Universität Hamburg
DER FORSCHUNG | DER LEHRE | DER BILDUNG

Fachbereich
Chemie

Development of heterogeneous and homogeneous metal oxide catalysts for green industrial processes

Cumulative Dissertation

with the aim of achieving a doctoral degree

Doctor rerum naturalium (Dr. rer. nat.)

at the Faculty of Mathematics, Informatics and Natural Sciences

Department of Chemistry

Institute of Technical and Macromolecular Chemistry

University of Hamburg

submitted by

Anne Wesner

Hamburg 2025

Biomass Catalysis Engineering

1. Evaluator Prof. Dr. Jakob Albert

Institute of Technical and Macromolecular Chemistry | Department of Chemistry

University of Hamburg

2. Evaluator Prof. Dr. Anders Riisager

Centre for Catalysis and Sustainable Chemistry | Department of Chemistry

Technical University of Denmark

1. Examiner Prof. Dr. Jakob Albert

Institute of Technical and Macromolecular Chemistry | Department of Chemistry

University of Hamburg

2. Examiner Prof. Dr. Lisa Vondung

Institute of Inorganic and Applied Chemistry | Department of Chemistry

University of Hamburg

3. Examiner Prof. Dr. Markus Fischer

Director of the Hamburg School of Food Science and of the Institute for Food Chemistry

University of Hamburg

Date of Disputation 28.11.2025

This study was conducted between January 2021 and December 2023 at the Institute of Technical and Macromolecular Chemistry of the University of Hamburg under the supervision of Prof. Dr.-Ing. habil. Jakob Albert.

The most effective way to do it, is to do it.

– *Amelia Earhart*

List of publications

Parts of this work and other studies have already been published in the following journals or presented as contributions at conferences.

Journals

- A. Wesner, N. Herrmann, L. Prawitt, A. Ortmann, J. Albert, M. J. Poller, Study of supported heteropolyacid catalysts for one step DME synthesis from CO_2 and H_2, *RSC Advances*, **2025**, *15*, pp. 38 - 47.
- A. Wesner, J.-C. Raabe, M. J. Poller, S. Meier, A. Riisager, J. Albert, Conversion of Sugars to Lactic Acid using Homogeneous Niobium-Substituted Polyoxometalate Catalysts, *Chem. Eur. J.*, **2024**, e202402649.
- A. Wesner, M. P. Papajewski, L. Schidowski, C. Ruhmlieb, M. J. Poller, J. Albert, Supported $H_8PV_5Mo_7O_{40}$ on activated carbon: Synthesis and Investigation of influencing factors for catalytic performance, *Daltons Trans.*, **2024**, *53*, pp. 14065-14076.
- A. Wesner, P. Kampe, N. Herrmann, S. Eller, C. Ruhmlieb, J. Albert, Indium-based Catalysts for CO_2 Hydrogenation to Methanol: Key aspects for Catalytic Performance, *ChemChatChem*, **2023**, *15*, e202301125.
- P. Kampe, N. Herrmann, A. Wesner, C. Ruhmlieb, J. Albert, Catalyst and Parameter Optimization Study for Slurry-Phase Methanol Synthesis Using Ni-Doped Indium-Based Catalysts, *ACS Sustainable Chem. Eng.,* **2023**, *11*, 14633 - 14644.
- P. Kampe, A. Wesner, P. Schühle, F. Hess, J. Albert, Effect of Conversion, Temperature and Feed Ratio on $In_2O_3/In(OH)_3$ Phase Transitions in Methanol Synthesis Catalysts: A Combined Experimental and Computational Study, *ChemPlusChem*, **2023**, *88*, e202300425.
- M. Sherbi, A. Wesner, V. Wisniewski, A. Bukowski, H. Velichkova, B. Fiedler, J. Albert, Superior CNT-supported bimetallic RuCu catalyst for the highly selective hydrogenolysis of glycerol to 1,2-propanediol, *Catal. Sci. Technol.*, **2021**, *11*, 6649 - 6653.

Conferences

- A. Wesner, P. Kampe, J. Albert, Indium-based Catalysts for CO_2 Hydrogenation to Methanol, *55. Jahrestreffen Deutscher Katalytiker*, **2022**, Weimar, Germany.
- A. Wesner, P. Kampe, J. Albert, CO_2 hydrogenation to methanol with Indium-based catalyst in a fixed bed reactor, *NaWuReT-YounGeCatS-Summerschool*, **2022**, Ulm, Germany.

Table of Content

List of Abbreviations and Symbols

Abbreviation	Meaning
AA	Alfa Aesar (ZrO2 from Alfa Aesar)
AC	Activated carbon
CMR	Carcinogenic, mutagenic and toxic to reproduction
CP	Co-precipitation
CR	Chemical reduction
DHA	Dihydroxyacetone
DKB-G	Norit Darco KBG
DME	Dimethyl ether
e.g.	For example (latin: exempli gratia)
et al.	And other (latin: et alia)
eq.	Equation
FA	Formic acid
GC	Gas chromatography
HPA	Heteropoly anion, heteropoly acid
HPLC	High-performance liquid chromatography
HSQC	Heteronuclear Single Quantum Coherence
ICP-OES	Inductively coupled plasma optical emission spectroscopy
IL	Ionic liquid
IPA	Isopoly anion
IR spectroscopy	Infrared spectroscopy
K10	Montmorillonit K10
LA	Lactic Acid
LPG	Liquid petroleum gas
M	Martin (synthetic procedure after Martin)
MCM-41	Mobil Composition of Matter No. 41
MeOH	Methanol
MOF	Metal organic framework
m-ZrO_2	Monoclinic ZrO_2
NASEur	Norit A Supra Eur
NCASPF	Norit CASP F
NGSX	Norit GSX
NMR	Nuclear magnetic resonance
OxFA	Oxidative conversion of biomass to formic acid
pH	Potential of hydrogen
ppm	Parts per million
POM	Polyoxometalate
R	Residual group
RedOx	Reduction/oxidation
rpm	Rotations per minute
S	Schühle (synthetic procedure after Schühle)
SEM-EDX	Scanning electron microscopy with energy dispersive X-ray spectroscopy
SG	Saint Gobain (ZrO_2 from Saint Gobain)
SOx	Sulphur oxides
SWV	Square wave voltammetry
TGA	Thermogravimetric analysis
TPD	Temperature programmed desorption
TPR	Temperature programmed reduction
UNFCCC	United Nations Framework Convention on Climate Change

Abbreviation	Meaning
USD	United States Dollar
WI	Wet impregnation
XPS	X-ray photoelectron spectroscopy
XRD	X-ray diffraction
ZSM-5	Zeolite Socony Mobil-5

POM abbreviation	Chemical formula
HPA-4	$H_7[PV_4Mo_8O_{40}]$
HPA-5 (or HPVMo)	$H_8[PV_5Mo_7O_{40}]$
HPInMo	$H_6[PInMo_{11}O_{40}]$
HPW	$H_3[PW_{12}O_{40}]$
HPVMo (or HPA-5)	$H_8[PV_5Mo_7O_{40}]$
HSiMo	$H_4[SiMo_{12}O_{40}]$
HSiW	$H_4[SiW_{12}O_{40}]$
NaMo	$Na_3[PMo_{12}O_{40}]$
$NaNb_2$	$Na_5[PNb_2Mo_{10}O_{40}]$
$NaNb_3$	$Na_6[PNb_3Mo_9O_{40}]$
NaV_3	$Na_6[PV_3Mo_9O_{40}]$
NaV_2Nb	$Na_6[PV_2NbMo_9O_{40}]$
$NaVNb_2$	$Na_6[PVNb_2Mo_9O_{40}]$

Formula symbol	Meaning	Unit
ϑ	Temperature	°C
ν	Rotational frequency	rpm
ρ	Volume fraction	vol.%
ω	Weight fraction	wt.%
m	Mass	kg (or g, Da)
n	Amount of substance	mol
P_{mass}	Productivity (based on mass of catalyst)	$g_{DME} \cdot g_{cat}^{-1} \cdot h^{-1}$
P_{mol}	Productivity (based on molar amount of active phase)	$mol_{DME} \cdot mol_{HPA}^{-1} \cdot h^{-1}$
$t_{reaction}$	Reaction time	h
V	volume	L
Yield	Y	%

1. Zusammenfassung

Katalysatoren sind nicht nur für die chemische und die Pharmaindustrie, sondern auch für die Herstellung von alltäglichen Produkten von essentieller Bedeutung. So durchlaufen rund 90 % aller weltweit hergestellten Produkte während ihrer Herstellung mindestens einen katalytischen Schritt. Der globale Katalysatormarkt wurde im Jahr 2020 auf 35,5 Milliarden US-Dollar geschätzt, rund ein Viertel des weltweiten Bruttosozialproduktes wird indirekt oder direkt über katalytische Prozesse erwirtschaftet. Bereits heute leisten Katalysatoren einen unverzichtbaren Beitrag zum Klima- und Umweltschutz - zwei der drängendsten Herausforderungen der gegenwärtigen Zeit. Für eine effiziente Nutzung bestehender fossiler Ressourcen, sowie für die Entwicklung neuer Prozesse zur Umsetzung nachhaltiger Rohstoffe ist die Forschung an leistungsfähigen Katalysatoren unabdingbar.[1,2]

In dieser Dissertation wird die Synthese, Charakterisierung und Anwendung von Metalloxid-Katalysatoren für die Umwandlung von Biomasse und CO_2 in wertvolle Plattformchemikalien untersucht. Kapitel 3 und 4 geben einen Überblick über die Herausforderungen im Bereich Klima und Energie, die eingesetzten Substrate (Biomasse und CO_2) und die Zielprodukte: Milchsäure, Ameisensäure, Dimethylether und Methanol. Darüber hinaus werden die in dieser Arbeit verwendeten Katalysatortypen, wie Polyoxometallate (POMs) sowie Katalysatoren auf Indium- und Kupferbasis, vorgestellt. Im kumulativen Teil (Kapitel 5) werden die verschiedenen Publikationen und deren Ergebnisse im Detail beschrieben. Dieser Teil gliedert sich in vier Studien, die jeweils spezifische katalytische Herausforderungen und Anwendungen thematisieren.

In der ersten Studie wurde die chemokatalytische Synthese von Milchsäure aus Biomasse mittels POMs untersucht. Der Fokus lag dabei auf dem Einfluss der sukzessiven Modifikation eines POMs durch Substitution der Gerüstmetalle mit Vanadium und Niob auf die katalytische Aktivität. Dabei diente das unsubstituierte POM $Na_3[PMo_{12}O_{40}]$ als Referenzkatalysator. Die Umwandlung von Dihydroxyaceton und verschiedenen Zuckern zu Milchsäure fand homogen katalysiert in Flüssigphase statt. Die höchste Aktivität beim Katalysatorscreening mit Dihydroxyaceton zeigte das zweifach mit Niob substituierte POM $Na_5[PNb_2Mo_{10}O_{40}]$ mit einer Ausbeute von 21 % und einem Umsatz von 97 %. $Na_5[PNb_2Mo_{10}O_{40}]$ konnte erfolgreich für die Synthese von Milchsäure aus sowohl einfachen Zucker wie Glucose, Fructose, Xylose und Mannose als auch für komplexere Disacharide wie Saccharose und Cellobiose eingesetzt werden.

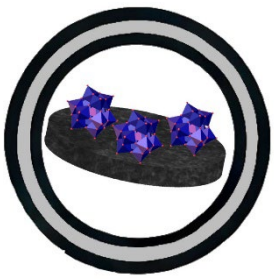

Die zweite Studie befasste sich mit der Heterogenisierung von Polyoxometallaten, am Beispiel der Trägerung von $H_8[PV_5Mo_7O_{40}]$ auf Aktivkohlen. Der Einfluss verschiedener physikalischer und chemischer Eigenschaften der Aktivkohlen als Trägermaterial, sowie die Auswirkungen unterschiedlicher Vor- und Nachbehandlungsmethoden von Aktivkohle auf die Trägerung von $H_8[PV_5Mo_7O_{40}]$ wurde untersucht. Die Katalysatoren wurden in Flüssigphasenreaktionen sowohl zur Umwandlung von Glucose in Ameisensäure unter O_2-Atmosphäre, als auch zu Milchsäure unter N_2-Atmosphäre getestet. Unter O_2-Atmosphäre zeigten die Katalysatoren eine hohe katalytische Aktivität mit Umsätzen von 68 - 78 % und Ausbeuten an Ameisensäure von 31 – 34 %. Jedoch waren die geträgerten Katalysatoren unter oxidativen Bedingungen nicht stabil, es kam zu hohem Leaching der aktiven Vanadiumspezies von über 68 %. Bei der Synthese von Milchsäure aus Glucose unter N_2-Atmosphäre zeigten sich vergleichbare Glucose-Umsätze von 65 - 71 %, sowie Ausbeuten an Milchsäure von durchgängig über 6 %. Das Leaching an aktiven Vanadiumspezies konnte deutlich reduziert werden auf unter 22 %.

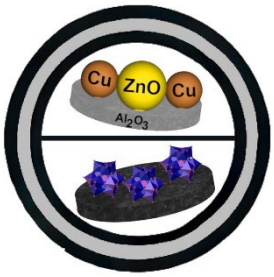

In der dritten Studie wurde die Direktsynthese von Dimethylether aus CO_2 in der Gasphase unter Einsatz heterogenisierter POMs untersucht. Für die Immobilisierung der Polyoxometallate wurden unterschiedliche Trägermaterialien wie Montmorillonit K10, Al_2O_3, ZrO_2, TiO_2 und Celite® 545 ausgewählt. Es wurden sowohl handelsübliche, unsubstituierte als auch erstmalig speziell entwickelte Übergangsmetall-substituierte POMs in einem bifunktionellen Katalysatorsystem zusammen mit dem kommerziellen Methanolsynthesekatalysator $Cu/ZnO/Al_2O_3$ zur Synthese von Dimethylether eingesetzt. Alle Katalysatorsysteme erwiesen sich als aktiv in der Dimethylether-Synthese, mit Ausbeuten an Dimethylether von 4 - 7 %. $H_4SiW_{12}O_{40}$ geträgert auf ZrO_2 zeigte die höchste katalytische Aktivität mit einer Dimethylether-Ausbeute von 7 %, was 54 % des erreichbaren thermodynamischen Gleichgewichts unter gegeben Reaktionsbedingungen entspricht. Auch bei wiederholtem Einsatz war der Katalysator chemisch und thermisch stabil.

Die vierte Studie befasste sich mit der Verbesserung des Methanolsynthesekatalysators für die Hydrierung von CO_2 zu Methanol. Dabei wurde In_2O_3/ZrO_2 als innovative Alternative zum etablierten kommerziellen Methanolsynthesekatalysator $Cu/ZnO/Al_2O_3$ eingesetzt. Es wurde der Einfluss von ZrO_2 als Trägermaterial für In_2O_3 und verschiedene Synthesemethoden zur Trägerung von In_2O_3 auf ZrO_2 untersucht. Zusätzlich wurde der Katalysator mit verschiedenen Metalloxiden, darunter CuO, CeO_2, MgO und NiO, dotiert, wobei das mit NiO modifizierte System die höchste Aktivität zeigte. Unter milden Reaktionsbedingungen konnte eine Methanolproduktivität von 0,221 g $MeOH \cdot g_{cat}^{-1} \cdot h^{-1}$ sowie ein CO_2-Umsatz von 5,7 % erzielt werden. Damit wurde die katalytische Performance des in der Literatur beschriebenen In_2O_3/ZrO_2-Vergleichskatalysators übertroffen. Zudem war der Katalysator in einen Langzeittest über 100 Stunden bei gleichbleibender Aktivität stabil.

Diese Studien verdeutlichen das Potenzial von Metalloxid-Katalysatoren zur effizienten und nachhaltigen Umwandlung erneuerbarer Ressourcen wie Biomasse und CO_2. Es konnte gezeigt werden, wie spezifische Modifikationen - etwa Heterogenisierung, Trägerwahl und Dotierung mit zusätzlichen Metallen - die katalytische Aktivität in einer Vielzahl von Anwendungen verbessern beziehungsweise ermöglichen können. Diese Erkenntnisse bieten wichtige Grundlagen für die Integration erneuerbarer Kohlenstoffquellen in industrielle Prozesse und bilden eine Brücke zwischen innovativem Katalysatordesign und praxisnahen, umweltfreundlichen Anwendungen.

2. Abstract

Catalysts are not only crucial for the chemical industry but also play a critical role in the pharmaceutical industry and the production of everyday goods. Over 90 % of all products manufactured globally undergo at least one catalytic step during their production. In 2020, the global catalyst market was valued at USD 35.5 billion, and it is projected to grow to USD 57.5 billion by 2030. Approximately one-quarter of the global gross domestic product is generated, either directly or indirectly, through catalytic processes. Catalysts already make an indispensable contribution to climate and environmental protection - two of the most pressing challenges of our time. To drive the development of new processes for the economic and ecological conversion of sustainable raw materials into valuable chemicals, research into highly effective catalysts is essential.[1,2]

This dissertation examines the synthesis, characterization, and application of metal oxide catalysts for converting biomass and CO_2 into valuable platform chemicals. The aim was to enhance catalytic reactivity and explore new catalytic applications. Chapters 3 and 4 cover the background on climate and energy challenges, the substrates (biomass and CO_2), and the target products, including lactic acid, formic acid, dimethyl ether, and methanol, alongside the catalyst classes of polyoxometalates (POMs) and In- and Cu-based metal catalysts. In the cumulative part (chapter 6), each experimental approach and outcome is discussed in detail. The cumulative part contains four studies, each addressing a distinct catalytic challenge and application. Collectively, the studies highlight the versatility of catalytic systems in transforming biomass and CO_2 into valuable products.

In the first study, the chemocatalytic synthesis of lactic acid from biomass using polyoxometalates was investigated. The focus layed on the impact of the successive modification of a POM trough substitution of scaffolding metals with V and Nb on the catalytic activity. The unsubstituted $Na_3[PMo_{12}O_{40}]$ served as the base catalyst. The conversion of dihydroxyacetone and various sugars to lactic acid was performed under homogeneous conditions in liquid phase. Among the tested catalysts, the two-times niobium-substituted POM $Na_5[PNb_2Mo_{10}O_{40}]$ proved to be the most active catalyst for the conversion of dihydroxyacetone, reaching a conversion of 97 % and a corresponding yield of 21 %. $Na_5[PNb_2Mo_{10}O_{40}]$ was also successfully applied for the synthesis of lactic acid from simple sugars such as, glucose, fructose, xylose, and mannose, as well as more complex disaccharides like sucrose and cellobiose.

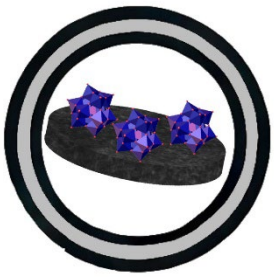

The second study addressed the heterogenization of polyoxometalates, specifically evaluating the immobilization of V-substituted $H_8[PV_5Mo_7O_{40}]$ on activated carbon. The influence of various physical and chemical properties of the activated carbon support, as well as the effects of different pre- and post-treatment methods on the successful immobilization of $H_8[PV_5Mo_7O_{40}]$, were investigated. The catalysts were tested in two applications: In liquid phase: for the conversion of biomass to formic acid under oxygen atmosphere, and the conversion of biomass to lactic acid under inert nitrogen atmosphere. Therefore, glucose was used as model compound for biomass. Under oxidative conditions, the catalysts demonstrated high catalytic activity with glucose conversion rates of 68 % to 78 % and formic acid yields of 31 % to 34 %. However, catalyst stability was limited by substantial leaching of the active vanadium species, exceeding 68 %, due to the harsh oxidative conditions. In contrast, under inert conditions, the conversion of glucose to lactic acid showed comparable conversion rates of 65 – 71 % and consistently yielded over 6 % LA. Importantly, vanadium leaching was substantially reduced to below 22 %.

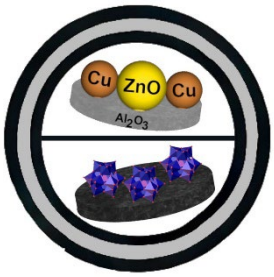

The third study explored the direct synthesis of dimethyl ether from CO_2 in the gas phase using heterogenized polyoxometalates. Various support materials, including *Montmorillonite K10*, Al_2O_3, ZrO_2, TiO_2, and *Celite® 545*, were tested for their suitability for the immobilization of POMs in catalytic applications. Both commercially available, unsubstituted POMs and custom-designed POMs were utilized in a bifunctional catalytic system alongside the commercial methanol synthesis catalyst $Cu/ZnO/Al_2O_3$. All tested catalyst systems proved to be active for dimethyl ether synthesis, achieving yields between 4 to 7 %. $H_4SiW_{12}O_{40}$ supported on ZrO_2 exhibiting the highest activity with yield of dimethyl ether of 7 %, reaching 54 % of the thermodynamic equilibrium yield under the applied conditions. Additionally, the catalyst showed as chemical and thermal stability in multiple runs.

In the fourth study, efforts were focused on improving the methanol synthesis catalyst for CO_2 hydrogenation by examining In_2O_3/ZrO_2 as a promising alternative to the conventional $Cu/ZnO/Al_2O_3$ catalyst. The influence of ZrO_2 as a support material and the effect of different methods for In_2O_3 deposition were evaluated. Additionally, metal oxides including CuO, CeO_2, MgO, and NiO were incorporated into the catalyst, with the NiO-modified system demonstrating the highest catalytic activity. Under mild reaction conditions, a methanol productivity of 0.221 $g_{MeOH} \cdot g_{cat}^{-1} \cdot h^{-1}$ and CO_2 conversion of 5.7 % was achieved, outperforming literature-reported In_2O_3/ZrO_2 system (0.159 $g_{MeOH} \cdot g_{cat}^{-1} \cdot h^{-1}$ and 4.4 %). Moreover, the catalyst exhibited long-term stability with consistent catalytic performance over 100 hours time-on-stream.

The collective insights from these studies underscore the immense potential of metal oxide catalysts in the efficient and sustainable conversion of renewable resources like biomass and CO_2. The results illustrate how specific modifications - such as heterogenization, support selection, and metal doping - can enhance catalytic performance across a range of applications. Looking ahead, these findings serve as a crucial step towards integrating renewable carbon sources in industrial-scale processes, bridging the gap between innovative catalyst design and practical, environmentally-friendly applications.

3. Introduction

Environmental risks, including extreme weather events, biodiversity loss, or natural resource shortages, represent some of the most pressing global challenges. These developments are direct consequences of the climate change, driven by anthropogenic greenhouse gas emissions. Data confirms that the average global surface temperature between 2011 and 2020 was 1.1 °C above the baseline level recorded from 1850 to 1900. The main contributor to this temperature increase is the combustion of fossil fuels, accounting for approximately 85 % of global greenhouse gas emissions in 2023. This has led to atmospheric CO_2 concentrations at their highest in two million years, increasing from 280 ppm in 1800 to 418 ppm in 2022. The impacts of human-induced climate change are already observable in the form of increasingly frequent and severe temperature and weather extremes.[3–5]

International environmental policy efforts began with the 1972 United Nations Conference on the Human Environment in Stockholm, widely regarded as the first global milestone in environmental protection. This was followed by the 1992 Earth Summit in Rio de Janeiro, where the United Nations Framework Convention on Climate Change (UNFCCC) was adopted, now signed by nearly every country worldwide. The UNFCCC's primary goal is to stabilize greenhouse gas emissions to prevent dangerous climate system interference. These international efforts culminated in the 2015 Paris Agreement, which established the ambitious target of limiting global warming to below 2 °C, and ideally to 1.5 °C. The European Union has also committed to this goal, aiming for climate neutrality by 2050, as established in the 2021 European Climate Law. Achieving this requires rapid and comprehensive greenhouse gas reduction. Germany has implemented this objective through its national Climate Change Act, which stipulates a reduction of greenhouse gas emissions by at least 65 % by 2030 and 88 % by 2040 compared to 1990 levels. Climate neutrality is to be achieved by 2045.[3,4,6]

Within this context, the chemical industry plays a crucial role. Accounting for 5 % of Germany's total greenhouse gas emissions (as of 2023), it remains one of the largest emission sources. Each year, the chemical industry produces around 24 million tons of materials largely derived from carbon-based chemicals, such as methanol or aromatic hydrocarbons. These compounds are primarily extracted from refinery products like naphtha, liquefied gas, and gas oil, as shown in Figure 1. To meet climate challenges and achieve net-zero emissions, the chemical industry is pursuing innovative strategies, including the electrification and flexibility of processes, the establishment of a circular economy, and the replacement of fossil-based raw materials with more sustainable, alternative sources.[7–9]

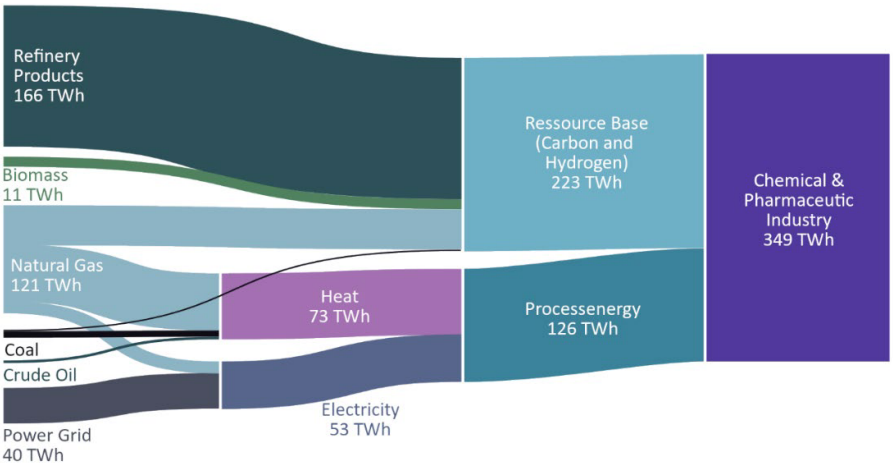

Figure 1: Resource and energy consumption in the German chemical-pharmaceutical industry (2019): Overview of the main raw materials and process energy sources, based on calorific value (heating value). Refinery products allocated to other sectors are not included. Adapted from *Münnich et al.*[7]

Annually, the chemical industry requires approximately 11 million tons of carbon to meet its production demands in Germany alone. Despite continuous efforts to implement circular economy strategies and improve recycling rates, a completely closed-loop carbon cycle remains unattainable. Consequently, the identification and utilization of alternative carbon sources are not only necessary but represent a strategic cornerstone for the long-term transformation of the chemical sector (Figure 2). Beyond the environmental advantages, such as minimizing greenhouse gas emissions, economic considerations are also increasingly relevant due to the limited availability of fossil resources. In this context, renewable carbon sources such as biomass and CO_2 offer promising alternatives. Biomass, derived from e.g. agricultural or forestry residues, offers the main advantage of being renewable. Meanwhile, CO_2, often regarded solely as a waste product, can be valorized as a raw material, transforming a significant emission source into a valuable feedstock for the chemical industry. [7–10]

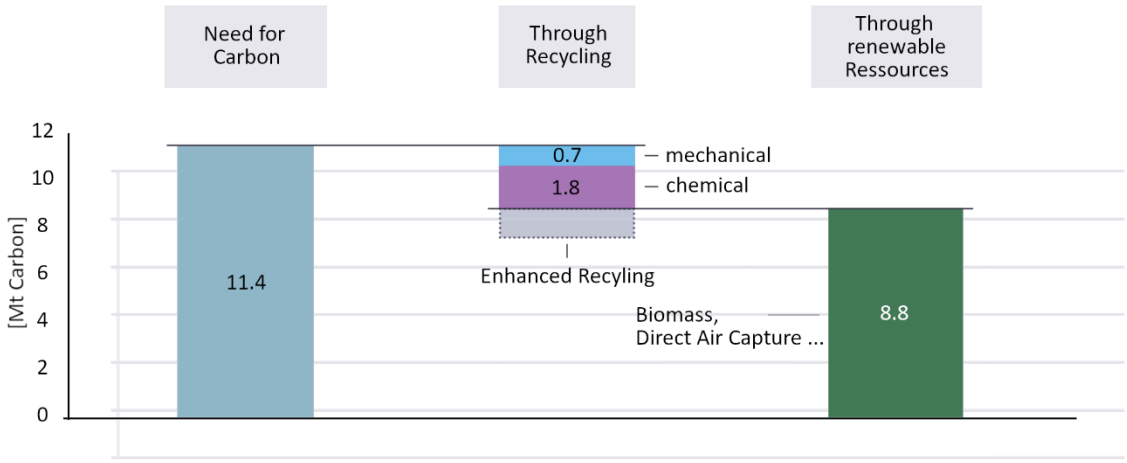

Figure 2: Estimated renewable carbon demand in the German chemical industry. Estimated recycling potential with 35 % for mechanical and 40 % for chemical recycling of post-consumer waste. Adapted from *Münnich et al.*[7]

Catalysis plays an indispensable and enabling role in most chemical processes, making it fundamental to advancing a more sustainable and environmentally friendly future. Its ability to accelerate chemical reactions as well as improve efficiency plays a critical factor in the resource and energy intensive chemical sector. For fossil-based processes, continuous catalyst optimization remains crucial to enhance resource efficiency, lower energy requirements, and reduce the formation of undesired by-products. Meanwhile, the development of innovative catalysts is crucial to enable a bio-based circular economy. This involves not only converting unavoidable waste but also tapping into new resources. The complexity associated with using CO_2 or biomass as renewable carbon sources demands extensive research and innovative catalytic approaches, as these processes are considerably more intricate than traditional fossil-based processes. Biomass, for example, comprises a broad range of biologically derived materials with highly diverse compositions and structures, requiring specific and adaptable catalytic systems for selective transformation. Likewise, the high thermodynamic stability of CO_2 demands advanced catalytic systems to facilitate its activation and conversion into value-added products. Overcoming these challenges and developing catalytic solutions for these challenges is a crucial step toward replacing fossil resources and supporting the chemical industry in moving toward a circular and more sustainable future.[2,11–13]

4. Theoretical Background

The theoretical section of this dissertation provides a comprehensive overview of the three key areas central to this dissertation. First, it examines the substrates utilized - CO_2 and biomass - focusing on their availability, sourcing methods, and potential roles within a sustainable economy. Their roles as alternative carbon sources are explored, highlighting their potential to decrease dependency on fossil-based feedstocks and their capacity to contribute to a circular carbon economy. Second, the discussion focuses on the target products of this thesis: lactic acid, formic acid, methanol, and dimethyl ether. Their industrial applications, economic significance, and conventional production methods are analyzed, providing a comprehensive understanding of their roles as platform chemicals in modern and sustainable chemical processes. The third focus is on the catalytic systems themselves, exploring the mechanisms and properties of the catalysts applied in this study. This includes insights into their activity, stability, and structural features that enable transformations of renewable carbon sources.

4.1 Biomass and CO_2 as Sustainable Resources

Renewable carbon includes all carbon sources that replace or circumvent the use of extra fossil carbon derived from the geosphere, thus preventing an escalation in atmospheric CO_2 concentrations. This encompasses carbon from three main sources: the biosphere, technosphere, and atmosphere. From the biosphere, renewable carbon is derived from various forms of biomass, including food crops and biogenic waste. In the technosphere and atmosphere, renewable carbon is sourced directly from CO_2 utilization through *Carbon Capture and Utilization*, which can involve carbon from both fossil-based and biogenic origins. Additionally, the technosphere supports the recycling of existing plastics and organic chemicals through various methods including mechanical, chemical, and enzymatic processes.[10] In the following chapter, the content focus on biomass and direct CO_2 utilization as alternative carbon sources, emphasizing their crucial role in decreasing dependence on fossil fuels.

4.1.1 Biomass

Biomass encompasses all carbon-containing compounds derived from biogenic sources As a renewable resource, it offers several advantages: it's versatile, easily storable, transportable, and largely considered CO_2-neutral. Notably, biomass is used for the production of biogas, such as methane, and liquid biofuels, including biodiesel and ethanol. In addition to its use as a carbon source, biomass is also utilized as an energy source, with energy generated from its combustion. In 2021, biomass contributed 9.7 % to Germany's primary energy supply, the largest share within the renewable energy sector. The total biomass on earth, estimated to contain about 550 gigatons of carbon, is predominantly composed of plant matter, which accounts for roughly 80 % of the total biomass. Bacterial biomass follows at approximately 15 %, while fungi, archaea, protists, animals, and viruses collectively contribute less than 10 %. This emphasizes the pivotal role of plant biomass not only in the in the earth's carbon cycle but also as a critical renewable carbon source for sustainable development.[12,14,15]

Within plant biomass, carbohydrates constitute roughly about two-thirds of the total composition, alongside other components such as lignin (approximately 20 %) and smaller fractions (approximately 5 %) comprising fats, proteins, terpenoids, alkaloids, and nucleic acids (Figure 3).[12,14–16] Carbohydrates are an essential component of human nutrition, being the main constituents of fruits, legumes or cereals.[9,17] Given their abundant availability, carbohydrates have become increasingly important as a sustainable resource for industrial applications, including the production of bio-based materials and chemicals.[15,18–22]

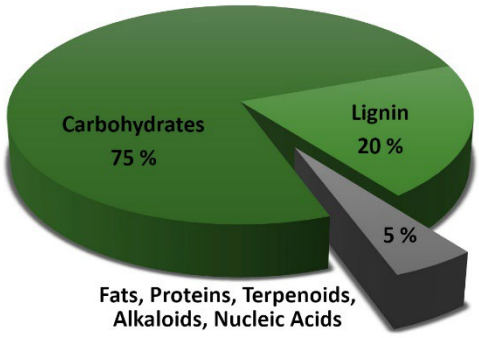

Figure 3: Composition of plant biomass. Adapted from *Lichtenthaler et al.*[9]

In this context, the *food vs. fuel* debate is particularly significant, addressing the competition between biomass utilization for food production versus biofuels. Critics argue that dedicating farmland to energy crops could decrease food availability and drive up global food prices. This issue peaked during the 2007/2008 food crisis, when rising food prices were attributed to increased bioenergy demand in Europe and the U.S. However, the causes of this crisis remain a topic of debate, with other factors such as increasing world population, rising global meat consumption or bad harvests also playing significant roles. As of 2016, 82 % of biomass in Germany was used for food and feed, while 14 % of agricultural land was dedicated to energy crops Figure 4), contributing only 8 % on Germany´s primary energy supply. An additional 2 % was allocated to industrial crops, which provided only a minimal share of the economy's raw materials. With land resources already constrained, balancing competing demands is critical. The 2022 Russo-Ukrainian War reignited the debate, with the German Ministry of the Environment advocating a decline or halt in biofuel crop cultivation to address food shortages, while proponents emphasized the role of bioenergy in diminishing reliance on fossil fuel imports, reducing the reliance on fossil fuels and combating climate change. Addressing both of these challenges requires thoughtful and sustainable strategies. These include reducing the agricultural land dedicated to animal feed production, utilizing biogenic residues and waste such as food and green waste, or organic refuse, as well as enhancing the efficiency of land use through innovative concepts and advanced technologies.[16,23]

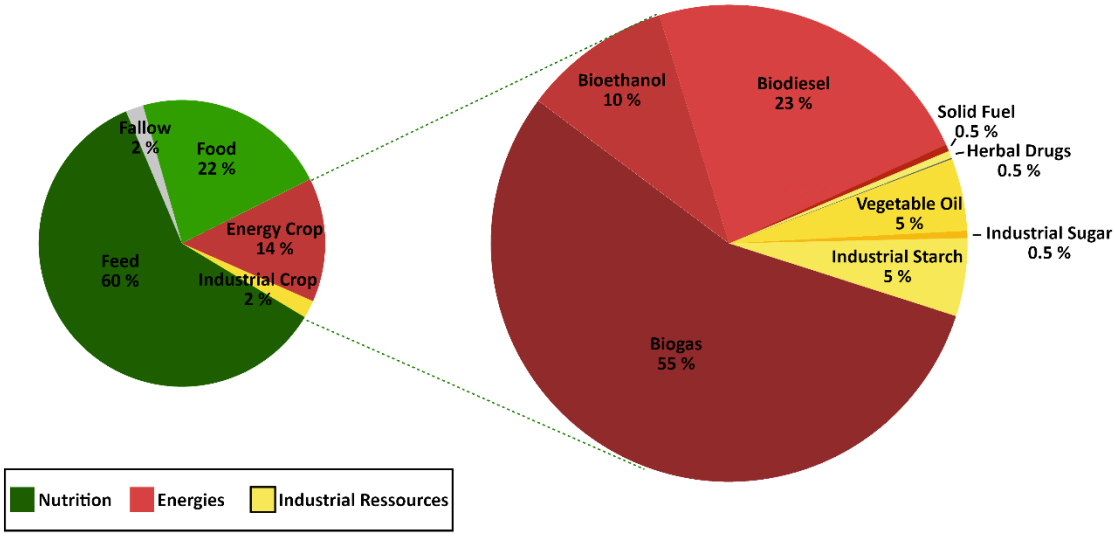

Figure 4: Distribution of agricultural land use in Germany (2016). Adapted from *Kircher et al.*[16]

Furthermore, optimizing biomass utilization is essential, with carbohydrate-containing biomass being particularly significant as it constitutes the largest share of biomass. Historically, carbohydrates were defined by the formula $C_n(OH_2)_n$, reflecting the origin of the term as *hydrates of carbon*. Nowadays, according to the *International Union of Pure and Applied Chemistry*, carbohydrates encompass not only monosaccharides, oligosaccharides, and polysaccharides but also derivatives formed through chemical modifications. These include carbonyl reduction to alditols, oxidation to carboxylic acids, or substitution of hydroxyl groups with functional groups such as hydrogen, amino, or thiol groups.[24]

Carbohydrate-containing biomass can be classified into three distinct classes according to its structural complexity and the nature and amount of its carbohydrate components: sugar-rich biomass, starch-rich biomass, and lignocellulosic biomass (Figure 5).[21,25,26]

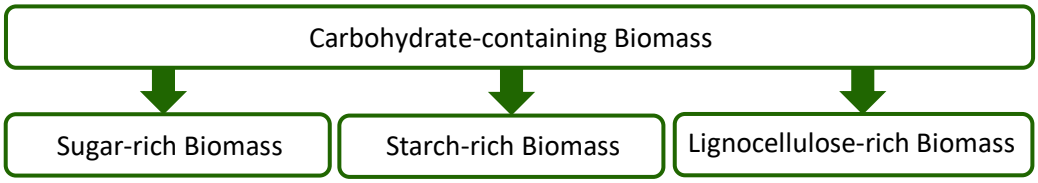

Figure 5: Classification of carbohydrate-based biomass.

The following subchapters will provide an overview of these categories.

Sucrose-rich Biomass

Sucrose (β-d-fructofuranosyl α-d-glucopyranoside), referred to as sugar in technical and legal terms, is the most prevalent disaccharide. It is composed of glucose and fructose units, represented by the formula $C_{12}H_{22}O_{11}$ (Figure 6). The two rings are arranged at a 90 ° angle to each other, the solid-state structure is stabilized by two hydrogen bonds linking the fructose and glucose units.[27–29]

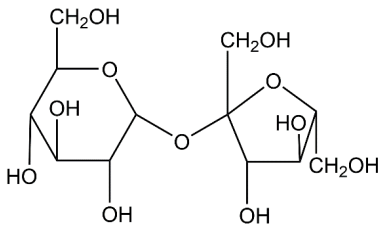

Figure 6: Structure of sucrose. Adapted from Schiweck.[27]

Sucrose is primarily known as sweetener in foods, with concentrations reaching up to 70 - 80 % in candies and 40 - 50 % in chocolates and jams. Approximately 72 % of sucrose is consumed by the sugar processing industry and craft trades, while the remaining 28 % is applied in fields such as the chemical industry. Sucrose esters are employed as emulsifiers and surfactants. Additionally, sucrose (and glucose) is utilized in fermentation for the production of complex antibiotics and vitamins that cannot be efficiently synthesized chemically, such as penicillin G, vitamin C, and spectinomycin.[9,27–29]

Sucrose is primarily obtained from sugar cane and sugar beet, grown largely in subtropical and tropical climates, with Brazil leading global production. Worldwide sugar production amounts to around 184 million tons per year, mainly sourced from Brazil, India, Thailand, and China.[28,30] The extraction

of sucrose is an extensive process that differs slightly between sugar beet and sugarcane. A schematic overview can be seen in Figure 7. For sugar beets, the process starts with washing after the harvesting and slicing the beets into thin strips, followed by extraction with water using a countercurrent system. The raw juice, containing 13 - 15 % sucrose, is purified by adding $CaCO_3$ and CO_2, for binding and precipitating unwanted impurities, such as proteins, pectins, amino acids, organic acids, and salts. The resulting thin juice is concentrated through evaporation, and crystallization is initiated by seeding with sucrose crystals, producing raw sugar. In the subsequent sugar refining process, raw sugar is dissolved in water, followed by purification and decolorization with activated carbon, diatomaceous earth, or specialized resins, yielding sucrose with 99.5 % purity. For sugarcane, processing begins with washing and shredding the harvested stalks. The cane fibers are mixed with water and pressed through rollers to extract raw juice, which contains 11 - 16 % sucrose. The raw juice is then clarified by heating and the addition of lime and flocculating agents, typically polyacrylamides. The remaining steps - concentration, crystallization, purification and refining - follow the same principles as for sugar beets.[31]

Figure 7: Schematic overview of the processing steps for sucrose-rich biomass. Adapted from Witzke.[25]

Starch-rich Biomass

Starch is a soft, white, tasteless, and odorless polymer synthesized and stored as an energy reserve in plant cells in the form of water-insoluble granules. As a primary energy source for various organisms, including fungi, bacteria, and animals, starch is composed of multiple glucose units. The simplest structure, amylose, consists of roughly 100 to 45,000 glucose units linked by α-1,4 glycoside bonds, forming a helical structure (Figure 8). Amylopectin, by contrast, has around 6,000 glucose units, with chains of 25 units linked by α-1,4 bonds, followed by branching via α-1,6 bonds (Figure 8). Plants typically exhibit an amylose-to-amylopectin ratio of about 4/1, with overall starch content varying by species. For instance, starch accounts for about 80 % of rice grain weight, 78 % of potatoes, and 68 % of wheat flour.[28,32,33] Around 61 % of starch is consumed in food, either directly (e.g. potatoes, cereals, corn, or cassava) or in processed products like bread and sweeteners. The remaining 39 % is used in non-food sectors, particularly in the paper industry for paper impregnation. Corn starch is also utilized in bioethanol production, while only 6 % of starch finds applications in the chemical industry, such as in fermentation processes, thermoplastic starch production, or bioethanol manufacturing.[28,33]

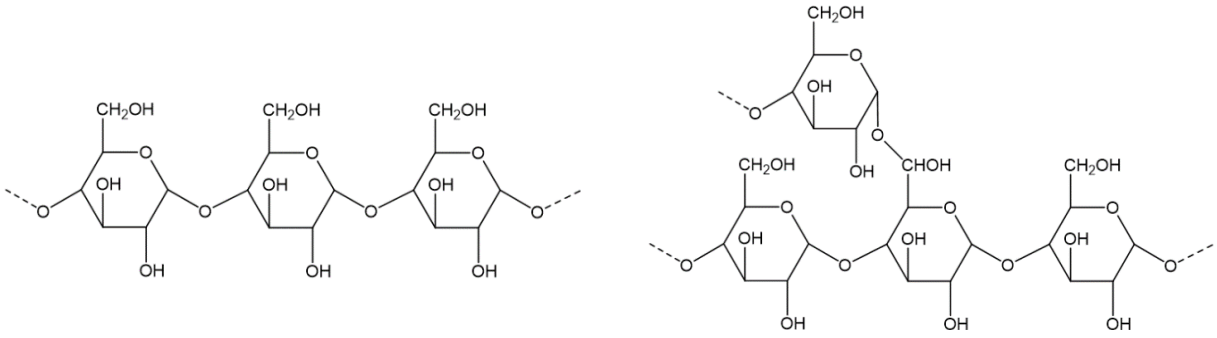

Figure 8: Structure of amylose (left) and amylopectin (right). Adapted from *Behr et al.*[28]

Approximately 135 million tons of starch are extracted worldwide each year, China being the largest producer.[34] Starch extraction (Figure 9) relies on the principle of wet milling, where plant cells are broken down, and the starch is released and washed out for separation. The complexity of wet milling process depends on the raw material. For corn, kernels are steeped in water to soften, then ground to separate starch from the oil-rich germ, fibers, and gluten. In potato processing, tubers are washed, shredded, and ground to rupture cell walls, releasing starch, which is then suspended in water and separated from fibers. For wheat, the grains are first milled and sieved, then mixed with water to form a dough-like mass, from which the starch is extracted. Regardless of the source, the extracted starch is then concentrated and dried for further processing. One significant application of starch is its conversion into sugar, wherefore industrial processes primarily use enzymatic hydrolysis. In the first step, α-amylases break down the starch into maltodextrins. Saccharification follows, where glucoamylases and pullulanases further convert maltodextrins into glucose. Finally, glucose can be partially isomerized into fructose using glucose isomerase.[28,35]

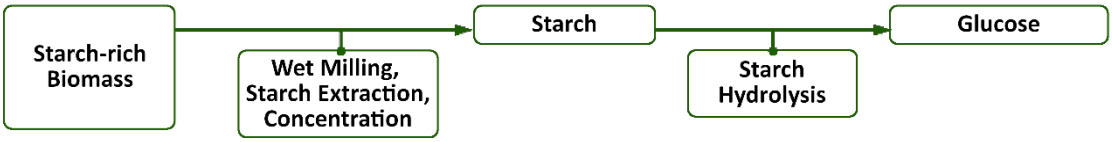

Figure 9: Schematic overview of the processing steps for starch-rich biomass. Adapted from Witzke.[25]

Lignocellulose-rich Biomass

Lignocellulosic biomass is the most abundant and economically viable renewable resource within plant biomass, providing a sustainable alternative to fossil fuels. This biomass forms the structural framework of plant cell walls, particularly in woody plants, and is mainly composed of the two polymeric carbohydrates cellulose (40 - 50 %) and hemicellulose (25 - 35 %) (Figure 10). It also includes a smaller fraction of the aromatic polymer lignin (15 - 20 %), a non-carbohydrate, and minor amounts of pectin, proteins, extractives, and ash.[19,36]

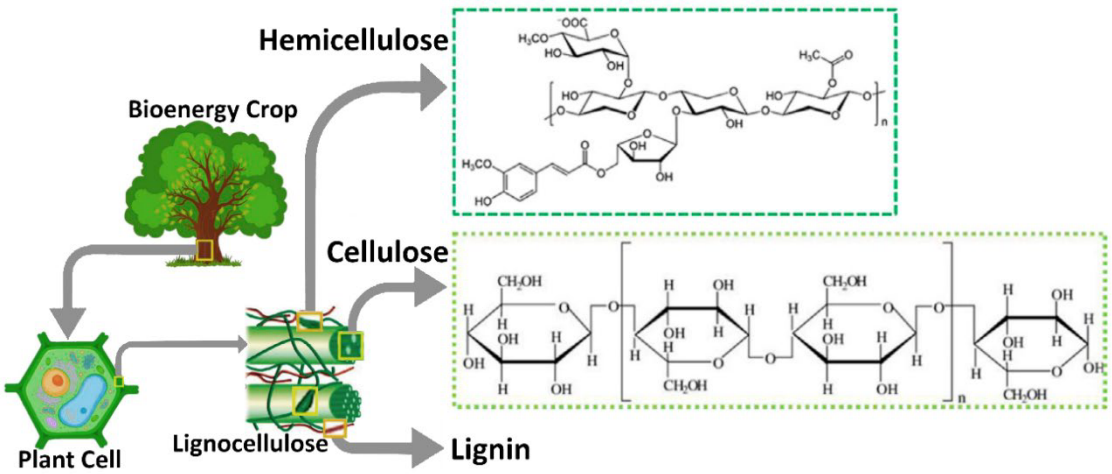

Figure 10: Composition of lignocellulosic biomass. Adapted from *Sankaran et al.*[37]

Cellulose, the most widely existing biopolymer in nature, is essential for the structural integrity of plant cell walls. It is found in plants like jute, flax, hemp, and particularly wood, constituting up to 50 %. Cellulose is also abundant in cotton seed hairs and grasses, contributing up to 30 % of their composition. Remarkably, this polymer is estimated to account for 40 - 50 % of all carbon present on earth.[19,38] Structurally, cellulose is a linear polysaccharide of 500 - 5000 D-glucose units, with molecular weights between 200,000 to 1 million Daltons. The glucose units are linked through β-1,4-glycosidic bonds, forming long polymer chains. These polymer chains cluster into fibrils, which are stabilized by hydrogen bonding and van der Waals interactions, thereby providing structural integrity to plants.[28,38,39] Cellulose is primarily used in pulp and paper production, with smaller quantities applied to produce regenerated cellulose fibers and various esters and ethers. Increasingly, cellulose is recognized as a sustainable feedstock for industrial applications, including the development of bio-based materials and chemicals.[15,18]

Hemicellulose is an integral component of plant cell walls, closely associated with cellulose and lignin, providing structural support and acting as scaffolds. Hemicelluloses form hydrogen bonds with cellulose, covalent bonds (primarily α-benzyl ether linkages) with lignin, and ester linkages with acetyl units and hydroxycinnamic acids. Hemicellulose is composed of polymeric hexosans and pentosans derived from a variety of monomers, such as glucose, mannose, galactose, rhamnose (hexosans), as well as arabinose and xylose (pentosans). The specific content and structure of hemicellulose vary depending on the plant type. For instance, hardwood and straw contain more xylans, while softwoods are rich in glucomannans.[19,20,22,38,40] The extraction of pure hemicellulose fractions on an industrial scale remains challenging. Current wood pulping processes often result in hemicellulose fractions that are contaminated with cellulose and lignin residues. This contamination limits hemicellulose utilization to *low-tech* sectors like energy, feed yeast, adhesives, and alcohol fermentation. Improved extraction and purification could unlock broader applications.[19,20,22]

In general, the deconstruction of lignocellulose-rich biomass (Figure 11) presents significant challenges, due to its dense structure and high lignin content, necessitating robust pretreatment processes. Pretreatment processes aim to disrupt the bonds between cellulose, hemicellulose, and lignin. Therefore, a variety of methods are employed, including physical processes (e.g. mechanical milling), physico-chemical approaches (e.g. Ammonia Fibre Explosion or Liquid Hot Water), chemical treatments (e.g. acids, bases, oxidizing agents, or organic solvents), or biological techniques utilizing fungi or microorganisms. These methods are often applied in combination, tailored to the specific properties of the raw material.[41] Following pretreatment, lignin, hemicellulose, and cellulose can be effectively separated for further processing. Enzymatic hydrolysis is then used to convert hemicellulose and cellulose into sugars. Cellulose hydrolysis is carried out by cellulases (e.g. endoglucanases, exoglucanases, and β-glucosidases), which sequentially cleave glycosidic bonds, yielding glucose monomers. Hemicellulose, due to its heterogeneous composition containing various monomers (e.g. xylans, mannans), requires a broader range of enzymes for effective hydrolysis. Industrially, xylanases (e.g. endoxylanases, β-xylosidases) are most commonly used to break down xylan chains, yielding xylose. Other sugars, such as mannose, galactose, or glucose, can be obtained by employing additional specific enzymes.[42]

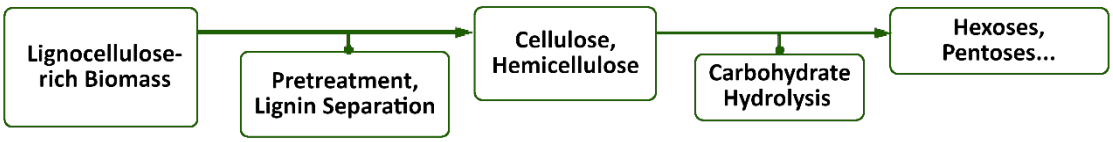

Figure 11: Schematic overview of the processing steps for lignocellulose-rich biomass. Adapted from Witzke.[25]

4.1.2 Carbon Dioxide

Carbon dioxide (CO_2) is a colorless, odorless, non-flammable gas that is soluble in water. At normal pressure, it sublimates at -78 °C from solid to gaseous state. It has a molecular weight of 44 Daltons and adopts a linear molecular structure, where carbon and oxygen are connected by both σ- and π-bonds with a bond length of 116.32 pm (Figure 12). These bonds exhibit polarization due to the disparate electronegativities of carbon and oxygen. Despite this polarity, the molecule lacks an overall electric dipole moment owing to its symmetric molecular arrangement (point group: D∞h). The chemical reactivity of CO_2 is strongly influenced by this bond polarization, primarily interacting with nucleophiles targeting the central carbon atom. These include neutral species with lone pairs (e.g. amines), electron-rich π-bonds (e.g. phenolates), and carbon-metal–σ-bonds (e.g. Grignard reagents). Moreover, CO_2 can coordinate with metals, altering its electron distribution and molecular geometry, thereby modifying its chemical reactivity.[13,43,44]

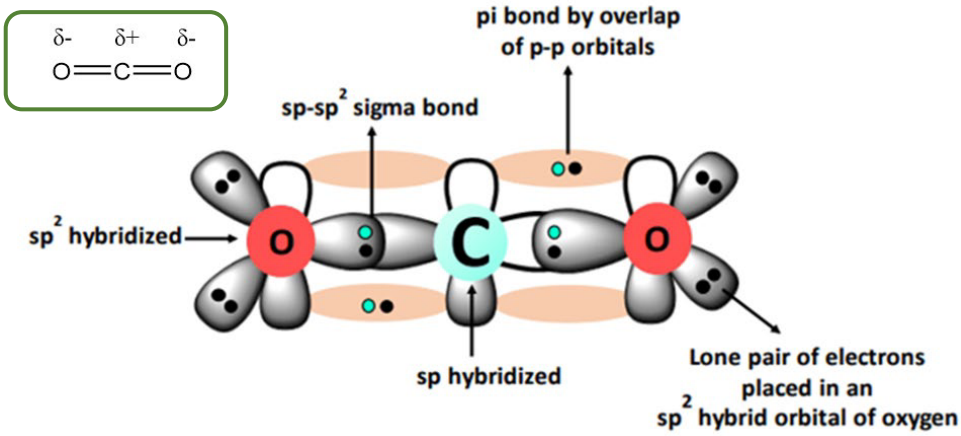

Figure 12: Structure of CO_2 and its hybridization. Adapted from Goyal.[45]

CO_2 is a natural component of Earth's atmosphere, alongside nitrogen and oxygen. Despite its relatively low concentration of about 0.038 %, it ranks among the most impactful greenhouse gases. CO_2 does not degrade on its own but is either physically stored in aquatic systems or converted into biomass through plant photosynthesis. Natural sources of CO_2 include volcanic emissions, as well as biological processes, such as animal and human respiration and the natural decomposition of organic material. Industrially, CO_2 has numerous applications, particularly in the food, pharmaceutical, and chemical industries, where it is used as a solvent in extraction and cleaning processes, as well as a refrigerant. Since the 1990s, CO_2 has increasingly become a focus of research, especially regarding its role in enhancing the greenhouse effect. Technologies for CO_2 capture and storage are gaining importance, both for mitigating climate impacts and for exploring CO_2 as a potential resource and sustainable alternative to fossil resources.[13,43,44,46,47]

Potential CO_2 sources for valorization include both atmospheric CO_2 and CO_2 point sources. Atmospheric CO_2, although abundant, its low concentration presents significant challenges for effective capture. Alternatively, point sources offer a more feasible solution for CO_2 utilization. These point sources can originate from biogenic processes, such as biofuel production (e.g. biogas or bioethanol) or the pulp and paper industry. An advantage of using CO_2 over biomass is the carbon uniformity it provides. Biomass, being heterogeneous and challenging to process, can be gasified to produce a uniform carbon source, yielding CO_2 and syngas. This method enables the effective use of

biogenic waste from industrial processes, households, and agricultural residues without competing with food production. Other major point sources of CO_2 include emissions from industrial processes such as iron and steel production, cement manufacturing, or other chemical processes (e.g. ethylene oxide or ammonia production). CO_2 emissions can be further categorized into energy-related emissions from power generation (e.g. biomass or waste combustion) and process-related emissions, directly resulting from production processes (e.g. iron and steel processing). The current amount of major CO_2 point sources in Germany, Europe, and worldwide is illustrated in Figure 13.[13,43,46,48,49]

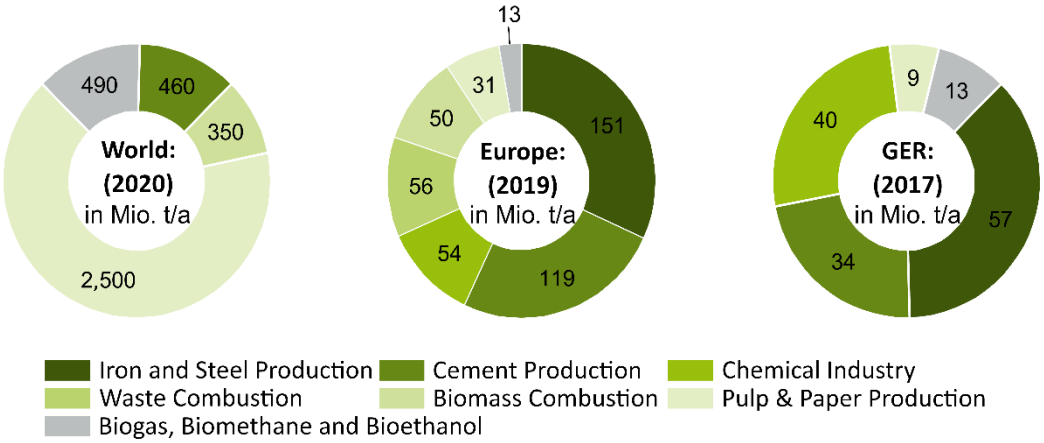

Figure 13: Major CO_2 point sources worldwide, in Europe and Germany. Adapted from *Schröder et al.*[48]

Depending on the CO_2 source, different capture processes are employed, including Pre-Combustion, Oxy-fuel Combustion, and Post-Combustion and Direct Air Capture (Figure 14).

Direct Air Capture captures CO_2 directly from ambient air by passing it through filters using large fans, where the CO_2 is captured and separated. Although Direct Air Capture is currently limited by high costs and significant energy requirements, it offers significant advantages, such as scalability, minimal land requirements, and high location flexibility. Facilities can be strategically placed in areas with abundant renewable energy, including hydrogen, allowing adaptation to regional conditions.[50,51]

CO_2 capture technologies for biogenic and industrial point sources are divided into Pre-Combustion, Oxy-fuel Combustion, and Post-Combustion. Pre-Combustion capture removes CO_2 before fossil fuel combustion by gasifying fuels like coal with steam and oxygen at elevated temperatures to produce syngas, composed mainly of CO and H_2. This syngas undergoes a subsequent water-gas shift reaction, converting CO into CO_2 and water, with CO_2 separated from the steam. Oxy-fuel Combustion, particularly suited for coal power plants, involves burning the fossil fuel in nearly pure oxygen (95 - 99 %) at elevated temperatures. The exhaust's water vapor is condensed, yielding CO_2 of high purity (around 90 %) without further processing. Post-Combustion carbon capture technology involves the removal of CO_2 from flue gases generated after fossil fuel combustion. These flue gases, containing impurities such as NO_x and SO_x, are filtered and scrubbed before CO_2 separation.[43,51,52]

The final separation of CO_2 from by-products, such as N_2 or SO_x, in Post-Combustion, Pre-Combustion, and Direct Air Capture processes employs various technologies, including adsorption, absorption, membrane systems, and cryogenic separation (Figure 14). The Oxy-fuel Combustion process, in contrast, is excluded here, as it relies on combustion with pure oxygen, resulting in emissions that primarily consist of water, which can be removed through condensation.[43,49]

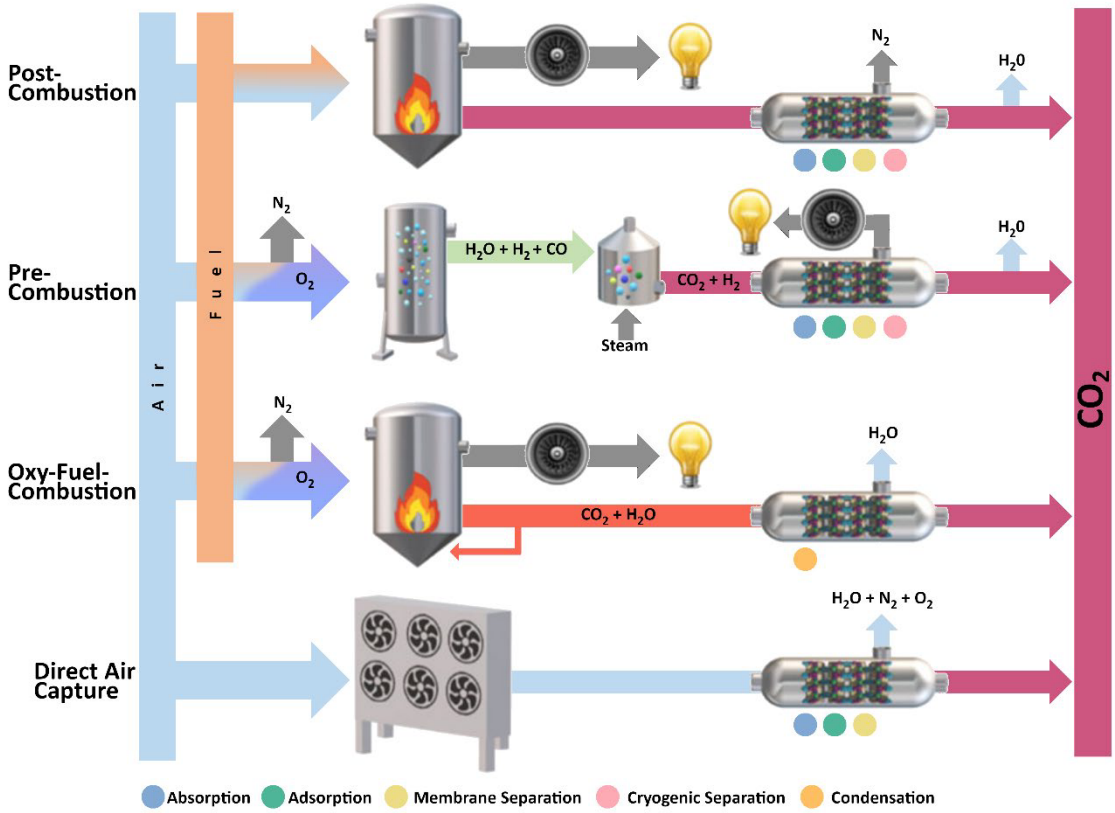

Figure 14: Processes for CO_2 capture: Post-Combustion, Pre-Combustion, Oxy–fuel Combustion and Direct Air Capture. Adapted from Pettinari.[53]

In adsorption-based CO_2 capture, CO_2 binds to adsorbents, typically solid materials, through physical interactions like van der Waals forces. Common adsorbents include activated carbon and zeolites, which are loaded under high pressure. Regeneration of the adsorbent is accomplished either by gradually lowering the pressure, potentially using a purge gas (pressure swing adsorption), or by heating the adsorbent material (temperature swing adsorption). Absorption processes are among the most commonly used methods for CO_2 capture from gas streams, with a distinction between physical and chemical absorption techniques. In physical absorption, CO_2 is reversibly dissolved in a liquid or porous solid. A typical example is pressurized water scrubbing, which relies on the different solubilities of gas components such as carbon dioxide, methane, hydrogen sulfide, and ammonia in water, allowing for their separation. Besides water, organic solvents such as methanol, propylene carbonate, N-methyl-2-pyrrolidone, dimethyl ether, and polyethylene glycol are also used. Chemical absorption often employs diluted aqueous amine solutions, such as ethanolamine or diethanolamine, which enable higher CO_2 loading than physical methods. Here, CO_2 reacts to form carbamates, with regeneration achieved by heating. Additional chemical processes involve potassium carbonate (*Benfield* and *SARGAS*), ammonia (*Chilled-Ammonia*), or amino acid salts (*Siemens-POSTCAP*). Another technique, carbonate looping employs solid absorbents, typically alkaline earth oxides like calcium oxide.[43,49]

Cryogenic methods capture CO_2 from exhaust or flue gas streams through condensation, sublimation, or distillation, using either low-temperature rectification or freezing CO_2 under elevated pressure. These approaches are particularly efficient for CO_2-rich gas streams, as energy demands increase substantially with lower CO_2 concentrations. Membrane processes, on the other hand, rely on membranes that separate CO_2 from other gases based on molecular size (porous membranes) or solubility (diffusion membranes). The separation is driven by the CO_2 partial pressure difference across

the membrane. These techniques are advantageous for their simple design, ease of operation, high safety, and low thermal energy requirement. However, the high energy demand for CO_2 compression can lead to increased costs.[43,49]

The capture of CO_2 from various sources differs significantly in terms of energy demands and associated costs, as illustrated in Figure 15 and Figure 16. The energy demand depends on the source and typically includes electricity (e.g. for compressors or pumps), heat (often supplied as steam), and fuel (for processes requiring additional combustion to generate sufficient heat). Dependent on the initial CO_2 concentration in the source, the effort and cost can vary greatly. The capture of atmospheric CO_2, for example, leads to increased energy demands and costs, due to its low concentration and therefore extensive capture process. In contrast, the CO_2 capture from industrial processes, such as natural gas or bioethanol production, is more efficient, requiring less energy and incurring lower costs due to higher CO_2 concentrations. However, as the world, respectively the EU, progresses toward climate neutrality by 2050 aligned with the *Paris Agreement* and the *European Green Deal*, the availability of CO_2 from fossil-based industrial sources is expected to decline. Remaining emissions will primarily stem from unavoidable process emissions, biogenic sources, and a small fraction of fossil emissions. As a result, the role of direct air capture is anticipated to grow significantly, providing an essential supplementary source of carbon. Achieving climate neutrality will also require substantial advancements in the efficiency and scalability of all CO_2 capture processes, ensuring that carbon is captured and utilized in the most sustainable and cost-effective manner.[49,54,55]

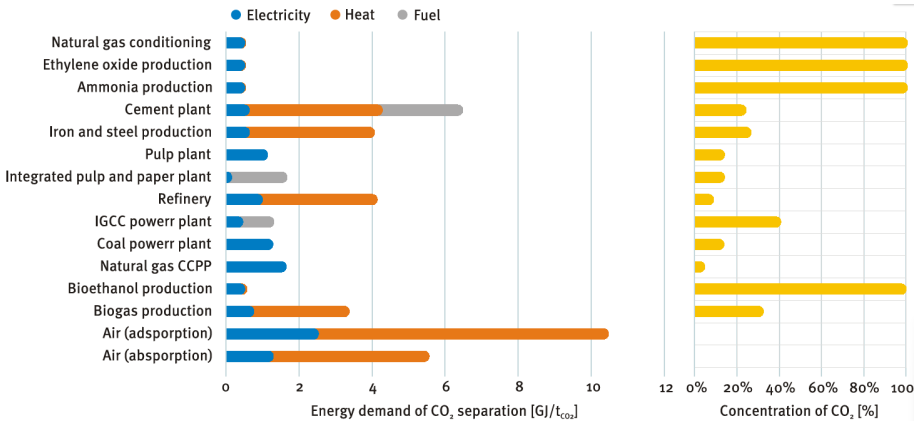

Figure 15: Energy demands for CO_2 capture from various sources with respective CO_2 concentrations.[55]

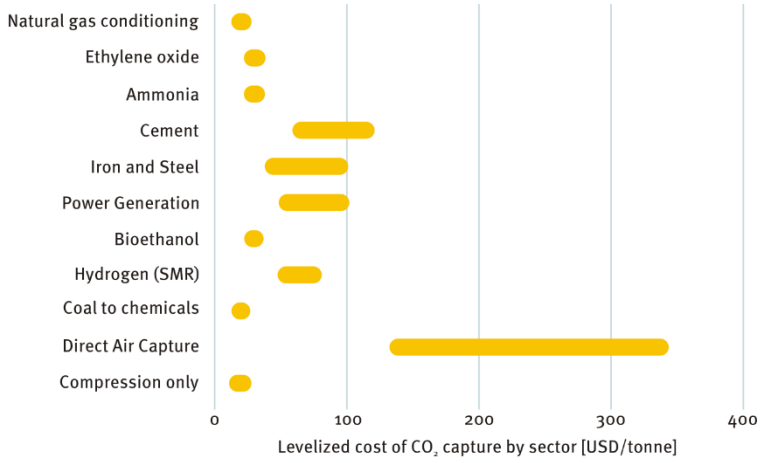

Figure 16: Costs associated with CO_2 capture from various sources.[55]

4.2 Products

Rising energy demand and the depletion of fossil resources highlight the necessity of renewable feedstocks such as biomass and CO_2. This dissertation investigates four representative products derived from these sustainable resources: formic acid (FA), lactic acid (LA), methanol (MeOH), and dimethyl ether (DME), which hold significant industrial relevance. Formic acid is utilized in the textile and rubber industries and is increasingly studied as a hydrogen storage medium. Lactic acid, essential for biodegradable plastics, plays a pivotal role in reducing reliance on fossil-based materials and is ranked among the top ten renewable chemicals. Methanol, a fundamental building block for various essential products, holds promise in future energy systems, especially as a hydrogen carrier. Dimethyl ether stands out as a low-emission alternative fuel, also widely used as a solvent and feedstock in the chemical industry. The following chapter provides an in-depth analysis of the chemical and physical properties, significance, and industrial applications of these compounds, alongside the conventional and emerging synthesis routes utilizing biomass and CO_2.

4.2.1 Lactic Acid

Lactic acid, or 2-hydroxypropionic acid, represents the simplest hydroxycarboxylic acid with the molecular formula $C_3H_6O_3$. (Figure 17). It exists in two optically active isomeric forms: L-(+)-lactic acid and D-(-)-lactic acid. In its anhydrous form, LA appears as a white crystalline solid. Due to its high hygroscopicity, it is more commonly encountered as a colorless, odorless liquid with a purity of up to 90 %. The liquid contains a substantial proportion of lactoyllactic acid along with other oligomeric impurities. This arises from LA, possessing both alcohol and acid functional groups, readily undergoes intermolecular esterification, resulting in the formation of esters such as lactoyllactic acid or lactide, a cyclic ester. LA is soluble in water, ethanol, diethyl ether, and acetone. It has a molecular weight of 90.08 g/mol, a melting point between 18 - 33 °C, and a boiling point ranging from 125 - 140 °C, although accurate determination of these properties remains challenging due to difficulties in synthesizing anhydrous LA.[56–58] LA is naturally produced as a racemic mixture during the fermentation of lactose, induced by LA bacteria. It also occurs in gastric juice, sauerkraut, beer, wine, and pickled cucumbers. In the muscles of the human body, LA forms from pyruvic acid in small concentrations, where elevated concentrations during physical exertion can lead to muscle cramps.[59]

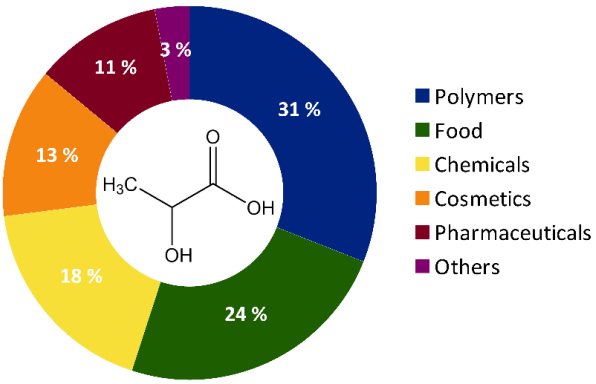

Figure 17: Structure and applications of lactic acid. Adapted from *Huang et al.*[60]

The global market for LA was valued at USD 3.5 billion in 2022 and is anticipated to surpass USD 7.9 billion by 2032, reflecting a compound annual growth rate of 8.7 %. LA is identified as one of the ten most important chemicals in the renewable feedstock sector (according to the U.S. Department

of Energy). LA and its derivatives, including salts and esters, hold significant importance in diverse sectors, ranging from the chemical and pharmaceutical industries to cosmetics and food industry. The food industry is the largest consumer, utilizing LA as a preservative, flavor enhancer, and acidulant. The most rapidly expanding application is the production of polylactic acid, a biodegradable plastic used in fibers and films. Polylactic acid is a sustainable alternative to fossil-based plastics, with applications spanning from food packaging to electronics, automotive parts, and medical devices.[56,57,60–62,63]

Approximately 90 % of LA in industry is produced via microbial fermentation of carbohydrates such as pentoses, hexoses, or easily hydrolysable polysaccharides, typically sourced from corn, sugarcane, and cassava. LA bacteria serve as the main microorganisms utilized in fermentation processes, alongside *Rhizopus*, *Streptococcus*, *Pediococcus*, *Sporolactobacillus inulinus*, *Bacillus coagulans*, and several yeasts.[58,64] Post-fermentation, a further processing for LA separation is required, including the removal of impurities from the feedstock, microbial by-products, and the microorganisms themselves. Additionally, lactate salts formed during fermentation must be converted into LA.[56] The conventional separation process for LA after fermentation involves the reaction of lime with the fermentation broth, to form calcium lactate, followed by its filtration and acidification with H_2SO_4, converting the calcium lactate into LA while precipitating gypsum ($CaSO_4 \cdot 2\ H_2O$) as a by-product. Following the removal of gypsum, the solution undergoes evaporation to achieve concentration, producing crude LA. The crude product often requires further purification steps such as liquid-liquid extraction, crystallization, or distillation to meet the desired specifications. Separation and purification often contribute to over 50 % of the overall production expenses. This is compounded by the rising prices of lime and sulfuric acid and the need to manage large volumes of unavoidable gypsum waste, all complicating industrial attractiveness. Additionally, the dependency on well-established refined substrates like glucose limits scalability, while using crude sources like lignocellulosic biomass remains challenging, due to the presence of impurities and pretreatment requirements. To meet the growing demand for industrial LA innovative sustainable chemo-catalytic routes are essential to address these limitations and enhance the scalability of the process.[56,58,61,64]

Chemical synthesis of LA relies on fossil-based feedstocks, starting with the reaction of acetaldehyde, derived from petroleum, with hydrogen cyanide to produce lactonitrile. This intermediate is then hydrolyzed using HCl or H_2SO_4 to yield LA and the corresponding ammonium salt (Figure 18). Currently, this is the only commercially established chemical route, utilized by *Musashino Co., Ltd.* (Japan) and *Sterling Chemicals Inc.* (USA). However, no industrially viable chemical route utilizing renewable raw materials has yet been developed, highlighting a significant gap in sustainable LA production.[56,61,62,65]

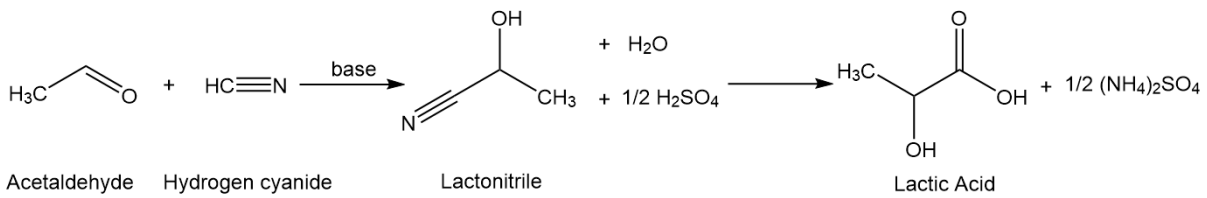

Figure 18: Reaction for synthesis of lactic acid from acetaldehyde and hydrogen cyanide. Adapted from *Münnich et al.*[7]

To bridge this gap, current research is directed at efficient chemo-catalytic approaches using renewable feedstocks, such as lignocellulosic biomass[66], cellulose[67], hemicellulose[68], sugars[69,70], and glycerol[71].Key approaches include the hydrothermal conversion of biomass with alkaline catalysts

(e.g. NaOH, $Ca(OH)_2$, KOH, $Ba(OH)_2$).[72] In these processes, an acidic solution is typically required to neutralize the base, along with hydrolysis and potential lactate formation to obtain pure LA. Acidic catalysts, including *Brønsted* and *Lewis* acid sites, have demonstrated effectiveness in converting carbohydrates to LA.[73] Research has investigated various acidic homogeneous catalysts, including $ErCl_3$[69], Al(III) and Cr(III) salts[74], and $ZnSO_4$[75], as well as heterogeneous catalysts such as Nb_2O_5[76], Sn-based catalysts[77], and zeolites[78].Recently, *Keggin*-type polyoxometalates (POMs) have emerged as highly effective catalysts for the biomass-to-LA conversion process under nitrogen atmosphere (see chapter 4.3).[79,80]

4.2.2 Formic Acid

Formic acid, also known as methanoic acid, is the simplest carboxylic acid with the molecular formula HCOOH and a planar structure (Figure 19). It is a colorless, transparent liquid, characterized by its highly corrosive nature and pungent odor. Inhalation of the vapors can irritate the lungs and eyes, and direct contact with the skin or eyes should be strictly avoided, as it may lead to severe chemical burns and irreversible tissue damage. Pure FA is highly hygroscopic, fully miscible with water and various polar solvents, while its miscibility with hydrocarbons is limited. It has a molecular weight of 46.03 g/mol. FA exhibits a relatively high melting point of 8.3 °C and a boiling point of 100.8 °C, which are elevated compared to similar organic compounds of equivalent molecular weight, attributed to its strong hydrogen bonds. It is the strongest unsubstituted alkyl carboxylic acid with a pKa of 3.74, making it ten times more acidic than acetic acid.[81,82] Naturally occurring in numerous organisms, FA is present in the venom glands of beetles, ants, and bees, as well as in caterpillar hairs, pine needles, nettles, various fruits, and as a salt in human urine. It is utilized by numerous plant and animal species, particularly in defensive and offensive venoms.[82,83] Notably, FA was detected as the first organic compound in space, with its first observation reported in the coma of comet C/1995 (Hale-Bopp).[84]

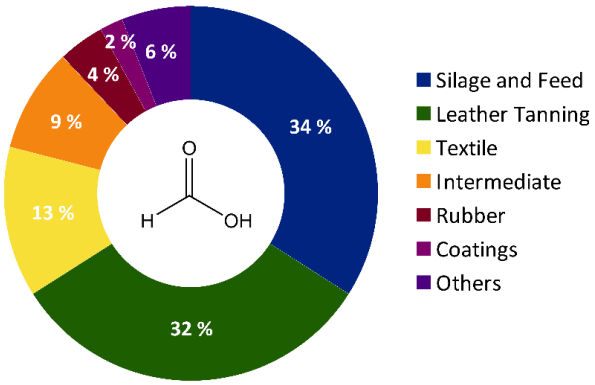

Figure 19: Structure and applications of formic acid. Adapted from OxFA GmbH.[85]

The global market for FA was estimated at USD 2.34 billion in 2024 and is projected to reach USD 3.43 billion by 2031, representing a compound annual growth rate of 5.6 %.[86] FA is used in dyeing processes, within the textile and leather industries, as well as in rubber production. It also serves as an intermediate in various chemical and pharmaceutical applications. Additionally, its use as a silage additive and preservative for green fodder is expected to grow significantly in the future. FA is also considered a promising energy- and hydrogen storage medium.[82,85]

Industrially, FA is produced from fossil-based feedstocks through the acidolysis of formate salts, oxidation of hydrocarbons, and hydrolysis of either methyl formate or formamide. The most widely

used method is the methyl formate route, which occurs in two steps (Figure 20). In the first step, methanol reacts with carbon monoxide in the presence of a basic catalyst, such as sodium or potassium methoxide, at around 80 °C and 45 bar to form methyl formate. In the second stage, methyl formate is hydrolyzed at temperatures between 100 - 140 °C to produce FA and methanol. The methanol is then recycled back into the process for further use.[82]

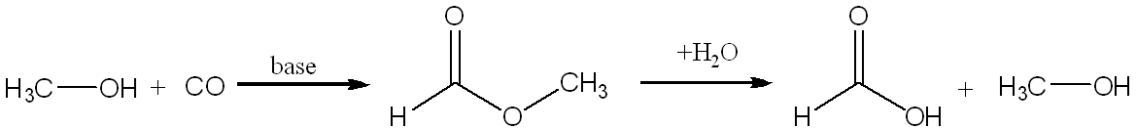

Figure 20: Reaction for synthesis of formic acid via methyl formate route. Adapted from *Reutemann et al.*[82]

Since 1983, research has been conducted on the production of biogenic FA from renewable resources, with *McGinnis et al.*[87] demonstrating the conversion of biomass into FA through high-temperature wet oxidation. Since then, numerous studies have explored the production of FA from biomass, including methods such as fast pyrolysis of sugars, cellulose, or hemicellulose [88] acid hydrolysis [89] and more novel approaches like electrocatalysis[90] or photocatalysis[91]. The most promising and extensively studied approach for producing FA from biomass is oxidative conversion encompassing wet and catalytic oxidation.[92] Wet oxidation is a hydrothermal treatment that utilizes air, oxygen, or hydrogen peroxide as oxidants at high temperatures (125 - 300 °C) and pressures ranging from 0.5 - 20 MPa.[93] Subcritical or supercritical water is a cost-effective, environmentally friendly solvent, offering versatility in converting various substrates, while having moderate yields and minimal by-products.[92] Wet oxidation has proven to be effective in converting various organic biomass sources, including cellulose [94,95], starch[96], various monosaccharides,[97] and organic waste such as dairy wastewater [94], domestic sludge[98], coconut husk,[99] and other agricultural residues like wheat stalk and corn cob.[100]. Catalytic oxidation, unlike wet oxidation, uses solvents other than water and combines an oxidant (mainly O_2) with a bifunctional catalyst containing both acidic (H^+) and redox active sites (such as V^{5+} or Fe^{3+}).[92] This catalyst may consist of combinations of two distinct catalysts, such as mixtures of H_2SO_4-$NaVO_3$.[101] Notably, polyoxometalates have proven to be outstanding catalysts for biomass oxidation due to their dual acidic and oxidative sites (chapter 4.3).[102]

4.2.3 Methanol

Methanol or methyl alcohol, is the simplest alcohol with the molecular formula CH_3OH (Figure 21). It is a colorless, volatile, and highly flammable liquid with a faint alcoholic odor. MeOH vapors can form explosive mixtures with air in concentrations between 7 % and 37 %. Due to its toxicity, MeOH is hazardous upon inhalation, ingestion, or skin contact, potentially causing symptoms such as headache, dizziness, nausea, and, in severe cases, blindness or death. This toxicity arises from its metabolization to formaldehyde and FA in the liver. MeOH is fully miscible with water and most organic solvents, with a melting point of -97.6 °C and a boiling point of 64.7 °C, resulting from hydrogen bonding between hydroxyl groups.[103,104] MeOH occurs naturally in certain plants, such as cotton plants, some grasses, and heracleum fruit. In its conjugated forms, as esters or ethers, MeOH is present in the pectin of fruits, contributing to structural support, and in lignin, where it is produced through the enzymatic breakdown of pectin and lignin. MeOH is also prevalent in space. Notably, a vast MeOH cloud spanning 463 billion kilometers was discovered within the Milky Way in 2006. Additionally, MeOH is an important molecular marker for identifying star-forming regions in astronomical research.[104,105]

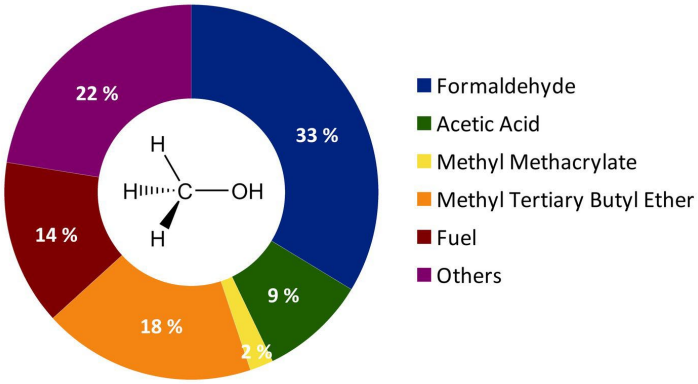

Figure 21: Structure and applications of MeOH. Adapted from Srivastava.[106]

The global MeOH market was valued at USD 32.8 billion in 2023 and is projected to reach USD 47.91 billion by 2032, with a compound annual growth rate of 4.8 %.[107] MeOH ranks among the most widely produced chemicals globally, with a global production capacity of 150 million tons (2020). It serves as a highly versatile building block for numerous essential chemicals, including acetic acid, formaldehyde, and methyl- and vinyl acetates (Figure 21). Additionally, MeOH can be blended with gasoline for use in modified engines or utilized directly as a fuel. One of the most promising future application is its use as a hydrogen carrier or as a feedstock for DME production.[104,108]

Industrially, MeOH is primarily produced from fossil-derived synthesis gas (syngas), a mixture mainly consisting of carbon monoxide, hydrogen, and trace amounts of carbon dioxide. Syngas is produced from various feedstocks, including natural gas, coal, and even biomass, whereby the preferred one is the production through steam reforming from natural gas, due to its low amount of impurities such as sulfur or heavy metals. In an exothermic reaction, CO and CO_2 are converted into MeOH (eq. 1 and eq. 2). Therefore, MEOH production is optimized under conditions of high pressure and low temperature, with the equilibrium composition determining the maximum achievable conversion. Additionally, through water-gas-shift reaction, CO can also be converted into CO_2 (eq. 3). The process employs Cu-based catalysts, with $Cu/ZnO/Al_2O_3$ being the most widely used.[103,104,109]

$$CO + 2\,H_2 \rightleftharpoons CH_3OH \qquad \Delta H_{298\,K} = -91\ \text{kJ/mol} \qquad \text{eq.1}$$

$$CO_2 + 3\,H_2 \rightleftharpoons CH_3OH + H_2O \qquad \Delta H_{298\,K} = -49\ \text{kJ/mol} \qquad \text{eq.2}$$

$$CO + H_2O \rightleftharpoons CO_2 + H_2 \qquad \Delta H_{298\,K} = -42\ \text{kJ/mol} \qquad \text{eq.3}$$

An innovative alternative to fossil-based MeOH production is the synthesis of *green methanol*, derived directly from hydrogen and pure CO_2. The CO_2 is sourced from the atmosphere or industrial point sources (chapter 4.1), while the hydrogen for this process is produced via water electrolysis (Figure 22), using renewable electricity from sources like solar and wind. This hydrogen can not only serve as a feedstock for MeOH synthesis but also as an energy storage medium for intermittent renewable energy. Other potential methods for hydrogen production include biomass pyrolysis, steam or oxygen gasification, and reforming of biomass-derived products like ethanol or methane.[104,108]

MeOH synthesis from H_2 and CO_2 is technically competitive with conventional syngas-based methods, although it remains less economically viable. Nonetheless, the growing global emphasis on reducing CO_2 emissions has intensified industrial interest in this sustainable process.[104,108,110] The first pilot plant for *green methanol* synthesis, with a production capacity of 50 kg/day, was established in Japan using a Cu-based catalyst modified with ZnO,ZrO_2,Al_2O_3 and Ga_2O_3 catalysts.[111] Currently, in Denmark,

the first commercial-scale green MeOH plant is under construction, developed by *European Energy A/S*, with an anticipated annual production capacity of up to 42,000 tons.[112]

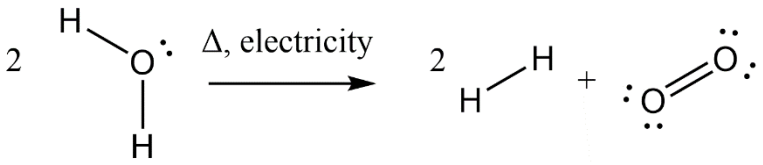

Figure 22: Reaction for generation of hydrogen from water electrolysis. Adapted from *Basile et al*.[108]

MeOH synthesis from H_2 and CO_2 is technically competitive with conventional syngas-based methods, although it remains less economically viable. Nonetheless, the growing global emphasis on reducing CO_2 emissions has intensified industrial interest in this sustainable process.[104,108,110] The first pilot plant for *green methanol* synthesis, with a production capacity of 50 kg/day, was established in Japan using a Cu-based catalyst modified with ZnO,ZrO_2,Al_2O_3 and Ga_2O_3 catalysts.[111] Currently, in Denmark, the first commercial-scale green MeOH plant is under construction, developed by *European Energy A/S*, with an anticipated annual production capacity of up to 42,000 tons.[112]

Cu-based catalysts remain the benchmark for MeOH synthesis from CO-rich syngas but exhibit significant limitations when applied to direct CO_2 hydrogenation. The concurrent formation of water during CO_2 hydrogenation (eq. 3) accelerates Cu particle crystallization, resulting in sintering and catalyst deactivation. This inherent weakness underscores the need for water-tolerant catalysts with improved stability for industrial MeOH synthesis. Current research is addressing this issue by exploring alternatives that can sustain performance in the presence of water. In_2O_3-based catalysts emerge as a promising alternative, offering improved resistance to deactivation and high efficiency (chapter 4.3).[113]

4.2.3 Dimethyl Ether

Dimethyl ether also known as methoxymethane, is the simplest aliphatic ether with the molecular formula C_2H_6O (Figure 23). Under standard conditions, DME is a colorless, nearly odorless, non-toxic but highly flammable gas. DME vapors can form explosive mixtures with air at concentrations between 3 vol.% and 17 vol.%. It is miscible with most polar and nonpolar organic solvents but only partially soluble in water (5.7 % at 20 °C, 1 bar). Unlike many other aliphatic ethers, DME is resistant to auto-oxidation and peroxide formation, maintaining its stability in atmospheric oxygen, which is crucial for industrial applications.[114] DME is primarily synthesized for industrial purposes and does not naturally occur in significant quantities in the environment. It was detected in a distant protoplanetary disk, marking the largest organic molecule found in such a region. This discovery is significant as it suggests that complex organic molecules, which are potential precursors to life, may rain down on forming planets, giving insight on how life might originate on planets.[115]

The global market for DME was valued at USD 8.69 billion in 2023 and is projected to reach USD 25.4 billion by 2036, with a compound annual growth rate of 8.6 %.[116] DME is widely used as an aerosol propellant in products like hair sprays and lacquers or as a chemical feedstock for basic chemicals such as dimethyl sulfate, methyl lactate, and acetic acid. Furthermore, DME is employed in blending with liquefied petroleum gas (LPG), and is gaining attention as a potential diesel fuel substitute as well as an alternative to LPG, as its chemical and physical properties closely resemble conventional fuels. These properties include a low autoignition temperature and a vapor pressure

similar to liquified petroleum gas, making it compatible with existing infrastructure. DME is environmentally friendly, with a low global warming potential, short atmospheric half-life, and low CO and NO_x emissions, due to the absence of C–C bonds in its molecular structure and its high oxygen content. Furthermore, DME combustion results in substantially lower particulate emissions compared to conventional fuels.[109,114,117]

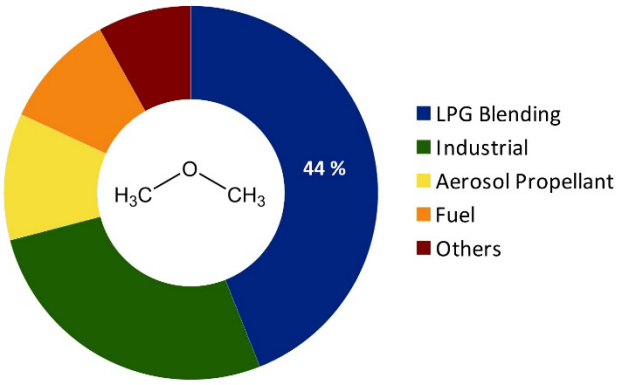

Figure 23: Structure and applications of DME. Not all numbers exactly specified. Adapted from market.us.[118]

Industrially, DME is predominantly synthesized through a two-step process. In the first stage, MeOH is produced from fossil-based syngas (eq. 1) using a Cu-based catalyst (see chapter 4.2.3.). The second stage involves the dehydration of the produced MeOH in a separate reactor, catalyzed by solid acid catalysts such as zeolites or Al_2O_3, to form DME (eq. 4).[109,119] A more efficient approach is the direct one-step synthesis of DME, converting CO with H_2, using a bifunctional catalyst, a combined mixture of the MeOH synthesis and the MeOH dehydration catalyst. Commercially, the only process for the direct conversion of syngas into DME is from *JFE Holdings Inc.* in Japan, with a production capacity of 5 tons per day.[46,108]

$$2\,CO + 4\,H_2 \rightleftharpoons 2\,CH_3OH \qquad \Delta H_{298\,K} = -181\ \text{kJ/mol} \qquad \text{eq.1}$$

$$2\,CH_3OH \rightleftharpoons CH_3OCH_3 + H_2O \qquad \Delta H_{298\,K} = -24\ \text{kJ/mol} \qquad \text{eq.4}$$

An innovative approach to sustainable DME production is the direct one-step synthesis of *green dimethyl ether* from CO_2. This process uses hydrogen produced via water electrolysis, and CO_2 captured from the atmosphere or industrial emissions as feedstocks, analogous to the *green methanol* process discussed in chapter 4.2.3. Similar to the one-step DME synthesis from syngas, this process employs a bifunctional catalyst system to enable the direct conversion of CO_2 and H_2 into DME. Thermodynamically, direct DME synthesis offers several advantages. The continuous removal of MeOH from the reaction, through its subsequent conversion to DME, shifts the overall equilibrium toward greater product yields. Moreover, this streamlined process provides faster reaction rates and simplified operations.[109]

Nevertheless, catalysts commonly used for the direct DME synthesis from CO_2 still face challenges related to limited space-time yields and long-time-stability.[120] The catalyst systems required for DME formation from CO_2 are similar to those used for DME production from CO. A bifunctional catalyst system is required, consisting of a MeOH synthesis catalyst, followed by an acidic catalyst for the dehydration of MeOH to DME.[121] The limitations and drawbacks of commercial MeOH synthesis

catalysts are already discussed in chapter 4.2.3.. The acidic catalyst must meet specific requirements. For the acidic component, a high density of active sites with moderate acidity is essential, as excessive acidity can lead to the formation of hydrocarbons and coke. The catalyst should also operate effectively at low temperatures, as this promotes high DME selectivity and inhibits CO formation (Figure 24). Additionally, resistance to water deactivation is crucial due to the substantial amount of water produced during the reaction.[121–123] The acidic catalysts commonly used for MeOH dehydration in industry are the metal oxide Al_2O_3 and the zeolite ZSM-5.[124] Alternative materials like mesoporous silicates as metal-doped MCM-41[125] or aluminophosphates[126] have been investigated, but are not yet widely adopted commercially. Al_2O_3, while effective for CO hydrogenation, suffers from water adsorption during CO_2 hydrogenation, which inhibits its active sites.[127] Zeolites like ZSM-5, on the other hand, often produce undesired by-products such as methane or other hydrocarbons, due to the excessively strong acidic sites.[128] To overcome the drawbacks of using Al_2O_3 or zeolites for MeOH dehydration, an alternative emerges in the form of *Keggin*-type heteropoly acids (HPAs) (chapter 4.3).

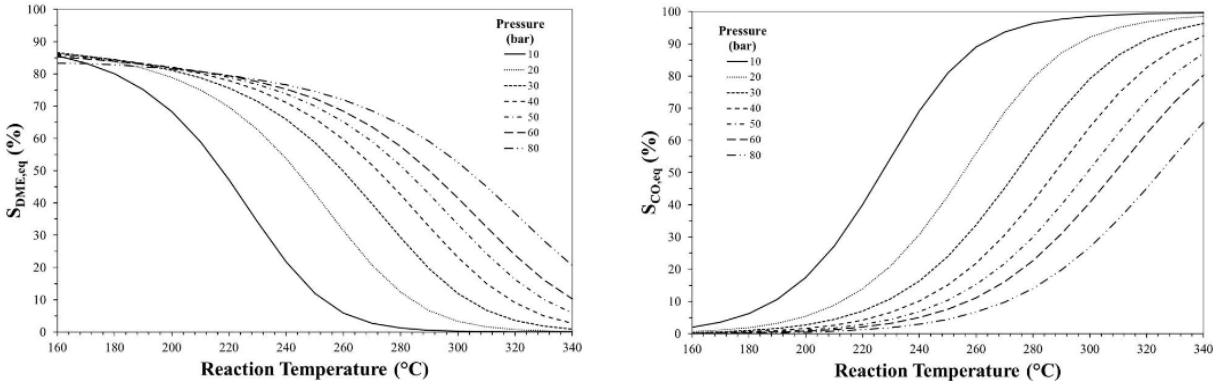

Figure 24: Effect of temperature (left) and pressure (right) on selectivity of DME and CO, with initial H_2/CO_2 ratio of 3/1.[129]

4.3 Catalysts

Catalysts are essential for organic transformations and compound synthesis, playing a pivotal role in the efficient utilization and conversion of sustainable resources. Metal-based catalysts stand out due to their versatility, ranging from simple metal salts and oxides to intricate coordination complexes, all demonstrating high catalytic efficiency. Their adaptability allows their application in both homogeneous and heterogeneous catalysis, making them integral to processes spanning academic research and industrial applications.[130]

This chapter gives an overview of the key catalysts employed in this study, specifically polyoxometalates as well as Indium- and Cu-based catalysts, categorized into homogeneous and heterogeneous catalysis. These catalysts were instrumental for synthesizing the compounds discussed in chapter 4.2, derived from sustainable carbon sources like biomass and CO_2 (chapter 4.1). This section will delve into their chemical and physical properties, catalytic performance, and the reaction mechanisms involved.

4.3.1 Homogeneous Metal Oxide Catalysts

In homogeneous catalysis, the catalyst is in the same phase as the reactants, which leads to notable benefits. One of these benefits is the minimal influence of mass transfer limitations, due to the uniform phase distribution. This type of catalysis provides substantial catalyst flexibility, allowing for a wide range of modifications and tailored designs. Furthermore, homogeneous catalysis is known for

achieving high selectivity and activity, which is beneficial for targeting specific reactions. Homogeneous catalysis also operates effectively under relatively mild conditions in terms of temperature and pressure, making it a valuable approach for sensitive or energy-efficient processes.[131]

Among homogeneous catalysts, POMs represent a particularly intriguing class, characterized by their structural complexity and adaptable properties. Their unique features enable a broad spectrum of catalytic functions, underscoring their significance and making them an ideal subject for further exploration.[132–135]

4.3.1.1 Polyoxometalates: History and Fundamentals

Polyoxometalates are distinct polyanionic structures, primarily composed of early transition metals such as V, Nb, Ta, Mo, and W, which are connected by oxo ligands. These metal atoms are usually present in their highest oxidation state, typically represented as $[MO_x]^{n-}$ building units. The most prevalent metal ions in POM structures are V, Mo, and W, all in their highest oxidation states.[132,136,137]

In 1826, *Berzelius* first described a yellow precipitate formed by the reaction of excess ammonium molybdate with H_3PO_4, which is now known as $(NH_4)_3[PMo_{12}O_{40}]$.[138] The first structural determination of a POM occurred in 1933 when *Keggin* determined the structure of $H_3[PW_{12}O_{40}] \cdot n\,H_2O$. This structure gave rise to a whole subclass of POMs, known as *Keggin*-type polyanions, characterized by the general formula $[XM_{12}O_{40}]^{n-}$.[139] Later, *Evans*' research led to the determination of the crystal structure of the $[TeMo_6O_{24}]^{6-}$ polyanion, whose structure had been previously proposed by *Anderson*, leading to the naming of the *Anderson-Evans* subclass.[140] In 1953, *Dawson* corrected the structure earlier proposed by *Wells* and determined the correct structure of the $[P_2W_{18}O_{62}]^{6-}$ polyanion.[141] That same year, *Lindqvist* introduced the structure of the $[Nb_6O_{19}]^{8-}$ polyanion, which lent its name to another subclass of POMs.[142]

Nowadays, POMs exhibit a wide range of sizes and structures, with the number of metal atoms varying from just a few to several hundred. One of the largest examples is a macroscopic molybdenum-cluster $Na_{48}[H_xMo_{368}O_{1032}(H_2O)_{240}(SO_4)_{48}] \cdot$ approximately 1000 H_2O, with a massive diameter of 6 nm, comparable to the macromolecule hemoglobin.[143] From the first mentions in the 19th century, to the structural determination about 100 years later, research has shifted towards understanding the properties and potential applications. Today, POMs are recognized for their diverse chemical compositions, structures, and unique physicochemical properties.[132,133,138–143,144]

4.3.1.2 Structure, Classification and Synthesis of Polyoxometalates

Based on their chemical composition, POMs are classified into isopolyanions (IPAs), $[M_xO_y]^{n-}$, consisting of pure metal oxide frameworks without heteroatoms, and heteropolyanions (HPAs), $[X_nM_xO_y]^{n-}$, where additional heteroanions are included alongside the metal centers, such as $[SiO_4]^{4-}$ or $[PO_4]^{3-}$. HPAs are generally more stable than IPAs and represent one of the most extensively studied subgroups of polyoxometalates. They are typically obtained as heteropolysalts or, in their protonated form, as heteropoly acids.[132,136]

IPAs and HPAs, such as those shown in Figure 25, exhibit various structural types. The *Lindqvist* -type structure with the $[M_6O_{19}]^{n-}$ polyanionic structure is one of the simplest, featuring an octahedral arrangement of six octahedrals. The best known structure is the *Keggin*-type structure, characterized by a central heteroatom (like P, Si, or B) surrounded by twelve metal atoms, often Mo or W, forming a tetrahedral shell ($[XM_{12}O_{40}]^{n-}$). Another important type is the *Wells-Dawson*-type structure, comprising eighteen metal atoms in two groups, typically described by

$[X_2M_{18}O_{62}]^{n-}$. Lastly, the *Anderson-Evans*-type structure has a central octahedron surrounded by a hexagonal ring of metal-oxo octahedrals ($[XM_6O_{24}]^{n-}$) and is notable for its versatility.[145]

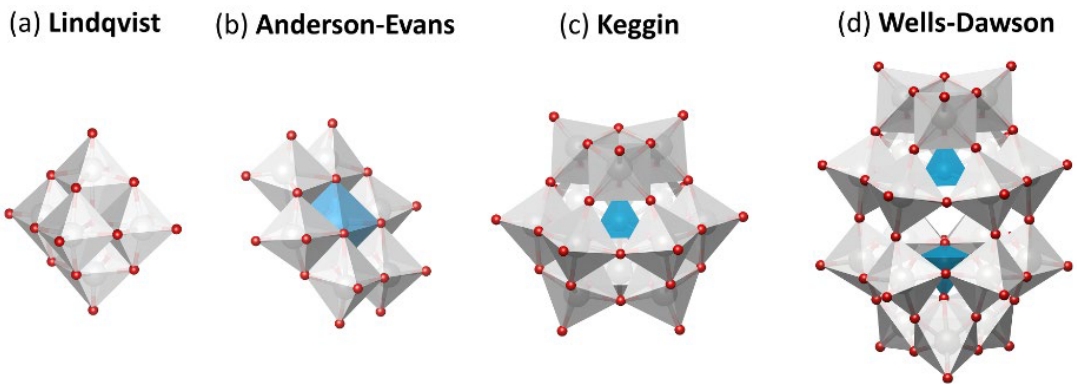

Figure 25: Polyhedral representation of several examples of iso- and heteropolyanions. a) *Lindqvist* ($[M_6O_{19}]^{n-}$), (b) *Anderson-Evans* ($[XM_6O_{24}]^{n-}$), (c) *Keggin* ($[XM_{12}O_{40}]^{n-}$), and (d) *Wells-Dawson* ($[X_2M_{18}O_{62}]^{n-}$). Oxygen in red, {MO_6} octahedra in grey, {XO_6} and {XO_4} polyhedral in blue (X = a heteroatom).[146]

The synthesis of both HPAs and IPAs typically occurs in aqueous solution through the condensation of simple mononuclear oxoanions (equations 5 - 7). Polyanions can often be crystallized as salts from stoichiometrically acidified mixtures from room temperature, owing to favorable equilibrium constants and rapid formation rates. While the stoichiometric ratios from synthesis equations are generally reliable, successful crystallization may require excess heteroatoms or precise adjustments to temperature and pH value. Key factors influencing synthesis include pH value, temperature, concentration, the type of anions and heteroatoms, reducing agents, and additional ligands. Besides the conventional methods, recent advancements in POM synthesis have explored alternative approaches, such as hydrothermal synthesis and the use of ionic liquids (ILs), offering new pathways for the creation of novel POM structures.[132,134]

$$7\ MoO_4^{2-} + 8\ H^+ \rightarrow\ [Mo_7O_{24}]^{6-} + 4\ H_2O \qquad \text{eq.5}$$

$$6\ MoO_4^{2-} + Cr(H_2O)_6^{3+} + 6\ H^+ \rightarrow [Cr(OH)_6Mo_6O_{18}]^{3-} + 6\ H_2O \qquad \text{eq.6}$$

$$12\ WO_4^{2-} + HPO_4^{2-} + 23\ H^+ \rightarrow [PW_{12}O_{40}]^{3-} + 12\ H_2O \qquad \text{eq.7}$$

An established strategy for modifying the properties of heteropolyoxometalates (HPAs) involves the targeted substitution of addenda atoms, such as molybdenum or tungsten, with catalytically active transition metals. These structural modifications allow for the controlled tuning of catalytic functionality, as the incorporated transition metals can act as active sites themselves. Such substitutions open up a broad range of applications, including hydrogen evolution, oxidative processes like water oxidation, CO_2 reduction, and transformations of organic substrates. Depending on the substitution pattern, either single transition metals can be introduced or combinations of different metals can be incorporated. A classical example is the vanadium-containing Keggin-type phosphomolybdates, such as $H_{3+x}[PV_xMo_{12-x}O_{40}]$, first reported by Odyakov and Zhizhina. Analogous modifications have also been described for other POM frameworks, including Wells–Dawson- and Lindqvist-type structures, where vanadium partially replaces tungsten (e.g., $K_{6+x}[P_2V_xW_{18-x}O_{62}]$ and $K_{2+x}[V_xW_{6-x}O_{19}]$).

4.3.1.3 Properties and Applications of Polyoxometalates

POMs possess an impressive array of chemical and physical properties that can be precisely modified by adjusting molecular size, composition, structure, and charge. They are known for their high thermal stability, their resistance to oxidation in solution, and high solubility across a wide range of polar and nonpolar solvents. POMs also exhibit significant acidity, remarkable redox activity, and remain stable even during multiple electron-transfer processes.[133,147] The structural and electronic versatility of POMs enables their application in diverse areas. These range from pharmaceuticals - acting as antiviral, antibacterial, and anticancer agents - to magnetic materials and energy storage. Notably, their catalytic properties represent one of their most important applications.[136,148]

POMs, and HPAs in particular, are highly versatile catalysts with multiple active sites, including protons, oxygen atoms, and metal centers. Protons in these catalysts act as *Brønsted* acids, promoting acid-catalyzed reactions. Additionally, certain oxygen atoms, especially those in lacunary sites with high negative charges, display sufficient basicity to act as active sites in base-catalyzed reactions. Notably, the metal centers in POM catalysts are central to their efficiency in oxidation and redox reactions. *Keggin*-type HPAs have gained extensive attention in catalysis research due to their superior structural stability. Building on the versatile catalytic properties of POMs, their applications extend to diverse chemical valorization processes. They are used in industrial processes like the hydration of propene, isobutene, and *n*-butene to alcohols; the oxidation of methacrolein; the polymerization of THF; and the esterification of acetic acid with ethylene to produce ethyl acetate.[149]

An established strategy for modifying the properties of Keggin-HPAs involves the targeted substitution of addenda atoms, such as molybdenum or tungsten, with catalytically active transition metals. These structural modifications allow for the controlled tuning of catalytic functionality, as the incorporated transition metals can act as active sites themselves. Such substitutions open up a broad range of applications, including hydrogen evolution, oxidative processes like water oxidation, CO_2 reduction, and transformations of organic substrates. Depending on the substitution pattern, either single transition metals can be introduced or combinations of different metals can be incorporated. A well-known example are vanadium-containing *Keggin*-type POMs, such as $H_{3+x}[PV_xMo_{12-x}O_{40}]$, first reported by Odyakov and Zhizhina. Analogous modifications have also been described for other POM frameworks, including *Wells-Dawson*- and *Lindqvist*-type structures, where vanadium partially replaces tungsten (e.g., $K_{6+x}[P_2V_xW_{18-x}O_{62}]$ and $K_{2+x}[V_xW_{6-x}O_{19}]$).[150]

The following sections explore specific sustainable catalytic uses of POMs, focusing on their roles in biomass conversion, as well as in acid-catalyzed reactions such as the synthesis of dimethyl ether.

4.3.1.4 Polyoxometalates as Catalysts

Conversion of Biomass to Lactic Acid

So far, research on POMs for LA production has primarily concentrated on the oxidation of glycerol, which is an attractive starting material due to its abundant availability, particularly as a by-product of biodiesel production.[151] Both homogeneous and heterogeneous systems with POMs have demonstrated promising results. For instance, with simple $H_3[PMo_{12}O_{40}]$ and $H_3[PMo_{12}O_{40}]/C$,[152] or $AlPMo_{12}O_{40}$ and $CrPMo_{12}O_{40}$[153] and novel lysine-acid-functionalized POMs ($Ly_xH_{3-x}[PMo_{12}O_{40}]$)[154] as well as $H_3[PMo_{12}O_{40}]$ embedded in a lipid-like bilayer on graphene oxide.[155] The conversion of biomass, especially lignocellulosic biomass, to LA is both a promising but challenging process. Existing research and catalytic systems for the conversion of various types of biomass are discussed in chapter 4.2.1.

The desired pathway for acid-catalyzed LA formation, starting from glucose, begins with the isomerization of glucose to fructose (Figure 26). This is followed by a retro-aldol condensation, yielding dihydroxyacetone (DHA) and glyceraldehyde as intermediates. These intermediates are then dehydrated to form pyruvaldehyde, from which upon rehydration LA is formed, the target product of this reaction. When POMs are used as catalysts, some alternative side reactions may occur. Glyceraldehyde can be oxidized to glyceric acid, which may undergo C–C bond cleavage, producing glycolic acid and ultimately FA. Additionally, glyceraldehyde can decarboxylate to form acetaldehyde, which can either be further oxidized to glyoxal or converted into acetic acid.[79,156]

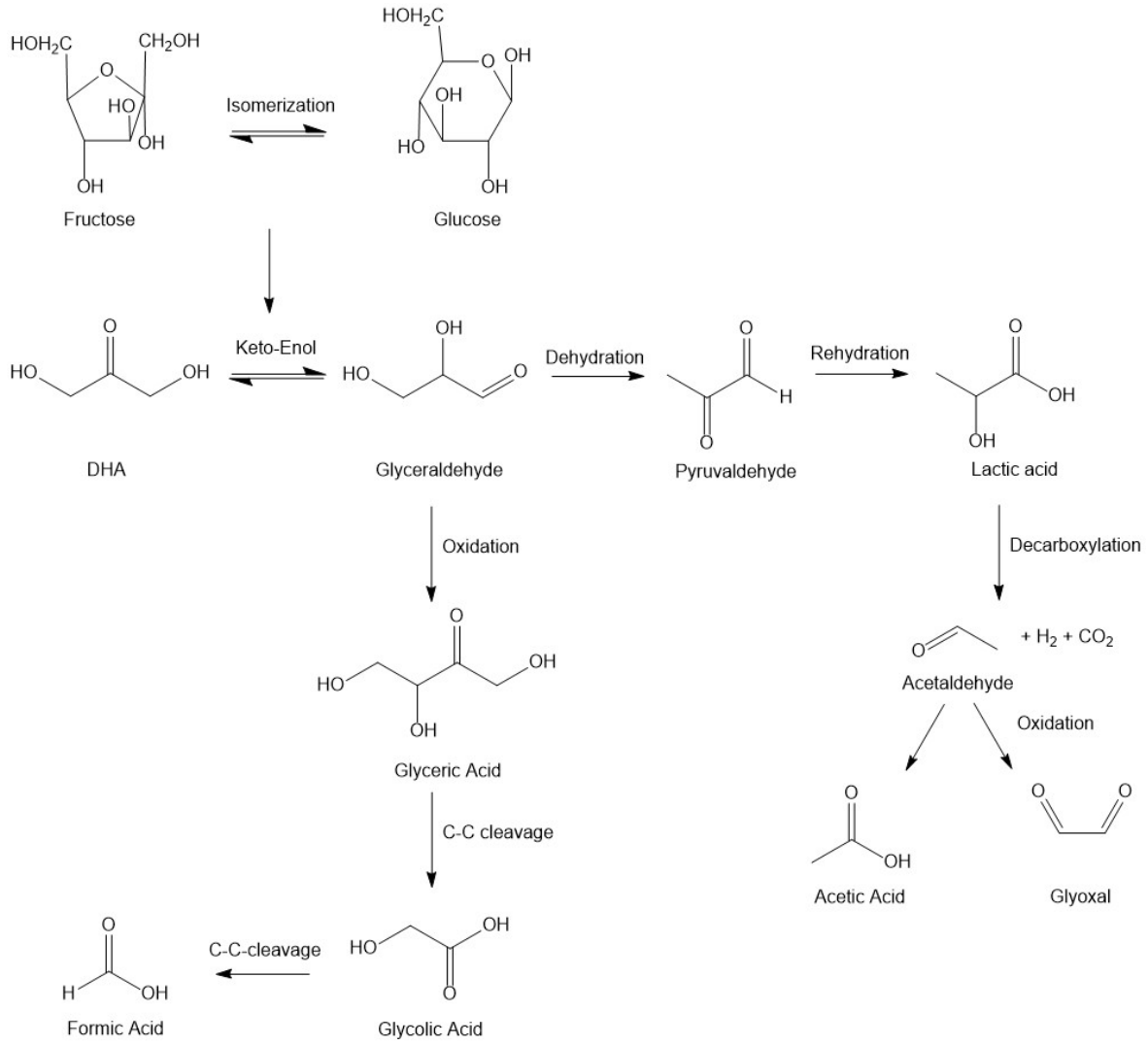

Figure 26: Reaction pathways for glucose conversion to lactic acid.[157]

Albert et al. investigated the use of POMs as catalysts for glucose conversion into lactic acid. Within this work, alongside other V-containing compounds ($VOSO_4$ and NH_4VO_3), the catalysts $H_4[PV_1Mo_{11}O_{40}]$ and $H_8[PV_5Mo_7O_{40}]$ (HPA-5) were employed achieving a LA yield of 12.8 % using HPA-5.[79] It was demonstrated that paramagnetic, acid-bound vanadyl species were responsible for the conversion of glucose to LA.[79,156] *Voß et al.* further explored the catalytic potential of different *Keggin*-type and *Lindqvist*-type polyoxometalates as switchable catalysts, enabling the production of either FA or LA by simply changing the reaction atmosphere from O_2 to N_2. Using $H_6[PV_3Mo_9O_{40}]$, they achieved a 40 %

yield of LA from glyceraldehyde as the substrate within a reaction time of 1.[80] More recently, *Marianou et al.* demonstrated the conversion of complex cellulose to LA, with supported $H_4[SiW_{12}O_{40}]/SiO_2$-$Al_2O_3$ being the most efficient catalyst, achieving a 23.5 % yield of LA and a cellulose conversion rate of 61.2 % after 24 hours.[158] Apart from these studies, research into the use of POMs for LA production remains limited and underexplored, highlighting the need for further investigation to fully realize their potential in this field.

Conversion of Biomass to Formic Acid

Keggin-type HPAs have proven to be highly effective catalysts for oxidation reactions. *Wölfel et al.* investigated the use of *Keggin*-type HPA $H_5[PV_2Mo_{10}O_{40}]$ for the selective and complete conversion of water-soluble carbohydrates to FA.[102] $H_5[PV_2Mo_{10}O_{40}]$ was also capable of converting complex feedstocks, such as pomace, cane trash, waste paper, cyanobacteria, and wood, into FA under mild conditions (90 °C and 30 bar molecular O_2) utilizing p-toluene sulfonic acid as an additive.[159] Further research led to the utilization of a more efficient catalyst HPA-5, which exhibited enhanced catalytic activity due to its higher V-content.[160,161] This advancement in catalyst design led to the development of the first commercial process for bio-based FA production, known as the *OxFA* process, achieving a notable FA yield of 85 % under mild conditions of 20 bar O_2 and 90 °C utilizing HPA-5.[162,163] Additionally, the OxFA process is being considered for integration with *Fischer-Tropsch* synthesis to enable the production of green liquid fuels.[162]

The Vanadium atoms serve as the catalytically active centers in *Keggin*-type HPAs. During the oxidation of glucose or other substrates, these vanadium species undergo reduction, but are subsequently re-oxidized by molecular oxygen, returning the catalyst to its original state (Figure 27). This also explains the exceptional catalytic performance of HPA-5, which can be largely attributed to its high concentration of V^{5+} species. Under conditions of low oxygen pressure, the reoxidation of the reduced POM catalyst typically limits the reaction rate. However, under *OxFA* conditions with 30 bar oxygen, the rate determining step shifts to biomass oxidation.[27,160,161,164,165]

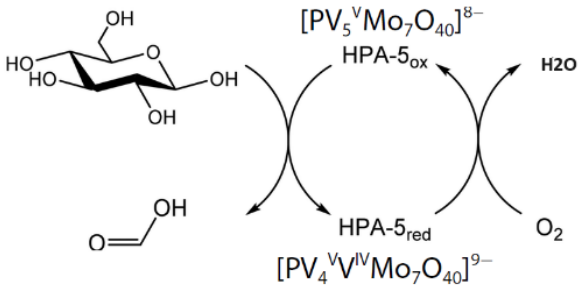

Figure 27: Catalytic cycle of the *OxFA* process. Adapted from *He et al*. and *Poller et al.*[166]

In general, the conversion of biomass can be divided into two key steps: (a) oxidative cleavage of C-C bonds in the substrate enabled by the catalyst and (b) regeneration of the POM catalyst through re-oxidation by molecular oxygen.[161] A detailed reaction sequence is outlined in Figure 28. The initial step involves an oxidative C–C bond cleavage by the elimination of water, resulting in erythrose and glyoxal as intermediates. In a subsequent oxidation step, erythrose is further converted into glyoxal and glycolaldehyde through the insertion of an additional oxygen atom from the POM catalyst, again

with concurrent water loss. In the final step, both glyoxal and glycolaldehyde are oxidized to form formic acid and carbon dioxide.[102,167,168]

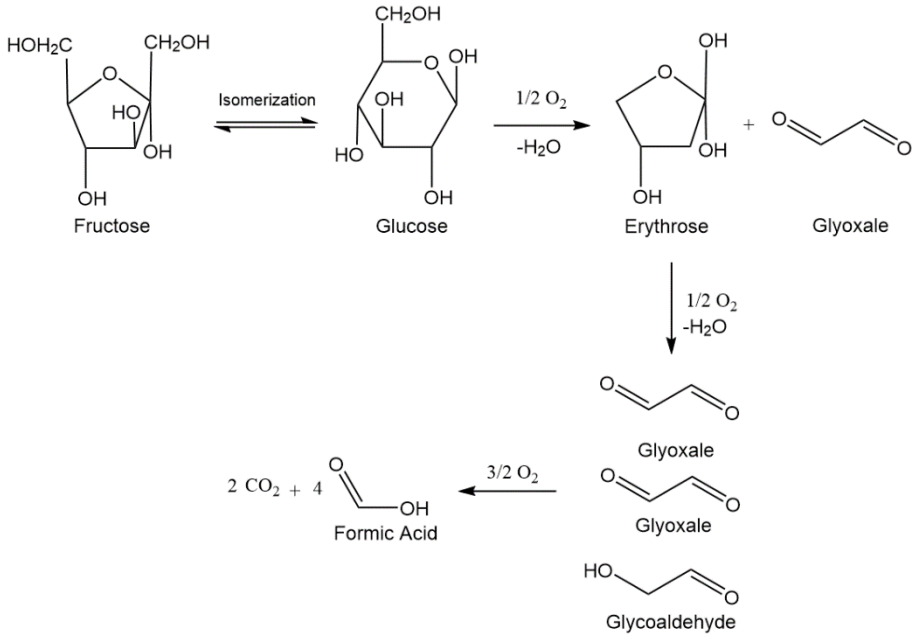

Figure 28: Reaction pathways for glucose conversion to formic acid.[168]

Conversion of CO_2 to DME

POMs exhibiting remarkable catalytic activity in the synthesis of DME and have been subject of various studies.[169,170–172] One of their key features is the presence of a high density of *Brønsted* acidic sites, which not only exhibit greater water tolerance compared to the *Lewis* acidic sites of γ-Al_2O_3 but also promote high catalytic activity at lower temperatures. This is particularly important, as it avoids the formation of undesirable by-products, such as hydrocarbons and coke.[121,123,173] *Alhaarbi et al.* could demonstrate an exhibited superior catalytic performance for DME formation from MeOH for various tungsten Keggin-type HPAs compared to H-ZSM-5 catalysts.[174] *Peinado et al.* further explored the catalytic potential of POMs by supporting $H_4[SiW_{12}O_{40}]$ on various materials, such as boron nitride, CeO_2, ZrO_2, SiO_2, TiO_2, and Al_2O_3. Their study showed that $H_4[SiW_{12}O_{40}]$, especially supported on ZrO_2, TiO_2, or SiO_2 created strong catalyst-support interactions, leading to enhanced catalytic activity compared to bulk $H_4[SiW_{12}O_{40}]$, and even outperformed conventional γ-Al_2O_3.[172] Similarly, *Ladeira et al.* found that TiO_2-supported $H_3[PW_{12}O_{40}]$ and $H_4[SiW_{12}O_{40}]$ displayed improved catalytic performance compared to the bulk HPAs due to weaker water interactions, allowing for faster exchange between MeOH and water, as well as better access of MeOH to catalytic active sites.[175] Other catalysts with notable activity include unsupported $H_3[PW_{12}O_{40}]$[176] as well as vanadium substituted $H_3[PW_{12}O_{40}]$ ($H_{3+x}[PW_{12-x}V_xO_{40}]$)[177],$H_3[PW_{12}O_{40}]$/BN[178] and $H_3[PW_{12}O_{40}]$/MCM-41[179].

POMs have not only been applied in the single MeOH dehydration step but have also been incorporated into bifunctional catalyst systems for direct CO_2 hydrogenation to DME. A notable recent approach utilized Cu/ZnO/ZrO_2 as the metallic function, combined with $H_4[SiW_{12}O_{40}]$ supported on Al_2O_3 or ZrO_2 as the acidic center, in a physical mixture. This study provided the first experimental and theoretical proof that direct DME synthesis from CO_2 is favorable compared to DME synthesis from MeOH, achieving higher CO_2 conversion and DME yields.[180] Other catalyst systems involved Cu/ZrO_2 combined with $H_3[PMo_{12}O_{40}]$/K10[170] or $H_3[PW_{12}O_{40}]$/K10[170] as well as halloysite nanotube-supported

CuZnO-$H_3PW_{12}O_{40}$.[181] *Kubas et al.* explored physical mixtures of Cu/ZnO/ZrO_2 and $H_3[PW_{12}O_{40}]$ or $H_4[SiW_{12}O_{40}]$ supported on different materials (e.g. γ-Al_2O_3, ZrO_2), testing 45 different combinations, with the supported $H_4[SiW_{12}O_{40}]$ demonstrating high stability and outperforming zeolite-based catalysts.[171]

Despite the promising advancements in using POMs for DME synthesis, research in the direct synthesis of DME from CO_2 is limited to the studies mentioned, which are particularly lacking an exploration of more diverse and substituted POM structures. Until yet, studies have primarily focused on a narrow range of unsubstituted, commercially available HPAs, indicating a significant opportunity for further investigation into novel POM-based catalysts. Expanding the scope of research in this field could unlock new catalytic possibilities and further improve the efficiency and sustainability of DME production from CO_2.

The CO_2 hydrogenation process to DME involves four main reactions, paralleling those of CO hydrogenation outlined in chapter 4.2.3. The process begins with the hydrogenation of CO_2 to MeOH (eq.2), followed by the dehydration of MeOH to DME (eq.4). Side reactions include the reverse water-gas shift reaction, producing CO and H_2O (eq.6), as well as MeOH formation from CO (eq.1). The overall reaction results in two molecules of CO_2 converting into one molecule of DME and three molecules of H_2O.[120,121,171]

$CO_2 + 3\,H_2 \rightleftharpoons CH_3OH + H_2O$	$\Delta H_{298\,K}$ = - 49 kJ/mol	eq.2
$2\,CH_3OH \rightarrow CH_3OCH_3 + H_2O$	$\Delta H_{298\,K}$ = - 24 kJ/mol	eq.4
$CO_2 + H_2 \rightleftharpoons CO + H_2O$	$\Delta H_{298\,K}$ = 42 kJ/mol	eq.6
$CO + 2\,H_2 \rightarrow CH_3OH$	$\Delta H_{298\,K}$ = - 91 kJ/mol	eq.1

4.3.2 Heterogeneous Metal Oxide Catalysts

In heterogeneous catalysis, the catalyst exists in a different phase than the reactants, commonly used as a solid interacting with gaseous or liquid reactants. This phase distinction offers several advantages compared to homogeneous systems, particularly in terms of catalyst recovery and recyclability, as the catalyst can be more easily separated from the reaction mixture. Heterogeneous catalysts also generally exhibit high thermal stability, allowing them to perform effectively under elevated temperatures and pressures. This makes them ideal for large-scale industrial processes where durability and ease of handling are critical.[182,183]

4.3.2.1 Heterogenization of Polyoxometalates

One of the challenges associated with the use of POMs as catalysts, particularly in industry, stems from their use in homogeneous catalysis, which presents several inherent limitations. These include extensive and cost-effective recovery and recycling. As well as the considerable difficulty in regenerating deactivated or “aged” catalytic species. Consequently, significant research has been directed towards their heterogenization in order to combine the intrinsic catalytic benefits of POMs with the resilience and ease of handling required in industrial settings. The heterogenization of POMs can be classified into two main strategies: solidification and immobilization (Figure 29).[182–184]

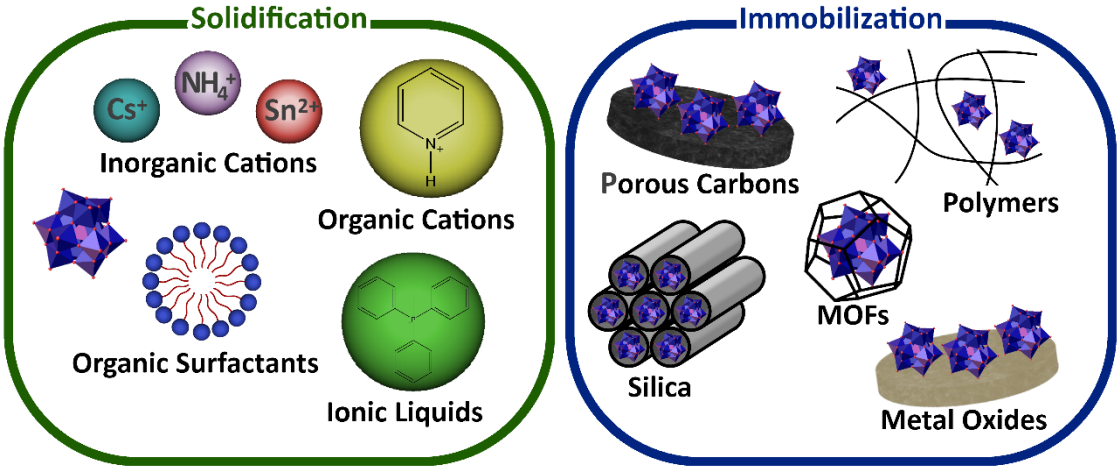

Figure 29: Methods for heterogenization of polyoxometalates. Adapted from *Mizuno et al.*[185] and *Zhou et al.*[186]

Solidification involves the transformation of homogeneous POMs into insoluble, complexed ionic materials by replacing the commonly used H^+ counterions of polyanions with suitable cations. These counter-cations are selected based on their composition, charge, size, shape, and hydrophobicity, and may include inorganic cations (e.g. NH_4^+, Cs^+, Na^+, K^+) or organic cations (e.g. amines, phosphides, surfactants, or ionic liquids (ILs)). Typically, this process is achieved via precipitation from aqueous POM solutions. Large alkali metals and transition metals are commonly used as counterions, and research increasingly aims to adapt these materials for more sustainable applications.[184–187] A notable example is the Cs-substituted $Cs_xH_{4-x}[SiW_{12}O_{40}]$ catalyst developed by *Pesaresi et al.* with catalytic activity for the transesterification of C4 and C8 triglycerides, used for biodiesel production.[188] Organic counterions - compared to inorganic counterions - provide a broader range of modification options for POM anions due to their diverse functional groups. This allows adjustments to surface properties, such as hydrophilicity or hydrophobicity, and improves the compatibility to organic substrates, making them well-suited for liquid-phase organic reactions. Commonly used organic modifiers include amines, surfactants, and ionic liquids.[186] *Zhao et al.* prepared amino acid-functionalized $H_3[PW_{12}O_{40}]$ catalysts, which were successfully applied for the simultaneous transesterification of triglycerides and esterification of fatty acids in a one-pot biodiesel production, even for low-quality feedstocks.[189] Similarly, *Rafiee et al.* synthesized phosphotungstate-based POM-ILs using sulfonated pyridinium cations, demonstrating their efficiency in the selective oxidation of thioethers and thiophenes, as well as in model-oil desulfurization, suggesting potential in real diesel desulfurization.[190] Nevertheless, a significant challenge in solidification remains the formation of complexes with small particle sizes, particularly in metal-POM complexes. These complexes often form colloidal dispersions, complicating catalyst separation and limiting scalability for industrial applications.[184]

Immobilization, on the other hand, entails anchoring POMs onto support materials through adsorption, covalent bonding, or counter-ion exchange. The immobilization of POMs on porous supports allows for highly and uniformly dispersed active centers. Advances in materials science have introduced new functional supports, accelerating the development of immobilized POM catalysts. A key challenge in designing efficient heterogeneous POM catalysts lies in selecting the appropriate polyanions and supports to create optimal microenvironments, such as pore structure and surface properties, tailored to specific reactions. A wide range of supports have been utilized for the immobilization of POMs, such as mesoporous silica, metal-organic frameworks (MOFs), polymers, metal oxides, magnetic nanoparticles, porous carbons, and zeolites. Immobilization methods encompass techniques such as impregnation, sol-gel processes, electrostatic interactions, ion

exchange, encapsulation, substitution, and covalent grafting. The most frequently used method for immobilizing POM-based compounds is the traditional, simple wet impregnation of POMs onto inert solid supports.[184,186,191] Significant efforts have been dedicated to advancing sustainable applications with supported POMs. For example, *Zhang et al.* demonstrated that $H_3[PW_{12}O_{40}]$ encapsulated within the MOF MIL-101 serves as an efficient and reusable catalyst for the dehydration of carbohydrates - especially fructose - into 5-hydroxymethylfurfural, a platform chemical for producing liquid fuels and fine chemicals.[192] Beyond increasing surface area and enhancing the stability of POMs, immobilization has also been shown to improve catalytic activity. For example, in aerobic oxidations, POMs supported on activated carbon (AC) demonstrated significantly higher catalytic performance compared to other high-surface-area supports like SiO_2 and Al_2O_3.[185] *Neumann et al.* suggested that, for POM/AC complexes, the quinone species on the surface of activated carbon act as co-catalysts. These quinones interact with the POMs to form semiquinone intermediates, thereby significantly enhancing the oxidative strength of the system.[193] Supported POMs also have been successfully applied for the direct synthesis of DME from CO_2, as discussed in chapter 4.3.1.

4.3.2.2 $Cu/ZnO/Al_2O_3$ for Synthesis of Methanol

The industrial production of MeOH began in the 1920s with a high-pressure process patented by *BASF AG* utilizing syngas from coal gasification. The catalysts, based on zinc/chromium oxide, were particularly resistant to catalyst poisons from syngas such as sulfur and chlorine. However, achieving satisfactory MeOH yields of more than 10 % required high operational conditions (350 - 400 °C, 300 bar), also leading to methane and other light hydrocarbons as by-products. Due to its high energy demands and inefficiency, this method was phased out by the mid-1980s. In 1966, *Imperial Chemical Industries* developed a more efficient process operating at 300 °C and 100 bar. This improvement was made possible by the usage of sulfur-free syngas derived from methane steam reforming, allowing for the employment of Cu/ZnO catalysts stabilized with Al_2O_3. These Cu-based catalysts exhibited higher activity and selectivity than the previously used $ZnO\text{-}Cr_2O_3$ catalysts. Reducing the operating temperature also helped minimize the formation of light hydrocarbons as by-products. *Lurgi GmbH* further optimized this process, reducing operating conditions to 250 - 350 °C and 40 - 50 bar. Today, $Cu/ZnO/Al_2O_3$ catalysts form the foundation for most modern MeOH synthesis processes, except in cases where sulfur contaminants are present. The composition of these catalysts varies depending on the manufacturer, with CuO content ranging from 20 – 80 wt.%, ZnO from 15 – 50 wt.%, and Al_2O_3 between 4 – 30 wt.% (Figure 30).[103,108,183]

Manufacturer	Cu (wt%)	Zn (wt%)	Al (wt%)	Other
IFP	45–70	15–35	4–20	Zr-2–18
Synetix (formerly ICI)	20–35	15–50	4–20	Mg
BASF	38.5	48.8	12.9	Rare earth oxide-5
Shell	71	24	12	
Sud Chemie	65	22	31	
DuPont	50	19	17	
United Catalysts	62	21	17	
Haldor Topsoe MK-121	>55	21–25	8–10	
Mitsubishi Gas Chemical Company	63.6	33.4	3	
Ammonia Casale	30	50	3	Cr (16)
Lonza	40	20		Zr (40)
AIST, RITE	45.2	27.1	4.5	Zr (22.6) Si (0.6)
YKK Corporation	76.3	11	12.7	

Figure 30: Methanol synthesis catalysts - Key manufacturers and specifications.[108] Adapted and originally published from *Bozzano*.[194]

Despite its widespread industrial use, the exact mechanism and active phase of the $Cu/ZnO/Al_2O_3$ catalyst in MeOH synthesis have long remained uncertain. *Klötzer et al.* clarified that the catalytic pathway and active phase are significantly influenced by the composition of the reaction gas (Figure 31). CO_2 hydrogenation proceeds via formate and methoxy intermediates, while CO reduction predominantly follows the methoxy pathway. Under CO_2-rich conditions, ZnO tends to form clusters or nanoparticles, whereas Cu-Zn surface alloy is favored in the presence of pure CO. These findings underscore the role of CO in promoting the formation of the Zn-Cu alloy, which acts as the active phase and enhances the efficiency of CO_2-to-MeOH conversion.[195]

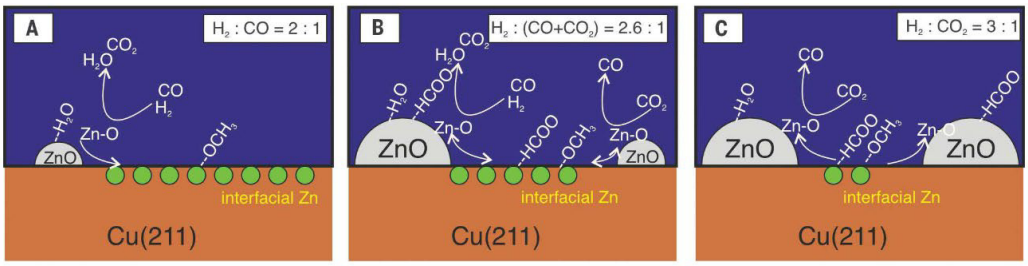

Figure 31: Illustration of the Zn/ZnO/Cu(211) surface reaction dynamics for methanol synthesis, influenced by the transition from CO-rich reducing conditions (A) to CO_2-rich oxidizing environments (C).[195]

The co-precipitation method is currently the most widely adopted technique for producing $Cu\text{-}ZnO\text{-}Al_2O_3$ catalyst systems. This method typically involves precipitating metal salts with basic agents such as sodium carbonate or ammonium carbonate under controlled conditions, including concentration, temperature, stirring speed, and pH value. The material undergoes a drying phase at approximately 120 °C, after which it is calcined at temperatures between 300 - 500 °C, transforming it into finely dispersed metal oxides. These oxides are then shaped into cylindrical pellets with typical dimensions of 4 – 6 mm in both diameter and height, which represent the commercial catalyst forms. For MeOH synthesis, the catalyst is first reduced using hydrogen (0.5 - 2 %) under a nitrogen atmosphere at temperatures between 150 - 250 °C. In its active state, the Cu surface area of commercial catalysts ranges from 20 - 30 m^2/g.

Typically, $Cu/ZnO/Al_2O_3$ catalysts have a lifespan of about two years, with around one-third of their activity being lost within the first 1000 operational hours. This loss is often compensated by gradually increasing the reaction temperature. Deactivation can occur through various mechanisms, such as catalyst poisoning from syngas impurities and thermally induced sintering, both of which contribute to a decline in catalytic performance. While innovations in syngas production have significantly decreased poisoning effects, thermal deactivation mechanisms such as sintering or phase segregation remain persistent issues. Catalyst sintering is exacerbated by the presence of H_2O, which poses a particular challenge in MeOH synthesis from CO_2, due to the large amounts of H_2O, generated in the process. Numerous research groups focus on creating novel catalyst systems for MeOH synthesis by exploring alternative formulations and materials. The most straightforward modifications often involve $Cu/ZnO/Al_2O_3$ catalyst systems enhanced with various dopants. While these dopants may lead to slight improvements, they typically do not result in drastic changes to overall catalyst longevity.[44,103,108]

4.3.2.3 In_2O_3/ZrO_2 for Synthesis of Methanol

One promising approach as alternative catalyst for the conversion of CO_2 to MeOH are catalysts based on In_2O_3 to avoid the drawbacks of conventional $Cu/ZnO/ZrO_2$ catalysts. In_2O_3 is a wide-bandgap

semiconductor, featuring a direct bandgap of approximately 2.8 - 2.9 eV. It crystallizes mainly in its body-centered cubic most stable bixbyite-type structure. When doped with tin, it exhibits high electrical conductivity alongside transparency in the visible spectrum, making it an effective material for use as transparent electrodes in applications like flat-panel displays and solar cells.[196] Due to their physiochemical properties and redox properties, In_2O_3-based materials are also promising for use in gas and biosensing applications[197], as well as in catalytic reactions such as in photocatalytic or electrochemical reactions[198], denitrification reactions [199] or in MeOH steam reforming[200].

Bielz et al. demonstrated, through MeOH steam reforming and hydrogenation experiments, that In_2O_3 features oxygen vacancies under conditions relevant to MeOH synthesis.[201] *Ye et al.* had previously conducted theoretical analyses of CO_2 hydrogenation on In_2O_3 using density functional theory, suggesting that In_2O_3 could be highly active for this conversion. Their findings revealed that oxygen vacancies facilitate both CO_2 activation and hydrogenation, while also stabilizing critical intermediates.[202,203] *Sun et al.*[204] provided the first experimental evidence of the effectiveness of In_2O_3 in CO_2-to-MeOH conversion, though with only moderate MeOH yield (7.1 %) and selectivity (55 %) at 330 °C and 40 bar. A breakthrough came in 2016, when *Martin et al.* achieved a remarkable 100 % selectivity for MeOH by supporting In_2O_3 on ZrO_2 under conditions comparable to those in industrial applications.[205]

Ye et al. initially proposed a mechanism (Figure 32), suggesting that the reaction proceeds via a defective In_2O_3 surface with oxygen vacancies. In this pathway, CO_2 binds to surface oxygen atoms, leading to the formation of carbonate-like species. Simultaneously, H_2 dissociates upon adsorption, forming surface hydroxyl groups.[202,206]

The concentration of oxygen vacancies on In_2O_3 appears to be the key factor influencing MeOH synthesis efficiency. Studies have shown that variations in the concentration of oxygen vacancies can directly impact catalytic performance.[207] *Nørskov et al*. demonstrated that an In_2O_3(110) surface with a higher degree of reduction and abundant oxygen vacancies performs less effectively in MeOH synthesis compared to an In_2O_3(111) surface with fewer vacancies.[208] Additionally, *Zhang et al.* examined the connection between the concentration of oxygen vacancies and the reduction level of In_2O_3 and an elevated MeOH yield.[209] Despite its favorable activity and high MeOH selectivity, In_2O_3 often faces deactivation at higher temperatures due to over-reduction. Studies have shown that only surface oxygen vacancies in In_2O_3 are beneficial for MeOH synthesis from CO_2 hydrogenation. However, the diffusion of these vacancies into the bulk leads to further reduction, which diminishes catalyst stability. While surface re-oxidation of reduced In_2O_3 particles can occur through interaction with CO_2, restoring the fully oxidized bulk structure generally requires oxygen.[208,210]

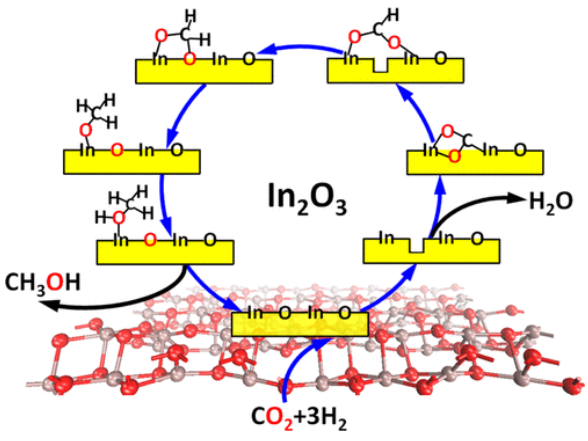

Figure 32: Reaction mechanism for CO_2 hydrogenation to methanol.[202]

The catalytic activity of In_2O_3, influenced by its reduction level and concentration of oxygen vacancies, can be enhanced through specific modifications that promote primarily vacancy formation. One approach involves supporting In_2O_3 on materials like ZrO_2, while another effective method is doping with metals such as Pd or Pt.[207,211]

Among various ZrO_2 supports, monoclinic ZrO_2 has proven particularly effective, enhancing both CO_2 adsorption and the dispersion of In_2O_3.[212] Studies by *Tsoukalou et al.* demonstrated that the ZrO_2 phase significantly impacts the structural and catalytic properties of nanocrystalline In_2O_3, showing that the monoclinic lattice stabilizes In_2O_3 and prevents over-reduction to In^0 during CO_2 hydrogenation to MeOH.[213] This was further corroborated by in situ spectroscopic measurements by *Zhang et al.*[209] *Frei et al.* reported that monoclinic ZrO_2 notably enhances catalytic activity. This effect arises because the epitaxial alignment of In_2O_3 on m-ZrO_2 enables a highly dispersed active oxide layer. The less ideal lattice match of the monoclinic phase introduces tensile strain, fostering additional oxygen vacancies within the In_2O_3 structure.[214] Furthermore, electron transfer from m-ZrO_2 to In_2O_3 is essential for boosting MeOH synthesis activity, by facilitating H_2 dissociation and accelerating the conversion of HCOO* to CH_3O* through hydrogenation.[215]

An alternative approach to enhancing In_2O_3 catalysts involves doping with various metals to generate additional active sites and facilitate H_2 activation. Many studies have focused on In-metal alloys, predominantly incorporating palladium as the second metal.[206] InPd alloys, in particular, have demonstrated improved stability and enhanced MeOH selectivity (> 80 %) compared to conventional $Cu/ZnO/Al_2O_3$ catalysts.[216] Palladium nanoparticles are known to promote efficient hydrogen dissociation, providing the necessary hydrogen for hydrogenation reactions while simultaneously preserving the density of oxygen vacancies.[217] Other noble and transition metals, including Pt[218], Rh[219], Ru[220], Au[221], Al[222], Ni[223] or Cu[224] have also been employed to dope In_2O_3. These metals enhance the catalyst's performance by facilitating CO_2 activation, stabilizing intermediates, improving H_2 activation, or introducing more oxygen vacancies as active sites, each contributing to a significant boost in catalytic activity.[206]

5. Objective of the Thesis

This work focuses on exploring various catalytic systems pivotal for implementing sustainable chemical processes. Specifically, metal-oxide based catalysts were investigated, with a particular focus on two representative systems: polyoxometalates (POMs) and indium oxide (In_2O_3)-based catalysts. POMs were studied in both liquid-phase reactions, enabling the selective conversion of biomass-derived substrates into lactic and formic acid, and in gas-phase reactions, where their combined acid–redox properties were applied in CO_2 hydrogenation to dimethyl ether. In contrast, In_2O_3-based catalysts were studied for gas-phase hydrogenation from CO2 to methanol.

The catalysts were specifically designed, synthesized, and systematically investigated to address critical aspects such as stability, activity under varying conditions, and adaptability to different reaction pathways. These efforts contribute to developing scalable and sustainable solutions for replacing fossil-based feedstocks with renewable alternatives, thereby aligning chemical production with the principles of a circular and climate-neutral economy.

6. Cumulative Section and Synopsis

This chapter weaves together the outcomes of multiple studies and provides a comprehensive synopsis of the thesis, offering an overview of the progress made in developing catalytic systems for specific chemical transformations. The first part address a homogeneous (first study) and heterogeneous (second study) liquid-phase reactions to transform biomass into lactic acid (LA) and formic acid (FA). Meanwhile, the third and fourth study shift to gas-phase reactions, focusing on CO_2 hydrogenation for the production of dimethyl ether (DME) (third study) and methanol (MeOH) (forth study). Connections between the studies are explored to illustrate how they complement one another, building a comprehensive picture of the research progress.

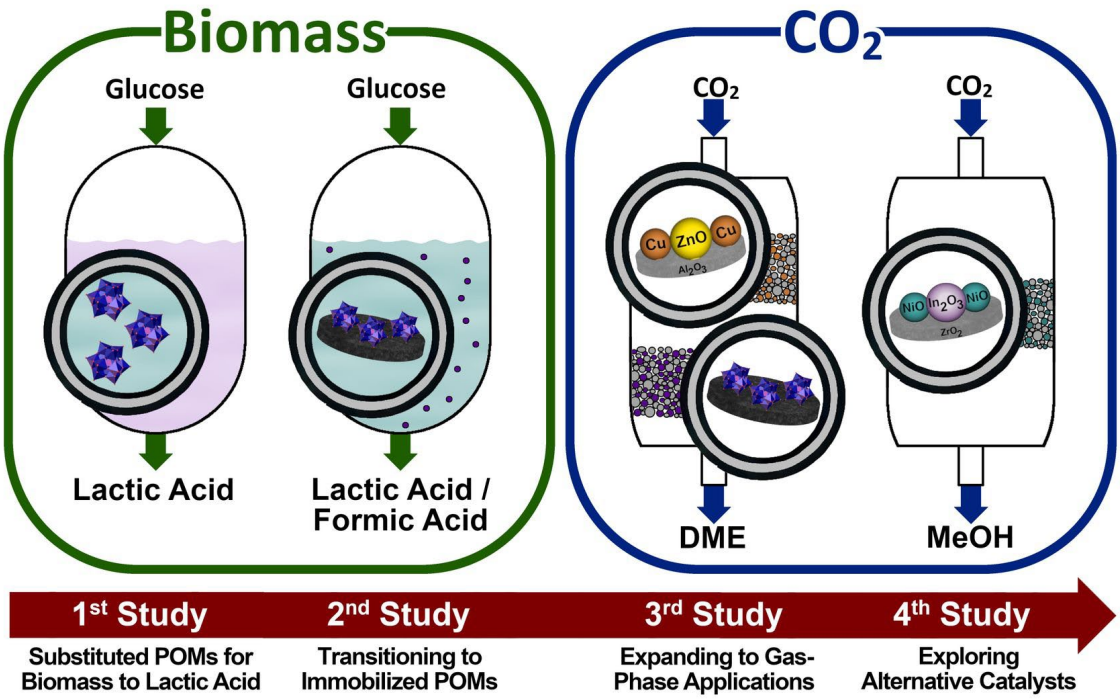

Figure 33: Overview of the research conducted in this thesis.

The aim of this chapter is to highlight how these studies contribute to the understanding and advancement of catalytic systems, emphasizing their objectives, methodologies, and key outcomes. The chapter is divided into four subchapters, each corresponding to a peer-reviewed publication. These subchapters focus on specific catalytic applications, illustrating the individual contributions of each study to the overall research objectives:

6.1 Substituted Polyoxometalates for Liquid-Phase Conversion of Biomass to Lactic Acid, in:

A. Wesner, J.-C. Raabe, M. J. Poller, S. Meier, A. Riisager, J. Albert, Conversion of Sugars to Lactic Acid using homogeneous Niobium-substituted Polyoxometalate Catalysts, *Chem. Eur. J.*, **2024**, e202402649.

6.2. Transitioning to Immobilized Systems: Liquid-Phase Conversion of Biomass to Lactic and Formic Acid, in:
A. Wesner, M. Papajewski, L. Schidowski, C. Ruhmlieb, M. Poller, Supported $H_8PV_5Mo_7O_{40}$ on activated carbon: Synthesis and Investigation of influencing factors for catalytic performance, *Daltons Trans.*, **2024**, *53*, pp. 14065-14076.

6.3. Expanding to Gas-Phase Applications: Immobilized Polyoxometalates for CO_2 Conversion to Dimethyl ether, in:
A. Wesner, N. Herrmann, L. Prawitt, A. Ortmann, J. Albert, M. J. Poller, Study of supported heteropolyacid catalysts for one step DME synthesis from CO_2 and H_2, *RSC Advances*, **2025**, *15*, pp. 38-47.

6.4. Exploring Alternative Catalysts: In_2O_3-Based Catalysts for Gas-Phase CO_2 Conversion to Methanol, in:
A. Wesner, P. Kampe, N. Herrmann, S. Eller, C. Ruhmlieb, J. Albert, Indium-based Catalysts for CO_2 Hydrogenation to Methanol: Key aspects for Catalytic Performance, *ChemChatChem*, **2023**, *15*, e202301125.

6.1 Substituted Polyoxometalates for Conversion of Biomass to Lactic Acid

The first study focuses on the exploration of specific element-substituted POMs as catalysts for the homogeneous catalyzed conversion of biomass into lactic acid, a versatile platform chemical with significant industrial applications. Building on the established potential of biomass as a renewable feedstock, this study delves into optimizing its catalytic conversion using tailored POM systems. Although previous research has demonstrated the feasibility of using POMs for this purpose, the field still requires a deeper understanding of how structural modifications influence catalytic performance. This study addresses this knowledge gaps by exploring the impact of heteroatom substitution and evaluating how these modifications influence the catalytic activity for the chemo catalytic synthesis of lactic acid. Through this approach, this study aimed to deepen the understanding of POMs in transforming biomass-derived substrates to lactic acid and to enhance their potential as versatile and effective catalysts for sustainable biomass conversion.

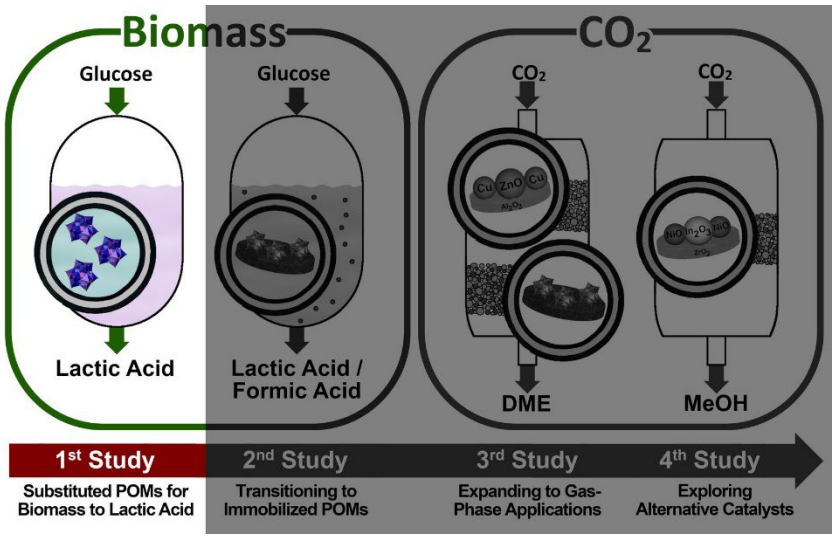

Figure 34: Scope of the first study: Substituted POMs for biomass to lactic acid.

Therefore, specific element-substituted POMs in the form of heteropolysalts were utilized. The base catalyst, $Na_3[PMo_{12}O_{40}]$, was systematically modified by substituting molybdenum with varying amounts of V and Nb. These substitutions ranged from the Vanadium-rich $Na_6[PV_3Mo_9O_{40}]$ to mixed substitutions such as $Na_6[PV_2NbMo_9O_{40}]$ and $Na_6[PVNb_2Mo_9O_{40}]$, and finally to the niobium-dominant $Na_5[PNb_2Mo_{10}O_{40}]$ ($NaNb_2$) and $Na_6[PNb_3Mo_9O_{40}]$. For catalyst screening, dihydroxyacetone was selected as a model substrate, as it represents a simple carbohydrate and a key intermediate in the breakdown of higher carbohydrates.[225] Reactions were carried out in the liquid phase under nitrogen atmosphere using water as the reaction medium. Substituting the catalyst with vanadium and niobium consistently improved the lactic acid yield, with $Na_5[PNb_2Mo_{10}O_{40}]$ emerging as the most active catalyst. Building on this, $Na_5[PNb_2Mo_{10}O_{40}]$ was tested with more complex substrates, including monosaccharides (glucose, fructose, mannose, xylose) and disaccharides (sucrose, cellobiose). Lactic acid was successfully produced in all reactions, though black solid residues (humins) were observed as by-products. Structural stability of the catalyst after reaction was confirmed through Infrared and Raman spectroscopy as well as elemental analysis, demonstrating its robustness under the applied reaction conditions. These results highlight the potential of Nb-substituted POMs not only as effective catalysts for lactic acid synthesis but also as robust systems for broader applications in biomass conversion.

Chemistry–A European Journal
Research Article
doi.org/10.1002/chem.202402649
Chemistry Europe
European Chemical Societies Publishing
www.chemeurj.org

Conversion of Sugars to Lactic Acid using Homogeneous Niobium-Substituted Polyoxometalate Catalysts

Anne Wesner,[a] Jan-Christian Raabe,[a] Maximilian J. Poller,[a] Sebastian Meier,[b] Anders Riisager,[b] and Jakob Albert*[a]

The catalytic conversion of biomass into high-value chemicals is an increasing field of research. This study uniquely investigates the use of various Keggin-type heteropoly salts (HPS) for the chemical conversion of sugars into lactic acid under mild conditions of 160 °C and 20 bar N_2. In the first phase, Nb– and V–substituted HPSs were employed to synthesize lactic acid from dihydroxyacetone, an intermediate in the conversion of sugars to lactic acid. Results indicated that increasing the Nb content within the Keggin structure enhances the yield of lactic acid while reducing the formation of the byproduct acetaldehyde. A correlation was established between the redox activity of the HPS and the catalytic performance. The most active catalyst, $Na_5[PNb_2Mo_{10}O_{40}]$, ($NaNb_2$) achieved a lactic acid yield of 20.9% after 1 h of reaction. In the second phase of the study, $NaNb_2$ was applied for the conversion of different sugars including glucose, fructose, mannose, sucrose, xylose, and cellobiose. It was demonstrated that the catalyst remains active for complex hexoses, achieving lactic acid yields of up to 12%. Post-mortem analysis using infrared (IR) and Raman spectroscopy, nuclear magnetic resonance (NMR), and inductively coupled plasma optical emission spectrometry (ICP-OES) confirmed the stability of $NaNb_2$.

Introduction

Addressing the urgent challenge of replacing fossil resources, which currently fulfill over 90% of our energy and chemical needs, is crucial for mitigating carbon emissions and fostering sustainable development. Biomass, a globally available resource, emerges as a promising alternative feedstock for the production of platform chemicals. It has the potential to partially, or in certain cases fully, replace the current fossil raw materials in established chemical processes. A central focus for future research lies in developing new and innovative processes for utilizing alternative raw materials, such as biomass.[1]

Lactic acid (LA) is a highly valuable chemical, which is widely used in food as well as in the pharmaceutical or cosmetics industry. Furthermore, it can be used as a polymer precursor for the synthesis of polylactic acid as a biodegradable polymer, which contributes to reducing microplastic pollution.[2] The global demand for LA was 3.5 billion USD in 2022 and is expected to rise to 7.9 billion USD in 2032 due to the increasing demand for biodegradable plastic as well as fermented products such as yoghurt or butter.[3] Yet, the existing anaerobic fermentation method for the production of LA is plagued by drawbacks such as high costs and energy demand, long reaction times due to the low reaction rate, low productivity, and the generation of waste salts.[4] Additionally, biological processes are very sensitive to changes of pH or temperature.

Driven by advantages like high productivity and cost-effectiveness, attention has been turned to alternative and more efficient chemo–catalytic routes for LA production from biomass.[4b,5] In these chemical routes, the retro-aldol reaction of carbohydrates is the rate determining step in the conversion to LA or other valuable C2-C4 chemicals. Most of these processes are heterogeneously catalyzed by zeolites.[6] However, some homogeneous catalysts, such as $Ca(OH)_2$,[7] Sn halides,[8] Al(III) and Cr(II) salts[9] or YCl_3,[10] have also been employed. Vanadium salts, especially $VOSO_4$, have also been applied as non-toxic and cheap catalysts for the conversion of sugars to LA in an aqueous solution.[11] However, only a few studies were able to produce LA under mild conditions (below 200 °C).

Recently, Keggin-type polyoxometalates (POM) have been shown to be promising catalysts for the conversion of biomass to LA under nitrogen atmosphere.[12] Keggin-type POMs have the general molecular formula $[XM_{12}O_{40}]^{n-}$, where the metal positions M are preferably occupied by transition-metals from Group 6 of the periodic table (Mo or W) in their highest oxidation states. The position X is a placeholder for hetero-elements such as P or Si. Since the Keggin structure requires the presence of a hetero-element, this type of POM structure belongs to the class of heteropolyanions (HPA).[13] The properties of a Keggin structure are significantly influenced by the choice of cations (e.g. alkali metal cations). These compounds are then called heteropolysalts (HPS) whereby the counter-cation determines the solubility properties and acidity of these compounds.[14]

[a] A. Wesner, J.-C. Raabe, M. J. Poller, J. Albert
Institute of Technical and Macromolecular Chemistry, University of Hamburg, Bundesstraße 45, 20146 Hamburg, Germany
+49-(0)40 42838 4209
E-mail: jakob.albert@uni-hamburg.de
[b] S. Meier, A. Riisager
Department of Chemistry, Technical University of Denmark, Kemitorvet, 2800 Kgs. Lyngby, Denmark

Supporting information for this article is available on the WWW under https://doi.org/10.1002/chem.202402649

Through extensive research on Keggin-type POMs in the last decades, their potential as RedOx catalysts was discovered, as the metals are able to accept or release one or more electrons without structural changes.[15] In particular, the selective substitution of one or more framework metals with RedOx active transition elements like vanadium in its oxidation state +V (V^V) gave the POMs new properties that prove to be extremely useful in homogeneous RedOx catalytic applications.[16] From a synthetic point of view, V^V can be incorporated into the Keggin structure without much effort via a classic self-assembly synthesis.[17] However, the incorporation of the homologous Nb^V proves to be significantly more challenging since there are no water-soluble Nb^V precursor compounds readily available that can be used for this synthesis approach. An exception is the hexaniobate anion $[Nb_6O_{19}]^{8-}$, which is stable in highly alkaline aqueous solutions.[18] The latter was used in a recently published study for the synthesis of Nb^V substituted Keggin-type POMs via the formation of the Keggin-Lacunary anion $[PMo_9O_{34}]^{9-}$.[19]

Nb-based solid species, such as niobium oxides (e.g. Nb_2O_5) or mixed oxides (e.g. Nb_2O_5-Al_2O_3, Nb_2O_5-TiO_2), niobic acid/hydrated niobium pentoxide ($Nb_2O_5{\cdot}nH_2O$), niobium phosphate ($NbOPO_4$) or niobium molybdate ($LiNbMoO_6$), are utilized in a variety of catalytic applications, including photocatalysis, oxidation, dehydration and epimerization reactions.[20] However, research on homogeneous catalysis using Nb–based catalysts is exceedingly rare,[21] highlighting a significant need for further exploration in this area. This study therefore focuses on Nb–containing HPSs in homogeneous catalysis for converting sugars and sugar derivatives into LA.

Experimental Methods

Catalyst Preparation and Characterization

The original procedures for synthesis and characterization of the employed catalysts are published in a previous study.[19] Catalysts were characterized by elemental analysis via inductively coupled plasma optical emission spectroscopy(ICP-OES) and atomic absorption spectroscopy (AAS) to verify the elemental composition. The hydration water content was determined via thermogravimetric analysis (TGA). The integrity of the Keggin-type structure was verified by infrared (IR) spectroscopy (solid-state characterization). Analysis in aqueous solution was done by using nuclear magnetic resonance (NMR) spectroscopy via ^{31}P–NMR and ^{51}V–NMR, high-resolution ^{1}H-^{13}C heteronuclear single quantum coherence (HSQC) spectroscopy and square–wave–voltammetry (SWV). Comprehensive description of all catalysts is given in the Supplementary Information.

Catalyst Testing and Evaluation

All experiments for catalyst screening were performed in a 20 mL custom–built stainless–steel autoclave, with a glass inlet vial. For each experiment, 42 mg of catalyst and 100 mg substrate, both dissolved in 4 g H_2O, as well as a magnetic stirrer, coated with polytetrafluoroethylene, were added to the inlet vial. The vial was placed in the reactor, which was then closed and flushed three times with 25 bar of N_2 to remove residual air. Afterwards, the reactor was positioned in a temperature–controlled aluminum heating block and the reaction temperature was set to 160 °C and magnetic stirring (1000 rpm) was switched on. After one hour of reaction time, the stirring was stopped, and the reactor was immediately removed from the heating block and placed into an ice–cooled water bath. Once the reactor had cooled down to room temperature, it was vented. The glass vial containing the reaction solution was then removed from the reactor for analysis by High–Performance Liquid Chromatography (HPLC).

The conversion rates for all substrates (X), the yields for all products (Y), selectivities (S) and carbon balances (Cb) were calculated using the Equations (1–4) below:

$$X = \frac{n_{substrate,initial} - n_{substrate,final}}{n_{substrate,\ initial}} \cdot 100\,\% \quad (1)$$

$$Y = \frac{n_{product}}{n_{substrate,\ initial}} \cdot 100\,\% \quad (2)$$

$$S = \frac{Y}{X} \cdot 100\,\% \quad (3)$$

$$Cb = \frac{n_{C,initial}}{n_{C,final}} \cdot 100\,\% \quad (4)$$

In this context, $n_{substrate,initial}$ represents the initial quantity of substrate utilized, while $n_{substrate,final}$ indicates the amount of substrate remaining at the end of the reaction and $n_{product}$ is the amount of the desired product determined by HPLC. $n_{c,initial}$ and $n_{c,final}$ represent the total amount of carbon before and after reaction.

Results and discussion

Screening HPSs for Conversion of Dihydroxyacetone (DHA) into Lactic Acid (LA)

In the first part of the study, a variety of transition-metal substituted Keggin-type HPAs in the form of water-soluble sodium salts (HPSs) were employed for the transformation of DHA into LA in aqueous solution. The choice of sodium as a cation is a result of the synthetic procedure, which requires the use of precursors containing Na^+.[19] The exchange of the cation would require complex post-synthesis treatments such as crystallization or extractive removal using diethyl ether.

The catalysts used included the unsubstituted $Na_3[PMo_{12}O_{40}]$ (NaMo) as a benchmark and vanadium-substituted $Na_6[PV_3Mo_9O_{40}]$ (NaV_3) based on a former study.[12a] Additionally, various vanadium–niobium substituted HPSs were also tested, including $Na_6[PV_2NbMo_9O_{40}]$ (NaV_2Nb), $Na_6[PVNb_2Mo_9O_{40}]$ ($NaVNb_2$), $Na_4[PNbMo_{11}O_{40}]$ (NaNb), $Na_5[PNb_2Mo_{10}O_{40}]$ ($NaNb_2$), and $Na_6[PNb_3Mo_9O_{40}]$ ($NaNb_3$). All catalysts were subjected to comprehensive characterization using elemental and compositional analysis (ICP-OES, AAS, and TGA), optical and nuclear spectroscopy (FTIR/Raman, and NMR), as well as electrochemical analysis (SWV). Further details are reported in the Supplementary Information.

For the catalytic conversion of DHA to LA, the HPS were dissolved in an aqueous DHA solution, which was heated to 160 °C under an atmosphere of 20 bar N_2 for a duration of 1 h. These conditions were chosen based on previous work by D. Voß et al., who described nearly full conversion of glucose under these conditions.[12a] The desired reaction pathway proceeds from DHA through a keto–enol tautomerism of glyceraldehyde, followed by conversion via pyruvaldehyde to LA (Figure 1). The obtained yields of reaction products, as well as conversion rates for the various catalysts are summarized in Figure 2. Full details, including comprehensive mass balances, are provided in Tables S1 and S2.

In the control experiment without a catalyst, a conversion of DHA to pyruvaldehyde was determined (Y_{PA} = 21 %), of which only a minor fraction was already transformed into LA (Y_{LA} = 2.6 %). Upon addition of the synthesized HPSs, the conversion to pyruvaldehyde increased from 23 % (control) to 75 % (NaMo) and 85 % (NaV_3) whereas the respective LA yield increased to just above 8 % (Figure 2, Table S1).

Using Nb-substituted HPSs, the conversion of DHA increased further to 92–97 % (Figure 2, Table S1). Moreover, also the yield of LA steadily rose, starting at 10 % with NaV_2Nb, to 12 % with $NaVNb_2$ and 16 % with NaNb, and reaching a maximum of 21 % using $NaNb_2$ and $NaNb_3$. The increasing yield of LA was associated with the subsequent substitution of vanadium by niobium within the Keggin structure. Notably, the trend in the yield of undesired acetaldehyde was the exact opposite. The yield of acetaldehyde for the unsubstituted NaMo was 11 %, and with increasing substitution of vanadium by niobium, the yield of acetaldehyde decreased from 20 % (NaV_3) to 11 % ($NaNb_2$ and $NaNb_3$). These results suggest that LA undergoes further chemical conversion for lower niobium–content, leading to further oxidation into acetaldehyde (Figure 1).

A hypothesis for the differing behavior of HPSs with varying V or Nb content is that the redox properties, altered by metal substitution, are responsible for driving the predominant reaction mechanism. Therefore, SWV measurements of the different HPSs were conducted in aqueous solution. The determined redox potential is critical for assessing the oxidative properties of the catalyst. HPSs exhibit various two–electron redox processes, which can be modulated by the incorporation of various elements into the Keggin structure.[19,22]

SWV measurements (Figure 3) indicate that incorporating vanadium into NaMo induces a shift towards higher redox potentials compared to −380 mV for NaMo, for instance −370 mV for $NaVNb_2$, −345 mV for NaV_2Nb or −330 mV (NaV_3), respectively. Moreover, multiple peaks are observed in the voltammograms, for instance at −525 mV and −160 mV (NaV_3). This observation can likely be attributed to the additional redox processes of vanadium species, such as between V^V and V^{IV}.[22,23] These results help to explain the catalytic performance of NaMo in comparison to NaV_3. The increase in conversion from 75 % (NaMo) to 85 % (NaV_3) can be attributed to the incorporation of

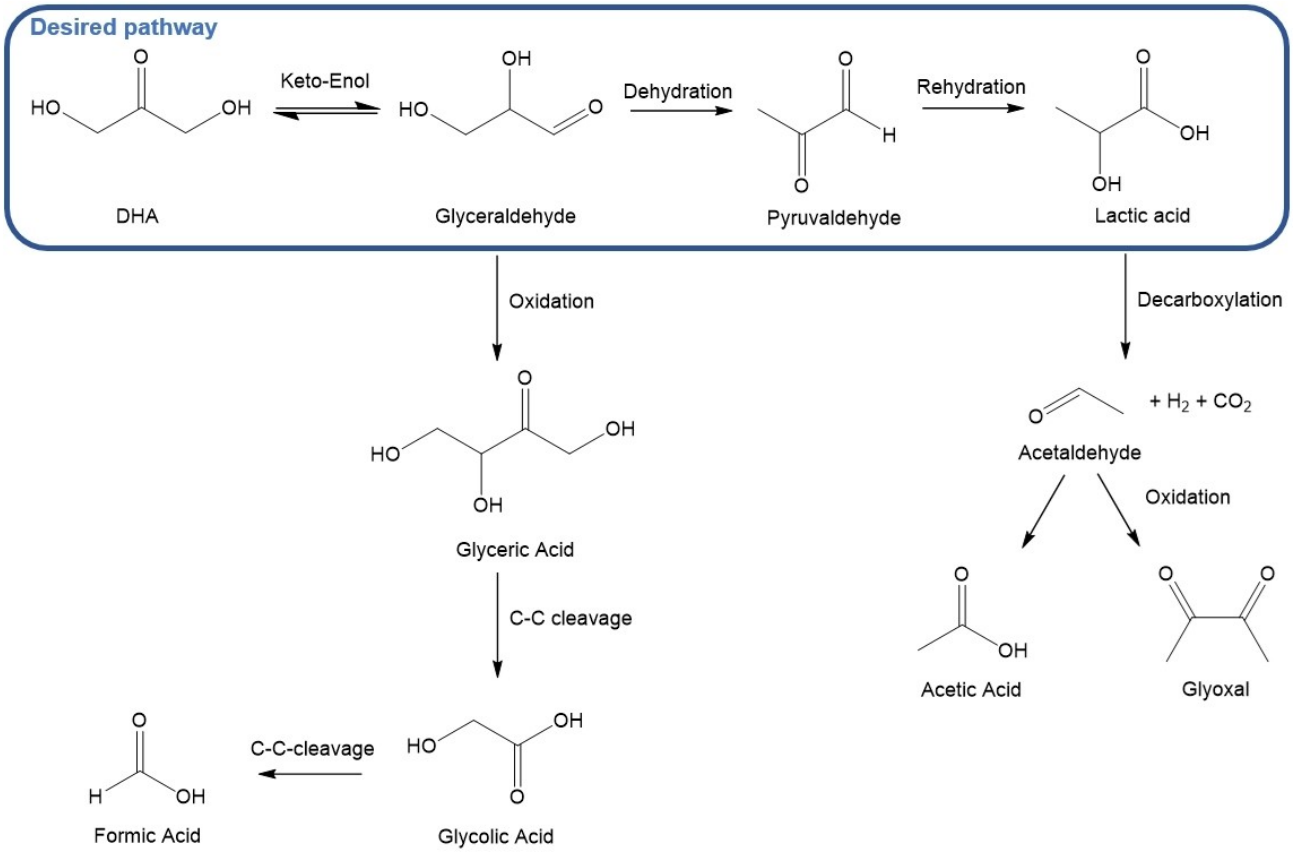

Figure 1. Desired reaction pathway and side reactions for the conversion of DHA to LA.[12a,20d]

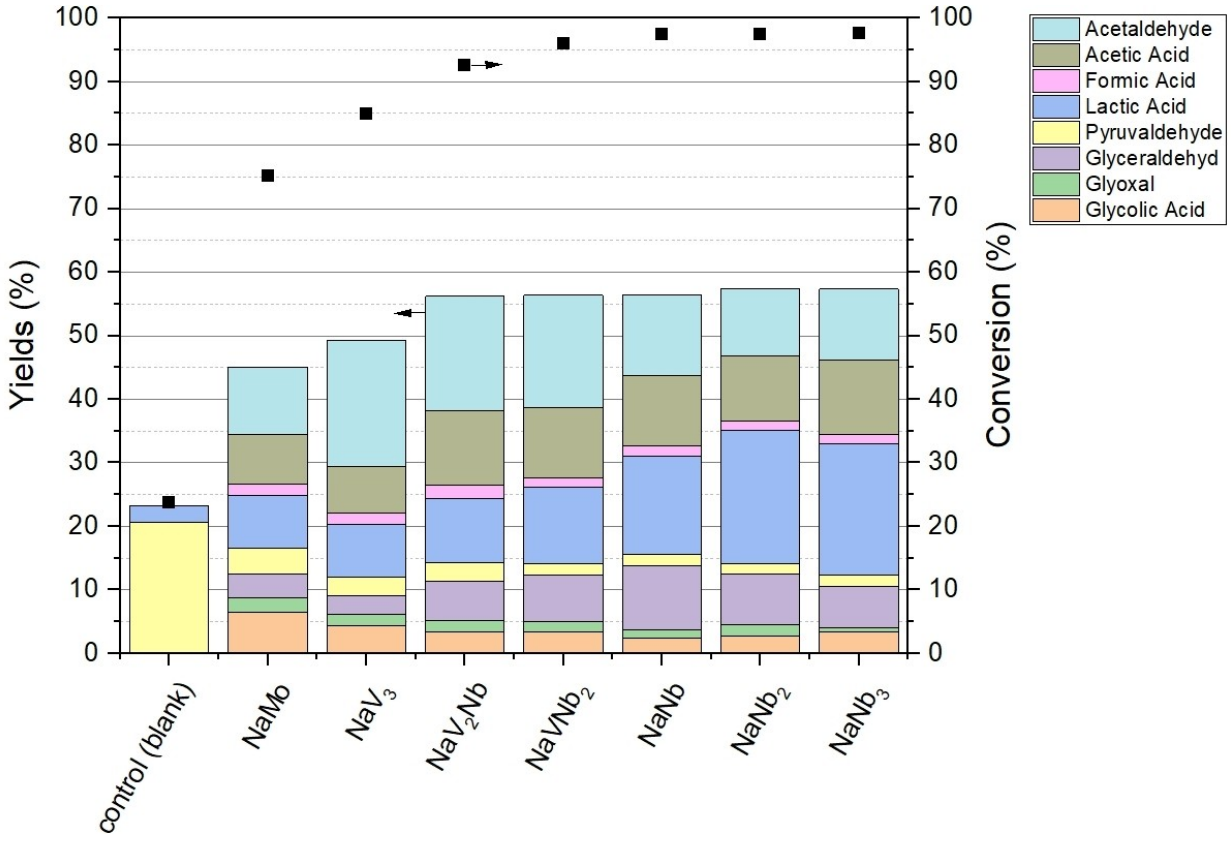

Figure 2. Conversion and product yields of HPS screening for the conversion of DHA into LA. Reaction conditions: 42 mg catalyst, 100 mg substrate, 4 g H_2O, 160 °C, 20 bar N_2, 1000 rpm, 1 h.

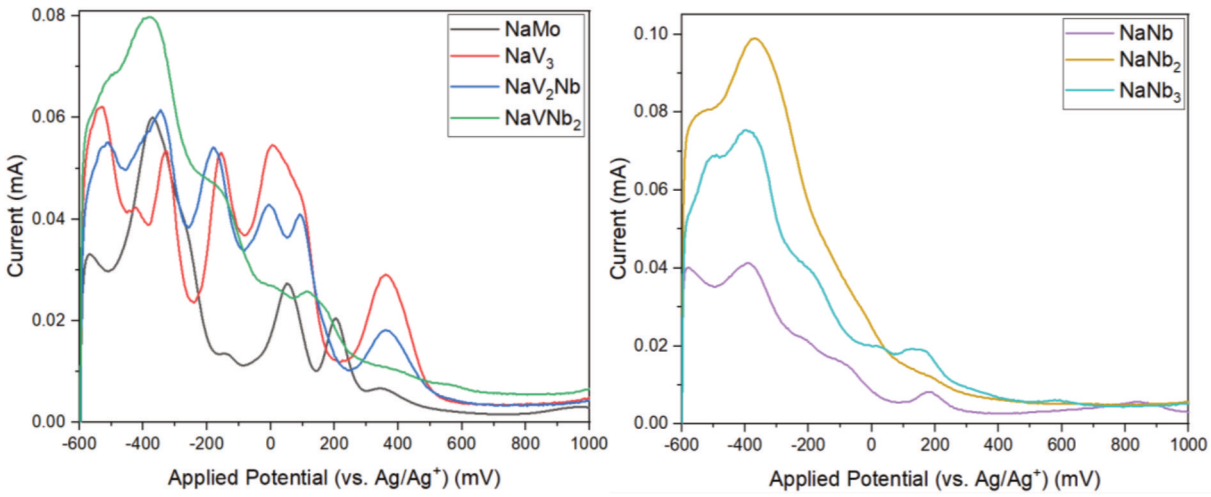

Figure 3. SWV measurements of unsubstituted, V-substituted HPSs (left) and Nb-substituted HPSs (right).[19]

vanadium into the Keggin structure with the paramagnetic, acid–bound vanadyl species being primarily responsible for facilitating the formation of LA.[12b] However, the strong oxidative properties of NaV_3 lead to decarboxylation of the formed LA into acetaldehyde. While the yield of LA remains constant at 8% for both NaMo and NaV_3, the yield of acetaldehyde nearly doubles, increasing from 11% (NaMo) to 20% (NaV_3) after vanadium incorporation.[12b,19]

In the case of the solely vanadium–substituted NaV_3, a more pronounced redox activity is evident compared to the mixed V–Nb HPSs. As the substitution of vanadium with niobium increases, the redox potential is further reduced; $NaNb_2$ exhibits

the lowest redox potential, marginally higher than that of $NaNb_3$ (−395 mV for NaNb, −370 mV for $NaNb_2$ and −400 mV for $NaNb_3$, respectively). This reduced redox activity in niobium–rich HPSs correlates with a diminished decarboxylation of LA to acetaldehyde, as the vanadium-substituted systems, with their higher redox activity, promote this consecutive reaction.[12b,19]

Besides the formation of acetaldehyde from DHA, secondary products are formed through oxidation and decarboxylation (Figure 1), including acetic acid, formic acid, or glycolic acid (Figure 2). The carbon balance was closed to at least 60% for the liquid phase in all experiments, whereas the most of the remaining carbon likely was present as gaseous or solid byproducts. As demonstrated in previous studies,[12a,24] a portion of DHA is likely converted into CO_2 because the system was not completely free of oxygen. Additionally, the catalyst, in its initial oxidized state, may facilitate the partial or complete oxidation of DHA to CO_2.[12b,16c,25] CO_2 was not quantified due to the focus of this study on LA formation and the analysis of the liquid phase. Secondly, the formation of dark–colored solids was observed. Due to the small scale of the reaction setup, the formed solid could not be analyzed in detail; however, it is assumed that DHA underwent oligomerization during the reaction (Figure 4).[12a,26] These factors collectively contribute to the incomplete closure of the carbon balance.

As a preliminary conclusion from the catalyst screening experiments, a clear relationship between redox activity and product selectivity for DHA conversion under inert atmosphere could be revealed. Moreover, it was demonstrated that the target product, LA, can be synthesized from DHA with favorable yields up to 21% under non-optimized conditions using the novel $NaNb_2$ HPS as a catalyst. To provide a synthetic route from more directly bio–based molecules, the study progressed from using the simple molecule DHA as a substrate to testing the efficiency of $NaNb_2$ for converting more complex sugars into LA.

Substrate Scope for Production of LA using $NaNb_2$ as a Catalyst

In the second part of the study, the most promising $NaNb_2$ catalyst was utilized for converting a range of sugars (hexoses and pentoses) into LA, encompassing glucose, fructose, mannose, sucrose, xylose, and cellobiose (Figure 5). Full details, including comprehensive mass balances, are provided in Figure S2 and Tables S3 and S4. The reaction pathway for the conversion of sugars to LA is shown in Figure 5.[26b,27] In the control experiments without catalyst, the conversion of sugars was found to be negligible with no LA produced from any of the sugars tested (Table S3). Upon employing $NaNb_2$ as a catalyst, the conversion for the monosaccharides increased significantly, ranging from 77% (for glucose and mannose) over 92% (xylose) up to 100% (for fructose) (Figure 6). The latter full conversion indicates that the retro–aldol condensation pathway predominantly involves fructose. Initially, glucose isomerizes to fructose, a thermodynamically favoured reaction. Subsequently, fructose undergoes a [3 + 3] retro–aldol reaction, leading to the formation of intermediate DHA, which subsequently is converted to LA (Figure 5). Additionally, via the consequent removal of fructose by subsequent retro–aldol condensation, further conversion of glucose to fructose occurred.[28] The disaccharide sucrose, composed of glucose and fructose linked by an α,β–1,2–glycosidic bond, also showed complete conversion. In contrast, the disaccharide cellobiose, which consists of two glucose molecules connected by α,β–1,4–glycosidic linkage, exhibits a significantly lower conversion rate of merely 36%. This disparity in the conversions can be attributed to the high hydrolysis stability of cellobiose, whereas sucrose readily dissociates into its monomers.[29]

LA yields were very similar for all sugars ranging from 10% (glucose) to 12% (xylose). The byproducts identified aligned with those observed in the conversion process of DHA described above. Notably, neither glyoxal nor glycolic acid could be detected among the reaction products, indicating that transformation does not proceed to C2 compounds within the reaction timeframe, as it was the case when starting with DHA. The presence of acetic acid and formic acid among the reaction

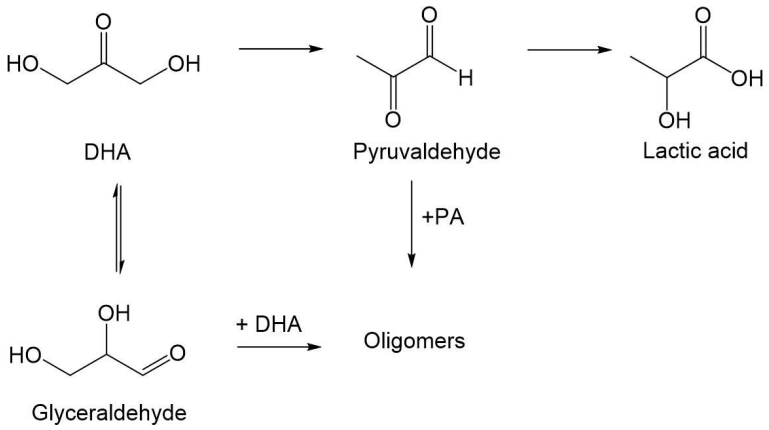

Figure 4. Undesired oligomerization of DHA.[26a]

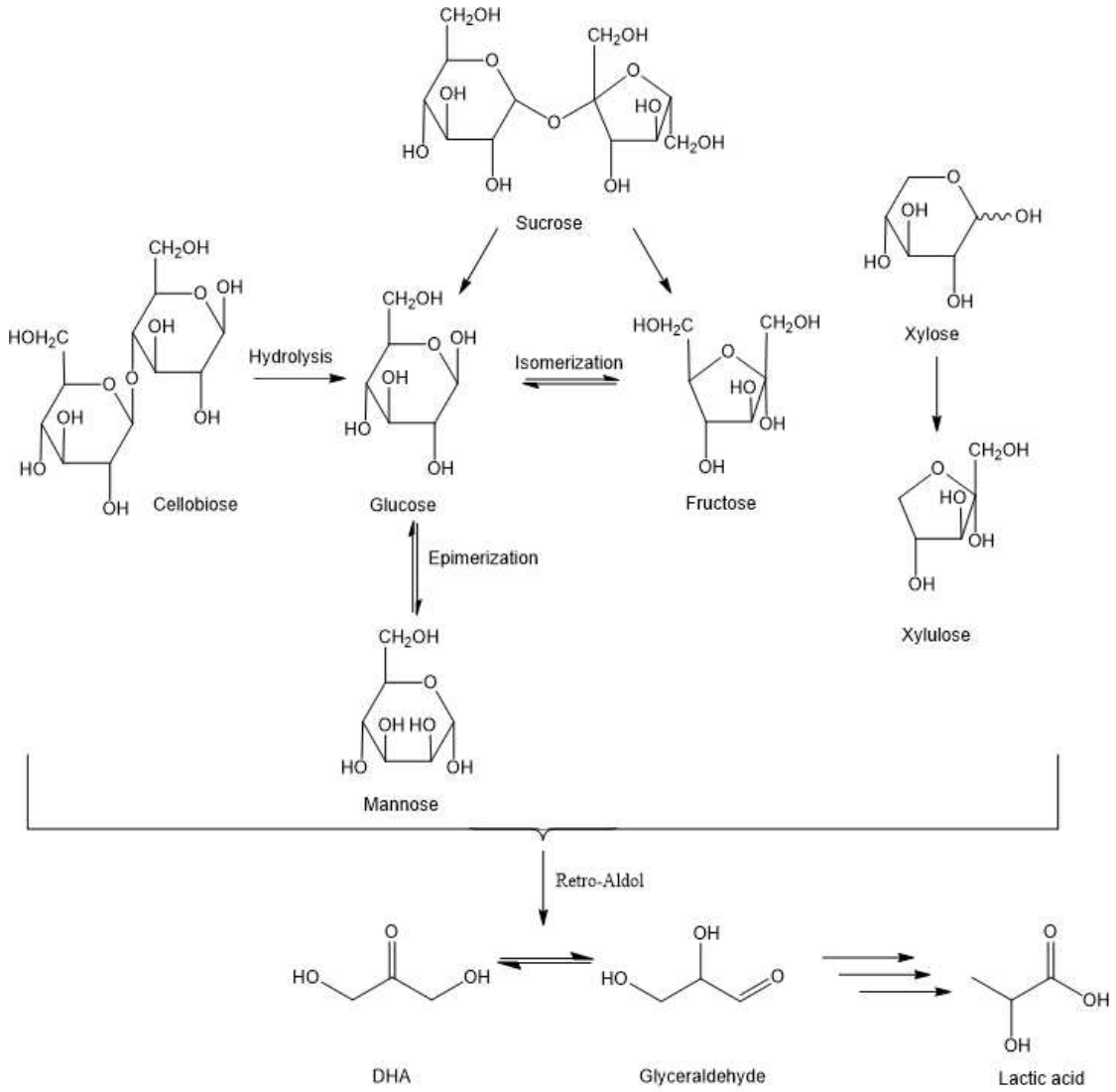

Figure 5. Reaction pathways for the conversion of sugars into LA.[26b,27]

products as C1 and C2 compounds, respectively, suggests the catalytic action partly remain oxidative in nature. This observation implies that the transformation may deviate from the reaction pathway depicted in Figure 1, occurring through alternative oxidative degradation mechanisms or via the retro–aldol cleavage of DHA.

The carbon balance for the conversion of different sugars can be closed to a maximum of 83% (glucose) in the liquid phase (Table S4). The remaining carbon is again anticipated to be partly in the gas phase in the form of CO_2. Moreover, a black solid remained after reaction like for the transformation seen with DHA. Presumably, a fraction of the sugars is converted into humins, which is possible through the acid–catalyzed transformation of carbohydrates at high temperatures up to 250 °C. These humins can be formed through various pathways, including aldol condensation of the sugars or etherification.[30] The quantitative assessment of the solids is impeded by the small scale of the reaction setup. However, residues were investigated using IR spectroscopy, which displayed the characteristic bands indicative of humins derived from sugars, such as for unsubstituted furans at 1600 cm^{-1} and the CH plane vibrations at 750 and 795 cm^{-1}.[31] Additionally, bands for ethers, as well as carbonyl and aliphatic vibrations, were identifiable. The IR bands and their corresponding assignment can be found in Table S5 and Figure S3.

To further investigate the incomplete carbon balance, additional byproducts of representative sugars were analyzed using HSQC spectroscopy using the anomeric region as structural reporter groups (Table S6). Glucose (hexose), xylose (pentose), and cellobiose (disaccharide) were selected as exemplary substrates. The analysis revealed the presence of various stereoisomers formed by isomerization of the aldoses. Specifically, for glucose, the stereoisomers allose and altrose were detected (Figure S4). For xylose, the isomers arabinose, ribose, and lyxose were identified (Figure S5). In the case of cellobiose, various other disaccharides were present as evidenced by the presence of β-glycosidic bonds in various products, although they were not identified due to the lack of

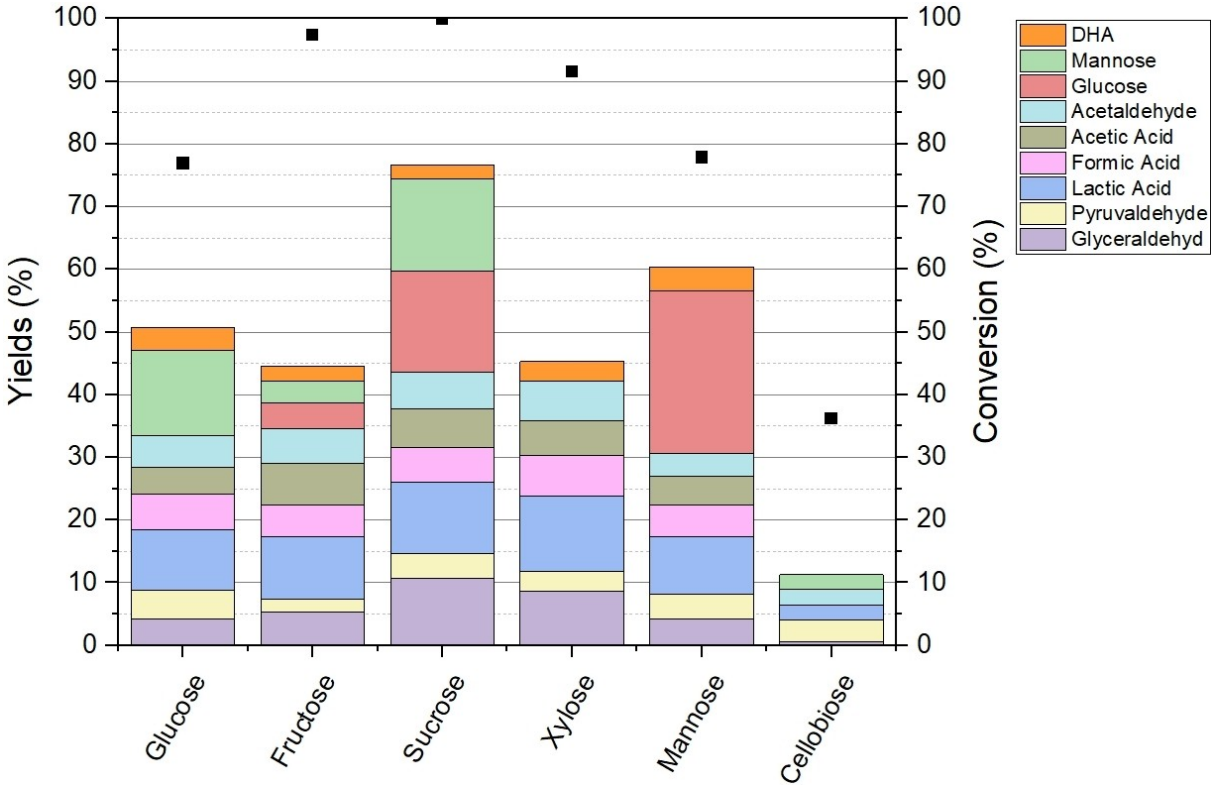

Figure 6. Conversion and product yields of the screening of different sugars into LA with $NaNb_2$. Reaction conditions: 42 mg catalyst, 100 mg substrate, 4 g H_2O, 160 °C, 20 bar N_2, 1000 rpm, 1 h.

suitable reference standards. Hence, the analyses corroborate that the reactions to some extend are reversible, leading to isomerization of the original substrate.

Post-Reaction Catalyst Analysis

The stability of the most promising $NaNb_2$ catalyst was evaluated post reaction. Therefore, the crude reaction solution from the experiment using glucose as substrate was characterized via ^{31}P NMR and Raman spectroscopy, as well as ICP–OES.

The comparison of the Raman spectra of the aqueous solution before and after the reaction (Figure 7), confirmed the preservation of the Keggin structure's characteristic vibration bands, notably at 200 cm^{-1} and 970 cm^{-1}, indicating the stability of the catalyst under reaction conditions.[32]

ICP-OES analysis of the aqueous reaction solutions confirmed the stoichiometry of $NaNb_2$ that maintained the Mo:P:Nb ratio. This observation indicated that no niobium oxide precipitated during catalysis, as evidenced by the consistency in the molar ratios (Table 1).

In addition to spectral and elemental analysis, the pH values of the reaction solutions were measured both before and after the reaction (Table S7). Prior to the reaction, the pH values ranged between 3.4 and 3.6, due to the dissociation of the dissolved $NaNb_2$ in water. After the reaction, a decrease in pH was observed, from 2.8 for cellobiose to 1.9 for glucose and mannose, which can be attributed to the formation of organic acids. Figure S6 shows the ^{31}P NMR spectra of the $NaNb_2$ catalyst dissolved in H_2O in comparison with an aqueous solution of $NaNb_2$ acidified to the lowest post-reaction pH value of 1.9. The spectra are very complex, which can be attributed to various isomer species (positional isomers and structural isomers) and the different dissociation species that form depending on the pH value. The reaction solution was further treated with elemental bromine for re-oxidation of the catalyst, which was necessary to avoid paramagnetic species leading to

Table 1. ICP-OES analysis of $NaNb_2$, before and after reaction.

	Na (mg/L)	Mo (mg/L)	Nb (mg/L)	P (mg/L)	Mo:P:Nb molar ratio[a]
$NaNb_2$ before reaction	558	4540	148	841	10.5:1.1:2.0
$NaNb_2$ after reaction	511	4799	156	934	10.0:1.0:2.0

[a] Calculated via the molar mass of individual elements, normalized to Nb as reference.

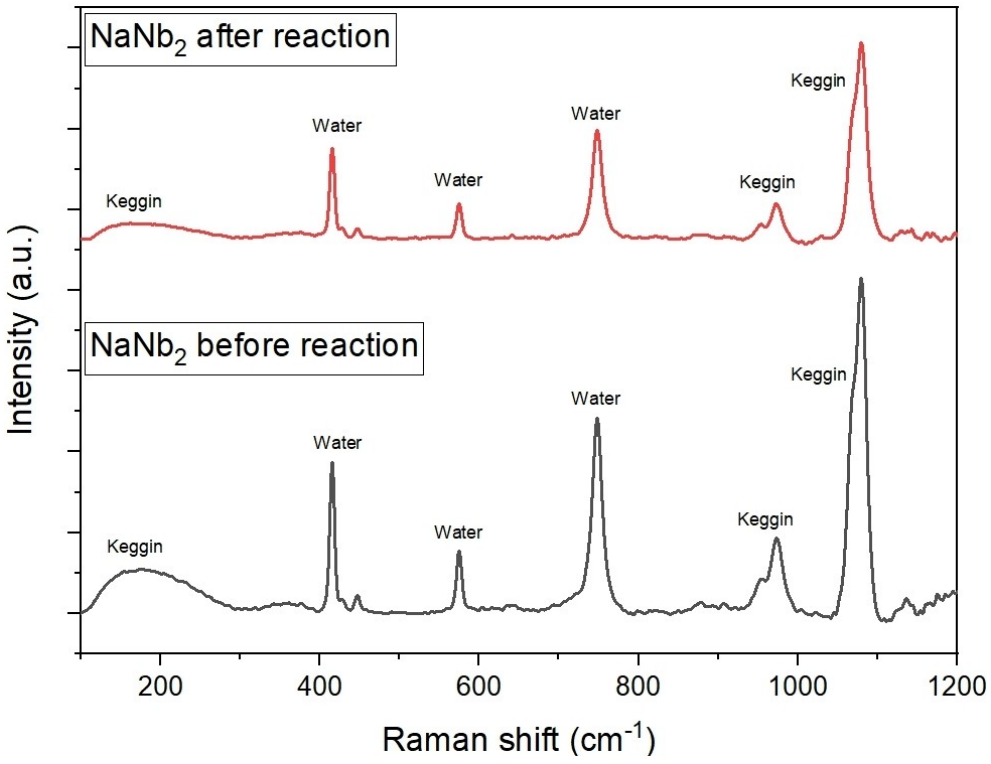

Figure 7. Raman spectra of the $NaNb_2$ catalyst before and after reaction using glucose as a substrate.

high background noise. The spectrum of the bromine treated solution highlights the impact of pH such as substrates or reaction products on the formation of pH-dependent dissociation species. The signal at −3.7 ppm can be attributed to the intact $NaNb_2$, whereas other signals represent different dissociative and structural isomers of the Keggin structure.

Conclusions

In summary, the study demonstrates that niobium–substituted HPSs are catalytically active for converting complex sugars into LA under mild reaction conditions of 160 °C and 20 bar N_2, providing a rare example of using niobium–based POMs in homogeneous catalysis.

Using DHA as a C3 model substrate for catalyst screening, the POMs redox activity was found to directly influence the product selectivity. Substituting vanadium with niobium enhances the formation of LA, with $NaNb_2$ being the most promising catalyst achieving a yield of LA of 21 % in just one hour reaction time. Notably, the catalyst could also successfully be applied to more complex substrates including C5-C12 sugars, successfully converting them into LA with yields of up to 12 %. Additionally, the catalyst's stability under the applied reaction conditions was confirmed through comprehensive post analysis of the crude reaction solution. This stability ensures that the catalyst can be used effectively without degradation over the course of the reaction. These findings highlight the potential of niobium-substituted POMs as promising catalysts for future applications in sustainable chemical synthesis, particularly in the bioconversion of renewable resources into valuable platform chemicals.

Acknowledgements

Funded by the European Union (ERC, BioValCat, Project 101086573). Views and opinions expressed are however those of the author(s) only and do not necessarily reflect those of the European Union or the European Research Council. Neither the European Union nor the granting authority can be held responsible for them. The authors gratefully acknowledge the central analytical services of the Chemistry Department at UHH for carrying out ICP-OES, NMR, and Raman measurements. Furthermore, A.W. thanks ERASMUS+ for a mobility for traineeships scholarship and DTU Chemistry for hosting and providing the infrastructure for this study. High-field 2D NMR spectra were acquired on the 800 MHz NMR instrument of the NMR Center DTU funded by the Villum Foundation. Open Access funding enabled and organized by Projekt DEAL.

Conflict of Interests

The authors have disclosed that there are no competing financial interests or personal relationships that could have influenced the work reported in this paper.

Data Availability Statement

The data that support the findings of this study are available from the corresponding author upon reasonable request.

Keywords: Lactic acid · Niobium-substituted heteropoly salts · Polyoxometalates · Biomass conversion

[1] a) D. R. Dodds, R. A. Gross, *Science* **2007**, *318*, 1250–1251; b) L. T. Mika, E. Cséfalvay, Á. Németh, *Chem. Rev.* **2018**, *118*, 505–613.
[2] J. Kim, Y.-M. Kim, V. R. Lebaka, Y.-J. Wee, *Fermentation* **2022**, *8*, 609.
[3] a) Precedence Research, "Lactic Acid Market Size, Share, and Trends 2024 to 2034", to be found under https://www.precedenceresearch.com/lactic-acid-market, 2022; b) R. Alves de Oliveira, A. Komesu, C. E. Vaz Rossell, R. Maciel Filho, *Biochem. Eng. J.* **2018**, *133*, 219–239.
[4] a) M. Dusselier, P. van Wouwe, A. Dewaele, E. Makshina, B. F. Sels, *Energy Environ. Sci.* **2013**, *6*, 1415–1442; b) P. Mäki-Arvela, I. L. Simakova, T. Salmi, D. Y. Murzin, *Chem. Rev.* **2014**, *114*, 1909–1971.
[5] A. R. E. Hansen, P. R. Jensen, S. Meier, *Catal. Sci. Technol.* **2023**, *13*, 362–371.
[6] a) M. S. Holm, S. Saravanamurugan, E. Taarning, *Science* **2010**, *328*, 602–605; b) Y. Zhang, H. Luo, L. Kong, X. Zhao, G. Miao, L. Zhu, S. Li, Y. Sun, *Green Chem.* **2020**, *22*, 7333–7336.
[7] S. Lux, M. Siebenhofer, *Catal. Sci. Technol.* **2013**, *3*, 1380–1385.
[8] Y. Hayashi, Y. Sasaki, *Chem. Commun.* **2005**, 2716–2718.
[9] C. B. Rasrendra, I. G. B. N. Makertihartha, S. Adisasmito, H. J. Heeres, *Top. Catal.* **2010**, *53*, 1241–1247.
[10] S. Xu, J. Li, J. Li, Y. Wu, Y. Xiao, C. Hu, *iScience* **2019**, *12*, 132–140.
[11] Z. Tang, W. Deng, Y. Wang, E. Zhu, X. Wan, Q. Zhang, Y. Wang, *ChemSusChem* **2014**, *7*, 1557–1567.
[12] a) D. Voß, R. Dietrich, M. Stuckart, J. Albert, *ACS Omega* **2020**, *5*, 19082–19091; b) J. Albert, M. Mendt, M. Mozer, D. Voß, *Appl. Catal. A: Gen.* **2019**, *570*, 262–270.
[13] J.-C. Raabe, F. Jameel, M. Stein, J. Albert, M. J. Poller, *Dalton Trans.* **2024**, *53*, 454–466.
[14] a) M. Ammam, *J. Mater. Chem. A* **2013**, *1*, 6291–6312; b) C. L. Hill, C. M. Prosser-McCartha, *Coord. Chem. Rev.* **1995**, *143*, 407–455.
[15] a) N. Mizuno, K. Kamata, K. Yamaguchi, *Top. Catal.* **2010**, *53*, 876–893; b) A. Patel, N. Narkhede, S. Singh, S. Pathan, *Catal. Rev. Sci. Eng.* **2016**, *58*, 337–370; c) J.-C. Raabe, M. J. Poller, D. Voß, J. Albert, *ChemSusChem* **2023**, *16*, e202300072.
[16] a) J. Albert, R. Wölfel, A. Bösmann, P. Wasserscheid, *Energy Environ. Sci.* **2012**, *5*, 7956–7962; b) J. Albert, D. Lüders, A. Bösmann, D. M. Guldi, P. Wasserscheid, *Green Chem.* **2014**, *16*, 226–237; c) S. Maerten, C. Kumpidet, D. Voß, A. Bukowski, P. Wasserscheid, J. Albert, *Green Chem.* **2020**, *22*, 4311–4320; d) B. Bertleff, M. S. Haider, J. Claußnitzer, W. Korth, P. Wasserscheid, A. Jess, J. Albert, *Energy Fuels* **2020**, *34*, 8099–8109.
[17] a) J.-C. Raabe, J. Albert, M. J. Poller, *Chem. Eur. J.* **2022**, *28*, e202201084; b) J.-C. Raabe, J. Aceituno Cruz, J. Albert, M. J. Poller, *Inorganics* **2023**, *11*, 138.
[18] a) V. G. Maiorov, A. I. Nikolaev, V. K. Kopkov, V. Y. Kuznetsov, N. L. Mikhailova, *Russ. J. Appl. Chem.* **2011**, *84*, 1137–1140; b) M. Nyman, T. M. Alam, F. Bonhomme, M. A. Rodriguez, C. S. Frazer, M. E. Welk, *J. Clust. Sci.* **2006**, *17*, 197–219.
[19] J.-C. Raabe, T. Esser, F. Jameel, M. Stein, J. Albert, M. J. Poller, *Inorg. Chem. Front.* **2023**, *10*, 4854–4868.
[20] a) S. Kang, R. Miao, J. Guo, J. Fu, *Catal. Today* **2021**, *374*, 61–76; b) M. Ziolek, *Catal. Today* **2003**, *78*, 47–64; c) K. Tanabe, *Catal. Today* **2003**, *78*, 65–77; d) A. Takagaki, S. Furusato, R. Kikuchi, S. T. Oyama, *ChemSusChem* **2015**, *8*, 3769–3772.
[21] S. Kikkawa, Y. Fujiki, V. Chudatemiya, H. Nagakari, K. Shibusawa, J. Hirayama, N. Nakatani, S. Yamazoe, *Angew. Chem. Int. Ed.* **2024**, *63*, e202401526.
[22] T. Esser, A. Wassenberg, J.-C. Raabe, D. Voß, J. Albert, *ACS Sustain. Chem. Eng.* **2024**, *12*, 543–560.
[23] J.-C. Raabe, T. Esser, M. J. Poller, J. Albert, *Catal. Today* **2024**, *441*, 114899.
[24] A. Wesner, M. P. Papajewski, L. Schidowski, C. Ruhmlieb, M. J. Poller, J. Albert, *Dalton Trans.* **2024**, *53*, 14065–14076.
[25] J. Li, D.-J. Ding, L. Deng, Q.-X. Guo, Y. Fu, *ChemSusChem* **2012**, *5*, 1313–1318.
[26] a) A. Takagaki, H. Goto, R. Kikuchi, S. T. Oyama, *Appl. Catal. A: Gen.* **2019**, *570*, 200–208; b) M. Xia, W. Dong, Z. Shen, S. Xiao, W. Chen, M. Gu, Y. Zhang, *Sustain. Energy Fuels.* **2020**, *4*, 5327–5338.
[27] Z. Li, P. Wu, J. Pang, X. Li, S. Zhai, M. Zheng, *Catalysts* **2023**, *13*, 545.
[28] a) Y. Zhang, J. Cao, Y. Zhou, Y. Li, L. Li, X. Xie, *Cellulose* **2023**, *30*, 3523–3537; b) T. Liu, J. Wang, H. Cui, J. Wang, *Green Chem.* **2023**, *25*, 4565–4576; c) S. Yamaguchi, T. Baba, *Molecules* **2016**, *21*, 937.
[29] a) J. Reichert, J. Albert, *ACS Sustain. Chem. Eng.* **2017**, *5*, 7383–7392; b) M. Marzo, A. Gervasini, P. Carniti, *Carbohydr. Res.* **2012**, *347*, 23–31.
[30] a) I. van Zandvoort, Y. Wang, C. B. Rasrendra, E. R. H. van Eck, P. C. A. Bruijnincx, H. J. Heeres, B. M. Weckhuysen, *ChemSusChem* **2013**, *6*, 1745–1758; b) G. Tsilomelekis, M. J. Orella, Z. Lin, Z. Cheng, W. Zheng, V. Nikolakis, D. G. Vlachos, *Green Chem.* **2016**, *18*, 1983–1993; c) M. Sevilla, A. B. Fuertes, *Carbon* **2009**, *47*, 2281–2289; d) N. Kutrakul, A. Liu, S. Ratchahat, P. Posoknistakul, N. Laosiripojana, K. C.-W. Wu, C. Sakdaronnarong, *Chem. Eng. Res. Des.* **2022**, *187*, 549–569.
[31] A. Wassenberg, T. Esser, M. J. Poller, J. Albert, *Materials* **2023**, *16*, 2864.
[32] J.-C. Raabe, L. Hombach, M. J. Poller, A. Collauto, M. M. Roessler, A. Vorholt, A. K. Beine, J. Albert, *ChemCatChem* **2024**, *16*, e202400395.

Manuscript received: July 12, 2024
Accepted manuscript online: September 24, 2024
Version of record online: ■■, ■■

6.2 Transitioning to Immobilized Polyoxometalates: Liquid-Phase Conversion of Biomass to Lactic and Formic Acid

The second study focuses on improving POM catalysts by transitioning from homogeneous to heterogenized systems through immobilization. While the first study explored specific element-substituted POMs for the homogeneous conversion of biomass into lactic acid, their industrial applicability is limited by challenges related to catalyst separation and reusability. Heterogeneous catalysts offer a solution to these issues, enabling improved scalability aligning with industrial demands. This study explores the heterogenization of POMs to overcome these limitations while maintaining or enhancing their catalytic performance for the liquid-phase conversion of biomass into lactic and FA. By shifting from homogeneous to heterogeneous systems, this work expands the potential of POM-based catalysts and bridges the gap between laboratory-scale research and industrial applications, showcasing the practicality of immobilized POMs in sustainable chemical processes.

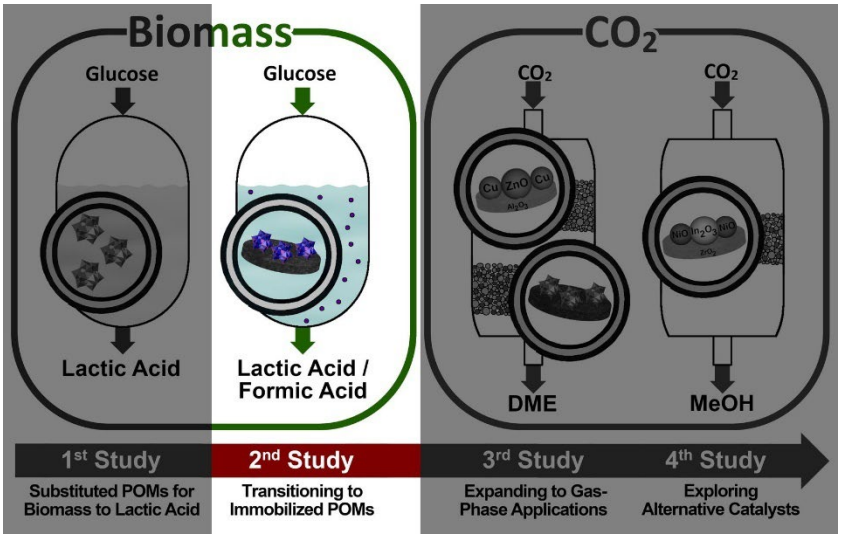

Figure 35: Scope of the second study: Transitioning to immobilized POMs.

The *Keggin*-type POM $H_8[PV_5Mo_7O_{40}]$ (HPA-5) was selected as a model catalyst for immobilization due to its unique combination of *Brønsted* acidity and redox activity, making it particularly suitable for industrial applications in sustainable chemistry. HPA-5 was systematically immobilized on various activated carbons with differing chemical and physical properties. Among these, the activated carbon CW20 exhibited the highest HPA-5 loading while maintaining the *Keggin* structure post-immobilization. CW20 was then subjected to oxidative and reductive pretreatments, as well as thermal posttreatments. Thereby, the impact of surface modifications, such as variations in functional groups and oxygen content on the deposition of HPA-5 was investigated. The supported catalysts were evaluated for glucose conversion to FA under oxygen atmosphere and to lactic acid under nitrogen atmosphere, using glucose as a model substrate due to its simplicity as a carbohydrate. In the oxidation to FA, harsh oxidative conditions led to extensive leaching of immobilized HPA-5, making it unsuitable for this reaction. However, in the conversion to lactic acid under nitrogen, the HPA-5/CW20 catalyst, prepared via wet impregnation without additional treatments, demonstrated high catalytic activity with drastically diminished leaching. This highlights the stability of the immobilized system under these conditions. This study demonstrates the potential of immobilized POM catalysts for biomass conversion, addressing leaching, stability, and industrial relevance in lactic acid synthesis.

Dalton Transactions

ROYAL SOCIETY OF CHEMISTRY

PAPER

View Article Online
View Journal | View Issue

Cite this: *Dalton Trans.*, 2024, **53**, 14065

Supported $H_8PV_5Mo_7O_{40}$ on activated carbon: Synthesis and Investigation of influencing factors for catalytic performance†

Anne Wesner,[a] Max P. Papajewski,[a] Leon Schidowski,[a] Charlotte Ruhmlieb,[b] Maximilian J. Poller [a] and Jakob Albert *[a]

Polyoxometalates (POMs), in particular the Keggin-type HPA-5 ($H_8PV_5Mo_7O_{40}$) are widely established as effective catalysts for acid- and redox-catalyzed reactions. Yet, they are mainly used as homogeneous catalysts, which poses challenges regarding catalyst separation. This study explores the synthesis of supported HPA-5, and its application as a heterogeneous catalyst for biomass conversion, focusing on activated carbons with diverse chemical and physical properties as support materials. Characterization of these carbons gives insights into the influence of surface area, oxygen content, and acidity on HPA adsorption and stability. Activated carbon CW20, was found to be the best support due to its high vanadium loading and effective preservation of the HPA-5 structure. It underwent various pre- and post-treatments, and the obtained supported catalysts were evaluated for their catalytic performance in converting glucose under both oxidative (OxFA process) and inert (Retro-Aldol condensation) conditions. Notably, HPA-5 supported on CW20 emerged as an exceptional catalyst for the retro-aldol condensation of glucose to lactic acid, achieving a selectivity of 15% and a conversion rate of 71%, with only minimal vanadium leaching.

Received 6th May 2024,
Accepted 29th July 2024

DOI: 10.1039/d4dt01336k

rsc.li/dalton

Introduction

Biomass emerges as a sustainable and environmentally carbon neutral alternative to traditional fossil resources, including oil, coal, or natural gas. The development of efficient catalysts for the conversion of biomass into valuable chemicals is a pivotal step advancing towards a sustainable economy.[1,2]

In this context, polyoxometalates (POMs) are highly promising materials. They represent a group of anionic metal–oxide clusters, exhibiting a wide array of electronic and structural characteristics. They are well established as catalysts for acid- or redox-catalyzed reactions.[3–7] One of the most commonly used POM subclasses in this context are Keggin-type heteropoly acids (HPAs), which are defined by the formula $[XM_{12}O_{40}]^{n-}$ (X = P, Si, V *etc.* and M = Mo, W, V *etc.*).[6,8,9] These HPAs have demonstrated a high efficiency and versatility in the conversion of lignocellulosic biomass into monosaccharides and subsequently into various valuable platform chemicals.[10–14]

Keggin-type Mo–V–P HPAs, especially HPA-5 ($H_8PV_5Mo_7O_{40}$), have been successfully applied as catalysts for the selective oxidation of biomass to formic acid (known as OxFA process). This process involves partial, catalytic and selective oxidation of biogenic substrates under mild conditions (90 °C, ≤ 30 bar oxygen), using O_2 as an oxidant and H_2O as solvent.[15–17] Formic acid is a product with versatile applications, primarily used in feed industry and silage aid, but also in textile, pharmaceutical, leather, and rubber sectors. It also serves as storable and transportable secondary energy carrier, which can be decomposed either into CO and H_2O, or CO_2 and H_2 for energy and material utilization.[18] Furthermore, the same HPAs have been employed for the formation of lactic acid under mild conditions and nitrogen atmosphere, which is identified as one of NREL's top 12 value-added chemicals derived from biomass. Lactic acid is applied as a polymer precursor for polylactic acid, a biodegradable and bio-based plastic, in pharmaceutical and cosmetic applications as well as for the fermentation of food.[19–21]

Due to their good solubility in water, HPAs are typically employed as homogeneous catalysts. While beneficial for selectivity and conversion, this poses challenges for their separation and reuse. Consequently, several efforts have been

[a]*Institute of Technical and Macromolecular Chemistry, University of Hamburg, Bundesstraße 45, 20146 Hamburg, Germany*
[b]*Institute of Physical Chemistry, University of Hamburg, Grindelallee 117, 20146 Hamburg, Germany. E-mail: jakob.albert@uni-hamburg.de*
† Electronic supplementary information (ESI) available. See DOI: https://doi.org/10.1039/d4dt01336k

undertaken to heterogenize HPAs. The primary strategies for heterogenizing HPAs involve complexation with inorganic or organic cations or immobilization onto supports, *e.g.*, *via* covalent binding (grafting), encapsulation in porous structures, or impregnation.[22–25]

Activated carbon is particularly effective as a support for HPAs due to its high surface area, diverse porosity, cost-effectiveness, accessibility, recyclability, and pH stability. Consequently, this material has been frequently used for the heterogenization of HPAs due to its advantageous properties.[24,26–31] $H_4SiW_{12}O_{40}$, when supported on activated carbon, has demonstrated efficient hydrolysis of cellobiose and seaweed into sugars under microwave irradiation.[32] Furthermore, $H_4SiW_{12}O_{40}$/activated carbon, has been effectively employed for the selective hydrolysis of starch to glucose.[33] In a similar vein, the $H_3PW_{12}O_{40}$/activated carbon composite has been successfully used in catalyzing the hydrolysis of cellulose and hemicellulose.[34,35] Nevertheless, the potential of carbon-supported HPAs in biomass conversion beyond these examples remains largely unexplored.[23] Furthermore, the nature of the adsorption of HPA to activated carbon, including if it is of chemical or physical nature, still remains unclear.[26,35,36]

In this study, HPA-5, well-known for its bifunctionality both as acid and redox catalyst, was systematically impregnated onto a variety of activated carbons, varying in different physical (such as surface area, pore volume and morphology) and chemical characteristics (including elemental composition, surface acid sites, and functional groups). This was done to assess the impact of these properties on the suitability as a support material for HPA-5. Subsequently, the most suitable activated carbon was selected for impregnation using different synthetic methods. The catalytic activity and leaching stability of this system were then evaluated in two different multiphasic reactions, specifically the oxidation of glucose into formic acid as well as the retro-aldol condensation of glucose into lactic acid.

Experimental

Materials and catalyst preparation

Unless specified otherwise, all chemicals were obtained commercially and used as received without further purification. A range of activated carbons was purchased from Cabot, including Norit SXPlus (NSXPlus), Norit A Supra Eur (NASEur), Norit GSX (NGSX), Norit CASP F (NCASPF), and Norit Darco KBG (DKB-G), while CW20 was acquired from Silcarbon.

The HPA-5 bulk catalyst was synthesized according to a previously published procedure.[9,37] The successful synthesis was confirmed by IR spectroscopy and elemental analysis (see Fig. S1 and Table S1†).

Initially, for testing different activated carbons as support materials (chapter: *Supporting HPA-5 on different activated carbons*), wet impregnation was employed to support HPA-5 onto all activated carbons (experimental series 1, **E1**). For this process, 4.99 g (3.11 mmol) HPA-5 was dissolved in 250 ml of H_2O adjusted to a pH range of 2–3, and 7.02 g of the selected activated carbon was suspended into the solution. The suspension was stirred at 50 °C for 3 hours at 100 rpm using a rotary evaporator. The solid was subsequently filtered off, washed with H_2O until neutral pH was achieved, and then dried overnight (see Fig. 6).

Additionally, activated carbon CW20 was chosen to test various synthesis methods (experimental series) for impregnation (chapter: *Supporting HPA-5 on CW20 using various synthesis methods*). Different pre- and post-treatments additionally to the general wetness-impregnation procedure (see Fig. 6) were utilized. In experimental series 2 (**E2**), oxidative pre-treatment was performed in concentrated 65 wt% HNO_3 at 90 °C for 3 hours as pre-treatment. Series 3 (**E3**) incorporated an additional post-treatment, heating the catalyst to 200 °C at 2 K min^{-1} for 5 hours. Series 4 (**E4**) applied the same post-treatment as **E3**, but without any pre-treatment of the activated carbon. Finally, series 5 (**E5**) used reductive pre-treatment, heating the carbon to 400 °C for 4 hours under an atmosphere of 95% N_2/5% H_2 (100 l h^{-1}).

Catalyst characterization

The elemental analysis of all catalysts was conducted using Inductively Coupled Plasma-Optical Emission Spectroscopy (ICP-OES). Powder X-Ray Diffraction (XRD) techniques were utilized to investigate their crystalline structures. Nitrogen physisorption measurements were applied to ascertain the porosity, pore volume, and overall surface area. Catalyst morphology and metal distribution were explored through Scanning Electron Microscopy (SEM) along with Energy-Dispersive X-ray Spectroscopy (EDX). The acidity parameters of the synthesized catalysts were assessed *via* NH_3-Temperature Programmed Desorption (NH_3-TPD), Boehm titration method, and Point of Zero Charge analysis. Furthermore, Infrared (IR) and Raman spectroscopy were employed for structural characterization. Comprehensive descriptions of all characterization methods are given in the ESI.†

Catalytic evaluation and determination of catalytic parameters

Catalytic experiments were carried out in a three-fold plant in stainless steel reactors. Analysis of both liquid and gaseous products were conducted using High Performance Liquid Chromatography (HPLC) and Gas Chromatography (GC), respectively. The examination of the utilized catalysts was carried out *via* ICP-OES and IR. Detailed descriptions of the catalytic evaluation, as well as the equations used for calculating catalytic parameters, such as conversion (X), yield (Y) and selectivity (S), are provided in the ESI.†

Results and discussion

Characterization of activated carbons

Initially, all activated carbons were characterized according to their textural and chemical features. X-Ray diffraction (Fig. S2†) confirms the presence of crystalline graphitic carbon with characteristic diffraction patterns between 15–30° (002

Table 1 Elemental and textural properties of pure activated carbons

	NSXPlus	NASEur	NGSX	CW20	NCASPF	DKB-G
Elemental analysis						
Al (wt%)	0.95	—	0.09	0.05	—	—
Fe (wt%)	—	—	0.07	—-	—	—
P (wt%)	—	—	—	1.50	1.25	1.47
C (wt%)	88.74	94.38	88.35	82.61	76.97	76.80
H (wt%)	0.68	0.46	1.33	2.21	3.18	2.89
N (wt%)	—	—	—	—	—	—
O (wt%)	2.47	3.49	5.18	8.74	13.93	17.22
Textural properties						
Specific surface area ($m^2\ g^{-1}$)	923	1771	736	1500	1544	1341
Pore volumina ($mL\ g^{-1}$)	0.65	0.90	0.62	1.32	1.22	1.45
∅ pore diameter (nm)	7.35	1.69	7.21	16.48	14.93	11.61
Boehm titration						
Surface acidity ($mmol\ g^{-1}$)	55.0	55.5	69.0	188.0	248.0	303.5
Surface basicity ($mmol\ g^{-1}$)	57.0	82.0	61.5	45.0	0.0	0.0
Carboxylic groups ($mmol\ g^{-1}$)	5.0	0.0	5.5	39.0	94.0	102.5
Lactonic groups ($mmol\ g^{-1}$)	9.0	7.0	32.5	113.0	118.0	185.5
Phenolic groups ($mmol\ g^{-1}$)	41.0	51.5	31.0	36.0	36.0	15.5
NH_3-TPD acidity						
Low (150–500 °C)	0.04	0.08	0.11	1.00	2.15	2.49
High (500–700 °C)	0.00	0.06	0.07	1.00	1.61	2.45
Total	0.01	0.07	0.08	1.00	1.79	2.46
Point of zero charge (pH)	8.80	8.65	7.40	5.74	2.87	2.62

reflection) and 40–50° (001 reflection).[38,39] Elemental analysis indicates negligible impurities with minor traces of Al, Fe, and P (Table 1). The activated carbons exhibit varying carbon, hydrogen, and oxygen contents. Oxygen amount ranges from 3.49 wt% (NSXPlus) to 17.22 wt% (DKB-G), the carbon amount accordingly from 88.74 wt% (NSXPlus) to 76.80 wt% (DKB-G). Hydrogen content varies from 0.68 wt% (NSXPlus) to 3.18 wt% (NCASPF) (Table 1).

Specific surface areas range from 736 $m^2\ g^{-1}$ (NASEur) to 1544 $m^2\ g^{-1}$ (NCASPF), with pore diameters spanning from 1.69 nm (NASEur) to 16.48 nm (CW20) (Table 1, Fig. S2 and S3†). Microscopy data (Fig. S5–10†) indicate the presence of agglomerates comprising nanoscopic substructures across all samples. Therefore, it is essential to differentiate between various surface types: firstly, the outermost surface of the sample, followed by the surface area formed by interstices between agglomerates and substructures, and lastly, nanoporous regions within the samples. These features are important to evaluate the inner surface area of the sample and are discernible in certain areas under SEM examination.

The points of zero charge range from pH 2.62 (DKB-G) to pH 8.80 (NSXPlus). Determined surface acidities range from 55 μmol g^{-1} for NSXPlus to 304 μmol g^{-1} for DKB-G, surface basicities from 0 μmol g^{-1} for DKB-G to 57 μmol g^{-1} for NSXPlus (Table 1). Notably, there is a correlation between oxygen content, point of zero charge, and surface characteristics (Fig. 2 and Fig. S11†). Activated carbon contains various surface oxide groups with different acidities such as strongly acidic carboxylic acids, acidic phenolic groups, or weakly acidic lactonic groups (Table S2†).[40,41] These functional groups can also be separately determined using the Boehm method.[42,43] An increase in surface acidity aligns with a higher amount of carboxylic and lactonic groups, while the quantity of phenolic groups remains relatively constant (Table 1). NH_3-TPD for activated carbons with an oxygen amount under 6 wt% (NSXPlus, NASEur, NGSX) indicates negligible amounts of interactions with NH_3, for activated carbons, however, with a significantly higher amount of oxygen over 6 wt% (CW20, NCASPF, DKB-G) weak and middle (150–500 °C) as well as strong (500–700 °C) interactions can be seen (Fig. 1). NH_3-TPD measurements agree with the results of point of zero charge measurements and acidity determined by Boehm method (Fig. 2). Therefore, it is hypothesized that the surface acidity is directly related to the amount of oxygen groups on the surface (Fig. 2).

Raman spectroscopy analysis shows the presence of the D-band at approximately 1330 cm^{-1}, indicative of disordered sp^2-hybridized rings in carbon (Fig. S12†).[44,45] The IR spectra (Fig. 1) for activated carbons with over 6 wt% oxygen content (CW20, NCASPF, DKB-G) display bands of various surface groups. For instance, bands indicating the presence of alcohol, phenol, and carboxylic groups are observed between 1000–1300 cm^{-1}, as well as for C=C bonds and surface quinones between 1500–1700 cm^{-1}.[46] The exact positions of surface groups in activated carbons are listed in Table S3.† Due to the overlap of all bands, precise assignment of surface groups is challenging. Interestingly, the IR spectra of the groups with lower oxygen content (less than 6 wt%, for NSXPlus, NASEur, NGSX), exhibit very high absorption, resulting in either no or only very weak bands.

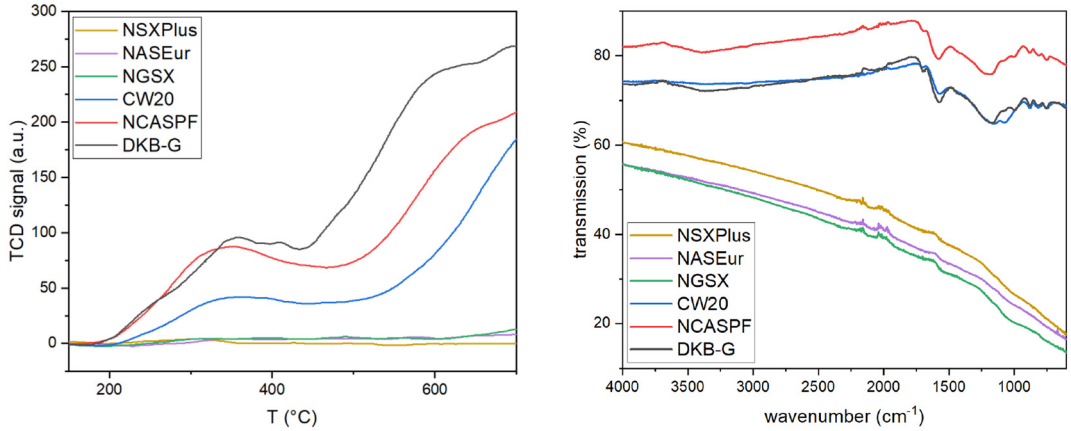

Fig. 1 NH_3-TPD acidity (left) and Infrared spectra of pure activated carbons (right).

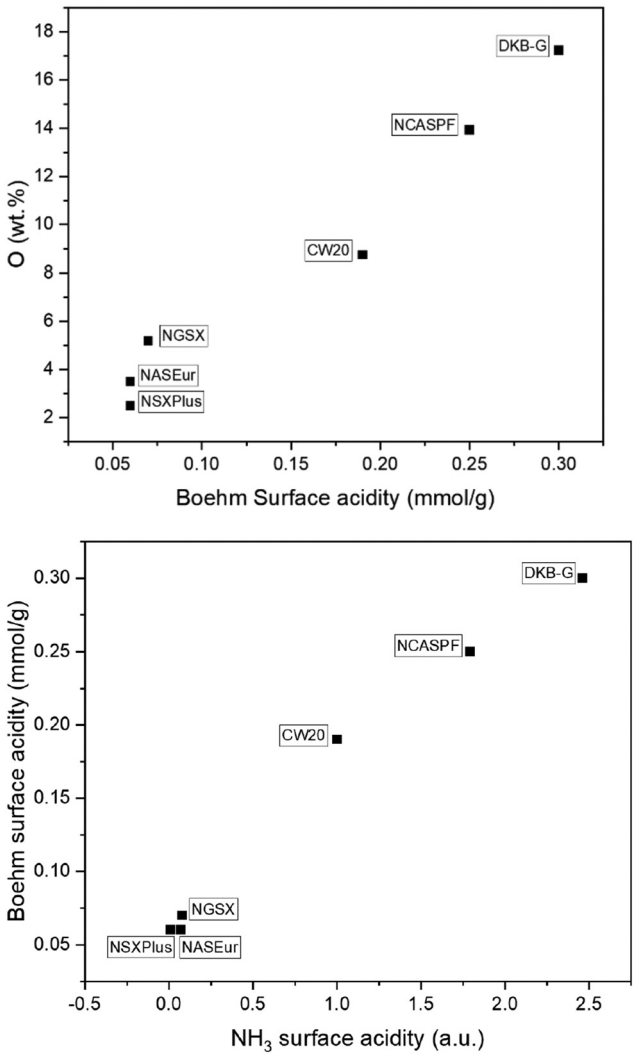

Fig. 2 Correlation between oxygen content and acidity (top) and between Boehm and NH_3 surface acidity (bottom).

Supporting HPA-5 on different activated carbons. The characterized activated carbons were impregnated with HPA-5 using wetness impregnation applying the same synthesis method for all samples (**E1**) (Fig. 6).

IR spectra show that the impregnation on CW20, NCASPF, and DKB-G was successful (Fig. 3). The concise IR bands of HPA-5 can be distinguished: 1049–1060 cm^{-1} (P═O vibration), 945–962 cm^{-1} (M_t═O), 866–877 cm^{-1} (M–O–M_{vertex}),

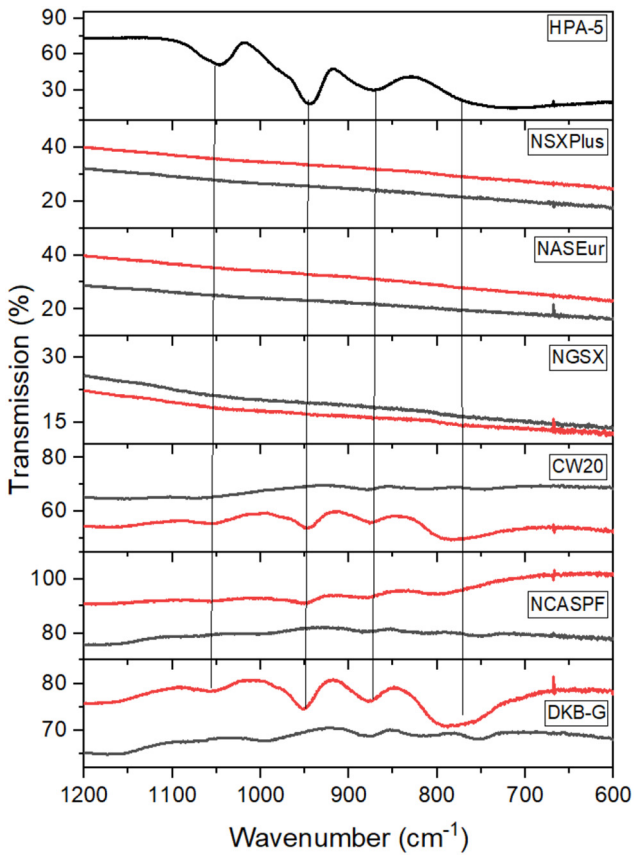

Fig. 3 IR-spectra of HPA-5 impregnated carbons, red – impregnated, black – pure activated carbon.

Table 2 Elemental analysis of impregnated carbons

Loading	NSXPlus	NASEur	NGSX	CW20	NCASPF	DKB-G	HPA-5 ($H_8PV_5Mo_7O_{40}$)
Mo (wt%)	5.85	7.45	4.39	8.06	7.64	6.7	17.4
P (wt%)	0.23	0.26	0.17	1.17	0.64	0.69	0.8
V (wt%)	1.74	2.34	1.22	2.32	2.03	1.82	6.6
Molar ratio Mo : V	7.7 : 4.3	7.6 : 4.4	7.9 : 4.1	7.8 : 4.2	8.0 : 4.0	7.9 : 4.1	7.0 : 5.0

643–767 cm^{-1} ($M–O–M_{edge}$).[9] For NSXPlus, NASEur and NGSX no reflexes could be detected, which can either be due to no HPA-5 being present on these activated carbons because of overall high absorption, or because of decomposition of the Keggin structure through the non-acidic character of these activated carbons.[47] Positively charged surfaces can adsorb anionic HPA clusters due to electrostatic interactions.[48] Consequently, since successful deposition of HPA-5 on these activated carbons could not be confirmed, they were excluded from further investigations.

Furthermore, Raman spectroscopy and XRD were employed for analytical investigations. Raman spectra of pure HPA 5 displayed the characteristic vibrational bands indicative of the Keggin structure, as well as additional bands below 800 cm^{-1}, which correspond to M–O–M vibrations (Fig. S13†).[9] XRD analysis revealed distinct diffraction patterns at 27.6°, 27.7°, and 27.9° for the pure HPA-5 catalyst (Fig. S14†), corresponding to the Miller indices [3 1 4], [2 4 0], and [3 1 1], respectively, as determined from single-crystal X-ray diffraction data in a previous study.[9] However, using Raman and XRD, no clear signals for HPA-5 were observed on the impregnated samples at all (Fig. S13 and S14†), suggesting that these methods are not suitable for this kind of investigation.

SEM reveals no significant alteration in morphology due to impregnation (Fig. S16–21†). SEM-EDX analysis and ICP-OES confirm the successful impregnation of HPA-5 onto the supports. SEM-EDX mapping shows a microscopic homogeneous distribution of Mo, V, and P (Fig. S15†). Table 2 presents the ICP-OES results, listing the content of Mo, P, and V for each activated carbon compared to the desired HPA-5 loading (right column). Additionally, the molar ratios of Mo to V for each sample have been calculated and are also displayed in the table in comparison to the desired ratio of HPA-5 (right column). The impregnation process achieves approximately 35% of the targeted HPA-5 loading on the supports (CW20 and NASEur), with the remainder not adsorbed and leached during subsequent washing. All activated carbons exhibit a molar ratio of Mo : V of approximately 8 : 4, which suggests the presence of HPA-4 ($H_7PV_4Mo_8O_{40}$) instead of HPA-5. The reason for this might be the differences in stability and charge of the HPA resulting in different interaction strengths with the carbon surface. Literature indicates that Keggin structures experience a reduction in stability as the degree of substitution increases. The preferential formation of HPA-4 over HPA-5 might be due to the enhanced dissociation of HPA-5, which can also facilitate the formation of lower substituted POMs.[37]

The quantities of adsorbed HPA-5 vary depending on the used carbon material, with CW20 and NASEur showing the highest loadings. Interestingly, there is no overall correlation observable between the oxygen content and the loading of the catalysts (Fig. 4). Other studies have suggested that surface oxygen groups play a stabilizing role,[35] however, this was not confirmed in this study, which involved a wide variety of activated carbons. Additionally, some studies indicate that the stabilization of supported HPAs may also be influenced by van

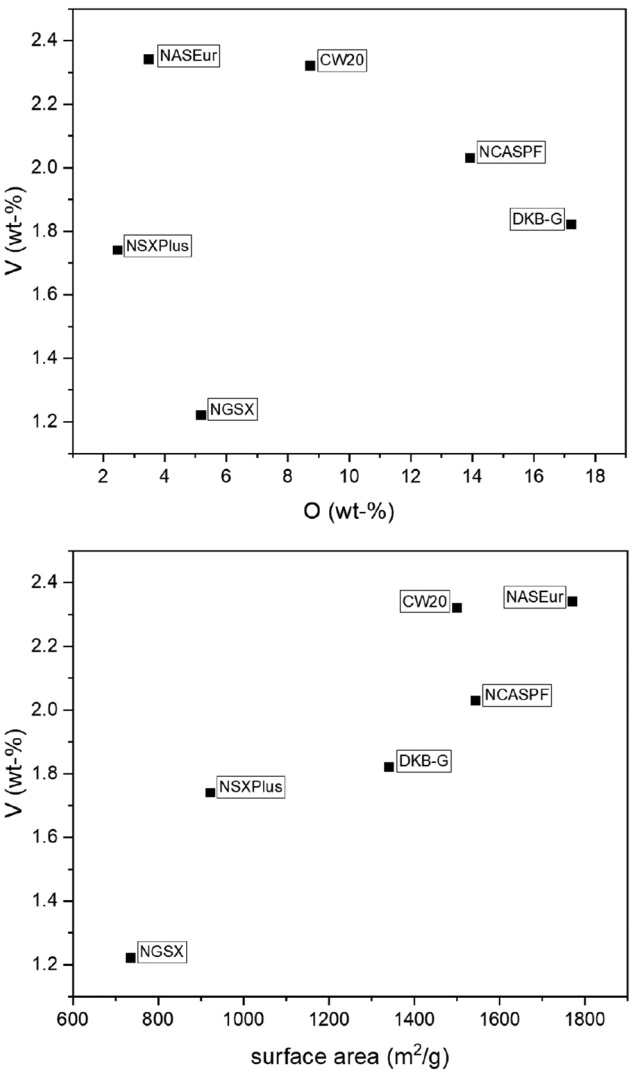

Fig. 4 Correlation between amount of oxygen and vanadium loading (top) and between surface area and vanadium loading (bottom).

der Waals forces, hydrogen bonding, or the exchange of the terminal oxygen atom (O_t) in the HPA structure.[35,49] Vanadium loading on the activated carbons shows a correlation with their surface area (Fig. 4). As the surface area increases, the vanadium loading also rises from 1.22 wt% for NGSX with a surface area of 736 m^2 to twice as much at 2.34 wt% for NASEur, corresponding to a surface area of 1771 m^2. The increased POM loading with higher porosity was also observed in previous studies.[35,50] Interestingly, we observed that CW20, compared to NASEur, even with a smaller surface area of only 1500 m^2 exhibits the equal vanadium loading of 2.32 wt% V. When the vanadium content is related to the surfaces of the two activated carbons, CW20 shows a higher loading of 15.47 wt V m^{-2} g^{-1} compared to NASEur with 13.21 wt V m^{-2} g^{-1} (Fig. 5).

As a conclusion, it can be stated that the specific surface area has a greater influence on the impregnation efficiency than the surface oxygen or the acidity of the surface. CW20 and NASEur show the highest loadings of HPA. However, the low surface acidity of NASEur could have led to the destruction of the Keggin structure of the POMs. While the individual elements Mo, V, P could be detected by elemental analysis, the Keggin structure could not be conclusively identified using spectroscopic and X-ray analytical methods for this activated carbon. Since CW20 exhibited the highest vanadium loading as well as preservation of the POM structure, this activated carbon was chosen for subsequent experiments to try out advanced synthesis techniques.

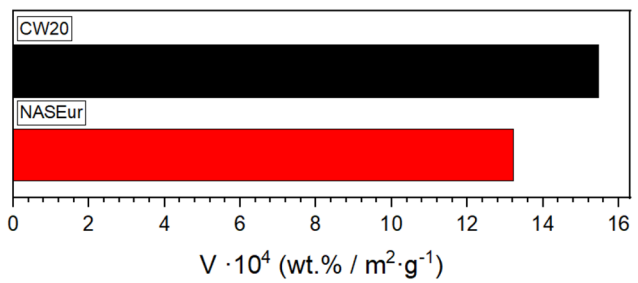

Fig. 5 Vanadium loading of CW20 and NASEur related to surface area.

Supporting HPA-5 on CW20 using various synthesis methods. To determine the influence of common pre- and post-treatment procedures for activated carbon on HPA-5 impregnation, various synthesis approaches (in the following reffered to as experimental series, **E2** to **E5**) were employed using CW20 (Fig. 6). This investigation aimed specifically at assessing how changes in surface chemistry, achieved through targeted modifications of functional groups and oxygen content, as well as subsequent treatments of the impregnated catalysts, influence the deposition of HPA-5. The catalytic performance of these catalysts was tested in the conversion of biomass under oxidative or inert conditions.

For the experimental investigation, CW20 underwent diverse pretreatment protocols in distinct experimental series. Specifically, CW20 was applied in its untreated form, subjected to oxidative pretreatment using 65 wt% HNO_3 for 3 hours (**E2**), and alternatively, reductively pretreated at 400 °C for 4 hours (**E5**) using a reductive gas mixture composed of 5% hydrogen and 95% nitrogen.

Due to the oxidative pretreatment, the surface area and pore volume decrease from 1500 m^2 g^{-1} and 1.32 mL g^{-1} (CW20) to 357 m^2 g^{-1} and 0.26 mL g^{-1} ($CW20_{ox}$), respectively (Table 3, Fig. S22 and S23†). The oxygen content increases from 8.74 wt% to 35.88 wt%, while the carbon content correspondingly decreases from 82.61 wt% to 58.05 wt%. It is observed that the acidity of the activated carbon increases. The point of zero charge shifts from pH 5.74 to pH 1.69 and NH_3-TPD reveals a more than fivefold increase of acidity compared to pure CW20. Measurements according to Boehm indicate that the density of acidic functional groups increases from 188 to 500 µmol g^{-1}. There is an increased formation of carboxyl groups, while the relative proportion of phenolic and lactonic groups decreases. IR spectra indicate an increase in bands in the range between 1500–2000 cm^{-1}, which can be attributed to

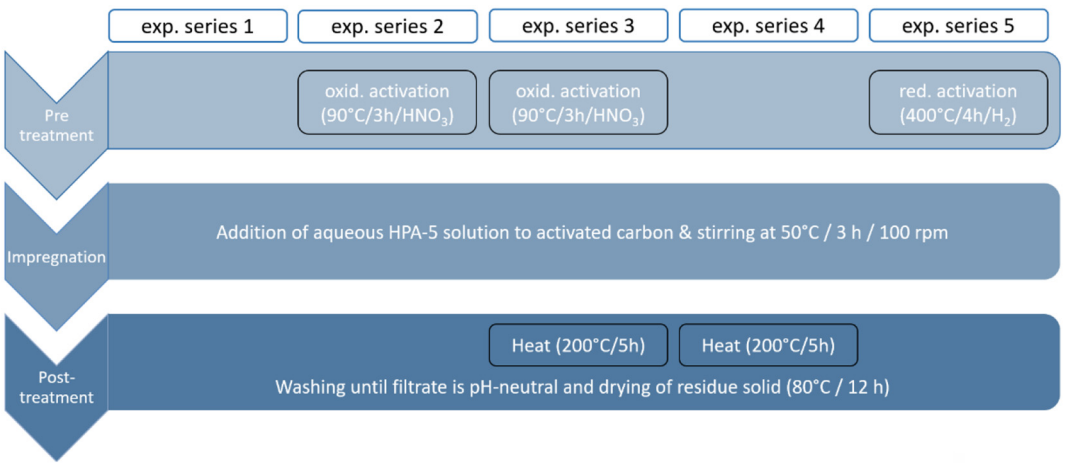

Fig. 6 Different experimental series with pre- and post-treatments for impregnation of activated carbon.

Table 3 Elemental and textural properties of untreated CW20 and pretreated $CW20_{ox.}$ and $CW20_{red}$

	CW20	$CW20_{ox}$	$CW20_{red}$
Elemental analysis			
C (wt%)	82.61	58.05	82.58
H (wt%)	2.21	2.28	2.18
N (wt%)	—	0.3	—
O (wt%)	8.74	35.88	9.44
Textural properties			
Specific surface area ($m^2\ g^{-1}$)	1500	357	1527
Pore volumina ($mL\ g^{-1}$)	1.32	0.26	1.38
∅ pore diameter (nm)	16.48	2.61	20.42
Boehm titration			
Surface acidity ($\mu mol\ g^{-1}$)	188.0	500.0	182.5
Surface basicity ($\mu mol\ g^{-1}$)	45.0	0.00	28.0
Carboxylic groups ($\mu mol\ g^{-1}$)	39.0	473.5	29.5
Lactonic groups ($\mu mol\ g^{-1}$)	113.0	58.5	380.5
Phenolic groups ($\mu mol\ g^{-1}$)	36.0	0.00	0.00
NH_3-TPD acidity			
Low (150–500 °C)	1.00	9.63	0.47
High (500–700 °C)	1.00	4.03	1.28
Total	1.00	5.84	1.02
Point of zero charge (pH)	5.74	1.69	5.44

the increase in carboxyl groups (Table 3 and Fig. 7). The SEM images (Fig. S24–26†) reveal that the pure CW20 is composed of nanosized grains and agglomerates whereas the structures of the oxidized CW20 are in the order of micrometers in size. Therefore, the overall roughness of the oxidized sample appears significantly larger. Interestingly, the images of the reduced CW20 again resemble the size distribution and roughness of the pure CW20.

Due to the reductive pretreatment, there are neither significant changes in the textural properties, surface area nor the pore volumina remain the same. The oxygen content rises slightly to 9.44 wt%, possibly as a result of the removal of weakly bound impurities from the surface. Furthermore, the reductive pretreatment also results in the adsorption of nitrogen onto the surface of $CW20_{red}$ (0.3 wt%), which is present in the reductive gas, and could lead to nitrogen containing surface groups (Table 3). The acidity change is not significant within the margin of measurement error. The point of zero charge decreases from 5.74 to 5.44 and NH_3-TPD shows a slightly change to higher acidity (Table 3 and Fig. 7) from 1 to 1.28. Reductive pretreatment shows no significant changes in the IR spectrum compared to CW20 (Fig. 7).

For all experimental series, SEM-EDX mapping shows a microscopic homogeneous distribution of Mo, V, and P (Fig. S30†). In the impregnation process of both untreated and pretreated activated carbon, differences are observed in the adsorbed quantity of HPA-5 (Table 4). For the untreated (**E1**) and reductively pretreated activated carbon (**E5**), vanadium amounts of 2.32 wt% (**E1**) and 2.54 wt% (**E5**) are detected, with a molar ratio of Mo : V of 7.8 : 4.2 (**E1**) and 7.4 : 4.6 (**E5**) respectively. The Keggin structure is preserved according to IR analysis (Fig. 8) for untreated (**E1**) as well as reductively pretreated activated carbon (**E5**). However, the oxidatively pretreated activated carbon (**E2**) results in only a 1.67 wt% V loading, with a Mo : V molar ratio of 1.5 : 10.5. This is attributed to the low adsorption of molybdenum, with just 0.46 wt%. The lack of successful impregnation is likely due to the significantly reduced surface area of $CW20_{ox}$, which is only 357 $m^2\ g^{-1}$ and the change of surface oxygen groups. Furthermore, IR spectra show the absence of a discernible Keggin structure.

The experimental series involving $CW20_{ox}$ was further expanded by incorporating a post-treatment step (**E3**), where, following the initial impregnation, the activated carbon and HPA-5 were heated to 200 °C for 3 hours before washing. The same procedure was applied to untreated CW20 for comparison (**E4**). The results indicate that post-treatment led to a significantly higher vanadium loading of 7.58 wt% V (**E3**) and 7.03 wt% V (**E4**), compared to standard impregnation, with a molar ratio of Mo : V of 6.3 : 5.7 (**E3**) and 6.0 : 6.0 (**E4**), respectively. This exceeded the anticipated vanadium amount of 6.6 wt%. These findings demonstrate the substantial impact of post-treatment on the impregnation efficiency. IR spectra indicate a preserved Keggin structure. The TGA analysis revealed that the majority of mass loss occurred during the heating

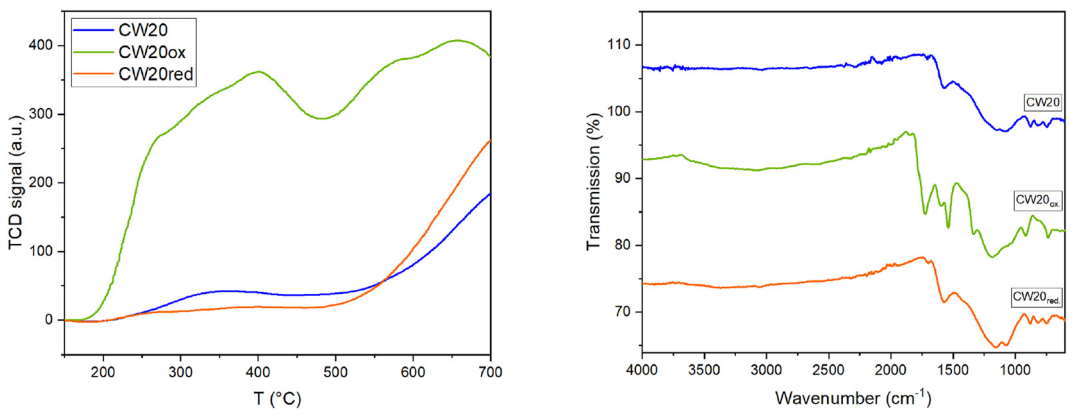

Fig. 7 NH_3-TPD acidity (left) and IR-spectra (right) of untreated CW20 and pretreated $CW20_{ox}$ and $CW20_{red}$.

Table 4 Elemental analysis of CW20 after impregnation for different experimental series, before and after reaction

	E1	E2	E3	E4	E5	HPA-5$_{the.}$
Before reaction						
Mo (wt%)	8.06	0.46	15.88	12.94	7.61	17.4
P (wt%)	1.17	0.64	1.20	1.43	1.22	0.8
V (wt%)	2.32	1.67	7.58	7.03	2.54	6.6
Molar ratio Mo : V	7.8 : 4.2	1.5 : 10.5	6.3 : 5.7	6.0 : 6.0	7.4 : 4.6	7.0 : 5.0
After formic acid formation						
Mo (wt%)	6.33	<1	5.62	4.57	4.18	
P (wt%)	0.94	0.43	1.14	0.85	0.69	
V (wt%)	0.59	<0.5	2.46	2.27	0.54	
Molar ratio Mo : V	10.1 : 1.9	—	6.6 : 5.4	6.2 : 5.8	9.7 : 2.3	
Leaching of V (%)	75	100	68	68	79	
After lactic acid formation						
Mo (wt%)	7.07	0.43	6.41	5.97	6.77	
P (wt%)	0.86	0.45	0.76	0.90	0.21	
V (wt%)	1.92	1.62	5.98	5.85	2.00	
Molar ratio Mo : V	7.9 : 4.1	1.5 : 10.5	4.4 : 7.6	4.2 : 7.8	7.7 : 4.3	
Leaching of V (%)	17	3	21	17	21	

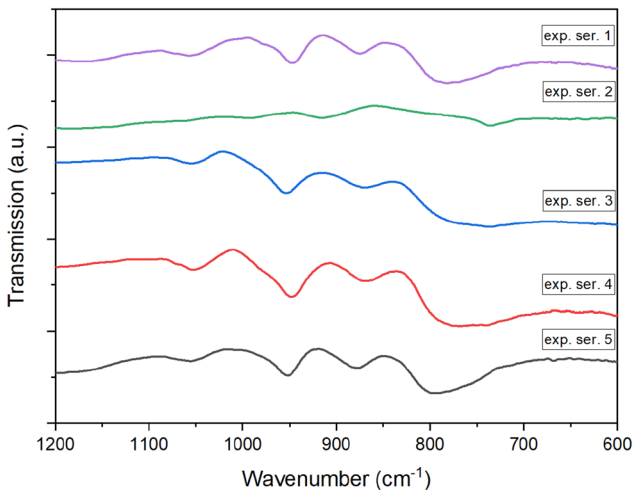

Fig. 8 IR-spectra of CW20 after HPA-5 impregnation for different experimental series.

phase up to 200 °C. Mass-spectroscopic analysis indicates that this loss predominantly corresponds to a molecular mass of 18 g mol^{-1} (Fig. S27–29†), suggesting it to be water loss. The enhancement in loading can be further attributed to the removal of hydroxyl groups from the activated carbon surface, facilitating the formation of ether or ester-like bonds between the surface oxygen of the activated carbon and the HPA. The release of an additional oxygen atom from water detachment not only contributes to the overall mass reduction but also potentially leads to higher POM loading and the observed elevated Mo : V ratio.

Applying supported HPA-5 for the catalytic conversion of glucose. In order to further assess the influence of the various pre- and post-treatments during the catalyst synthesis, the different catalysts (HPA-5 on CW20, **E1** to **E5**) were tested for several biomass transformation reactions. First, they were applied for the oxidative conversion of glucose to formic acid (OxFA process),[15] and secondly, they were tested for the retro-aldol reaction converting glucose to lactic acid under an inert atmosphere.[19] In both reactions catalytic activity and stability of the catalysts (leaching) were assessed.

Simplified reaction pathways for the oxidative conversion and retro-aldol reaction are illustrated in Fig. 9. The conversion of glucose to formic acid and lactic acid, respectively, proceeds *via* dihydroxyacetone and glyceraldehyde, catalyzed by different vanadium species. Detailed descriptions of the mechanisms for both reactions are extensively documented in the literature.[51–56]

Oxidative conversion of glucose analogous to the OxFA process

For the oxidative conversion of glucose, the supported HPA-5 catalyst was suspended in an aqueous solution of glucose, the mixture was heated to 90 °C under an atmosphere of 20 bar O_2 in a steel pressure reactor for 6 hours (see ESI†), analogous to the commercial OxFA process. After the reaction, the composition of the gas phase was investigated with GC, while the liquid phase was analyzed with HPLC. The results are summarized in Fig. 10.

The homogeneous HPA-5 as a benchmark shows a glucose conversion of 76% after 6 h reaction time, with a selectivity towards formic acid of 54% and a FA-yield of 41%. This is in very good alignment with previous literature, evidencing the successful execution of the experiments in this study.[57]

The conversion of glucose for all heterogeneous catalysts is between 68% to 78%, except for **E2** with just 54%. This experiment also shows the lowest yield of formic acid with just 24% likely due to unsuccessful impregnation in this series as mentioned before (Table 4). The yield towards formic acid for the other supported catalysts is between 31% to 34% (**E3**), and therefore below the homogeneous HPA-5. The selectivity to formic acid for all catalysts ranges from 40% (E1) to 51% (E3). Interestingly, despite the reduced vanadium content in the

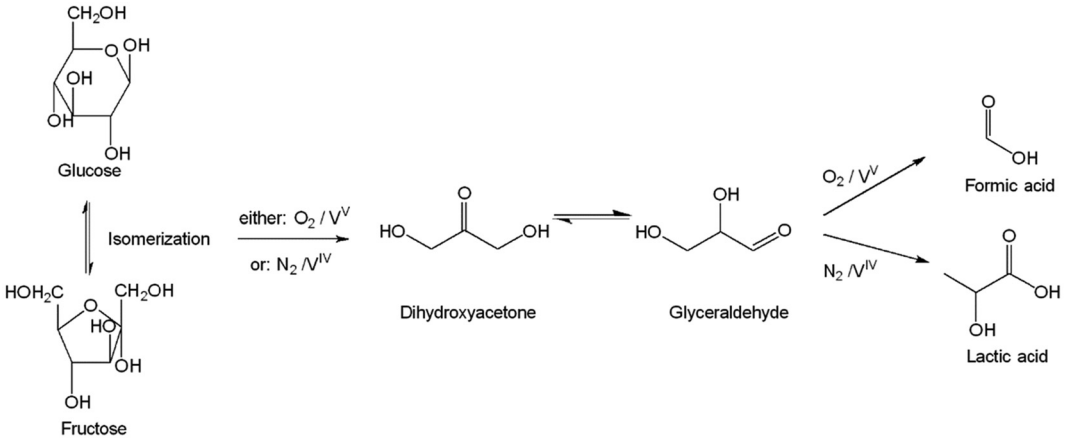

Fig. 9 Simplified reaction pathways for conversion of glucose to formic acid or lactic acid.[51–56]

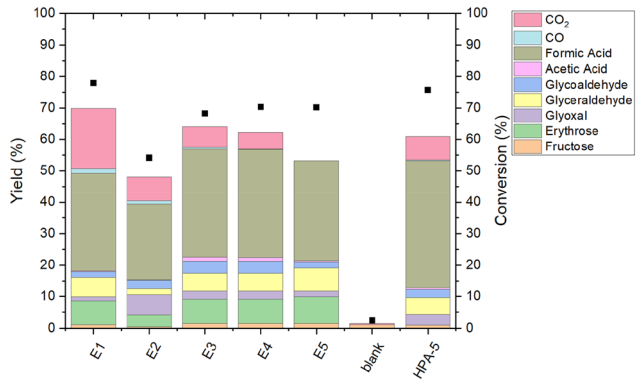

Fig. 10 Catalytic performance of HPA-5/CW-20 for glucose oxidation to formic acid. Reaction conditions: glucose 3.603 g (20 mmol), catalyst 1.821 g (pure HPA-5: 1.14 mmol), 45 ml H_2O, 90 °C, 20 bar O_2, 1000 rpm, 6 h.

supported catalysts compared to pure homogeneous HPA-5, the results demonstrate a catalytic activity comparable to that of homogeneous HPA-5.

Due to the promising results for E1, this experimental series was reproduced. Data showed sufficient reproducibility (Table S5†).

With respect to catalyst stability, leaching of vanadium exceeds 68% across all experimental series (Table 4), probably due to reaction conditions that disrupt the bond between HPA and the activated carbon support. The initial pH value above 2.5 decreases to below 1.4 by the end of the reaction (Table S4†), matching the pH of pure HPA-5 in solution, where HPA exists in a dissociated state. The Keggin structure of HPA-5 remains intact post-reaction in all catalysts, except, as expected, in **E2**, where it was not initially present (Fig. S36†).

In summary, the use of HPA-5 supported on CW-20 activated carbon demonstrates promising catalytic activity in the OxFA process for oxidatively converting glucose to formic acid, but is not suitable due to the high leaching of vanadium.

Inert conversion of glucose analogous to retro-aldol-condensation

For the retro-aldol condensation of glucose, the HPA-5/CW-20 catalyst was suspended in an aqueous solution of glucose, the mixture was heated to 160 °C under an atmosphere of 20 bar N_2 in a steel (1.4571) pressure reactor for 1 hour (see ESI†). After reaction, the composition of the gas phase was investigated with GC, while the liquid phase was analyzed with HPLC. The results are summarized in Fig. 11.

As a benchmark, the homogeneous HPA-5 shows a glucose conversion of 71%, with a selectivity towards lactic acid of 15% and a LA-yield of 10% (Fig. 11). In literature, conversion of 28% and a yield of lactic acid of 13% was achieved under identical reaction conditions but for 3 hours reaction time and use of 1 mmol glucose and 0.1 mmol HPA-5, respectively.[51]

For all heterogeneous catalysts, the glucose conversion ranges between 65% to 71%, the selectivity towards lactic acid between 9% to 15%, the yield consistently exceeds 6% (Table S6†). Interestingly, the HPA-5/CW-20 catalyst syn-

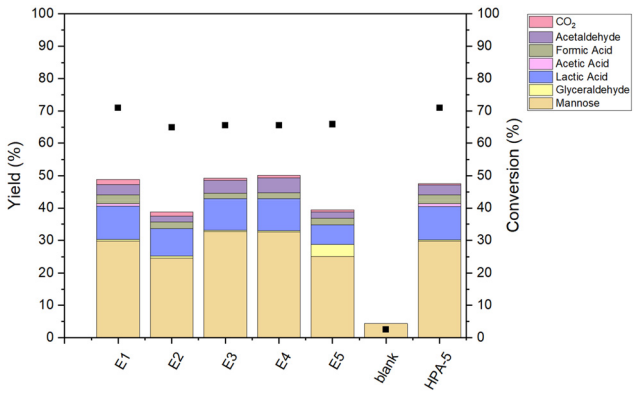

Fig. 11 Catalytic performance of HPA-5/CW-20 for glucose conversion to lactic acid. Reaction conditions: glucose 1.032 g (20 mmol), catalyst 0.406 g (pure HPA-5: 1.14 mmol), 40 ml H_2O, 160 °C, 20 bar N_2, 1000 rpm, 1 h.

thesized without pre- and post-treatment (**E1**) closely matches the catalytic performance of the homogeneous HPA-5, showing a conversion of 71% and a lactic acid yield of 11%, whereby only low leaching occurs (see below). This comparison indicates that the reaction is heterogeneously catalyzed, rather than being driven solely by the leached fraction of HPA. Additionally, the lower amount of HPA on the catalyst's surface resulted in overall higher activity than the homogeneous HPA-5.

Infrared spectroscopy further verifies the preservation of the Keggin structure across all other catalysts (**E3–E5**). Across all experimental series, the leaching related to vanadium is below 22% (Table 4). Furthermore, in experimental series with post-treatments (3 and 4), more than half of the molybdenum is leached, indicating weaker bonding than vanadium. Compared to the oxidative conditions of the OxFA process, significantly less leaching occurs, also indicating disruptive behavior of oxidative conditions for the HPA–AC bonds (Table 4). The initial pH value of 2.9 decreased to no lower than 2.41 in all catalysts, suggesting less dissociation of the POM under these conditions than in the OxFA process with a final pH of around 1.39 (Table S4†). Collectively, both the elemental analysis and IR spectroscopy demonstrate that the supported catalysts are substantially more stable under the conditions of the retro-aldol condensation than under oxidative conditions. Interestingly, the increased temperature of 160 °C, in comparison to the OxFA process at 90 °C, does not significantly affect the stability of the catalyst compared to the pH value. The higher decrease in pH value in the OxFA process is predominantly attributable to the accumulation of acidic reaction products, notably formic and acetic acid, which contribute to a decrease in pH. Subsequently, when developing supported HPAs, it is important to consider the post-reaction pH value to ensure catalyst stability.

Conclusions

In this study, HPA-5 was successfully supported on various activated carbons using a simple wetness impregnation method. SEM analyses show a homogeneous dispersion of HPA on the various carbon supports. For activated carbons, IR spectra confirmed the preservation of the Keggin structure. Elemental analysis indicated that not HPA-5, but lower substituted POMs could be adsorbed onto activated carbon, probably due to a decrease in stability with an increasing degree of substitution by vanadium.

The activated carbon CW20 was chosen for its ability to retain a high vanadium content and preserve the POM structure. It underwent various pre- and post-treatments aimed at optimizing the synthesis methodologies. Remarkably, CW20, when subjected to simple wetness impregnation without additional pre- or post-treatment, exhibited catalytic activity comparable to the homogeneous HPA-5 catalyst. This resulted in a selectivity for lactic acid of 15% and a glucose conversion of 71%.

Author contributions

Anne Wesner performed catalyst synthesis and characterization, data interpretation and conceptual planning of the experimental workflow, and wrote the manuscript draft. Leon Schidowski and Max Papajewski carried out the catalytic experiments. Maximilian J. Poller participated in planning and supervision of the experimental workflow, interpretation of data, and reviewing the manuscript. Charlotte Ruhmlieb provided valuable insights for data interpretation through scientific discussions, especially for SEM studies. Jakob Albert was responsible for acquisition of funding and resources, as well as project supervision and manuscript review.

Data availability

The data that support the findings of this study are available on request from the corresponding author, JA.

Conflicts of interest

There are no conflicts to declare.

Acknowledgements

The authors gratefully acknowledge Cabot for providing activated carbon samples. The central analytical services of the Chemistry Department at UHH are gratefully acknowledged for carrying out ICP-OES, SEM, Raman, and XRD measurements. Furthermore, we thank Moritz Hilgers for carrying out point of zero charge measurements during his research internship. This research was partially funded by OxFA GmbH.

References

1 P. Sudarsanam, R. Zhong, S. van den Bosch, S. M. Coman, V. I. Parvulescu and B. F. Sels, Functionalised heterogeneous catalysts for sustainable biomass valorisation, *Chem. Soc. Rev.*, 2018, **47**, 8349–8402.
2 V. K. Vaithyanathan, B. Goyette and R. Rajagopal, A critical review of the transformation of biomass into commodity chemicals: Prominence of pretreatments, *Environ. Challenges*, 2023, **11**, 100700.
3 J. Zhong, J. Pérez-Ramírez and N. Yan, Biomass valorisation over polyoxometalate-based catalysts, *Green Chem.*, 2021, **23**, 18–36.
4 N. I. Gumerova and A. Rompel, Synthesis, structures and applications of electron-rich polyoxometalates, *Nat. Rev. Chem.*, 2018, **2**, 0112.
5 I. V. Kozhevnikov, Catalysis by Heteropoly Acids and Multicomponent Polyoxometalates in Liquid-Phase Reactions, *Chem. Rev.*, 1998, **98**, 171–198.

6 M. T. Pope and A. Müller, Polyoxometalate Chemistry: An Old Field with New Dimensions in Several Disciplines, *Angew. Chem., Int. Ed. Engl.*, 1991, **30**, 34–48.
7 T. Okuhara, N. Mizuno and M. Misono, Catalytic Chemistry of Heteropoly Compounds, in *Advances in Catalysis*, Elsevier, 1996, pp. 113–252.
8 M. T. Pope, Heteropoly and isopoly oxometalates, in *Inorganic Chemistry Concepts Vol. 8*, Springer, Berlin, Heidelberg, New York, Tokyo, 1983.
9 J.-C. Raabe, M. J. Poller, D. Voß and J. Albert, H8 PV5 Mo7 O40 - A Unique Polyoxometalate for Acid and RedOx Catalysis: Synthesis, Characterization, and Modern Applications in Green Chemical Processes, *ChemSusChem*, 2023, **16**, e202300072.
10 Y. Ogasawara, S. Itagaki, K. Yamaguchi and N. Mizuno, Saccharification of natural lignocellulose biomass and polysaccharides by highly negatively charged heteropolyacids in concentrated aqueous solution, *ChemSusChem*, 2011, **4**, 519–525.
11 J. Tian, J. Wang, S. Zhao, C. Jiang, X. Zhang and X. Wang, Hydrolysis of cellulose by the heteropoly acid H3PW12O40, *Cellulose*, 2010, **17**, 587–594.
12 K. Shimizu, H. Furukawa, N. Kobayashi, Y. Itaya and A. Satsuma, Effects of Brønsted and Lewis acidities on activity and selectivity of heteropolyacid-based catalysts for hydrolysis of cellobiose and cellulose, *Green Chem.*, 2009, **11**, 1627.
13 L. M. Sanchez, H. J. Thomas, M. J. Climent, G. P. Romanelli and S. Iborra, Heteropolycompounds as catalysts for biomass product transformations, *Catal. Rev.*, 2016, **58**, 497–586.
14 W. Deng, Q. Zhang and Y. Wang, Polyoxometalates as efficient catalysts for transformations of cellulose into platform chemicals, *Dalton Trans.*, 2012, **41**, 9817–9831.
15 J. Albert, R. Wölfel, A. Bösmann and P. Wasserscheid, Selective oxidation of complex, water-insoluble biomass to formic acid using additives as reaction accelerators, *Energy Environ. Sci.*, 2012, **5**(7), 7956–7962.
16 J. Albert, D. Lüders, A. Bösmann, D. M. Guldi and P. Wasserscheid, Spectroscopic and electrochemical characterization of heteropoly acids for their optimized application in selective biomass oxidation to formic acid, *Green Chem.*, 2014, **16**(1), 226–237.
17 J. Albert and P. Wasserscheid, Expanding the scope of biogenic substrates for the selective production of formic acid from water-insoluble and wet waste biomass, *Green Chem.*, 2015, **17**(12), 5164–5171.
18 J. Hietala, A. Vuori, P. Johnsson, I. Pollari, W. Reutemann and H. Kieczka, Formic Acid, in *Ullmann's Encyclopedia of Industrial Chemistry*, Wiley, 2003, pp. 1–22.
19 D. Voß, R. Dietrich, M. Stuckart and J. Albert, Switchable Catalytic Polyoxometalate-Based Systems for Biomass Conversion to Carboxylic Acids, *ACS Omega*, 2020, **5**, 19082–19091.
20 M. J. Biddy, C. Scarlata and C. Kinchin, *Chemicals from Biomass: A Market Assessment of Bioproducts with Near-Term Potential*, NREL/TP-5100-65509, Denver, 2016.
21 R. Datta and M. Henry, Lactic acid: recent advances in products, processes and technologies—a review, *J. Chem. Technol. Biotechnol.*, 2006, **81**, 1119–1129.
22 E. Rafiee and S. Eavani, Heterogenization of heteropoly compounds: a review of their structure and synthesis, *RSC Adv.*, 2016, **6**, 46433–46466.
23 L. Hombach, N. Simitsis, J. T. Vossen, A. J. Vorholt and A. K. Beine, Solidified and Immobilized Heteropolyacids for the Valorization of Lignocellulose, *ChemCatChem*, 2022, **14**, e202101838.
24 Y. Wu, X. Ye, X. Yang, X. Wang, W. Chu and Y. Hu, Heterogenization of Heteropolyacids: A General Discussion on the Preparation of Supported Acid Catalysts, *Ind. Eng. Chem. Res.*, 1996, **35**, 2546–2560.
25 Y. Zhou, G. Chen, Z. Long and J. Wang, Recent advances in polyoxometalate-based heterogeneous catalytic materials for liquid-phase organic transformations, *RSC Adv.*, 2014, **4**, 42092–42113.
26 M. A. Schwegler, P. Vinke, M. van der Eijk and H. van Bekkum, Activated carbon as a support for heteropolyanion catalysts, *Appl. Catal., A*, 1992, **80**, 41–57.
27 Y. Izumi and K. Urabe, Catalysis of heteropoly acids entrapped in activated carbon, *Chem. Lett.*, 1981, **10**, 663–666.
28 M. N. Timofeeva, M. M. Matrosova, T. V. Reshetenko, L. B. Avdeeva, E. A. Paukshtis, A. A. Budneva, A. L. Chuvilin and V. A. Likholobov, Adsorption of H3PW12O40 by porous carbon materials, *Russ. Chem. Bull.*, 2002, **51**, 243–248.
29 Y. Izumi, Catalysis by heterogeneous supported heteropoly acid, *J. Catal.*, 1983, **84**, 402–409.
30 Y. Yang, K. Chiang and N. Burke, Porous carbon-supported catalysts for energy and environmental applications: A short review, *Catal. Today*, 2011, **178**, 197–205.
31 M. Almohalla, I. Rodríguez-Ramos and A. Guerrero-Ruiz, Comparative study of three heteropolyacids supported on carbon materials as catalysts for ethylene production from bioethanol, *Catal. Sci. Technol.*, 2017, **7**, 1892–1901.
32 S. Tsubaki, K. Oono, A. Onda, T. Ueda, T. Mitani and M. Hiraoka, Microwave-assisted hydrolysis of biomass over activated carbon supported polyoxometalates, *RSC Adv.*, 2017, **7**, 12346–12350.
33 V. B. Kumar, I. N. Pulidindi and A. Gedanken, Selective conversion of starch to glucose using carbon based solid acid catalyst, *Renewable Energy*, 2015, **78**, 141–145.
34 S. d. A. Carminati, A. C. C. Arantes, A. C. S. d. Oliveira and M. L. Bianchi, Enhancing the sugars production yieldby supporting H3PW12O40 heteropoly acid on activated carbon for use as catalyst in hydrolysis of cellulose, *Matéria*, 2018, **23**, e12260.
35 L. Hombach, N. Hausen, A. G. Manjón, C. Scheu, H. Kraffczyk, M. Rose, J. Albert and A. K. Beine, Carbon supported polyoxometalates as recyclable solid acid catalysts in aqueous reactions, *Appl. Catal., A*, 2023, **666**, 119392.
36 R. Ghubayra, R. Yahya, E. F. Kozhevnikova and I. V. Kozhevnikov, Oxidative desulfurization of model diesel

fuel catalyzed by carbon-supported heteropoly acids: Effect of carbon support, *Fuel*, 2021, **301**, 121083.

37 J.-C. Raabe, J. Aceituno Cruz, J. Albert and M. J. Poller, Comparative Spectroscopic and Electrochemical Study of V(v)-Substituted Keggin-Type Phosphomolybdates and -Tungstates, *Inorganics*, 2023, **11**, 138.

38 X.-Y. Liu, M. Huang, H.-L. Ma, Z.-Q. Zhang, J.-M. Gao, Y.-L. Zhu, X.-J. Han and X.-Y. Guo, Preparation of a carbon-based solid acid catalyst by sulfonating activated carbon in a chemical reduction process, *Molecules*, 2010, **15**, 7188–7196.

39 B. S. Girgis, Y. M. Temerk, M. M. Gadelrab and I. D. Abdullah, X-ray Diffraction Patterns of Activated Carbons Prepared under Various Conditions, *Carbon Lett.*, 2007, **8**, 95–100.

40 M. S. Shafeeyan, W. M. A. W. Daud, A. Houshmand and A. Shamiri, A review on surface modification of activated carbon for carbon dioxide adsorption, *J. Anal. Appl. Pyrolysis*, 2010, **89**, 143–151.

41 U. Zielke, K. J. Hüttinger and W. P. Hoffman, Surface-oxidized carbon fibers: I. Surface structure and chemistry, *Carbon*, 1996, **34**, 983–998.

42 H.-P. Boehm, Functional Groups on the Surfaces of Solids, *Angew. Chem., Int. Ed. Engl.*, 1966, **5**, 533–544.

43 H. Boehm, Surface oxides on carbon and their analysis: a critical assessment, *Carbon*, 2002, **40**, 145–149.

44 P. Kurzweil and O. K. Dietlmeier, *Elektrochemische Speicher: Superkondensatoren, Batterien, Elektrolyse-Wasserstoff, Rechtliche Grundlagen*, 1. Aufl. 2015, Springer Vieweg, Wiesbaden, 2015.

45 N. Shimodaira and A. Masui, Raman spectroscopic investigations of activated carbon materials, *J. Appl. Phys.*, 2002, **92**, 902–909.

46 P. E. Fanning and M. Vannice, A DRIFTS study of the formation of surface groups on carbon by oxidation, *Carbon*, 1993, **31**, 721–730.

47 G. Marcì, E. García-López, M. Bellardita, F. Parisi, C. Colbeau-Justin, S. Sorgues, L. F. Liotta and L. Palmisano, Keggin heteropolyacid H3PW12O40 supported on different oxides for catalytic and catalytic photo-assisted propene hydration, *Phys. Chem. Chem. Phys.*, 2013, **15**, 13329–13342.

48 W. Qi, W. Liu, S. Liu, B. Zhang, X. Gu, X. Guo and D. Su, Heteropoly Acid/Carbon Nanotube Hybrid Materials as Efficient Solid–Acid Catalysts, *ChemCatChem*, 2014, **6**, 2613–2620.

49 J. Breibeck, N. I. Gumerova and A. Rompel, Oxo-Replaced Polyoxometalates: There Is More than Oxygen, *ACS Org. Inorg. Au*, 2022, **2**, 477–495.

50 J. Alcañiz-Monge, G. Trautwein, S. Parres-Esclapez and J. A. Maciá-Agulló, Influence of microporosity of activated carbons as a support of polyoxometalates, *Microporous Mesoporous Mater.*, 2008, **115**, 440–446.

51 J. Albert, M. Mendt, M. Mozer and D. Voß, Explaining the role of vanadium in homogeneous glucose transformation reactions using NMR and EPR spectroscopy, *Appl. Catal., A*, 2019, **570**, 262–270.

52 T. Lu, M. Niu, Y. Hou, W. Wu, S. Ren and F. Yang, Catalytic oxidation of cellulose to formic acid in H 5 PV 2 Mo 10 O 40 + H 2 SO 4 aqueous solution with molecular oxygen, *Green Chem.*, 2016, **18**, 4725–4732.

53 Z. Tang, W. Deng, Y. Wang, E. Zhu, X. Wan, Q. Zhang and Y. Wang, Transformation of cellulose and its derived carbohydrates into formic and lactic acids catalyzed by vanadyl cations, *ChemSusChem*, 2014, **7**, 1557–1567.

54 H. Wang, M. Wang, J. Shang, Y. Ren, B. Yue and H. He, H3PMo12O40 Immobilized on Amine Functionalized SBA-15 as a Catalyst for Aldose Epimerization, *Materials*, 2020, **13**, 507.

55 Z. Li, P. Wu, J. Pang, X. Li, S. Zhai and M. Zheng, Catalytic Conversion of Sugars into Lactic Acid via a RuOx/MoS2 Catalyst, *Catalysts*, 2023, **13**, 545.

56 M. Xia, W. Dong, Z. Shen, S. Xiao, W. Chen, M. Gu and Y. Zhang, Efficient production of lactic acid from biomass-derived carbohydrates under synergistic effects of indium and tin in In–Sn-Beta zeolites, *Sustainable Energy Fuels*, 2020, **4**, 5327–5338.

57 J. Reichert, B. Brunner, A. Jess, P. Wasserscheid and J. Albert, Biomass oxidation to formic acid in aqueous media using polyoxometalate catalysts – boosting FA selectivity by in situ extraction, *Energy Environ. Sci.*, 2015, **8**, 2985–2990.

6.3 Expanding to Gas-Phase Applications: Immobilized Polyoxometalates for CO_2 Conversion to Dimethyl Ether

The third study focuses on broadening the application of immobilized POM catalysts into gas-phase reactions, marking a shift from the liquid-phase reactions in the first and second study. While the first study focused on homogeneous POM catalysts and the second study explored their heterogenized form for biomass conversion, the third study targets the gas-phase conversion of CO_2 into DME, a valuable chemical and alternative fuel. Gas-phase reactions offer distinct advantages for industrial applications, including diminishing leaching issues, simplifying catalyst separation and recovery, and facilitating operation under continuous flow conditions.[226] This study aims to demonstrate the adaptability and efficiency of immobilized POMs in such systems, aligning with the broader goal of advancing renewable carbon utilization in industrial-scale catalysis.

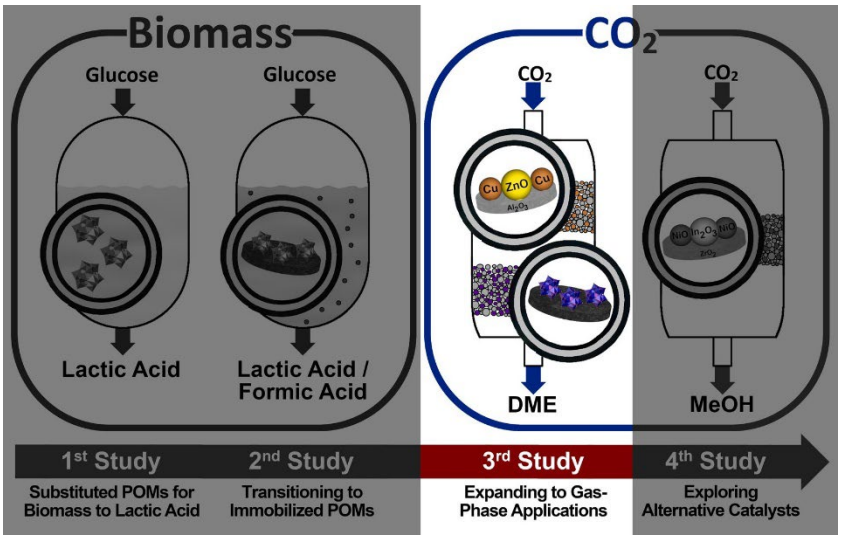

Figure 36: Scope of the third study: Expanding to gas-phase applications.

The bifunctional catalytic system utilized in this study combined a commercial methanol synthesis catalyst, $Cu/ZnO/Al_2O_3$, with a POM catalyst for methanol dehydration, enabling the direct synthesis of DME from CO_2. In the first phase of the study, various conventional and custom-designed POMs were immobilized on *Montmorillonite K10* to evaluate the influence of framework metals (Mo, W), heteroatoms (P, Si), and overall charge variations on the catalytic activity. All supported catalysts were tested in a fixed-bed reactor for the direct synthesis of DME from CO_2, with $H_4[SiW_{12}O_{40}]$ supported on K10 (HSiW/K10) emerging as the most effective catalyst. The second phase examined the influence of support materials on the catalytic performance of HSiW. Immobilization on ZrO_2 as support significantly enhanced catalytic activity, attributed to homogeneous distribution and enhanced accessibility of acid sites. The performance of the $HSiW/ZrO_2$ catalyst was compared to that of a reference catalyst prepared via a literature-reported synthesis method. Both catalysts were tested under identical reaction conditions, demonstrating comparable activity and highlighting the robustness of $HSiW/ZrO_2$ regardless of the synthesis approach. These findings underscore the suitability of ZrO_2 as a support material for gas-phase reactions, providing a stable platform for POM immobilization. This work highlights the potential of POM-based systems, particularly $HSiW/ZrO_2$, for scalable and sustainable CO_2-to-DME conversion.

RSC Advances

PAPER

View Article Online
View Journal | View Issue

Cite this: *RSC Adv.*, 2025, **15**, 38

Study of supported heteropolyacid catalysts for one-step DME synthesis from CO_2 and H_2†

Anne Wesner, Nick Herrmann, Lasse Prawitt, Angela Ortmann, Jakob Albert and Maximilian J. Poller *

Received 8th November 2024
Accepted 16th December 2024

DOI: 10.1039/d4ra07964g

rsc.li/rsc-advances

Dimethyl ether (DME) is a versatile molecule, gaining increasing interest as a viable hydrogen and energy storage solution, pivotal for the transitioning from fossil fuels to environmentally friendly and sustainable energy supply. This research explores a novel approach for the direct conversion of CO_2 to DME in a fixed-bed reactor, combining the $Cu/ZnO/Al_2O_3$ methanol synthesis catalyst with supported heteropolyacids (HPAs). First, various HPAs, both commercially available and custom-synthesized, were immobilized on Montmorillonite K10. Using a wet impregnation procedure an almost ideal mono-layer of HPA on the support was achieved. The catalysts were further evaluated for their efficiency in direct synthesis of DME from CO_2/H_2 in combination with the $Cu/ZnO/Al_2O_3$ catalyst. Among the catalysts tested, tungstosilicic acid (HSiW) supported on K10 exhibited the most promising performance, achieving a DME yield (Y_{DME}) of 7.06% and a molar productivity (P_{mol}) of 77.84 mol_{DME} mol_{HPA}^{-1} h^{-1}. In a subsequent step, further tests using HSiW on various support materials identified ZrO_2 as the most effective support, increasing the molar productivity to 125.44 mol_{DME} mol_{HPA}^{-1} h^{-1}, while maintaining the DME yield. The results highlight the potential of applying HPA-based catalysts for sustainable DME synthesis directly from CO_2, emphasizing the critical role of the catalyst support for optimizing catalytic performance.

Introduction

In view of climate change and geopolitical challenges, Europe is turning to renewable energy sources like the sun and wind to reduce dependence on fossil fuels. However, aligning renewable electricity supply with demand is challenging. A viable solution is converting surplus electricity into so-called 'green' hydrogen *via* electrolysis, which can then be transformed into methanol (MeOH) or dimethyl ether (DME), effectively storing the hydrogen.[1,2] DME offers a higher volumetric energy density of 21 MJ L^{-1} compared to hydrogen with 8.5 MJ L^{-1},[3] is environmentally benign, and easily liquefies under slightly elevated pressure for use with existing liquid gas infrastructure. It already has several applications from propellant to diesel substitute, highlighting its potential as a green energy solution.[4–6]

Typically, DME is produced in a two-step process: first, converting syngas (CO/H_2) to methanol using a $Cu/ZnO/Al_2O_3$ catalyst, then, in a second step, dehydrating MeOH into DME with a solid acid catalyst.[7,8] A more efficient approach is the direct synthesis, converting CO or CO_2 with H_2 into DME in one step. This method has several advantages, such as simplified operational procedures, increased reaction rates and enhanced equilibrium conversion, achieved through the continuous removal of MeOH as an intermediate from the reaction mixture. Although this process is not yet ready for commercial application, it has gained significant interest from major players in the DME production industry, such as Topsoe, Air Products & Chemicals for its efficiency and potential.[9,10]

The conversion of CO_2 to DME *via* catalytic hydrogenation is favored from a thermodynamic perspective (eqn (1)). This process requires two different catalytic functionalities: a metallic catalyst for the conversion of CO_2 to methanol, and a solid acid catalyst for the subsequent dehydration of methanol to DME.[8,11]

$$2CO_2 + 6H_2 \leftrightarrow CH_3OCH_3 + 3H_2O \quad \Delta H_{298\ K} = -123\ kJ\ mol^{-1} \tag{1}$$

Within the scientific literature, various catalysts with Brønsted or Lewis acidic functionalities have shown to be effective for dehydrating MeOH to DME, with performance depending on the acidic sites' density and strength. Weak and medium acid centers favor DME production, while very strong acid centers may cause formation of other hydrocarbons and coke.[12–14] Notable catalysts include γ-Al_2O_3, H-ZSM-5, mesoporous silicates such as MCM-41[15] or aluminophosphates,[16]

Institute of Technical and Macromolecular Chemistry, University of Hamburg, Bundesstraße 45, Hamburg 20146, Germany. E-mail: maximilian.poller@uni-hamburg.de; Tel: +49 40 42838 3172

† Electronic supplementary information (ESI) available. See DOI: https://doi.org/10.1039/d4ra07964g

whereby Al_2O_3 and H-ZSM-5 are most commonly used.[8,17] Al_2O_3 faces challenges due to the adsorption of water produced during the reaction, which inhibits the active sites.[18] Conversely, in zeolites like H-ZSM-5, there is a tendency to generate methane or other hydrocarbons as undesirable by-products due to the excessively strong acidic sites.[19]

To overcome the drawbacks of using alumina or zeolites for methanol dehydration, an alternative emerges in the form of Keggin-type heteropolyacids (HPAs) immobilized on supports with high surface areas.[20,21] These anionic metal-oxide clusters, with the general formula $[XM_{12}O_{40}]^{n-}$, feature a central heteroatom X (typically P or Si) and a metal atom M (usually Mo or W). Their properties can be customized by modifying counterions or metal atoms, tailoring charge, acidity, and pH stability for optimal catalytic performance.[22–24] Due to their low surface area (approximately 5–10 $m^2\ g^{-1}$), HPAs benefit significantly from being supported on high surface area supports (such as TiO_2, SiO_2, ZrO_2). This approach gains enhanced access to active centers, boosting their activity in methanol dehydration.[6,25–27]

Attributable to their high Brønsted acidity, lacking the excessively strong acidic sites of zeolites, HPAs exhibit remarkable catalytic activity in the dehydration of methanol and have been subject of various studies.[9,12,20,25,28–31] These studies highlight the strong catalytic performance of HPAs, especially supported $H_3PW_{12}O_{40}$ (HPW) and $H_4SiW_{12}O_{40}$ (HSiW) due to their high acidity.[30,32] In some instances, these have even outperformed the catalytic activity of H-ZSM-5.[33] Notably, HPW supported on MCM-41 exhibited a 100% selectivity towards DME from MeOH at equilibrium conversion.[34] The inherent advantages of HPAs, such as operating under mild conditions, minimizing byproduct formation, thermal stability and resisting deactivation by water, make them especially promising for converting methanol to DME.[9]

To the best of our knowledge, only a limited range of unsubstituted, commercially available HPAs have been utilized in DME synthesis. In this study, the research scope is extended to include transition-metal substituted HPAs to examine the effects of incorporating different heteroatoms such as vanadium and indium. The incorporation of these heteroatoms allow for the modification of the acid sites within the HPAs.[35] This study aims to explore how varying the acidity through different heteroatoms influences their performance as catalysts in the conversion of methanol to DME. Additionally, this research marks the first instance where both commercial and specially designed catalysts have been evaluated under uniform experimental conditions, enabling a detailed comparative and comprehensive analysis of their catalytic performance. Moreover, diverse supports were employed to further investigate the HPA–support interactions.

Experimental methods

The following HPAs were supported on Montmorillonite K10 (K10) *via* wet impregnation: $H_4SiW_{12}O_{40}$ (HSiW), $H_3PMo_{12}O_{40}$ (HPMo), $H_3PW_{12}O_{40}$ (HPW), $H_8PV_5Mo_7O_{40}$ (HPVMo), $H_6PInMo_{11}O_{40}$ (HPInMo), and $H_4SiMo_{12}O_{40}$ (HSiMo). Furthermore, HSiW was supported on different carriers (Al_2O_3, ZrO_2 TiO_2, Celite® 545), using the same method. The supports and catalysts were characterized *via* inductively coupled plasma optical emission spectroscopy (ICP-OES), N_2-physisorption, X-ray diffraction (XRD), NH_3-temperature programmed desorption (NH_3-TPD), scanning electron microscopy (SEM) and infrared spectroscopy (IR). All catalysts were tested in combination with the commercially available $Cu/ZnO/Al_2O_3$ methanol synthesis catalyst in a fixed-bed reactor (Fig. S1†), whereby the two catalyst materials were arranged in two layers separated by a layer of glass wool (Fig. S2†). The reaction conditions were set at 250 °C and 50 bar, with a gas hourly space velocity (GHSV) of 10 000 h^{-1}, and a feed gas composition of H_2/CO_2 at a ratio of 3 : 1. The gas-phase was analyzed using online gas chromatography (Fig. S3†). An in-depth description of the catalyst synthesis and characterization[35–38] including all used chemicals (Table S1†), the catalytic experiments[39] and the catalytic evaluation, can be found in the ESI.†

Results and discussion

Initially, monolayers of various HPAs, including both commercially available and custom-synthesized variants, were deposited on K10 and their performance was evaluated as part of a bifunctional catalyst system together with commercial $Cu/ZnO/Al_2O_3$ catalyst for DME synthesis. Subsequently, the most promising HPA from the initial screening was combined with different support materials, and their catalytic performance in DME synthesis was systematically evaluated.

HPA catalyst selection for DME synthesis – supporting of various HPAs on K10

Synthesis of various supported HPAs on K10. Initially, various HPAs were immobilized on montmorillonite K10 (K10) as carrier. K10 was chosen as support material based on its previously reported performance, which results from its thermal stability, high surface area, excellent adsorption capacity, and excellent mechanical properties.[12,40] The acidic properties of K10 can be enhanced through impregnation with HPAs.[41] The range of HPAs included commercial available HPAs ($H_4SiW_{12}O_{40}$ – HSiW, $H_3PMo_{12}O_{40}$ – HPMo, and $H_3PW_{12}O_{40}$ – HPW) as well as specially synthesized HPAs ($H_8PV_5Mo_7O_{40}$ – HPVMo, $H_6PInMo_{11}O_{40}$ – HPInMo, and $H_4SiMo_{12}O_{40}$ – HSiMo). This selection covers a range of different framework elements (Mo, W), different heteroelements (P, Si), and different charges, resulting in differences concerning the number of protons and their acidic strength.

N_2 physisorption data reveal that K10, as expected, is a mesoporous layered silicate with an average pore radius just below 2 nm (Table 1). A single Keggin molecule possesses a diameter of approximately 1 nm, indicating that HPA molecules can infiltrate the pores and potentially cover the entire surface area.[35] The application of HPAs on K10 results in a reduction of the BET surface area by about half in all samples, additionally, a significant decrease in pore volume is also

Table 1 Textural properties, results of elemental analysis and NH_3-TPD analysis of supported HPAs on K10

Catalyst	HSiW	HPMo	HPW	HPVMo	HPInMo	HSiMo	Pure K10
Textural properties							
S_{BET} ($m^2\ g^{-1}$)	97	100	102	112	106	108	215
Ø pore diameter (nm)	1.96	1.97	1.97	1.97	1.96	1.96	1.97
Pore volume (mL g^{-1})	0.05	0.09	0.05	0.06	0.10	0.06	0.28
Elemental analysis							
W or Mo (wt%)	29.45	20.27	33.53	12.55	23.51	21.50	—
HPA (wt%)	38.42	32.14	43.77	41.15	34.05	30.00	—
$Loading_{eff}$ ($\mu mol_{HPA}\ g_{cat}^{-1}$)	130	180	150	190	220	190	—
$Loading_{theor}$ ($\mu mol_{HPA}\ g_{cat}^{-1}$)	160	190	160	200	190	190	—
NH_3-TPD-normalized adsorption capacity	1.00	1.91	1.02	1.44	2.48	1.36	0.48
Per mass catalyst	1.00	1.91	1.02	1.44	2.48	1.36	0.48
Per molar mass HPA	1.00	1.38	0.88	0.98	1.46	0.93	—

observed. This finding aligns with previous studies, which additionally demonstrated an increase in micropore volume upon impregnation of K10 using HPMo and HPW.[12]

The impregnation of K10 with HPAs aimed at achieving a monolayer of HPA on the entire surface of the support material. The results of elemental analysis (Table 1) were used for the calculation of effective loading ($Loading_{eff}$), which is compared to the maximum theoretical loading ($Loading_{theor}$) to evaluate the impregnation efficiency. Elemental analysis indicates that the impregnation of all HPAs was successful, achieving the target $Loading_{theor}$. For HPMo, HPInMo, and HSiMo, a higher $Loading_{eff}$ is observed, which may be attributed to measurement inaccuracies in the elemental analysis.

SEM-EDX mapping indicates macroscopic homogeneous distribution of the HPA on the support (Fig. 1 and S4†). Combined with the $Loading_{eff}$ values, which align with the predicted $Loading_{theor}$, this supports the assumption that monolayer coverage has been achieved.

SEM indicates no change in morphology of the catalyst due to the synthesis procedure (Fig. S5†). The preservation of the HPA structure upon supporting on K10 is evident in the IR spectra (Fig. 2 and S6†), apparent by the characteristic Keggin vibration bands: 1049–1060 cm^{-1} for P–O vibration, 945–962 cm^{-1} for $M{=}O_{terminal}$, 866–877 cm^{-1} for $M{-}O{-}M_{vertex}$, and 643–767 cm^{-1} for $M{-}O{-}M_{edge}$.[35] K10 itself displays a very broad vibration band at 1027 cm^{-1} from the stretching vibration of Si–O groups,[42] which overlaps with the P=O vibration of the HPAs.

Additionally, the samples were characterized by X-ray diffraction (Fig. S7†). It is evident that the characteristic peaks of the support material were preserved after the synthesis, indicating the structure remained intact. However, a reduction in the intensity of the diffraction peaks of pure K10 is observed following impregnation, indicative of a partial loss of crystallinity due to the impregnation process.[41,43] Furthermore, no peaks corresponding to the HPAs are detected, this is attributed to the insufficient quantity of HPA on the support, resulting in background noise predominance.

NH_3-TPD data (Table 1 and Fig. 3) indicate varying acidities among the different supported HPAs. It is evident that supporting the HPAs on K10 results in increased acidity compared to pure K10 for all HPAs. The supported catalysts themselves exhibit distinct acidity strengths (Table 1). For instance, HPInMo demonstrates a five-fold higher normalized adsorption capacity of 2.48, related to mass of the catalyst, compared to commercially available HSiW (1.00) and HPW (1.02). The supported, unsubstituted HPMo exhibits a relatively high adsorption capacity of 1.91. In contrast, the incorporation of vanadium

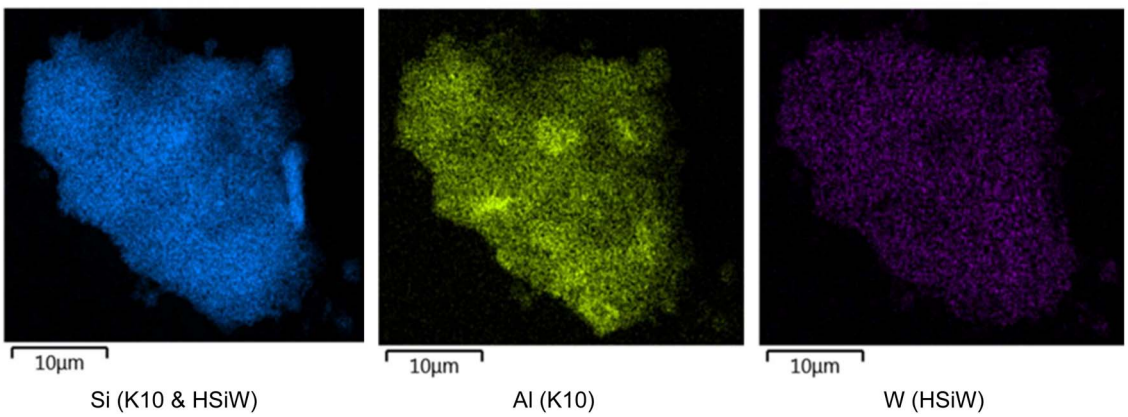

Fig. 1 Exemplary SEM EDX-mapping of HSiW supported on K10.

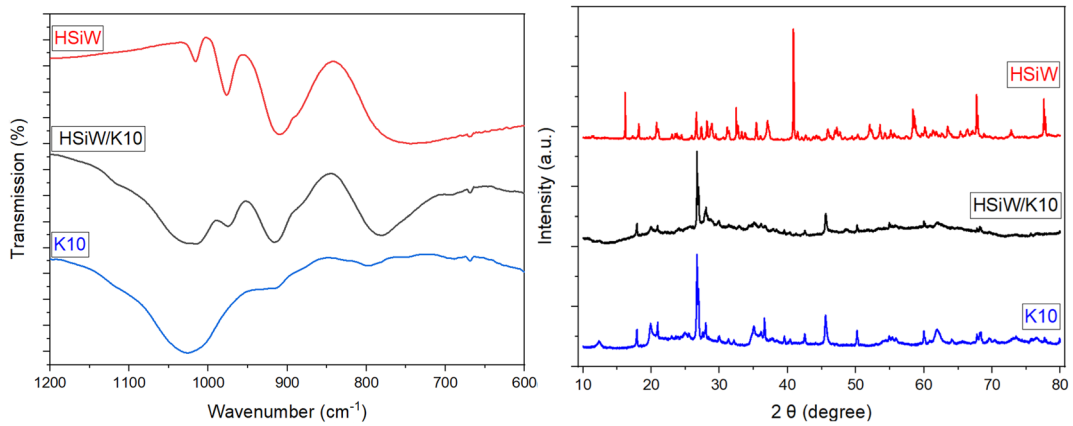

Fig. 2 Exemplary IR spectra (left) and XRD (right) of pure HSiW (red line), HSiW supported on K10 (black line) and pure K10 (blue line).

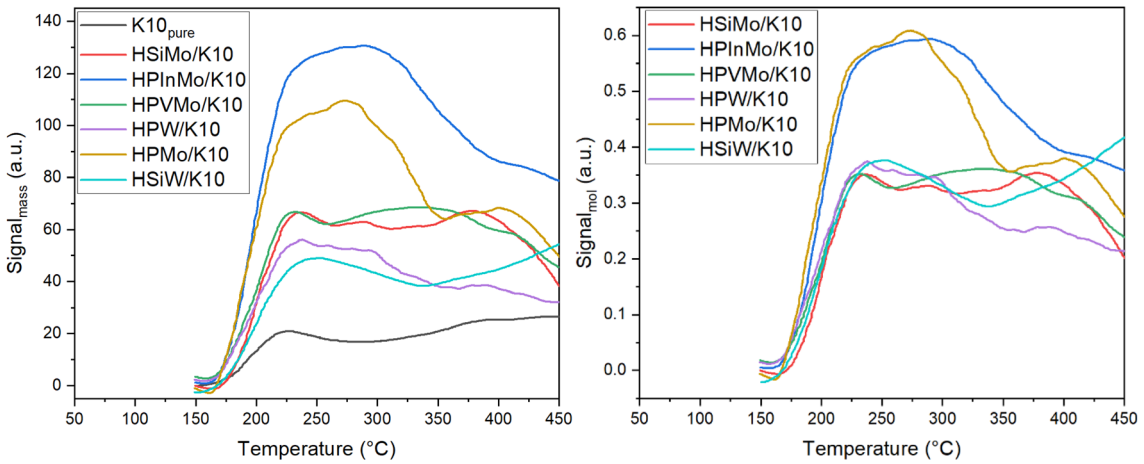

Fig. 3 NH_3-TPD analysis of HPAs supported on K10, normalized to mass of catalyst (left) and normalized to molar mass of supported HPA (right).

(HPVMo) reduces this capacity to 1.44, while HSiMo exhibits an even lower adsorption capacity of 1.36. Thus, incorporation of different heteroatoms allows for targeted adjustment of the acidity of supported HPAs, allowing specific investigation in this study into the impact of acidity on catalytic activity in DME synthesis.

Catalytic performance of supported HPAs on K10. All supported HPAs were tested in combination with the commercial $Cu/ZnO/Al_2O_3$ methanol synthesis catalyst for single-stage DME synthesis from a 3/1 H_2/CO_2 mixture (Fig. 4 and Table S2†). Pure K10 already shows a DME yield of 4.76%, resulting from its own acidic sites (Fig. 3 and Table 1). Impregnation with HPInMo and HPVMo results in a decrease in catalytic activity (Y_{DME} = 4.69% and 3.95%) compared to pure K10. This reduction in activity could be attributed to the decreased surface area of these HPAs, leading to fewer active sites available on the K10 surface. This limitation could not be compensated by the catalytic efficiency of the HPAs, despite their elevated acidity, which was determined by NH_3-TPD. Conversely, after impregnation of K10 with HPW and HSiMo, slight increases in catalytic activity were observed, yielding DME of 5.73% and 5.24% respectively,

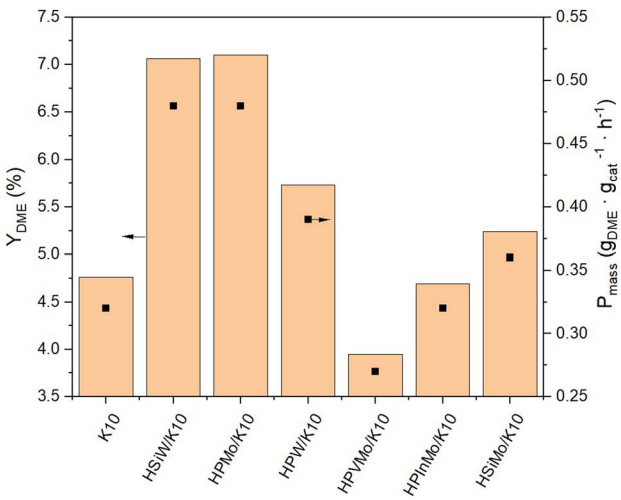

Fig. 4 Yield of DME Y_{DME} and productivity P_{mass} of HPAs supported on K10. Reaction conditions: T = 250 °C, p = 50 bar, H_2/CO_2 3/1, GHSV = 10 000 h^{-1}.

marginally surpassing the performance of pure K10. The highest yields, exceeding 7%, were achieved using HSiW and HPMo impregnated on K10. Under the chosen operating conditions, the thermodynamic DME equilibrium yield of 13%, calculated using the property method Soave–Redlich–Kwong in ASPEN Plus, was not attained using the bifunctional catalyst system, due to the low residence time applied in our setup. The maximum was 54% of equilibrium yield with HPMo/K10 and HSiW/K10.

NH_3-TPD data (Table 1) reveal no direct correlation between the measured acidity and catalytic activity. For instance, impregnation of K10 with HPInMo increases the acidity fivefold, yet the DME yield decreases post-impregnation compared to pure K10. Conversely, K10 impregnated with HSiW and HPMo, which exhibit the highest catalytic activity, show an acidity increase by just two and four times, respectively, compared to pure K10. This discrepancy can be attributed to the reactions being conducted under optimal conditions for methanol synthesis,[44] where especially the Brønsted acidic sites of the heteropoly acids have a negligible impact on DME formation.[41] These conditions were chosen to maximize methanol yield for its subsequent conversion to DME, but leading to no acidity–activity correlation.

The DME selectivities S_{DME} for each supported HPA catalyst follow the same trend as for Y_{DME} (Fig. S8†). The combined selectivities of DME and MeOH make up approximately 50%, with the remaining 50% attributed to the by-product CO (Table S2†) resulting from the competing reverse water–gas-shift (RWGS) reaction. This indicates that in each experiment conducted, the $Cu/ZnO/Al_2O_3$ catalyst produced almost an equal amount of MeOH and CO, as no further reaction of CO occurs on the DME catalyst.[45] Consequently, the comparison of DME synthesis activities of the catalysts for the second reaction step is based on consistent conditions.

The productivity P_{mass} follows the same trend as the DME yield (Y_{DME}), as a consistent mass of catalyst was used across all synthesis experiments (Fig. 4). However, due to the varying molar masses of the individual HPAs, the molar-based productivity P_{mol} shows significant differences (Fig. 5). Here too, HSiW and HPMo on K10 exhibit the highest productivities with 77.84 and 59.40 $mol_{DME}\ mol_{HPA}^{-1}\ h^{-1}$, respectively, with HSiW/K10 having a higher productivity than HPMo/K10 due to its lower molar mass. HPVMo/K10 and HPInMo/K10 continue to show the lowest P_{mol} (both around 30 $mol_{DME}\ mol_{HPA}^{-1}\ h^{-1}$). The comparison of data between HSiW, HPW, HSiMo, and HPMo on K10 is interesting. Among the tungstates, the Si-containing HPA achieves better results, while HPMo catalyzes the reaction more efficiently than both HSiMo and HPW. Thus, it cannot be stated that either of the metals (W or Mo) offers an advantage, nor is there a trend favoring a central hetero atom (Si or P).

The IR spectra indicate that the Keggin structure is preserved after the reaction across all catalysts (Fig. S9†). The Keggin bands are most distinct for the HSiW/K10 and HPW/K10 catalysts. For all molybdenum-containing HPAs, the vibrational bands are identifiable but exhibit weaker intensity. Additionally, all of the molybdates show a dark blue coloration after the reaction (Fig. S10†), suggesting a reduction process has occurred during the reaction to form molybdenum blue (eqn (2)).[46,47] The darker coloration and weakening of IR bands indicate that this reduction is incomplete, suggesting the presence of the reduced species of the catalyst as well as poorer catalyst stability.

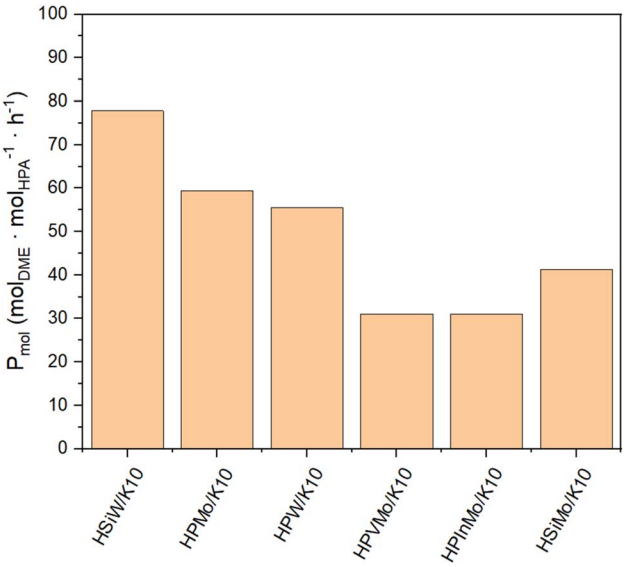

Fig. 5 Productivity P_{mol} of HPAs supported on K10. Reaction conditions: $T = 250$ °C, $p = 50$ bar, H_2/CO_2 3/1, GHSV = 10 000 h^{-1}.

$$[PMo_{12}^{VI}O_{40}]^{3-} + 4e^- \rightleftharpoons [PMo_4^{V}Mo_8^{VI}O_{40}]^{7-} \quad (2)$$

As an interim conclusion, it is notable that the impregnation of K10 with HSiW and HPMo particularly lead to increased DME yields compared to pure K10. By considering molar-based productivity P_{mol}, HSiW/K10 is identified as the most efficient catalyst. To validate these findings, the reproducibility of the experimental procedure was investigated using HSiW/K10 in multiple repetitions. These experiments resulted in consistent yields and selectivities for the by-products, MeOH and CO, as well as stable catalyst productivity across the experiments (Fig. S11 and Table S3†), and thereby confirmed the initial results.

Support selection for DME synthesis – supporting HSiW on different supports

Following the identification of HSiW as the optimal HPA for DME synthesis, its performance was further evaluated on various support materials. To this end, HSiW was immobilized on ZrO_2, Al_2O_3, TiO_2, and Celite® 545 (hereafter simply referred to as Celite). Celite, primarily composed of SiO_2, possesses a unique internal structure with vacuoles surrounded by interconnected pores within its silica walls, providing an ideal surface for physical adsorption. Due to its adsorptive and insulating properties, Celite is widely used in applications such as filtration, chromatography, and mild abrasives.[48] ZrO_2, Al_2O_3, and TiO_2, on the other hand, are established support materials

for supported catalysts, valued for their stability and compatibility with a variety of catalytic processes.[49–52] The influence of support materials in enhancing the catalytic activity of HPAs for DME synthesis is pivotal, as demonstrated in previous studies, which have highlighted the beneficial effects of utilizing various supports such as SiO_2 or TiO_2 for HPAs.[25,53] However, detailed analyses of the support's influence for HPAs remain insufficiently explored in existing research.

The amount of HSiW used for synthesis was adjusted to the surface area of each support to create a monolayer. The impregnation was carried out as described above. In Table 2 the elemental analysis as well as the effective loading $Loading_{eff}$ and the maximum theoretical loading $Loading_{theor}$ and the point of zero charge of the supports are listed. For all supports, the actual and theoretical loadings closely match, indicating complete impregnation of HSiW on each support. IR spectra confirm the preservation of the Keggin structure of all supported catalysts (Fig. S12†).

Celite, like K10, represents another silicate used for supporting HSiW. It exhibits a notably low surface area of just 1 $m^2\ g^{-1}$ and no measurable pore volume (Table 2). The minimal surface area measured can be attributed to Celite's very large pores of ≥200 nm, visible in SEM (Fig. S13†). These pores are too large to be quantified using the available BET measurement equipment. Post-impregnation, SEM images indicate pore blockage (Fig. S13†), and the clustering effect increases the measured surface area to 4.35 $m^2\ g^{-1}$.

For the three oxide materials (ZrO_2, Al_2O_3, and TiO_2), SEM images (Fig. S13†), combined with SEM-EDX images (Fig. S14†), indicate that the particles remain approximately the same size, thus undamaged post-synthesis, and reveal a homogeneous distribution of the HPA across the entire surface. Among these materials, ZrO_2 has the smallest surface area at 91 $m^2\ g^{-1}$, while Al_2O_3 possesses the largest of 277 $m^2\ g^{-1}$. Post-impregnation, the surface areas of Al_2O_3 and TiO_2 decrease by approximately 40%, with a significant reduction in pore volumes as well. Conversely, ZrO_2 shows only an 11% reduction of surface area, with smaller decreases in pore radius and volume, suggesting a particularly uniform distribution of HPA molecules across the entire surface of the support (Table 2).

The supported catalysts as well as the supports themselves were employed in the synthesis of DME (Fig. 6). Among the tested supports, pure K10 demonstrates significant inherent catalytic activity. The incorporation of HPAs onto the supports invariably lead to an enhanced catalytic performance compared to the unmodified supports. The DME yield across all HPA-modified catalysts is observed to be around 7%, with a P_{mass} of 0.5 $g_{DME}\ g_{cat}^{-1}\ h^{-1}$. Due to the limited precision of the measurements, the productivity data do not decisively distinguish the most effective HPA-support combination. Remarkably, the mass-normalized productivity of unsupported HSiW, matches that of the supported catalyst materials.

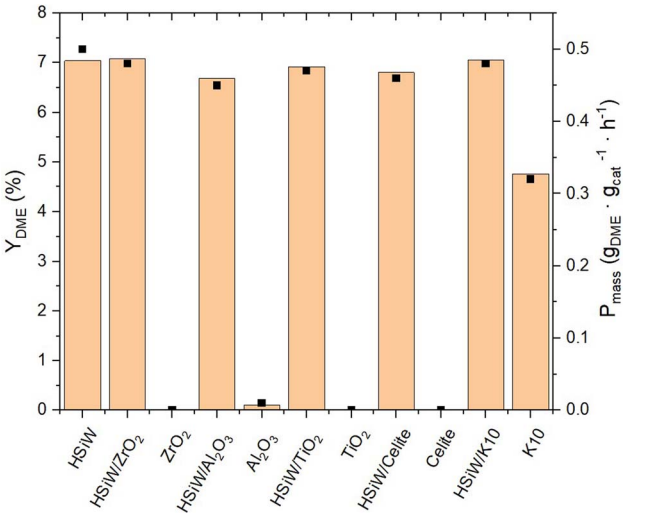

Fig. 6 Yield of DME Y_{DME} and productivity P_{mass} of HSiW on different supports. Reaction conditions: T = 250 °C, p = 50 bar, H_2/CO_2 3/1, GHSV = 10 000 h^{-1}.

When normalizing productivity to the molar amount of catalyst (Fig. 7), unsupported HSiW exhibits the lowest productivity of 35.77 $mol_{DME}\ mol_{HPA}^{-1}\ h^{-1}$. For each support, it is observed that the catalytic activity is consistently enhanced by the support material. This enhancement is attributed to the generally increased surface area, which improves accessibility to active sites crucial for converting MeOH to DME. Interestingly, catalytic activity does not directly correlate solely with higher surface area and therefore with a higher loading of the HSiW monolayer. Impregnation on Celite slightly increases

Table 2 Textural properties and results of elemental analysis of HSiW on different supports

	HSiW/ZrO_2	ZrO_2	HSiW/Al_2O_3	Al_2O_3	HSiW/TiO_2	TiO_2	HSiW/Celite	Celite
Textural properties								
S_{BET} ($m^2\ g^{-1}$)	81	91	161	277	106	163	4	1
Ø pore diameter (nm)	3.40	4.07	1.97	4.48	1.86	2.37	1.57	1.85
Pore volume (mL g^{-1})	0.18	0.28	0.23	0.75	0.13	0.33	0.01	0.00
Point of zero charge		6.52		7.6		5.9		7.08
Elemental analysis								
W (wt%)	18.32	—	33.24	—	28.91	—	45.02	—
HPA (wt%)	27.19	—	49.34	—	42.91	—	68.81	—
$Loading_{eff}$ ($\mu mol_{HPA}\ g_{cat}^{-1}$)	80	—	150	—	130	—	210	—
$Loading_{theor}$ ($\mu mol_{HPA}\ g_{cat}^{-1}$)	90	—	150	—	120	—	210	—

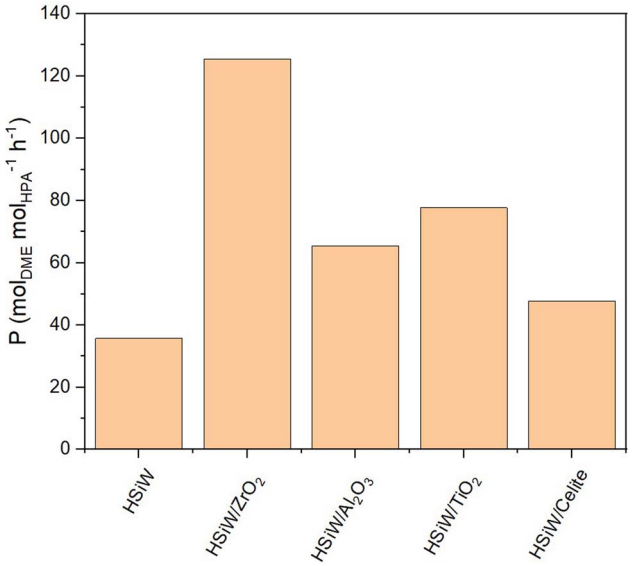

Fig. 7 Productivity P_{mol} of HSiW on different supports. Reaction conditions: T = 250 °C, p = 50 bar, H_2/CO_2 3/1, GHSV = 10 000 h^{-1}.

P_{mol} to 47.68 mol$_{DME}$ mol$_{HPA}^{-1}$ h^{-1}, followed by HSiW on Al_2O_3, TiO_2 and K10, with the HSiW/ZrO_2 as combination achieving the highest P_{mol} of 125.44 mol$_{DME}$ mol$_{HPA}^{-1}$ h^{-1}. This suggests a cooperative effect between the support and the HPA, which enhances the catalytic activity.

As previously demonstrated and confirmed in this section, the combined selectivities of DME and MeOH consistently make up about 50%, with the remaining 50% attributed to the by-product CO (Fig. S15 and Table S4†). This steady result indicates that MeOH production by Cu/ZnO/Al_2O_3 catalyst remains consistent across all experiments, with no further CO conversion by the supported HPA catalyst. This allows for a fair comparison of the DME formation by the supported HPAs in the second reaction step under uniform conditions. The pure supports used for the HPA catalysts showed no catalytic activity for DME synthesis, except for K10, which shows partial conversion of MeOH to DME without any HPA supported.

NH_3-TPD analysis (Fig. S16†) indicates that catalytic activity also does not directly correlate with measured Brønsted acidity. Specifically, HSiW/ZrO_2 exhibits the second highest acidity after HSiW/Al_2O_3. These findings suggest additional factors influencing catalytic activity beyond surface area and Brønsted acidity. Previous studies indicate that ZrO_2 provides additional sites for methanol adsorption, enhancing methanol conversion and leading to higher DME production.[25,54] SEM-EDX analysis and N_2-physisorption also confirm that despite ZrO_2's smaller surface area, it is fully and uniformly covered by HPA after impregnation, ensuring optimal catalytic activity through enhanced accessibility of acid sites, highlighting ZrO_2 as an exceptional support material.

Comparative analysis with previously-reported catalyst

The most effective catalyst identified in this study, hereafter referred to as HSiW/ZrO_2^W, was compared with the leading literature-reported catalyst for DME synthesis from CO_2, HSiW/ZrO_2^K, as reported by Kubas *et al.*[21] To enable a direct comparison of the catalytic performance, the catalyst was synthesized following the method outlined by Kubas,[21] with equivalent HPA-unit loading of 1 HPA unit per nm^2 of, and subsequently tested under identical reaction conditions.

Table 3 Catalytic Results for HPA/ZrO_2 of current study (HPA/ZrO_2^W) *vs.* catalyst from literature (HPA/ZrO_2^K). Reaction conditions: T = 250 °C, p = 50 bar, H_2/CO_2 3/1, GHSV = 10 000 h^{-1}

Catalyst	HSiW/ZrO_2^W	HSiW/ZrO_2^K
X_{CO_2} (%)	19.36	18.70
Y_{MeOH} (%)	3.32	3.40
Y_{DME} (%)	7.08	6.88
Y_{CO} (%)	12.50	11.85
S_{MeOH} (%)	14.50	15.36
S_{DME} (%)	30.91	31.09
S_{CO} (%)	54.59	53.55
P_{mass} (g$_{DME}$ g$_{cat}^{-1}$ h^{-1})	0.48	0.47
P_{mol} (mol$_{DME}$ mol$_{HPA}^{-1}$ h^{-1})	125.44	108.67

The catalytic performance (Table 3) of HSiW/ZrO_2^K shows generally good agreement with HSiW/ZrO_2^W, with slightly higher values for DME yield (Y_{DME} = 7.08%) and selectivity (S_{DME} = 30.91%) for HSiW/ZrO_2^K, compared to HSiW/ZrO_2^W with Y_{DME} = 6.88% and S_{DME} = 31.09%. The mass-specific productivities for both catalysts are equivalent, with P_{mass} = 0.48 g$_{DME}$ g$_{cat}^{-1}$ h^{-1} (HSiW/ZrO_2^W) and 0.47 g$_{DME}$ g$_{cat}^{-1}$ h^{-1} (HSiW/ZrO_2^K). However, due to lower HPA loading, the molar productivity of our HSiW/ZrO_2^W is higher compared to the HSiW/ZrO_2^K catalyst reported by Kubas *et al.*,[21] indicating a possible improvement in HPA dispersion resulting from the synthesis method we used in this study.

Overall, the comparison underscores the enhanced catalytic activity of HSiW supported on ZrO_2 as a robust support material, irrespective of specific synthesis or reaction conditions. This study further demonstrates, through the use of tailored heteropoly acid catalysts and a range of supports, that parameters such as support surface area, pore size, and the tuned acidity of heteropoly acids do not have a definitive impact on catalytic activity. Notably, HSiW/ZrO_2 consistently outperforms other polyoxometalates, although the exact underlying mechanisms remain unclear and warrant further investigation.

Conclusions

In this study, various HPA catalysts were employed for the single-step synthesis of DME. Therefore, bifunctional catalyst systems, combining commercial Cu/ZnO/Al_2O_3 catalyst with supported HPAs, have been prepared. Both commercial HPAs (HPW, HPMo, HSiW) and specially synthesized HPAs (HPVMo, HPInMo, HSiMo) were used. The successful impregnation of K10 montmorillonite with monolayers of various HPAs was confirmed by a range of analytical techniques including ICP-OES, SEM-EDX, and N_2-physisorption. Subsequently, these catalysts were evaluated, in combination with a methanol synthesis catalyst, for their DME synthesis activity in a fixed-bed

reactor. HSiW emerged as the most effective catalyst in this screening, achieving a DME yield of 7.06% (53% of the equilibrium yield) and a molar productivity of 77.84 mol_{DME} mol_{HPA}^{-1} h^{-1}. Upon impregnation onto different supports, HSiW supported on ZrO_2 proved to be the optimal catalyst, enhancing the molar productivity up to 125.44 mol_{DME} mol_{HPA}^{-1} h^{-1}. Overall, we evaluated an unprecedented range of heteropolyacids and support materials for this reaction. The results highlight that, beyond the strengths and numbers of acidic centers, the uniform dispersion of HSiW on ZrO_2 enhances accessibility to catalytic active sites.

Data availability

The data supporting our article with the title "Study of supported heteropolyacid catalysts for one step DME synthesis from CO_2 and H_2" have been included as part of the ESI.† Further information is available on request.

Author contributions

Anne Wesner was responsible for synthesis and characterization of the catalysts, interpreting data, conceptualizing the experimental workflow, and drafting the manuscript. Nick Herrmann performed supervision and design of catalytic experiments. Lasse Prawitt and Angela Ortmann carried out the catalyst synthesis as well as characterization and conducted all catalytic experiments. Prof. Jakob Albert provided infrastructure and equipment. As principal investigator, Dr Maximilian J. Poller was responsible for conceptualization of this project, acquired financial support, coordinated and supervised the project. All authors contributed to the discussion of the work and the scientific writing.

Conflicts of interest

There are no conflicts to declare.

Acknowledgements

We gratefully acknowledge the central analytical services of the Chemistry Department at UHH for carrying out ICP-OES (Dr Dirk Eifler and his team), SEM (Dr Charlotte Ruhmlieb and her team), and XRD (Dr Frank Hoffmann and Isabelle Nevoigt) measurements. Furthermore, we thank Philipp Kampe for his advice concerning the operation of the fixed bed reactor setup, and Dr Jan-Christian Raabe for his support concerning the synthesis of HPAs. We also thank Hauke Heller for providing access to the BET apparatus and Sandra König for her valuable guidance in operating the BET device. This project was funded by the "Behörde für Wissenschaft, Forschung, Gleichstellung und Bezirke" of the Free Hanseatic City of Hamburg (BWFGB) *via* the Hamburg Innovation GmbH through the Call4Transfer funding program (grant number C4T839).

References

1 P. Schühle, R. Stöber, M. Semmel, A. Schaadt, R. Szolak, S. Thill, M. Alders, C. Hebling, P. Wasserscheid and O. Salem, Dimethyl ether/CO_2 – a hitherto underestimated H_2 storage cycle, *Energy Environ. Sci.*, 2023, **16**, 3002–3013.
2 E. Pawelczyk, N. Łukasik, I. Wysocka, A. Rogala and J. Gębicki, Recent Progress on Hydrogen Storage and Production Using Chemical Hydrogen Carriers, *Energies*, 2022, **15**, 4964.
3 M. Hilgers, *Alternative Antriebe und Ergänzungen zum konventionellen Antrieb*, Springer Fachmedien Wiesbaden, Wiesbaden, 2016.
4 Z. Azizi, M. Rezaeimanesh, T. Tohidian and M. R. Rahimpour, Dimethyl ether: a review of technologies and production challenges, *Chem. Eng. Process.: Process Intensif.*, 2014, **82**, 150–172.
5 E. Catizzone, G. Bonura, M. Migliori, F. Frusteri and G. Giordano, CO_2 Recycling to Dimethyl Ether: State-of-the-Art and Perspectives, *Mol.*, 2018, **23**, 31.
6 N. Mota, E. M. Ordoñez, B. Pawelec, J. L. G. Fierro and R. M. Navarro, Direct Synthesis of Dimethyl Ether from CO_2: Recent Advances in Bifunctional/Hybrid Catalytic Systems, *Catalysts*, 2021, **11**, 411.
7 S. Banivaheb, S. Pitter, K. H. Delgado, M. Rubin, J. Sauer and R. Dittmeyer, Recent Progress in Direct DME Synthesis and Potential of Bifunctional Catalysts, *Chem. Ing. Tech.*, 2022, **94**, 240–255.
8 K. Krim, A. Sachse, A. Le Valant, Y. Pouilloux and S. Hocine, One Step Dimethyl Ether (DME) Synthesis from CO_2 Hydrogenation over Hybrid Catalysts Containing Cu/ZnO/Al_2O_3 and Nano-Sized Hollow ZSM-5 Zeolites, *Catal. Lett.*, 2023, **153**, 83–94.
9 C. Peinado, D. Liuzzi, S. N. Sluijter, G. Skorikova, J. Boon, S. Guffanti, G. Groppi and S. Rojas, Review and perspective: Next generation DME synthesis technologies for the energy transition, *Chem. Eng. J.*, 2024, **479**, 147494.
10 A. Akhoondi, A. I. Osman and A. A. Eslami, Direct catalytic production of dimethyl ether from CO and CO_2: a review, *Synth. Sinter.*, 2021, **1**, 105–125.
11 C. Liu and Z. Liu, Perspective on CO_2 Hydrogenation for Dimethyl Ether Economy, *Catalysts*, 2022, **12**, 1375.
12 A. Kornas, M. Śliwa, M. Ruggiero-Mikołajczyk, K. Samson, J. Podobiński, R. Karcz, D. Duraczyńska, D. Rutkowska-Zbik and R. Grabowski, Direct hydrogenation of CO_2 to dimethyl ether (DME) over hybrid catalysts containing CuO/ZrO_2 as a metallic function and heteropolyacids as an acidic function, *React. Kinet., Mech. Catal.*, 2020, **130**, 179–194.
13 Y. Fu, T. Hong, J. Chen, A. Auroux and J. Shen, Surface acidity and the dehydration of methanol to dimethyl ether, *Thermochim. Acta*, 2005, **434**, 22–26.
14 L. Travalloni, A. C. Gomes, A. B. Gaspar and M. A. Da Silva, Methanol conversion over acid solid catalysts, *Catal. Today*, 2008, **133–135**, 406–412.

15 D. VARIŞLI, K. C. TOKAY, A. ÇİFTÇİ, T. DOĞU and G. DOĞU, Methanol dehydration reaction to produce clean diesel alternative dimethylether over mesoporous aluminosilicate-based catalysts, *Turk. J. Chem.*, 2009, **33**(3), 355–366.

16 W. Dai, W. Kong, G. Wu, N. Li, L. Li and N. Guan, Catalytic dehydration of methanol to dimethyl ether over aluminophosphate and silico-aluminophosphate molecular sieves, *Catal. Commun.*, 2011, **12**, 535–538.

17 H. Bateni and C. Able, Development of Heterogeneous Catalysts for Dehydration of Methanol to Dimethyl Ether: A Review, *Catal. Ind.*, 2019, **11**, 7–33.

18 M. Xu, J. H. Lunsford, D. Goodman and A. Bhattacharyya, Synthesis of dimethyl ether (DME) from methanol over solid-acid catalysts, *Appl. Catal., A*, 1997, **149**, 289–301.

19 N. Khandan, M. Kazemeini and M. Aghaziarati, Determining an optimum catalyst for liquid-phase dehydration of methanol to dimethyl ether, *Appl. Catal., A*, 2008, **349**, 6–12.

20 D. Kubas, J. M. Beck, E. Kasisari, T. Schätzler, A. Becherer, A. Fischer and I. Krossing, From CO_2 to DME: Enhancement through Heteropoly Acids from a Catalyst Screening and Stability Study, *ACS Omega*, 2023, **8**, 15203–15216.

21 D. Kubas, M. Semmel, O. Salem and I. Krossing, Is Direct DME Synthesis Superior to Methanol Production in Carbon Dioxide Valorization? From Thermodynamic Predictions to Experimental Confirmation, *ACS Catal.*, 2023, **13**, 3960–3970.

22 M. T. Pope, *Heteropoly and Isopoly Oxometalates*, Springer Berlin, Berlin, 2013.

23 M. T. Pope and A. Müller, Polyoxometalate Chemistry: An Old Field with New Dimensions in Several Disciplines, *Angew. Chem., Int. Ed. Engl.*, 1991, **30**, 34–48.

24 N. I. Gumerova and A. Rompel, Synthesis, structures and applications of electron-rich polyoxometalates, *Nat. Rev. Chem*, 2018, **2**, 0112.

25 C. Peinado, D. Liuzzi, R. M. Ladera-Gallardo, M. Retuerto, M. Ojeda, M. A. Peña and S. Rojas, Effects of support and reaction pressure for the synthesis of dimethyl ether over heteropolyacid catalysts, *Sci. Rep.*, 2020, **10**, 8551.

26 E. Millán, N. Mota, R. Guil-López, B. Pawelec, J. L. García Fierro and R. M. Navarro, Direct Synthesis of Dimethyl Ether from Syngas on Bifunctional Hybrid Catalysts Based on Supported H3PW12O40 and Cu-ZnO(Al): Effect of Heteropolyacid Loading on Hybrid Structure and Catalytic Activity, *Catalysts*, 2020, **10**, 1071.

27 A. Wesner, M. P. Papajewski, L. Schidowski, C. Ruhmlieb, M. J. Poller and J. Albert, Supported H8PV5Mo7O40 on activated carbon: synthesis and investigation of influencing factors for catalytic performance, *Dalton Trans.*, 2024, **53**, 14065–14076.

28 H. HAYASHI, The properties of heteropoly acids and the conversion of methanol to hydrocarbons, *J. Catal.*, 1982, **77**, 473–484.

29 F. M. Ebeid, L. Ali and F. F. Abdalla, Conversion Of Methanol Over Metal-Salts Of 12-Molybdophosphoric Acid, *Indian J. Biochem.*, 1992, **31**, 921–928.

30 R. M. Ladera, M. Ojeda, J. L. G. Fierro and S. Rojas, TiO_2-supported heteropoly acid catalysts for dehydration of methanol to dimethyl ether: relevance of dispersion and support interaction, *Catal. Sci. Technol.*, 2015, **5**, 484–491.

31 W. Alharbi, E. F. Kozhevnikova and I. V. Kozhevnikov, Dehydration of Methanol to Dimethyl Ether over Heteropoly Acid Catalysts: The Relationship between Reaction Rate and Catalyst Acid Strength, *ACS Catal.*, 2015, **5**, 7186–7193.

32 R. M. Ladera, J. L. G. Fierro, M. Ojeda and S. Rojas, TiO_2-supported heteropoly acids for low-temperature synthesis of dimethyl ether from methanol, *J. Catal.*, 2014, **312**, 195–203.

33 B. P. Karaman and N. Oktar, Tungstophosphoric acid incorporated hierarchical HZSM-5 catalysts for direct synthesis of dimethyl ether, *Int. J. Hydrogen Energy*, 2020, **45**, 34793–34804.

34 A. Ciftci, D. Varisli, K. C. Tokay, N. A. Sezgi and T. Dogu, Dimethyl ether, diethyl ether & ethylene from alcohols over tungstophosphoric acid based mesoporous catalysts, *Chem. Eng. J.*, 2012, **207–208**, 85–93.

35 J.-C. Raabe, M. J. Poller, D. Voß and J. Albert, H8 PV5 Mo7 O40 - A Unique Polyoxometalate for Acid and RedOx Catalysis: Synthesis, Characterization, and Modern Applications in Green Chemical Processes, *ChemSusChem*, 2023, **16**, e202300072.

36 J.-C. Raabe, J. Aceituno Cruz, J. Albert and M. J. Poller, Comparative Spectroscopic and Electrochemical Study of V(V)-Substituted Keggin-Type Phosphomolybdates and -Tungstates, *Inorganics*, 2023, **11**, 138.

37 V. F. Odyakov and E. G. Zhizhina, A novel method of the synthesis of molybdovanadophosphoric heteropoly acid solutions, *React. Kinet. Catal. Lett.*, 2008, **95**, 21–28.

38 J. D. H. Strickland, The Preparation and Properties of Silicomolybdic Acid. I. The Properties of Alpha Silicomolybdic Acid, *J. Am. Chem. Soc.*, 1952, **74**, 862–867.

39 A. Wesner, P. Kampe, N. Herrmann, S. Eller, C. Ruhmlieb and J. Albert, Indium-based Catalysts for CO_2 Hydrogenation to Methanol: Key Aspects for Catalytic Performance, *ChemCatChem*, 2023, **15**, e202301125.

40 J. Zhao, X. Zheng, Q. Liu, M. Xu, S. Yang and M. Zeng, Chitosan supported Pd^0 nanoparticles encaged in Al or Al-Fe pillared montmorillonite and their catalytic activities in Sonogashira coupling reactions, *Appl. Clay Sci.*, 2020, **195**, 105721.

41 M. Śliwa, K. Samson, M. Ruggiero-Mikołajczyk, A. Żelazny and R. Grabowski, Influence of Montmorillonite K10 Modification with Tungstophosphoric Acid on Hybrid Catalyst Activity in Direct Dimethyl Ether Synthesis from Syngas, *Catal. Lett.*, 2014, **144**, 1884–1893.

42 Z. Danková, A. Mockovčiaková and S. Dolinská, Influence of ultrasound irradiation on cadmium cations adsorption by montmorillonite, *Desalin. Water Treat.*, 2014, **52**, 5462–5469.

43 G. D. Yadav and N. Kirthivasan, Synthesis of bisphenol-A: comparison of efficacy of ion exchange resin catalysts vis-à-vis heteropolyacid supported on clay and kinetic modelling, *Appl. Catal., A*, 1997, **154**, 29–53.

44 I. Kiendl, H. Schmaderer, N. Schödel and H. Klein, Experimentelle und theoretische Betrachtungen der Methanol- und direkten DME-Synthese im Labor- und Technikums-Maßstab, *Chem. Ing. Tech.*, 2020, **92**, 736–745.
45 P. Kampe, N. Herrmann, C. Ruhmlieb, M. Finsel, O. Korup, R. Horn and J. Albert, Spatially Resolved Reaction Profiles of CO_2 Hydrogenation to Methanol Using In-Based Catalysts in a Compact Profile Reactor, *ACS Sustainable Chem. Eng.*, 2024, **12**, 9541–9549.
46 A. Müller, J. Meyer, E. Krickemeyer and E. Diemann, Molybdenum Blue: A 200 Year Old Mystery Unveiled, *Angew. Chem., Int. Ed. Engl.*, 1996, **35**, 1206–1208.
47 J. N. Barrows, G. B. Jameson and M. T. Pope, Structure of a heteropoly blue. The four-electron reduced .beta.-12-molybdophosphate anion, *J. Am. Chem. Soc.*, 1985, **107**, 1771–1773.
48 V. Pace, J. V. Sinisterra and A. R. Alcantara, A. Celite-Supported Reagents in Organic Synthesis: An Overview, *COC*, 2010, **14**, 2384–2408.
49 K. Tanabe, Surface and catalytic properties of ZrO_2, *Mater. Chem. Phys.*, 1985, **13**, 347–364.
50 M. Trueba and S. P. Trasatti, γ-Alumina as a Support for Catalysts: A Review of Fundamental Aspects, *Eur. J. Inorg. Chem.*, 2005, **2005**, 3393–3403.
51 S. Bagheri, N. M. Julkapli and S. B. A. Hamid, Titanium dioxide as a catalyst support in heterogeneous catalysis, *Sci. World J.*, 2014, **2014**, 727496.
52 T. W. van Deelen, C. H. Mejía and K. P. Jong, de Control of metal-support interactions in heterogeneous catalysts to enhance activity and selectivity, *Nat. Catal.*, 2019, **2**, 955–970.
53 J. Schnee, A. Eggermont and E. M. Gaigneaux, Boron Nitride: A Support for Highly Active Heteropolyacids in the Methanol-to-DME Reaction, *ACS Catal.*, 2017, **7**, 4011–4017.
54 E. Rafiee and S. Eavani, Heterogenization of heteropoly compounds: a review of their structure and synthesis, *RSC Adv.*, 2016, **6**, 46433–46466.

6.4 Exploring Alternative Catalysts: In_2O_3-based Catalysts for CO_2 Conversion to Methanol:

The fourth study explores the development of In_2O_3-based catalysts as an alternative for the gas-phase conversion of CO_2 to methanol. Study one to three investigated the application of POMs in homogeneous and heterogeneous catalysis - covering biomass conversion in liquid-phase systems (first and second study) and CO_2-to-DME synthesis in gas-phase systems (third study). In the third study, the bifunctional system of the commercial $Cu/ZnO/Al_2O_3$ catalyst for CO_2 hydrogenation to methanol combined with POMs for the subsequent dehydration to DME, exhibited high catalytic activity. Despite its industrial relevance, the $Cu/ZnO/Al_2O_3$ catalyst faces significant drawbacks, particularly deactivation caused by water, a by-product of methanol synthesis to CO_2. To address these limitations, In_2O_3-based catalysts, which are already recognized for their stability and activity in CO_2 hydrogenation, were evaluated and further optimized.

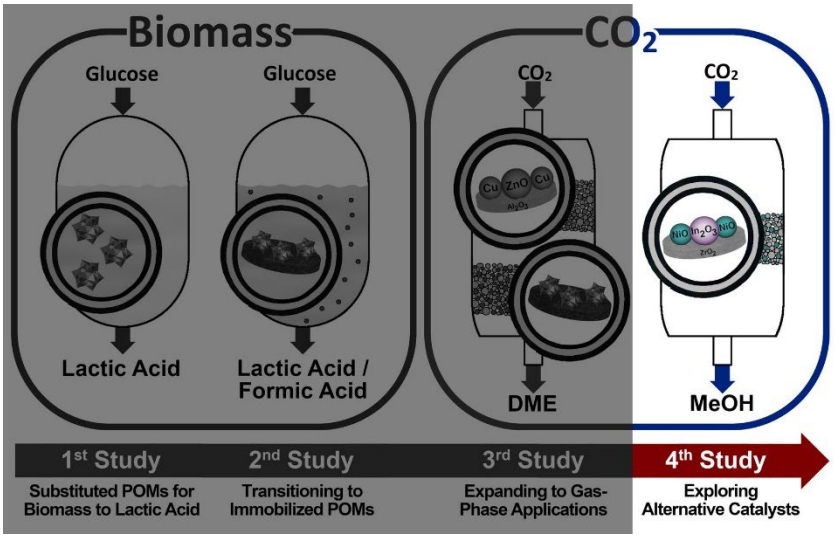

Figure 37: Scope of the fourth study: Exploring alternative catalysts.

This study systematically investigated In_2O_3-based catalysts for CO_2 hydrogenation to methanol, focusing on support material properties, preparation techniques, and promoter effects. A primary focus was placed on the role of ZrO_2 as a support material. Different types of ZrO_2, varying in combination with different preparation methods for In_2O_3/ZrO_2 catalysts were evaluated. Beyond support optimization, the study explored the effect of incorporating metal oxide promoters, such as CeO_2, MgO, CuO, and NiO, into the In_2O_3/ZrO_2 catalyst system. Among the tested promoters, NiO emerged as the most promising promoter, enhancing methanol productivity and CO_2 conversion. The incorporation of NiO in In_2O_3/ZrO_2 catalyst was further optimized by testing different synthesis methods, including chemical reduction, co-precipitation, and wet impregnation. Hereby, the utilization of wet impregnation showed the best results, yielding a highly active $NiO\text{-}In_2O_3/ZrO_2$ catalyst. To assess the industrial viability of the optimized $NiO\text{-}In_2O_3/ZrO_2$ catalyst, long-term stability tests were conducted, where the catalyst maintained high performance over 100 hours time-on-stream. Post-reaction characterization revealed no structural or morphological degradation, confirming its robustness under industrially relevant conditions. This study underscores the potential of $NiO\text{-}In_2O_3/ZrO_2$ as a robust and scalable alternative for methanol synthesis, by addressing the challenges present in catalyst preparation, support material interactions, and promoter optimization.

ChemCatChem

Research Article
doi.org/10.1002/cctc.202301125

Chemistry Europe
European Chemical Societies Publishing

www.chemcatchem.org

Indium-based Catalysts for CO_2 Hydrogenation to Methanol: Key Aspects for Catalytic Performance

Anne Wesner[+],[a] Philipp Kampe[+],[a] Nick Herrmann,[a] Sebastian Eller,[a] Charlotte Ruhmlieb,[b] and Jakob Albert*[a]

CO_2 hydrogenation utilizing sustainably produced hydrogen and CO_2 derived from industrial exhaust gas represents a pivotal technology for chemical energy storage and climate change mitigation. This work aims to identify the best combination of catalyst support, synthesis method and promotor for In_2O_3/ZrO_2 catalysts in a typical fixed-bed configuration. Intense characterization using ICP-OES, XRD, XPS, N_2-physisorption, CO_2-TPD, H_2-TPR and SEM-EDX provide molecular insights into the different effects caused by various synthesis methods and doping elements. Doping the most promising In_2O_3/ZrO_2 (M-SG) catalyst with 0.7 wt.% NiO by wetness impregnation using an ethanol/water mixture as a solvent, an increased methanol production rate of 0.497 $g_{MeOH} \cdot g_{cat}^{-1} \cdot h^{-1}$ could already be achieved at 250 °C. Hereby, the low amount of highly dispersed NiO promotes H_2 activation via hydrogen spillover, leading to sustained catalytic activity for 100 hours of time-on-stream.

Introduction

The worldwide demand for energy is growing continuously, fossil resources are depleting, and atmospheric CO_2 levels are on the rise.[1] As a result, there is a growing significance placed on the generation of energy from renewable sources such as solar, wind and biomass, as well as the capture, storage and use of CO_2 as a valuable raw material.[2,3,4] In this context, methanol (MeOH) produced by electrolysis hydrogen and captured CO_2 has emerged as an efficient approach [Equation (1)].

$$CO_2 + 3\ H_2 \rightleftharpoons CH_3OH + H_2O \qquad \Delta H_R = -50\ kJ\,mol^{-1} \tag{1}$$

Additionally, methanol forms the basis for various bulk chemicals, such as formaldehyde and olefins.[4] However, the endothermic reverse water gas shift (RWGS) reaction [Equation (2)] considerably reduces the methanol selectivity under typical reaction conditions (200–300 °C, 50–100 bar).[5] Moreover, CO as a by-product can also undergo hydrogenation to form methanol [Equation (3)].

$$CO_2 + H_2 \rightleftharpoons CO + H_2O \qquad \Delta H_R = +41\ kJ\,mol^{-1} \tag{2}$$

$$CO + 2\ H_2 \rightleftharpoons CH_3OH \qquad \Delta H_R = -91\ kJ\,mol^{-1} \tag{3}$$

For commercial applications, copper-based catalysts such as $Cu/ZnO/Al_2O_3$ are typically used for methanol synthesis from mixed syngas ($CO/CO_2/H_2$). Cu as an active metal facilitates hydrogen spillover, whereby active H atoms are generated on the metal surface through H_2-dissociation on the Cu-surface and subsequently migrate to the support material.[6,7] In recent mechanistic studies involving CuZnO-containing catalysts, selectivity loss has been observed not only through the RWGS reaction but also trough an additional pathway involving CO formation via methanol decomposition.[8] However, this catalyst exhibits limited activity for CO_2 hydrogenation due to deactivation caused by the by-product H_2O.[9] Moreover, temperatures exceeding 280 °C lead to thermal sintering of Cu, that impairs catalytic performance even further.[10]

Recently, In_2O_3/ZrO_2 catalysts have demonstrated to be highly efficient catalysts for hydrogenation of CO_2 to methanol in several studies.[11–14] Under typical reaction conditions of $T = 200$–275 °C and $p = 35$–75 bar, In_2O_3 generates oxygen vacancies that activate CO_2 for the formation of formate ($HCOO^-$).[15] The In_3O_5 ensemble adjacent to the vacancy stabilizes the heterolytic splitting of H_2. As a result, the formation of CO through RWGS is inhibited, leading to an increased methanol selectivity.[14,16] The combination of In_2O_3 and ZrO_2 as a support achieved a synergistic effect at the interface between oxygen vacancy defects of the oxides.[17] Adjusting the right particle size and morphology control are key factors for preparing Indium-based catalysts with high activity.[18] The ZrO_2 carrier plays a crucial role in preventing the sintering of In_2O_3, thus ensuring long-time-stability of the

[a] A. Wesner,[+] P. Kampe,[+] N. Herrmann, S. Eller, Prof. Dr. J. Albert
Institute of Technical and Macromolecular Chemistry
Universität Hamburg
Bundesstraße 45, 20146 Hamburg (Germany)
E-mail: jakob.albert@uni-hamburg.de

[b] Dr. C. Ruhmlieb
Institute of Physical Chemistry
Universität Hamburg
Grindelallee 117, 20146 Hamburg (Germany)

[+] These authors contributed equally to this work and therefore share first authorship.

Supporting information for this article is available on the WWW under https://doi.org/10.1002/cctc.202301125

catalyst. According to proposed mechanisms, the oxygen vacancy filled after methanol desorption is regenerated through its hydrogenation by water formation.[19] The composition of reducing and oxidizing components in the gas phase under common reaction conditions of CO_2 hydrogenation maintains the equilibrium between surface oxygen atoms and vacancies. This balanced configuration maintains the catalyst in an active state and hinders its deactivation.[20] Moreover, phase-transitions caused by fluctuating conditions like hydrogen drop out caused by intermittent hydrogen sources like electrolysis may affect the catalytic performance of Indium-based catalysts.[21]

The present study reveals the influence of different ZrO_2 carriers on In_2O_3/ZrO_2 catalysts, as well as the impact of different preparation methods in gas-phase CO_2 hydrogenation to methanol. Additionally, the impact of doping In_2O_3/ZrO_2 with various metal oxides (CeO_2, MgO, CuO, NiO) was investigated, as this has proven to increase the performance in slurry-phase CO_2 hydrogenation to methanol.[22] Hereby, Ni and Cu might enhance H_2 dissociation and migration to the support surface, promoting oxygen vacancy formation pushing the system to higher methanol productivity.[23,24] Another approach involved increasing the CO_2 adsorption capacity of In_2O_3/ZrO_2 by adding basic materials, such as Mg or Ce. On the one hand, Mg-based oxides are used as basic supports for Cu in CO_2 hydrogenation.[25] CeO_2, on the other hand, serves as a catalyst for CO oxidation to CO_2 through generation of oxygen vacancies. These vacancies could also be active for CO_2 hydrogenation and enhance methanol selectivity.[26]

Results and Discussion

Impact of different ZrO_2-supports on the catalytic performance of In_2O_3/ZrO_2-catalysts

ZrO_2 as a support material for In_2O_3 has shown to optimize oxygen vacancy formation being beneficial for CO_2 activation and effectively prevents sintering of In_2O_3, as proven by stability tests over 1000 h time-on-stream.[12,14,27] The use of monoclinic ZrO_2 for supporting In_2O_3 allows epitaxial growth of In_2O_3, whereby the mismatching of the crystal lattices leads to formation of tensile forces. This, in turn, promotes the formation of an increased number of oxygen vacancies in In_2O_3, enhancing its catalytic properties. Additionally, vacancies in ZrO_2 being close to In_2O_3 may also interact and enforce methanol synthesis.[12,14,25,28]

There are two established In_2O_3/ZrO_2 catalysts reported in literature, both utilizing monoclinic ZrO_2 as a support material.[12,13] However, they exhibit distinct catalytic performance regarding methanol synthesis via CO_2 hydrogenation, despite containing the same amount of In. Therefore, in the following discussion, we will investigate the main characteristics of two different commercial monoclinic ZrO_2 supports for In_2O_3, referred to as Alfa Aesar (AA) and Saint Gobain (SG), and their influence on the resulting catalytic performance for CO_2 hydrogenation to methanol.

Synthesis procedures as described in the literature were utilized for the preparation of In_2O_3/ZrO_2-catalysts (see Supplementary methods). Throughout this study, In_2O_3/ZrO_2 catalysts used and prepared by Schühle et al.[13] will be referred to as SAA, and In_2O_3/ZrO_2 catalysts used and prepared by Martin et al.[12] as M-SG. Both catalysts were used for CO_2 hydrogenation to methanol at elevated reaction temperatures (250, 275 or 300 °C) and pressures (50 or 75 bar) in a high-pressure continuous-flow fixed-bed reactor setup (Figure S1). To put the In-based catalysts in perspective with the commercial Cu-based catalyst for methanol synthesis, we compared the methanol productivity at 250 °C for the same pressures (50 and 75 bar) at 250 °C. The commercial $Cu/ZnO/Al_2O_3$ catalyst shows a methanol productivity of $P_{cat} = 0.964\ g_{MeOH}\ g_{cat}^{-1} \cdot h^{-1}$. (Figure S2).

Figure 1 summarizes the main catalytic results for In_2O_3/ZrO_2-catalysts at both pressure levels. In detail, In_2O_3/ZrO_2 (M-SG) shows both, higher P_{cat} and Y_{MeOH}, independently of the applied reaction conditions (Table S1). A maximum methanol productivity of $0.470\ g_{MeOH} \cdot g_{cat}^{-1} \cdot h^{-1}$ for In_2O_3/ZrO_2 (M-SG) was achieved at 300 °C and 75 bar, whereby only $0.330\ g_{MeOH} \cdot g_{cat}^{-1} \cdot h^{-1}$ were achieved using In_2O_3/ZrO_2 (S-AA). Moreover, In_2O_3/ZrO_2 (M-SG) yielded a maximum Y_{MeOH} of 10.0% compared to In_2O_3/ZrO_2 (S-AA) with a Y_{MeOH} of only 6.8%. The equilibrium yield of methanol (12.9%, dotted line) was simulated for 300 °C and 75 bar using the property method Soave-Redlich-Kwong in ASPEN Plus. The experimental standard deviations of two different catalyst batches were determined by calculating the arithmetic means at the highest P_{cat} (Figure S3, Table S2).

Initial analysis of the ZrO_2 supports by ICP-OES (Table 1) confirmed high purity of both materials. XRD diffraction patterns confirmed a monoclinic crystal lattice for both ZrO_2 supports with characteristic-111 and 111 reflections at 28.18° and 31.47°, respectively, as well as smaller broad reflection for the 022 crystal lattices at 50.12° (Figure S6a). SEM analysis showed alike morphology for both supports (Figure S5a, b). Notably, ZrO_2 (SG) exhibited a significantly higher surface area than ZrO_2 (AA) with a BET-surface of 89 m^2/g vs. 51 m^2/g.

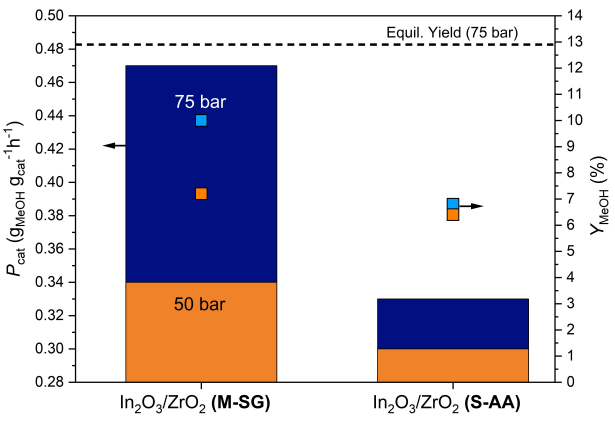

Figure 1. Evolution of productivity (left) and methanol yield (right) in dependency of total pressure $p = 50$ bar (orange) and $p = 75$ bar (blue) for different ZrO_2 supports (SG or AA). Simulated equilibrium yield at $T = 300$ °C and $p = 75$ bar. Reaction conditions: $CO_2/H_2 = 1/3$; $GHSV = 8400\ h^{-1}$; $TOS = 3$ h; $T = 300$ °C; $h_{bed} = 5.1 \pm 0.1$ cm.

Table 1. Textural properties of ZrO_2 and In_2O_3/ZrO_2.

	In (wt.%)[a]	Zr (wt.%)[a]	S_{BET} (m^2/g)[b]	∅ pore radius (nm)[b]	pore volume (cm^3/g)[b]	particle size (nm)[c]
ZrO_2 (SG)	–	65.48	89.35	4.07	0.292	–
ZrO_2 (AA)	–	66.49	51.27	5.69	0.238	–
In_2O_3/ZrO_2 (M-SG)	11.08	56.28	75.96	3.39	0.214	11.84
In_2O_3/ZrO_2 (S-AA)	11.11	56.28	44.97	5.67	0.174	16.91
In_2O_3/ZrO_2 (S-SG)	9.82	56.52	75.36	3.70	0.222	11.77
In_2O_3/ZrO_2 (M-AA)	10.91	60.33	49.14	5.71	0.203	16.91

[a] Determined by ICP-OES. [b] Measured by N_2-physisorption. [c] Calculated using the Scherrer equation (Equation S1) based on the In_2O_3 (222) reflection in the XRD diffractograms (Figure S6a).

Furthermore, the average pore volume of ZrO_2 (SG) of 0.292 cm^3/g was higher than for ZrO_2 (AA) with 0.238 cm^3/g (Table 1). The average pore diameters for both ZrO_2 range in the mesoporous area between 4–6 nm.[29,30] Both supports, however, showed only weak interactions with CO_2, as evident from the CO_2-TPD spectra (Figure 2a), that exhibit a desorption peak between 100–300 °C, that can be assigned to physisorbed CO_2.[31,32] Desorption peaks assigned to chemisorbed CO_2 through thermally induced oxygen vacancies can be observed in a small amount.[12,30] Nevertheless, ZrO_2 (AA) demonstrates slightly less interaction with CO_2 compared to ZrO_2 (SG) in the low temperature area (Figure 2a, Table S3). In H_2-TPR, negligible interactions with H_2 were observed for both support materials (Figure 2b, Table S4).

Elemental analysis confirmed the desired In loading of ~10 wt.% for both In_2O_3/ZrO_2 (M-SG) and In_2O_3/ZrO_2 (S-AA) catalysts (Table 1). Moreover, the incorporation of In_2O_3 in the monoclinic ZrO_2 structure was evident due to an additional pattern at 30.59° in XRD, assigned to 222 reflection of In_2O_3 (Figure S6a). SEM analysis revealed no significant change in morphology throughout the synthesis process (Figure S5) SEM-EDX mapping further confirmed an overall homogeneous distribution of each element on the catalyst surface (Figure 3).

After impregnation, the surface area decreases equally byabout 12% for both catalysts, along with a reduction of pore radius and volume (Table 1, Figure S6b). This observation indicates the agglomeration of In_2O_3 on the ZrO_2 surface as well as within the pores. Notably, the chemisorptive properties of the catalysts exhibited distinct changes compared to pure ZrO_2. As anticipated, the incorporation of In_2O_3 into the crystalline framework results in a shift of CO_2 desorption peaks to higher temperatures as well as an increased CO_2 desorption signal intensity, indicating an enhanced capacity to bind CO_2 (Figure 2a, Table S3). These results are in good agreement with literature.[12,14,26,33] CO_2 adsorption of In_2O_3/ZrO_2 (M-SG) exhibited those of In_2O_3/ZrO_2 (S-AA) in both strength and capacity (Table S3). Between 250 °C and 350 °C the formation of an oxygen vacancy between two In atoms allows the bridging coordination of CO_2.[12] The desorption peak in this range for In_2O_3/ZrO_2 (M-SG) shows a higher CO_2 uptake and therefore more surface In atoms are available leading to less bulk-In compared to In_2O_3/ZrO_2 (S-AA).

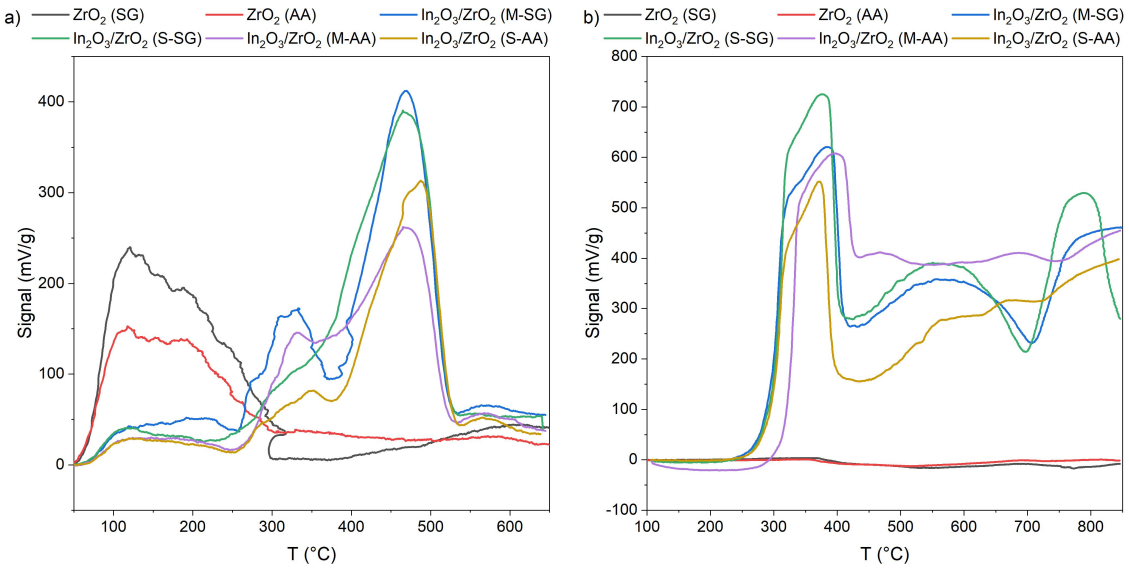

Figure 2. Chemisorptive analysis of different ZrO_2 supports (AA and SG) and In_2O_3/ZrO_2 catalysts (S-SG, S-AA and M-SG, M-AA): a) CO_2-TPD and b) H_2-TPR.

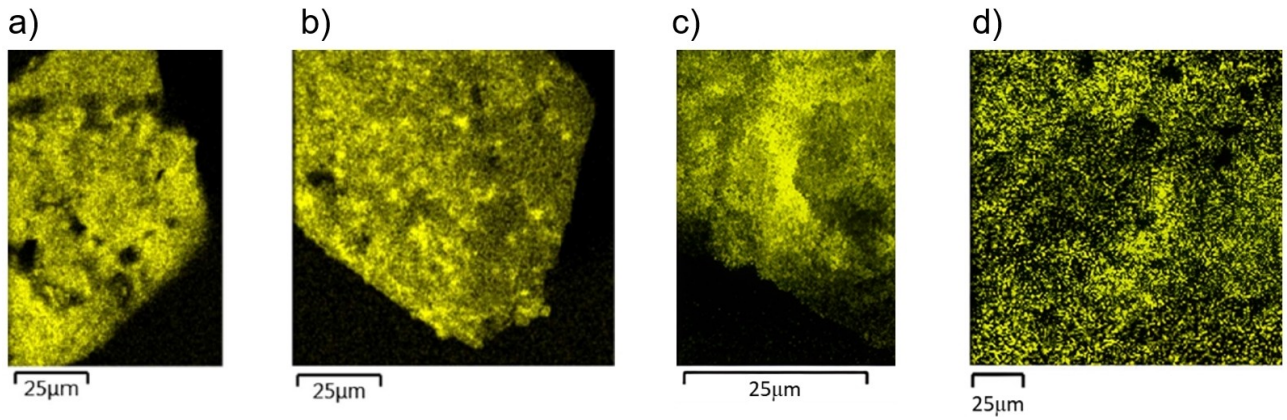

Figure 3. SEM-EDX mapping elemental analysis of In for a) In_2O_3/ZrO_2 (S-AA), b) In_2O_3/ZrO_2 (M-SG), c) In_2O_3/ZrO_2 (S-SG) and d) In_2O_3/ZrO_2 (M-AA).

Results of H_2-TPR revealed a significant increase in the surface reducibility of In_2O_3/ZrO_2 catalysts compared to pure ZrO_2. Furthermore, the reduction capacity of In_2O_3/ZrO_2 (M-SG) exhibits those of In_2O_3/ZrO_2 (S-AA) (Figure 2b). The TPR profile of In_2O_3/ZrO_2 (M-SG) showed two reduction peaks between around 100–420 °C and 420–470 °C, assigned to the reduction of surface species of In_2O_3 (100–420 °C)[32] and reduction of bulk In_2O_3 (> 420 °C).[34] Notably, In_2O_3/ZrO_2 (M-SG) exhibits higher H_2 adsorption capacity at lower temperatures, indicating and increased propensity for hydrogen dissociation during methanol synthesis (Table S4).[35]

Impact of synthesis method on the catalytic performance of In_2O_3/ZrO_2 catalysts

Besides the different ZrO_2 supports (AA or SG), there is also a disparity in the synthesis method between In_2O_3/ZrO_2 (S-AA) and In_2O_3/ZrO_2 (M-SG). Martin (M) et al.[12] utilize a solvent system containing ethanol and water (74/26 H_2O/EtOH v/v), whereas Schühle et al.[13] (S) employ pure water. Furthermore, (M) uses a substantially higher amount of solvent (47 $mL_{solvent}/g_{ZrO_2}$) in comparison to (S) with 20 $mL_{solvent}/g_{ZrO_2}$. Moreover, the synthesis procedure of (M) involves a significantly longer stirring time for synthesis of five hours comparing to (S) where the solvent is evaporated immediately after mixing the suspension without further stirring.

The aim of our study was to identify the determining key factors being responsible for the observed different catalytic activities of In_2O_3/ZrO_2 (S-AA) and In_2O_3/ZrO_2 (M-SG). Therefore, also hybrid catalysts were prepared by combining the original ZrO_2-supports with the respective corresponding synthesis method. This resulted in In_2O_3/ZrO_2 (S-AA or S-SG) and In_2O_3/ZrO_2 (M-AA or M-SG). For In_2O_3/ZrO_2 (M-AA), the standard deviations of experimental procedure out of four experiments and two different batches were calculated (Figure S3 and Table S2).

A comparison of the CO_2 hydrogenation activity at 300 °C and 75 bar displays significant differences in the used ZrO_2 as well as synthesis method with regard both to productivity and yield (Figure 4). Generally, catalysts prepared according to (M) showed higher P_{cat} (around 0.4402–0.470 $g_{MeOH} \cdot g_{cat}^{-1} \cdot h^{-1}$) than catalysts prepared according to (S) with only 0.320–0.399 $g_{MeOH} \cdot g_{cat}^{-1} \cdot h^{-1}$. Moreover, the ZrO_2 supports applied by (SG) gave better results than the one of (AA), related to the mass of catalyst.

Examining the productivity $P_{surface}$ normalized to the surface area (Table 1) for all In_2O_3/ZrO_2 catalysts, the discernible impact of the synthesis method is evident (Figure S4). Whether considering ZrO_2 (SG) catalysts with $P_{surface} = 5.29$ and 6.19 $mg_{MeOH} \cdot m^{-2} \cdot h^{-1}$ (S-SG or M-SG) or ZrO_2 (AA) with $P_{surface} =$ 7.12 and 8.18 $mg_{MeOH} \cdot m^{-2} \cdot h^{-1}$ (S-AA or M-AA), it can be seen, that catalysts prepared using the synthesis procedure of (M) exhibit higher normalized productivity. Nevertheless, the catalytic results show that the surface area of the employed ZrO_2 is the most significant influence on catalytic activity, while the synthesis method has a subordinated influence on the catalytic activity for CO_2-hydrogenation.

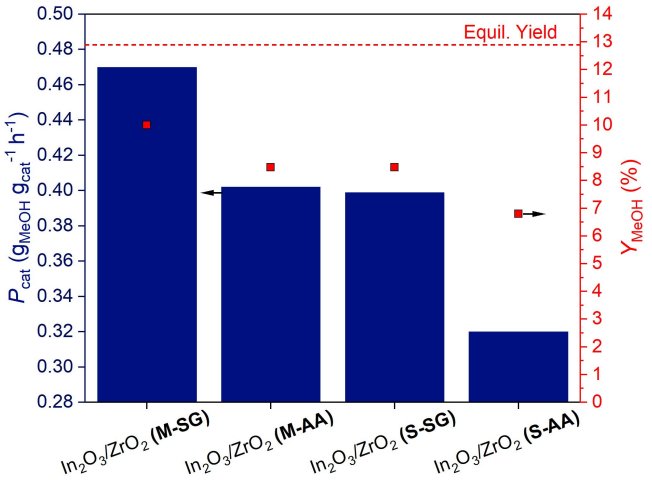

Figure 4. Influence of different ZrO_2 (SG or AA) supports and synthesis methods (M or S) on methanol yield and productivity in comparison to the calculated equilibrium yield. Reaction conditions: $CO_2/H_2 = 1/3$; GHSV = 8400 h^{-1}; *TOS* = 3 h; *T* = 300 °C; *p* = 75 bar; $h_{bed} = 5.1 \pm 0.1$ cm.

Elemental analysis of all catalysts confirmed the same amount of In loading of around 10 wt.% (Table 1). XRD diffraction patterns of all In_2O_3/ZrO_2 show characteristic patterns for monoclinic ZrO_2 as well as cubic In_2O_3 (Figure S6a). According to SEM analysis, no morphological changes can be observed due to the synthesis procedure (Figure S5, c–f). Furthermore, SEM-EDX mapping shows that In is dispersed homogeneously on ZrO_2 on a macroscopic level. Furthermore, no significant differences in the distribution of In_2O_3 on ZrO_2 for the different catalysts could be displayed (Figure 3). Additionally, the crystallite size of In_2O_3 on ZrO_2 was determined using the Scherrer-Debye equation (Equation S1, Table 1).[36] Despite an overall homogeneous distribution, it is evident that the particle size is influenced by the type of ZrO_2 used rather than the synthesis method. Specifically, when ZrO_2 (SG) was employed, particle sizes were consistently smaller, with 11.84 nm for In_2O_3/ZrO_2 (M-SG) and 11.77 nm for In_2O_3/ZrO_2 (S-SG). In contrast, the use of ZrO_2 (AA) as a support resulted in a larger particle size of 16.91 nm for both In_2O_3/ZrO_2 (M-AA) and In_2O_3/ZrO_2 (S-AA). The smaller crystallite sizes observed with ZrO_2 (SG) as support correlate with higher catalytic performance.

Interestingly, chemisorptive data show that the catalysts differ significantly with respect to their adsorption as well as reduction behaviour. CO_2-TPD results show that In_2O_3/ZrO_2 catalysts based on ZrO_2 (SG) have overall higher as well as stronger CO_2 binding capacities than those based on ZrO_2 (AA), which confirms stronger interactions between In_2O_3 and ZrO_2 (SG) (Figure 2a and Table S3). Regardless of the support used, the synthesis procedure of (M) leads to catalysts with overall higher CO_2 adsorption. Additionally, H_2-TPR data show a strong dependency of the used ZrO_2 and the synthesis procedure. In detail, using ZrO_2 (AA) with the synthesis method of (M) enhanced the reduction capacity of 0.8 (In_2O_3/ZrO_2 (S-AA)) to the same amount as for the ZrO_2-based SG catalysts with 1.06 (In_2O_3/ZrO_2 (M-AA)) (Figure 2b and Table S4).

Physisorptive analysis show, however, that the surface area as well as the pore volume of In_2O_3/ZrO_2 (M-AA) with 49.14 m^2/g and 0.203 cm^3/g is higher than for In_2O_3/ZrO_2 (S-AA) with 44.97 m^2/g and 0.174 cm^3/g (Table 1). Through the longer stirring time employed by (M) and the use of more solvent, it is possible that the metal particles have been able to gain access to enter the pores and thereby prevent their blocking.[37,38] Additionally, there could be an effect of the solvent. Using ethanol instead of water as solvent for the impregnation lowers the polarity and could cause stronger interactions between In_2O_3 and ZrO_2. This can be seen in the TPR results of ZrO_2 (AA)-based catalysts, where more species have been formed, which are reduced at higher temperatures, indicating formation of bulk In_2O_3 (Figure 2b and Table S4).[38,39] This effect is not as strong for ZrO_2 (SG) based catalysts, which is due the overall higher surface area of ZrO_2, decreasing the influence of the synthesis method.

Effect of Cu-, Ni-, Mg-, or Ce-as promotors on the catalytic performance of In_2O_3/ZrO_2 catalysts

To further enhance the catalytic performance of In_2O_3/ZrO_2 in CO_2 hydrogenation to methanol, various promotors (Cu, Ni, Mg, Ce) were added to the In_2O_3/ZrO_2 catalyst. These materials can enhance the formation of methanol in different ways. On the one hand side, basic materials like Ce as well as Mg can catalyze oxidation of in-situ formed CO by the competing RWGS reaction further to CO_2, resulting in the formation of additional oxygen vacancies.[2,19,23] Furthermore, it was shown that Ce and Mg as promotors can enhance the CO_2 adsorption capacity.[40] Cu as well as Ni have the property of enhancing hydrogen spillover, whereby the atomic hydrogen takes part in the consecutive hydrogenation of carbon containing surface species to form methanol.[7,41] In this study, the influence of different metal promotors for the In_2O_3/ZrO_2 (M-SG) catalyzed CO_2 hydrogenation to methanol was examined. Therefore, ZrO_2 (SG) as the most promising support was chosen and impregnated with In_2O_3 together with the respective promotors via co-precipitation (for detailed description see Supporting Information).

To evaluate the different catalytic activities of the various promoters, this study was carried out at 250 °C and 75 bar since lower reaction kinetics and theoretically higher equilibrium yield of MeOH $Y_{Eq.,MeOH}$ = 28.9% would be possible (calculated by the property method Soave-Redlich-Kwong in ASPEN Plus). Figure 5 shows a higher productivity of the Ce-promoted In_2O_3/ZrO_2 (0.083 $g_{MeOH} \cdot g_{cat}^{-1} \cdot h^{-1}$) compared to the Mg-promoted In_2O_3/ZrO_2 (0.049 $g_{MeOH} \cdot g_{cat}^{-1} \cdot h^{-1}$), but both metals decrease the catalytic activity of the pristine In_2O_3/ZrO_2 (M-SG) of 0.159 $g_{MeOH} \cdot g_{cat}^{-1} \cdot h^{-1}$ while keeping the selectivity S_{MeOH} of about 80%. Promoting the catalyst with Cu also downgrades the productivity (P_{cat} = 0.088 $g_{MeOH} \cdot g_{cat}^{-1} \cdot h^{-1}$) while only slightly decreasing the selectivity (S_{MeOH} = 75%). In contrast, the addition of Ni to In_2O_3/ZrO_2 catalysts increases the catalytic performance up to 0.221 $g_{MeOH} \cdot g_{cat}^{-1} \cdot h^{-1}$ compared to the unmodified In_2O_3/ZrO_2 (M-SG) with only a slight selectivity decrease to S_{MeOH} = 66%.

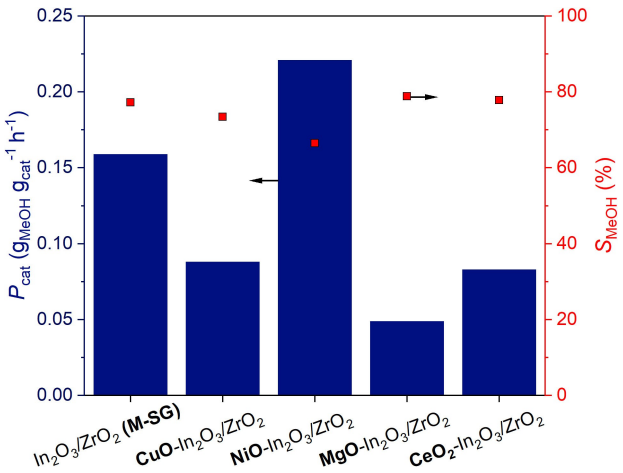

Figure 5. Catalytic performance of CuO-, NiO-, MgO- and CeO-promoted In_2O_3/ZrO_2 compared to In_2O_3/ZrO_2 (M-SG) Reaction conditions: CO_2/H_2 = 1/3; GHSV = 8300 h^{-1}; *TOS* = 3 h; *T* = 250 °C; *p* = 75 bar; h_{bed} = 5.1 ± 0.1 cm.

Table 2. Textural properties of metal promoted In_2O_3/ZrO_2.

	Cu/Ni/Mg/Ce (wt.%)[a]	In (wt.%)[a]	Zr (wt.%)[a]	S_{BET} (m^2/g)[b]	Ø pore radius (nm)[b]	pore volume (cm^3/g)[b]
CuO-In_2O_3/ZrO_2	7.66	6.37	55.55	79.78	4.07	0.324
NiO-In_2O_3/ZrO_2	6.40	7.76	50.12	88.93	3.70	0.260
MgO-In_2O_3/ZrO_2	2.62	8.95	48.66	88.82	3.71	0.270
CeO_2-In_2O_3/ZrO_2	5.11	6.95	52.84	87.87	4.05	0.256

[a] Determined by ICP-OES. [b] Measured by N_2-physisorption.

ICP-OES elemental analysis confirmed the successful impregnation of ZrO_2 with In_2O_3 and the respective promotor (Table 2), while SEM analysis revealed no change in morphology after impregnation (Figure S8). However, precipitation was not complete, as the desired loading of 10 wt.% for both, In and the respective promotor, could only be achieved up to 8 wt.%. XRD data show, that only patterns of ZrO_2 can be observed, but none of In_2O_3 or the respective promotors, indicating both exist in an amorphous state (Figure S9a). To assess the potential impact of slight variations in metal loadings on the catalytic performance, we examined also P_{metal} next to P_{cat}. P_{metal} involves normalizing productivity to the quantity of all active metals (Table 2), including Indium and the respective promotor. The enhanced catalytic activity of NiO-In_2O_3/ZrO_2 remains evident even when accounting all active surface species. P_{metal} of NiO-In_2O_3/ZrO_2 with 1.563 $g_{MeOH} \cdot g_{metal}^{-1} \cdot h^{-1}$ is higher than for pure In_2O_3/ZrO_2 with 1.437 $g_{MeOH} \cdot g_{metal}^{-1} \cdot h^{-1}$ (Figure S7). The conversion of CO_2 was 5.7% using the NiO-In_2O_3/ZrO_2 catalyst compared to 4.4% using the pure In_2O_3/ZrO_2 catalyst.

XPS analysis was performed to examine in which oxidation state the respective metals are present. XPS survey spectra of all catalysts exhibit the expected peaks for Zr3d, In3d, O1s as well as a C1s peak, that can be attributed to surface impurities from the measurements (Figure 6). Each spectrum shows peaks corresponding to the presence of the promotor (Cu, Ni, Mg and Ce). The XPS deconvolution results reveal that In is only present as In_2O_3 in the catalyst and no metallic In^0 is present. The In3d signals in the XPS spectra are observed at binding energy values of approximately 445 eV (for In3d 5/2) and 453 eV (for In3d 3/2) (Figure S10a).[42,43]

Interestingly, XPS analysis further confirm that Cu, Ni, Mg and Ce are all present in their oxidized form before and after reaction (Figure S10b–e). Cu2p spectra of CuO-In_2O_3/ZrO_2 reveal that Cu is present in its oxidized form as CuO with characteristic signals at 933 and 942 eV with a splitting of 19.8 eV.[42–44] For NiO, the Ni2p spectra exhibit mainly signals corresponding to NiO at 855 and 873 eV.[20,45] Mg is identified as magnesium oxide (MgO) based on the characteristic binding energy at 1305 eV.[46] Ce3d spectra could be depicted into three regions with binding energy values of 882, 897 and 915 eV, that can be assigned to CeO_2.[47]

Physisorptive data show that synthesis via co-precipitation just led to a slight decrease of the BET-surface. All metal-promoted catalysts show BET-surfaces around 89 m^2/g (Ni, Ce,

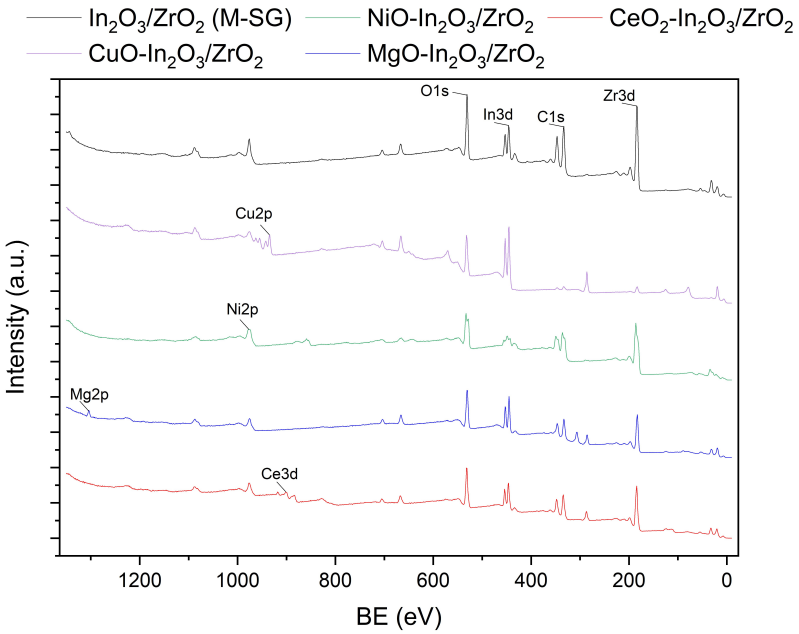

Figure 6. XPS survey spectra of In_2O_3/ZrO_2 (M-SG), as well as CuO-, NiO-, MgO-, and CeO_2- promoted In_2O_3/ZrO_2.

Mg) or 80 m^2/g (Cu). Therefore, incorporation of the metals via co-precipitation leads to higher surface areas compared to wetness impregnation as for In_2O_3/ZrO_2 (M-SG) with 76 m^2/g. Range of pore sizes with overall pore radii of 3.7 to 4.1 nm as well as pore volumes with 0.26–0.32 cm^3/g for the metal-incorporated In_2O_3/ZrO_2 catalysts are higher than for In_2O_3/ZrO_2 (M-SG) with 3.4 nm and 0.21 cm^3/g, respectively (Table 2, Figure S9b). This suggests the presence of all metal oxides on the surface, but no penetration into the pores, as well as formation of agglomerates.

The incorporation of the promotors also leads to a change in CO_2 adsorption capacity (Figure 7a). In detail, adding MgO, CuO & NiO to In_2O_3 lead to a higher overall CO_2 adsorption capacity compared to the non-promoted catalyst (In_2O_3/ZrO_2 (M-SG)) by a factor of more than 1.5 (see Table S5). In the case of CeO_2, the adsorption capacity decreases by a factor of 0.8. The presence of NiO on the In_2O_3/ZrO_2-catalyst facilitates the reduction of the catalyst surface, as evidenced by the shift to lower temperatures required for H_2 adsorption in H_2-TPR experiments (Figure 7b). Overall, both higher CO_2 adsorption as well as easier reducibility contribute to a higher methanol productivity.

The decrease in activity for the CuO-In_2O_3/ZrO_2 catalyst compared to In_2O_3/ZrO_2 (M-SG) is significant in terms of both productivity and selectivity (Figure 5). This can be attributed to the differences in chemisorptive properties. When examining the CO_2-TPD data, it is observed that the overall CO_2 adsorption capacity of CuO-In_2O_3/ZrO_2 is higher. However, the temperature required for CO_2 desorption is also significantly elevated compared to In_2O_3/ZrO_2 (M-SG). Compared to In_2O_3/ZrO_2 (M-SG) with the highest CO_2 desorption temperature at 470 °C, the required temperature for CO_2 desorption increased about 100 °C up to 570 °C when CuO is incorporated (Figure 7a, Table S5). This indicates that the catalyst has a strong affinity for CO_2 adsorption, but the adsorption strength is excessive for efficient methanol production in subsequent steps. In H_2-TPR data, a notable baseline shift is observed at higher temperatures (> 690 °C) for CuO-In_2O_3/ZrO_2 (Figure 7b, Table S6). This indicates that the bulk material is reduced and hydrogen evolves at higher temperatures.

Among all the catalysts studied, MgO-In_2O_3/ZrO_2 exhibited the lowest catalytic activity. This can be attributed to the unexpected decrease in CO_2 adsorption capacity strength, indicating weaker CO_2 adsorption at the catalyst's surface (Figure 7a, Table S5). Additionally, the incorporation of Mg results in a decrease in the reducibility of the catalyst, as evident from the H_2-TPR data (Figure 7b, Table S6).

In case of the CeO_2-In_2O_3/ZrO_2 catalyst compared to the non-promoted (In_2O_3/ZrO_2 (M-SG)), there is a decrease in overall adsorption capacity (Figure 7a, Table S5). This could be attributed to the formation of In_2O_3 and CeO_2 clusters, as observed in the EDX mapping analysis (Figure 8b). The inhomogeneous distribution of these clusters may hinder the adsorption of CO_2 and result in reduced adsorption capacity. This finding is also consistent with the TPR data (Figure 7b, Table S6) that shows a shift to higher reduction temperatures and lower reduction capacity for the CeO_2-In_2O_3/ZrO_2 catalyst, resulting from bulk formation. This, in turn, leads to a decrease in productivity.

In conclusion, particularly the incorporation of NiO significantly enhances the catalytic performance. The hydrogen spillover effect facilitates H_2 adsorption, subsequently improving H_2 dissociation and migration to the support surface, resulting in higher methanol productivity and CO_2 conversion. This mechanism fosters the formation of oxygen vacancies, resulting in higher methanol productivity of the system. This enhancement is proven by chemisorptive analysis, showing significantly higher levels of both adsorbed CO_2 or H_2 compared to all other catalysts.

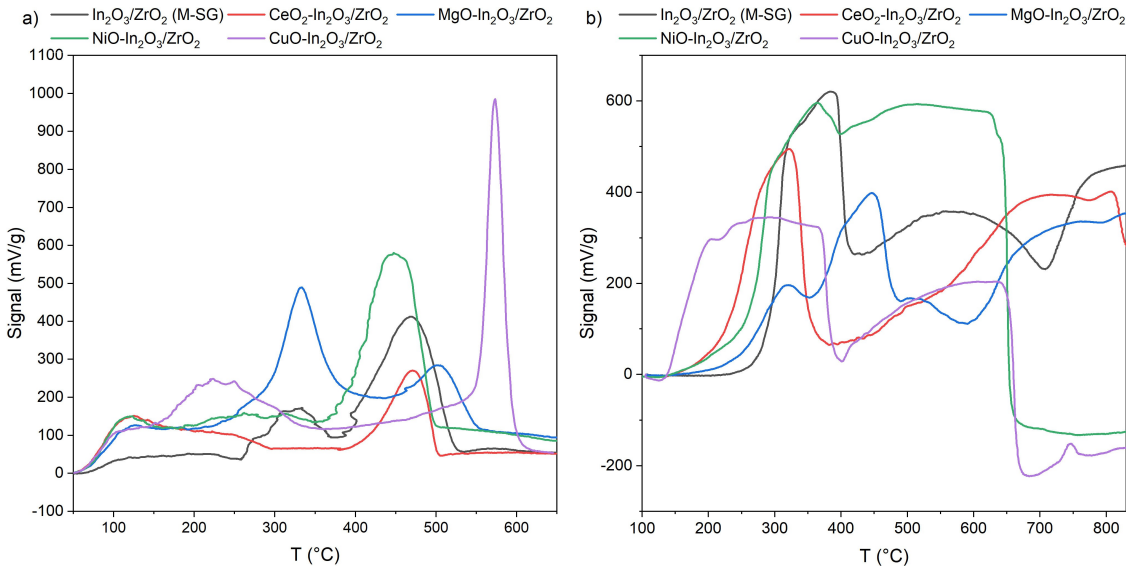

Figure 7. Chemisorptive analysis of CuO-, NiO-, MgO- and CeO_2-promoted In_2O_3/ZrO_2 compared to In_2O_3/ZrO_2 (M-SG): a) CO_2-TPD and b) H_2-TPR.

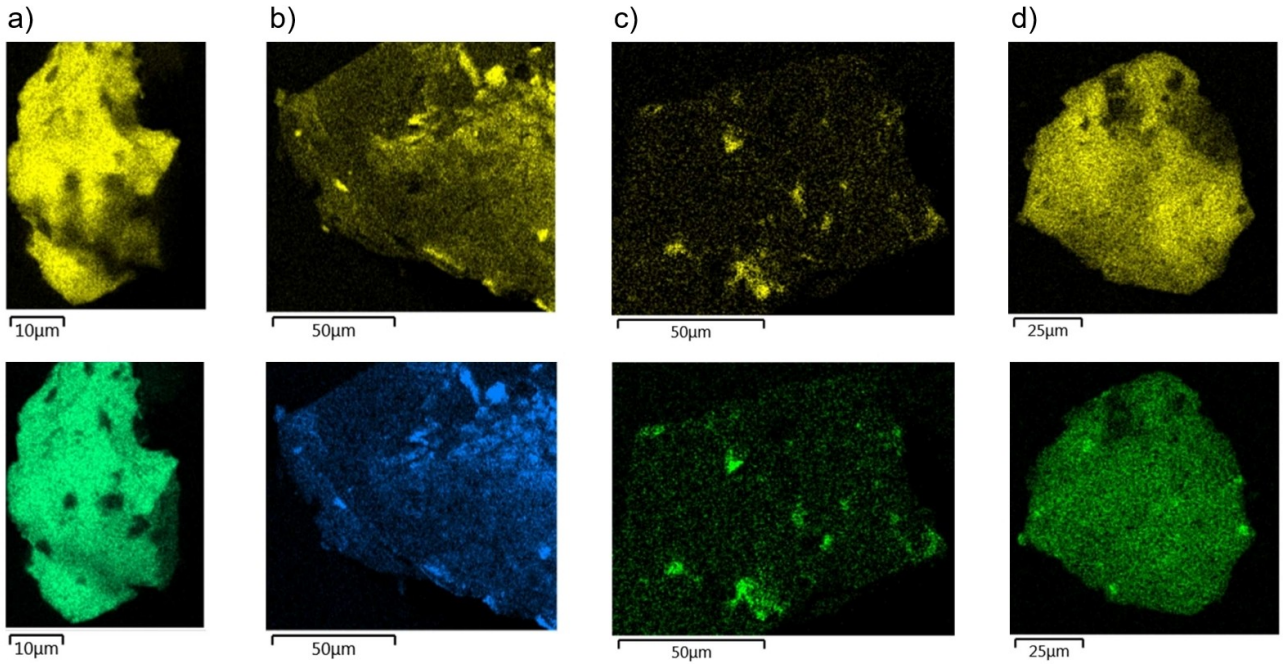

Figure 8. SEM-EDX elemental mapping images of a) NiO-In_2O_3/ZrO_2, b) CeO_2-In_2O_3/ZrO_2, c) MgO-In_2O_3/ZrO_2 and d) CuO-In_2O_3/ZrO_2. Top: In distribution (yellow); Bottom: metal promotor (green/blue).

Combination of NiO-promoting and optimized synthesis method on the catalytic performance of In_2O_3/ZrO_2 catalysts

Different synthesis methods were employed to incorporate the best performing NiO-promotor into In_2O_3/ZrO_2 catalysts, namely chemical reduction (CR), co-precipitation (CP), and wetness impregnation (WI). These NiO-incorporated In_2O_3/ZrO_2 catalysts were further evaluated for their catalytic performance in the CO_2 hydrogenation to methanol. Table 3 shows the textural composition of the synthesized catalysts.

ICP-OES elemental analysis confirmed the successful incorporation of Ni into the In_2O_3/ZrO_2 catalyst using all three preparation methods (Table 3). Interestingly, only 0.32 wt% of Ni could be incorporated via CR, while 0.69 resp. 0.76 wt% Ni could be incorporated by CP and WI at an overall constant In loading of around 10.5 wt%. Furthermore, XPS analysis indicate also the presence of NiO in all catalysts for the various synthesis methods. (Figure 9). The Ni2p core level spectrum of all catalysts shows again binding energies at 855 and 873 eV, which refer to Ni^{2+} species (Figure S13).[20,45]

Physisorptive data show only small deviations in surface area (74–80 m^2/g) as well as pore volume (0.216–0.258 cm^3/g)

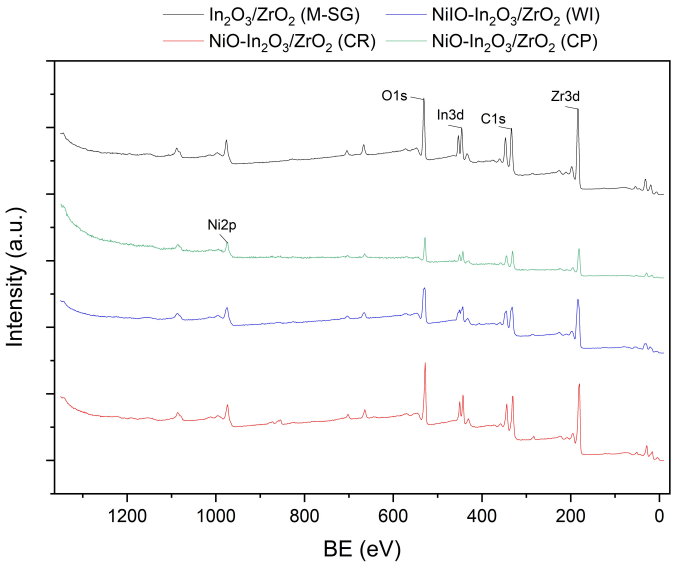

Figure 9. XPS survey spectra of NiO-In_2O_3/ZrO_2 prepared by WI, CR or CP compared with In_2O_3/ZrO_2 (M-SG).

Table 3. Textural composition of NiO-In_2O_3/ZrO_2 catalysts prepared by Wi, CR and CP.

	Ni (wt.%)[a]	In (wt.%)[a]	Zr (wt.%)[a]	S_{BET} (m^2/g)[b]	∅ pore radius (nm)[b]	pore volume (cm^3/g)[b]
NiO-In_2O_3/ZrO_2 (WI)	0.76	10.48	53.85	80.66	3.70	0.216
NiO-In_2O_3/ZrO_2 (CR)	0.32	10.64	53.40	74.37	3.70	0.223
NiO-In_2O_3/ZrO_2 (CP)	0.69	10.63	58.09	78.82	4.06	0.258

[a] Determined by ICP-OES. [b] Measured by N_2-physisorption.

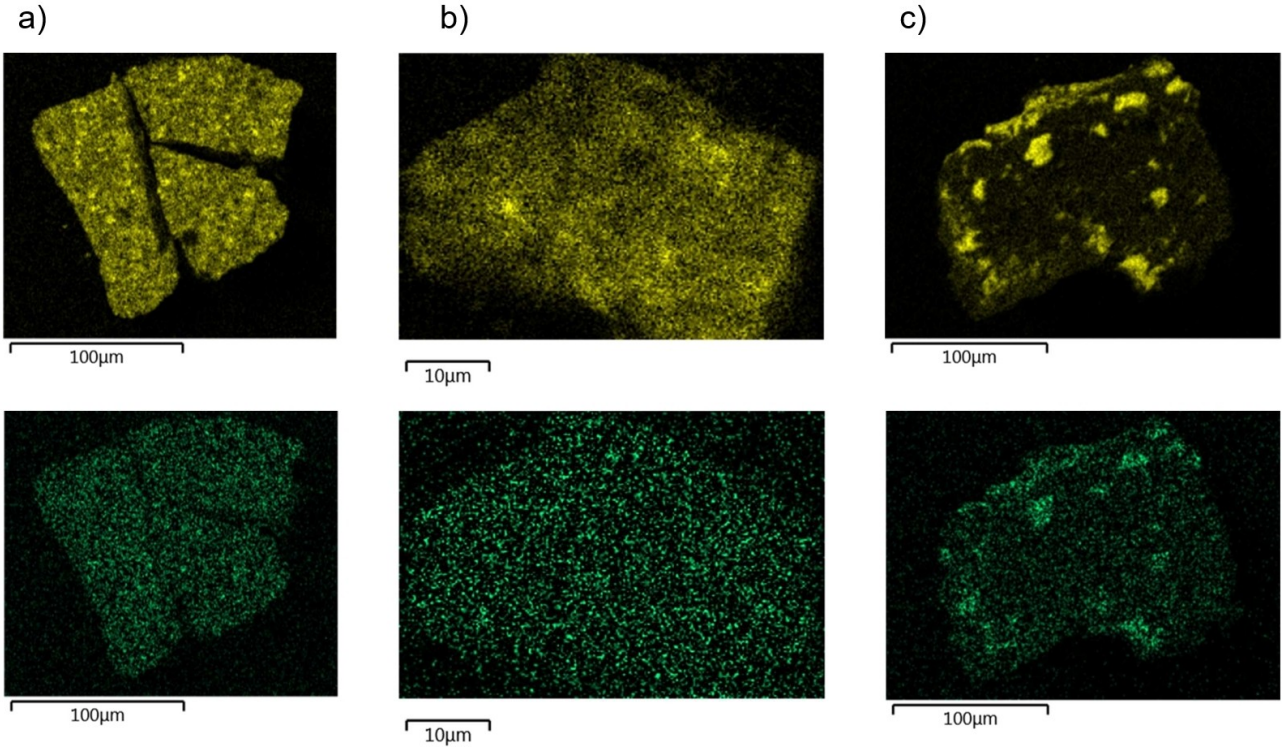

Figure 10. SEM-EDX elemental mapping images of Ni-In_2O_3/ZrO_2 prepared by a) WI, b) CR and c) CP. Top: In distribution (yellow); bottom: Ni distribution (green).

after impregnation for all preparation methods. However, the pore size distribution is nearly similar for the three synthesis methods with a medium pore size of 10 nm (Table 3, Figure S11b). Moreover, XRD data confirm patterns for crystalline In_2O_3 and ZrO_2, except for NiO-In_2O_3/ZrO_2 (CP), as already seen before, where just patterns for ZrO_2 are present, indicating an amorphous structure for In_2O_3. Furthermore, no distinct patterns can be seen for NiO in the diffractogram, indicating amorphous or nanocrystalline NiO species (Figure S11a).

SEM analysis was conducted to investigate the morphological changes after impregnation with Ni through the different synthesis techniques. No changes could be revealed in the morphology of the ZrO_2 supported catalysts after impregnation with In_2O_3 and NiO for all synthesis methods (Figure S12). Furthermore, SEM-EDX mapping demonstrates a macroscopic homogeneous distribution of both In and Ni for NiO-In_2O_3/ZrO_2 (WI) (Figure 10). The formation of agglomerates could be further supported by H_2-TPR analysis, where a baseline shift of NiO-In_2O_3/ZrO_2 (CR) could be deduced (see Figure 11b).

The overall H_2-reduction and CO_2 adsorption capacity of NiO-In_2O_3/ZrO_2 (CR) (0.72/0.87) as well as NiO-In_2O_3/ZrO_2 (CP) (0.96/0.91) are lower than for the pristine In_2O_3/ZrO_2 (M-SG) (Tables S7, S8). This indicates a poorer reducibility, explained by formation of agglomerates. NiO-In_2O_3/ZrO_2 (WI) exhibit improved H_2-reduction properties with 1.19 as well as increased CO_2 capacity values with 1.69. This can be explained by the formation of electronic defects by incorporation of NiO via WI as well as the already discussed H_2-spillover by Jiang et al.[55] (Figure 11a and b, Tables S7 and S8).

Figure 12 shows methanol productivities as well as selectivities for the four different synthesized catalysts. Compared to the non-promoted In_2O_3/ZrO_2 (M-SG) catalyst giving a productivity of $P_{cat} = 0.475\ g_{MeOH} \cdot g_{cat}^{-1} \cdot h^{-1}$, the productivity decreased if NiO is incorporated via CR, yielding a productivity of only $0.39\ g_{MeOH} \cdot g_{cat}^{-1} \cdot h^{-1}$. Moreover, NiO-$In_2O_3/ZrO_2$ (CP) and NiO-In_2O_3/ZrO_2 (WI) showed a higher methanol productivity of 0.482 and $0.497\ g_{MeOH} \cdot g_{cat}^{-1} \cdot h^{-1}$, respectively, when compared to In_2O_3/ZrO_2 (M-SG). Regarding selectivity, no significant decrease could be observed for any synthesis method.

Long-term stability of the NiO-In_2O_3/ZrO_2 (WI) catalyst

Finally, the MeOH productivity of the best performing NiO-In_2O_3/ZrO_2 (WI) catalyst was investigated for 100 h time-on-stream (Figure 13). After 12 h, the catalyst exhibited a maximum productivity of $0.162\ g_{MeOH} \cdot g_{cat}^{-1} \cdot h^{-1}$ at 250 °C and 75 bar. The MeOH productivity slightly decreased to $0.149\ g_{MeOH} \cdot g_{cat}^{-1} \cdot h^{-1}$ after 100 h. Moreover, no methane could be detected by GC analysis (Figure S14).

Post-mortem studies of the catalyst further revealed its stability. In detail, ICP-OES analysis indicate no leaching after 100 h *TOS*. Data of pre-reaction material (In-wt.% of 10.48, Zr-wt.% of 53.85 and Ni-wt.% of 0.76) are well in line with data of post-reaction material (In-wt.% of 10.36, Zr-wt.% of 53.39 and Ni-wt.% of 0.73), respectively. XRD patterns provide evidence of unchanged crystalline structure of In_2O_3 and ZrO_2 (Figure 14). Furthermore, no changes in morphology could be

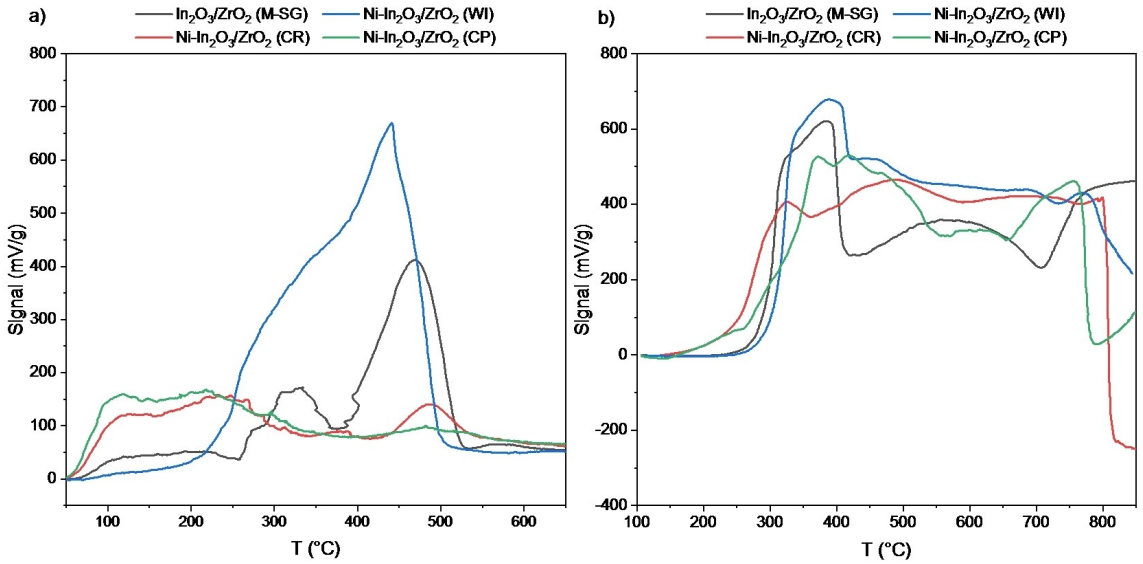

Figure 11. Chemisorptive analysis of NiO-In_2O_3/ZrO_2 prepared by WI, CR or CP compared to In_2O_3/ZrO_2 (M-SG): a) CO_2-TPD and b) H_2 TPR.

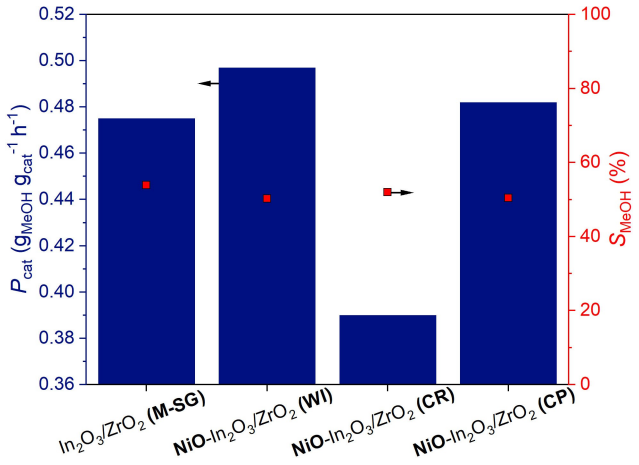

Figure 12. Impact of different synthesis methods for NiO-In_2O_3/ZrO_2 on the methanol productivity and selectivity. Reaction conditions: $CO_2/H_2 = 1/3$; GHSV = 8600 h^{-1}; *TOS* = 3 h; *T* = 300 °C; *p* = 75 bar; $h_{bed} = 5.1 \pm 0.1$ cm.

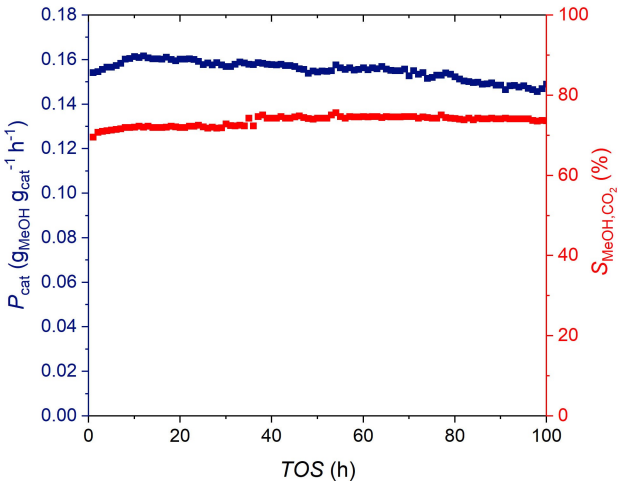

Figure 13. Stability of NiO-In_2O_3/ZrO_2 (WI) recorded over 100 h *TOS*, Reaction conditions: $CO_2/H_2 = 1/3$; GHSV = 4600 h^{-1}; *T* = 250 °C; *p* = 75 bar; $h_{bed} = 5.0$ cm.

observed in SEM (Figure 15). Finally, EDX-Mapping also shows no formation of agglomerates (Figure S15).

Conclusions

In this work, various In_2O_3/ZrO_2 catalysts have been investigated for their application in methanol synthesis. Hereby, different support materials, metal promotors as well as synthesis methods were applied to identify the best combination for gas-phase methanol synthesis. In detail, In_2O_3/ZrO_2 (M-SG) shows both higher P_{MeOH} and Y_{MeOH} independently of the applied reaction conditions with a maximum methanol productivity of 4.25 $g_{MeOH} \cdot g_{In}^{-1} \cdot h^{-1}$ at 300 °C and 75 bar compared to In_2O_3/ZrO_2 (S-AA) mainly due to its higher surface area. Moreover, only a disparity in the synthesis method could be revealed. In the next step, several metals were used as promotors for the In_2O_3/ZrO_2

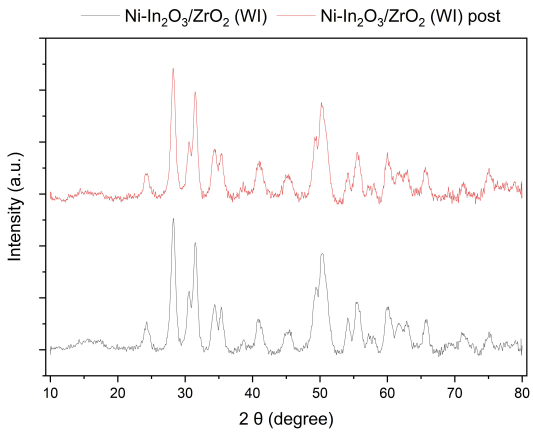

Figure 14. XRD patterns of NiO-In_2O_3/ZrO_2 (WI) before (black) and after (red) reaction.

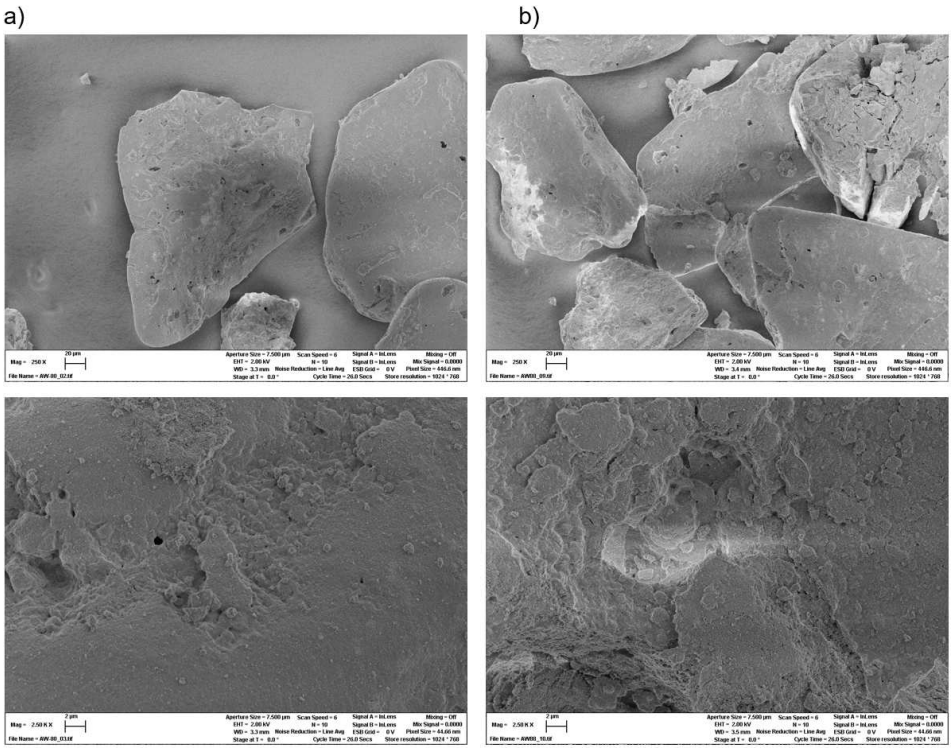

Figure 15. SEM images of Ni-In_2O_3/ZrO_2 (WI) before a) and after reaction b).

(M-SG) catalyst in order to further enhance its productivity. Hereby, the NiO-In_2O_3/ZrO_2 (M-SG) catalyst showed the best performance. Regarding the synthesis method, wetness impregnation using a water/ethanol solvent system has been found to be the most efficient preparation method for the incorporation of Ni into the In_2O_3/ZrO_2 (M-SG) catalyst. Overall, the NiO-promoted catalyst shows improved catalytic activity as well as stability because of a facilitated H_2-spillover and strong electronic interactions with the ZrO_2 support. The methanol productivity of In_2O_3/ZrO_2 (M-SG) could be increased from 0.475 $g_{MeOH} \cdot g_{cat}^{-1} \cdot h^{-1}$ to 0.497 $g_{MeOH} \cdot g_{cat}^{-1} \cdot h^{-1}$ by the addition of 0.8 wt% Ni without any methane formation. Finally, the NiO-In_2O_3/ZrO_2 catalyst remains stable and active over 100 h on stream paving the way for future applications in green methanol synthesis.

Experimental

Materials and catalyst preparation

All chemicals were obtained commercially and used as received without further purification. The In_2O_3/ZrO_2 catalysts were synthesized using wetness impregnation (WI) technique using different ZrO_2 supports. Furthermore, the dopants (Ni, Cu, Ce, Mg) have been incorporated either via wetness impregnation (WI), chemical reduction (CR) or co-precipitation (CP). Comprehensive description of the catalyst preparation can be found in the Supporting Information.

Catalyst characterization

The elemental compositions of all catalysts were determined using inductively coupled plasma optical emission spectroscopy (ICP-OES). The crystalline structure was analyzed via powder X-Ray diffraction (XRD), additional information about the oxidation states were obtained using X-ray photoelectron spectroscopy (XPS). The porosity, pore volume (BJH) as well as total surface area (BET) were determined by N_2-physisorption measurements. Scanning electron microscopy (SEM) and energy-dispersive X-ray spectroscopy (EDX) revealed catalyst morphology and metal dispersion. Chemisorptive properties were evaluated by CO_2-temperature-programmed desorption (CO_2-TPD) and H_2-temperature-programmed reduction (H_2-TPR). Comprehensive descriptions of all characterization methods are given in the Supporting Information.

Catalyst testing / Catalytic evaluation

All experiments were performed in a high-pressure continuous-flow fixed-bed reactor setup (see Figure S1). Usually, 4.0 to 5.0 g of catalyst were loaded into the reactor and fixated by a bed of quartz wool. Prior to the reaction, the catalyst was pretreated at 200 °C under flowing N_2 (300 $NmL \cdot min^{-1}$) for 1 hour. Subsequently, the temperature was set to 300 °C and a reaction gas mixture with a CO_2/H_2 stoichiometric ratio of 1/3 was fed using a flow rate of 1200 $Nml \cdot min^{-1}$ into the reactor ($GHSV = 8400–8600\ h^{-1}$, Equation S7), which was pressurized to 50 or 75 bar, respectively. Catalysts were tested for 3 h under steady-state conditions for performance comparison. Details of the experimental setup as well as equations for the calculation of the yield Y_{MeOH}, selectivity S_{MeOH}, CO_2 conversion X_{CO2} and productivity P_{cat}, $P_{surface}$, P_{metal} are provided in the Supporting Information.

Acknowledgements

The authors acknowledge Dr. Michael Pabel from Saint-Gobain NorPro for supply of ZrO_2 and Dr. Leonhard Schill from DTU Lyngby for performing XPS measurements. The Central Analytics Department of UHH is gratefully acknowledged for Elemental analysis, X-ray diffraction and Electron microscopy. Open access provided by Project DEAL. Open Access funding enabled and organized by Projekt DEAL.

Conflict of Interests

There are no conflicts to declare.

Data Availability Statement

Research data are not shared.

Keywords: CO_2 hydrogenation · hydrogen spillover · indium-based catalysts · methanol synthesis

[1] a) C. Panzone, R. Philippe, A. Chappaz, P. Fongarland, A. Bengaouer, *J. CO_2 Util.* **2020**, *38*, 314–347; b) M. Aresta, A. Dibenedetto, A. Angelini, *Chem. Rev.* **2014**, *114*, 1709–1742.
[2] R.-P. Ye, et al., *Nat. Commun.* **2019**, *10*, 5698.
[3] a) P. Gao, L. Zhang, S. Li, Z. Zhou, Y. Sun, *ACS Cent. Sci.* **2020**, *6*, 1657–1670; b) E. S. Rubin, H. Mantripragada, A. Marks, P. Versteeg, J. Kitchin, *Prog. Energy Combust. Sci.* **2012**, *38*, 630–671.
[4] A. Álvarez, A. Bansode, A. Urakawa, A. V. Bavykina, T. A. Wezendonk, M. Makkee, J. Gascon, F. Kapteijn, *Chem. Rev.* **2017**, *117*, 9804–9838.
[5] P. W. Andreas Jess, *Chemical Technology*, Wiley-VCH, Weinheim, **2013**, 685–686.
[6] W.-J. Shen, K.-W. Jun, H.-S. Choi, K.-W. Lee, *Korean J. Chem. Eng.* **2000**, *17*, 210–216.
[7] K.-D. Jung, A. T. Bell, *J. Catal.* **2000**, *193*, 207–223.
[8] N. Ortner, D. Zhao, H. Mena, J. Weiß, H. Lund, S. Bartling, S. Wohlrab, U. Armbruster, E. V. Kondratenko, *ACS Catal.* **2023**, *13*, 60–71.
[9] F. Studt, M. Behrens, E. L. Kunkes, N. Thomas, S. Zander, A. Tarasov, J. Schumann, E. Frei, J. B. Varley, F. Abild-Petersen, J. K. Norskov, R. Schlögl, *ChemCatChem* **2015**, *7*, 1105–1111.
[10] M. V. Twigg, M. S. Spencer, *Appl. Catal. A: General* **2001**, *212*, 161–174.
[11] P. Schühle, M. Schmidt, L. Schill, A. Riisager, P. Wasserscheid, J. Albert, *Catal. Sci. Technol.* **2020**, *10*, 7309–7322.
[12] O. Martin, A. J. Martín, C. Mondelli, S. Mitchell, T. F. Segawa, R. Hauert, C. Drouilly, D. Curulla-Ferré, J. Pérez-Ramírez, *Angew. Chem. Int. Ed.* **2016**, *55*, 6261–6265.
[13] P. Schühle, S. Reichenberger, G. Marzun, J. Albert, *Chem. Ing. Tech.* **2021**, *93*, 585–593.
[14] M. S. Frei, C. Mondelli, A. Cesarini, F. Krumeich, R. Hauert, J. A. Stewart, D. Curulla Ferré, J. Pérez-Ramírez, *ACS Catal.* **2020**, *10*, 1133–1145.
[15] J. Ye, C. Liu, D. Mei, Q. Ge, *ACS Catal.* **2013**, *3*, 1296–1306.
[16] K. Sun, Z. Fan, J. Ye, J. Yan, Q. Ge, Y. Li, W. He, W. Yang, C. Liu, *J. CO_2 Util.* **2015**, *12*, 1–6.
[17] Y. Wei, F. Liu, J. Ma, C. Yang, X. Wang, J. Cao, *J. Mol. Catal.* **2022**, *525*, 112354.
[18] K. Lau, P. Schühle, S.-X. Liang, F. de Kock, J. Albert, S. Reichenberger, *ACS Appl. Energ. Mater.* **2021**, *4*, 9206–9215.
[19] S. Dang, B. Qin, Y. Yang, H. Wang, J. Cai, Y. Han, S. Li, P. Gao, Y. Sun, *Sci. Adv.* **2020**, *6*, eaaz2060.
[20] M. Dou, M. Zhang, Y. Chen, Y. Yu, *Catal. Lett.* **2018**, *148*, 3723–3731.
[21] P. Kampe, A. Wesner, P. Schühle, F. Hess, J. Albert, *ChemPlusChem* **2023**, *88*, e202300425.
[22] P. Kampe, N. Herrmann, A. Wesner, C. Ruhmlieb, J. Albert, *ACS Sustainable Chem. Eng.* **2023**, *11*, 14633–14644.
[23] X. Jia, K. Sun, J. Wang, C. Shen, C. Liu, *J. Energy Chem.* **2020**, *50*, 409–415.
[24] M. S. Frei, C. Mondelli, R. García-Muelas, J. Morales-Vidal, M. Philipp, O. V. Safonova, N. López, J. A. Stewart, D. C. Ferré, J. Pérez-Ramírez, *Nat. Commun.* **2021**, *12*, 1960.
[25] N. Nomura, T. Tagawa, S. Goto, *React. Kinet. Catal. Lett.* **1997**, *63*, 21–25.
[26] S. Dey, G. C. Dhal, *Materials Science for Energy Technologies* **2020**, *3*, 6–24.
[27] K. Pokrovski, K. T. Jung, A. T. Bell, *Langmuir* **2001**, *17*, 4297–4303.
[28] J. Wang, G. Zhang, J. Zhu, X. Zhang, F. Ding, A. Zhang, X. Guo, C. Song, *ACS Catal.* **2021**, 1406–1423.
[29] K. S. W. Sing, *Pure Appl. Chem.* **1985**, *57*, 603–619.
[30] M. Thommes, *Chem. Int.* **2016**, *38*, 25.
[31] P. Sharma, P. Hoang Ho, J. Shao, D. Creaser, L. Olsson, *Fuel* **2023**, *331*, 125878.
[32] T.-y. Chen, C. Cao, T.-b. Chen, X. Ding, H. Huang, L. Shen, X. Cao, M. Zhu, J. Xu, J. Gao, Y.-F. Han, *ACS Catal.* **2019**, 8785–8797.
[33] P. Gao, et al., *ACS Catal.* **2018**, *8*, 571–578.
[34] C.-Y. Chou, R. F. Lobo, *Appl. Catal. A: General* **2019**, *583*, 117144.
[35] a) M. Bowker, *ChemCatChem* **2019**, *11*, 4238–4246; b) J. Zhong, X. Yang, Z. Wu, B. Liang, Y. Huang, T. Zhang, *Chem. Soc. Rev.* **2020**, *49*, 1385–1413.
[36] A. Monshi, M. R. Foroughi, M. R. Monshi, *WJNSE* **2012**, *02*, 154–160.
[37] A. V. Neimark, L. I. Kheifets, V. B. Fenelonov, *Ind. Eng. Chem. Prod. Res. Dev.* **1981**, *20*, 439–450.
[38] P. Munnik, P. E. de Jongh, K. P. de Jong, *Chem. Rev.* **2015**, *115*, 6687–6718.
[39] a) C. Li, W. Ying, F. Cao, H. Zhang, D. Fang, *Pet. Sci. Technol.* **2008**, *26*, 704–716; b) M. Tao, X. Meng, Y. Lv, Z. Bian, Z. Xin, *Fuel* **2016**, *165*, 289–297; c) F. T. Zangeneh, S. Mehrazma, S. Sahebdelfar, *Fuel Process. Technol.* **2013**, *109*, 118–123.
[40] Maria C. Bacariza, Inês Graça, Suse S. Bebiano, José M. Lopes, Carlos Henriques, B. Zhao, Y. Pan, C. Liu, *Catal. Today* **2012**, *194*, 60–64.
[41] a) Y. Yao, D. W. Goodman, *J. Mol. Catal. A: Chemical* **2014**, *383–384*, 239–242; b) Z. Zhang, C. Shen, K. Sun, C. Liu, *Catal. Commun.* **2022**, *162*, 106386.
[42] I. N. Reddy, C enkata Reddy, M. Cho, J. Shim, D. Kim, *Mater. Res. Express* **2017**, *4*, 86406.
[43] J. Chastain, J. F. Moulder, *Handbook of X-ray photoelectron spectroscopy. A reference book of standard spectra for identification and interpretation of XPS data*, Physical Electronics, Eden Prairie, Minn., **1992**, 29–30.
[44] M. C. Biesinger, L. W. Lau, A. R. Gerson, R. S. Smart, *Appl. Surf. Sci.* **2010**, *257*, 887–898.
[45] M. C. Biesinger, *Surf. Interface Anal.* **2017**, *49*, 1325–1334.
[46] a) N. C. Haider, J. Alonso, W. E. Swartz, *Z. Naturforsch. A* **1975**, *30*, 1485–1490; b) F. Khairallah, A. Glisenti, *Surf. Sci. Spectra* **2006**, *13*, 58–71.
[47] a) E. Bêche, P. Charvin, D. Perarnau, S. Abanades, G. Flamant, *Surf. Interface Anal.* **2008**, *40*, 264–267; b) X. Jiang, X. Li, J. Wang, D. Long, L. Ling, W. Qiao, *Catal. Sci. Technol.* **2018**, *8*, 2740–2749.

Manuscript received: September 7, 2023
Revised manuscript received: October 27, 2023
Accepted manuscript online: October 28, 2023
Version of record online: November 27, 2023

7. Comprehensive Discussion

In this chapter, the results presented in the cumulative section are systematically analyzed and contextualized within the framework of this dissertation. Building on the overarching aim of developing catalytic systems for sustainable chemical processes, this discussion revisits on the catalytic systems developed for the transformation of biomass into platform chemicals such as lactic acid (LA) and formic acid (FA), alongside the conversion of CO_2 into methanol (MeOH) and dimethyl ether (DME). The aim is to consolidate the findings by assessing the catalytic performance, scalability, and robustness of the systems developed. The discussion highlights the role of POMs in both liquid-phase and gas-phase reactions, their heterogenization for improved practicality, and their application in bifunctional catalytic systems for CO_2-to-DME conversion. Furthermore, the exploration of In_2O_3-based catalysts for methanol synthesis is also reviewed, focusing on the modifications that enhanced their performance and their potential for industrial applications. Through this detailed analysis, the chapter provides a critical perspective on the strengths and limitations of the developed systems, identifying essential factors driving catalytic efficiency and stability for the investigated reactions.

7.1 Substituted Polyoxometalates for Conversion of Biomass to Lactic Acid

The first study explored the application of element-substituted POMs in the form of heteropolysalts as catalysts for the synthesis of LA from biomass. Biomass, as a renewable and abundant resource, offers significant potential for sustainable chemical production. However, its efficient transformation requires advanced catalytic systems. This study explored how modifications to POMs, particularly through heteroatom substitution, influence catalytic performance, aiming to optimize LA synthesis and enhance biomass valorization.

The base catalyst, $Na_3[PMo_{12}O_{40}]$ (NaMo), was systematically altered by substituting Mo with different ratios of vanadium and niobium. The substitutions yielded a series of catalysts, ranging from the vanadium-rich $Na_6[PV_3Mo_9O_{40}]$ (NaV_3) to mixed compositions like $Na_6[PV_2NbMo_9O_{40}]$ (NaV_2Nb) and $Na_6[PVNb_2Mo_9O_{40}]$ ($NaVNb_2$), culminating in the niobium-dominant $Na_5[PNb_2Mo_{10}O_{40}]$ ($NaNb_2$) and $Na_6[PNb_3Mo_9O_{40}]$ ($NaNb_3$). Detailed characterization of the catalysts confirmed the preservation of the *Keggin* structure using infrared spectroscopy (IR spectroscopy), while elemental and thermogravimetric analyses verified their elemental composition and water content. Nuclear magnetic resonance (NMR) spectroscopy, including ^{31}P-NMR and ^{51}V-NMR, was used to verify the structural integrity in solution, square wave voltammetry (SWV) measurements were employed for the determination of the redox potential in aqueous solution.

Dihydroxyacetone (DHA) was selected as the model substrate for catalytic screening due to its role as an intermediate in the degradation of more complex carbohydrates. All catalysts were evaluated in liquid-phase reactions carried out under a nitrogen atmosphere at mild conditions (160 °C, 20 bar N_2) with water serving as the reaction medium (Figure 38). Product analysis was conducted using high performance liquid chromatography (HPLC). Substituting NaMo with vanadium and niobium led to significant improvements in LA yield as well as conversion rates of DHA. While NaMo and NaV_3 achieved LA yields of 8.3 % with conversions of 75 % (NaMo) and 85 % (NaV_3), higher niobium content resulted in even greater performance. Yields of LA increased to 10 % (NaV_2Nb), 12 % ($NaVNb_2$), and 21 % ($NaNb_2$), with corresponding conversions of 93 % (NaV_2Nb), 96 % ($NaVNb_2$), and 97 % ($NaNb_2$). Simultaneously, acetaldehyde yields decreased from 20 % (NaV_3) to 11 % ($NaNb_2$), reflecting enhanced selectivity toward LA. The overall carbon balance was only approximately 60 %, attributed to the formation of gaseous products such as CO_2 and CO, as well as insoluble solid residues likely caused by the oligomerization of DHA. These by-products were not investigated further within the scope of this study.

Further analysis of the catalysts revealed a strong correlation between the redox properties of the POMs and their performance in the LA synthesis. Catalysts with higher niobium content demonstrated improved catalytic efficiency towards LA, due to the suppression of side reactions observed in vanadium-substituted POMs. Further SWV measurements provided valuable insights into the redox properties of the catalysts and their correlation with product selectivity in DHA conversion under inert conditions. Vanadium substitution into NaMo enhances the redox potential, resulting in increased DHA conversion and LA formation. However, the elevated redox activity also promotes undesired side reactions, such as the decarboxylation of LA into acetaldehyde. This highlights the dual role of vanadium in catalyzing desired reactions while driving side reactions. In contrast, the progressive substitution with niobium reduces the redox potential, effectively suppressing these consecutive reactions and improving selectivity towards LA.

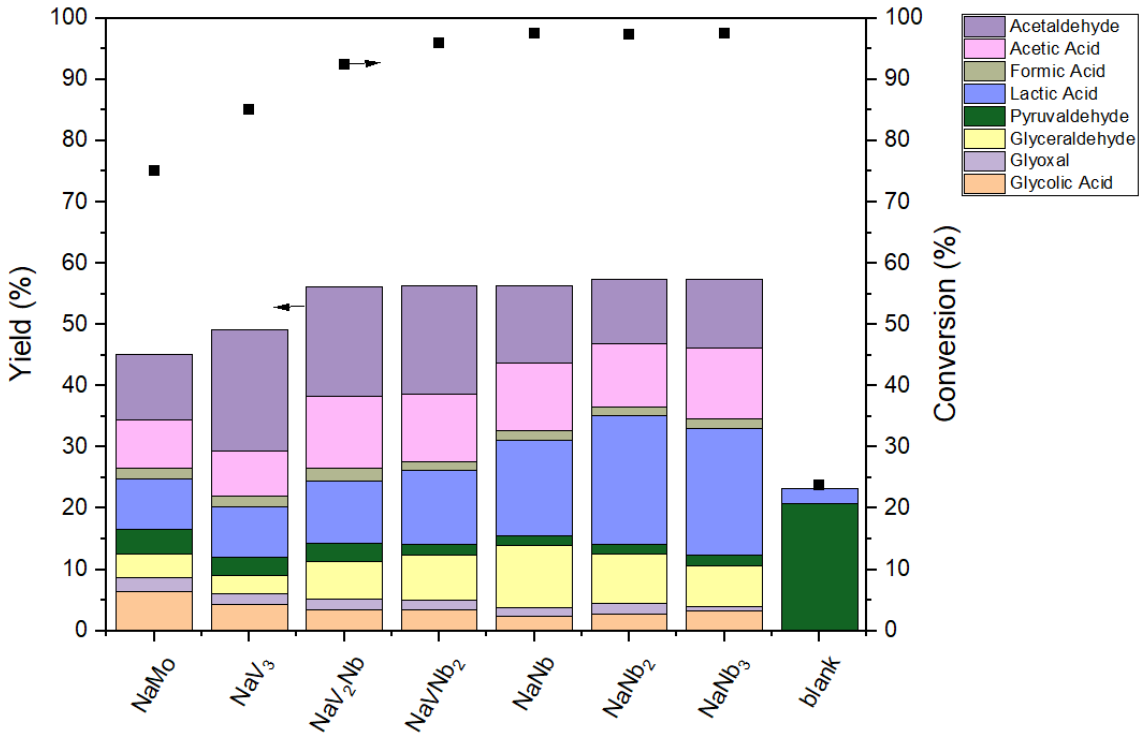

Figure 38: Conversion and product yields of catalyst screening for the conversion of DHA into lactic acid. Reaction conditions: m_{cat} = 42 mg, $m_{substrate}$ = 100 mg, $m_{solvent}$ = 4 g H_2O, ϑ = 160 °C, p = 20 bar N_2, ν = 1000 rpm, $t_{reaction}$ = 1 h. Adapted from *Wesner et al.*[157]

Expanding the scope beyond DHA, $NaNb_2$, identified as the most efficient catalyst during the screening, was further evaluated for the conversion of more complex sugars into LA. Monosaccharides such as fructose, glucose, mannose, and xylose, as well as disaccharides like sucrose and cellobiose, were tested. High conversion rates were observed for monosaccharides, with fructose demonstrating full conversion, benefiting from its direct retro-aldol condensation pathway to LA. In contrast, glucose showed lower conversion rates of 77 % as it requires an isomerization step to fructose before participating in the retro-aldol reaction. For the disaccharides, sucrose displayed full conversion, whereas cellobiose showed a significantly lower conversion rate of 36 %, likely due to its hydrolysis-resistant glyosidic bonds. Despite variations in conversion rates, LA yields were comparable for all sugars, ranging from 10 % (glucose) to 12 % (xylose). Carbon balances reached up to 83 % for glucose, with unaccounted carbon likely forming CO_2 or humins, the latter confirmed through IR

spectroscopy. Additionally, Heteronuclear Single Quantum Coherence (HSQC) spectroscopy identified stereoisomers as minor by-products, highlighting complex isomerization pathways.

The stability of the $NaNb_2$ catalyst was thoroughly examined after the reaction. For this purpose, the crude reaction mixture obtained from the glucose conversion experiment was analyzed using ^{31}P-NMR, Raman spectroscopy, and elemental analysis. The elemental analysis confirmed the stoichiometry of $NaNb_2$, maintaining the expected Mo/P/Nb ratio of 10/1/2, indicating no niobium oxide precipitation occurred during the catalytic reaction. Raman spectroscopy further verified the preservation of the *Keggin* structure through characteristic spectral bands (Figure 39). Additionally, the ^{31}P-NMR spectrum showed a distinct signal at 3.7 ppm, attributed to the intact $NaNb_2$, demonstrating that the catalyst remained structurally stable under the applied reaction conditions (Figure 39).

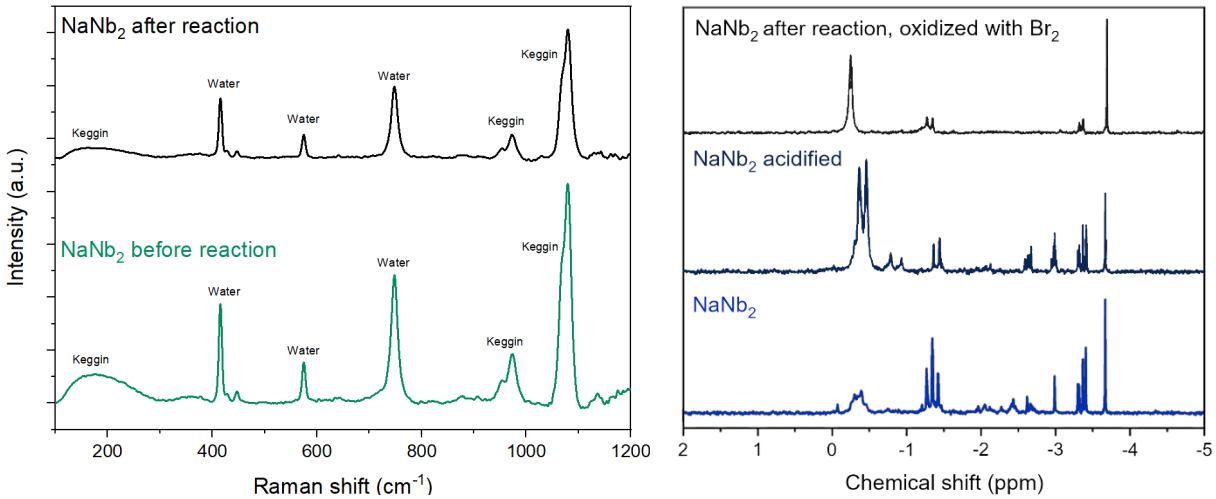

Figure 39: Raman spectra of the $NaNb_2$ catalyst before and after reaction using glucose as a substrate (left). ^{31}P-NMR spectra of $NaNb_2$ in aqueous solution (bottom), $NaNb_2$ in aqueous solution acidified to the pH value of the reaction solutions and of $NaNb_2$ in the reaction solution, oxidized with elemental bromine (right). Adapted from *Wesner et al.*[157]

The results underscore the potential of $NaNb_2$ as a robust and efficient catalyst for the selective conversion of biomass-derived substrates into LA. Notably, this system represents one of the few reported examples of niobium-based homogeneous catalysis—most commonly, niobium is applied in the form of Nb_2O_5 as a heterogeneous catalyst, with only very few homogeneous systems described in the literature, such as $K_8Nb_6O_{19}$.[227] The enhanced catalytic performance, combined with its structural stability under reaction conditions, highlights the significance of tailored POMs for sustainable chemical processes. These results not only deepen the understanding of structure-activity relationships in POMs but also pave the way for developing more effective catalytic systems for the efficient conversion of biomass-derived substrates.

7.2 Transitioning to Immobilized POMs: Liquid-Phase Conversion of Biomass to Lactic and Formic Acid

The second study focused on overcoming the limitations of POM catalysts in industrial biomass conversion by transitioning from homogeneous to heterogenized systems. While the homogeneous, element-substituted POMs explored in the first study demonstrated strong catalytic performance in LA synthesis, challenges such as catalyst separation and reusability restricted the use. This study addressed these challenges by immobilizing POMs onto solid supports, facilitating their use as

heterogeneous catalysts for the liquid-phase transformation of biomass into LA and FA. This study also aimed to investigate key factors influencing POM immobilization, the nature of POM-support interactions, and their impact on catalytic efficiency in biomass conversion processes.

The Keggin-type POM $H_8[PV_5Mo_7O_{40}]$ (HPA-5) was selected as a model catalyst for immobilization due to its well-established Brønsted acidity and redox properties. It has been effectively applied in FA synthesis, and this study examined its potential for biomass conversion to LA. HPA-5 was immobilized on activated carbons (ACs) with a range of physical and chemical characteristics, such as pore structure, surface area, oxygen content, and acidity. All pure support and the supported HPA-5/AC catalysts underwent extensive characterization, such as X-ray diffraction (XRD) for crystalline structure, N_2-physisorption for porosity, and SEM-EDX (Scanning electron microscopy with energy dispersive X-ray spectroscopy) for morphology and metal distribution. Acidity was assessed using NH_3 Temperature Programmed Desorption (TPD), *Boehm* titration, and Point of Zero Charge measurements, while IR and Raman spectroscopy provided structural insights.

The activated carbons utilized in this study, encompassing Norit SXPlus (NSXPlus), Norit A Supra Eur (NASEur), Norit GSX (NGSX), Norit CASP F (NCASPF), and Norit Darco KBG (DKB-G), were obtained from *Cabot*. Additionally, CW20 was supplied by *Silcarbon*. The characterization of activated carbons revealed crystalline graphitic carbon via XRD and negligible impurities of Al, Fe, and P according to elemental analysis. Oxygen content varied from 3.5 wt.% (NSXPlus) to 17.2 wt.% (DKB-G), with corresponding carbon levels ranging 76.8 wt.% (NSXPlus) to 88.7 wt.% (DKB-G). Specific surface areas ranged from 736 m^2/g (NASEur) to 1544 m^2/g (NCASPF), while pore diameters spanned 1.7 nm (NASEur) to 16.5 nm (CW20). Surface acidities and basicities, determined by the *Boehm* method, revealed that higher oxygen content increased surface acidity due to greater amounts of carboxylic and lactonic groups, while phenolic groups remained relatively unaffected. NH_3-TPD measurements confirmed this trend, showing significant NH_3 interactions for carbons with oxygen content above 6 wt.%, while those with less oxygen showed negligible interactions. This trend aligns with point of zero charge data, establishing a direct link between oxygenated surface groups and acidity. Raman and IR spectroscopy detected surface functional groups such as carboxylic acids, phenols, and quinones, with stronger signals in carbons containing more oxygen.

HPA-5 was impregnated onto activated carbons using wet impregnation methods, with IR confirming successful deposition on CW20, NCASPF, and DKB-G. In contrast, NSXPlus, NASEur, and NGSX failed to show signals, likely due to either high absorption or decomposition of the *Keggin* structure. As a result, the latter materials were excluded from further analysis. SEM-EDX analysis revealed a homogeneous distribution of Mo, V, and P across the carbon surface. Elemental analysis indicated molar ratios corresponding to HPA-4 ($H_7[PV_4Mo_8O_{40}]$) rather than the expected HPA-5. This can be attributed to the lower stability of HPA-5 as higher substitution levels weaken the *Keggin* structure, leading to dissociation under the impregnation conditions. This process favors the reformation of more stable, lower-substituted structures such as HPA-4. Notably, no clear correlation between surface oxygen content and loading was observed, contrasting previous studies suggesting a stabilizing role of oxygen groups (Figure 40). Vanadium loading correlated with surface area, with CW20 and NASEur achieving the highest loadings (Figure 40). However, CW20 exhibited superior impregnation efficiency relative to its surface area and preserved the *Keggin* structure, unlike NASEur, where structural degradation was observed.

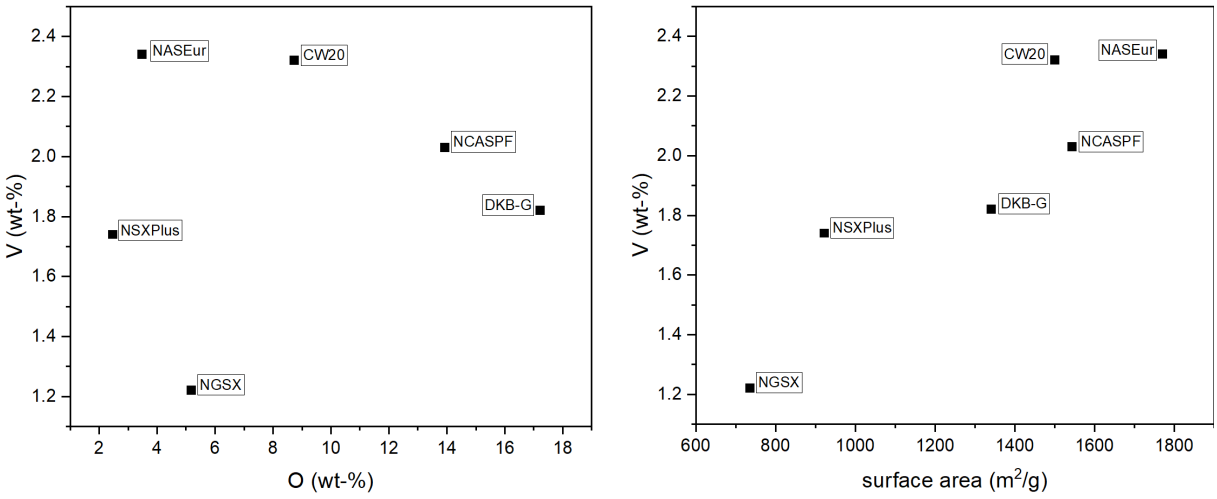

Figure 40: Correlation between amount of oxygen and vanadium loading (left) and between surface area and vanadium loading (right).[228]

Building on these findings, CW20 was further investigated under varying pre- and post-treatment conditions to assess their impact on HPA-5 impregnation and catalytic efficiency. The applied treatments were categorized into five experimental series (E1–E5) for comparative analysis (Figure 41). This investigation specifically focused on understanding how modifications in surface chemistry, such as targeted modifications of functional groups and oxygen content changes, as well as subsequent treatments of impregnated catalysts, affect HPA-5 deposition and structural integrity. CW20 as support for impregnation was either utilized untreated (E1), oxidatively pretreated with HNO_3 (E2), or reductively pretreated with H_2/N_2 gas (E5).

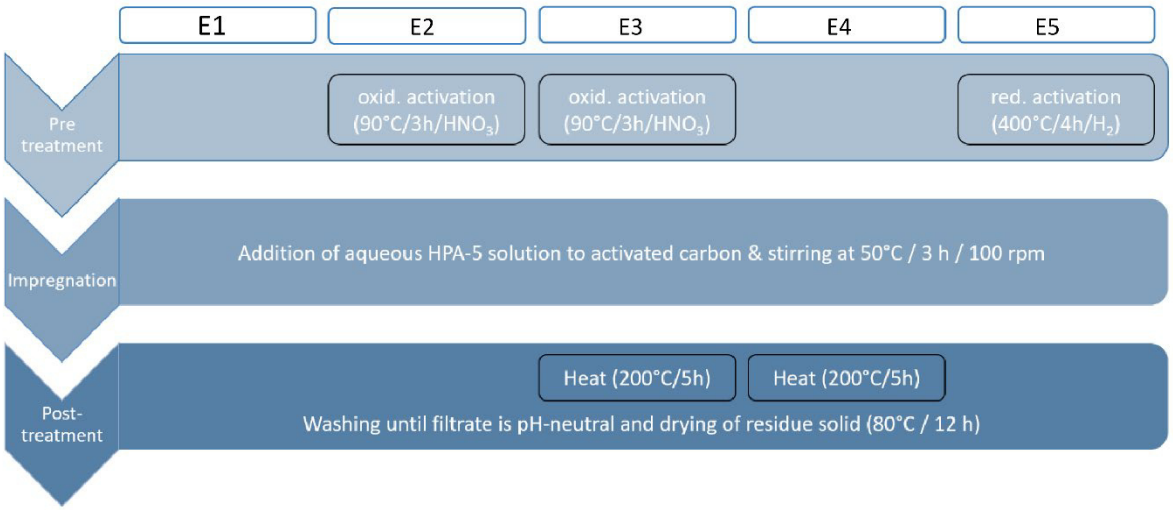

Figure 41: Varying pre- und posttreatments for impregnation of HPA-5 on activated carbon. Adapted from *Wesner et al.*[228]

Oxidative pretreatment drastically reduced the surface area and pore volume of CW20, decreasing from 1500 m²/g and 1.3 ml/g to 357 m²/g and 0.3 ml/g, respectively. Simultaneously, oxygen content increased from 8.7 wt.% to 35.9 wt.%, accompanied by a rise in acidity from 188 µmol/g to 500 µmol/g. This increase in acidity was attributed to a higher concentration of carboxyl groups, while phenolic and

lactonic groups diminished, as confirmed by *Boehm* titration method. This resulted in lower HPA-5 loading with a vanadium loading of 1.7 wt.% and structural degradation of HPA-5. In contrast, reductive pretreatment maintained the surface area and pore volume with minimal alterations to surface acidity, achieving a vanadium loading of 2.5 wt.% with a Mo/V molar ratio of 7.4/4.6, comparable to impregnation of untreated CW20 (E1). Post-treatment after impregnation (E3, E4) significantly improved vanadium loading to 7.6 wt.% and 7.0 wt.%, while preserving the *Keggin* structure. This enhancement was attributed to water removal, facilitating the formation of ether or ester-like bonds between HPA and the carbon surface.

Expanding on the evaluation of pre- and post-treatment effects, HPA-5/CW20 catalysts (E1-E5) were tested in two biomass transformation reactions: the oxidative conversion of glucose to FA and the inert conversion of glucose to LA. The oxidative process, carried out at 90 °C under 20 bar O_2 for 6 hours, showed varying results among the catalysts (Figure 42). Homogeneous HPA-5, used as a benchmark, achieved a 76 % glucose conversion and a FA yield of 41 %, consistent with literature data and confirming experimental reliability. Despite the decreased vanadium content, the supported catalysts demonstrated activity comparable to homogeneous HPA-5. All supported catalysts demonstrated glucose conversion rates of 68 % to 78 % and FA yields of 31 % to 34 % (E1-E5), except for oxidatively pretreated CW20 (E2). Untreated CW20 (E1) showed the most promising results among the supported catalysts, achieving a 68 % glucose conversion and a FA yield of 31 %. Oxidative pretreatment (E2) resulted in significantly lower performance, with only 54 % glucose conversion and a 24 % FA yield, due to reduced HPA-5 loading and the loss of structural integrity. High vanadium leaching (> 68 %) was observed across all catalysts under these conditions, attributed to the acidic environment (pH < 1.4) destabilizing the HPA structure.

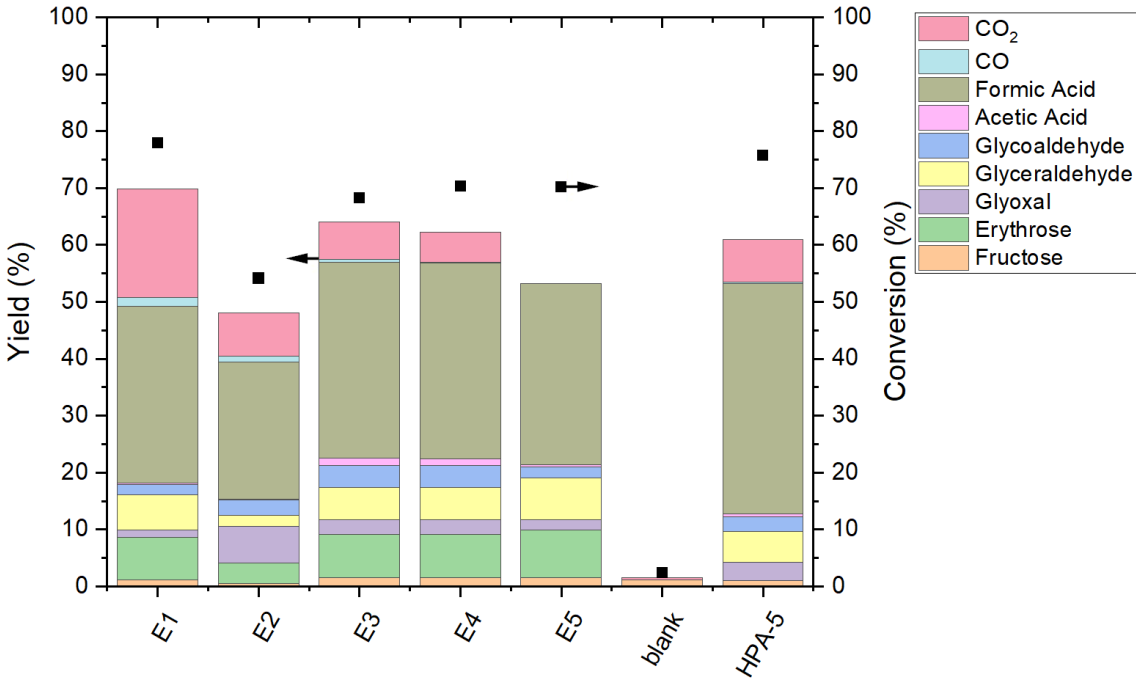

Figure 42: Conversion and product yields of HPA-5/CW20 for glucose oxidation to formic acid. Reaction conditions: m_{cat} = 1.821 g, $m_{substrate}$ = 3.603 g, $m_{solvent}$ = 45 g H_2O, ϑ = 90 °C, p = 20 bar O_2, ν = 1000 rpm, $t_{reaction}$ = 6 h. Adapted from *Wesner et al.*[228]

The conversion of glucose under inert conditions was conducted at 160 °C under 20 bar N_2 for 1 hour (Figure 43). The homogeneous HPA-5, serving as a benchmark, achieved a glucose conversion of 71 % and a LA yield of 10 %. Among the heterogeneous catalysts, conversions ranged from 65 % to 71 %, with LA yields consistently above 6 %. Notably, the HPA-5/CW-20 catalyst without pre- or post-treatment (E1), exhibited similar effectiveness to homogeneous HPA-5, with a glucose conversion of 71 % and a LA yield of 11 %. Post-treated catalysts (E3, E4) displayed increased vanadium loading but did not significantly outperform E1. Leaching was minimal under inert conditions, with vanadium loss remaining below 22 % for all catalysts Interestingly, E1 demonstrated not only high catalytic activity but also remarkable stability, as confirmed by its IR spectrum, which preserved the *Keggin* structure and a low vanadium leaching rate of just 11 %.

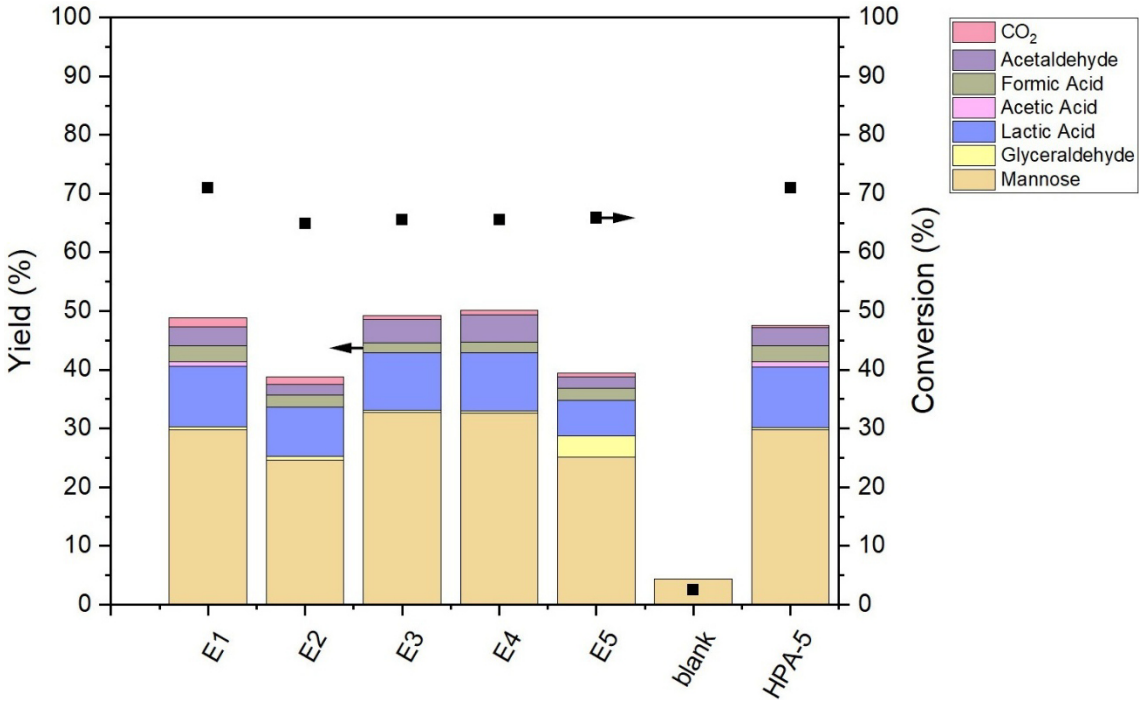

Figure 43: Conversion and product yields of HPA-5/CW20 for glucose conversion to lactic acid. Reaction conditions: m_{cat} = 0.406 g, $m_{substrate}$ = 1.032 g, $m_{solvent}$ = 40 g H_2O, ϑ = 160 °C, p = 20 bar N_2, ν = 1000 rpm, $t_{reaction}$ = 1 h. Adapted from *Wesner et al*.[228]

The findings from the second study emphasize the potential of immobilized HPA-5/CW20 catalysts in addressing key challenges associated with homogeneous POM systems. The catalytic performance and stability of E1 – without further pre- or posttreatment of HPA-5/CW20- particularly in glucose conversion to LA, underscores the potential of these heterogeneous catalysts for industrial applications. These results underline the importance of optimizing catalyst treatments and process conditions to enhance performance. Overall, this study provides valuable insights into the development of tailored, immobilized POM catalysts for sustainable biomass conversion processes.

7.3 Expanding to Gas-Phase Applications: Immobilized Polyoxometalates for CO_2 Conversion to Dimethyl Ether

The third study built upon the insights gained from the liquid-phase investigations of the first and second study, shifting the focus to gas-phase applications of immobilized POMs. While the earlier

studies centered on converting biomass into valuable chemicals, this section explored the potential of CO_2 as a renewable carbon source. Gas-phase reactions, a cornerstone of industrial chemistry, presented unique advantages such as decreased catalyst leaching, simplified separation, and suitability for continuous flow systems—critical for large-scale production. The direct conversion of CO_2 into DME, was investigated. By targeting CO_2 as a renewable carbon source, this section investigated the role of immobilized POMs in gas-phase systems, addressing environmental challenges while expanding their applicability to sustainable gas-phase processes.

To maintain consistency within this dissertation, certain nomenclature terminology has been adjusted compared to the original publication. Specifically, the polyoxometalate $H_8[PV_5Mo_7O_{40}]$ is referred to as HPA-5 instead of HPVMo in the following discussion.

A bifunctional catalytic system was utilized to facilitate the CO_2-to-DME conversion. This system combined the commercial MeOH synthesis catalyst $Cu/ZnO/Al_2O_3$ for the hydrogenation of CO_2 to MeOH, which was used for all experiments, and a series of immobilized POM-based catalysts for the subsequent dehydration of MeOH to DME. Comprehensive characterization of these catalysts included N_2-physisorption for porosity, SEM-EDX for morphology and elemental distribution, NH_3-TPD measurements for acidity, as well as IR spectroscopy for structural analysis. Catalyst performance was evaluated in a fixed-bed reactor at 250 °C and 50 bar, with a gas hourly space velocity (GHSV) of 10,000 h^{-1} and a feed gas composition of H_2/CO_2 at a 3/1 ratio. The resulting gas-phase products were analyzed via online gas chromatography (GC). The MeOH productivity was calculated either based on the mass of the catalyst (P_{mass}) or on the molar mass of the catalyst (P_{mol}).

The first phase of the study involved supporting various POMs, including commercial $H_4[SiW_{12}O_{40}]$ (HSiW), $H_3[PMo_{12}O_{40}]$ (HPMo) and $H_3[PW_{12}O_{40}]$ (HPW), as well as tailor-made $H_8[PV_5Mo_7O_{40}]$ (HPA-5), $H_6[PInMo_{11}O_{40}]$ (HPInMo), and $H_4[SiMo_{12}O_{40}]$ (HSiMo), on *Montmorillonite K10* (K10). This selection incorporates differing framework compositions (Mo, W), heteroelements (P, Si), and charge levels, leading to variations in proton quantity and their associated acidity. Building on the supported catalysts, physisorption analysis revealed a halving of the surface area and a significant decrease in pore volume for all K10-supported HPAs compared to the pure support. Elemental analysis confirmed successful impregnation, with SEM-EDX indicating a macroscopic homogeneous distribution of the HPA on the support. XRD analysis indicated that the K10 structure remained largely intact, though a slight loss of crystallinity was observed. Notably, peaks corresponding to the HPAs were absent, attributed to their low loading and the predominance of background noise. NH_3-TPD results highlighted variations in acidity across the catalysts. HPInMo exhibited the highest acidity with a NH_3 adsorption capacity of 2.5, followed by HPMo (1.9) and HPA-5 (1.4), while commercial catalysts HSiW and HPW showed comparatively lower adsorption capacities of 1.0. These findings confirm that incorporation of heteroatoms proved effective in tailoring acidity, enabling a detailed investigation into the relationship between acidic properties and catalytic efficiency in DME synthesis.

To assess the catalytic performance of the supported HPAs, the bifunctional system combining $Cu/ZnO/Al_2O_3$ for MeOH synthesis and K10-supported HPAs for MeOH dehydration was evaluated for DME production (Figure 44). Pure K10 exhibited a DME yield of 4.8 %, attributed to its inherent acidity. However, HPInMo and HPA-5-supported catalysts showed lower yields of 4.7 % and 4.0 %, respectively, likely due to decreased surface area and diminished active site availability. In contrast, HPW and HSiMo slightly outperformed K10, yielding 5.7 % and 5.2 %, respectively, indicating moderate improvements in catalytic performance. HSiW/K10 and HPMo/K10 displayed superior performance, achieving over 7 % DME yield and reaching 54 % of the thermodynamic equilibrium yield under the applied conditions. Notably, for HPInMo/K10, despite a fivefold increase in acidity, DME yields were lower than for K10 alone, indicating that acidity alone is insufficient to predict catalytic activity. The mass-based productivity (P_{mass}) aligns with the DME yield, as the same amount of catalyst was utilized

in all synthesis experiments. However, regarding the molar-based productivities P_{mol}, HSiW/K10 stands out with P_{mol} reaching 77.84 $mol_{DME} \cdot mol_{HPA}^{-1} \cdot h^{-1}$, surpassing HPMo/K10 due to its lower molar mass. HSiW/K10 also demonstrates higher catalytic activity than the tungstate-based HPW, suggesting a strong influence of silicon in enhancing its performance. However, this trend is not consistent across the molybdenum-based catalysts, where HPMo outperforms HSiMo, so no distinct advantage of tungsten over molybdenum, or silicon over phosphor as heteroatoms can be concluded. Despite these mixed results, HSiW/K10 proved to be the most efficient catalyst overall, with reproducibility tests confirming stable yields and selectivity.

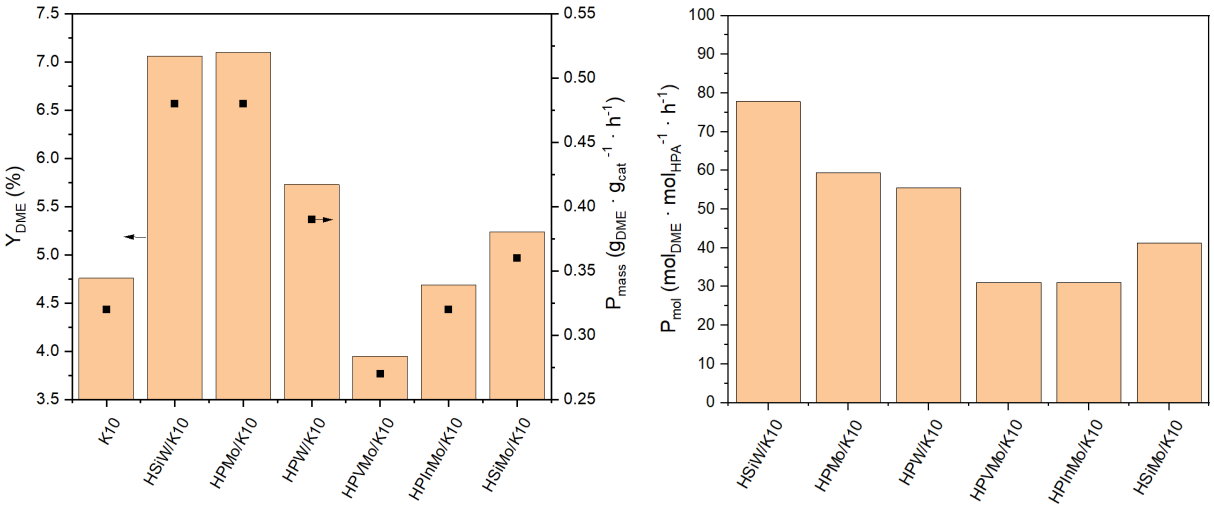

Figure 44: Yield of DME Y_{DME} and productivity P_{mass} (left) and Productivity P_{mol} (right) of HPAs supported on K10. Reaction conditions: m_{cat} = 2.5 g, ϑ = 250 °C, p = 50 bar H_2/CO_2, H_2/CO_2 ratio = 3/1, GHSV = 10000 h^{-1}. Adapted from *Wesner et al.*[229]

Following the identification of HSiW as a highly effective catalyst, its performance on various supports, including ZrO_2, Al_2O_3, TiO_2, and *Celite®*, was systematically evaluated. IR spectroscopy confirming the structural stability of the *Keggin* unit post-reaction across all supports. *Celite*, despite being characterized by a minimal surface area of 1 m^2/g, exhibited large pores that facilitated uniform HSiW distribution, as confirmed by SEM-EDX, slightly improving productivity (47.7 $mol_{DME} \cdot mol_{HPA} \cdot h^{-1}$) compared to unsupported HSiW. Among oxide supports, Al_2O_3 and TiO_2 showed a substantial decrease in surface area and pore volume post-impregnation, while ZrO_2 retained 89 % of its surface area, indicating a more highly uniform HPA dispersion. Detailed characterization via SEM-EDX corroborated these findings. NH_3-TPD analysis revealed variations in acidity, with HSiW/Al_2O_3 exhibiting the highest *Brønsted* acidity. However, catalytic activity was not solely correlated with acidity, ZrO_2-supported HSiW, with moderate acidity, outperformed all other catalysts with a productivity of 125.4 $mol_{DME} \cdot mol_{HPA} \cdot h^{-1}$ (Figure 45), likely due to enhanced MeOH adsorption enabled by its surface properties. Overall, the findings underscore the critical influence of support properties, with ZrO_2 emerging as an exceptional material for catalytic efficiency in DME synthesis.

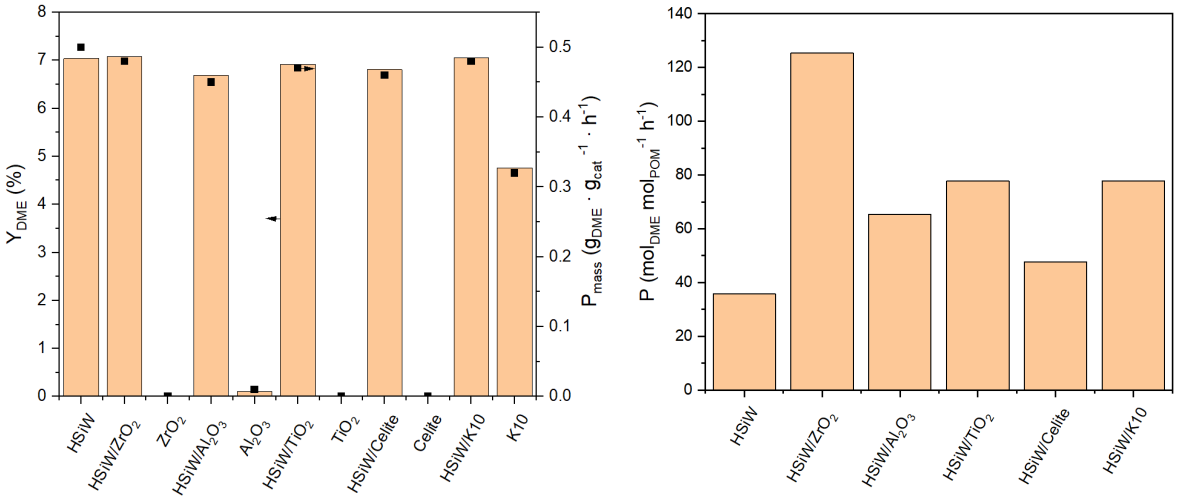

Figure 45: Yield of DME Y_{DME} and productivity P_{mass} (left) and productivity P_{mol} (right) of HSiW on different supports. Reaction conditions: m_{cat} = 2.5 g, ϑ = 250 °C, p = 50 bar H_2/CO_2, H_2/CO_2 ratio = 3/1, GHSV = 10000 h^{-1}. Adapted from *Wesner et al.* [229]

To benchmark the catalytic performance of HSiW/ZrO_2 developed in this study, it was compared with a widely recognized ZrO_2-supported HSiW catalyst from the literature, known for its high efficiency in DME synthesis from CO_2.[180] The literature catalyst was synthesized following the reported method, maintaining identical HPA loading conditions and tested under identical reaction conditions as the previous catalysts in this study. The comparative analysis revealed that the DME yields of the two catalysts were similar, with the literature catalyst achieving 7.09 % and the HSiW/ZrO_2 developed in this study reaching 6.9 %. Both catalysts exhibited nearly identical P_{mass} of approximately 0.5 $g_{DME} \cdot g_{cat}^{-1} \cdot h^{-1}$. However, P_{mol} of the catalyst synthesized within this study was notably higher, attributed to the improved dispersion of HPA achieved through its tailored synthesis method.

In this study, an extensive range of heteropolyacids was systematically evaluated for DME synthesis, highlighting the inclusion of numerous catalysts that had not been previously investigated. HSiW emerged as the standout catalyst, achieving remarkable catalytic activity, especially when supported on ZrO_2. The uniform dispersion of HSiW on ZrO_2 emerged as a critical factor, enhancing activity beyond what could be attributed to strength or density of acidic centers alone. These results not only highlight the versatility of POMs but also underline the potential of immobilized POMs in advancing efficient and sustainable gas-phase reactions.

7.4 Exploring Alternative Catalysts: In_2O_3-based Catalysts for CO_2 Conversion to Methanol

The fourth study moves beyond the POM systems investigated in earlier sections to explore In_2O_3-based catalysts for CO_2 hydrogenation to MeOH. While the bifunctional systems in the third study, combining Cu/ZnO/Al_2O_3 and POMs, demonstrating high efficiency for CO_2-to-DME conversion, the industrial drawbacks of Cu/ZnO/Al_2O_3 to deactivation by water highlights the need for more robust alternatives. In_2O_3-based catalysts are recognized for their stability and activity in MeOH production, making them a promising option for overcoming these obstacles. This chapter examines their catalytic properties and focuses on optimization strategies to enhance their performance. By addressing these aspects, the study aims to expand the range of catalytic systems available for large-scale CO_2 utilization in green chemistry.

To maintain consistency within this dissertation, certain nomenclature terminology has been adjusted compared to the original publication. Specifically, mass-based productivity P_{cat} is referred to as P_{mass} in the following discussion.

This study examined two key factors: the role of ZrO_2 as a support for In_2O_3 and the incorporation of different metal(oxides) into In_2O_3. In the first part, the impact of supporting In_2O_3 on ZrO_2 was investigated using two well-established In_2O_3/ZrO_2 catalysts from the literature - In_2O_3/ZrO_2 (S-AA) and In_2O_3/ZrO_2 (M-SG). These catalysts, which differ in their textural properties and synthesis methods, served as a basis for evaluating how impregnation and support characteristics influence catalytic performance. Here, S and M repnt the specific synthesis procedures, while AA and SG refer to the respective ZrO_2 supports used in their preparation. This research further explored the addition of metal oxides like NiO, CeO_2, MgO, or CuO to In_2O_3. Special attention was directed toward incorporating NiO using diverse synthesis methods, including wet impregnation, co-precipitation, and chemical reduction. The catalytic performance was assessed in a fixed-bed reactor under conditions of CO_2/H_2 ratio of 1/3, GHSV near 8000 h^{-1}, temperatures of 250 °C or 300 °C and pressures of 50 bar or 75 bar. The MeOH productivity was calculated either based on the mass of the catalyst (P_{mass}) or on the surface area of the catalyst ($P_{surface}$). Comprehensive catalyst characterization was performed to correlate structural and chemical properties with catalytic performance. Elemental analysis verified the composition, while XRD provided detailed information on crystal structure. XPS (X-ray photoelectron spectroscopy) measurements elucidated surface oxidation states, and N_2-physisorption characterized textural properties, such as surface area and pore volume. Morphology and dispersion of active metals were studied using SEM-EDX, while CO_2-TPD and H_2-TPR (Temperature-programmed reduction) were used for the determination of chemisorptive and reduction properties.

As a support material for In_2O_3, ZrO_2 promotes the generation of oxygen vacancies crucial for CO_2 activation and plays a key role in preventing the sintering of In_2O_3. Therefore, the investigation of ZrO_2 as support material, as well as the study of impregnation methods are key factors for optimizing catalytic performance. Two literature-reported catalysts, In_2O_3/ZrO_2 (S-AA) and In_2O_3/ZrO_2 (M-SG), served as benchmarks. Both studied supports - ZrO_2 (AA) and ZrO_2 (SG) exhibited a monoclinic crystal structure, as confirmed by XRD, but also provided distinct differences. ZrO_2 (SG) is characterized by a higher surface area (89 m^2/g) and larger pore volume (0.29 cm^3/g) compared to ZrO_2 (AA) (51 m^2/g and 0.24 cm^3/g), whereby these structural properties directly impacted the dispersion of In_2O_3 and the resulting chemisorptive characteristics. While both catalysts achieved the targeted In_2O_3-loading of around 10 wt.%, CO_2-TPD and H_2-TPR measurements highlighted the superior capacity of In_2O_3/ZrO_2 (M-SG) for CO_2 activation and hydrogen dissociation. This was reflected in higher MeOH productivity (P_{mass} = 0.470 $g_{MeOH} \cdot g_{cat}^{-1} \cdot h^{-1}$) and yield ($Y_{DME}$ = 10.0 %) of In_2O_3/ZrO_2 (M-SG) compared to In_2O_3/ZrO_2 (S-AA), with 0.330 $g_{MeOH} \cdot g_{cat}^{-1} \cdot h^{-1}$ and 6.8 %, respectively. Furthermore, the influence of synthesis methodologies on In_2O_3/ZrO_2 catalysts was evaluated, highlighting the interplay between preparation techniques and catalytic performance (Figure 46). The (M) method, utilizes an ethanol/water solvent system with a volume ratio of 74/26, and an extended stirring time of 5 hours, while the (S) method uses pure water as solvent with immediate solvent evaporation. To investigate the impact of these variables, both synthesis approaches were applied to ZrO_2 (AA) and ZrO_2 (SG), resulting in four hybrid catalysts: In_2O_3/ZrO_2 (M-AA), In_2O_3/ZrO_2 (S-AA), In_2O_3/ZrO_2 (M-SG), and In_2O_3/ZrO_2 (S-SG). Catalysts prepared with the (M) method consistently outperformed their (S) counterparts, achieving MeOH productivities of 0.470 $g_{MeOH} \cdot g_{cat}^{-1} \cdot h^{-1}$ (In_2O_3/ZrO_2 (M-SG)) and 0.440 $g_{MeOH} \cdot g_{cat}^{-1} \cdot h^{-1}$ (In_2O_3/ZrO_2 (M-AA), compared to 0.330 $g_{MeOH} \cdot g_{cat}^{-1} \cdot h^{-1}$ (In_2O_3/ZrO_2 (S-AA)) and 0.320 $g_{MeOH} \cdot g_{cat}^{-1} \cdot h^{-1}$ (In_2O_3/ZrO_2 (S-SG). Although the (M) method demonstrated superior performance, the selection of ZrO_2 as the support material proved to be the crucial factor in determining catalytic efficiency. This is particularly evident when comparing the productivities normalized to the surface areas, where In_2O_3/ZrO_2 (M-SG) achieved a higher productivity of 6.19 $mg_{MeOH} \cdot m^{-2} \cdot h^{-1}$, surpassing In_2O_3/ZrO_2 (S-SG) with 5.29 $mg_{MeOH} \cdot m^{-2} \cdot h^{-1}$ (Figure 46).

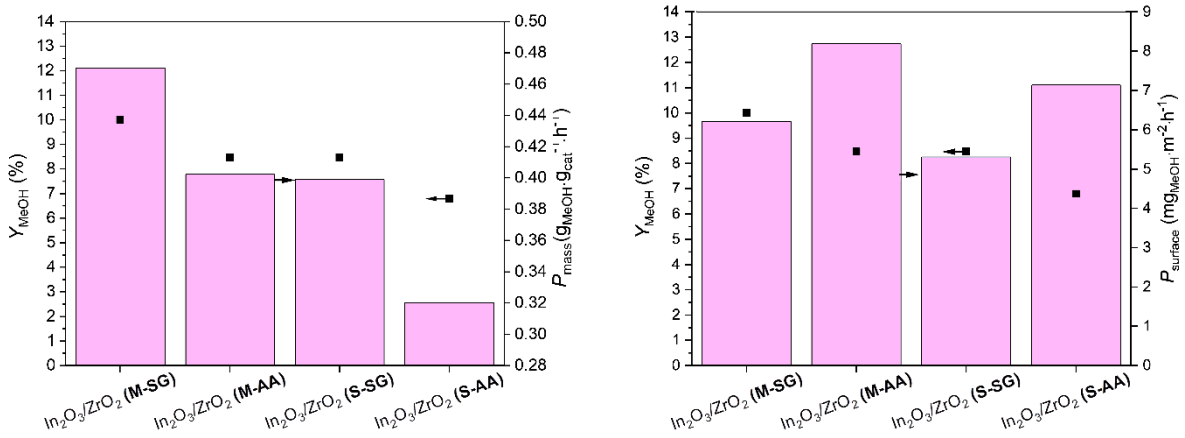

Figure 46: Influence of different ZrO_2 (SG or AA) supports and synthesis methods (M or S) on methanol yield and productivity based on the amount of catalyst P_{mass} (left) and on productivity based on the specific surfaces (right). Reaction conditions: m_{cat} =4 - 5 g, ϑ = 300 °C, p = 75 bar H_2/CO_2, H_2/CO_2 ratio = 3/1, GHSV = 8400 h^{-1}. Adapted from *Wesner et al.*[230]

To further enhance the catalytic activity of CO_2 hydrogenation to MeOH, various promoters (NiO, CuO, MgO, CeO_2) were incorporated into the catalyst system. Catalysts were prepared using co-precipitation, yielding a consistent and a significant surface area of around 89 m^2/g (except CuO with around 80 m^2/g), alongside uniform pore sizes and volumes. Elemental analysis verified the successful deposition of In_2O_3 and the respective promoter onto the ZrO_2 support, while XPS analysis confirmed that all metals were present in their oxidized states. CO_2-TPD revealed lower overall adsorption capacity for CeO_2-In_2O_3/ZrO_2 compared to pure In_2O_3/ZrO_2, likely attributed to forming of agglomerates, as confirmed by SEM-EDX mapping analysis. In contrast, for NiO-, CuO- and MgO-promoted catalysts significantly higher adsorption capacity was observed. Thereby, while CuO increased CO_2 adsorption capacity, also the adsorption strength increases, shifting the CO_2-desorption temperature to around 570 °C compared to around 470 °C for pure In_2O_3/ZrO_2, indicating strong CO_2-adsorption. In contrast, incorporation with MgO leads to a decrease in CO_2-desorption temperature, indicating only weak CO_2-adsorption strength. The NiO-promoted In_2O_3/ZrO_2 catalyst demonstrates alongside improved CO_2 adsorption capacity an enhanced surface reducibility, confirmed by H_2-TPR analysis, suggesting a higher catalytic activity for MeOH production. The findings align closely with the measured catalytic performance (Figure 47). NiO-In_2O_3/ZrO_2 demonstrated superior catalytic performance, achieving a MeOH productivity of 0.221 $g_{MeOH} \cdot g_{cat}^{-1} \cdot h^{-1}$ and CO_2 conversion of 5.7 %, outperforming the unmodified In_2O_3/ZrO_2 catalyst (0.159 $g_{MeOH} \cdot g_{cat}^{-1} \cdot h^{-1}$ and 4.4 %). In comparison, incorporation of CuO- and MgO reduced productivity to 0.088 $g_{MeOH} \cdot g_{cat}^{-1} \cdot h^{-1}$ and 0.049 $g_{MeOH} \cdot g_{cat}^{-1} \cdot h^{-1}$, respectively. These results underscore the interplay between chemisorptive properties and catalytic productivity, with NiO emerging as the most effective promoter for enhancing CO_2 hydrogenation to MeOH.

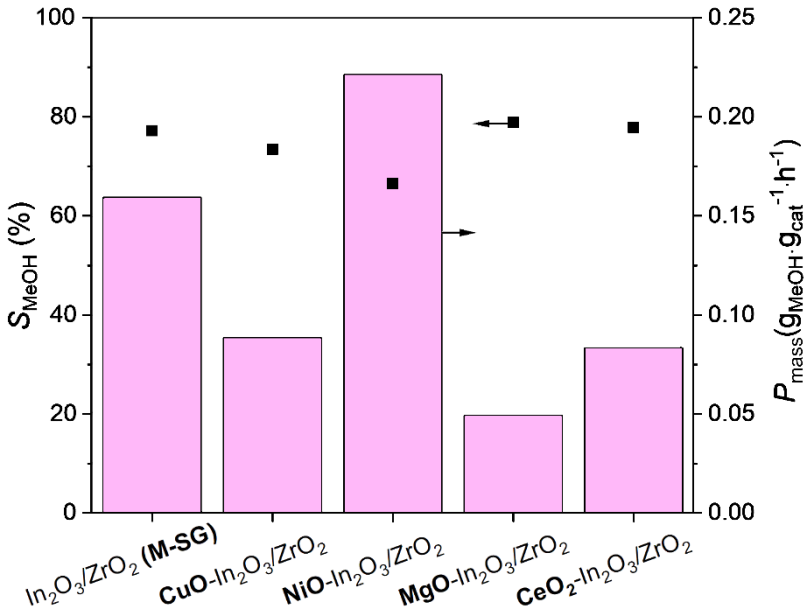

Figure 47: Catalytic performance of CuO-, NiO-, MgO- and CeO-promoted In_2O_3/ZrO_2 compared to In_2O_3/ZrO_2 (M-SG). Reaction conditions: m_{cat} =4 - 5 g, ϑ = 250 °C, p = 75 bar H_2/CO_2, H_2/CO_2 ratio = 3/1, GHSV = 8300 h^{-1}. Adapted from *Wesner et al.*[230]

To further optimize the catalytic performance of In_2O_3/ZrO_2 catalysts for CO_2 hydrogenation to MeOH, three synthesis methods - chemical reduction (CR), co-precipitation (CP), and wet impregnation (WI) - were employed to incorporate the NiO promoter. Elemental analysis confirmed successful NiO incorporation in all cases, with loadings of 0.32 wt.% (CR), 0.69 wt.% (CP), and 0.76 wt.% (WI), while maintaining a consistent In content of around 10.5 wt.%. Physisorptive data revealed minimal variation in surface area (74 - 80 m^2/g) and pore volume (0.216 - 0.258 cm^3/g) across the methods, with uniform pore size distributions around 10 nm. XPS confirmed the presence of Ni^{2+} species, while XRD and SEM-EDX suggested amorphous or nanocrystalline NiO structures with homogeneous metal dispersion. Catalytic evaluations (Figure 48) showed that NiO-In_2O_3/ZrO_2 (WI) achieved the highest MeOH productivity of 0.497 $g_{MeOH} \cdot g_{cat}^{-1} \cdot h^{-1}$, surpassing both the unmodified In_2O_3/ZrO_2 catalyst (0.475 $g_{MeOH} \cdot g_{cat}^{-1} \cdot h^{-1}$ and NiO-In_2O_3/ZrO_2 prepared via CR (0.390 $g_{MeOH} \cdot g_{cat}^{-1} \cdot h^{-1}$) or CP (0.482 $g_{MeOH} \cdot g_{cat}^{-1} \cdot h^{-1}$). The superior performance of WI-derived catalyst can be attributed to its improved H_2 reduction capacity of 1.19 and improved CO_2 adsorption capacity of 1.69. These values significantly surpass those the unmodified In_2O_3/ZrO_2, as well as for CR- and the CP-derived counterparts, likely due to the formation of agglomerates. The superior properties of the WI-derived catalyst can be linked to the formation of electronic defects during the impregnation process, which increase active sites for CO_2 adsorption and promote efficient hydrogen spillover. Long-term stability tests confirmed robust performance over 100 hours time-on-stream, with only a marginal decline in productivity (from 0.162 to 0.149 $g_{MeOH} \cdot g_{cat}^{-1} \cdot h^{-1}$), no methane formation, and no significant leaching or structural changes, as evidenced by elemental and XRD analyses.

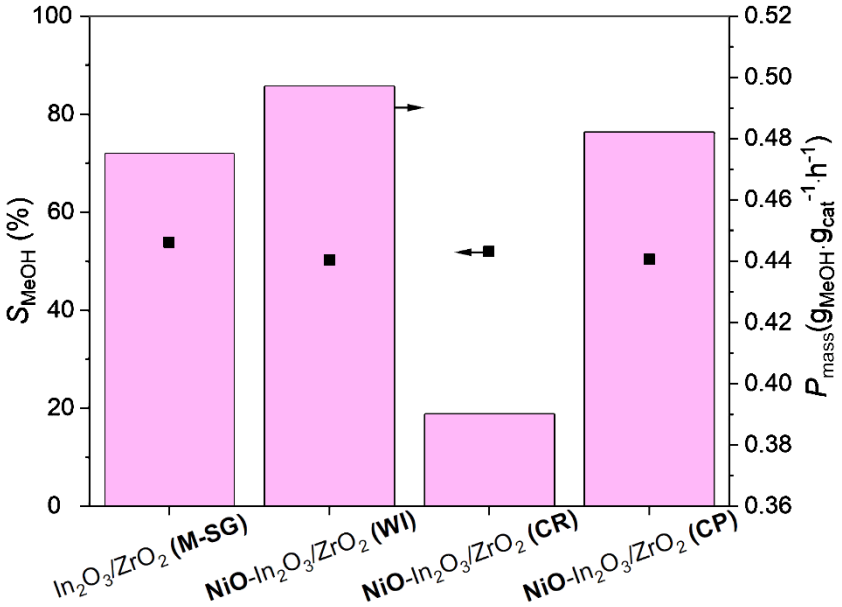

Figure 48: Impact of different synthesis methods for NiO-In_2O_3/ZrO_2 on the methanol productivity and selectivity. Reaction conditions: mcat = 4 - 5 g, ϑ = 300 °C, p = 75 bar H_2/CO_2, H_2/CO_2 ratio = 3/1, GHSV = 8600 h^{-1} (left). Adapted from *Wesner et al.*[230]

The comprehensive evaluation of In_2O_3-based catalysts highlights their significant potential as a robust and industrially relevant alternative for CO_2 hydrogenation to MeOH. By systematically investigating the effects of ZrO_2 supports, synthesis methods, and promoter incorporation, this study demonstrated the importance of optimizing catalyst composition and preparation to enhance performance. These findings underscore the interplay of structural, chemisorptive, and electronic properties in driving catalytic efficiency. NiO emerged as the most effective promoter, particularly when incorporated via wet impregnation, achieving superior MeOH productivity and long-term stability.

7.5 Conclusion of the Comprehensive Discussion

In conclusion, this work addressed the problems associated with the catalytic conversion of renewable carbon sources such as biomass and CO_2. Given the complexity and variability of these alternative feedstocks, the development of efficient, stable, and adaptable catalytic systems is essential for their successful integration into chemical production processes. The results of this work provide detailed insights into the catalytic conversion of renewable carbon sources through the targeted use of various metal oxide-based systems in different reaction environments.

The first study investigated the production of the platform chemical lactic acid from renewable, bio-based, starting materials, specifically the homogeneous catalytic conversion of biomass to lactic acid using specifically element-substituted POMs. $Na_3[PMo_{12}O_{40}]$ served as the base catalyst, systematically modified through partial substitution of molybdenum with vanadium and niobium. Among the catalysts tested, $Na_5[PNb_2Mo_{10}O_{40}]$ achieved the highest lactic acid yields from dihydroxyacetone of 21 % and also showed catalytic activity with various mono- and disaccharides. The structural stability of the catalyst after reaction was confirmed by spectroscopic and elemental analyses, highlighting its robustness and suitability for biomass conversion in aqueous media. Nevertheless, the technical and industrial implementation of such homogeneously catalyzed processes is challenged by the difficulties of catalysts separation and recycling. To overcome these limitations of the homogeneously catalyzed systems, the second study focused on immobilizing POMs on solid supports. For this purpose, $H_8[PV_5Mo_7O_{40}]$ was immobilized on various activated carbons, with CW20 providing the highest loading while preserving the Keggin structure. Catalytic tests using glucose as a model substrate demonstrated that the immobilized catalyst effectively converted glucose to lactic acid under a nitrogen atmosphere with a glucose conversion of 71 % and a LA yield of 11 %., with vanadium leaching of 11 %. However, significant leaching of > 68 % occurred under oxidative conditions, limiting its applicability for formic acid production. The study highlights the potential of immobilized POM catalysts for biomass conversion and emphasizes the importance of tailored catalyst preparation and optimized process conditions for improved performance.

The third study further explored the field of application of heterogenized POM catalysts. By combining immobilized POMs with a $Cu/ZnO/Al_2O_3$ catalyst in a bifunctional system they could be employed for the direct conversion of CO_2 to dimethyl ether in a heterogeneous gas-solid system. In this study, a huge variety of custom-made POMs was evaluated for this reaction. Ultimately, $H_4[SiW_{12}O_{40}]$ supported on ZrO_2 exhibited the highest activity, with a yield of dimethyl ether of 7 %, reaching 54 % of the thermodynamic equilibrium yield under the applied conditions. The catalytic performance was attributed to improved dispersion and acid site accessibility. The system enabled stable DME production and performed comparably to established reference catalysts. However, the additional water formation, resulting from the use of CO2 and the subsequent condensation to DME, is expected to lead to a decreased stability of the $Cu/ZnO/Al_2O_3$ catalyst. Therefore, the fourth study focused on developing an In_2O_3-based catalysts for CO_2 hydrogenation to methanol as an alternative to the water-sensitive $Cu/ZnO/Al_2O_3$ system. Various types of supports, promoters and synthesis methods were evaluated. NiO was found to be the most effective promoter, especially when incorporated via wet impregnation. The resulting $NiO–In_2O_3/ZrO_2$ catalyst showed high methanol productivity of 0.221 $g_{MeOH} \cdot g_{cat}^{-1} \cdot h^{-1}$ and maintained consistent catalytic activity during extended testing, confirming its structural stability and industrial applicability.

Together, these studies demonstrate, that rational catalyst design—ranging from element substitution to immobilization and promoter integration—can significantly improve the performance and stability of metal oxide-based systems. By tailoring catalytic systems to the requirements of both biomass and CO_2 valorization, this work contributes to developing efficient technologies for renewable carbon utilization in sustainable future-oriented chemical processes.

8. References

[1] N. Mittal, E. Prasad, *Catalyst Market Size, Share, Competitive Landscape and Trend Analysis Report, by Type, Process and Application,* in: https://www.alliedmarketresearch.com/catalysts-market, **2021.** Accessed 23.08.2024.

[2] C. Asmelash, A. Bardow, M. Beller, *Roadmap der deutschen Katalyseforschung*. *KATALYSE: Eine interdisziplinäre Schlüsseltechnologie zur nachhaltigen Wirtschaftsentwicklung*, Frankfurt am Main, **2023**.

[3] H. Lee, K. Calvin, D. Dasgupta, G. Krinner, A. Mukherji, P. W. Thorne, C. Trisos, J. Romero, P. Aldunce, K. Barrett et al., *Climate Change 2023: Synthesis Report. Contribution of Working Groups I, II and III to the Sixth Assessment Report of the Intergovernmental Panel on Climate Change*, Intergovernmental Panel on Climate Change (IPCC), Geneva, **2023**.

[4] M. Anderl, A. Bartel, J. Bürger, M. Gössel, M. Haydn, H. Heinfeller, C. Heller, A. Heuber, T. Köther, T. Krutzler, *Klimaschutzbericht 2023*, Wien, **2023**.

[5] E. Cavaciuti-Wishart, S. Heading, K. Kohler, *The global Risks Report 2024*. 19th Edition, Holtzbrinck Publishing Group, Geneva, **2024**.

[6] a) P. Boudes, *United Nations Conference on the Human Environment,* in: https://www.britannica.com/topic/United-Nations-Conference-on-the-Human-Environment, **2014.** Accessed 04.09.2024.; b) Presse- und Informationsamt der Bundesregierung, *Klimaschutzgesetz und Klimaschutzprogramm,* in: https://www.bundesregierung.de/breg-de/service/archiv/klimaschutzgesetz-2197410, **2025.** Accessed 23.05.2025.

[7] P. Münnich, J. Somers, J. Metz, U. Tillmann, C. Oliveira, R. Hermanns, A. Kalousdian, R. Meys, A. Bardow, B. Winter, *Chemie im Wandel. Die drei Grundpfeiler für die Transformation chemischer Wertschöpfungsketten*, Berlin, **2023**.

[8] F. Joas, W. Witecka, T. Lenck, F. Peter, F. Seiler, *Klimaneutrale Industrie*. *Schlüsseltechnologien und Politikoptionen für Stahl, Chemie und Zement*, Berlin, **2020**.

[9] F. W. Lichtenthaler, *Carbohydrates as Organic Raw Materials*, in: Ullmann's Encyclopedia of Industrial Chemistry, Wiley-VCH Verlag GmbH & Co. KGaA, Weinheim, Germany, **2000**, pp. 583–616.

[10] M. Carus, L. Dammer, A. Raschka, P. Skoczinski, Renewable carbon: Key to a sustainable and future-oriented chemical and plastic industry: Definition, strategy, measures and potential, *Greenh. Gases: Sci. Technol.*, **2020**, *10*, pp. 488–505.

[11] P. Barbaro, C. Bianchini, *Catalysis for Sustainable Energy Production*, Wiley VCH Verlag GmbH & Co. KGaA, Weinheim, **2009**.

[12] M. Kaltschmitt, K. Stampfer, *Energie aus Biomasse*. *Ressourcen und Bereitstellung*, Springer Vieweg, Heidelberg, **2024**.

[13] P. Styring, E. A. Quadrelli, K. Armstrong (Eds.) *Carbon dioxide utilisation*. *Closing the carbon cycle*, Elsevier, Amsterdam, **2015**.

[14] Y. M. Bar-On, R. Phillips, R. Milo, The biomass distribution on Earth, *Proc. Natl. Acad. Sci. U. S. A.*, **2018**, *115*, pp. 6506–6511.

[15] A. Tursi, A review on biomass: importance, chemistry, classification, and conversion, *Biofuel Res. J.*, **2019**, *6*, pp. 962–979.

[16] M. Kircher, *Zirkuläre Bioökonomie*, Springer Fachmedien Wiesbaden, Wiesbaden, **2023**.

[17] C. Stylianopoulos, *Carbohydrates: Chemistry and Classification*, in: Encyclopedia of Human Nutrition, Elsevier, **2013**, pp. 265–271.

[18] D. Klemm, B. Heublein, H.-P. Fink, A. Bohn, Cellulose: faszinierendes Biopolymer und nachhaltiger Rohstoff, *Angew. Chem.*, **2005**, *117*, pp. 3422–3458.

[19] B. Kamm, P. R. Gruber, M. Kamm, *Biorefineries-Industrial Processes and Products*, Wiley VCH Verlag GmbH & Co. KGaA, Weinheim, **2005**.

[20] P. Gatenholm, M. Tenkanen, *Hemicelluloses*. *Science and technology*, Oxford University Press, Washington, D.C., **2003**.

[21] B. Kamm, M. Kamm, Das Konzept der Bioraffinerie – Produktion von Plattformchemikalien und Finalprodukten, *Chemie Ingenieur Technik*, **2007**, *79*, pp. 592–603.

[22] T. Heinze, *Polysaccharides I*, Springer-Verlag, Berlin/Heidelberg, **2005**.

[23] a) A. Meier, *Tank oder Teller: Der Streit über den Einsatz von Biokraftstoffen belastet die Ampel,* in: https://www.tagesspiegel.de/politik/der-streit-uber-den-einsatz-von-biokraftstoffen-belastet-die-ampel-8586784.html, **2022.** Accessed 18.01.2025.; b) G. Klepper, N. Schmitz, J. Henke, *Biokraftstoffe – Zeit für eine Neubewertung,* in: https://www.deutsches-klima-konsortium.de/news/biokraftstoffe-zeit-fuer-eine-neubewertung/, **2015.** Accessed 16.12.2024.

[24] G. P. Moss, P. A. S. Smith, D. Tavernier, Glossary of class names of organic compounds and reactivity intermediates based on structure (IUPAC Recommendations 1995), *Pure Appl. Chem.*, **1995**, *67*, pp. 1307–1375.

[25] L. Witzke, Alternative Kraftstoffe für die dieselmotorische Verbrennung aus kohlenhydrathaltigen Biomassen und basierend auf bio- und chemisch-katalytischen Herstellverfahren, *Dissertation*, TU Braunschweig, Wiesbaden, **2017**.

[26] G. Ramalingam, A. K. Priya, L. Gnanasekaran, S. Rajendran, T. K. Hoang, Biomass and waste derived silica, activated carbon and ammonia-based materials for energy-related applications – A review, *Fuel*, **2024**, *355*.

[27] H. Schiweck, M. Clarke, G. Pollach, *Sugar*, in: Ullmann's Encyclopedia of Industrial Chemistry, Wiley VCH Verlag GmbH & Co. KGaA, Weinheim, **2012**, pp. 557–626.

[28] A. Behr, T. Seidensticker, *Chemistry of Renewables*. *An Introduction*, Springer Berlin / Heidelberg, Berlin, Heidelberg, **2021**.

[29] Y. Queneau, S. Jarosz, B. Lewandowski, J. Fitremann, Sucrose chemistry and applications of sucrochemicals, *Adv. Carbohydr. Chem. Biochem.*, **2007**, *61*, pp. 217–292.

[30] United States Department of Agriculture, *Sugar: World Markets and Trade,* in: https://fas.usda.gov/data/sugar-world-markets-and-trade-05232024, **2024.** Accessed 17.07.2024.

[31] A. Lützen, J. Seibel, *Saccharose,* in: https://roempp.thieme.de/lexicon/RD-19-00037, **2007.** Accessed 17.07.2024.

[32] B. O. Fraser-Reid, K. Tatsuta, J. Thiem, *Glycoscience. Chemistry and Chemical Biology*, Springer Berlin/Heidelberg, Berlin, Heidelberg, **2008**.

[33] S. Vaz Jr., *Biomass and Green Chemistry*. *Building a Renewable Pathway*, Springer International Publishing, Cham, **2018**.

[34] -, *Global Market for Starch and Starch Products,* in: https://www.gov.mb.ca/agriculture/markets-and-statistics/trade-statistics/pubs/starch-world-market.pdf, **2023.** Accessed 23.05.2025.

[35] a) D. Osteroth, *Taschenbuch für Lebensmittelchemiker und -technologen*, Springer Berlin Heidelberg, Berlin, Heidelberg, **1991**; b) -, *Stärkeindustrie | Herstellung,* in: https://www.vgms.de/staerkeindustrie/staerkeindustrie/herstellung, **-.** Accessed 17.12.2024.; c) K.-D. Jany, *Enzyme für die Stärkehydrolyse - Gewinnung von HFCS-Sirup und Maltodextrinen,* in: https://www.biotech-enzymes.com/enzyme-fuer-die-staerkeverzuckerung-gewinnung-von-hfcs-sirup-und-maltodextrinen, **-.** Accessed 17.12.2024.

[36] a) I. Alawad, H. Ibrahim, Pretreatment of agricultural lignocellulosic biomass for fermentable sugar: opportunities, challenges, and future trends, *Biomass Conv. Bioref.*, **2022**, *14*, pp. 6155–6183; b) C.-H. Zhou, X. Xia, C.-X. Lin, D.-S. Tong, J. Beltramini, Catalytic conversion of lignocellulosic biomass to fine chemicals and fuels, *Chem. Soc. Rev.*, **2011**, *40*, pp. 5588–5617.

[37] R. Sankaran, K. Markandan, K. S. Khoo, C. K. Cheng, V. Ashokkumar, B. Deepanraj, P. L. Show, The Expansion of Lignocellulose Biomass Conversion Into Bioenergy via Nanobiotechnology, *Front. Nanotechnol.*, **2021**, *3*.

[38] F. Dalena, A. Basile, C. Rossi, *Bioenergy systems for the future*. *Prospects for biofuels and biohydrogen*, Woodhead Publishing, Kidlington, **2017**.

[39] J. M. Berg, J. L. Tymoczko, G. J. Gatto, L. Stryer, *Biochemie*, Springer Berlin / Heidelberg, Berlin, Heidelberg, **2018**.

[40] M. N. Belgacem, A. Gandini, *Monomers, polymers and composites from renewable resources*, Elsevier, Amsterdam, **2009**.

[41] L. Olsson, *Biofuels*, Springer Berlin / Heidelberg, Berlin, Heidelberg, **2007**.

[42] A. B. Gunjal, N. N. Patil, S. S. Shinde, *Enzymes in Degradation of the Lignocellulosic Wastes*, Springer International Publishing, Cham, **2020**.

[43] M. Fischedick, K. Görner, M. Thomeczek, *CO_2: Abtrennung, Speicherung, Nutzung. Ganzheitliche Bewertung im Bereich von Energiewirtschaft und Industrie*, Springer Berlin, Berlin, **2013**.

[44] M. de Falco, G. Iaquaniello, G. Centi, *CO_2: A Valuable Source of Carbon*, Springer London, London, **2013**.

[45] V. Goyal, *CO_2 lewis structure, molecular geometry, bond angle, shape,* in: https://topblogtenz.com/carbon-dioxide-co2-lewis-structure-molecular-geometry-bond-angle-hybridization/, **2023.** Accessed 18.12.2023.

[46] M. Kircher, T. Schwarz, *CO_2 und CO - Nachhaltige Kohlenstoffquellen für die Kreislaufwirtschaft*, Springer Spektrum, Berlin, Heidelberg, **2020**.

[47] D. Wolf-Gladrow, Der Ozean als Teil des globalen Kohlenstoff-Kreislaufs, *UWSF - Z Umweltchem. Ökotox.*, **1992**, *4*, pp. 20–24.

[48] J. Schröder, K. Naumann, *Monitoring erneuerbarer Energien im Verkehr*, DBFZ Deutsches Biomasseforschungszentrum gemeinnützige GmbH, **2022**.

[49] T. Fröhlich, S. Blömer, D. Münter, L.-A. Brischke, *CO_2 Quellen für die PtX Herstellung in Deutschland*. *Technologien, Umweltwirkung, Verfügbarkeit*, Heidelberg, **2019**.

[50] a) C. Breyer, M. Fasihi, C. Bajamundi, F. Creutzig, Direct Air Capture of CO_2 : A Key Technology for Ambitious Climate Change Mitigation, *Joule*, **2019**, *3*, pp. 2053–2057; b) M. Erans, E. S. Sanz-Pérez, D. P. Hanak, Z. Clulow, D. M. Reiner, G. A. Mutch, Direct air capture: process technology, techno-economic and socio-political challenges, *Energy Environ. Sci.*, **2022**, *15*, pp. 1360–1405.

[51] Y. Himeda, *CO_2 Hydrogenation Catalysis*, Wiley VCH Verlag GmbH & Co. KGaA, Weinheim, **2021**.

[52] D. Alalaiwat, E. Khan, Current status and future scenarios of carbon capture from power plants emission: a review, *Rev. Environ. Sci. Biotechnol.*, **2023**, *22*, pp. 799–822.

[53] C. Pettinari, A. Tombesi, Metal–organic frameworks for carbon dioxide capture, *MRS Energy Sustain.*, **2020**, *7*.

[54] P. Kasten, C. Heinemann, *Kein Selbstläufer: Klimaschutz und Nachhaltigkeit durch PtX*. *Diskussion der Anforderungen und erste Ansätze für Nachweiskriterien für eine klimafreundliche und nachhaltige Produktion von PtX-Stoffen*, Berlin, **2019**.

[55] A. R. Alagu, C. Boumrifak, L. F. López González, *Carbon for Power-to-X. Suitable CO_2 sources and integration in PtX value chains*, Frankfurt am Main, **2024**.

[56] J. N. Starr, G. Westhoff, *Lactic Acid*, in: Ullmann's Encyclopedia of Industrial Chemistry, Wiley-VCH Verlag GmbH & Co. KGaA, Weinheim, Germany, **2000**, pp. 1–8.

[57] S. M. Ameen, G. Caruso, *Lactic Acid in the Food Industry*, Springer International Publishing, Cham, **2017**.

[58] R. A. Auras, L.-T. Lim, S. E. M. Selke, H. Tsuji, *Poly(lactic acid): Synthesis, structures, properties, processing, applications, and end of life*, John Wiley & Sons Inc., New Jersey, **2022**.

[59] A. Wollrab, *Organische Chemie*, Springer Berlin / Heidelberg, Berlin, Heidelberg, **2014**.

[60] Y. Huang, Y. Wang, N. Shang, P. Li, Microbial Fermentation Processes of Lactic Acid: Challenges, Solutions, and Future Prospects, *Foods*, **2023**, *12*.

[61] A. Pandey, *Current developments in biotechnology and bioengineering*. *Production, isolation and purification of industrial products*, Elsevier, Amsterdam, **2017**.

[62] S.-T. Yang, H. A. El Ensashy, N. Thongchul, *Bioprocessing Technologies in Integrated Biorefinery for Production of Biofuels*, John Wiley & Sons Inc., New Jersey, **2013**.

[63] a) J. J. Bozell, G. R. Petersen, Technology development for the production of biobased products from biorefinery carbohydrates—the US Department of Energy's "Top 10" revisited, *Green Chem.*, **2010**, *12*, pp. 539–554; b) S. Bidway, *Lactic Acid Market Size, Share, and Trends 2024 to 2034,* in: https://www.precedenceresearch.com/lactic-acid-market, **2024.** Accessed 22.07.2024.

[64] M. Dusselier, P. van Wouwe, A. Dewaele, E. Makshina, B. F. Sels, Lactic acid as a platform chemical in the biobased economy: the role of chemocatalysis, *Energy Environ. Sci.*, **2013**, *6*, p. 1415.

[65] J. Ren, *Biodegradable Poly(Lactic Acid): Synthesis, Modification, Processing and Applications*, Springer Berlin / Heidelberg, Berlin, Heidelberg, **2011**.

[66] K. H. Kim, C. S. Kim, Y. Wang, C. G. Yoo, Integrated Process for the Production of Lactic Acid from Lignocellulosic Biomass: From Biomass Fractionation and Characterization to Chemocatalytic Conversion with Lanthanum(III) Triflate, *Ind. Eng. Chem. Res.*, **2020**, *59*, pp. 10832–10839.

[67] N. Shi, Q. Liu, X. He, H. Cen, R. Ju, Y. Zhang, L. Ma, Production of lactic acid from cellulose catalyzed by easily prepared solid $Al_2(WO_4)_3$, *Bioresour. Technol. Rep.*, **2019**, *5*, pp. 66–73.

[68] L. Yang, J. Su, S. Carl, J. G. Lynam, X. Yang, H. Lin, Catalytic conversion of hemicellulosic biomass to lactic acid in pH neutral aqueous phase media, *Appl. Catal. B: Environ.*, **2015**, *162*, pp. 149–157.

[69] H. Ma, P. Tingelstad, de Chen, Lactic acid production by catalytic conversion of glucose: An experimental and techno-economic evaluation, *Catal. Today*, **2023**, *408*, pp. 2–8.

[70] D. Esposito, M. Antonietti, Chemical conversion of sugars to lactic acid by alkaline hydrothermal processes, *ChemSusChem*, **2013**, *6*, pp. 989–992.

[71] L. Chen, S. Ren, X. P. Ye, Glycerol conversion to lactic acid with sodium hydroxide as a homogeneous catalyst in a fed-batch reactor, *React. Kinet. Mech. Catal.*, **2015**, *114*, pp. 93–108.

[72] a) X. Yan, F. Jin, K. Tohji, T. Moriya, H. Enomoto, Production of lactic acid from glucose by alkaline hydrothermal reaction, *J. Mater. Sci.*, **2007**, *42*, pp. 9995–9999; b) Z. Shen, F. Jin, Y. Zhang, B. Wu, A. Kishita, K. Tohji, H. Kishida, Effect of Alkaline Catalysts on Hydrothermal Conversion of Glycerin into Lactic Acid, *Ind. Eng. Chem. Res.*, **2009**, *48*, pp. 8920–8925; c) L. Li, F. Shen, R. L. Smith, X. Qi, Quantitative chemocatalytic production of lactic acid from glucose under anaerobic conditions at room temperature, *Green Chem.*, **2017**, *19*, pp. 76–81; d) H. Kishida, F. Jin, X. Yan, T. Moriya, H. Enomoto, Formation of lactic acid from glycolaldehyde by alkaline hydrothermal reaction, *Carbohydr. Res.*, **2006**, *341*, pp. 2619–2623.

[73] S. Saravanamurugan, H. Li, A. Riisager, A. Pandey, *Biomass, biofuels, biochemicals: Recent advances in development of platform chemicals*, Elsevier, Amsterdam, **2020**.

[74] C. B. Rasrendra, I. G. B. N. Makertihartha, S. Adisasmito, H. J. Heeres, Green Chemicals from d-glucose: Systematic Studies on Catalytic Effects of Inorganic Salts on the Chemo-Selectivity and Yield in Aqueous Solutions, *Top. Catal.*, **2010**, *53*, pp. 1241–1247.

[75] M. Bicker, S. Endres, L. Ott, H. Vogel, Catalytical conversion of carbohydrates in subcritical water: A new chemical process for lactic acid production, *J. Mol. Catal. A Chem.*, **2005**, *239*, pp. 151–157.

[76] D. Cao, W. Cai, W. Tao, S. Zhang, D. Wang, D. Huang, Lactic Acid Production from Glucose Over a Novel Nb_2O_5 Nanorod Catalyst, *Catal. Lett.*, **2017**, *147*, pp. 926–933.

[77] J. Barros dos Santos, N. José Araújo de Albuquerque, C. Lúcia de Paiva e Silva Zanta, M. Roberto Meneghetti, S. Margareti Plentz Meneghetti, Fructose conversion in the presence of Sn(IV) catalysts exhibiting high selectivity to lactic acid, *RSC Adv.*, **2015**, *5*, pp. 90952–90959.

[78] a) F.-F. Wang, H.-Z. Wu, H.-F. Ren, C.-L. Liu, C.-L. Xu, W.-S. Dong, Er/β-zeolite-catalyzed one-pot conversion of cellulose to lactic acid, *J. Porous Mater.*, **2017**, *24*, pp. 697–706; b) Y. Zhang, H. Luo, L. Kong, X. Zhao, G. Miao, L. Zhu, S. Li, Y. Sun, Highly efficient production of lactic acid from xylose using Sn-beta catalysts, *Green Chem.*, **2020**, *22*, pp. 7333–7336.

[79] J. Albert, M. Mendt, M. Mozer, D. Voß, Explaining the role of vanadium in homogeneous glucose transformation reactions using NMR and EPR spectroscopy, *Appl. Catal. A: Gen.*, **2019**, *570*, pp. 262–270.

[80] D. Voß, R. Dietrich, M. Stuckart, J. Albert, Switchable Catalytic Polyoxometalate-Based Systems for Biomass Conversion to Carboxylic Acids, *ACS omega*, **2020**, *5*, pp. 19082–19091.

[81] a) J. E. Prue, A. J. Read, Acidity constant of formic acid, *Trans. Faraday Soc.*, **1966**, *62*, p. 1271; b) K. P. C. Vollhardt, N. E. Schore, *Organic chemistry*. *Structure and function*, W. H. Freeman and Company, New York, **2011**.

[82] W. Reutemann, H. Kieczka, *Formic Acid*, in: Ullmann's Encyclopedia of Industrial Chemistry, Wiley VCH Verlag GmbH & Co. KGaA, Weinheim, **2012**.

[83] H.-D. Jakubke, R. Karcher, *Ameisensäure,* in: https://www.spektrum.de/lexikon/chemie/ameisensaeure/361, **1998.** Accessed 24.07.2024.

[84] D. Bockelée-Morvan, D. C. Lis, J. E. Wink, J. Despois, R. Crovisier, R. Bachiller, D. J. Benford, N. Biver, P. Colom, E. Davies et al., New molecules found in comet C/1995 O1 (Hale-Bopp), *Astron. Astrophys.*, **2000**, pp. 1101–1114.

[85] -, *Markets,* in: https://www.oxfa.eu/en/markets/, **-.** Accessed 21.12.2024.

[86] P. Pandey, *Formic Acid Market to Develop New Growth Story Formic Acid Market to Develop New Growth Story 2024 - 2031,* in: https://www.openpr.com/news/3583376/formic-acid-market-to-develop-new-growth-story-2024-2031-basf, **2024.** Accessed 24.07.2024.

[87] G. D. McGinnis, W. W. Wilson, S. E. Prince, C. C. Chen, Conversion of biomass into chemicals with high-temperature wet oxidation, *Ind. Eng. Chem. Prod. Res. Dev.*, **1983**, *22*, pp. 633–636.

[88] a) R. Vinu, L. J. Broadbelt, A mechanistic model of fast pyrolysis of glucose-based carbohydrates to predict bio-oil composition, *Energy Environ. Sci.*, **2012**, *5*, pp. 9808–9826; b) P. R. Patwardhan, R. C. Brown, B. H. Shanks, Product distribution from the fast pyrolysis of hemicellulose, *ChemSusChem*, **2011**, *4*, pp. 636–643.

[89] a) T. Flannelly, M. Lopes, L. Kupiainen, S. Dooley, J. J. Leahy, Non-stoichiometric formation of formic and levulinic acids from the hydrolysis of biomass derived hexose carbohydrates, *RSC Adv.*, **2016**, *6*, pp. 5797–5804; b) K. Świątek, S. Gaag, A. Klier, A. Kruse, J. Sauer, D. Steinbach, Acid Hydrolysis of Lignocellulosic Biomass: Sugars and Furfurals Formation, *Catalysts*, **2020**, *10*; c) Y. Sun, L. Lin, C. Pang, H. Deng, H. Peng, J. Li, B. He, S. Liu, Hydrolysis of Cotton Fiber Cellulose in Formic Acid, *Energy Fuels*, **2007**, *21*, pp. 2386–2389.

[90] a) V. P. Muiuane, M. Ferreira, P. Bignet, A. P. Bettencourt, P. Parpot, Production of formic acid from biomass-based compounds using a filter press type electrolyzer, *J. Environ. Chem. Eng.*, **2013**, *1*, pp. 1237–1244; b) K. Natsui, H. Iwakawa, N. Ikemiya, K. Nakata, Y. Einaga, Stable and Highly Efficient Electrochemical Production of Formic Acid from Carbon Dioxide Using Diamond Electrodes, *Angew. Chem.*, **2018**, *57*, pp. 2639–2643.

[91] a) B. Jin, G. Yao, X. Wang, K. Ding, F. Jin, Photocatalytic Oxidation of Glucose into Formate on Nano TiO_2 Catalyst, *ACS Sustain. Chem. Eng.*, **2017**, *5*, pp. 6377–6381; b) Q. Zhang, Y. Ge, C. Yang, B. Zhang, K. Deng, Enhanced photocatalytic performance for oxidation of glucose to value-added organic acids in water using iron thioporphyrazine modified SnO_2, *Green Chem.*, **2019**, *21*, pp. 5019–5029.

[92] F. Shen, R. L. Smith Jr., J. Li, H. Guo, X. Zhang, X. Qi, Critical assessment of reaction pathways for conversion of agricultural waste biomass into formic acid, *Green Chem.*, **2021**, *23*, pp. 1536–1561.

[93] M. J. Dietrich, T. L. Randall, P. J. Canney, Wet air oxidation of hazardous organics in wastewater, *Environ. Prog.*, **1985**, *4*, pp. 171–177.

[94] L. Calvo, D. Vallejo, Formation of Organic Acids during the Hydrolysis and Oxidation of Several Wastes in Sub- and Supercritical Water, *Ind. Eng. Chem. Res.*, **2002**, *41*, pp. 6503–6509.

[95] R. Robert, S. Barbati, N. Ricq, M. Ambrosio, Intermediates in wet oxidation of cellulose: identification of hydroxyl radical and characterization of hydrogen peroxide, *Water Res.*, **2002**, *36*, pp. 4821–4829.

[96] C. Wang, X. Chen, M. Qi, J. Wu, G. Gözaydın, N. Yan, H. Zhong, F. Jin, Room temperature, near-quantitative conversion of glucose into formic acid, *Green Chem.*, **2019**, *21*, pp. 6089–6096.

[97] a) F. Jin, J. Yun, G. Li, A. Kishita, K. Tohji, H. Enomoto, Hydrothermal conversion of carbohydrate biomass into formic acid at mild temperatures, *Green Chem.*, **2008**, *10*, p. 612; b) J. Yun, G. Yao, F. Jin, H. Zhong, A. Kishita, K. Tohji, H. Enomoto, L. Wang, Low-temperature and highly efficient conversion of saccharides into formic acid under hydrothermal conditions, *AICHE J.*, **2016**, *62*, pp. 3657–3663.

[98] A. T. Quitain, M. Faisal, K. Kang, H. Daimon, K. Fujie, Low-molecular-weight carboxylic acids produced from hydrothermal treatment of organic wastes, *J. Hazard. Mater.*, **2002**, *93*, pp. 209–220.

[99] K. Ding, Y. Le, G. Yao, Z. Ma, B. Jin, J. Wang, F. Jin, A rapid and efficient hydrothermal conversion of coconut husk into formic acid and acetic acid, *Process Biochem.*, **2018**, *68*, pp. 131–135.

[100] P. Gao, G. Li, F. Yang, X.-N. Lv, H. Fan, L. Meng, X.-Q. Yu, Preparation of lactic acid, formic acid and acetic acid from cotton cellulose by the alkaline pre-treatment and hydrothermal degradation, *Ind. Crops Prod.*, **2013**, *48*, pp. 61–67.

[101] M. Niu, Y. Hou, S. Ren, W. Wu, K. N. Marsh, Conversion of wheat straw into formic acid in $NaVO_3$–H_2SO_4 aqueous solution with molecular oxygen, *Green Chem.*, **2015**, *17*, pp. 453–459.

[102] R. Wölfel, N. Taccardi, A. Bösmann, P. Wasserscheid, Selective catalytic conversion of biobased carbohydrates to formic acid using molecular oxygen, *Green Chem.*, **2011**, *13*, pp. 2759–2763.

[103] J. Ott, V. Gronemann, F. Pontzen, E. Fiedler, G. Grossmann, D. B. Kersebohm, G. Weiss, C. Witte, *Methanol*, in: Ullmann's Encyclopedia of Industrial Chemistry, Wiley VCH Verlag GmbH & Co. KGaA, Weinheim, **2012**.

[104] M. Bertau, H. Offermanns, L. Plass, F. Schmidt, H.-J. Wernicke, *Methanol: The Basic Chemical and Energy Feedstock of the Future*, Springer Berlin / Heidelberg, Berlin, Heidelberg, **2014**.

[105] a) L. Harvey-Smith, R. J. Cohen, Discovery of large-scale methanol and hydroxyl maser filaments in W3(OH), *Mon. Not. R. Astron. Soc.*, **2006**, *371*, pp. 1550–1558; b) S. Leurini, Methanol: a diagnostic tool for star formation, *Dissertation*, Rheinische Friedrich-Wilhelms-Universität Bonn, **2004**.

[106] R. K. Srivastava, P. K. Sarangi, L. Bhatia, A. K. Singh, K. P. Shadangi, Conversion of methane to methanol: technologies and future challenges, *Biomass Conv. Bioref.*, **2022**, *12*, pp. 1851–1875.

[107] S. Bidwai, *Methanol Market Size, Share, and Trends 2024 to 2034,* in: https://www.precedenceresearch.com/methanol-market, **2024.** Accessed 19.01.2025.

[108] A. Basile, F. Dalena, *Methanol*. *Science and Engineering*, Elsevier, Amsterdam, **2017**.

[109] D. Wawrzyńczak, I. Majchrzak-Kucęba, C. Pevida, G. Bonura, R. Nogueira, M. de Falco, *The Carbon Chain in Carbon Dioxide Industrial Utilization Technologies*, CRC Press, Boca Raton, **2022**.

[110] M. Aresta, A. Dibenedetto, Utilisation of CO_2 as a chemical feedstock: opportunities and challenges, *Dalton Trans.*, **2007**, pp. 2975–2992.

[111] K. Ushikoshi, K. Moria, T. Watanabe, M. Takeuchi, M. Saito, A 50 kg/day class test plant for methanol synthesis from CO_2 and H_2, *Stud. Surf. Sci. Catal.*, **1998**, *114*, pp. 357–362.

[112] N. Skafte, *The world's largest green methanol plant fuels green shipping and industry,* in: https://stateofgreen.com/en/solutions/the-worlds-largest-green-methanol-plant-fuels-green-shipping-and-industry/, **2024.** Accessed 19.01.2025.

[113] a) M. Hillestad, Direct hydrogenation of carbon dioxide to methanol: Systematic generation of multi-stage designs, *J. CO2 Util.*, **2023**, *74*; b) S. G. Jadhav, P. D. Vaidya, B. M. Bhanage, J. B. Joshi, Catalytic carbon dioxide hydrogenation to methanol: A review of recent studies, *Chem. Eng. Res. Des.*, **2014**, *92*, pp. 2557–2567.

[114] M. Müller, U. Hübsch, *Dimethyl Ether*, in: Ullmann's Encyclopedia of Industrial Chemistry, Wiley-VCH Verlag GmbH & Co. KGaA, Weinheim, Germany, **2000**.

[115] N. G. C. Brunken, A. S. Booth, M. Leemker, P. Nazari, N. van der Marel, E. F. van Dishoeck, A major asymmetric ice trap in a planet-forming disk, *A&A*, **2022**, *659*, A29.

[116] R. Baghel, *Dimethyl Ether (DME) Market Size & Share,* in: https://www.researchnester.com/reports/dimethyl-ether-market/3501, **2024.** Accessed 22.08.2024.

[117] W. Maus, *Zukünftige Kraftstoffe*. *Energiewende des Transports als ein weltweites Klimaziel*, Springer Berlin / Heidelberg, Berlin, Heidelberg, **2019**.

[118] R. Baghei, *Global Dimethyl Ether Market,* in: https://market.us/report/dimethyl-ether-market/, **2024.** Accessed 19.01.2025.

[119] a) X. Bao, Y. Xu, *Natural gas conversion VII*. *Proceedings of the 7th Natural Gas Conversion Symposium, June 6-10, 2004, Dalian, China*, Elsevier, Amsterdam, **2004**; b) N. Dahmen, E. Henrich, E. Dinjus, F. Weirich, The bioliq® bioslurry gasification process for the production of biosynfuels, organic chemicals, and energy, *Energy Sustain. Soc.*, **2012**, *2*.

[120] C. Liu, Z. Liu, Perspective on CO2 Hydrogenation for Dimethyl Ether Economy, *Catalysts*, **2022**, *12*.

[121] E. Catizzone, G. Bonura, M. Migliori, F. Frusteri, G. Giordano, CO_2 Recycling to Dimethyl Ether: State-of-the-Art and Perspectives, *Molecules*, **2017**, *23*.

[122] Y. Fu, T. Hong, Chen, Jieping, A. Auroux, J. Shen, Surface acidity and the dehydration of methanol to dimethyl ether, *Thermochim. Acta 434*, **2005**, *434*, pp. 22–26.

[123] A. Ghosh, D. Nag, R. Chatterjee, A. Singha, P. S. Dash, B. Choudhury, A. Bhaumik, CO 2 to dimethyl ether (DME): structural and functional insights of hybrid catalysts, *Catal. Sci. Technol.*, **2024**, *14*, pp. 1387–1427.

[124] a) K. Krim, A. Sachse, A. Le Valant, Y. Pouilloux, S. Hocine, One Step Dimethyl Ether (DME) Synthesis from CO2 Hydrogenation over Hybrid Catalysts Containing Cu/ZnO/Al2O3 and Nano-Sized Hollow ZSM-5 Zeolites, *Catal. Lett.*, **2023**, *153*, pp. 83–94; b) H. Bateni, C. Able, Development of Heterogeneous Catalysts for Dehydration of Methanol to Dimethyl Ether: A Review, *Catal. Ind.*, **2019**, *11*, pp. 7–33.

[125] S. P. Naik, V. Bui, T. Ryu, J. D. Miller, W. Zmierczak, Al-MCM-41 as methanol dehydration catalyst, *Applied Catalysis A: General*, **2010**, *381*, pp. 183–190.

[126] W. Dai, W. Kong, G. Wu, N. Li, L. Li, N. Guan, Catalytic dehydration of methanol to dimethyl ether over aluminophosphate and silico-aluminophosphate molecular sieves, *Catal. Commun.*, **2011**, *12*, pp. 535–538.

[127] M. Xu, J. H. Lunsford, D. Goodman, A. Bhattacharyya, Synthesis of dimethyl ether (DME) from methanol over solid-acid catalysts, *Appl. Catal. A-Gen.*, **1997**, *149*, pp. 289–301.

[128] N. Khandan, M. Kazemeini, M. Aghaziarati, Determining an optimum catalyst for liquid-phase dehydration of methanol to dimethyl ether, *Appl. Catal. A-Gen.*, **2008**, *349*, pp. 6–12.

[129] E. Catizzone, G. Bonura, M. Migliori, F. Frusteri, G. Giordano, *On the Effectiveness of Zeolite-Based Catalysts in the CO_2 Recycling to DME: State of the Art and Perspectives*, **2017**.

[130] M. Sutradhar, Metal-Based Catalysts in Organic Synthesis, *Catalysts*, **2021**, *10*.

[131] A. Behr, *Angewandte homogene Katalyse*, Wiley VCH Verlag GmbH & Co. KGaA, Weinheim, **2008**.

[132] K. R. Poeppelmeier, J. Reedijk, *Comprehensive inorganic chemistry II*. *From elements to applications*, Elsevier, Amsterdam, **2013**.

[133] M. T. Pope, A. Müller, Polyoxometalate Chemistry: An Old Field with New Dimensions in Several Disciplines, *Angew. Chem. Int. Ed. Engl.*, **1991**, *30*, pp. 34–48.

[134] M. T. Pope, *Heteropoly and isopoly oxometalates*, Springer, Berlin, Heidelberg, New York, Tokyo, **1983**.

[135] R. Klaewkla, M. Arend, W. F., *A Review of Mass Transfer Controlling the Reaction Rate in Heterogeneous Catalytic Systems*, in: Mass Transfer - Advanced Aspects (Ed.: H. Nakajima), InTech, **2011**.

[136] R. van Eldik, L. Cronin, *Advances in Inorganic Chemistry*. *Polyoxometalate chemistry*, Elsevier Academic Press, Amsterdam, **2017**.

[137] M. T. Pope, A. Müller, *Polyoxometalate chemistry*. *From topology via self-assembly to applications*, Kluwer Academic Publishers, Dordrecht, **2001**.

[138] J. J. Berzelius, Beitrag zur näheren Kenntniss des Molybdäns, *Ann. Phys.*, **1826**, *82*, pp. 369–392.

[139] J. F. KEGGIN, Structure of the Molecule of 12-Phosphotungstic Acid, *Nature*, **1933**, *131*, pp. 908–909.

[140] H. T. Evans, THE CRYSTAL STRUCTURES OF AMMONIUM AND POTASSIUM MOLYBDOTELLURATES, *J. Am. Chem. Soc.*, **1948**, *70*, pp. 1291–1292.

[141] B. Dawson, The structure of the 9(18)-heteropoly anion in potassium 9(18)-tungstophosphate, $K_6(P_2W_{18}O_{62})$.14 H_2O, *Acta Crystallogr.*, **1953**, *6*, pp. 113–126.

[142] I. Lindqvist, The structure of the hexaniobate ion in $7Na_2O\cdot 6Nb_2O_5\cdot 32\ H_2O$, *Ark Kemi*, , *1953*, pp. 247–250.

[143] A. Müller, E. Beckmann, H. Bögge, M. Schmidtmann, A. Dress, Inorganic Chemistry Goes Protein Size: A Mo368 Nano-Hedgehog Initiating Nanochemistry by Symmetry Breaking, *Angew. Chem. Int. Ed.*, **2002**, *41*, pp. 1162–1167.

[144] a) J. R. Galán-Mascarós, U. Kortz, Special issue on Polyoxometalates, *Acta crystallogr., C Struct. chem.*, **2018**, *74*, pp. 1180–1181; b) M. J. W. Budych, K. Staszak, A. Bajek, F. Pniewski, R. Jastrząb, M. Staszak, B. Tylkowski, K. Wieszczycka, The future of polyoxymetalates for biological and chemical apllications, *Coord. Chem. Rev.*, **2023**, *493*.

[145] a) B. Rathee, M. Wati, R. Sindhu, S. Sindhu, Applications of Polyoxometalates (A Review), *Orient. J. Chem.*, **2022**, *38*, pp. 327–335; b) M. T. Pope, *Polyoxometalates*, in: Encyclopedia of Inorganic Chemistry (Eds.: R. B. King, R. H. Crabtree, C. M. Lukehart, D. A. Atwood, R. A. Scott), Wiley, **2005**.

[146] D. E. Salazar Marcano, T. N. Parac-Vogt, Hybrid functional materials merging polyoxometalates and biomolecules: From synthesis to applications, *Coord. Chem. Rev.*, **2024**, *518*.

[147] W. Deng, Q. Zhang, Y. Wang, Polyoxometalates as efficient catalysts for transformations of cellulose into platform chemicals, *Dalton Trans.*, **2012**, *41*, pp. 9817–9831.

[148] a) Y. Zhang, J. Liu, S.-L. Li, Z.-M. Su, Y.-Q. Lan, Polyoxometalate-based materials for sustainable and clean energy conversion and storage, *EnergyChem*, **2019**, *1*; b) T. Yamase, Anti-tumor, -viral, and -bacterial activities of polyoxometalates for realizing an inorganic drug, *J. Mater. Chem.*, **2005**, *15*, pp. 4773–4782.

[149] a) M. T. Pope, A. Müller, W. N. Lipscomb, J. Maruani, *Polyoxometalates: From Platonic Solids to Anti-Retroviral Activity*, Springer Netherlands, Dordrecht, **1994**; b) M. Misono, *Heterogeneous Catalysis of Mixed Oxides: Perovskite and Heteropoly Catalysts*, Elsevier, Amsterdam, **2013**; c) S.-S. Wang, G.-Y. Yang, Recent advances in polyoxometalate-catalyzed reactions, *Chem. Rev.*, **2015**, *115*, pp. 4893–4962.

[150] a) Z. Wang, X. Xin, M. Zhang, Z. Li, H. Lv, G.-Y. Yang, Recent advances of mixed-transition-metal-substituted polyoxometalates, *Sci. China Chem.*, **2022**, *65*, pp. 1515–1525; b) J.-C. Raabe, Zu Gast bei den Polyoxometallaten: Entwicklung und katalytische Anwendung, *Dissertation*, Universität Hamburg, Hamburg, **2024**; c) V. F. Odyakov, E. G. Zhizhina, New process for preparing aqueous solutions of Mo-V-phosphoric heteropoly acids, *Russ. J. Inorg. Chem.*, **2009**, *54*, pp. 361–367; d) S. Himeno, M. Takamoto, T. Ueda, Synthesis, characterisation and voltammetric study of a β-Keggin-type [PW12O40]3− complex, *Journal of Electroanalytical Chemistry*, **1999**, *465*, pp. 129–135; e) I. V. Kozhevnikov, Catalysis by Heteropoly Acids and Multicomponent Polyoxometalates in Liquid-

Phase Reactions, *Chemical reviews*, **1998**, *98*, pp. 171–198; f) L. Pauling, THE MOLECULAR STRUCTURE OF THE TUNGSTOSILICATES AND RELATED COMPOUNDS, *J. Am. Chem. Soc.*, **1929**, *51*, pp. 2868–2880.

[151] a) R. Christoph, B. Schmidt, U. Steinberner, W. Dilla, R. Karinen, *Glycerol*, in: Ullmann's Encyclopedia of Industrial Chemistry, Wiley-VCH Verlag GmbH & Co. KGaA, Weinheim, Germany, **2000**; b) J. Zhong, J. Pérez-Ramírez, N. Yan, Biomass valorisation over polyoxometalate-based catalysts, *Green Chem.*, **2021**, *23*, pp. 18–36.

[152] M. Tao, X. Yi, I. Delidovich, R. Palkovits, J. Shi, X. Wang, Hetropolyacid-Catalyzed Oxidation of Glycerol into Lactic Acid under Mild Base-Free Conditions, *ChemSusChem*, **2015**, *8*, pp. 4195–4201.

[153] M. Tao, D. Zhang, X. Deng, X. Li, J. Shi, X. Wang, Lewis-acid-promoted catalytic cascade conversion of glycerol to lactic acid by polyoxometalates, *Chem. Commun.*, **2016**, *52*, pp. 3332–3335.

[154] M. Tao, N. Sun, Y. Li, S. Wang, X. Wang, The fabrication of trifunctional polyoxometalate hybrids for the cascade conversion of glycerol to lactic acid, *Catal. Sci. Technol.*, **2020**, *10*, pp. 207–214.

[155] M. Tao, N. Sun, Y. Li, T. Tong, M. Wielicako, S. Wang, X. Wang, Heteropolyacids embedded in a lipid bilayer covalently bonded to graphene oxide for the facile one-pot conversion of glycerol to lactic acid, *J. Mater. Chem. A*, **2017**, *5*, pp. 8325–8333.

[156] Z. Tang, W. Deng, Y. Wang, E. Zhu, X. Wan, Q. Zhang, Y. Wang, Transformation of cellulose and its derived carbohydrates into formic and lactic acids catalyzed by vanadyl cations, *ChemSusChem*, **2014**, *7*, pp. 1557–1567.

[157] A. Wesner, J.-C. Raabe, M. J. Poller, S. Meier, A. Riisager, J. Albert, Conversion of Sugars to Lactic Acid using Homogeneous Niobium-Substituted Polyoxometalate Catalysts, *Chem. Eur. J.*, **2024**, e202402649.

[158] A. A. Marianou, C. C. Michailof, D. Ipsakis, K. Triantafyllidis, A. A. Lappas, Cellulose conversion into lactic acid over supported HPA catalysts, *Green Chem.*, **2019**, *21*, pp. 6161–6178.

[159] a) J. Albert, R. Wölfel, A. Bösmann, P. Wasserscheid, Selective oxidation of complex, water-insoluble biomass to formic acid using additives as reaction accelerators, *Energy Environ. Sci.*, **2012**, *5*, pp. 7956–7962; b) J. Albert, P. Wasserscheid, Expanding the scope of biogenic substrates for the selective production of formic acid from water-insoluble and wet waste biomass, *Green Chem.*, **2015**, *17*, pp. 5164–5171.

[160] J. Reichert, J. Albert, Detailed Kinetic Investigations on the Selective Oxidation of Biomass to Formic Acid (OxFA Process) Using Model Substrates and Real Biomass, *ACS Sustain. Chem. Eng.*, **2017**, *5*, pp. 7383–7392.

[161] J. Albert, D. Lüders, A. Bösmann, D. M. Guldi, P. Wasserscheid, Spectroscopic and electrochemical characterization of heteropoly acids for their optimized application in selective biomass oxidation to formic acid, *Green Chem.*, **2014**, *16*, pp. 226–237.

[162] J. Albert, A. Jess, C. Kern, F. Pöhlmann, K. Glowienka, P. Wasserscheid, Formic Acid-Based Fischer–Tropsch Synthesis for Green Fuel Production from Wet Waste Biomass and Renewable Excess Energy, *ACS Sustain. Chem. Eng.*, **2016**, *4*, pp. 5078–5086.

[163] OxFA GmbH, in: https://www.oxfa.eu, **[Jahr ermittelt fehlt!].** Accessed 24.07.2024.

[164] E. G. Zhizhina, V. F. Odyakov, M. V. Simonova, K. I. Matveev, Kinetics of Oxidation of Reduced Phosphorus-Molybdenum-Vanadium Heteropoly Acid Species with Dioxygen in Aqueous Solutions, *Kinet. Catal.*, **2005**, *46*, pp. 354–363.

[165] J.-C. Raabe, M. J. Poller, D. Voß, J. Albert, $H_8PV_5Mo_7O_{40}$ - A Unique Polyoxometalate for Acid and RedOx Catalysis: Synthesis, Characterization, and Modern Applications in Green Chemical Processes, *ChemSusChem*, **2023**, *16*.

[166] a) Z. He, Y. Hou, J. Wei, S. Ren, W. Wu, Efficient catalytic oxidation of biomass to formic acid coupled with low-energy formaldehyde production from methanol, *Green Chem.*, **2024**, *26*, pp.

2170–2182; b) M. J. Poller, S. Bönisch, B. Bertleff, J.-C. Raabe, A. Görling, J. Albert, Elucidating activating and deactivating effects of carboxylic acids on polyoxometalate-catalysed three-phase liquid–liquid-gas reactions, *Chem. Eng. Sci.*, **2022**, *264*.

[167] a) J. Albert, Chemische Wertschöpfung aus Biomasse mittels selektiver katalytischer Oxidation zu Ameisensäure (FA) - der Erlanger OxFA-Prozess, *Dissertation*, FAU, Erlangen, **2015**; b) J. Piera, J.-E. Bäckvall, Catalytic oxidation of organic substrates by molecular oxygen and hydrogen peroxide by multistep electron transfer--a biomimetic approach, *Angew. Chem. Int. Ed.*, **2008**, *47*, pp. 3506–3523.

[168] S. Maerten, C. Kumpidet, D. Voß, A. Bukowski, P. Wasserscheid, J. Albert, Glucose oxidation to formic acid and methyl formate in perfect selectivity, *Green Chem.*, **2020**, *22*, pp. 4311–4320.

[169] a) C. Peinado, D. Liuzzi, S. N. Sluijter, G. Skorikova, J. Boon, S. Guffanti, G. Groppi, S. Rojas, Review and perspective: Next generation DME synthesis technologies for the energy transition, *Chem. Eng. J.*, **2024**, *479*; b) H. HAYASHI, The properties of heteropoly acids and the conversion of methanol to hydrocarbons, *Journal of Catalysis*, **1982**, *77*, pp. 473–484; c) F. M. Ebeid, L. Ali, Abdalla, FF, CONVERSION OF METHANOL OVER METAL-SALTS OF 12-MOLYBDOPHOSPHORIC ACID, *Indian Journal of Chemistry*, **1992**, *31*, pp. 921–928; d) R. M. Ladera, M. Ojeda, J. L. G. Fierro, S. Rojas, TiO 2 -supported heteropoly acid catalysts for dehydration of methanol to dimethyl ether: relevance of dispersion and support interaction, *Catal. Sci. Technol.*, **2015**, *5*, pp. 484–491; e) W. Alharbi, E. F. Kozhevnikova, I. V. Kozhevnikov, Dehydration of Methanol to Dimethyl Ether over Heteropoly Acid Catalysts: The Relationship between Reaction Rate and Catalyst Acid Strength, *ACS Catal.*, **2015**, *5*, pp. 7186–7193.

[170] A. Kornas, M. Śliwa, M. Ruggiero-Mikołajczyk, K. Samson, J. Podobiński, R. Karcz, D. Duraczyńska, D. Rutkowska-Zbik, R. Grabowski, Direct hydrogenation of CO_2 to dimethyl ether (DME) over hybrid catalysts containing CuO/ZrO_2 as a metallic function and heteropolyacids as an acidic function, *React. Kinet. Mech. Catal.*, **2020**, *130*, pp. 179–194.

[171] D. Kubas, J. M. Beck, E. Kasisari, T. Schätzler, A. Becherer, A. Fischer, I. Krossing, From CO_2 to DME: Enhancement through Heteropoly Acids from a Catalyst Screening and Stability Study, *ACS omega*, **2023**, *8*, pp. 15203–15216.

[172] C. Peinado, D. Liuzzi, R. M. Ladera-Gallardo, M. Retuerto, M. Ojeda, M. A. Peña, S. Rojas, Effects of support and reaction pressure for the synthesis of dimethyl ether over heteropolyacid catalysts, *Sci. Rep.*, **2020**, *10*.

[173] P. Huber, F. Studt, P. N. Plessow, Reactivity of Surface Lewis and Brønsted Acid Sites in Zeolite Catalysis: A Computational Case Study of DME Synthesis Using H-SSZ-13, *J. Phys. Chem. C*, **2022**, *126*, pp. 5896–5905.

[174] W. Alharbi, E. F. Kozhevnikova, I. V. Kozhenikov, Dehydration of Methanol to Dimethyl Ether over Heteropoly Acid Catalysts: The Relationship between Reaction Rate and Catalyst Acid Strength, *ACS Catal.*, **2015**, *5*, pp. 7186–7193.

[175] R.-M. Ladera, J. Fierro, M. Ojeda, S. Rojas, TiO_2-supported heteropoly acids for low-temperature synthesis of dimethyl ether from methanol, *J. Catal.*, **2014**, *312*, pp. 195–203.

[176] J. Schnee, L. Fusaro, C. Aprile, E. M. Gaigneaux, Keggin $H_3PW_{12}O_{40}$ pore blockage by coke can be reversible in the gas phase methanol-to-DME reaction, *Catal. Sci. Technol.*, **2017**, *7*, pp. 6151–6160.

[177] L. Nakka, J. E. Molinari, I. E. Wachs, Surface and bulk aspects of mixed oxide catalytic nanoparticles: oxidation and dehydration of CH_3OH by polyoxometallates, *J. Am. Chem. Soc.*, **2009**, *131*, pp. 15544–15554.

[178] J. Schnee, A. Eggermont, E. M. Gaigneaux, Boron Nitride: A Support for Highly Active Heteropolyacids in the Methanol-to-DME Reaction, *ACS Catal.*, **2017**, *7*, pp. 4011–4017.

[179] A. Ciftci, D. Varisli, K. Cem Tokay, N. Aslı Sezgi, T. Dogu, Dimethyl ether, diethyl ether & ethylene from alcohols over tungstophosphoric acid based mesoporous catalysts, *Chemical Engineering Journal*, **2012**, *207-208*, pp. 85–93.

[180] D. Kubas, M. Gierse, O. Salem, I. Krossing, Is Direct DME Synthesis Superior to Methanol Production in Carbon Dioxide Valorization? From Thermodynamic Predictions to Experimental Confirmation, *ACS Catal.*, **2023**, *13*, pp. 3960–3970.

[181] M. Y. Mohamud, T. A. T. Abdullah, A. Ahmad, M. Ikram, A. Alir, M. L. P. Phey, W. Nabgan, Direct Synthesis of Dimethyl Ether from CO2 Hydrogenation over Core-Shell Nanotube Bi-Functional Catalyst, *Catalysts*, **2023**, *13*.

[182] A. Behr, D. W. Agar, J. Jörissen, *Einführung in die Technische Chemie*, Springer Berlin / Heidelberg, Berlin, Heidelberg, **2010**.

[183] W. Reschetilowski, *Einführung in die Heterogene Katalyse*, Springer Berlin/Heidelberg, Berlin, Heidelberg, **2015**.

[184] E. Rafiee, S. Eavani, Heterogenization of heteropoly compounds: a review of their structure and synthesis, *RSC Adv.*, **2016**, *6*, pp. 46433–46466.

[185] N. Mizuno, *Modern Heterogeneous Oxidation Catalysis*, Wiley VCH Verlag GmbH & Co. KGaA, Weinheim, **2009**.

[186] Y. Zhou, G. Chen, Z. Long, J. Wang, Recent advances in polyoxometalate-based heterogeneous catalytic materials for liquid-phase organic transformations, *RSC Adv.*, **2014**, *4*, pp. 42092–42113.

[187] M. Misono, Unique acid catalysis of heteropoly compounds (heteropolyoxometalates) in the solid state, *Chem. Commun.*, **2001**, pp. 1141–1152.

[188] L. Pesaresi, D. R. Brown, A. F. Lee, J. M. Montero, H. Williams, K. Wilson, Cs-doped $H_4SiW_{12}O_{40}$ catalysts for biodiesel applications, *Appl. Catal. A-Gen.*, **2009**, *360*, pp. 50–58.

[189] Q. Zhao, H. Wang, H. Zheng, Z. Sun, W. Shi, S. Wang, X. Wang, Z. Jiang, Acid–base bifunctional HPA nanocatalysts promoting heterogeneous transesterification and esterification reactions, *Catal. Sci. Technol.*, **2013**, *3*.

[190] E. Rafiee, S. Eavani, Organic–inorganic polyoxometalate based salts as thermoregulated phase-separable catalysts for selective oxidation of thioethers and thiophenes and deep desulfurization of model fuels, *J. Mol. Catal. A: Chem.*, **2013**, *380*, pp. 18–27.

[191] J.-J. Ye, C.-D. Wu, Immobilization of polyoxometalates in crystalline solids for highly efficient heterogeneous catalysis, *Dalton Trans.*, **2016**, *45*.

[192] Y. Zhang, V. Degirmenci, C. Li, E. J. M. Hensen, Phosphotungstic acid encapsulated in metal-organic framework as catalysts for carbohydrate dehydration to 5-hydroxymethylfurfural, *ChemSusChem*, **2011**, *4*, pp. 59–64.

[193] R. Neumann, A. M. Khenkin, I. Vigdergauz, Quinones as Co-Catalysts and Models for the Surface of Active Carbon in the Phosphovanadomolybdate-Catalyzed Aerobic Oxidation of Benzylic and Allylic Alcohols: Synthetic, Kinetic, and Mechanistic Aspects, *Chem. Eur. J.*, **2000**, *6*, pp. 875–882.

[194] G. Bozzano, F. Manenti, Efficient methanol synthesis: Perspectives, technologies and optimization strategies, *Progress in Energy and Combustion Science*, **2016**, *56*, pp. 71–105.

[195] P. Amann, B. Klötzer, D. Degerman, N. Köpfle, T. Götsch, P. Lömker, C. Rameshan, K. Ploner, D. Bikaljevic, H.-Y. Wang et al., The state of zinc in methanol synthesis over a Zn/ZnO/Cu(211) model catalyst, *Science*, **2022**, *376*, pp. 603–608.

[196] R. Fornari, *Single crystals of electronic materials*. *Growth and properties*, Woodhead Publishing, Duxford, **2019**.

[197] a) M. Chen, D. Cui, Z. Zhao, Di Kang, Z. Li, S. Albawardi, S. Alsageer, F. Alamri, A. Alhazmi, M. R. Amer et al., Highly sensitive, scalable, and rapid SARS-CoV-2 biosensor based on In_2O_3 nanoribbon transistors and phosphatase, *Nano Res.*, **2022**, *15*, pp. 5510–5516; b) A. Khort, Y. Haiduk, I. Taratyn, D. Moskovskikh, K. Podbolotov, A. Usenka, N. Lapchuk, V. Pankov, High-performance

selective NO_2 gas sensor based on In_2O_3-graphene-Cu nanocomposites, *Sci. Rep.*, **2023**, *13*; c) T. Waitz, T. Wagner, T. Sauerwald, C.-D. Kohl, M. Tiemann, Ordered Mesoporous In_2O_3: Synthesis by Structure Replication and Application as a Methane Gas Sensor, *Adv. Funct. Mater.*, **2009**, *19*, pp. 653–661.

[198] a) L. Luo, L. Fu, H. Liu, Y. Xu, J. Xing, C.-R. Chang, D.-Y. Yang, J. Tang, Synergy of Pd atoms and oxygen vacancies on In_2O_3 for methane conversion under visible light, *Nat. Commun.*, **2022**, *13*, p. 2930; b) K. K. Pawar, L. S. Chaudhary, S. S. Mali, T. S. Bhat, A. D. Sheikh, C. K. Hong, P. S. Patil, In_2O_3 nanocapsules for rapid photodegradation of crystal violet dye under sunlight, *J. Colloid Interface Sci.*, **2020**, *561*, pp. 287–297; c) C. I. Shaughnessy, D. T. Jantz, K. C. Leonard, Selective electrochemical CO 2 reduction to CO using in situ reduced In 2 O 3 nanocatalysts, *J. Mater. Chem. A*, **2017**, *5*, pp. 22743–22749.

[199] A. Gervasini, J. A. Perdigon-Melon, C. Guimon, A. Auroux, An in-depth study of supported In_2O_3 catalysts for the selective catalytic reduction of NO_x: the influence of the oxide support, *J. Phys. Chem. B*, **2006**, *110*, pp. 240–249.

[200] H. Lorenz, W. Jochum, B. Klötzer, M. Stöger-Pollach, S. Schwarz, K. Pfaller, S. Penner, Novel methanol steam reforming activity and selectivity of pure In_2O_3, *Appl. Catal. A-Gen.*, **2008**, *347*, pp. 34–42.

[201] T. Bielz, H. Lorenz, W. Jochum, R. Kaindl, F. Klauser, B. Klötzer, S. Penner, Hydrogen on In_2O_3: Reducibility, Bonding, Defect Formation, and Reactivity, *J. Phys. Chem. C*, **2010**, *114*, pp. 9022–9029.

[202] J. Ye, C. Liu, D. Mei, Q. Ge, Active Oxygen Vacancy Site for Methanol Synthesis from CO_2 Hydrogenation on In_2O_3 (110): A DFT Study, *ACS Catal.*, **2013**, *3*, pp. 1296–1306.

[203] J. Ye, C. Liu, Q. Ge, DFT Study of CO_2 Adsorption and Hydrogenation on the In_2O_3 Surface, *J. Phys. Chem. C*, **2012**, *116*, pp. 7817–7825.

[204] K. Sun, Z. Fan, J. Ye, J. Yan, Q. Ge, Y. Li, W. He, W. Yang, C. Liu, Hydrogenation of CO_2 to methanol over In_2O_3 catalyst, *J. CO2 Util.*, **2015**, *12*, pp. 1–6.

[205] O. Martin, A. J. Martín, C. Mondelli, S. Mitchell, T. F. Segawa, R. Hauert, C. Drouilly, D. Curulla-Ferré, J. Pérez-Ramírez, Indium Oxide as a Superior Catalyst for Methanol Synthesis by CO_2 Hydrogenation, *Angew. Chem.*, **2016**, *128*, pp. 6369–6373.

[206] J. Wang, G. Zhang, J. Zhu, X. Zhang, F. Ding, A. Zhang, X. Guo, C. Song, CO_2 Hydrogenation to Methanol over In_2O_3-Based Catalysts: From Mechanism to Catalyst Development, *ACS Catal.*, **2021**, *11*, pp. 1406–1423.

[207] W. Wang, K. Huo, Y. Wang, J. Xie, X. Sun, Y. He, M. Li, J. Liang, X. Gao, G. Yang et al., Rational Control of Oxygen Vacancy Density in In_2O_3 to Boost Methanol Synthesis from CO_2 Hydrogenation, *ACS Catal.*, **2024**, *14*, pp. 9887–9900.

[208] A. Cao, Z. Wang, H. Li, J. K. Nørskov, Relations between Surface Oxygen Vacancies and Activity of Methanol Formation from CO_2 Hydrogenation over In_2O_3 Surfaces, *ACS Catal.*, **2021**, *11*, pp. 1780–1786.

[209] X. Zhang, A. V. Kirilin, S. Rozeveld, J. H. Kang, G. Pollefeyt, D. F. Yancey, A. Chojecki, B. Vanchura, M. Blum, Support Effect and Surface Reconstruction in In_2O_3/m-ZrO_2 Catalyzed CO_2 Hydrogenation, *ACS Catal.*, **2022**, *12*, pp. 3868–3880.

[210] a) A. Tsoukalou, P. M. Abdala, D. Stoian, X. Huang, M.-G. Willinger, A. Fedorov, C. R. Müller, Structural Evolution and Dynamics of an In_2O_3 Catalyst for CO_2 Hydrogenation to Methanol: An Operando XAS-XRD and In Situ TEM Study, *J. Am. Chem. Soc.*, **2019**, *141*, pp. 13497–13505; b) M. Ziemba, M. Radtke, L. Schumacher, C. Hess, Aufklärung der CO_2-Hydrierung über In_2O_3-Nanopartikeln mittels Operando UV/Vis- und Impedanzspektroskopie, *Angew. Chem.*, **2022**, *134*.

[211] D. Cai, Y. Cai, K. B. Tan, G. Zhan, Recent Advances of Indium Oxide-Based Catalysts for CO_2 Hydrogenation to Methanol: Experimental and Theoretical, *Materials (Basel, Switzerland)*, **2023**, *16*.

[212] a) M. Dou, M. Zhang, Y. Chen, Y. Yu, Theoretical study of methanol synthesis from CO_2 and CO hydrogenation on the surface of ZrO_2 supported In_2O_3 catalyst, *Surf. Sci.*, **2018**, *672-673*, pp. 7–12; b) M. M. Zain, M. Mohammadi, N. Kamiuchi, A. R. Mohamed, Development of highly selective In_2O_3/ZrO_2 catalyst for hydrogenation of CO_2 to methanol: An insight into the catalyst preparation method, *Korean J. Chem. Eng.*, **2020**, *37*, pp. 1680–1689; c) M. S. Frei, C. Mondelli, J. Pérez-Ramírez, Development of In_2O_3-based Catalysts for CO_2-based Methanol Production, *Chimia*, **2020**, *74*, pp. 257–262.

[213] A. Tsoukalou, P. M. Abdala, A. Armutlulu, E. Willinger, A. Fedorov, C. R. Müller, Operando X-ray Absorption Spectroscopy Identifies a Monoclinic ZrO_2: In Solid Solution as the Active Phase for the Hydrogenation of CO_2 to Methanol, *ACS Catal.*, **2020**, *10*, pp. 10060–10067.

[214] M. S. Frei, C. Mondelli, A. Cesarini, F. Krumeich, R. Hauert, J. A. Stewart, D. Curulla Ferré, J. Pérez-Ramírez, Role of Zirconia in Indium Oxide-Catalyzed CO_2 Hydrogenation to Methanol, *ACS Catal.*, **2020**, *10*, pp. 1133–1145.

[215] C. Yang, C. Pei, R. Luo, S. Liu, Y. Wang, Z. Wang, Z.-J. Zhao, J. Gong, Strong Electronic Oxide-Support Interaction over In_2O_3/ZrO_2 for Highly Selective CO_2 Hydrogenation to Methanol, *J. Mater. Sci.*, **2020**, *142*, pp. 19523–19531.

[216] A. García-Trenco, A. Regoutz, E. R. White, D. J. Payne, M. S. Shaffer, C. K. Williams, PdIn intermetallic nanoparticles for the Hydrogenation of CO2 to Methanol, *Applied Catalysis B: Environmental*, **2018**, *220*, pp. 9–18.

[217] a) N. Rui, Z. Wang, K. Sun, J. Ye, Q. Ge, C. Liu, CO_2 hydrogenation to methanol over Pd/In_2O_3: effects of Pd and oxygen vacancy, *Appl. Catal. B: Environ.*, **2017**, *218*, pp. 488–497; b) M. S. Frei, C. Mondelli, R. García-Muelas, K. S. Kley, B. Puértolas, N. López, O. V. Safonova, J. A. Stewart, D. Curulla Ferré, J. Pérez-Ramírez, Atomic-scale engineering of indium oxide promotion by palladium for methanol production via CO_2 hydrogenation, *Nat. Commun.*, **2019**, *10*.

[218] a) K. Sun, N. Rui, Z. Zhang, Z. Sun, Q. Ge, C. Liu, A highly active Pt/In_2O_3 catalyst for CO_2 hydrogenation to methanol with enhanced stability, *Green Chem.*, **2020**, *22*, pp. 5059–5066; b) Z. Han, C. Tang, J. Wang, L. Li, C. Li, Atomically dispersed Pt^{n+} species as highly active sites in Pt/In_2O_3 catalysts for methanol synthesis from CO_2 hydrogenation, *J. Catal.*, **2021**, *394*, pp. 236–244.

[219] a) J. Wang, K. Sun, X. Jia, C. Liu, CO_2 hydrogenation to methanol over Rh/In_2O_3 catalyst, *Catal. Today*, **2021**, *365*, pp. 341–347; b) N. H. M. Dostagir, C. Thompson, H. Kobayashi, A. M. Karim, A. Fukuoka, A. Shrotri, Rh promoted In_2O_3 as a highly active catalyst for CO_2 hydrogenation to methanol, *Catal. Sci. Technol.*, **2020**, *10*, pp. 8196–8202.

[220] Q. Wu, C. Shen, N. Rui, K. Sun, C. Liu, Experimental and theoretical studies of CO_2 hydrogenation to methanol on Ru/In_2O_3, *J. CO2 Util.*, **2021**, *53*.

[221] Z. Lu, K. Sun, J. Wang, Z. Zhang, C. Liu, A Highly Active Au/In_2O_3-ZrO_2 Catalyst for Selective Hydrogenation of CO_2 to Methanol, *Catalysts*, **2020**, *10*.

[222] L. Liu, B. Mezari, N. Kosinov, E. J. M. Hensen, Al Promotion of In_2O_3 for CO_2 Hydrogenation to Methanol, *ACS Catal.*, **2023**, *13*, pp. 15730–15745.

[223] X. Jia, K. Sun, J. Wang, C. Shen, C. Liu, Selective hydrogenation of CO_2 to methanol over Ni/In_2O_3 catalyst, *Journal of Energy Chemistry*, **2020**, *50*, pp. 409–415.

[224] R. Zou, C. Shen, K. Sun, X. Ma, Z. Li, M. Li, C. Liu, CO_2 hydrogenation to methanol over the copper promoted In_2O_3 catalyst, *Journal of Energy Chemistry*, **2024**, *93*, pp. 135–145.

[225] D. Nelson, Cox M., *Principles of Biochemistry*, W. H. Freeman and Company, New York, **2013**.

[226] W. Reschetilowski, *Handbuch Chemische Reaktoren*. *Grundlagen und Anwendungen der Chemischen Reaktionstechnik*, Springer Berlin Heidelberg, Berlin, Heidelberg, **2020**.

[227] a) M. Ziolek, Niobium-containing catalysts—the state of the art, *Catalysis Today*, **2003**, *78*, pp. 47–64; b) L. Oliveira, M. Pereira, A. Pacheli Heitman, J. Filho, C. Oliveira, M. Ziolek, Niobium: The Focus on Catalytic Application in the Conversion of Biomass and Biomass Derivatives, *Molecules (Basel, Switzerland)*, **2023**, *28*.

[228] A. Wesner, M. P. Papajewski, L. Schidowski, C. Ruhmlieb, M. J. Poller, J. Albert, Supported $H_8PV_5Mo_7O_40$ on activated carbon: Synthesis and Investigation of influencing factors for catalytic performance, *Dalton transactions (Cambridge, England : 2003)*, **2024**, *53*, pp. 14065–14076.

[229] A. Wesner, N. Herrmann, L. Prawitt, A. Ortmann, J. Albert, M. J. Poller, Study of supported heteropolyacid catalysts for one-step DME synthesis from CO_2 and H_2, *RSC Adv.*, **2025**, *15*, pp. 38–47.

[230] A. Wesner, P. Kampe, N. Herrmann, S. Eller, C. Ruhmlieb, J. Albert, Indium-based Catalysts for CO 2 Hydrogenation to Methanol: Key Aspects for Catalytic Performance, *ChemCatChem*, **2023**, *15*.

[231] J.-C. Raabe, T. Esser, F. Jameel, M. Stein, J. Albert, M. J. Poller, Study on the incorporation of various elements into the Keggin lacunary-type phosphomolybdate [PMo 9 O 34] 9− and subsequent purification of the polyoxometalates by nanofiltration, *Inorg. Chem. Front.*, **2023**, *10*, pp. 4854–4868.

[232] J.-C. Raabe, J. Aceituno Cruz, J. Albert, M. J. Poller, Comparative Spectroscopic and Electrochemical Study of V(V)-Substituted Keggin-Type Phosphomolybdates and -Tungstates, *Inorganics*, **2023**, *11*, p. 138.

[233] V. F. Odyakov, E. G. Zhizhina, A novel method of the synthesis of molybdovanadophosphoric heteropoly acid solutions, *React Kinet Catal Lett*, **2008**, *95*, pp. 21–28.

[234] J. D. H. Strickland, The Preparation and Properties of Silicomolybdic Acid. I. The Properties of Alpha Silicomolybdic Acid, *J. Am. Chem. Soc.*, **1952**, *74*, pp. 862–867.

[235] P. Schuehle, S. Reichenberger, G. Marzun, J. Albert, Slurry phase hydrogenation of CO 2 to methanol using indium-based catalysts: Influence of reaction conditions and catalyst support, *Chemie Ingenieur Technik*, **2020**, *92*, p. 1258.

9. Appendix

9.1. List of Chemicals Used

Table 1: List of chemicals used, classified according to globally harmonized system of classification and labelling of chemicals (GHS).

Substance	Purity	GHS-symbol	Hazard precautionary Statement
Acetaldehyde	40 %		H225, H319, H341, H350, H335 P202, P210, P233, P240, P305 + P351 + P338, P308 + P313
Acetic acid	97 %		H226, H314 P102, P210, P243, P280, P303 + P361 + P353, P305 + P351 + P338, P310, P501
Aluminium oxide	n.s.	Not a hazardous substance according to GHS.	
Ammonia	99 %		H331, H314, H318, H400, H411
Celite® 545	n.s.		H372 P260, P264, P270, P314, P501
Cerium(III) nitrate hexahydrate	99.5 %		H272, H318, H410 P210, P220, P273, P280, P305 + P351 + P338, P371 + P380 + P375 -
Cellobiose	≥ 99 %,	Not a hazardous substance according to GHS.	
Copper based methanol synthesis catalyst	n.s.		H410 P273, P391, P501
Copper (II) nitrate trihydrate	99 %		H272, H314, H400, H411 P210, P220, P280, P305 + P351 + P338, P310, P371 + P380 + P375
CW20	-	Not a hazardous substance according to GHS.	
Dihydroxyacetone	85 %	Not a hazardous substance according to GHS.	
Disodium hydrogen phosphate	95 %,	Not a hazardous substance according to GHS.	
Erythrose	75 %,		
Formic acid	≥ 99 %		H226, H302, H314, H331 P210, P243, P280, P301 + P330+P331, P302 + P352, P304 + P340, P305 + P351 + P338, P308 + P310, P403 + P235

Fructose	≥ 99 %,	Not a hazardous substance according to GHS.
Glyceraldehyde	≥ 90 %,	Not a hazardous substance according to GHS.
Glycoaldehyde	100 %	Not a hazardous substance according to GHS.
Glycolic acid	50 %,	 H314, H332 P260, P271, P280, P303 + P361 + P353, P304 + P340 + P310, P305 + P351 + P338
Glyoxal	40 %,	 H314, H317, H335, H341 P202, P261, P280, P303 + P361 + P353, P304 + P340 + P310, P305 + P351 + P338
Glucose	≥ 99.5 %	Not a hazardous substance according to GHS.
Helium	≥ 99 %	 H280 P403
Hydrochloric acid	37 %	 H290, H314, H318, H335 P280, P260, P301 + P330 + P331, P302 + P352, P304 + P340, P305 + P351 + P338, P308 + P310
Hydrogen	100 %	 H220, H280 P210, P377, P403
Hydrogen peroxide	30 %	 H302, H318 P280, P301 + P330 + P331, P305 + P351 + P338, P308 + P310
Indium (III) hydroxide	99.8 %	 H315, H319 P280, P302 + P352, P332 + P313, P337 + P313
Indium (III) nitrate hydrate	≥ 99.999 %,	 H272, H315, H319 P332 + P313, P280, P371 + P380 + P375, P302 + P352, P337 + P313, P210, P220
Lactic acid	85 %	 H314, EUH071 P280, P303 + P361 + P353, P304 + P340 + P310, P305 + P351 + P338, P363
Magnesium nitrate hexahydrate	≥ 98 %	Not a hazardous substance according to GHS.
Mannose	≥ 99 %	Not a hazardous substance according to GHS.
Molybdenum oxide	99.5 %	 H319, H335, H351 P261, P305 + P351 + P338, P280
Montmorillonite K10	n.s.	Not a hazardous substance according to GHS.

Nickel (II) nitrate hexahydrate	n.s.		H272, H302 + H332, H315, H317, H318, H334, H341, H350, H360, H372, H410 P210, P273, P280, P301 + P312, P305 + P351 + P338, P308 + P313
Niobium(V) oxide	99.5 %	Not a hazardous substance according to GHS.	
Nitric acid	≥ 90 %		H272, H290, H330, H314, H318 P220, P280, P301 + P330 + P331, P303 + P361 + P353, P305 + P351 + P338, P310
Nitrogen	100 %		H280 P403
Norit A Supra Eur	n.s.	Not a hazardous substance according to GHS.	
Norit CASP F	n.s.	Not a hazardous substance according to GHS.	
Norit Darco KBG	n.s.	Not a hazardous substance according to GHS.	
Norit GSX	n.s.	Not a hazardous substance according to GHS.	
Norit SXPlus	n.s.	Not a hazardous substance according to GHS.	
Oxygen	100 %		H270, H280 P220, P244, P370 + P376, P403
Phosphomolybdic acid	≤ 100 %		H272, H314 P210, P220, P260, P280, P303 + P361 + P353, P305 + P351 + P338
Phosphoric acid	≥ 85 %		H290, H302, H314 P280, P301 + P330 + P331, P303 + P361 + P353, P305 + P351 + P338, P310
Phosphotungstic acid	≤ 100 %		H302, H314, H411 P260, P273, P280, P301 + P312, P303 + P361 + P353, P305 + P351 + P338
Potassium hydroxide	85 %		H290, H302, H314, H318 P280, P303 + P361 + P353, P305 + P351 + P338, P310
Pyruvaldehyde	40 %		H302, H318, H317, H341 P301 + P330 + P331, P302 + P352, P305 + P351 + P338, P310, P280
Silicotungstic acid	99 %		H315, H319, H335 P261, P264, P271, P280, P302 + P352, P305 + P351 + P338
Sodium bicarbonate	n.s.	Not a hazardous substance according to GHS.	
Sodium carbonate	≥ 99 %		H319 P305+P351+P338, P337+P313

Sodium hydroxide	≥99 %		H290, H314 P280, P301+P330+P331, P305+P351+P338
Sodium molybdate dihydrate	99.5 %	Not a hazardous substance according to GHS.	
Sodium nitrate	99		H272, H319 P220, P280, P305+P351+P338, P337+P313
Sodium vanadium oxide	96 %		H301, H332, H319, H361d, H372 P264, P301 + P310, P304 + P340, P337 + P313, P280
Sucrose	≥ 99.5 %,	Not a hazardous substance according to GHS.	
Titanium dioxide	n.s.		H351 P201, P280, P284, P308 + P313
Xylose	≥ 99 %,	Not a hazardous substance according to GHS.	
Zirconium dioxide	≥ 99 %	Not a hazardous substance according to GHS.	

9.2 Catalyst Preparation, Testing and Characterization

9.2.1 Catalyst Preparation and Testing

The synthesis procedures of the catalysts and the catalytic experiments are described individually for each study in the following sections.

9.2.1.1 Catalyst Preparation and Testing: Substituted Polyoxometalates for Liquid-Phase Conversion of Biomass to Lactic Acid

Catalyst Preparation

All polyoxometalates utilized in this study were synthesized by Dr. Jan-Christian Raabe, following a procedure that has been detailed described in an earlier publication.[231]

Catalyst Testing

Catalyst screening reactions were conducted in a 20 ml custom-designed stainless-steel autoclave fitted with a removable glass vial insert. Each experiment was set up by dissolving 42 mg of catalyst and 100 mg of the substrate in 4 g H_2O. A PTFE-coated magnetic stir bar was added to ensure effective mixing. The prepared vial was placed inside the reactor, which was then sealed and purged three times with nitrogen (25 bar) to eliminate residual oxygen.

The assembled autoclave was transferred to a pre-heated aluminum block maintained at 160 °C. Stirring was initiated at 1000 rpm, and the reaction was allowed to proceed for one hour. Upon completion, stirring was halted and the reactor was swiftly placed in an ice-cooled water bath to quench the reaction. After cooling to room temperature, the reactor was depressurized, and the glass vial was removed. The liquid reaction mixture was subsequently analyzed using high-performance liquid chromatography (HPLC).

9.2.1.2 Catalyst Preparation and Testing: Transitioning to Immobilized Systems: Liquid-Phase Conversion of Biomass to Lactic and Formic Acid

Catalyst Preparation

HPA-5

The bulk HPA-5 catalyst was prepared following a method described in the literature.[165,232] For the synthesis, 44.3 g MoO_3 were dissolved in 500 ml deionized H_2O together with 16.9 g of a 5 % H_3PO_4 solution under reflux, forming a clear yellow solution. In parallel, 20.0 g of V_2O_5 were suspended in 750 ml H_2O, cooled to 0 °C, and treated dropwise with 165 ml of 30 % H_2O_2, resulting in a red-brown solution with oxygen evolution. After complete dissolution, 3.0 g of 25 % H_3PO_4 were added. The vanadium solution was slowly combined with the refluxing molybdenum solution and the resulting mixture was refluxed for another hour. After cooling under reduced pressure, the product was filtered to yield a dark red or brown solid.

Supported Catalysts

Various activated carbons from Cabot: Norit SXPlus (NSXPlus), A Supra Eur (NASEur), GSX (NGSX), CASP F (NCASPF), and Darco KBG (DKB-G) - as well as CW20 from Silcarbon were used. In the initial experimental series (E1), HPA-5 was supported on each carbon via wet impregnation: 4.99 g (3.11 mmol) HPA-5 was dissolved in 250 ml H_2O (pH 2 - 3), then combined with 7.02 g of the respective

carbon. The mixture was stirred at 50 °C for 3 hours (100 rpm), followed by filtration, washing to neutral pH, and overnight drying (Fig. 6).

CW20 was selected for a series of further experimental series applying different pre- and post-treatment steps in addition to the general wet impregnation method (see Fig. 6). In experimental series 2 (E2), CW20 was subjected to oxidative pre-treatment by refluxing in concentrated nitric acid (65 wt.%) at 90 °C for 3 hours prior to impregnation. In E3, a thermal post-treatment was carried out after impregnation, heating the material to 200 °C at a rate of 2 $K \cdot min^{-1}$ for 5 hours. In E4, the same post-treatment conditions were applied without any pre-treatment of the carbon. In experimental series 5 (E5), CW20 underwent reductive pre-treatment by heating to 400 °C for 4 hours under a flow of 95 % N_2/5 % H_2 (100 $l \cdot h^{-1}$) prior to impregnation. A schematic overview of all synthesis is in chapter 8.2 (Figure 41).

Catalyst Testing

The catalytic tests were carried out using a three fold-plant, consisting of three 100 mL stainless steel autoclaves, with quartz glass liners placed inside (21 ml tare volume, 55 ml max capacity). Stirring was achieved with a gas-inducing stainless steel stirred. To ensure each reactor was equipped with a heating jacket, and temperatures were monitored at two positions – within the liquid phase and at the reactor wall. System pressure was recorded using both analog and digital gauges.

For oxidation reactions, 3.603 g glucose (20 mmol) and 1.821 g catalyst (equivalent to 1.14 mmol pure HPA-5) were added. For retro-aldol reactions, 1.032 g glucose (5.7 mmol) and 0.406 g catalyst (0.25 mmol HPA-5) were used. Each liner was filled with 45 ml (oxidation) or 40 ml (retro-aldol) of deionized water before being sealed into the reactor using five screws tightened to 15 Nm. To eliminate air, the system was purged three times with O_2 (oxidation) or N_2 (retro-aldol). Subsequently, the operating pressure was set to 20 bar, and the reactors were heated to 90 °C (oxidation) or 160 °C (retro-aldol), with stirring initiated at 300 rpm. Upon reaching the target temperature, stirring was increased to 1000 rpm, marking the start of the reaction. A comprehensive description can be found in chapter 9.5.2.

9.2.1.3 Catalyst Preparation and Testing: Expanding to Gas-Phase Applications: Immobilized Polyoxometalates for CO_2 Conversion to Dimethyl ether

Catalyst Preparation

$H_6PInMo_{11}O_{40}$ (HPInMo, HPA-5)

The bulk HPA-5 catalyst was prepared after modified method described in the literature.[233] MoO_3 (20.02 g) and H_3PO_4 (85 %; 1.47 g) were dissolved in 200 ml H_2O and refluxed under stirring for 2 hours, during which an additional 0.44 g of H_3PO_4 was added gradually. $In(OH)_3$ (2.10 g) was dissolved in 20 ml H_2O and 10 ml conc. HCl, and the resulting solution was added to the reaction mixture. Reflux was continued for another 30 minutes. The solvent was then removed by rotary evaporation (80 °C, 200 mbar, 200 rpm), and the product was thoroughly dried under vacuum at 80 °C (0 mbar, 200 rpm).

$H_4SiMo_{12}O_{40}$ (HSiMo)

The bulk HPA-5 catalyst was prepared after modified method described in the literature.[234] MoO_3 (34.55 g) was dissolved in 500 ml H_2O using NaOH (12.75 g). A separate Na_2SiO_3 solution (2.44 g) was added under vigorous stirring, yielding a yellow solution, which was acidified to pH 1.4 using HCl (1 mol/l). Extraction with diethyl ether was attempted but failed. Further acidification to pH 0.745 also showed no extraction into the organic phase. After concentrating both phases, 10.00 g of crude

product was collected and dissolved in H_2O (100 ml), forming a green-yellow solution with some insoluble material. Addition of HCl (37 %, 10 ml) and H_2O_2 (35 %, 10 ml) turned the solution bright yellow. The undissolved residue was filtered off. The filtrate was extracted multiple times with butyl acetate, turning the organic phase intensely yellow. After solvent removal, an amorphous green solid was obtained.

Supported Catalysts

Wet impregnation was employed to deposit a series of heteropoly acids on montmorillonite K10, including $H_4SiW_{12}O_{40}$, $H_3PMo_{12}O_{40}$, $H_3PW_{12}O_{40}$, $H_8PV_5Mo_7O_{40}$, $H_6PInMo_{11}O_{40}$, and $H_4SiMo_{12}O_{40}$. In a separate set of experiments, $H_4SiW_{12}O_{40}$ was additionally supported on alternative carriers such as Al_2O_3, ZrO_2, TiO_2, and Celite® 545, following the same impregnation protocol.

Prior to impregnation, the metal oxides (Al_2O_3, TiO_2, ZrO_2) were ground to a particle size of 80 – 250 µm using a mortar, while montmorillonite K10 and Celite® 545 were used as received. The amount of support was calculated according to surface area to ensure a heteropoly acid loading of 1 unit per nm². The HPA was dissolved in 500 ml of deionized H_2O and used at its resulting pH. After adding the support material, the suspension was stirred for 3 hours on a rotary evaporator (room temperature, 800 mbar, 111 rpm), followed by solvent removal at 80 °C and 200 mbar. The resulting solid was then dried at 100 °C for 20 hours.

Catalyst Testing

All catalytic tests were conducted in a stainless-steel fixed-bed reactor system, equipped with a heating jacket. A feed gas mixture containing 25 % CO_2 and 75 % H_2 was introduced into the reactor via calibrated mass flow controllers. Nitrogen served as an inert carrier and purge gas. System pressure was regulated downstream using a back-pressure valve, while the catalyst bed temperature was monitored by an internal thermocouple.

The reactor was loaded with 2.5 g of $Cu/ZnO/Al_2O_3$ catalyst and one supported catalyst, respectively, and diluted homogeneously with inert quartz beads. Quartz wool was placed in the middle for separation of the catalyst as well as at both ends of the reactor to secure the catalyst bed. Before initiating the reaction, all materials were treated at 250 °C under N_2 flow (300 $Nml \cdot min^{-1}$) for 30 minutes. For preforming, 10 % H_2 was added for an additional hour.

Following pre-treatment, the pressure was set to 50 bar, and a feed gas with a H_2/CO_2 ratio of 3/1was introduced at a flow rate of 1100 $Nml \cdot min^{-1}$. Gas-phase analysis was carried out via online gas chromatography at defined time intervals of 10, 20, 30, 60, 90, and 120 minutes. To stop the reaction, the feed gas was switched off, and the reactor was purged with nitrogen before being allowed to cool to ambient temperature. A comprehensive description can be found in chapter 9.5.3.

9.2.1.4 Catalyst Preparation and Testing: In_2O_3-based Catalysts for CO_2 Conversion to Methanol

Catalyst Preparation

In_2O_3/ZrO_2 catalysts

In_2O_3/ZrO_2 catalysts were prepared via impregnation based on methods described by Martin et al.[205] and Schühle et al.[235]. Two ZrO_2 supports were employed: one from Alfa Aesar (ZrO_2 (AA)) and one from Saint-Gobain (ZrO_2 (SG)), both ground to 80 – 250 µm prior to synthesis.

Synthesis of In_2O_3/ZrO_2 (M-AA)

6.84 g of $In(NO_3)_3 \cdot x\ H_2O$ was dissolved in 630 ml ethanol and 216 ml H_2O. 18 g ZrO_2 (AA) was added and stirred for 5 hours using a rotary evaporator. The mixture was dried at 65 °C (12 hours), then calcined at 300 °C (5 °C/min, 3 hours).

Synthesis of In_2O_3/ZrO_2 (S-AA)

10 g of $In(NO_3)_3 \cdot x\ H_2O$ was dissolved in 25 ml H_2O. 16.4 ml of this solution was mixed with 17.1 g ZrO_2 (AA). After solvent removal via rotary evaporation, the sample was dried (65 °C, 12 hours) and calcined (300 °C, 5 °C/min, 3 hours).

Synthesis of In_2O_3/ZrO_2 (M-SG)

6.84 g of $In(NO_3)_3 \cdot x\ H_2O$ was dissolved in 630 ml ethanol and 216 ml H_2O. 18 g ZrO_2 (SG) was added and stirred for 5 hours using a rotary evaporator. The mixture was dried at 65 °C (12 hours), then calcined at 300 °C (5 °C/min, 3 hours).

Synthesis of In_2O_3/ZrO_2 (S-SG)

10 g of $In(NO_3)_3 \cdot x\ H_2O$ was dissolved in 25 ml H_2O. 16.4 ml of this solution was mixed with 17.1 g ZrO_2 (SG). After solvent removal via rotary evaporation, the sample was dried (65 °C, 12 hours) and calcined (300 °C, 5 °C/min, 3 hours).

Synthesis of metal oxide-promoted In_2O_3/ZrO_2 catalysts

In_2O_3/ZrO_2 catalysts promoted with CeO_2, MgO, CuO, or NiO were prepared by co-precipitation, therefore 10 g of Na_2CO_3 were dissolved in 100 ml deionized water. A mixture containing $In(NO_3)_3 \cdot x\ H_2O$ and the respective metal nitrate or carbonate (calculated for 10 wt.% metal loading) was dissolved in 250 ml H_2O. The pH was adjusted to 9.2 with $NaHCO_3$ solution before adding 20 g of ZrO_2. The resulting suspension was stirred (111 rpm, room temperature, 800 mbar) for 1 hour using a rotary evaporator, diluted with 500 ml H_2O, and subsequently filtered and washed to neutral pH. Drying was carried out at 65 °C for 12 hours, followed by calcination at 300 °C for 3 hours.

Synthesis of metal oxide-promoted In_2O_3/ZrO_2 catalysts

NiO-promoted catalysts were also prepared by wet impregnation and chemical reduction. For wet impregnation 0.747 g of $Ni(NO_3)_2 \cdot 6\ H_2O$ were dissolved in 250 ml H_2O and added to 15 g In_2O_3/ZrO_2 (M-SG). After stirring (111 rpm, room temperature, 850 mbar, 1 hour), the solvent was evaporated, and the solid was dried and calcined as described above.

For chemical reduction 0.747 g $Ni(NO_3)_2 \cdot 6\ H_2O$ were dissolved in 250 ml H_2O with 15 g In_2O_3/ZrO_2 (M-SG). After stirring and heating to 80 °C, a NaOH solution (Ni/NaOH = 1/3 mol) and freshly prepared $NaBH_4$ (Ni/$NaBH_4$ = 1/4 mol) were added. The suspension was stirred for 2 hours (80 °C, 800 mbar), followed by pH-neutral washing and drying at 65 °C for 12 hours.

Catalyst Testing

All catalytic tests were conducted in a stainless-steel fixed-bed reactor system, equipped with a heating jacket. A feed gas mixture containing 25 % CO_2 and 75 % H_2 was introduced into the reactor via calibrated mass flow controllers. Nitrogen served as an inert carrier and purge gas. System pressure was regulated downstream using a back-pressure valve, while the catalyst bed temperature was monitored by an internal thermocouple. The reactor effluent was analyzed every 30 minutes by online gas chromatography, one methanizer (for CO and CO_2 detection), two flame ionization detectors (FID), and one thermal conductivity detector (TCD).

The reactor was loaded with 5.0 or 4.0 g of catalyst, which was sieved to a particle size of 80 – 250 µm, and diluted homogeneously with inert quartz beads. Quartz wool was placed at both ends to secure the catalyst bed. Before initiating the reaction, all materials were treated at 200 °C under N_2 flow (300 Nml · min^{-1}) for 1 hour. For Ni- and Cu-based systems, an additional reduction step was performed under 10 % H_2/N_2 (500 Nml · min^{-1}) at 200 °C for 1 hour.

Following pre-treatment, the catalyst bed was heated to 300 °C and a feed gas with a H_2/CO_2 ratio of 3/1 was introduced at a flow rate of 1200 Nml · min^{-1}. The reactor was pressurized to either 50 or 75 bar, depending on the experiment. All materials were tested under steady-state conditions for at least 3 hours to allow performance comparison. After testing, the system was cooled at 3 K · min^{-1} under N_2 flow (1000 Nml · min^{-1}) and the catalyst was recovered and stored under argon (grade 4.6, Heide Gas) for further analysis. A comprehensive description can be found in chapter 9.5.4.

9.2.2 Catalyst Characterization: Analytical Methods and Devices

The used methods and devices for characterization of the catalysts as well as analysis of the reaction products and solutions are described in the following sections:

Inductively Coupled Plasma Optical Emission Spectrometry (ICP-OES)

The elemental composition of the catalysts was analyzed by ICP-OES (ASCOR spectrometer by Spectro). Sodium as element was additionally quantified using flame atomic absorption spectrometry (F-AAS, Thermo, Solaar S Series). The emitted light from excited atoms was detected and evaluated to quantify the elemental content. Measurements were conducted at the Central Elemental Analysis Facility of the Department of Chemistry, University of Hamburg.

Dissolving of the samples was carried out using the following approaches:

- Pure POMs were either dissolved directly in water at room temperature, with gentle heating, or by adding 100 µL of conc. HNO_3 to 5 ml of H_2O to facilitate dissolution.
- Supported POM catalysts were digested using a mixture of aqua regia and conc. HF in a closed-vessel microwave digestion system (Anton Paar Multiwave 7000)
- In_2O_3/ZrO_2-based catalysts were dissolved in a mixture of 5 ml conc. H_2SO_4 and 1 ml conc. HNO_3.

CHNS (O)

Elemental analysis of carbon, hydrogen, nitrogen, and sulfur (CHNS) in the activated carbon samples was conducted using a "Euro EA3000" analyzer (EuroVector). The material was sealed in a tin capsule and combusted in a helium stream with added oxygen at approximately 1000 °C. The resulting combustion products were separated via gas chromatography and analyzed with a thermal conductivity detector.

Oxygen content was determined separately using the "Oxycube" analyzer (Elementar). The samples were weighed into silver capsules and subjected to pyrolysis at 1450 °C on nickel-coated carbon in a helium stream. The generated CO gas was captured, desorbed, and analyzed by TCD, enabling oxygen quantification via calibration against reference materials. All measurements were carried out at the Central Laboratory for Elemental Analysis, Department of Chemistry, University of Hamburg.

Thermogravimetric Analysis (TGA)

TGA measurements fro determination of the water content of the polyoxometalates were performed using a TG 209 F1 Libra instrument (NETZSCH). Data evaluation was carried out using the Proteus

software (NETZSCH). Approximately 20 mg of the respective sample was loaded into a crucible made of Al_2O_3 or borosilicate glass. The mass change was recorded over the course of the defined temperature ramp.

Nuclear Magnetic Resonance Spectroscopy (NMR)

NMR spectroscopy for characterization of the polyoxometalates was carried out on a Bruker AVANCE II 600 MHz instrument at room temperature. For this purpose, 70 mg of each sample was dissolved in 0.63 ml of diluted hydrochloric acid (pH 1), followed by the addition of 0.07 ml acetone-d_6. ^{31}P-NMR spectra were collected using 2048 scans, a spectral window of 40 ppm, and an offset of -1 ppm, with a relaxation time of 1 second. For ^{51}V-NMR analysis, 4096 scans were recorded using a spectral width of 400 ppm, a frequency offset of -520 ppm, and a shorter relaxation delay of 0.5 seconds.

Infrared Spectroscopy (IR)

For structural analysis, IR measurements were carried out in ATR mode using a Shimadzu QATR™-S system with a diamond prism. Spectra were collected in the wavenumber range of 400 – 4000 cm^{-1}. Following acquisition, baseline correction was applied and characteristic peaks were manually identified. The corrected spectral data were then converted into x/y format and saved as text files for further processing.

Raman Spectroscopy

Raman spectroscopy was conducted using a SENTERRA Raman microscope (Bruker Optik GmbH). Spectra were collected using a 20x objective and a 785 nm excitation laser. The measurement range spanned from 75 to 1525 cm^{-1}. For each sample, eight scans were recorded with an integration time of 16 seconds per scan. A glassy carbon electrode (3 mm diameter) served as the working electrode, while a silver/silver ion (Ag/Ag^+) electrode and a platinum wire were employed as reference and counter electrodes, respectively.

Square Wave Voltametry (SWV)

SWV measurements were carried out in an aqueous hydrochloric acid solution adjusted to pH 1, with an analyte concentration of 1 $mmol \cdot l^{-1}$, using an Ivium potentiostat. The electrode configuration consisted of a 3 mm glassy carbon working electrode, an Ag/Ag^+ reference electrode, and a platinum counter electrode. Parameters included a scan rate of 5 $mV \cdot s^{-1}$, a 20 mV modulation amplitude, and a frequency of 25 Hz.

High-Performance Liquid Chromatography (HPLC)

Quantitative and qualitative analysis of the reaction products was conducted by HPLC. The used system was either an Agilent 1200 Series or a SHIMADZU HPLC System, both equipped with a BIORAD Aminex HPX-87H column (300 mm · 7.8 mm) and a refractive index detector. A 0.0050 M aqueous solution of sulfuric acid served as the mobile phase.

N_2-Physisorption

The textural properties of all catalyst samples were determined by nitrogen physisorption. Activated carbons were measured on a SA3100 Surface Area Analyzer (Beckman Coulter) at the Interdisciplinary Centre for Analytics on the Nanoscale, while the supported POMs and In_2O_3-based catalysts were characterized using an Autosorb iQ MP/XR from Anton Paar. Comprehensive information on measurement procedures is provided in Chapter 9.5.

Powder X-ray Diffraction (p-XRD)

To investigate the crystalline structure of the catalyst powders, p-XRD analysis was employed. Measurements were carried out using a Panalytical MDP X'Pert Pro diffractometer equipped with a Cu Kα radiation source (λ = 0.1541 nm), operating in Bragg–Brentano geometry. Diffraction patterns were recorded in a 2θ range from 10° to 80° with a step size of 0.013° and a measurement time of 0.3 s per step. Data analysis was performed using the X'Pert HighScore Plus software.

Additionally, for In_2O_3-based catalysts, the average particle size where determined using Scherrer-Debye equation.

NH_3 Temperature Programmed Desorption (NH_3-TPD)

NH_3-TPD was applied to assess the surface acidity of both activated carbon materials and supported POM catalysts. Measurements were conducted on a ChemBET Pulsar TPD/TPR analyzer (Quantachrome Instruments). Prior to measurement, samples were pre-treated in helium (80 ml/min) - activated carbons at 130 °C and POM catalysts at 150 °C. After cooling to 100 – 130 °C, the materials were exposed to ammonia to ensure surface saturation, followed by helium purging to remove weakly adsorbed NH_3. Desorption profiles were recorded by heating the samples up to 450 °C (supported catalysts) or 750 °C (activated carbons) at 10 K/min. Desorbed ammonia was quantified via a thermal conductivity detector (TCD), and peak areas were integrated using Origin software. All values were normalized to a standard material (CW20 or $HSiW/ZrO_2$).

CO_2 Temperature Programmed Desorption (CO_2-TPD)

CO_2-TPD was performed using a ChemBET Pulsar instrument (Quantachrome Instruments) to evaluate CO_2 adsorption strength and capacity of In_2O_3-based catalysts. For each measurement, 0.3 g of the sample was pretreated in helium flow (80 ml/min) by heating to 200 °C at 10 K/min for one hour to remove surface-bound water. CO_2 was then introduced at the same temperature to allow surface adsorption, and the sample was cooled to 50 °C. Subsequently, desorption was initiated by heating to 700 °C under helium flow (80 ml/min, 10 °C/min), with the amount of desorbed CO_2 detected via a thermal conductivity detector.

Hydrogen Temperature Programmed Reduction (H_2-TPR)

H_2-TPR was conducted using a ChemBET Pulsar system (Quantachrome Instruments) to assess the surface reducibility of the In_2O_3-based catalysts. For each experiment, 0.3 g of the sample was pretreated in a nitrogen flow (80 ml/min) by heating to 180 °C (10 °C/min) for one hour to remove adsorbed water. After cooling to 100 °C, the sample was subjected to a reducing gas mixture (5 % H_2 in N_2, 80 ml/min), while being heated to 850 °C at a rate of 10 °C/min. Hydrogen consumption during reduction was monitored using a thermal conductivity detector.

Microscopy

The morphology and elemental distribution of the catalysts were investigated using scanning electron microscopy (SEM) and energy-dispersive X-ray spectroscopy (EDX). All measurements were conducted on a Leo 1550 Gemini SEM system. SEM images were obtained at an acceleration voltage of 2 kV with a 7.5 µm aperture. EDX elemental mapping was performed at 20 kV with a 30 µm aperture. A Silicon Drift Detector (Ultim Max 100, Oxford Instruments) in combination with AZtec software was used for detection for all analyses.

Point of Zero Charge Measurement (PZC)

To determine the PZC of the activated carbon samples, a series of sodium nitrate solutions (0.1 M, 40 ml each) were prepared and adjusted to pH values ranging from 2 to 11 using sodium hydroxide and nitric acid solutions of varying concentrations (0.1 M and 0.005 M). 200 mg of activated carbon was then added to each solution and stirred for 24 hours at 300 rpm. After equilibration, the suspensions were filtered and the final pH of each filtrate was measured. The PZC was determined by plotting the pH shift (ΔpH = pH_final − pH_initial) against the initial pH. The intersection point of the fitted linear section with ΔpH = 0 was defined as the point of zero charge.

Boehm Titration

The Boehm titration method was applied to quantify the oxygen-containing surface functional groups on the activated carbons. Therefore, four separate base solutions were prepared: 0.1 M NaOH, 0.05 M Na_2CO_3, and 0.1 M $NaHCO_3$, as well as 0.1 M HCl. Each 50 ml solution was combined with 2.00 g of activated carbon and stirred for 24 hours. After filtration of the suspensions, 10 ml of the resulting filtrates were titrated against HCl or NaOH using a Metrohm Eco Titrator to determine the amount of neutralized base or acid.

X-ray Photoelectron Spectroscopy (XPS)

The surface chemical composition and oxidation states of the catalysts were examined via XPS, performed on a Thermo Scientific system with Al Kα radiation (photon energy: 1484.6 eV) and a spot size of 400 µm. To compensate for surface charging, a flood gun was applied during analysis. The binding energies were calibrated using the C 1s peak at 284.8 eV. Spectral data were evaluated using Avantage software (version 4.87).

Gas Chromatography (GC)

The composition of the gaseous reaction products was determined using an online Bruker 450-GC gas chromatograph or a Varian 450-GC. Detailed methodological descriptions for each experimental study are provided in Chapter 9.5.

9.3 List of Figures

9.4 List of Tables

9.5 Supporting Information

9.5.1 Supporting Information of 1st study: Substituted Polyoxometalates for Liquid-Phase Conversion of Biomass to Lactic Acid

in: A. Wesner, J.-C. Raabe, M. J. Poller, S. Meier, A. Riisager, J. Albert, Conversion of Sugars to Lactic Acid using homogeneous Niobium-substituted Polyoxometalate Catalysts, *Chem. Eur. J.*, **2024**, e202402649.

Chemistry–A European Journal

Supporting Information

Conversion of Sugars to Lactic Acid using Homogeneous Niobium-Substituted Polyoxometalate Catalysts

Anne Wesner, Jan-Christian Raabe, Maximilian J. Poller, Sebastian Meier, Anders Riisager, and Jakob Albert*

Supporting Information

Conversion of Sugars to Lactic Acid using homogeneous Niobium-substituted Polyoxometalate Catalysts

Anne Wesner[a], Jan-Christian Raabe[a], Maximilian J. Poller[a], Sebastian Meier[b], Anders Riisager[b] and Jakob Albert[a]*

[a] Institute of Technical and Macromolecular Chemistry, University of Hamburg, Bundesstraße 45, 20146 Hamburg, Germany

[b] Department of Chemistry, Technical University of Denmark, Kemitorvet, 2800 Kgs. Lyngby, Denmark

* Contact details of the corresponding author: Phone: +49-(0)40 42838 4209; e-mail: jakob.albert@uni-hamburg.de

Table of contents

Catalyst preparation and characterization

The original synthesis procedures are published in a previous study.[1]

Synthesis of potassium hexaniobate $K_8Nb_6O_{19}$ as a precursor compound

In a typical procedure, diniobium pentoxide (22.63 g, 85.13 mmol, 1 equivalent) and potassium hydroxide (71.04 g, 1.27 mol, 14.87 equivalents) were mixed and added in small portions to a nickel crucible heated over a gas burner flame. The mixture was bubbling and the diniobium pentoxide was dissolved in the potassium hydroxide melt. After complete addition of both precursors, the reaction melt was heated until bubbling has stopped. The melt was dissolved in water, filtered and reduced to one-eighth of its volume under reduced pressure, resulting in a precipitation of a colorless solid. It was cooled to 4 °C overnight and the precipitate was collected by filtration and washed several times with cooled ethanol. After washing the solid was dried at 60 °C in an oven. A colorless solid (25.25 g) was obtained. The Nb^V content of the potassium hexaniobate was first determined using ICP-OES and the weights were calculated for the respective reaction procedures based on the Nb content, considering the stoichiometric ratios.

Synthesis and Characterization of $PNb_xMo_{12-x}O_{40}^{(3+x)-}$: ($Na_4[PNbMo_{11}O_{40}]$ (NaNb), $Na_5[PNb_2Mo_{10}O_{40}]$ ($NaNb_2$), $Na_6[PNb_3Mo_9O_{40}]$ ($NaNb_3$))

Synthesis of $PNb_xMo_{12-x}O_{40}^{(3+x)-}$: ($Na_4[PNbMo_{11}O_{40}]$ (NaNb), $Na_5[PNb_2Mo_{10}O_{40}]$ ($NaNb_2$), $Na_6[PNb_3Mo_9O_{40}]$ ($NaNb_3$))

The stoichiometry of P/Nb/Mo was ensured by weighing the precursors in the correct molar ratios. Sodium molybdate dihydrate (10.01 g for $Na_4[PNbMo_{11}O_{40}]$, 10.00 g for $Na_5[PNb_2Mo_{10}O_{40}]$ and 10.01 g for $Na_6[PNb_3Mo_9O_{40}]$) and disodium hydrogen phosphate (0.65 g for $Na_4[PNbMo_{11}O_{40}]$, 0.65 g for $Na_5[PNb_2Mo_{10}O_{40}]$ and 0.66 g for $Na_6[PNb_3Mo_9O_{40}]$) (stoichiometry 9:1) were dissolved in water (50 mL) and the pH was adjusted to ~1, forming a yellow, clear solution. To this solution, a solution of potassium hexaniobate (1.12 g for $Na_4[PNbMo_{11}O_{40}]$, 2.16 g for $Na_5[PNb_2Mo_{10}O_{40}]$ and 3.36 g for $Na_6[PNb_3Mo_9O_{40}]$) in a diluted aqueous hydrogen peroxide solution (1.5 %) (20 mL) was added and refluxed to form an orange or yellow reaction solution. For substitution degrees x = 1 and 2, sodium molybdate dihydrate (2.22 g for $Na_4[PNbMo_{11}O_{40}]$ and 1.11 g for $Na_5[PNb_2Mo_{10}O_{40}]$) was added in the required stoichiometry to fill the remaining vacancies of the lacunary species. The pH value was 5.142 (in the experiment for $Na_4[PNbMo_{11}O_{40}]$), 4.789 (in the experiment for $Na_5[PNb_2Mo_{10}O_{40}]$) and 5.450 (in the experiment for $Na_6[PNb_3Mo_9O_{40}]$) A clear, yellow reaction solution was then formed. The pH was adjusted to ~1.6 by adding a 37 % hydrochloric acid solution in water. The reaction solution was filtered and desalted using an established nanofiltration method.

The solution of potassium hexaniobate must be added directly to the reaction solution without delay, otherwise niobium(V) oxide may precipitate. The solution should therefore be freshly prepared and used immediately. After the above described solution has been added to the lacunary solution, the reaction mixture must be heated directly to prevent precipitation of niobium(V) oxide. It is recommended to use a preheated oil bath. Sometimes direct precipitate formation occurs after the addition of the potassium hexaniobate solution. This is not always a problem if the heating is fast enough, and a clear reaction solution form

Characterization of $Na_4[PNbMo_{11}O_{40}]$ (NaNb)

^{31}P-NMR: (242.9 MHz, H_2O/D_2O, 20 °C):*δ* (ppm) = -1.28, -1.37, -1.43, -2.99, -3.29, -3 .30, -3.36, -3.38, -3.66

IR (ATR): $\tilde{\nu}$ (cm^{-1}) = 3396 (w, O-H, H_2O), 1615 (O-H, hydration H_2O), 1058, 1034 (w, P-O), 944 (me, $M=O_t$), 859 (me, $(M\text{-}O\text{-}M)_{vertex}$), 741 (st, $(M\text{-}O\text{-}M)_{edge}$).

ICP-OES: Calculated for $Na_4[PNbMo_{11}O_{40}] \cdot 6\ H_2O$: 52.264 % Mo, 4.601 % Nb, 1.534 % P, 0.00 % K, 4.554 % Na. Found for $Na_4PNbMo_{11}O_{40} \cdot 6\ H_2O$: 44.77 % Mo, 4.33 % Nb, 1.17 % P 0.75 % K, 4.84 % Na. Data normalized to molybdenum. Na/K/P/Nb/Mo ratio: 4.96/0.45/0.893/1.10/11.

TGA: 4.933 % weight loss upon drying, this corresponds to 6 mol lattice water per mol of the POM.

Characterization of $Na_5[PNb_2Mo_{10}O_{40}]$ ($NaNb_2$)

^{31}P-NMR: (242.9 MHz, H_2O/D_2O, 20 °C):
δ (ppm) = -0.28, -0.36, -1.26, -1.33, -1.40, -2.45, -2.51, -2.63, -2.92, -2.96, -3.04, -3.0 9, -3.19, -3.27, -3.28, -3.33, -3.37, -3.46, -2.64.

IR (ATR): $\tilde{\nu}$ (cm^{-1}) = 3412 (w, O-H, H_2O), 1613 (O-H, hydration H_2O), 1049 (w, P-O), 947 (me, $M=O_t$), 856 (me, $(M\text{-}O\text{-}M)_{vertex}$), 757 (st, $(M\text{-}O\text{-}M)_{edge}$).

ICP-OES: Calculated for $Na_5[PNb_2Mo_{10}O_{40}] \cdot 5\ H_2O$: 47.467 % Mo, 9.193 % Nb, 1.532 % P, 0.00 % K, 5.687 % Na. Found for $Na_5PNb_2Mo_{10}O_{40} \cdot 5\ H_2O$: 47.74 % Mo, 8.456 % Nb, 1.50 % P 1.36 % K, 4.565 % Na. Data normalized to molybdenum. Na/K/P/Nb/Mo ratio: 3.99/0.70/0.98/1.83/10.

TGA: 4.652 % weight loss upon drying, this corresponds to 5 mol lattice water per mol of the POM.

Characterization $Na_6[PNb_3Mo_9O_{40}]$ ($NaNb_3$)

^{31}P-NMR: (242.9 MHz, H_2O/D_2O, 20 °C):
δ [ppm] = -2.36, -2.48, -2.52, -2.61, -2.73, -2.78, -2.91, -2.96, -3.04, -3.09, -3.18, -3.26 , -3.28, -3.33, -3.37, -3.63.

IR (ATR): $\tilde{\nu}$ (cm^{-1}) = 3388 (w, O-H, H_2O), 1613 (O-H, hydration H_2O), 1047 (w, P-O), 944 (me, $M=O_t$), 857 (me, $(M-O-M)_{vertex}$), 760 (st, $(M-O-M)_{edge}$).

ICP-OES: Calculated for $Na_6[PNb_3Mo_9O_{40}] \cdot 7\ H_2O$: 41.569 % Mo, 13.418 % Nb, 1.491 % P, 0.00 % K, 6.641 % Na. Found for $Na_6PNb_3Mo_9O_{40} \cdot 7\ H_2O$: 38.54 % Mo, 12.03 % Nb, 1.26 % P 2.37 % K, 4.30 % Na. Data normalized to molybdenum. Na/K/P/Nb/Mo ratio: 4.19/1.36/0.91/2.90/9.

TGA: 6.297 % weight loss upon drying, this corresponds to 7 mol lattice water per mol of the POM.

Synthesis and Characterization of $NaPV_xNb_yMo_9O_{40}^{(3+x)}$: ($Na_6[PV_2NbMo_9O_{40}]$ (NaV_2Nb), $Na_6[PVNb_2Mo_9O_{40}]$ ($NaVNb_2$))

Synthesis of $Na_6[PV_2NbMo_9O_{40}]$ (NaV_2Nb), $Na_6[PVNb_2Mo_9O_{40}]$ ($NaVNb_2$)

The stoichiometry of P/V/Mo was ensured by weighing the precursors in the correct molar ratios. Sodium molybdate dihydrate (15.00 g for $Na_6[PV_2NbMo_9O_{40}]$ and 10.00 g for $Na_6[PVNb_2Mo_9O_{40}]$) and disodium hydrogen phosphate (0.98 g for $Na_6[PV_2NbMo_9O_{40}]$ and 0.66 g for $Na_6[PVNb_2Mo_9O_{40}]$) (stoichiometry 9 : 1) were dissolved in water and the pH was adjusted to ~1, forming a yellow, clear solution. To this solution, a solution of sodium vanadate in water (1.68 g for $Na_6[PV_2NbMo_9O_{40}]$ and 0.56 g $Na_6[PVNb_2Mo_9O_{40}]$) was added and refluxed to form a red reaction solution, directly after the vanadate addition. A pH value of 5.351 (in the experiment for $Na_6[PV_2NbMo_9O_{40}]$) and 5.235 (in the experiment for $Na_6[PVNb_2Mo_9O_{40}]$) was measured. The pH was adjusted to ~1.6 by adding a 37 % hydrochloric acid solution in water. In the last step, the reaction solution was filtered and desalted using a nanofiltration approach. Sodium vanadium oxide dissolves in water after the aqueous suspension has been heated briefly.

Characterization of $Na_6[PV_2NbMo_9O_{40}]$ (NaV_2Nb)

^{31}P-NMR: (242.9 MHz, H_2O/D_2O, 20 °C): δ (ppm) = -2.50 to -4.30.

^{51}V-NMR (157.8 MHz, H_2O/D_2O, 20 °C): (ppm) = -517.7, -525.9, -531.3, -532.8, -533 .2, -533.8, -534.3, -535.7, -538.5, -540 to -546.

IR (ATR): $\tilde{\nu}$ [cm^{-1}] = 3374 (w, O-H, H_2O), 1610 (O-H, hydration H_2O), 1046 (w, P-O), 941 (me, M=O_t), 847 (me, (M-O-M)$_{vertex}$), 750 (st, (M-O-M)$_{edge}$).

ICP-OES: Calculated for $Na_6[PV_2NbMo_9O_{40}] \cdot 7\ H_2O$: 43.319 % Mo, 4.661 % Nb, 5.111 % V, 1.554 % P, 0.00 % K, 6.92 % Na. Found for $Na_6PV_2NbMo_9O_{40} \cdot 7\ H_2O$: 38.50 % Mo, 4.38 % Nb, 5.225 % V 1.52 % P 1.38 % K, 6.49 % Na. Data normalized to molybdenum. Na/K/P/V/Nb/Mo ratio: 6.33/0.792/1.10/2.3/1.06/9.

TGA: 5.901 % weight loss upon drying, this corresponds to 7 mol lattice water per mol of the POM.

Characterization of $Na_6[PVNb_2Mo_9O_{40}]$ ($NaVNb_2$)

^{31}P-NMR: (242.9 MHz, H_2O/D_2O, 20 °C):
δ (ppm) = -4.92, -5.08, -5.27 to -5.36, -5.49, -5.62, -5.69, -5.93, -5.96, -5.99, -6.04, -6.20, -6.30, -6.42, -6.43, -6.49, -6.54, -6.73, -6.77, -6.86, -6.88, -6.89, -6.90.

^{51}V-NMR (157.8 MHz, H_2O/D_2O, 20 °C):
δ (ppm) = -519.8, -527.9, -532.7, -533.7, -534.4, -535.4, -537.1, -545.1.

IR (ATR): $\tilde{\nu}$ (cm^{-1}) = 3391 (w, O-H, H_2O), 1615 (O-H, hydration H_2O), 1048 (w, P-O), 944 (me, $M=O_t$), 859 (me, $(M-O-M)_{vertex}$), 762 (st, $(M-O-M)_{edge}$).

ICP-OES: Calculated for $Na_6[PVNb_2Mo_9O_{40}] \cdot 5\ H_2O$: 43.191 % Mo, 9.294 % Nb, 2.548 % V, 1.549 % P, 0.00 % K, 6.90 % Na. Found for $Na_6PVNb_2Mo_9O_{40} \cdot 5\ H_2O$: 42.28 % Mo, 8.915 % Nb, 2.19 % V 1.46 % P 1.545 % K, 4.645 % Na. Data normalized to molybdenum. Na/K/P/V/Nb/Mo ratio: 4.13/0.81/0.964/0.880/1.96/9.

TGA: 4.077 % weight loss upon drying, this corresponds to 5 mol lattice water per mol of the POM.

Synthesis and Characterization of $Na_6[PV_3Mo_9O_{40}]$ (NaV_3)

Synthesis of $Na_6[PV_3Mo_9O_{40}]$ (NaV_3)

The stoichiometry of P/V/Mo was ensured by weighing the precursors in the correct molar ratios. Sodium molybdate dihydrate (10.00 g) and disodium hydrogen phosphate (0.66 g) (stoichiometry 9:1) were dissolved in water and the pH was adjusted to ~1, forming a yellow, clear solution. To this solution, a solution of sodium vanadate (1.68 g) in water was added and refluxed to form a red reaction solution, directly after the vanadium addition. A clear, red reaction solution was then formed. A pH value of 4.420 was measured. Finally, the reaction solution was filtered and desalted using a nanofiltration approach.

Characterization of $Na_6[PV_3Mo_9O_{40}]$ (NaV_3)

^{31}P-NMR (242.9 MHz, H_2O/D_2O, 20 °C):

δ [ppm] = -0.15, -2.70, -2.96, -3.02, -3.06, 3.26, -3.34, -3.42, -3.49, -3.52, -3.56, -3.62, -3.72, -4.05, -4.06, -4.13, -4.20, -4.21.

^{51}V-NMR (157.8 MHz, H_2O/D_2O, 20 °C):

δ [ppm] = -521.1, -532.0, -533.3, -533.6, -535.2, -536.8, -535.9, -540.8, -541.3, -542.9, -544, - 547.8, -549.4.

IR (ATR): $\tilde{\nu}$ [cm^{-1}] = 3561, 3307 (w, O-H, H_2O), 1618 (O-H, hydration H_2O), 1064, 1048 (w, P-O), 937 (me, M=O_t), 846 (me, (M-O-M)$_{vertex}$), 758 (st, (M-O-M)$_{edge}$).

ICP-OES: Calculated for $Na_6[PV_3Mo_9O_{40}] \cdot 8\ H_2O$: 43.846 % Mo, 7.76 % V, 1.573 % P, 0.00 % K, 7.004 % Na. Found for $Na_6PV_3Mo_9O_{40} \cdot 8\ H_2O$: 46.88 % Mo, 8.205 % V 1.61 % P 0.00 % K, 6.75 % Na. Data normalized to molybdenum. Na/K/P/V/Mo 5.41/0/0.957/2.97/9

TGA: 7.128 % weight loss upon drying, this corresponds to 8 mol lattice water per mol of the POM.

Synthesis and Characterization of $Na_3[PMo_{12}O_{40}]$ (NaMo)

Synthesis of $Na_3[PMo_{12}O_{40}]$ (NaMo)

The stoichiometry of P/Mo was ensured by weighing the precursors in the correct molar ratios. Sodium molybdate dihydrate (5 g) and a 85 % solution of phosphoric acid in water (0.199 g) (stoichiometry 12:1) were dissolved in water (50 mL) and the pH was adjusted to ~1, forming a yellow, clear solution. Finally, the reaction solution was filtered and desalted using a nanofiltration method.

Characterization of $Na_3[PMo_{12}O_{40}]$ (NaMo)

^{31}P-NMR (242.9 MHz, H_2O/D_2O, 20 °C):

δ [ppm] = -3.87.

IR (ATR): $\tilde{\nu}$ [cm^{-1}] = 3477 (w, o-H, H2O), 1616 (O-H, hydration H_2O), 1060 (w, P-O), 947 (me, M=O_t), 896 (m_e, $(M\text{-}O\text{-}M)_{vertex}$), 782 (st, $(M\text{-}O\text{-}M)_{edge}$).

ICP-OES: Calculated for $Na_3[PMo_{12}O_{40}]$ 8 H_2O: 56.565 % Mo, 1.522 % P, 0.00 % K, 3.389 % Na. Found for $Na_3PMo_{12}O_{40}$ 8 H_2O: 54.68 % Mo, 1.42 % P, 0.0007 % K, 10.85 % Na. Data normalized to molybdenum. Na/K/P/Mo 9.94/0/0.97/12.

TGA: 4.524 % weight loss upon drying, this corresponds to 8 mol lattice water per mol of the POM.

Analytical Methods

Inductively Coupled Plasma Optical Emission Spectroscopy and Atomic Absorption Spectrometry (ICP-OES and ICP-AAS)

Synthesized samples were analyzed using an ICP-OES-spectrometer for elemental analysis (Fa. Spectro, type ARCOS) for the elements Mo, V, Nb, and P (method ICP-OES). Na was determined with AAS-F (Fa. Thermo, type Solaar S Series), method: F-AAS without HKL).

Samples were dissolved as follows:

- NaMo, NaNb, $NaNb_3$, NaV_2Nb and $NaVNb_2$ were dissolved in water.
- $NaNb_2$ was dissolved in water and the solution was warmed to ensure complete dissolution.
- NaV_3 was dissolved in water (5 mL) and nitric acid (100 µL) was added.

Thermogravimetric Analysis (TGA)

TGA measurements were done on a TG 209 F1 Libra of NETZSCH. The resulting data were processed with the software Proteus from NETZSCH. For a single measurement, approximately 20 mg of the sample were weighted into a borosilicate-glass crucible. During measurement the change of mass was measured at the following temperature program:

- Heating to 30 °C with 10 K/min
- Stay at 30 °C for 15 minutes
- Heating to 350 °C with a heating rate of 10 K/min
- Stay at 350 °C for 30 minutes
- Cooling down to room temperature

Nuclear Magnetic Resonance Spectroscopy (NMR)

The NMR measurements were performed on a Bruker AVANCEII 600 MHz at room temperature. The samples were prepared by dissolution of the POM (70 mg) in diluted aqueous hydrochloric acid solution adjusted to pH 1 (0.63 mL) and acetone-d6 (0.07 mL) was added as deuterated solvent.

^{31}P-NMR spectra were measured as follows:

- Time Domain Data Sizes (TD): 32k
- Number of Scans (NS): 2k (= 2048)
- Transmitter Frequency Offset for Channel F1 (O1): -1 ppm
- Spectral Width (SW): 40 ppm
- Delay D1: 1 s.

^{51}V-NMR spectra were measured as follows:

- TD: 32k
- NS: 4k
- O1: -520 ppm
- SW: 400 ppm
- D1: 0.5 s

Infrared spectroscopy (IR)

The IR spectra were measured in attenuated total reflection (ATR) mode on a QATR™-S single-reflection ATR (with a diamond prism) from Shimadzu.

Raman spectroscopy

The Raman spectra were acquired using a SENTERRA Raman microscope from Bruker Optik GmbH, equipped with a 50-1000 µm aperture. The microscope was configured with a 20x objective, and the laser utilized had a wavelength of 785 nm. Spectral data were collected over a range of 75-1525 cm^{-1}. Each measurement was integrated over 16 seconds, with 8 scans per sample and a laser power setting of 10 mW.

Square-Wave-Voltammetry (SWV)

SWV measurements were done in aqueous, hydrochloric acid medium at pH 1 and a concentration of 1 mmol L^{-1} on an Ivium Potentiostat. During the measurement, the solution was purged with nitrogen. The working electrode was glassy carbon (diameter: 3 mm), the reference electrode was Ag/Ag^{+} and the counter electrode was platinum. All SWV measurements were done with a scan rate of 5 mV s^{-1}, a modulation amplitude of 20 mV and a frequency of 25 Hz.

High-Performance Liquid Chromatography (HPLC)

The determination and quantification of reaction products were carried out with HPLC. The undiluted reaction mixture was analyzed on an Agilent 1200 series HPLC (30 cm Aminex© HPX-87H column) with a RI detector using a 0.0050 M aqueous sulphuric acid solution as eluent. The time of the run was 60 min, at 30 ºC (column) and 35 °C (RI detector), with a flow of 0.3 ml min^{-1}.

^{1}H-^{13}C heteronuclear single quantum coherence spectroscopy (HSQC)

Soluble, organic post reaction products derived from reactions of glucose, sucrose, xylose and cellobiose were further quantified using high-field (18.7 T) NMR spectroscopy. To 500 μl of the samples, 50 μl of D_2O was added as an internal lock reference. The resultant sample volumes of 550 μl were transferred to 5 mm NMR sample tubes, which subsequently were placed into an 800 MHz Bruker Avance III instrument equipped with a 5 mm TCI cryoprobe. The samples were thermally equilibrated to 25°C. ^{1}H-^{13}C heteronuclear single quantum coherence (HSQC) spectra were recorded by acquiring 2048 and 256 complex data points sampling the FID for 183 ms and 42 ms in the direct and indirect dimensions, respectively. The spectral width was 14 ppm and 30 ppm in the ^{1}H and ^{13}C dimensions, respectively, where the ^{13}C dimensions was centered around the anomeric region with a carrier offset of 95 ppm. For each time point, 24 transients were summed up with an inter-scan relaxation delay of 1.0 seconds. Non uniform sampling was employed, speeding up acquisitions by reducing the fraction of sample data points in the indirect dimension to 30%, resulting in an overall experiment time of 75 minutes per sample. Spectra were

processed with zero filling to twice the number of acquired data points in both dimensions. Signals were assigned using previously described collections of reference compounds. [1,2] The signals for the identified carbohydrates were integrated in Bruker Topspin 3.5 pl7 software to yield relative fractions of the carbohydrate species including glucose, mannose, allose, altrose, all aldopentoses (xylose, ribose, lyxose and arabinose), and cellobiose, as well as other β-1,4 linked glycosides in the case of cellobiose substrate. The relative fractions resulting from these integrations were converted to absolute values by calibration relative to HPLC determinations of substrate signals in reactions using xylose and cellobiose as the substrate, and to HPLC determinations of the sum of glucose and mannose fractions in reactions using glucose, and sucrose substrates. This approach resulted in determinations that validated HPLC determinations in Tables S3 and S4 and yielded determinations in Table S6.

Supplementary catalytic results

Screening HPSs for conversion of dihydroxyacetone (DHA) into lactic acid (LA)

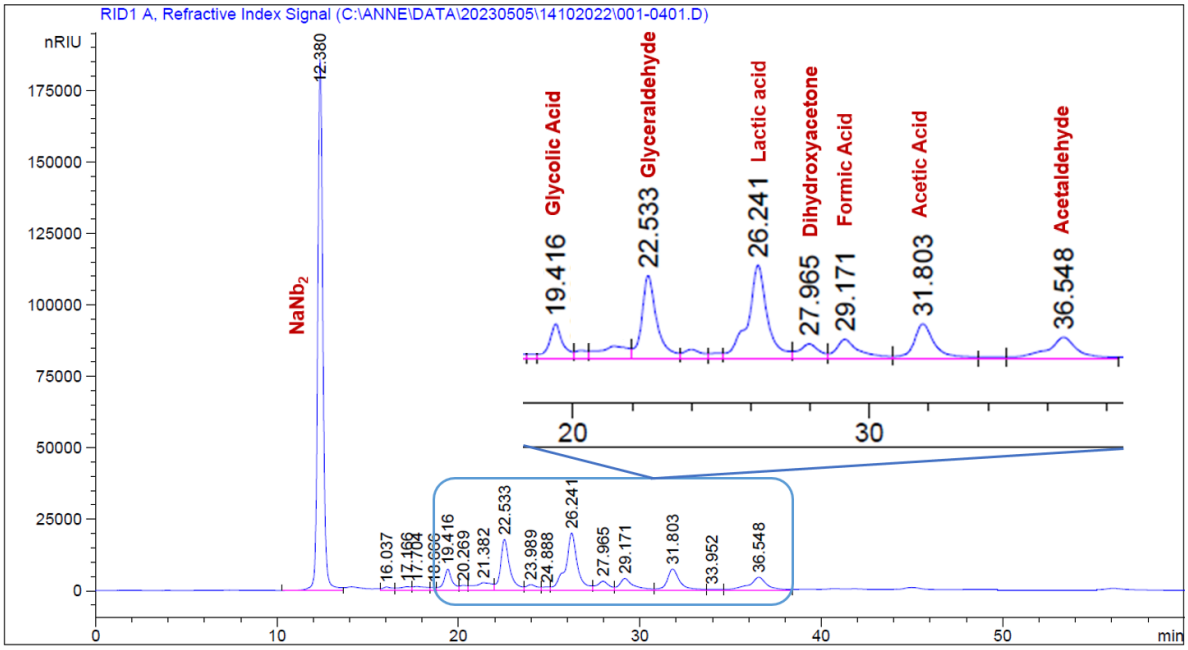

Figure S1: HPLC chromatogram displaying retention times of products from the catalytic conversion of DHA into LA with $NaNb_2$. Reaction conditions: 42 mg catalyst, 100 mg substrate, 4 g H_2O, 160 °C, 20 bar N_2, 1000 rpm, 1 h.

Table S1: Conversion and product yields for the conversion of DHA into LA.[a]

Catalyst	X (%)	Yields (%)							
		Y_{GA}	Y_{Gly}	Y_{GlycA}	Y_{PA}	Y_{LA}	Y_{FA}	Y_{AA}	Y_{AcA}
Control (blank)	23.7	0	0	0.	20.7	2.6	0	0	0
NaMo	75.2	6.4	2.3	3.8	4.0	8.3	1.8	7.9	10.6
NaV_3	85.0	4.4	1.7	3.1	2.9	8.3	1.7	7.4	19.8
NaV_2Nb	92.5	3.4	1.8	6.2	2.9	10.2	2.0	11.7	18.0
$NaVNb_2$	96.0	3.4	1.6	7.3	1.8	12.1	1.5	11.0	17.7
NaNb	97.5	2.4	1.3	10.1	1.7	15.4	1.7	11.0	12.7
$NaNb_2$	97.4	2.7	1.8	8.0	1.6	20.9	1.5	10.3	10.6
$NaNb_3$	97.2	3.3	0.6	6.6	1.7	20.7	1.6	11.6	11.2

[a] Reaction conditions: 42 mg catalyst, 100 mg substrate, 4 g H_2O, 160 °C, 20 bar N_2, 1000 rpm, 1 h. GA: glycolic acid, Gly: glyoxal, GlycA: glyceraldehyde, PA: pyruvaldehyde, LA: lactic acid, FA: formic acid, AA: acetic acid, AcA: acetaldehyde.

Table S2: Carbon balances and product selectivities for the conversion of DHA into LA.[a]

Catalyst	Cb (%)	Selectivities (%)							
		S_{GA}	S_{Gly}	S_{GlycA}	S_{PA}	S_{LA}	S_{FA}	S_{AA}	S_{AcA}
Control (blank)	100	0.0	0.0	0.0	87.3	11.0	0.0	0.0	0.0
NaMo	70	8.6	3.0	5.1	5.4	11.0	2.3	10.5	14.1
NaV_3	65	5.2	2.0	3.6	3.4	9.8	2.0	8.7	23.3
NaV_2	64	3.7	1.9	6.7	3.1	11.1	2.2	12.7	19.4
$NaVNb_2$	61	3.5	1.6	7.6	1.9	12.6	1.5	11.5	18.5
NaNb	59	2.5	1.4	10.4	1.8	15.9	1.7	11.3	13.0
$NaNb_2$	62	2.8	1.8	8.2	1.6	21.5	1.5	10.6	10.8
$NaNb_3$	60	3.4	0.7	6.8	1.8	21.3	1.6	12.0	11.5

[a] Reaction conditions: 42 mg catalyst, 100 mg substrate, 4 g H_2O, 160 °C, 20 bar N_2, 1000 rpm, 1 h. GA: glycolic acid, Gly: glyoxal, GlycA: glyceraldehyde, PA: pyruvaldehyde, LA: lactic acid, FA: formic acid, AA: acetic acid, AcA: acetaldehyde.

Substrate scope for production of LA using $NaNb_2$ as a catalyst

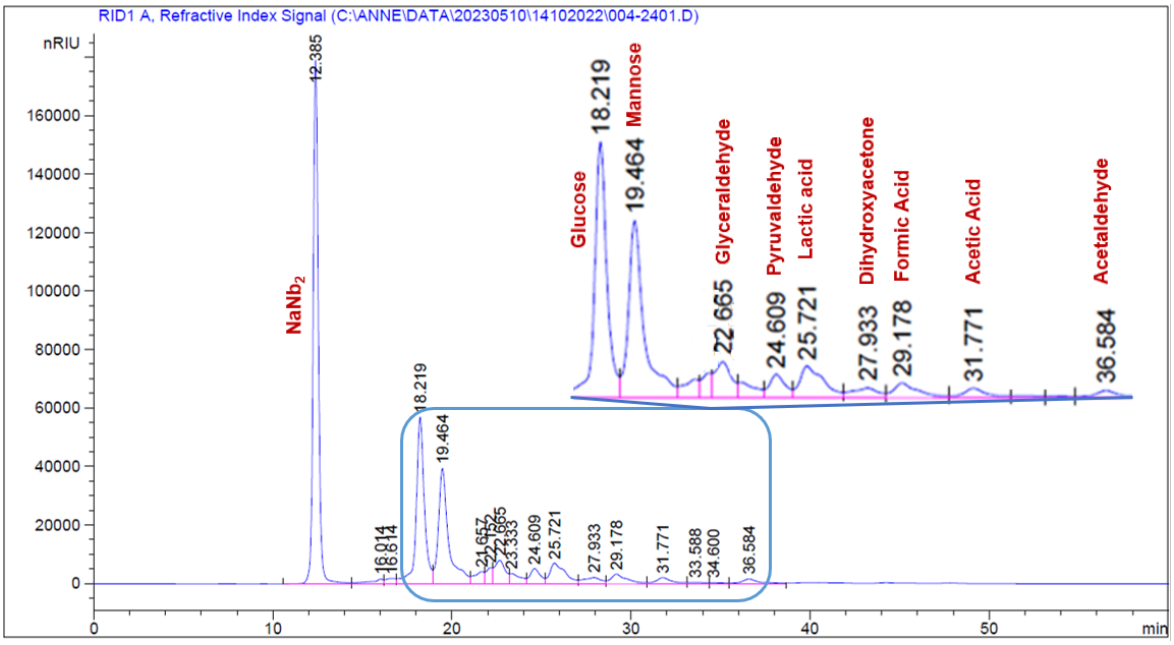

Figure S2: HPLC chromatogram displaying retention times of products from the catalytic conversion of glucose into LA with $NaNb_2$. Reaction conditions: 42 mg catalyst, 100 mg substrate, 4 g H_2O, 160 °C, 20 bar N_2, 1000 rpm, 1 h.

Table S3: Conversion and product yields for the conversion of different sugars into LA without catalyst (first entries) and with $NaNb_2$ (second entries).[a]

Substrate	X (%)	Yields (%)								
		Y_{DHA}	Y_{GlycA}	Y_{PA}	Y_{LA}	Y_{FA}	Y_{AA}	Y_{AcA}	Y_{Glu}	Y_{Man}
Glucose	0	0	0	0	0	0	0.0	0.0	-	0.0
Glucose	76.9	3.6	4.3	4.4	9.8	5.3	4.1	5.1	-	13.6
Fructose	0	0	0	0	0	0.0	0.0	0.0	0.0	0.0
Fructose	97.4	2.3	5.3	2.1	10.0	5.0	6.6	5.6	4.2	3.4
Sucrose	0	0	0	0	0	0.0	0	0.0	0.0	0.0
Sucrose	100	2.1	10.7	3.4	11.3	5.6	6.2	6.0	16.1	14.8
Xylose	0.0	0	0	0	0	0.0	0.0	0.0	0.0	0.0
Xylose	91.5	3.1	8.7	3.1	12.1	6.3	5.6	6.4	0.0	0.0
Mannose	0	0	0	0	0	0.0	0.0	0.0	0.0	-
Mannose	77.8	3.9	4.2	3.9	9.2	5.0	4.7	3.6	25.8	-
Cellobiose	2.9	0	0	0.0	0	0.0	0.0	0.0	0.0	0.0
Cellobiose	36.2	0	0.53	3.5	2.4	0.0	0.0	0.0	2.6	2.2

[a] Reaction conditions: 42 mg catalyst, 100 mg substrate, 4 g H_2O, 160 °C, 20 bar N_2, 1000 rpm, 1 h. DHA: dihydroxyacetone, GlycA: glyceraldehyde, PA: pyruvaldehyde, LA: lactic acid, FA: formic acid, AA: acetic acid, AcA: acetaldehyde, Glu: glucose, Man: mannose.

Table S4: Carbon balances and product selectivities for the conversion of different sugars into LA without catalyst (first entries) and with $NaNb_2$ (second entries).[a]

Substrate	Cb (%)	Selectivities (%)							
		S_{GlycA}	S_{PA}	S_{LA}	S_{FA}	S_{AA}	S_{AcA}	S_{Glu}	S_{Man}
Glucose	100	0.0	0.0	0.0	0.0	0.0	0.0	-	0.0
Glucose	83.4	5.6	5.8	12.7	6.9	5.4	6.7	-	17.7
Fructose	95.0	0.0	0.0	0.0	0.0	0.0	0.0	4.3	0.0
Fructose	44.1	5.5	2.2	10.3	5.1	6.8	5.7	1.9	3.5
Sucrose	100	0.0	0.0	0.0	0.0	0.0	0.0	0.0	0.0
Sucrose	73.2	10.7	4.0	11.3	5.6	6.2	5.9	16.1	14.8
Xylose	0.0	0.0	0.0	0.0	0.0	0.0	0.0	0.0	0.0
Xylose	49.3	9.5	3.4	13.2	6.9	6.1	7.0	0.0	0.0
Mannose	0.0	0.0	0.0	0.0	0.0	0.0	0.0	0.0	-
Mannose	52.8	5.4	5.1	11.8	6.4	6.1	4.7	33.2	-
Cellobiose	97.1	0.0	0.0	0.0	0.0	0.0	0.0	0.0	0.0
Cellobiose	74.6	1.5	9.6	6.6	6.6	0.0	0.0	7.2	6.1

[a] Reaction conditions: 42 mg catalyst, 100 mg substrate, 4 g H_2O, 160 °C, 20 bar N_2, 1000 rpm, 1 h. GlycA: glyceraldehyde, PA: pyruvaldehyde, LA: lactic acid, FA: formic acid, AA: acetic acid, AcA: acetaldehyde, Glu: glucose, Man: mannose.

Table S5: IR spectra band assignments.[2]

Wave number (cm^{-1})	Assignment
750 + 795	C-H Out of plane vibration substituted furan ring
965	C-H vibration furan ring
1020	C=C stretch vibrations
1090	C-O-C ether vibration
1160 + 1200	C-O-C deformation vibration furan ring
1295	C-H rocking vibration
1360	C-C framework vibration (furan) C6 sugars
1395	C-C framework vibration (furan) C5 sugars
1460	C-H aliphatic chain vibration
1510	C=C vibration aromatic couple bonds of polysubstituted furans
1600	C=C stretch vibration
1670	C=O carbonyl, aldehyde vibrations
1700	C=O stretch of acids, aldehydes and ketones

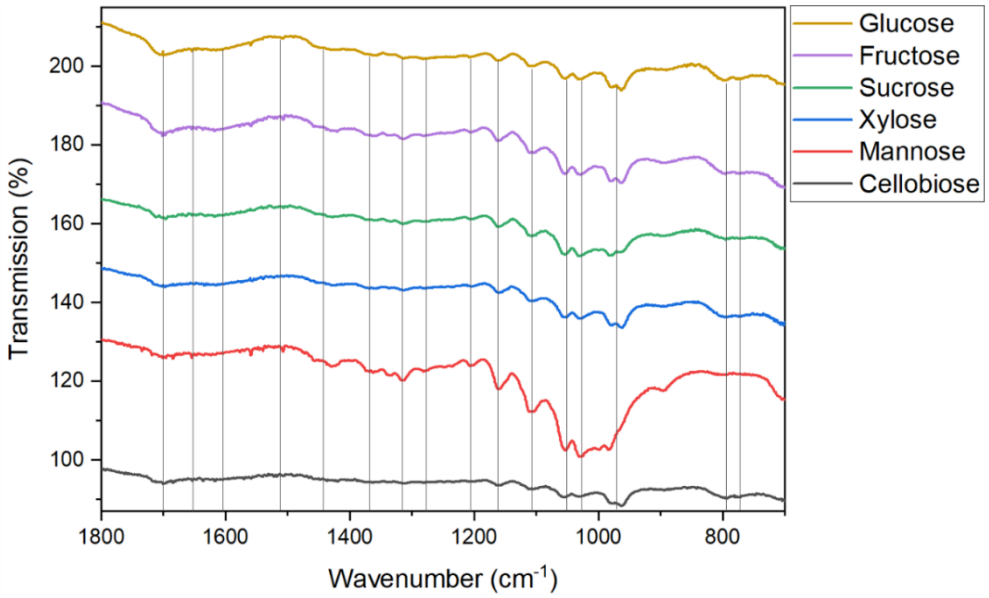

Figure S3: IR spectra of solid residues after the substrate screening experiments.

Table S6: Yields of selected by-products determined via NMR for the conversion of different sugars with $NaNb_2$.[a]

Substrate	Yields (%)						
	Y_{All}	Y_{Alt}	Y_{Xyl}	Y_{Ara}	Y_{Lyx}	Y_{Rib}	$Y_{other\ disacharides}$
Glucose	3.1	2.2	-	-	-	-	-
Xylose	-	-	-	7.0	5.5	2.4	-
Cellobiose	0.4	0.3	-	-	-	-	12.8

[a] Reaction conditions: 42 mg catalyst, 100 mg substrate, 4 g H_2O, 160 °C, 20 bar N_2, 1000 rpm, 1 h. All: allose, Alt: Altrose, Xyl: xylose, Ara: arabinose, Lux: lyxose, Rib: ribose.

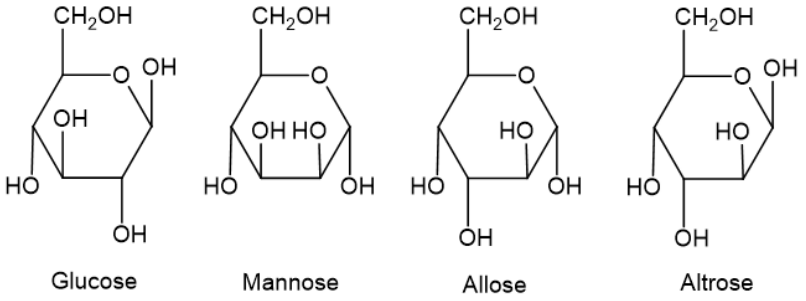

Figure S4: Structural formula of glucose and its isomers.

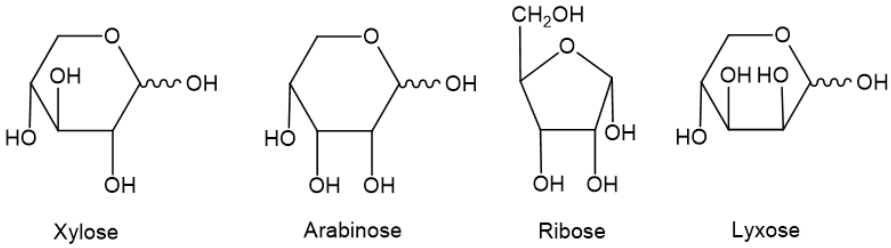

Figure S5: Structural formula of xylose and its isomers.

Post-reaction catalyst analysis

Table S7*:* pH-values for the conversion of different sugars into LA with $NaNb_2$ before ($pH_{initial}$) and after reaction (pH_{final}).[a]

Substrate	$pH_{initial}$	pH_{final}
Glucose	3.4	1.9
Fructose	3.5	2.1
Sucrose	3.6	2.4
Xylose	3.4	2.4
Mannose	3.4	1.9
Cellobiose	3.4	2.8

[a]Reaction conditions: 42 mg catalyst, 100 mg substrate, 4 g H_2O, 160 °C, 20 bar N_2, 1000 rpm, 1 h.

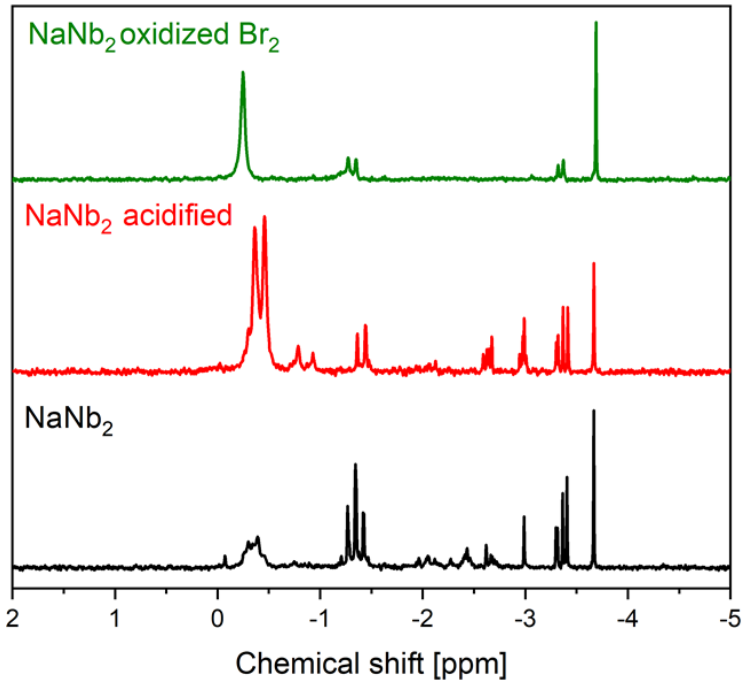

Figure S6: ^{31}P NMR spectra of $NaPNb_2$ in aqueous solution (bottom), $NaPNb_2$ in aqueous solution acidified to the pH value of the reaction solutions and of $NaPNb_2$ in the reaction solution, oxidized with elemental bromine.

References

[1] J.-C. Raabe, T. Esser, F. Jameel, M. Stein, J. Albert, M. J. Poller, *Inorg. Chem. Front.* **2023**, *10*, 4854.
[2] A. Wassenberg, T. Esser, M. J. Poller, J. Albert, *Materials* **2023**, *16,* e202300072.

9.5.2 Supporting Information of 2nd study: Transitioning to Immobilized Systems: Liquid-Phase Conversion of Biomass to Lactic and Formic Acid

in: A. Wesner, M. Papajewski, L. Schidowski, C. Ruhmlieb, M. Poller, Supported $H_8PV_5Mo_7O_{40}$ on activated carbon: Synthesis and Investigation of influencing factors for catalytic performance, *Daltons Trans*., **2024**, *53*, pp. 14065-14076.

Supported $H_8PV_5Mo_7O_{40}$ on activated carbon: Synthesis and Investigation of influencing factors for catalytic performance

– Supporting information –

Anne Wesner[a#], Max P. Papajewski[a], Leon Schidowski[a], Charlotte Ruhmlieb[b], Maximilian J. Poller[a], Jakob Albert[a*]

[a] Institute of Technical and Macromolecular Chemistry, University of Hamburg, Bundesstraße 45, 20146 Hamburg, Germany

[b] Institute of Physical Chemistry, University of Hamburg, Grindelallee 117, 20146 Hamburg, Germany

* Contact details of the corresponding author: jakob.albert@uni-hamburg.de

Supplementary catalyst characterization

Analysis methods

ICP-OES inorganic elemental analysis

Elemental analysis of each catalyst was conducted using inductively coupled plasma optical emission spectrometry (ICP-OES). Each sample, weighing 100 mg, was dissolved in a solution of 5 mL aqua regia and 1 mL concentrated HF using the Anton Paar Multiwave 7000 microwave system. The sample was then atomized in an argon plasma, and its elemental composition was quantified through optical emission spectrometry. This analysis was carried out with an ASCOR spectrometer (by Spectro) at the central element analysis service of the Department of Chemistry, University of Hamburg

CHNS(O) organic elemental analysis

CHNS analysis was employed to determine the composition of activated carbon using the "Euro EA3000" instrument by EuroVector. The sample was encapsulated in a tin capsule and combusted in a helium stream with oxygen addition at approximately 1000°C (Euro EA). The resulting combustion gases were separated gas chromatographically and analyzed using a thermal conductivity detector (WLD), which compared the thermal conductivity of the gas mixtures to that of pure helium. This allowed the determination of the CHNS content with the aid of standard substances.

For determination of oxygen content, the "Oxycube" device from Elementar (-OC) was utilized. Here, the substance was weighed into a silver capsule and pyrolyzed at 1450°C on nickel-coated carbon powder in a helium stream. The resulting combustion gases were separated through absorption and desorption processes and analyzed with a thermal conductivity detector (WLD), comparing the thermal conductivity of the produced CO with that of pure helium. The oxygen content was then determined based on a calibration with standard substances. This characterization was carried out at the Central Element Analysis Service of the Department of Chemistry, University of Hamburg.

N_2-physisorption

The textural properties of the activated carbons were determined using N_2-physisorption measurements. These measurements were conducted with the SA3100 Surface Area Analyzer from Beckman Coulter. Prior to the analysis, samples were degassed under vacuum at 50 °C for 10 hours. This characterization was performed at the Interdisciplinary Centre for Analytics in the Nanoscale (ICAN Centre). Average pore diameter was measured by following equation:

$$Ø\ pore\ diameter\ (nm) = \sum_i pore\ diameter_i \cdot incremental\ volume_i$$

XRD

Crystal structure determination was performed through powder X-ray diffraction (p-XRD) using a Panalytical MDP X'Pert Pro diffractometer, operating in Bragg-Brentano geometry with Cu Kα radiation (λ = 0.1541 nm). The diffraction angle was measured over a range of 10 to 80°, with a sampling rate of 0.013° every 0.3 seconds.

NH_3-TPD

Acidity was assessed using NH_3-Temperature Programmed Desorption (NH_3 TPD) on a ChemBET Pulsar device from Quantachrome Instruments. Samples weighing 0.06 g were initially purged with helium gas (80 mL/min) and heated to 130 °C at a rate of 10 K/min for an hour to eliminate surface water. NH_3 adsorption on the surface was conducted at the same temperature. Subsequently, the samples were heated to 750 °C under a helium flow (80 mL/min, 10 °C/min), and the desorbed NH_3 was detected using a Thermal Conductivity Detector (TCD). The integration of the NH_3-TPD spectra areas, indicative of weak to medium (150-500 °C) and strong (500-700 °C) acidity, was performed with Origin software, normalizing all measurements to the CW20 standard.

Microscopy

Scanning electron microscopy (SEM) and energy-dispersive X-ray spectroscopy (EDX) revealed catalyst morphology and metal dispersion. All measurements, including images and maps, were conducted using the "Leo 1550 Gemini" system. For the imaging, an acceleration voltage of 2 kV and an aperture of 7.5 µm diameter were employed. Conversely, all mappings were performed with an acceleration voltage of 20 kV and a 30 µm aperture. The Silicon Drift Detector (SDD) "Ultim Max 100" from Oxford Instruments, in conjunction with the "AZtec" software, was utilized as the detector for these analyses.

Point of zero charge measurement

For the determination of the point of zero charge in 40 mL of sodium nitrate solution (0.1 M), the pH was adjusted using sodium hydroxide solution (0.1 M and 0.005 M) and nitric acid (0.1 M and 0.005 M). The pH was set to values ranging from 2 to 11 to create ten solutions with varying pH levels ($ph_{initial}$). These solutions were then treated with activated carbon (200 mg). The suspensions were stirred for 24 hours at 300 rpm on magnetic stirrer plates. Subsequently, the suspensions were filtered, and the pH of the filtrate was determined (pH_{final}).

To determine the point of zero charge (PZC), the ΔpH (pH_final - pH_initial) of each solution was calculated and plotted against the initial pH value of the solution. The linear region of the curve was fitted, and the intersection point, where ΔpH = 0) was determined as the PZC.

Boehm titration

Boehm titration method was used to determine the oxygen functional groups. Initially, the following solutions were prepared: NaOH (0.1 M), Na_2CO_3 (0.05 M), $NaHCO_3$ (0.1 M), and HCl (0.1 M). Activated carbon (2.00 g) was suspended in each of these solutions (50 mL). The four resulting suspensions were stirred for 24 hours. After stirring, the suspensions were filtered. To determine the amount of substance, 10 mL of each filtrate was titrated with either HCl or NaOH using an Eco Titrator of Metrohm.[1]

Infrared spectroscopy

Infrared spectroscopy was employed for structural elucidation. Infrared spectra were acquired using an attenuated total reflection (ATR) setup, specifically a QATR™-S single-reflection ATR system with a diamond prism, manufactured by Shimadzu. The raw spectral data were processed to correct the baseline, and peak identification was conducted manually. Subsequently, the IR spectral data were converted and exported as x/y text files for further analysis.

Raman spectroscopy

Raman spectroscopy was applied to elucidate the surface chemistry and structural features of the catalysts. Raman spectroscopic measurements were conducted using a SENTERRA Raman microscope by Bruker Optik GmbH. The instrument's aperture was adjusted to 50 x 1000 µm, and a 20x objective lens was employed. The excitation laser, operating at a wavelength of 785 nm, facilitated measurements in the range of 75 cm^{-1} to 1525 cm^{-1}. The parameters for these measurements included an integration time of 16 seconds, a total of 8 scans, and a laser power set to 10 mW.

Thermogravimetric analysis

Thermogravimetric analysis (TGA) was performed utilizing a NETZSCH TG 209 F1 Libra instrument. Data processing was carried out using the NETZSCH Proteus software. For each analysis, 20 mg of the sample was weighed into an Al2O3 crucible, and mass changes were recorded in accordance with the applied temperature program. The temperature protocol involved a ramp up to 200°C at a rate of 2 K/min, maintained for 3 hours, followed by cooling down to room temperature. Throughout the measurements, a nitrogen flow of 20 mL/min was continuously passed through the instrument.

Characterization of HPA-5

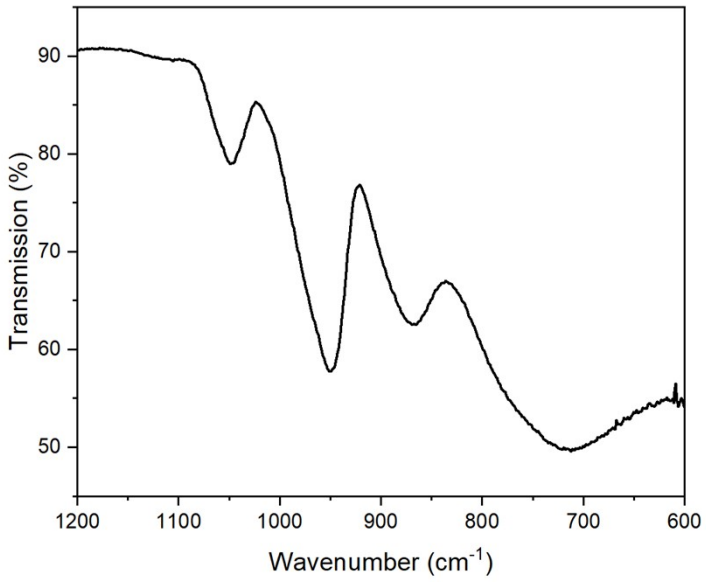

Figure S 1: Infrared spectra of bulk HPA-5.

Table S 1: Elemental and TGA analysis of bulk HPA-5.

	HPA-$5_{theor.}$	HPA-5
Loading[a]		
Mo (wt.%)[a]	41.84	36.19
P (wt.%)[a]	1.93	2.11
V (wt.%)[a]	15.87	13.86
Molar ratio Mo:V	7 : 5	7 : 5
Amount of Hydration water[b]		9.7 %

[a]determined via elemental analysis [b]determined via TGA analysis

Characterization of activated carbons

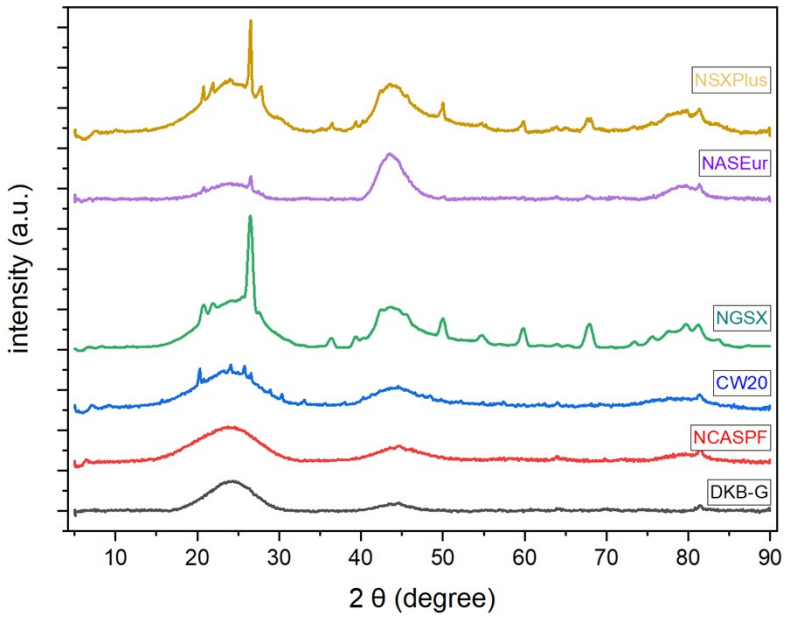

Figure S 2: XRD-diffractograms of pure activated carbons.

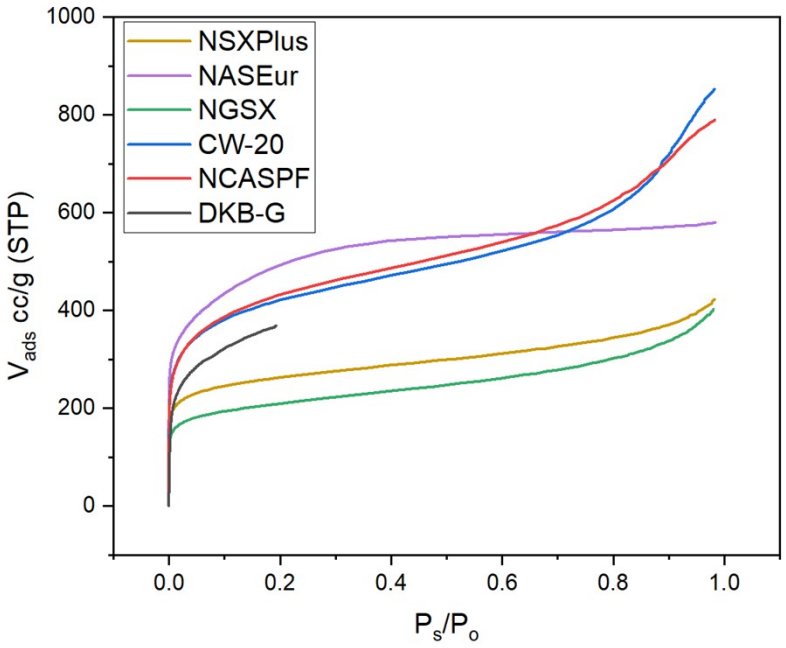

Figure S 3: Adsorption isotherms of pure activated carbons.

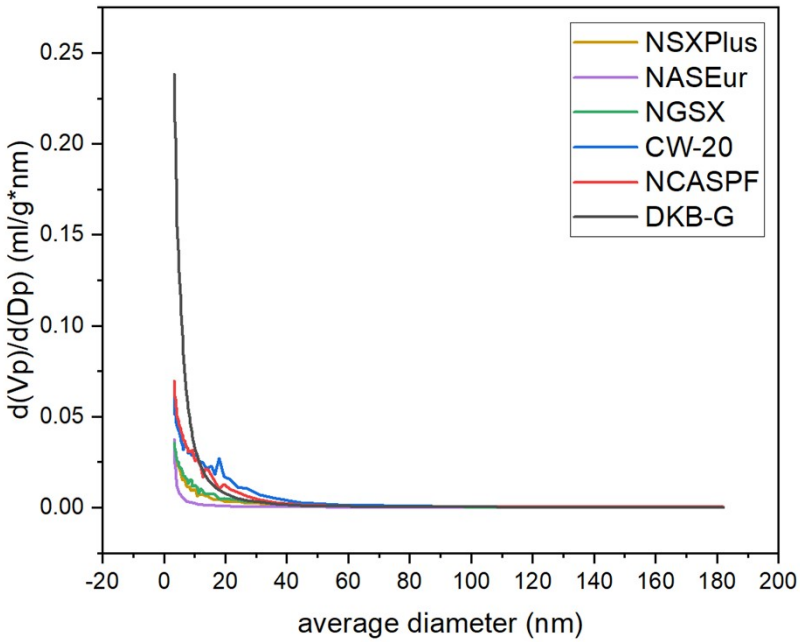

Figure S 4: Pore volumina of pure activated carbons.

Table S 2: Acidic properties of selected functional groups on carbon-based substrates.[2]

	Aqueous suspension
Carboxylic acid	Strong acidic
Anhdydrids	Strong acidic
Phenol	Acidic
Lactonic groups	Weakly acidic
Carbonyl groups	Weakly acidic
Pyrons	basic

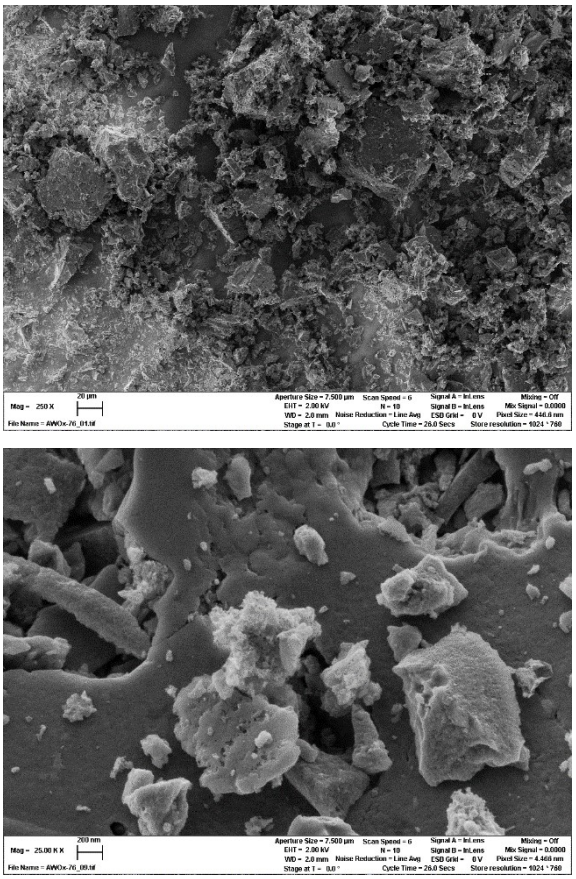

Figure S 5: SEM images of NSXPlus at magnifications of 250x and 25,000x.

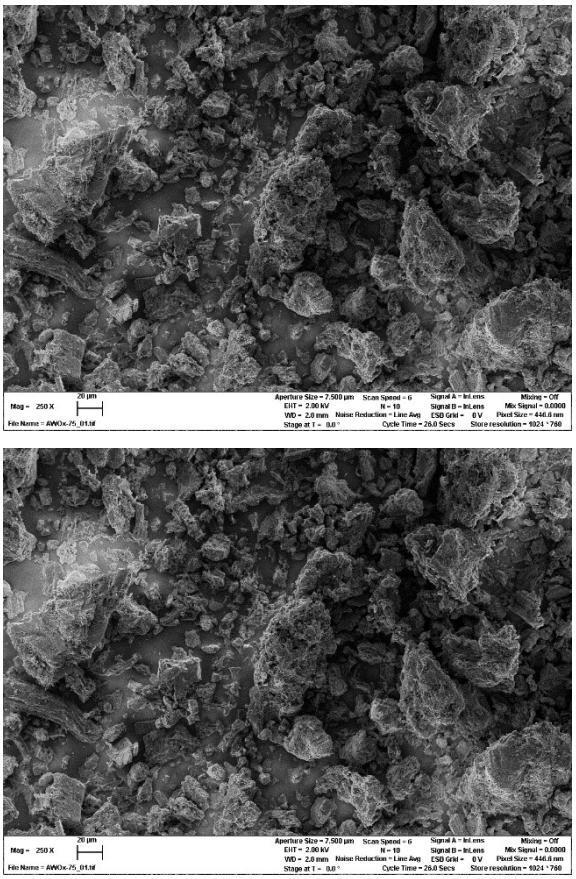

Figure S 6: SEM images of NASEur at magnifications of 250x and 25,000x.

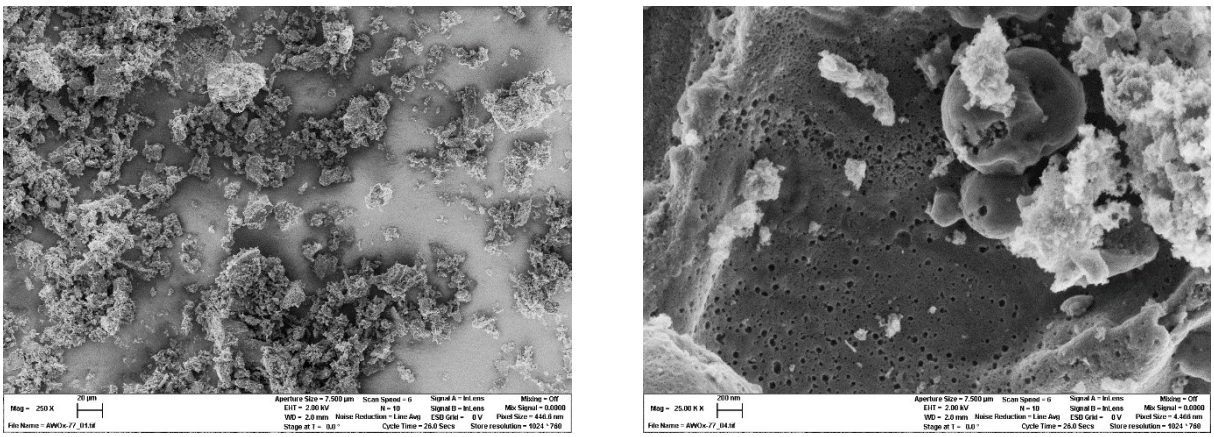

Figure S 7: SEM images of NGSX at magnifications of 250x and 25,000x.

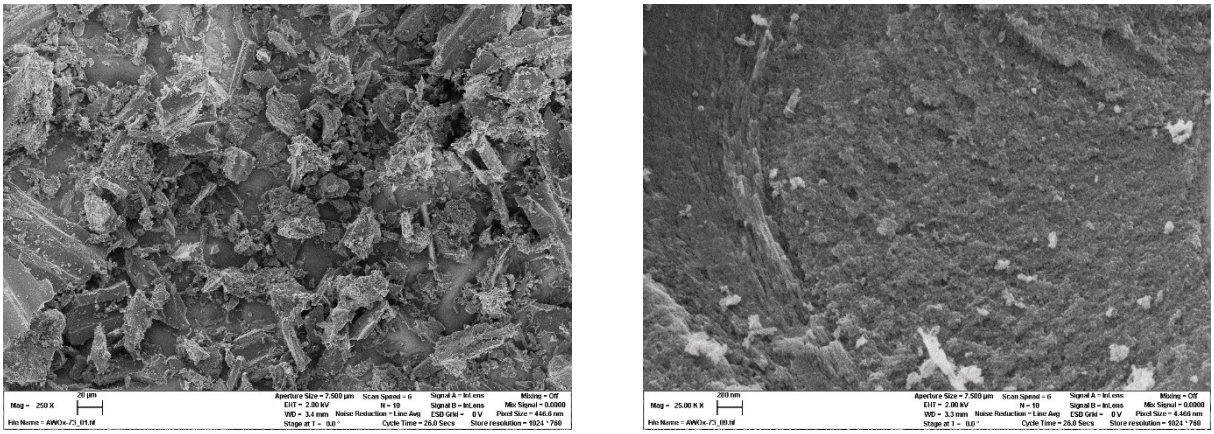

Figure S 8: SEM images of CW20 at magnifications of 250x and 25,000x.

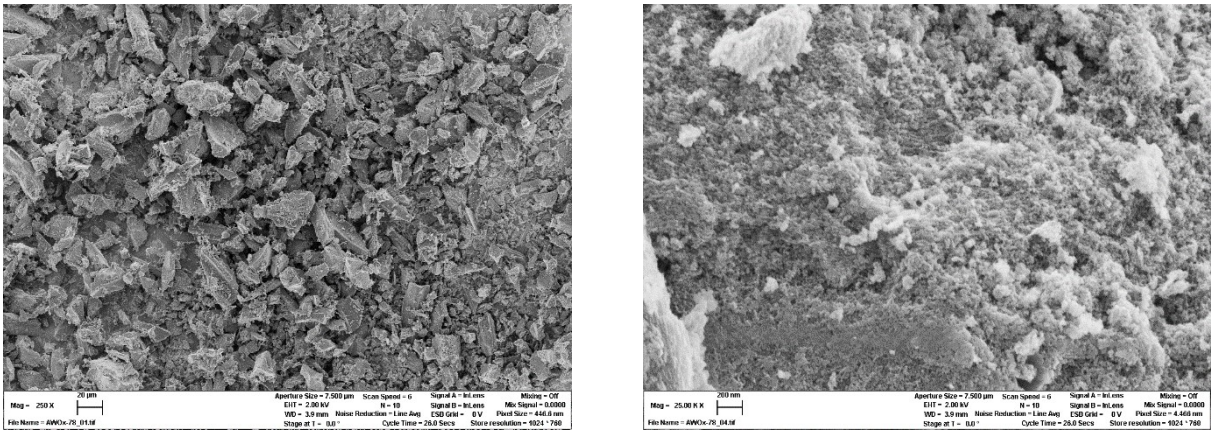

Figure S 9: SEM images of NCASPF at magnifications of 250x and 25,000x.

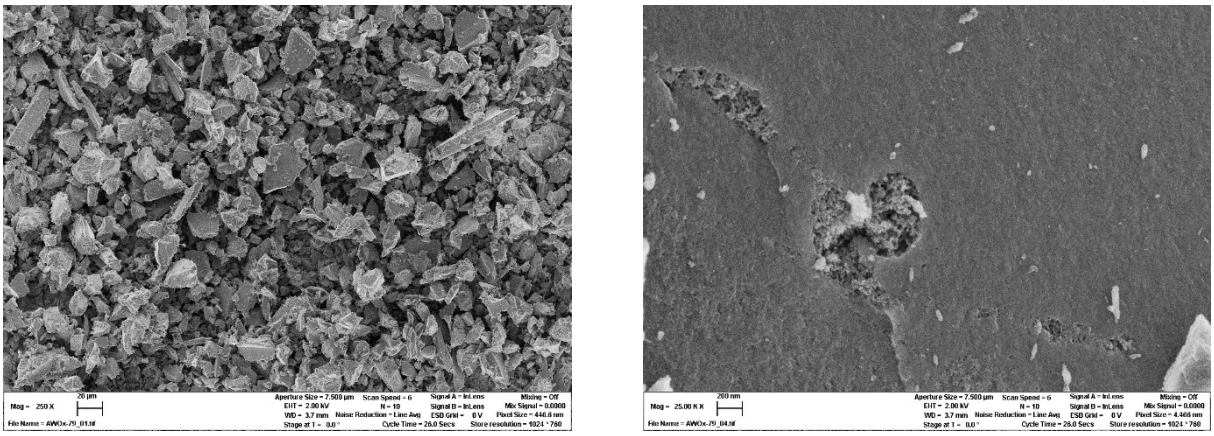

Figure S 10: SEM images of DKB-G at magnifications of 250x and 25,000x.

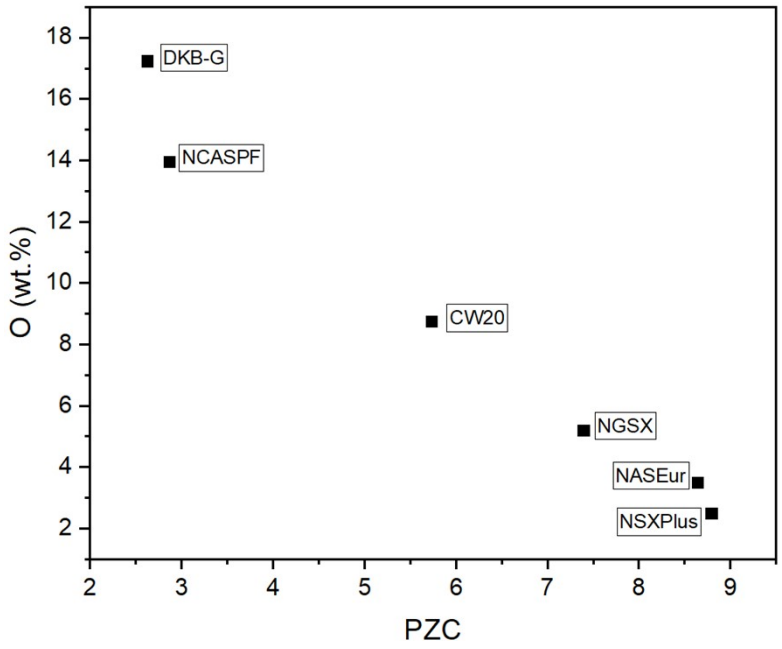

Figure S 11: Correlation between oxygen content and point of zero charge.

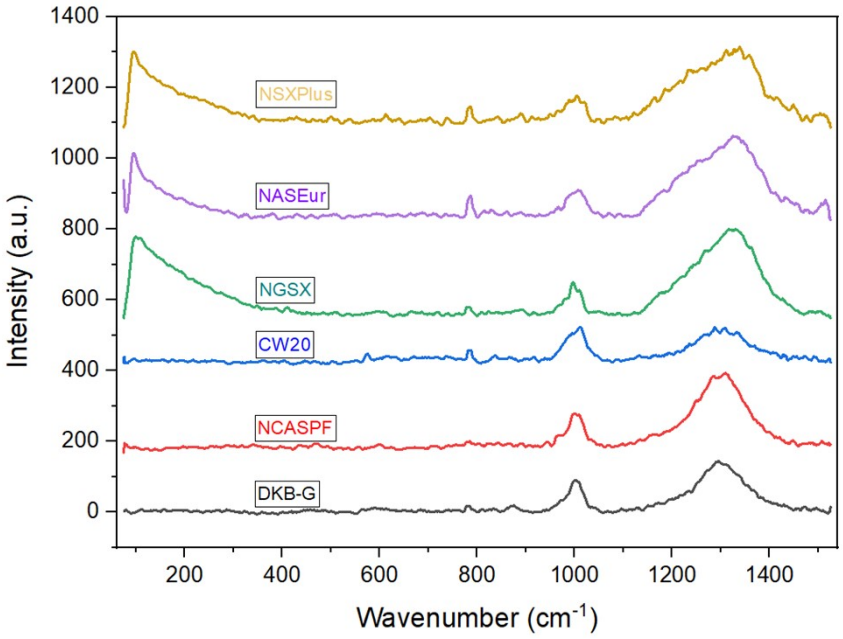

Figure S 12: Raman spectra of pure activated carbons.

Table S 3: positions of surface groups of activated carbons in infrared spectroscopy.[3]

	Assignment regions (cm-1)		
	1000-1500	1500-2050	2050-3700
C-O stretch of ethers	1000-1300		
Alcohols	1049-1276		3200-3640
Phenolic C-OH stretch	1000-1220		
Phenolic O-H bend/stretch	1160-1200		2500-3620
Carbonates	1100-1500	1590-1600	
Aromatics C=C stretching		1585-1600	
Quinones		1550-1680	
Carboxylic Acids (COOH)	1120-1200	1665-1760	2500-3300
Lactones	1160-1370	1675-1790	
Anhydrides	980-1300	1740-1880	
Ketones (C=C=O)			2080-2200
C-H stretch			2600-3000

HPA-5 supported on activated carbons

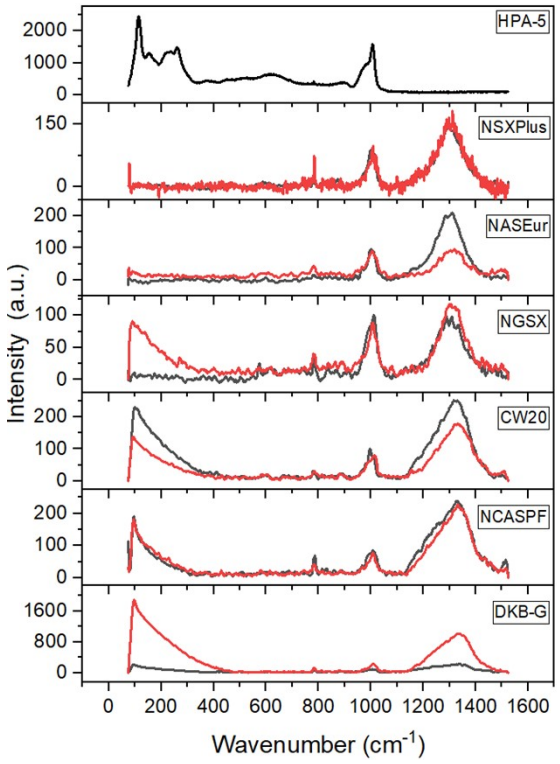

Figure S 13: Raman spectra of HPA-5 supported on various carbon materials.

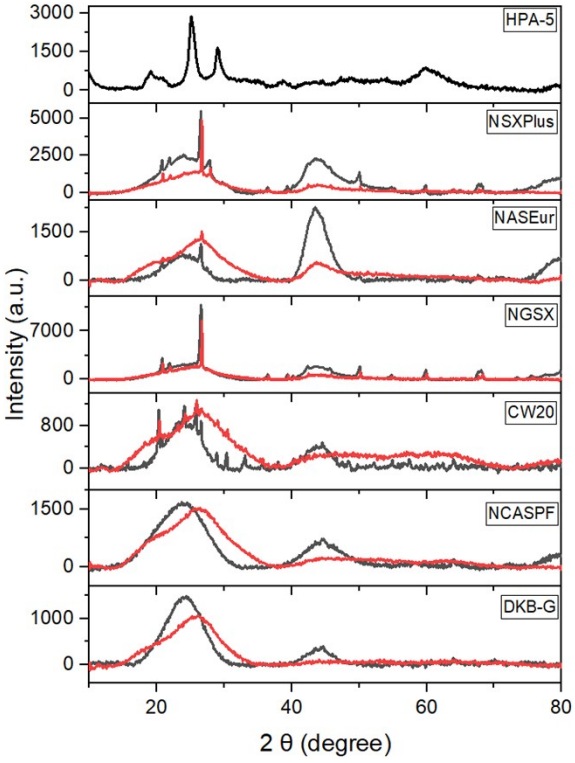

Figure S 14: XRD diffractograms of HPA-5 supported on various carbon materials.

NSXPlus

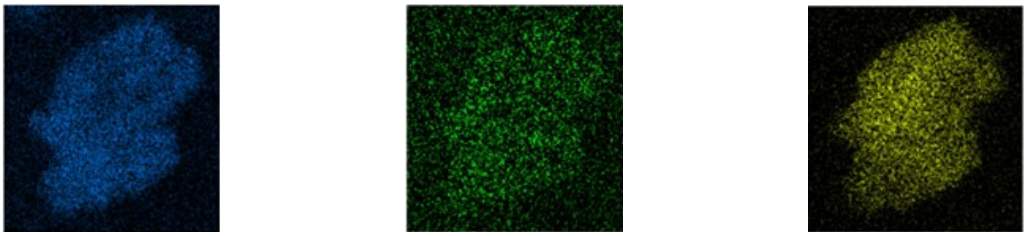

NASEur

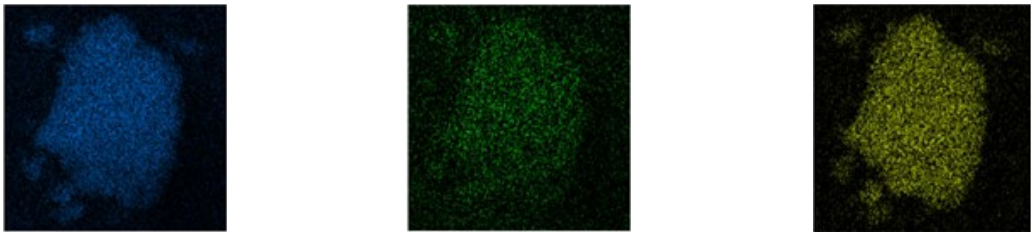

NGSX

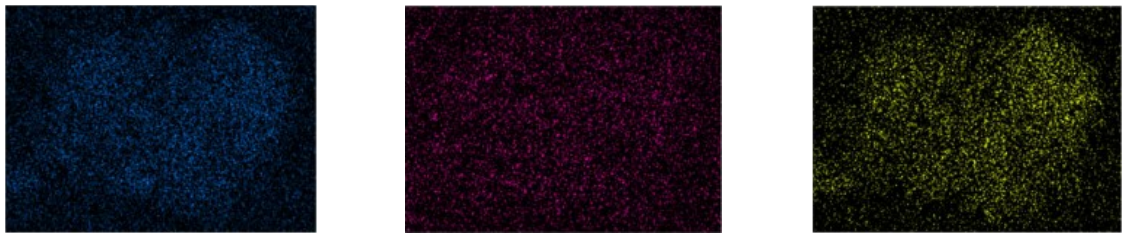

CW20

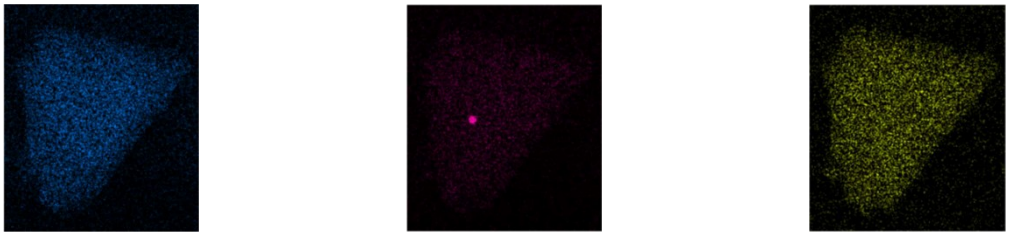

NCASPF

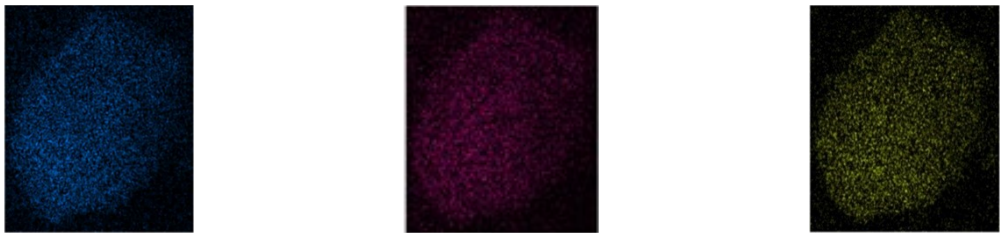

DKB-G

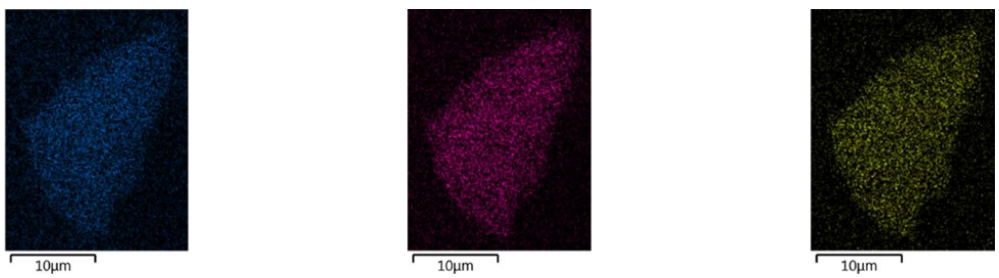

Figure S 15: SEM-EDX Mapping of impregnated carbons with Mo (blue), P (green & pink) and V (yellow).

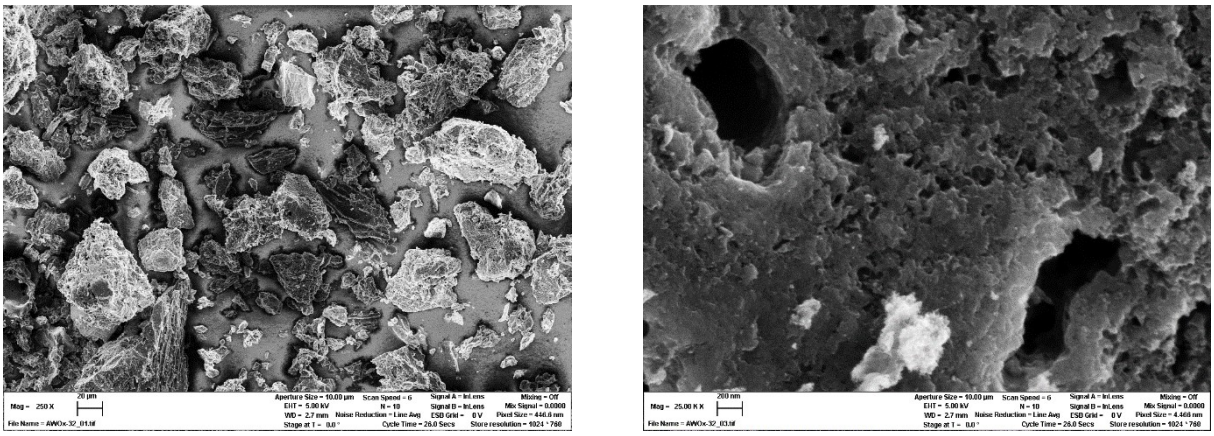

Figure S 16: SEM images of impregnated NSXPlus at magnifications of 250x and 25,000x.

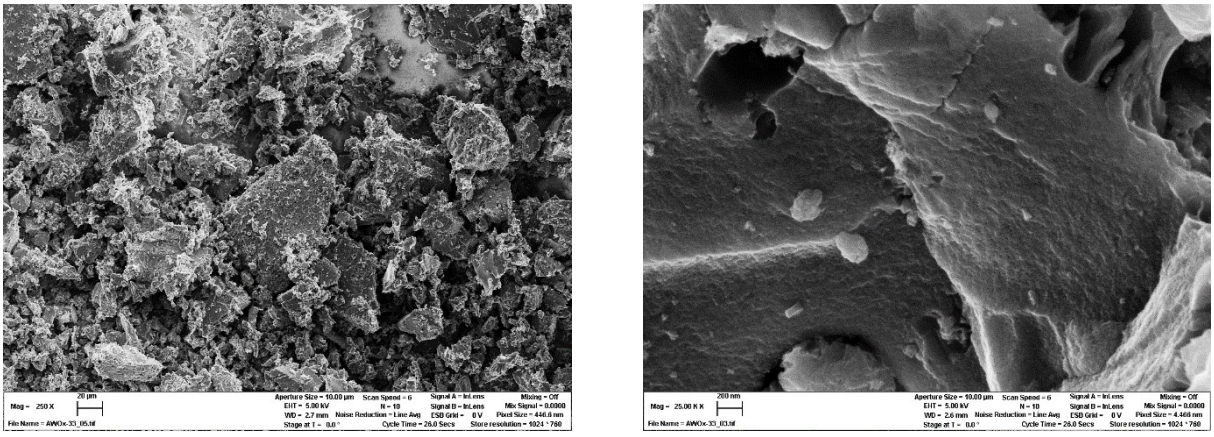

Figure S 17: SEM images of impregnated NASEur at magnifications of 250x and 25,000x.

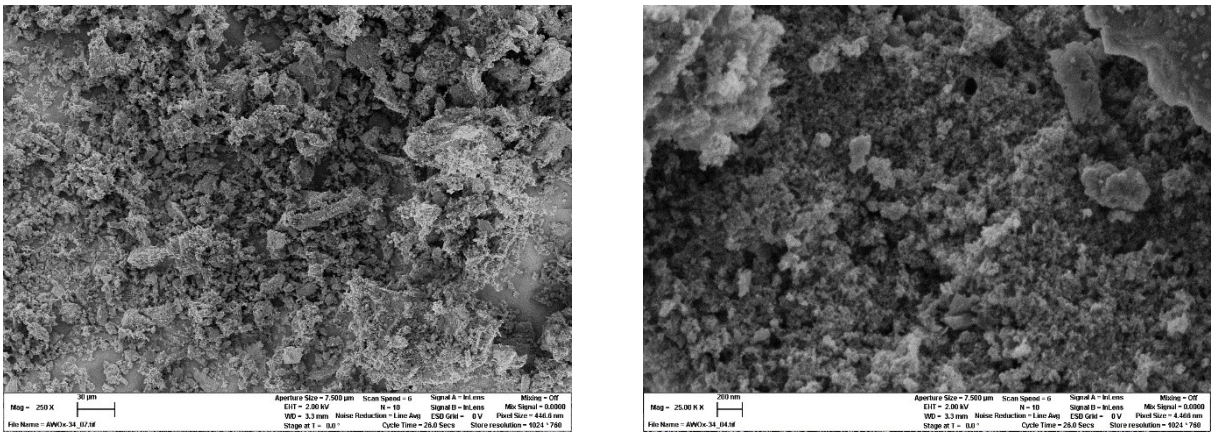

Figure S 18: SEM images of impregnated NGSX at magnifications of 250x and 25,000x.

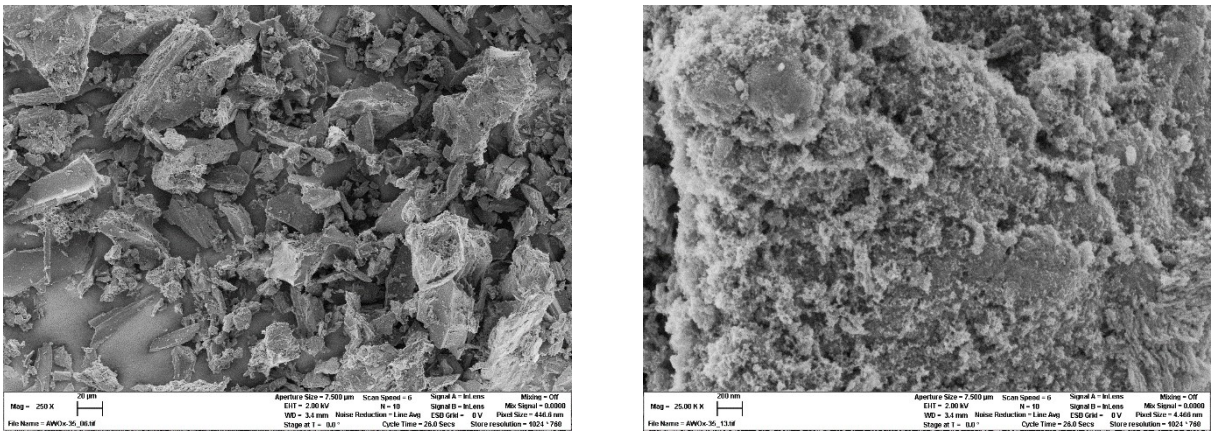

Figure S 19: SEM images of impregnated CW20 at magnifications of 250x and 25,000x.

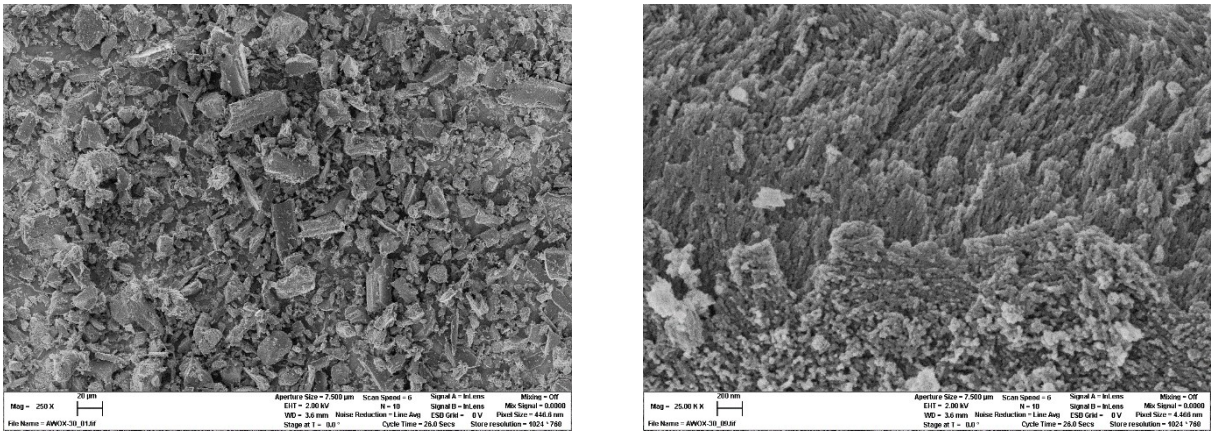

Figure S 20: SEM images of impregnated NCASPF at magnifications of 250x and 25,000x.

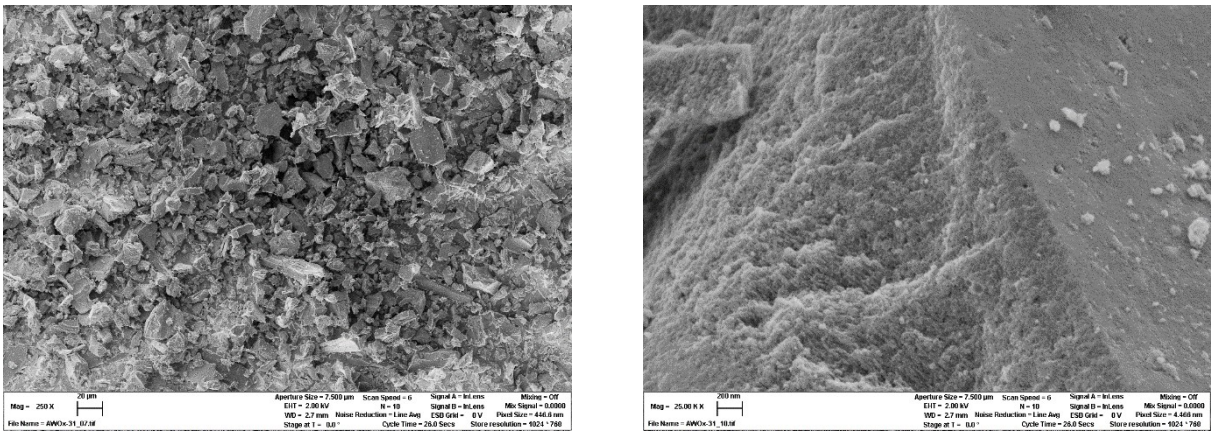

Figure S 21: SEM images of impregnated DKB-G at magnifications of 250x and 25,000x.

Supporting HPA-5 on CW20 by different synthesis methods

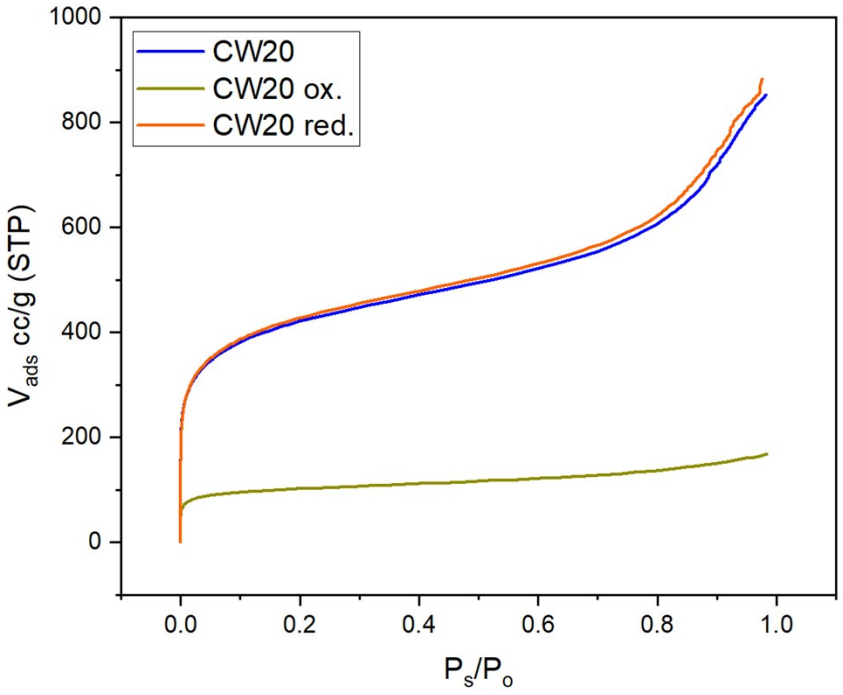

Figure S 22: Adsorption isotherms of untreated CW20 and pretreated $CW20_{ox.}$ and $CW20_{red.}$

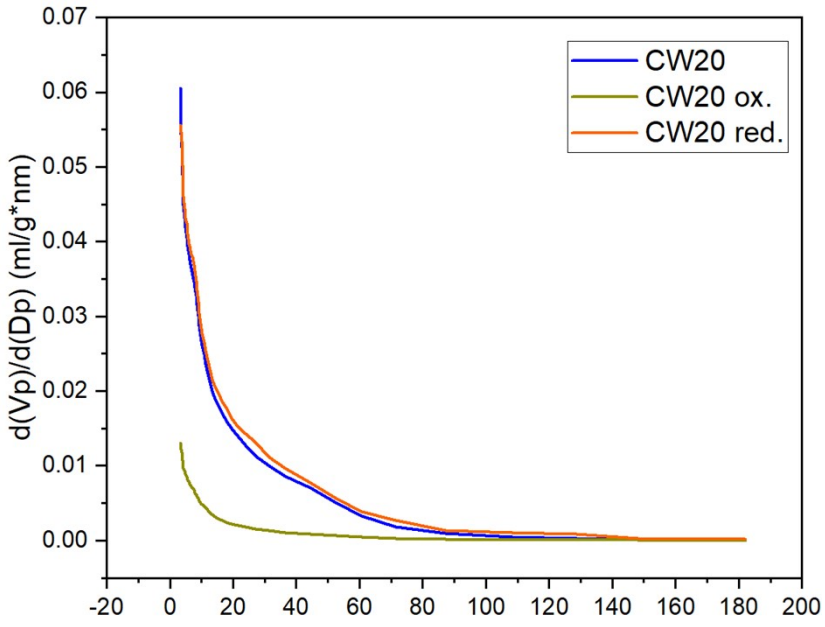

Figure S 23: Pore volumina of untreated CW20 and pretreated $CW20_{ox.}$ and $CW20_{red.}$

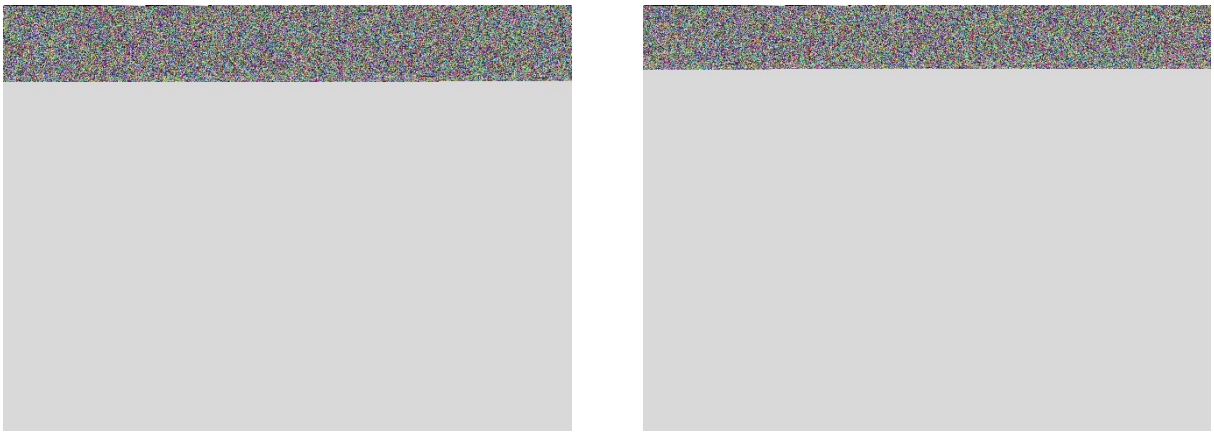

Figure S 24: SEM images of pure CW20 at magnifications of 250x and 25,000x.

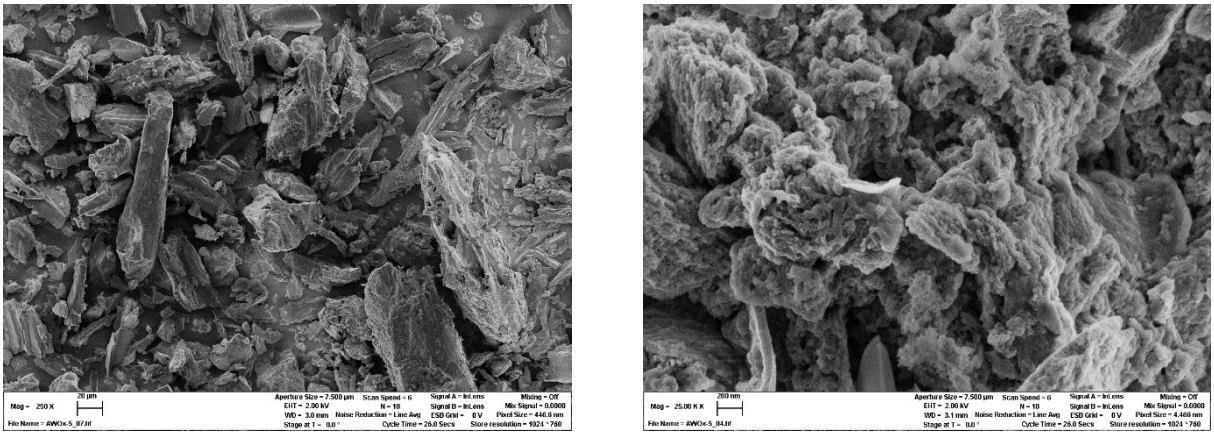

Figure S 25: SEM images of oxidized CW20 at magnifications of 250x and 25,000x.

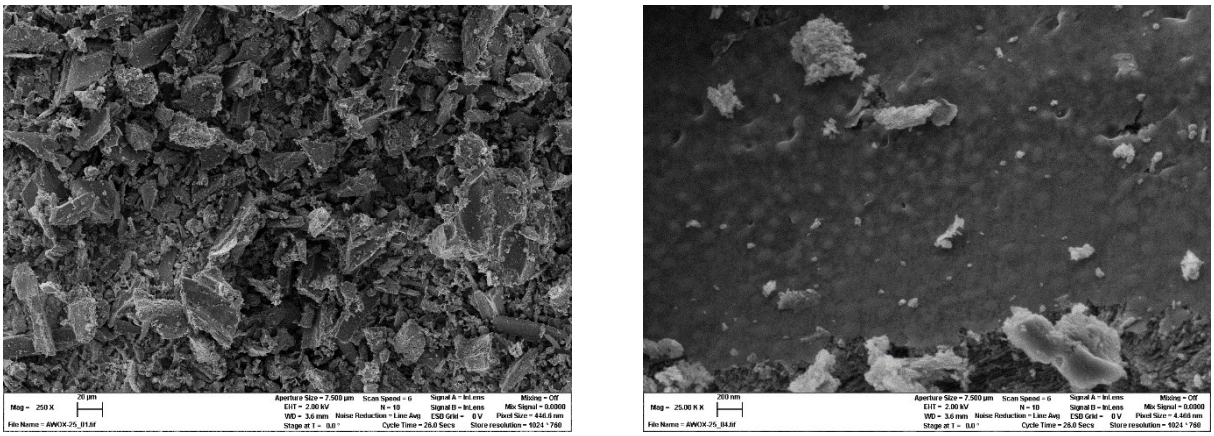

Figure S 26: SEM images of reduced CW20 at magnifications of 250x and 25,000x.

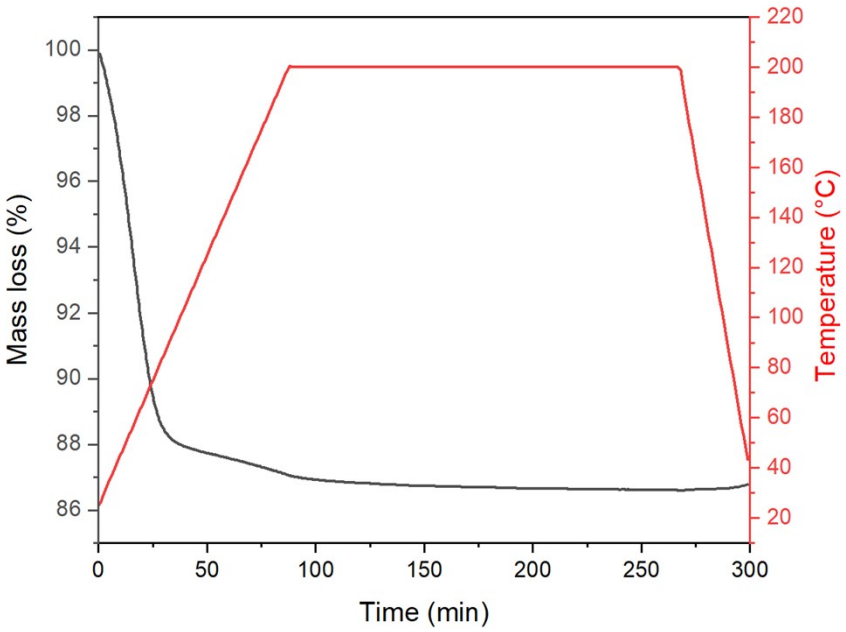

Figure S 27: TGA spectra of CW20 impregnated with HPA-5 (before washing).

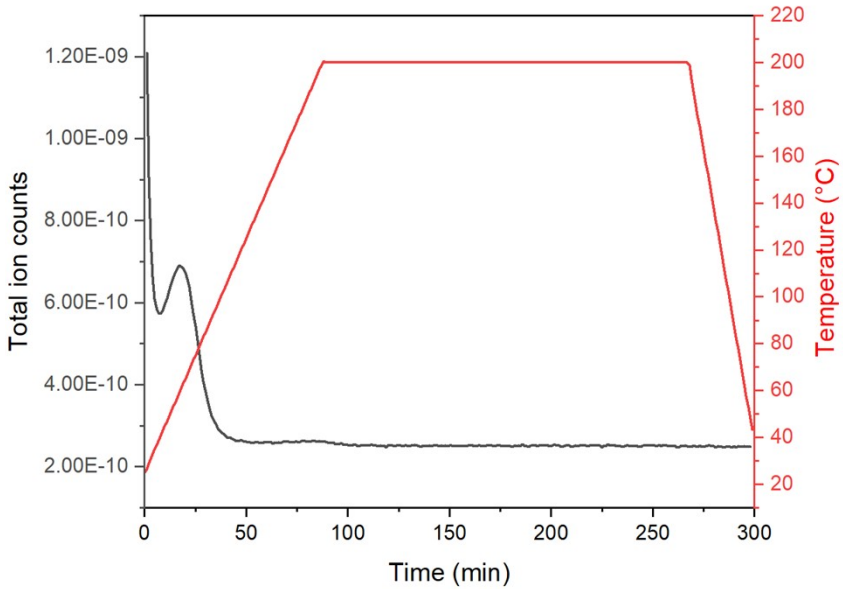

Figure S 28: Total ion counts (TIC) of TGA spectra of CW20 impregnated with HPA-5 (before washing).

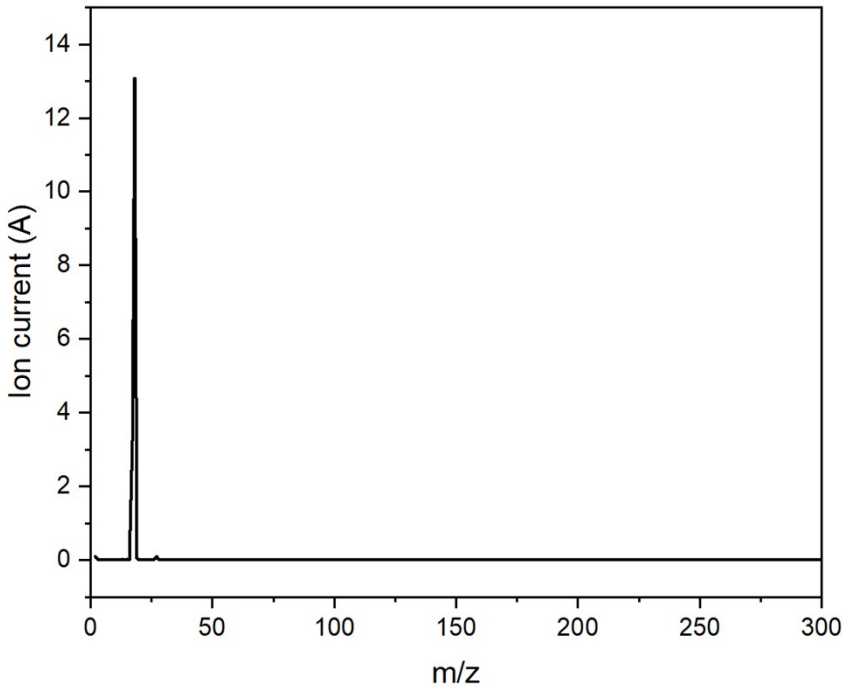

Figure S 29: m/z of maxima of maximum (TIC).

Experimental series 1

Experimental series 2

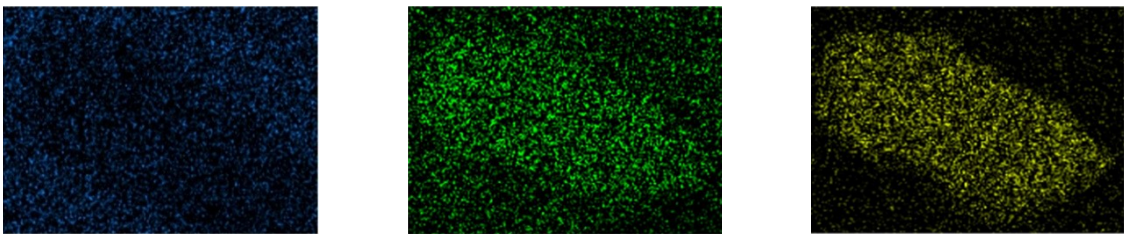

Experimental series 3

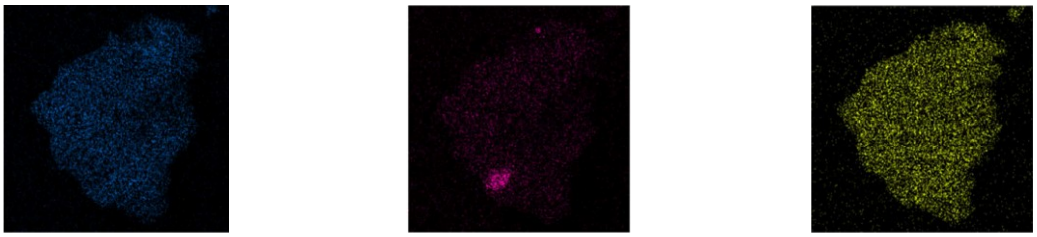

Experimental series 4

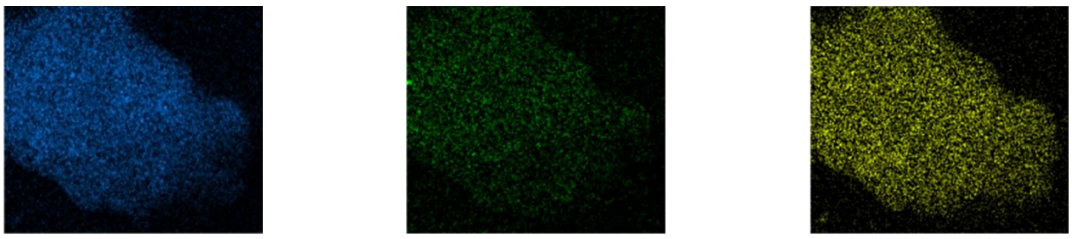

Experimental series 5

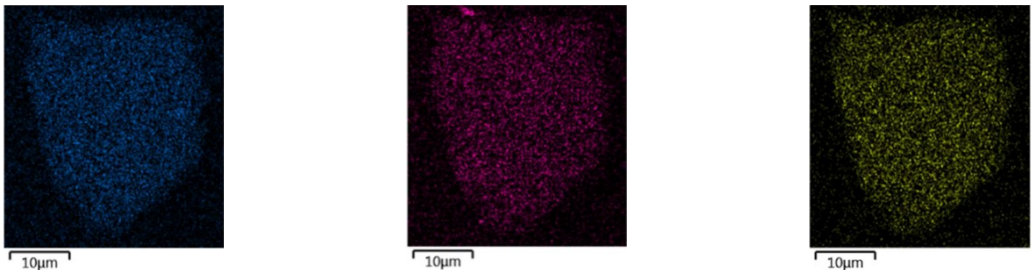

Figure S 30: SEM-EDX Mapping of CW20 after impregnation with different experimental series *with Mo (blue), P (green & pink) and V (yellow).*

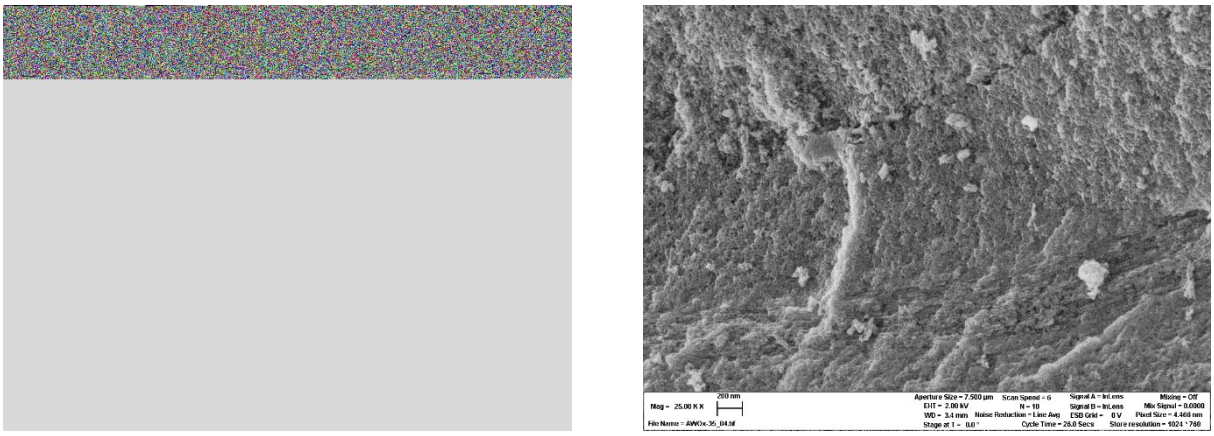

Figure S 31:SEM images of CW20_HPA-5 (exp. ser. 1) at magnifications of 250x and 25,000x.

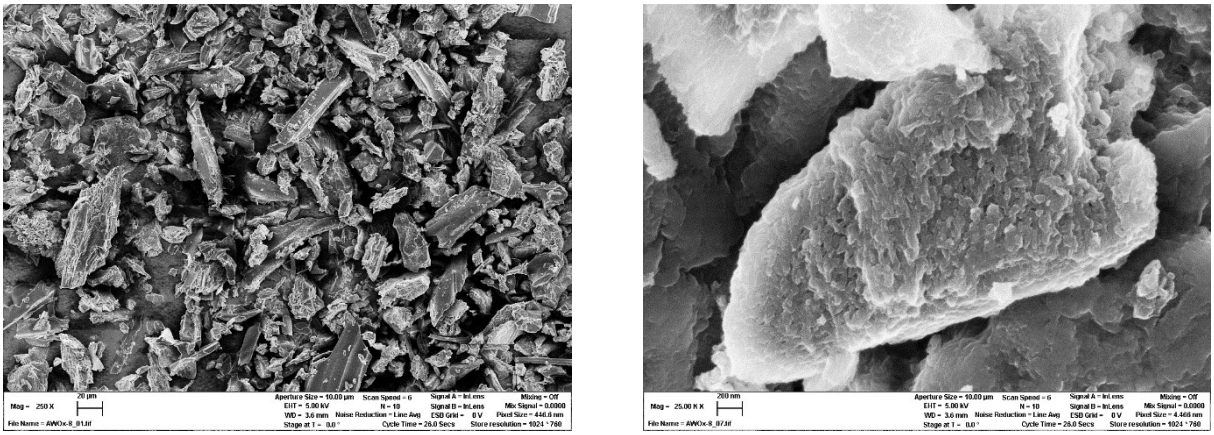

Figure S 32: SEM images of CW20_HPA-5 (exp. ser. 2) at magnifications of 250x and 25,000x.

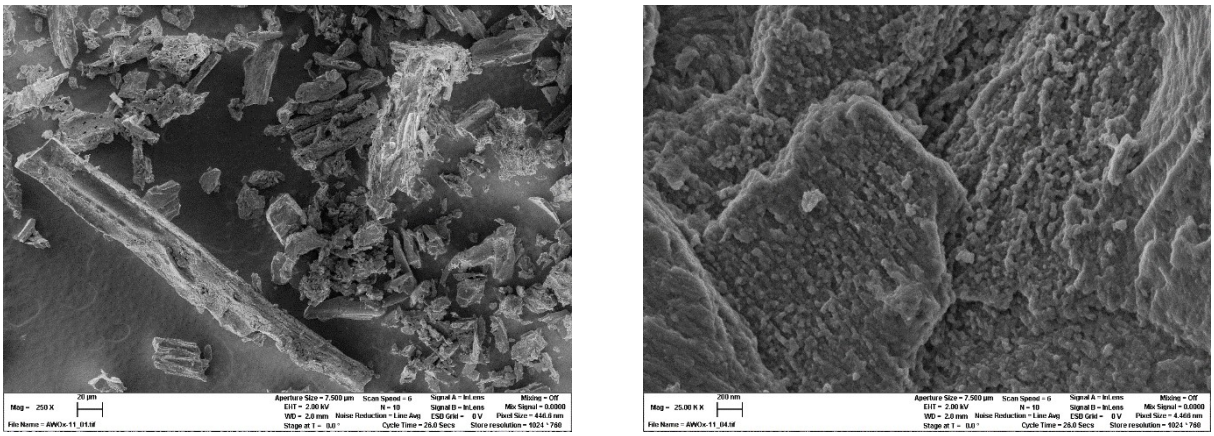

Figure S 33: SEM images of CW20_HPA-5 (exp. ser. 3) at magnifications of 250x and 25,000x.

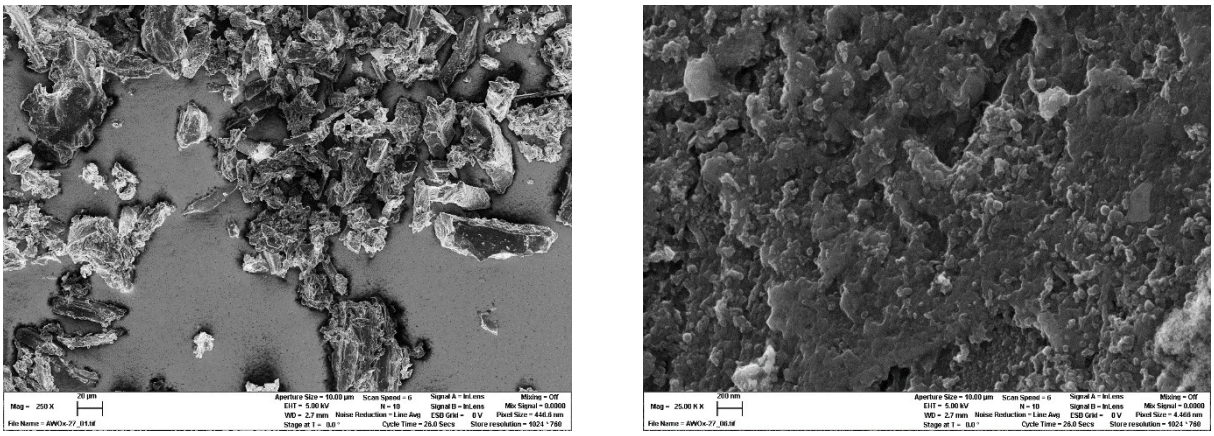

Figure S 34: SEM images of CW20_HPA-5 (exp. ser. 4) at magnifications of 250x and 25,000x.

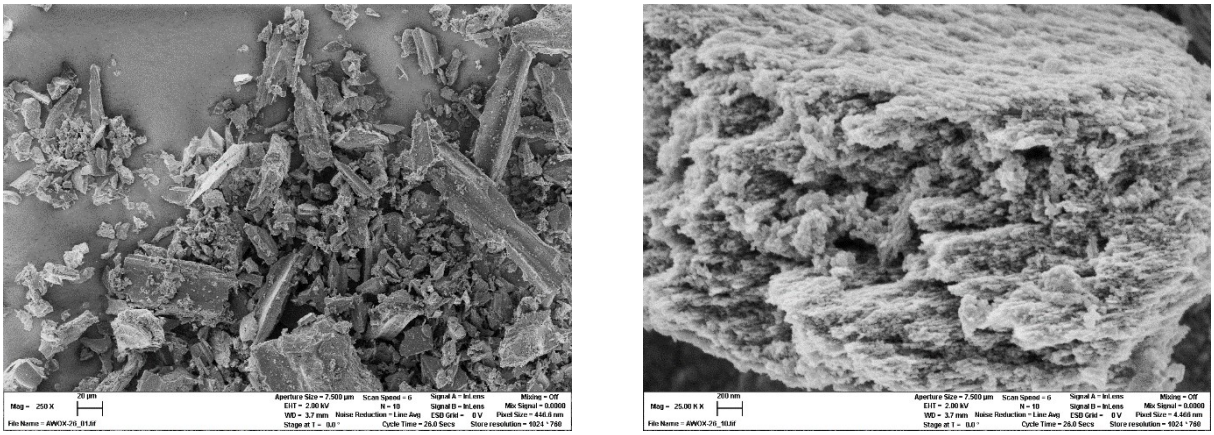

Figure S 35: SEM images of CW20_HPA-5 (exp. ser. 5) at magnifications of 250x and 25,000x.

Supplementary catalytic evaluation and determination of catalytic parameters

Catalytic experiments

The catalytic experiments were conducted in a three-fold plant consisting of three 100 mL stainless-steel (1.4571) reactor vessels made by HALMOSI. For stirring, a stainless-steel (1.4571) gas-entraining stirrer by Parr was used which was powered by an IKA Ministar 20. Graphite-based gaskets (Novaphit® MST/XP) were applied to provide reactor tightness. Each reactor was supplied with a heating jacket and two independent PT-100 thermostats measured the temperatures of the liquid phase inside the reactor and of the reactor wall. The pressure was measured both by analogous and digital pressure gages. Both temperature and pressure were regulated by Eurotherm controllers.

For the reaction, glass liners (21 mL tare volume) made of quartz glass fitting a maximum volume of 55 mL were utilized. For the oxidation, both glucose and catalyst were weighed and transferred to the glass liners – for glucose a mass of 3.603 g (20 mmol) and for the catalyst a mass of 1.821 g (pure HPA-5: 1.14 mmol). For the retro-aldol reaction, for glucose a mass of 1.032 g (5.7 mmol) and for the catalyst a mass of 0.406 g (pure HPA-5: 0.25 mmol)

Subsequently, the glass liner was filled with 45 mL (oxidation) or 40 ml (retro-aldol condensation) of deionized water. The glass liner was then transferred to the reactor vessel and the reactor was closed tightening five screws at a maximum torque of 15 Nm. To remove the air inside the reactor, three purges with O_2 were conducted. For the first two purges the pressure was elevated to 10 bar and for the last purge to 25 bar. The third purge at elevated pressure was also used to detect any leakages. The pressure was then set to 20 bar O_2 (oxidation) or N_2 (retro-aldol condensation), the stirrer was set to 300 rpm and the temperature was set to 90 °C (oxidation) or 160 °C (retro-aldol condensation). Once the temperature was reached, the stirrer was set to 1000 rpm, which was the reaction start point.

After 6 h (oxidation) or 1 h (retro-aldol condensation), the reaction was stopped by setting stirrers to 300 rpm, dismantling heating jackets and using pressurized air to cool down the reactors to 30 °C (approx. for 15 min). Gas samples were taken and the suspension inside the glass liners was filtered. Lastly, the filter cake was washed with 50 mL of water and dried for 24 h at 40 °C.

Analysis of substrates and reaction products

ICP-OES

Analogous to catalyst characterization

Infrared spectroscopy

Analogous to catalyst characterization

HPLC

The liquid reaction solution underwent quantitative analysis via High-Performance Liquid Chromatography (HPLC), employing a SHIMADZU HPLC system. This system was equipped with a BIORAD Aminex HPX-87H column (300 mm x 7.8 mm) and a refractive index detector for the analysis. For the conversion of glucose to formic acid, the HPLC analysis included an injection volume of 10 µL, a column temperature of 45 °C, and a flow rate of 0.5 ml/min. In the analysis of glucose conversion to lactic acid, the procedure involved an injection volume of 10 µL, a column temperature maintained at 30 °C, and a flow rate set at 0.3 ml/min.

HPLC determination of retention time and calibration for catalyst screening was performed using the following chemicals: glucose (n.a. Merck Milipore, 1.08337.1000), mannose (≥99 %, Sigma Aldrich, M2069-25G), fructose (≥99 %, VWR, 0226-1KG), glyoxal (40 %, Merck, 8206100100), glyceraldehyde (≥90 %, VWR, G5001-5G), erythrose, (75 %, Sigma Aldrich, E7625-1G), glycoaldehyde (), formic acid (99-100 %, AnalaR Normapur, 20318.322), acetic acid (79-81 %, Carl Roth, 20G164011), lactic acid (90 %, GPR Rectapur, 20356.298), acetaldehyde (≥99 %, VWR, 20877.265).

GC

Quantitative analysis of the gaseous reaction products was performed using a Varian 450-GC, which is equipped with column Shin Carbon ST (2 m · 0.75 mm) and with both a TCD-GC detector and an FID detector. The GC analysis protocol involved heating the system to 140°C at a rate of 15 K/min, followed by a holding period of 2.83 minutes. The TCD system operated with an argon flow at 300 °C, while the FID

was maintained at 200 °C, utilizing a hydrogen flow of 30 ml/min for combustion and an air flow of 310 mL/min.

Calculation of catalytic parameters

The conversion of glucose $X_{glucose}$ yield for all products (Y_P), the selectivities towards formic acid (S_{FA}) and lactic acid (S_{LA}), as well as the turnover-number (TON) were determined using the following equations:

$$X_{glucose} = \frac{n_{glucose,initial} - n_{glucose.\ final}}{n_{glucose.\ initial}} \cdot 100\ \% \quad \text{(S1)}$$

$$Y_P = \frac{n_p}{n_{glucose.\ initial}} \cdot 100\ \% \quad \text{(S2)}$$

$$S_{FA/LA} = \frac{Y_{FA/LA}}{X_{glucose}} \cdot 100\ \% \quad \text{(S3)}$$

Here, $n_{glucose,inital}$ represents the initial amount of glucose used, and $n_{glucose,final}$ denotes the amount of glucose remaining at the end of the reaction. N_p signifies the molar amount of specified product, n_{ps} encompasses the molar amounts of all resulting products.

Supplementary catalytic results and characterization

Applying supported HPA-5 for the catalytic conversion of glucose

Oxidative conversion of glucose analogous to the OxFA process

Table S 4: Catalytic parameters for conversion of glucose to formic acid.

	1	2	3	4	5	blank	HPA-5
	Yields (%)						
Fructose	1.13	0.49	1.57	1.57	1.49	1.22	1.07
Glyoxal	1.35	6.44	2.47	2.47	1.87	0.00	3.21
Glycerinaldehyde	6.08	2.02	5.73	5.72	7.30	0.00	5.34
Erythrose	7.50	3.60	7.64	7.63	8.39	0.00	0.00
Glycoaldehyde	1.80	2.62	3.82	3.82	1.95	0.00	0.00
Formic Acid	31.11	24.13	34.43	34.38	31.86	0.00	40.49
Acetic Acid	0.30	0.15	1.27	1.27	0.37	0.00	0.53
Carbon dioxide	19.07	7.56	6.69	5.31	0.01	0.30	7.37
Carbon monooxide	1.54	1.04	0.46	0.14	0.00	0.00	0.30
Selectivity to formic acid (%)	39.92	44.57	50.41	48.86	45.37	0.00	53.43
Conversion (%)	77.94	54.14	68.30	70.36	70.23	2.38	75.78
Carbon balance	91.94	93.92	95.80	91.96	83.02	99.13	85.15
Initial pH	2.59	2.64	2.86	2.56	2.64	3.84	1.25
Final pH	1.38	1.32	1.03	1.30	1.28	2.69	1.39

Table S 5: Catalytic parameters for conversion of glucose to formic acid: Experimental series 1 (1) and repetition (1_rep.).

	1	1_rep.
	Yields	
Fructose	1.13	1.35
Glyoxal	1.35	2.32
Glycerinaldehyde	6.08	6.63
Erythrose	7.50	4.80
Glycoaldehyde	1.80	1.80
Formic Acid	31.11	27.43
Acetic Acid	0.30	0.00
Carbon dioxide	19.07	12.32
Carbon monooxide	1.54	3.00
Selectivity to formic acid	39.92	37.56
Conversion	77.94	73.02
Carbon balance	91.94	84.44

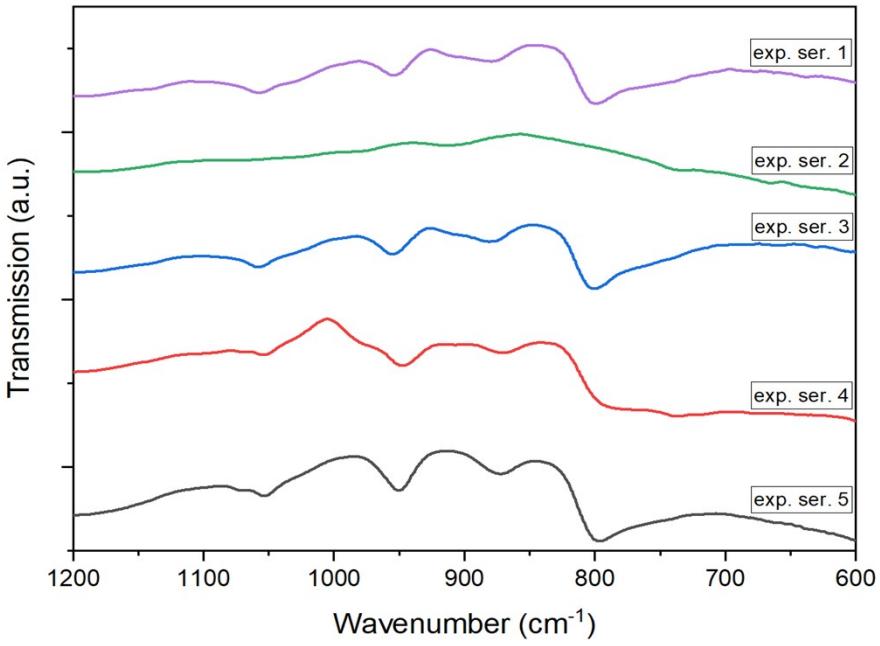

Figure S 36: IR-spectra of CW20 after impregnation with different experimental series after reaction (glucose to formic acid).

Inert conversion of glucose analogous to retro-aldol-condensation

Table S 6: Catalytic parameters for conversion of glucose to lactic acid.

	1	2	3	4	5	blank	HPA-5
	Yields (%)						
Mannose	29.79	24.69	32.75	32.65	25.19	4.34	29.74
Glyceraldehyde	0.45	0.58	0.34	0.40	3.54	0.00	0.45
Lactic Acid	10.32	8.44	9.76	9.82	6.07	0.00	10.30
Formic Acid	2.71	1.96	1.67	1.85	2.09	0.00	2.71
Acetic Acid	0.86	0.00	0.00	0.00	0.00	0.00	0.86
Acetaldehyde	3.09	1.78	4.09	4.58	1.88	0.00	3.09
CO_2	1.58	1.36	0.61	0.80	0.63	0.09	0.42
Selectivity to lactic acid (%)	14.55	13.00	14.88	14.98	9.22	0.00	14.51
Conversion	70.92	64.92	65.58	65.56	65.88	2.54	70.97
Carbon balance	77.90	73.89	83.64	84.55	73.52	100	76.59
Initial pH	2.96	3.16	2.93	2.97	3.40	5.77	1.92
Final pH	2.41	2.65	2.52	2.56	2.65	3.31	2.32

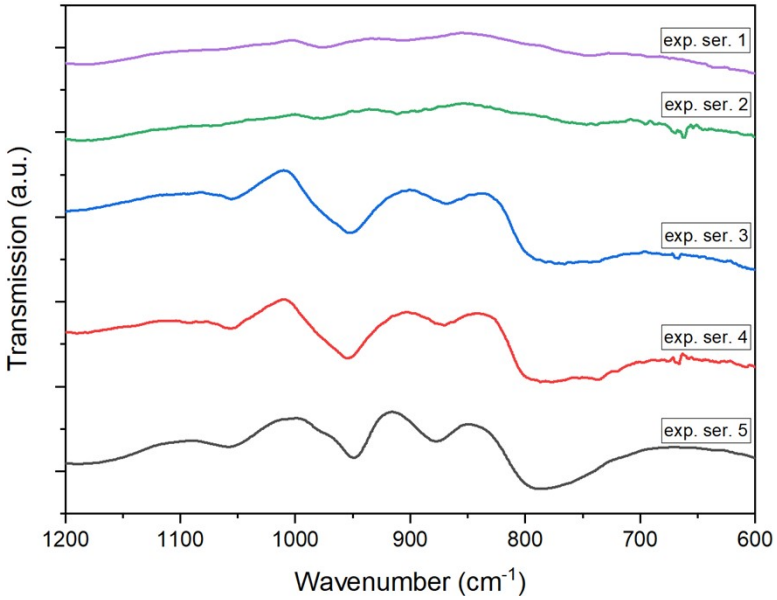

Figure S 37: IR-spectra of CW20 after impregnation with different experimental series after reaction (glucose to formic acid).

References

(1) Bandosz, T. J.; Jagiello, J.; Schwarz, J. A. Comparison of methods to assess surface acidic groups on activated carbons. *Anal. Chem.* **1992**, *64*, 891–895.

(2) Kohl, S. *Oberflächenoxide auf kohlenstoffbasierten Materialien.*, 2010.

(3) Fanning, P. E.; Vannice, M. A DRIFTS study of the formation of surface groups on carbon by oxidation. *Carbon* **1993**, *31*, 721–730.

9.5.3 Supporting Information of 3rd study: Expanding to Gas-Phase Applications: Immobilized Polyoxometalates for CO_2 Conversion to Dimethyl Ether

in: A. Wesner, N. Herrmann, L. Prawitt, A. Ortmann, J. Albert, M. J. Poller, Study of supported heteropolyacid catalysts for one step DME synthesis from CO_2 and H_2, *RSC Advances*, **2025**, *15*, pp. 38-47.

Study of supported heteropolyacid catalysts for one-step DME synthesis from CO_2 and H_2 – Supplementary Information

Anne Wesner[a#], Nick Herrmann[a], Lasse Prawitt[a], Angela Ortmann[a], Jakob Albert[a], Maximilian J. Poller[a*]

[a]Institute of Technical and Macromolecular Chemistry, University of Hamburg, Bundesstraße 45, 20146 Hamburg, Germany

* Contact details of the corresponding author: Phone: (+49)-40 42838 3172
e-mail: maximilian.poller@uni-hamburg.de

Table of Contents

Catalyst synthesis

All chemicals were used as received without further purification for the synthesis of all catalysts.

Table S 1: Chemicals used.

substance	purity / %	company	art.-no.
H_3PO_4	≥ 85	Grüssing	881303334
MoO_3	99.5	Thermo Scientific	206361000
$In(OH)_3$	99.8	Thermo Scientific	011855.18
HCl	n.s.	Thermo Scientific	15401327
$H_4SiW_{12}O_{40}$ x n H_2O	99	Sigma Aldrich	1006590100
Al_2O_3	n.s.	Thermo Scientific	43832
TiO_2	n.s.	Thermo Scientific	44429
Celite® 545	n.s.	Merck	1.02693.0000
Montmorillonite K10	n.s.	Sigma-Aldrich	69866
$Cu/ZnO/Al_2O_3$ catalyst	n.s.	Alfa Aesar	45776
$H_3PMo_{12}O_{40}$	≤ 100	Sigma-Aldrich	79560
$H_3PW_{12}O_{40}$	≤ 100	Sigma-Aldrich	P4006
$NaNO_3$	99	Grüssing	881216623
NaOH	99	Grüssing	881215841

Synthesis of HPAs

Synthesis of $H_6PInMo_{11}O_{40}$ *(HPInMo)*

MoO_3 (20.02 g) and H_3PO_4 (85 %; 1.47 g) were dissolved in water (200 ml) and refluxed with stirring for two hours. During this process, additional H_3PO_4 (0.44 g) was added incrementally. $In(OH)_3$ (2.10 g) was dissolved in 20 ml of water and 10 ml of conc. HCl and then added to the reaction mixture, which was further refluxed for 30 minutes. Subsequently, the solvent was evaporated using a rotary evaporator (80 °C, 200 mbar, 200 rpm), and the product was completely dried (80 °C, 0 mbar, 200 rpm). Synthesis was adapted according *Odyakov*.[1]

Synthesis of $H_8PV_5Mo_7O_{40}$ *(HPVMo)*

Firstly, MoO_3 (44.3 g) was dispersed in deionized water (500 ml) and mixed with a 25% aqueous H_3PO_4 solution (16.9 g). This mixture was heated to reflux, resulting in a clear yellow solution. Simultaneously, V_2O_5 (20.0 g) was suspended in H_2O (750 ml) and cooled down to 0°C. A 30% H_2O_2-solution (165 ml) was added dropwise while stirring, leading to the dissolution of V_2O_5 into a red/brown solution accompanied by gaseous

O_2 release. After complete dissolution, a 25% aqueous H_3PO_4 (3.0 g) was added and the mixture was stirred at ambient temperature. The V_2O_5-solution was then dropwise combined with the refluxing MoO_3-solution. The mixture was further refluxed for another hour, then allowed to cool to room temperature under reduced pressure, followed by filtration to obtain a red or dark brown solid.[2,3]

Synthesis of $H_4SiMo_{12}O_{40}$ (HSiMo).

MoO_3 (34.55 g) was suspended in 500 ml of H_2O and NaOH (12.75 g) was added until the solid was completely dissolved. Na_2SiO_3 (2.44 g) was solved in a few milliliters of H_2O and added to the molybdate while stirring vigorously. This gave a yellow solution which was acidified with HCl (1 mol/l) to pH 1.4. An unsuccessful attempt was made to extract the product from the acidic reaction solution using diethyl ether. The solution was acidified more to pH 0.745, but the organic phase remained colorless. Organic and aqueous phases were concentrated and 10.00 g of crude product was obtained. The crude product was then dissolved in 100 ml water. A greenish yellow solution was obtained and some white solid settled to the bottom. 10 ml HCl (37 %) and 10 ml H_2O_2 (35 %) were added and the solution turned bright yellow again. Since the white solid did not dissolve again it was filtered off. The filtrate was extracted with 10 x 50 ml $C_4H_8O_2$, causing the organic phase to turn intensely yellow, but the aqueous phase hardly decolorized at all. Lastly, the organic phase was concentrated to dryness and an amorphous green solid was obtained. Synthesis was adapted according Strickland.[4]

Supporting of HPAs

HPA catalyst selection for DME synthesis – Supporting of various HPAs on K10

Montmorillonite K10 was used as a support for various HPAs. For this purpose, 7.01 g of the HPA and 12.00 g of K10 were weighed, to achieve an HPA-unit loading of 1 HPA unit/nm^2. The HPAs that were impregnated included: $H_4SiW_{12}O_{40}$ (HSiW), $H_3PMo_{12}O_{40}$ (HPMo), $H_3PW_{12}O_{40}$ (HPW), $H_8PV_5Mo_7O_{40}$ (HPVMo), $H_6PInMo_{11}O_{40}$ (HPInMo), and $H_4SiMo_{12}O_{40}$ (HSiMo).

The HPA was dissolved in water (500 ml), and used at the resulting pH value without further adjustment, before the support was added. The suspension was mixed for three hours using a rotary evaporator (room temperature, 800 mbar, 111 rpm) and then the solvent was evaporated (80 °C, 200 mbar, 111 rpm). The product was dried for 20 hours at 100 °C.

Support selection for DME synthesis - Supporting HSiW on different supports

Different supports have been used for impregnation of HSiW: Al_2O_3, ZrO_2 TiO_2, Celite® 545. The metal oxides (Al_2O_3, TiO_2, ZrO_2) were initially ground using a mortar to achieve a particle size fraction ranging from 80 to 250 µm. Celite® 545 was used as received without any treatment. The synthesis procedure was analogous to that of different HPAs on K10.

Catalyst characterization

Inductively coupled plasma optical emission spectroscopy (ICP-OES)

The elemental composition of the catalysts was determined using ICP-OES. For microwave digestion, 10 to 20 mg of each catalyst was dissolved in a mixture of reverse aqua regia (HCl/HNO3 1:3) (5 ml) and 1 ml HF, then diluted to 50 ml. The sample was then atomized in an argon plasma. Quantification was based on the relative intensity of the element-specific spectral lines, using previously established calibration curves for the elements of interest. Measurements were carried out by the Central Element Analysis Service of the Department of Chemistry at the University of Hamburg, using an ASCOR spectrometer from Spectro.

N_2-physisorption

N_2-physisorption was performed to determine the textural properties of the materials. Measurements were conducted using an Autosorb iQ MP/XR instrument from Anton Paar, with Quantachrome® ASiQwin™ software utilized for data evaluation. The samples were degassed at 200°C for 10 hours under vacuum to remove surface water. The surface area was determined using the BET (Brunauer-Emmett-Teller) method, while pore volume and average pore diameter were derived from the BJH (Barrett-Joyner-Halenda) desorption isotherms.

X-ray diffraction (XRD)

The crystal structure of powdered catalysts was analyzed using XRD. This was conducted on a Panalytical MDP X'Pert Pro diffractometer, utilizing X-ray radiation generated at a copper source that diffracts off the lattice planes of the crystal samples. The diffraction pattern was recorded by a detector in the range of 10-80° with a scan rate of 0.013° per 0.3 seconds. The resulting diffractogram was processed and evaluated using X´Pert HighScore Plus software.

NH_3-Temperature Programmed Desorption (NH_3-TPD)

The acidity of the catalysts was determined using NH_3-TPD. Measurements were carried out on a Chembet Pulsar TPD/TPR analyzer from Quantachrome Instruments, the data were analyzed using the ASiQwin software. For this analysis, 160 mg of the catalyst was placed in a measurement cell and pre-treated at 150 °C for 1 hour under a helium flow of 80 ml/min to remove any adsorbed species. This was followed by cooling down of the sample to 100 °C and the adsorption of NH_3 at this temperature to saturate the catalyst's surface. Subsequently, loosely bound NH_3 was removed by flowing helium (80 ml/min) over the sample for 1 hour. Finally, TPD measurements were conducted from 150 to 450°C at a heating rate of 10 K/min. The amount of desorbed NH_3 was quantified using a Thermal Conductivity Detector (TCD). The areas under the NH_3-TPD curves, were integrated using Origin software. This analysis normalized all measurements against HSiW/ZrO_2 as standard to ensure consistency and comparability across the samples.

Microscopy

Scanning electron microscopy (SEM) measurements were employed to elucidate the metal dispersion and morphology of the catalysts. These measurements were carried out using a Leo 1550 Gemini scanning electron microscope from Zeiss. For SEM imaging, an acceleration voltage of 2 kV and an aperture diameter of 7.5 µm were utilized. Element distribution maps were created using an acceleration voltage of 20 kV and a 30 µm aperture. The Silicon Drift Detector Ultim Max 100 from Oxford Instruments, combined with AZtec software, was used as the detector. The mapping process for each sample required 10-15 minutes.

Point of zero charge measurement

The determination of the point of zero charge (PZC) for the supports was conducted with a Lab 850 pH meter from Fisher Scientific, using a SI Analytics BlueLine 14 pH electrode for precise pH measurements. To achieve a range of pH values from 2 to 11, adjustments were made in 40 ml of sodium nitrate solution (0.1 M) utilizing NaOH (0.1 M and 0.005 M) and HNO_3 (0.1 M and 0.05 M), thereby setting the initial pH

($pH_{initial}$) for each experiment. A suspension was then prepared by combining each solution with the support material and stirring continuously at 300 rpm for 24 hours. Subsequently, the pH of each solution was measured (pH_{final}). For analysis, the change in pH ($\Delta pH=pH_{final}-pH_{initial}$) was calculated for each suspension and plotted against $pH_{initial}$. The intersection of this line with the x-axis (where $\Delta pH=0$) was determined to be the PZC of the support material.

Infrared spectroscopy (IR)

IR was utilized for structural elucidation and specifically for the analysis of supported catalysts. Measurements were carried out using an IRSpirit equipped with a QUATR-S unit from Shimadzu, covering a range from 400 to 4000 cm^{-1}.

Catalytic evaluation and determination of catalytic parameters

Catalytic experiments

The experiments were carried out in a stainless steel (1.4571 grade) fixed-bed reactor with an internal diameter of 2 cm, capable of being enclosed by a heating jacket. The flow diagram for the reactor setup, including its peripherals and the connected gas chromatograph (GC), is depicted in Figure S 1.

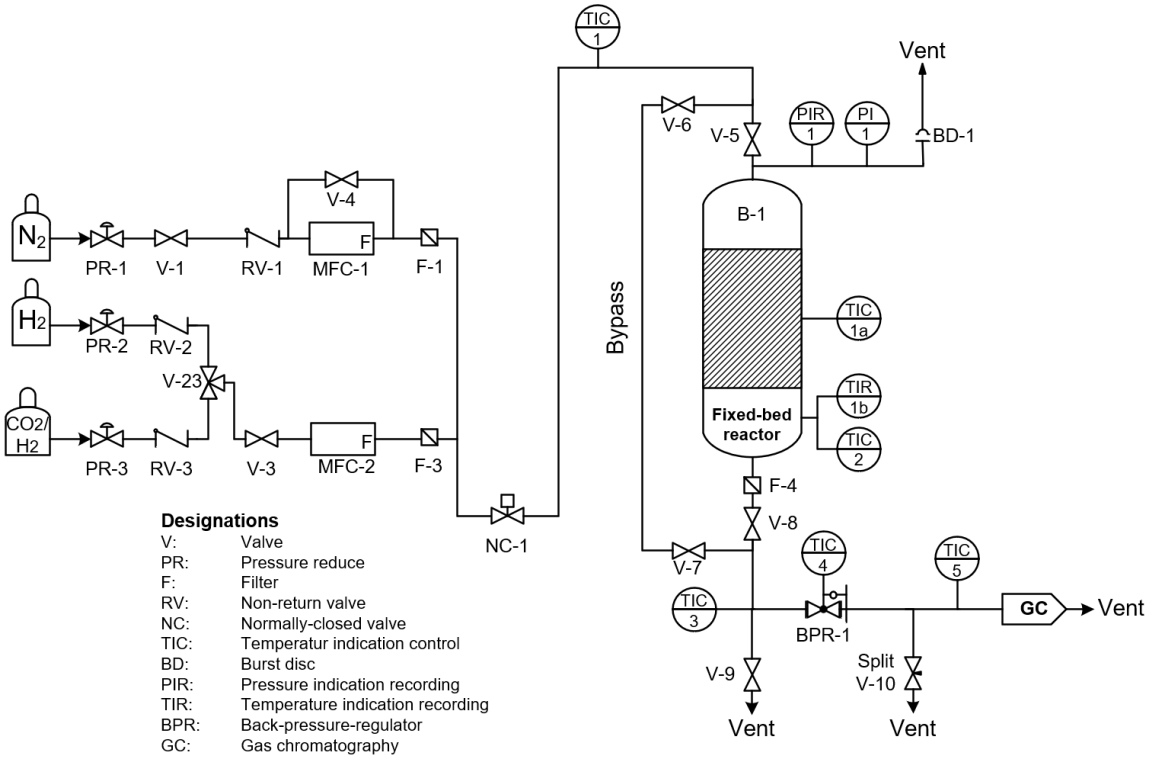

Figure S 1: Flow Diagram of the fixed-bed reactor setup.[5]

For each experiment, 2.5 g of $Cu/ZnO/Al_2O_3$-catalyst and the dehydration catalyst for converting methanol to DME were used. To achieve a bed height of 2 cm for each catalyst, the weighed catalysts were supplemented with inert glass beads (diameter 200-300 µm). Inside the reactor, the two catalysts were separated by a layer of glass wool (2 g). Figure S 2 schematically illustrates the catalyst packing within the reactor, with additional glass wool placed above the methanol catalyst to shape the flow profile and prevent catalyst swirling. The thermocouple (colored orange in Figure S 2) was positioned in the lower part of the methanol catalyst layer.

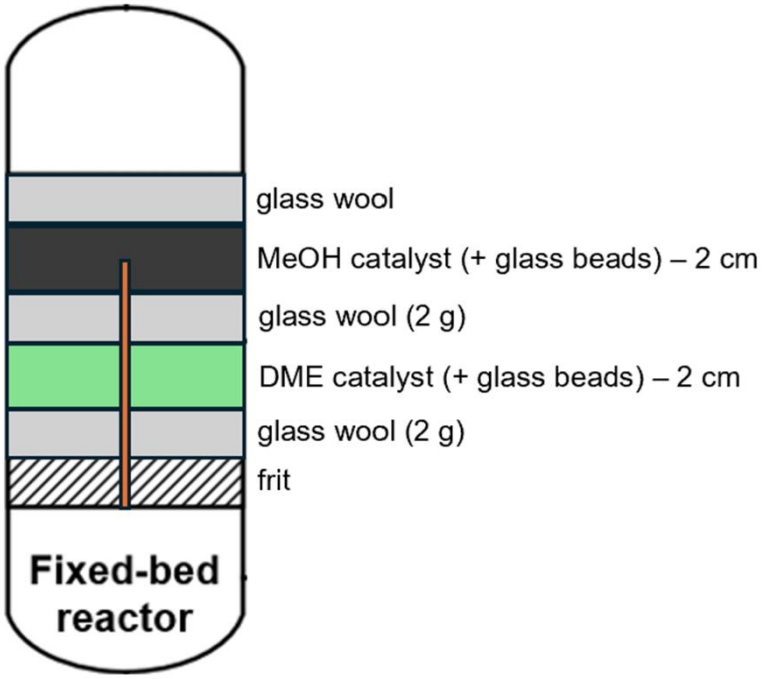

Figure S 2: Schematic Layout of the Catalyst Packing in the Reactor.

The reactor was heated to the reaction temperature of 250 °C under nitrogen flow (300 ml·min^{-1}) with a holding time of 30 minutes. For the one-hour preforming of the methanol catalyst, a gas flow containing 10 % hydrogen was introduced. Subsequently, N_2 was used to establish the reaction pressure of 50 bar. The introduction of the reaction gas (H_2/CO_2 in a 3 : 1 stoichiometric ratio, 1100 ml·min^{-1}) set the start of the reaction. The gas phase was analyzed using online GC after 10, 20, 30, 60, 90, and 120 minutes. To terminate the reaction, the supply of reaction gas was stopped, and the reactor setup was flushed with N_2 and cooled down to room temperature.

Analysis of reaction products via Gas-Chromatography (GC)

The composition of the gas phase at various stages of the reaction was analyzed using an online gas chromatograph Bruker 450-GC from Bruker. A schematic diagram of the GC setup can be seen in Figure S3. The gas was directly transported from the reactor to the GC through a heated gas line. The sample loop was filled with the gas to be analyzed, which was then injected into the column oven with argon as the carrier gas. Four separation columns installed in series and parallel (RT-Q-Bond, RT-U-Bond,

BRSwax, and BR-Molsieve 5A) were used to separate the gas into its components. Detection of MeOH and DME was carried out using the rear flame ionization detector (FID-rear). CO and CO_2 were measured using a methanizer unit at the middle flame ionization detector (FID-middle). Hydrogen was identified using the front thermal conductivity detector (TCD-front).

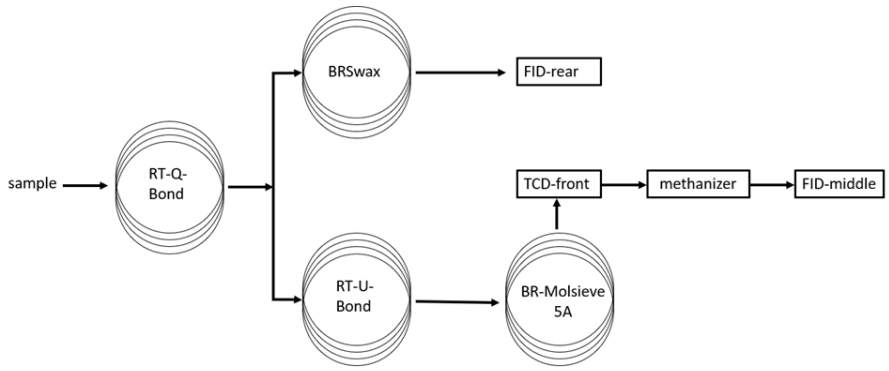

Figure S 3: Schematic Diagram of the Online Gas Chromatograph.

Calculation of catalytic parameters

Using ideal gas law

$$pV=nRT \qquad \text{Eq. 1}$$

the molar flow rate $\dot{n}_i$ of a component ii into the reactor can be calculated using equation 2.

$$\dot{n}_{i.in}= \frac{p_N \cdot y_{i.in} \cdot \dot{V}_N}{R \cdot T_N} \qquad \text{Eq. 2}$$

Here, p_N and T_N represent the standard pressure and standard temperature, respectively, *R* is the universal gas constant, $\dot{V}_N$ is the set volume flow rate, and $y_{i.in}$ is the fraction of component i in the input feed gas. The carbon balance of the reaction system is determined by the results of the online gas chromatography, using the average values of the measurements after 20 and 30 minutes for the fractions y_{out} of

the individual components. Firstly, the molar flow of the reactor outlet is calculated with equation 3, followed calculation of molar flow of each component with equation 4,

$$\dot{n}_{ges.out} = \frac{\dot{n}_{CO_2.\,in}}{y_{CO_2.out} + y_{CO.out} + y_{MeOH.out} + y_{DME.out}} \quad \text{Eq. 3}$$

$$n_{i.out} = \dot{n}_{ges.out} \cdot y_{i.out} \quad \text{Eq. 4}$$

Thus, yield (Y) and selectivity (S) can be determined using equations 5 and 6:

$$Y_i = \frac{\dot{n}_{i.out} - \dot{n}_{i.in}}{\dot{n}_{CO_2.\,in}} \cdot \frac{|\nu_{CO_2}|}{\nu_i} \cdot 100\ \% \quad \text{Eq. 5}$$

$$S_i = \frac{\dot{n}_{i.out} - \dot{n}_{i.in}}{\dot{n}_{CO_2.\,in} - \dot{n}_{CO_2.out}} \cdot \frac{|\nu_{CO_2}|}{\nu_i} \cdot 100\ \% \quad \text{Eq. 6}$$

The selectivities of the three exclusively detected gases at the outlet were subsequently normalized, due to:

$$S_{CO} + S_{DME} + S_{MeOH} = 100\ \% \quad \text{Eq. 7}$$

The productivity was calculated trough:

$$P_{cat} = \frac{\dot{n}_{DME.out} \cdot M_{DME}}{m_{cat}} \quad \text{Eq. 8}$$

To enhance the comparability of the HPAs, productivity was additionally calculated relative to the amount of catalyst used:

$$P_n = P_{cat} \cdot \frac{m_{cat}}{M_{DME} \cdot n_{HPA}} \quad \text{Eq. 9}$$

The CO_2 conversion rate X_{CO_2} and the gas hourly space velocity (GHSV) is determined using:

$$X_{CO_2} = \frac{\dot{n}_{CO_2.in} - \dot{n}_{CO_2.out}}{\dot{n}_{CO_2.\,in}} \cdot 100\ \%$$ Eq. 10

$$GHSV = \frac{\dot{V}_N}{V_{cat}}$$ Eq. 11

Effective molar loading was calculated from the mass fraction of the metal in the catalyst determined by ICP-OES, w_M, the mass fraction of that same metal in the HPA, $w_{M.HPA}$, and the molar mass of the HPA, M_{HPA}.

$$Loading_{eff} = \frac{w_M}{M_{HPA} \cdot w_{M.HPA}}$$ Eq. 12

Theoretical loading was calculated assuming all HPA material used in the synthesis was transferred onto the support.

$$Loading_{theo} = \frac{m_{HPA}}{(m_{HPA} + m_{support}) \cdot M_{HPA}}$$ Eq. 13

The arithmetic mean $\bar{x}$ and the standard deviation σ are determined according to:

$$\bar{x} = \frac{1}{n} \sum_{i=1}^{n} x_i$$ Eq. 14

$$\sigma = \sqrt{\frac{\sum_{i=1}^{n} (x_i - \bar{x})^2}{n-1}}$$ Eq. 15

Whereby *n* is he number of trials and x_i the measured value in the respective trial *i*.

Supplementary results and discussion

HPA catalyst selection for DME synthesis – Supporting of various HPAs on K10

HSiW/K10

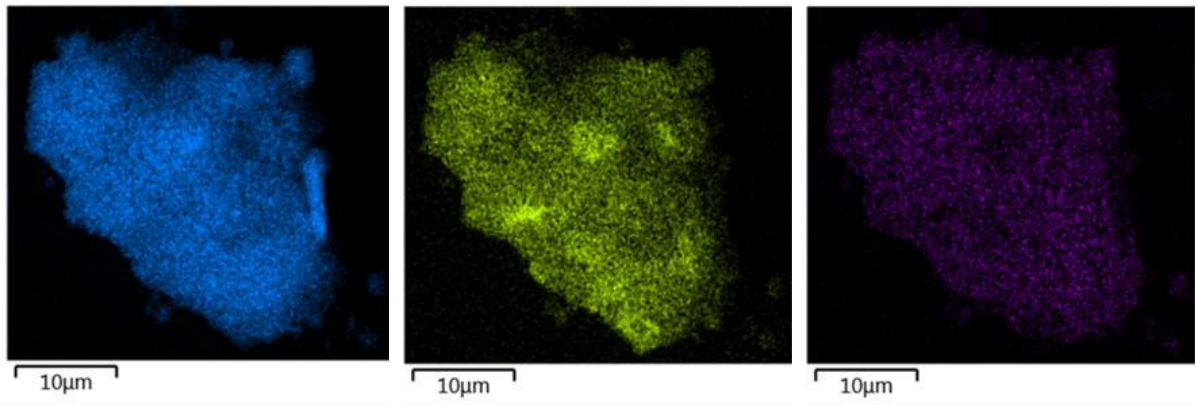

Si (K10 & HSIW) Al (K10) W

HPMo/K10

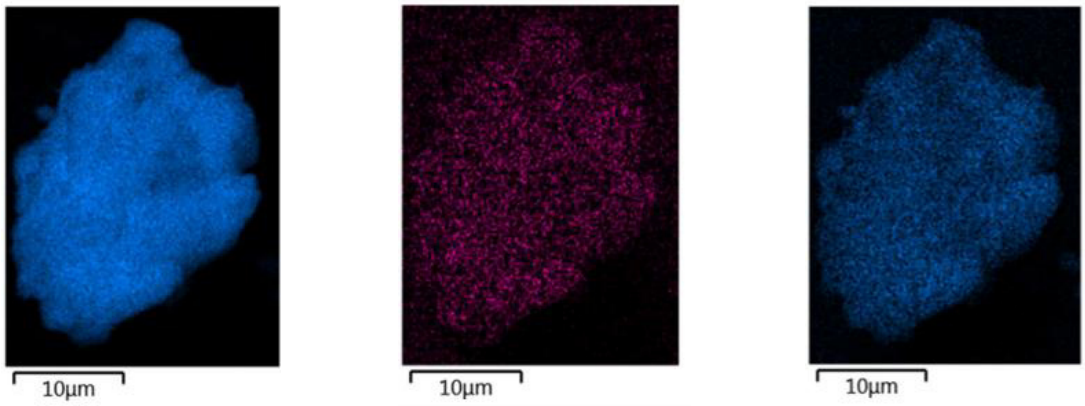

Si (K10) P Mo

HPW/K10

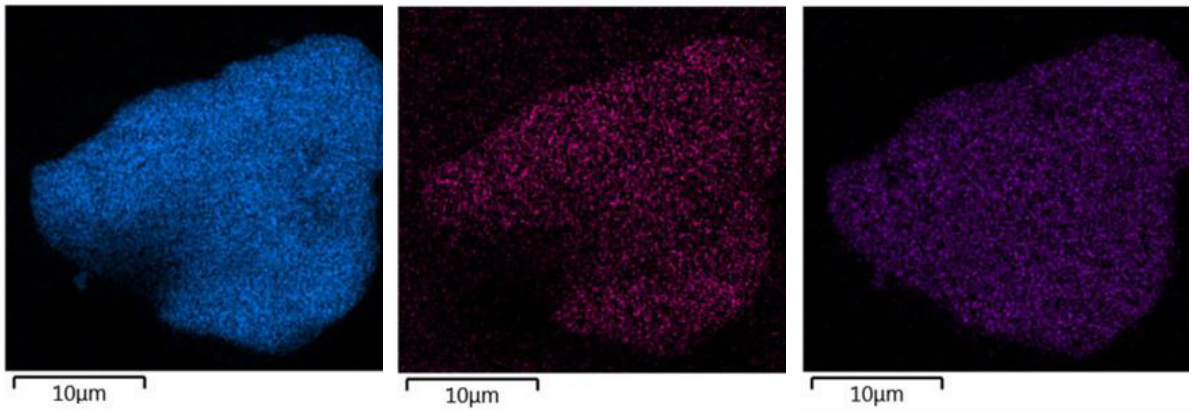

Si (K10) P W

HPVMo/K10

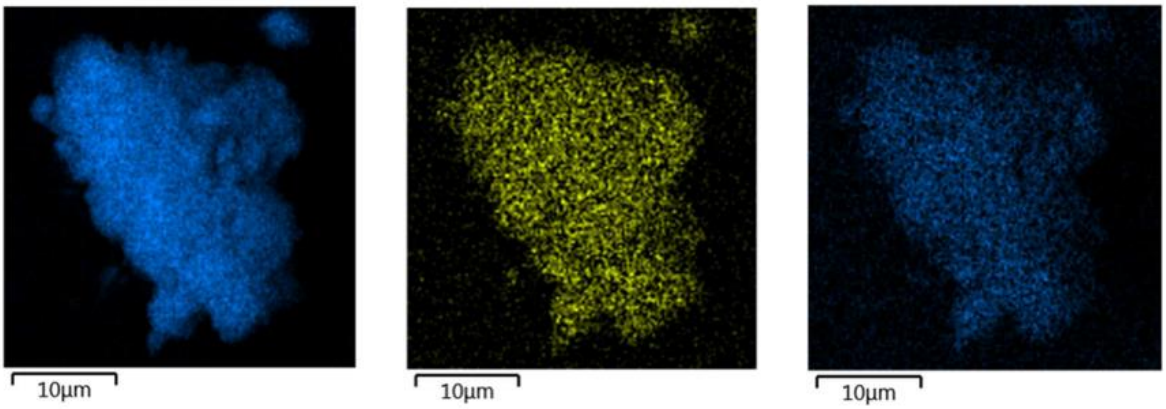

Si (K10) V Mo

HPInMo/K10

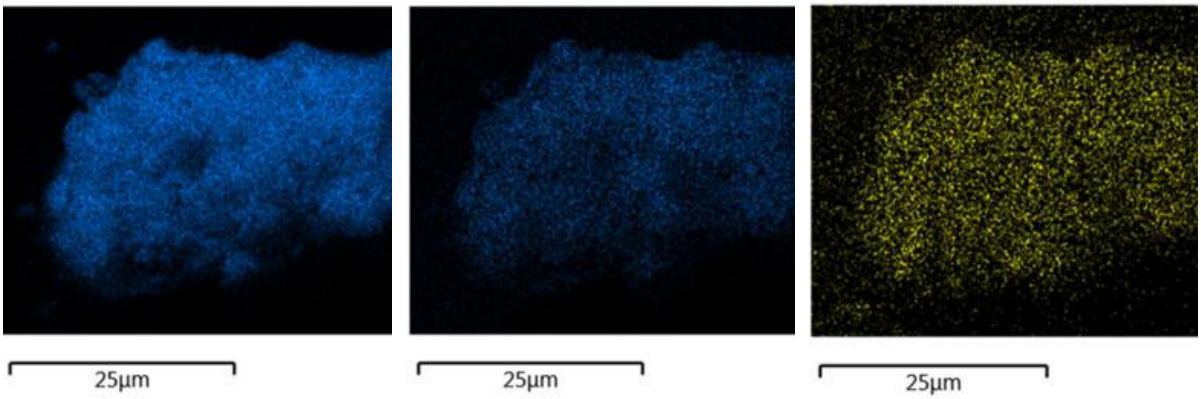

Si (K10) Mo In

HSiMo/K10

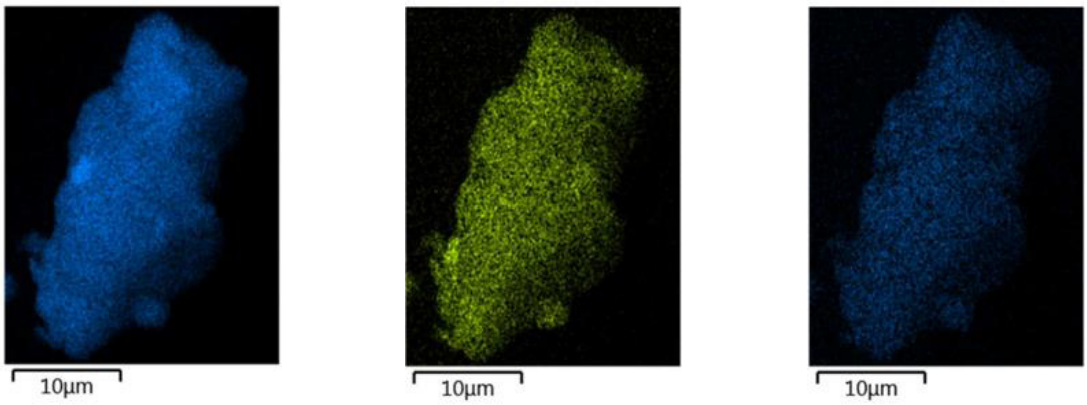

Si (K10 & HSiMo) Al (K10) Mo

Figure S 4: SEM EDX-Mapping of HPAs supported on K10

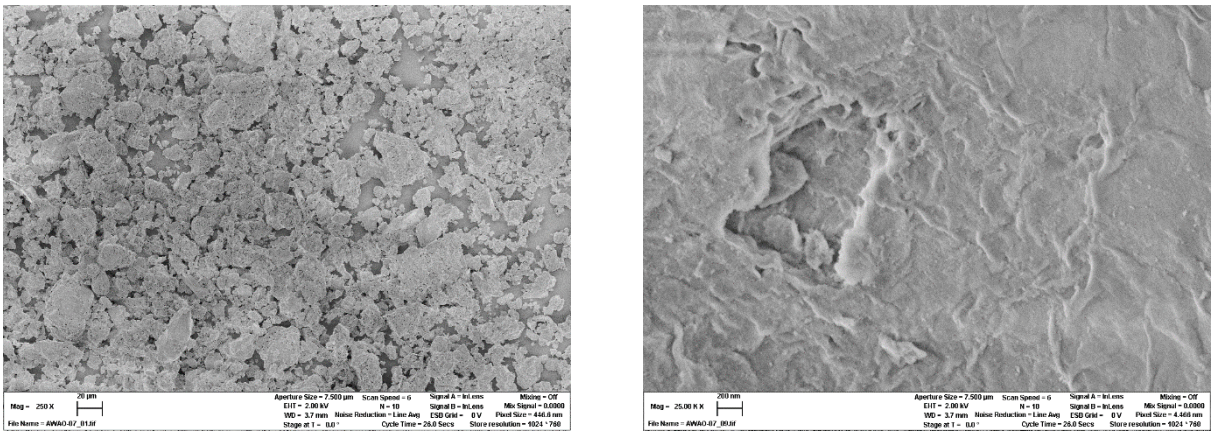

SEM images of HSiW/K10 at magnifications of 250x and 25,000x.

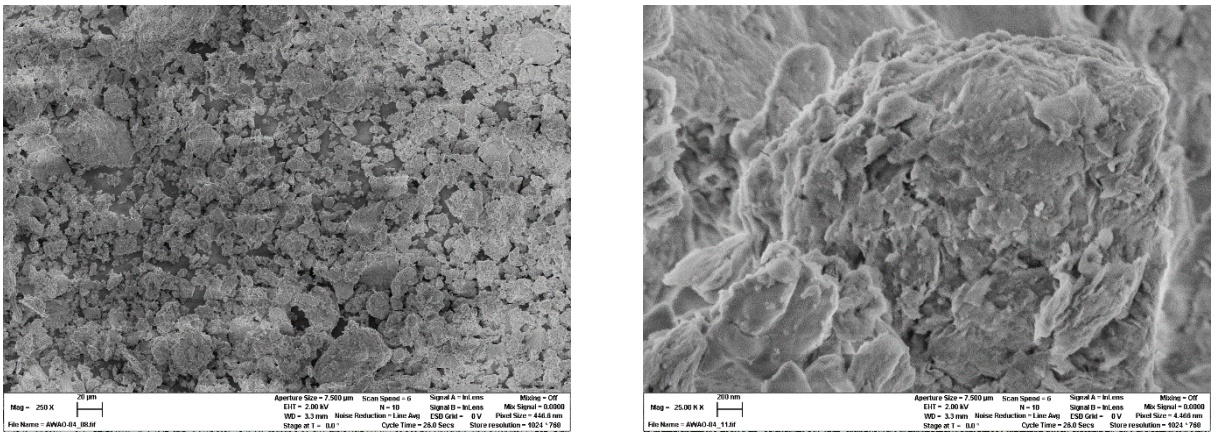

SEM images of HPMo/K10 at magnifications of 250x and 25,000x.

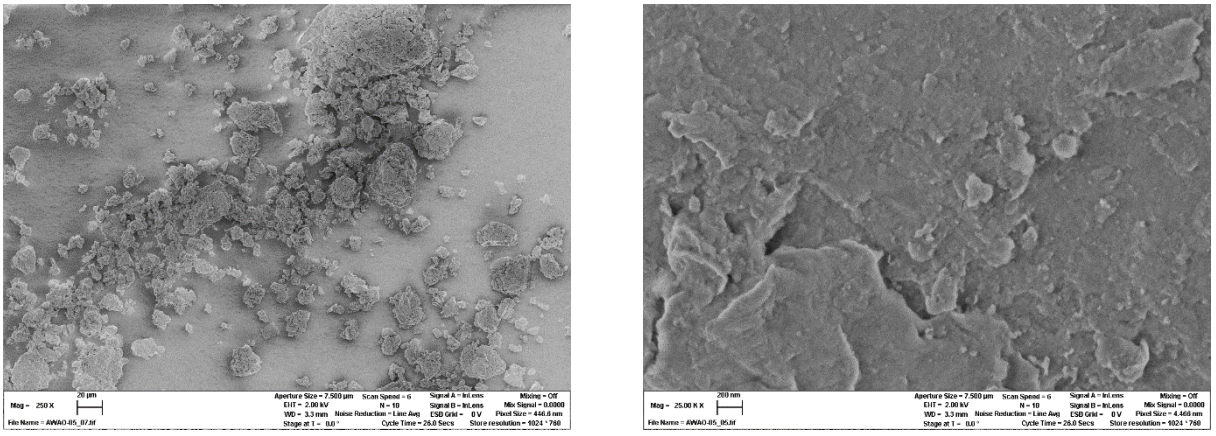

SEM images of HPW/K10 at magnifications of 250x and 25,000x.

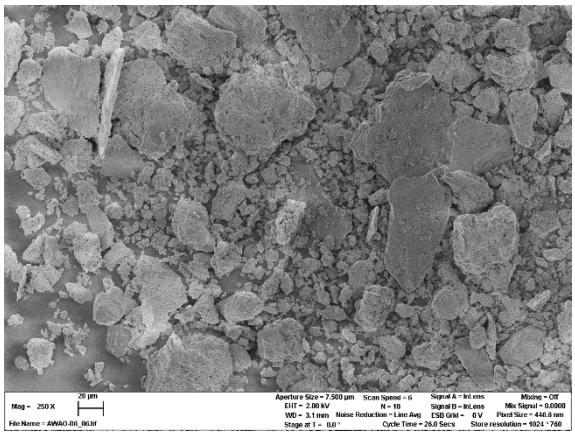

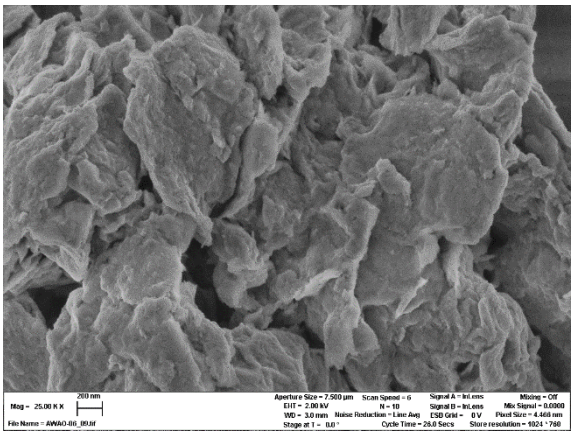

SEM images of HPVMo/K10 at magnifications of 250x and 25,000x.

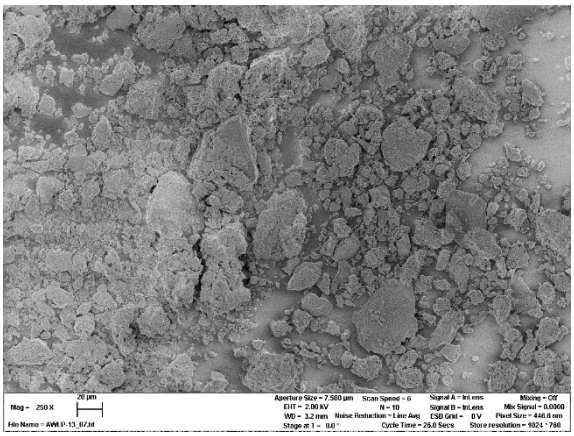

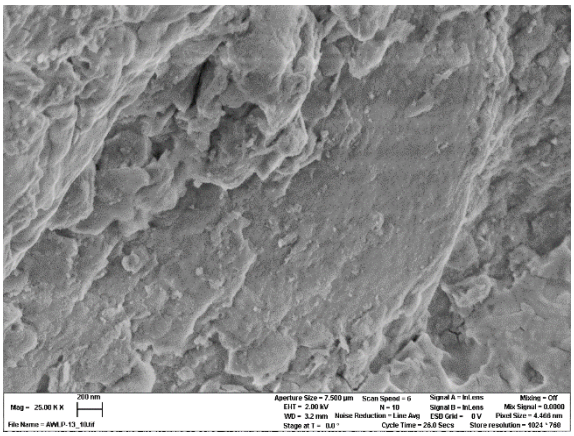

SEM images of HPInMo/K10 at magnifications of 250x and 25,000x.

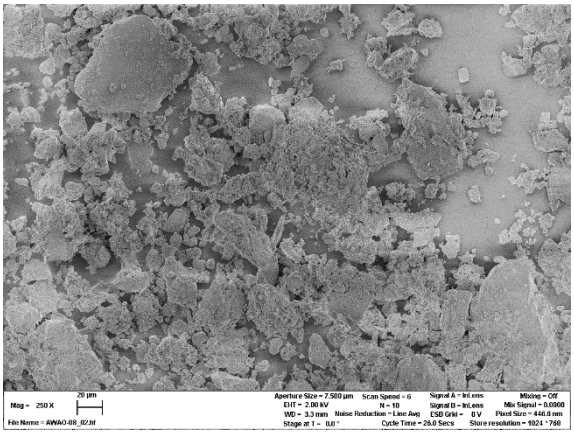

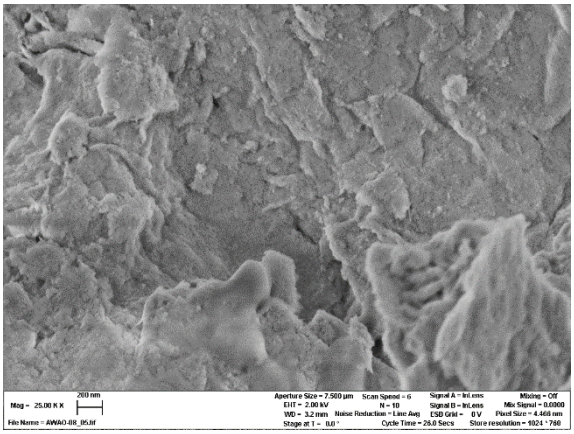

SEM images of HSiMo/K10 at magnifications of 250x and 25,000x.

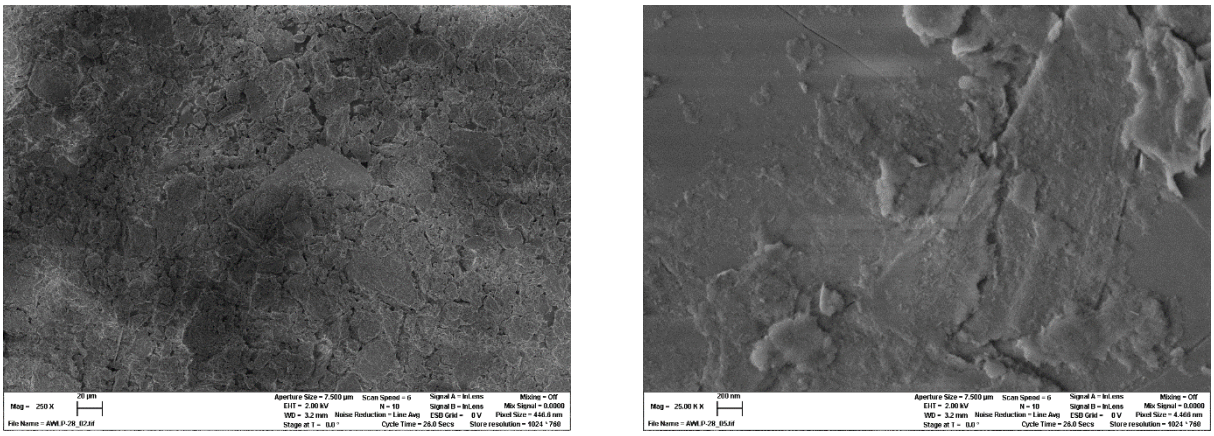

SEM images of K10 at magnifications of 250x and 25,000x.

Figure S 5: SEM Images of HPAs supported on K10.

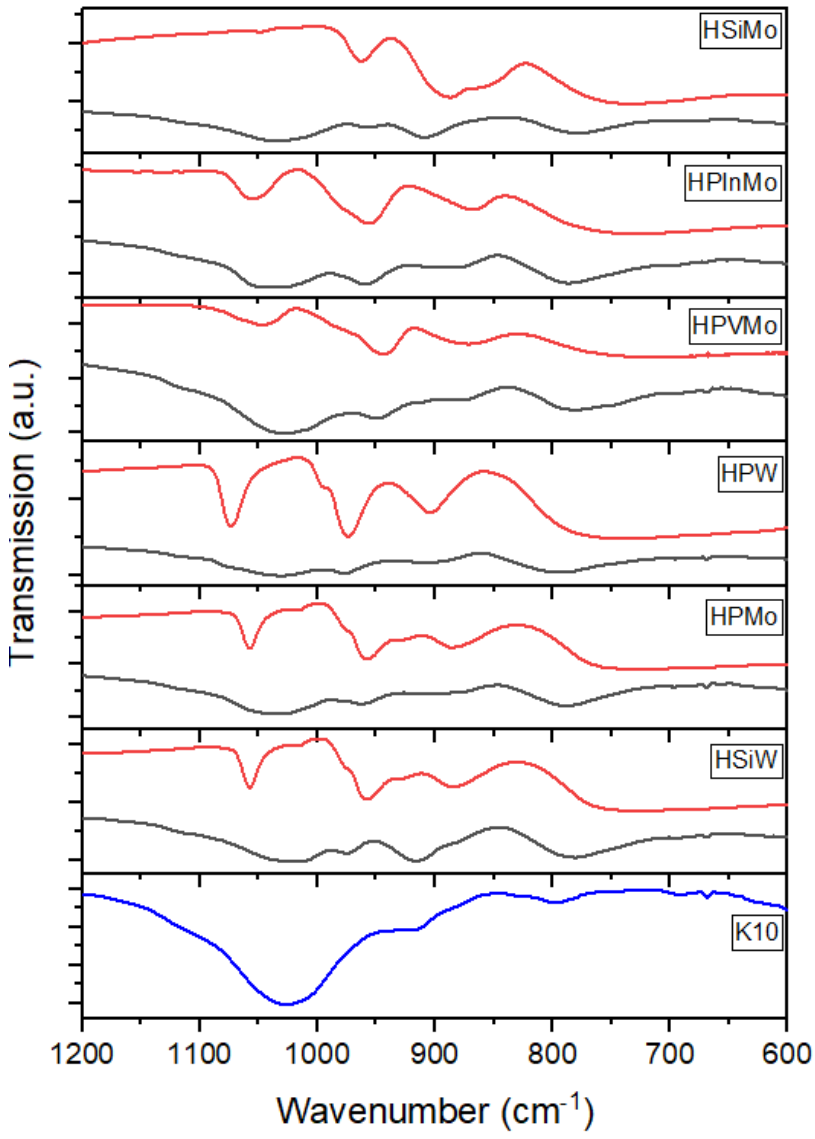

Figure S 6: IR spectra of pure (red line) and HPAs supported on K10 (black line) and pure K10 (blue).

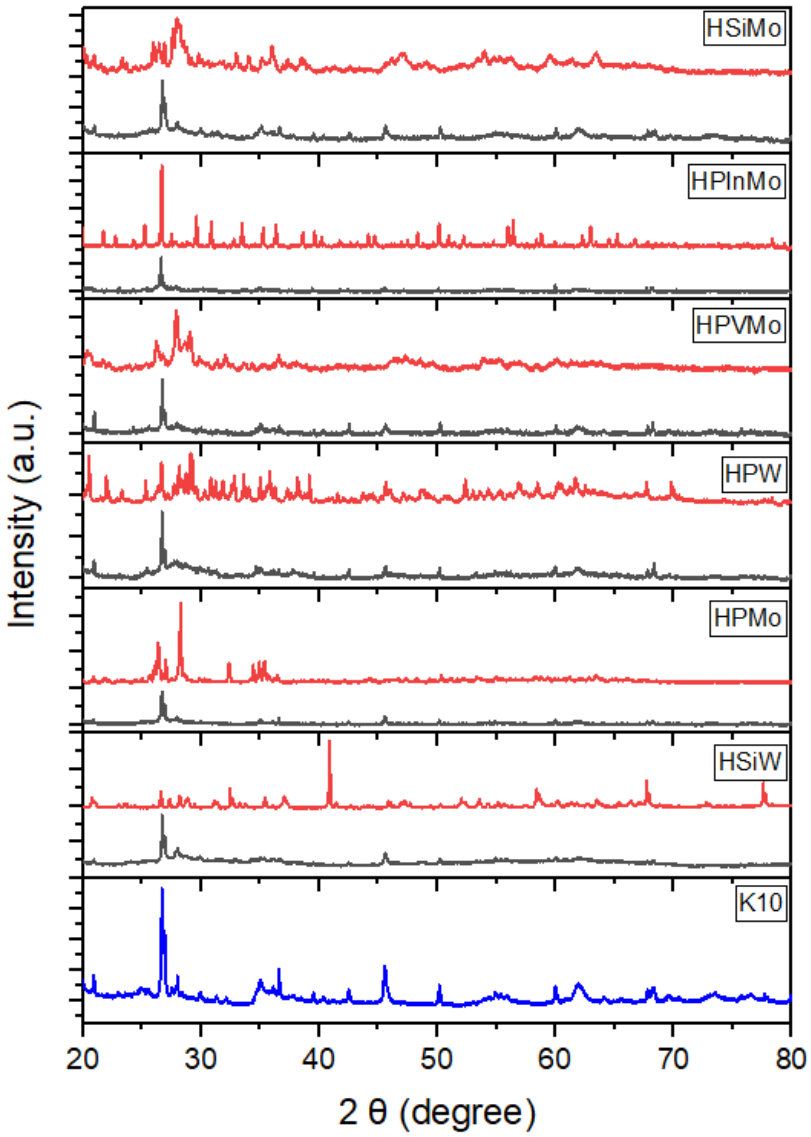

Figure S 7: XRD analytics of pure (red line) and HPAs supported on K10 (black line) and pure K10 (blue).

Table S 2: Catalytic results of HPAs supported on K10. Reaction conditions: T = 250 °C, p = 50 bar, H_2/CO_2 3/1, GHSV = 10000 h^{-1}.

catalyst	HSiW	HPMo	HPW	HPVMo	HPInMo	HSiMo	Pure K10
X_{CO_2} (%)	18.85	18.78	20.27	20.31	20.45.	19.96	19.89
Y_{MeOH} (%)	3.88	3.96	5.41	6.98	6.51	5.58	5.86
Y_{DME} (%)	7.06	7.10	5.73	3.95	4.69	5.24	4.76
Y_{CO} (%)	11.44	11.27	11.99	11.36	11.60	11.75	11.64
S_{MeOH} (%)	17.36	17.73	23.39	31.34	28.54	24.74	26.34
S_{DME} (%)	31.54	31.81	24.78	17.71	20.58	23.21	21.38
S_{CO} (%)	51.11	50.46	51.82	50.95	50.87	52.05	52.28
P_{mass} ($g_{DME}\ g_{cat}^{-1}\ h^{-1}$)	0.48	0.48	0.39	0.27	0.32	0.36	0.32
P_{mol} ($mol_{DME}\ mol_{HPA}^{-1}\ h^{-1}$)	77.84	59.40	55.53	31.12	31.00	41.30	-

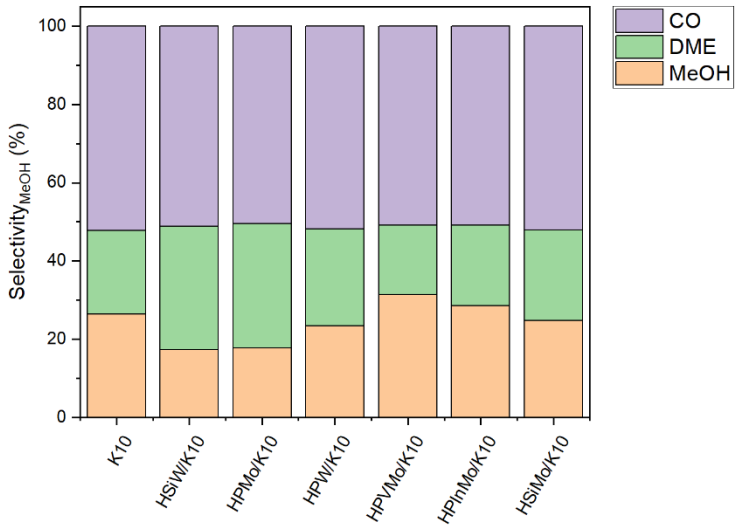

Figure S 8: Selectivities of HPAs supported on K10. Reaction conditions: T = 250 °C, p = 50 bar, H_2/CO_2 3/1, GHSV = 10000 h^{-1}.

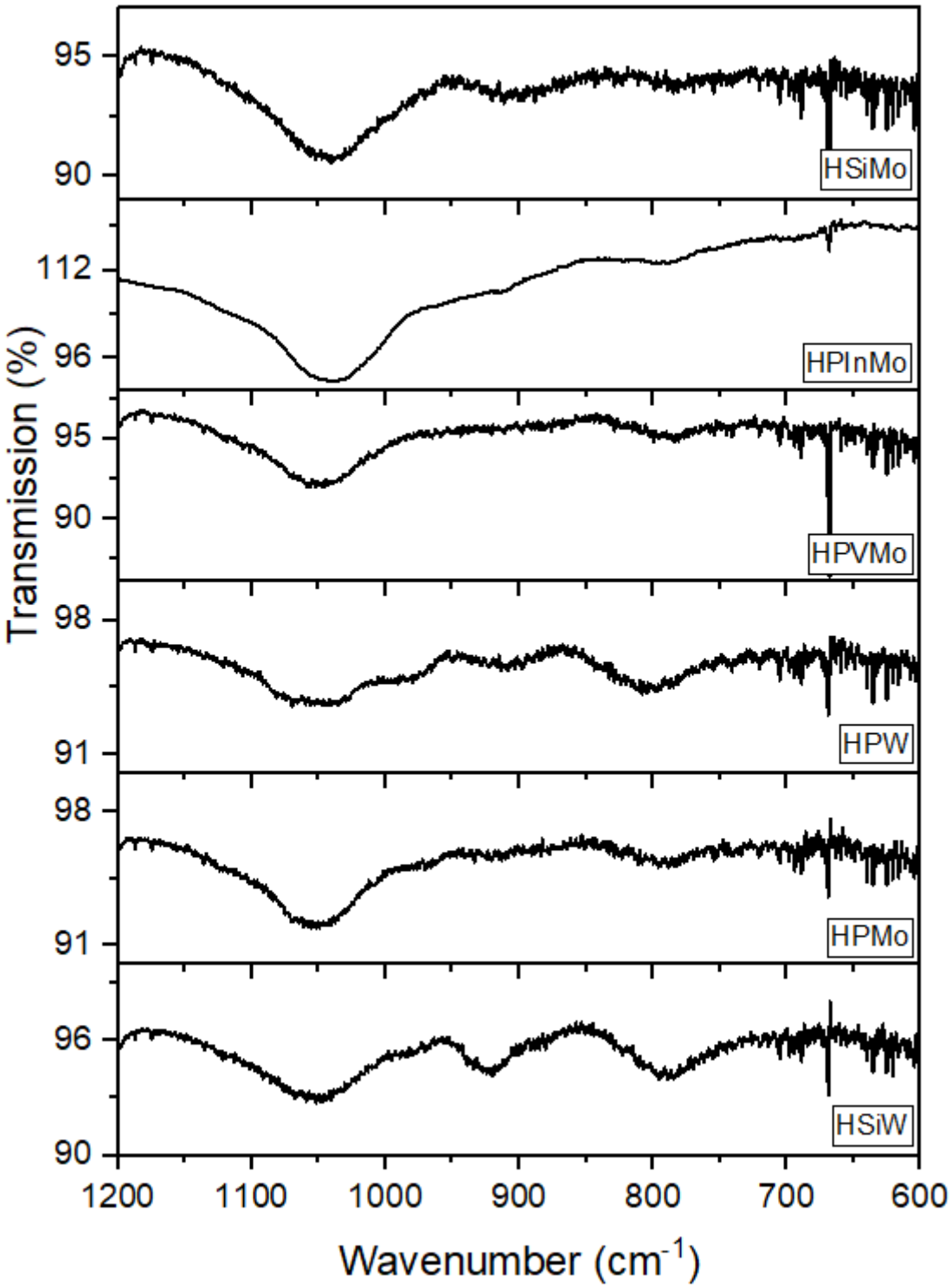

Figure S 9:IR analytics of HPAs supported on K10 after reaction.

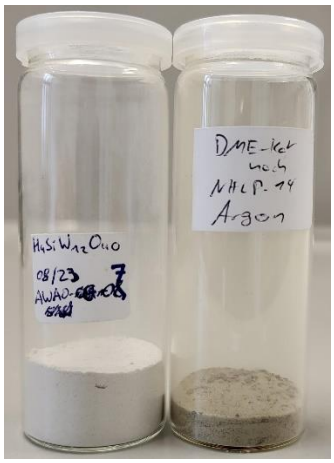

HSiW/K10

HPMo/K10

HPW/K10

HPVMo/K10

HPInMo/K10

HSiMo/K10

Figure S 10: HPAs supported on K10 before (left) and after use (right) in DME synthesis.

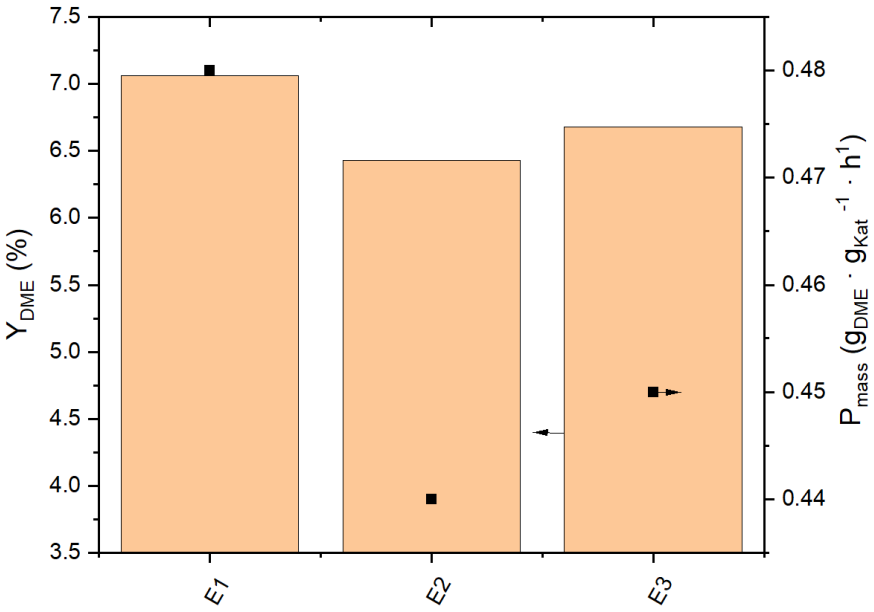

Figure S 11: Yield of DME Y_{DME} and productivity P_{mass} of reproduction experiments E1-E3 with HSiW/K10. Reaction conditions: T = 250 °C, p = 50 bar, H_2/CO_2 3/1, GHSV = 10000 h^{-1}.

Table S 3: Catalytic results of reproduction experiments using Cu/ZnO/Al_2O_3 and HSiW/K10 as catalysts. Reaction conditions: T = 250 °C, p = 50 bar, H_2/CO_2 3/1, GHSV = 10000 h^{-1}.

	E1	E2	E3	E4*	Mean value (E1-E3)	Standard deviation (E1-E3)
X_{CO_2} (%)	18.85	19.96	19.92	20.72	19.58	0.63
Y_{MeOH} (%)	3.88	4.79	4.31	6.38	4.33	0.46
Y_{DME} (%)	7.06	6.43	6.68	5.38	6.72	0.32
Y_{CO} (%)	11.44	11.96	12.27	11.65	11.89	0.42
S_{MeOH} (%)	17.36	20.65	18.54	27.24	18.85	1.67
S_{DME} (%)	31.54	27.73	28.72	22.99	29.33	1.98
S_{CO} (%)	51.11	51.62	52.74	49.77	51.82	0.83
P_{mass} (g_{DME} g_{cat}^{-1} h^{-1})	0.48	0.44	0.45	0.37	0.46	0.02

*In reproduction experiment E4, a reduced DME yield of 5.38% is noted, likely due to a measurement error, as the CO_2 conversion and CO yield are consistent with the other experiments, suggesting proper catalyst packing. Potential errors, such as incorrect DME catalyst layer packing or gas flow rate settings to the gas chromatograph, might contribute to lower detected DME levels. Consequently, E4 was excluded from the mean and standard deviation calculations to ensure accuracy.

Support selection for DME synthesis - Supporting HSiW on different supports

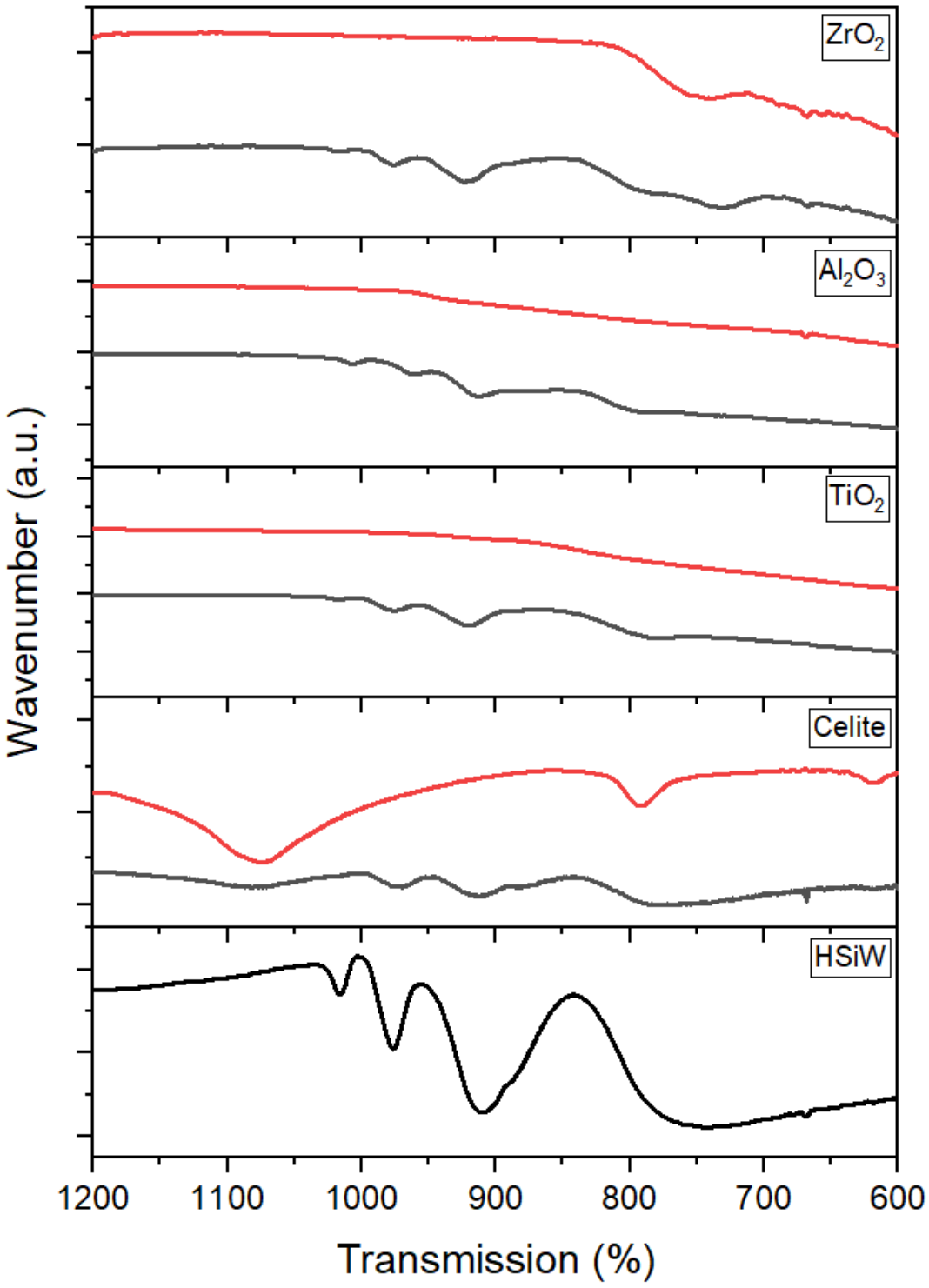

Figure S 12: IR analytics of pure supports (red line) and supported HSiW (black line).

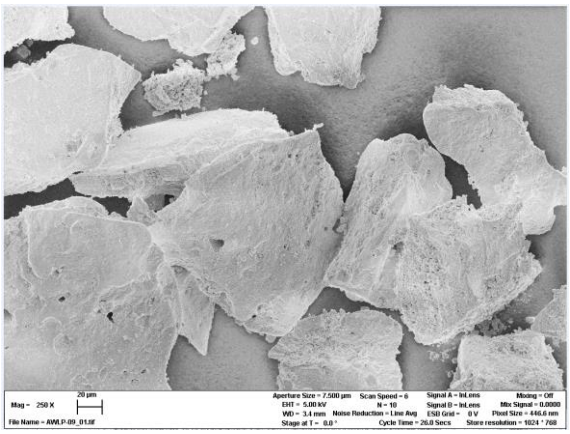

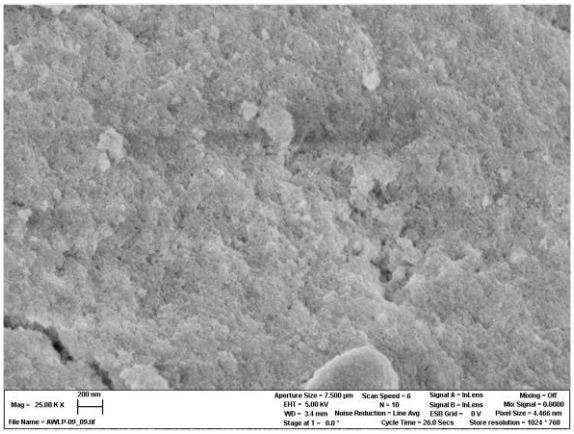

SEM images of HSiW/ZrO_2 at magnifications of 250x and 25,000x.

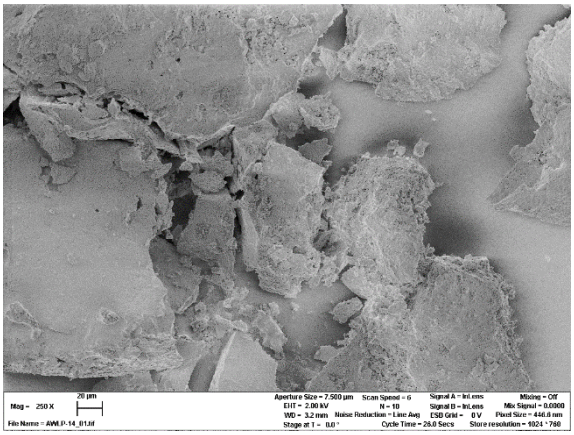

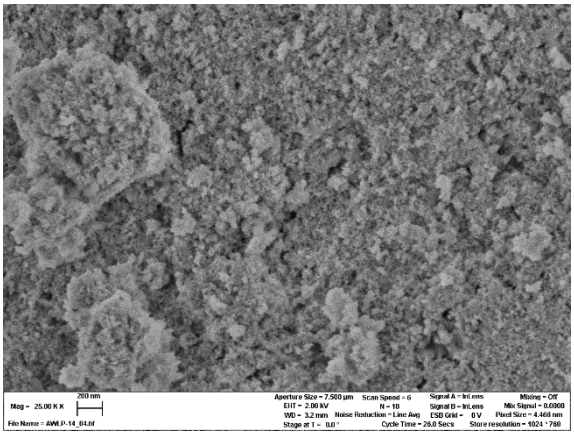

SEM images of ZrO_2 at magnifications of 250x and 25,000x.

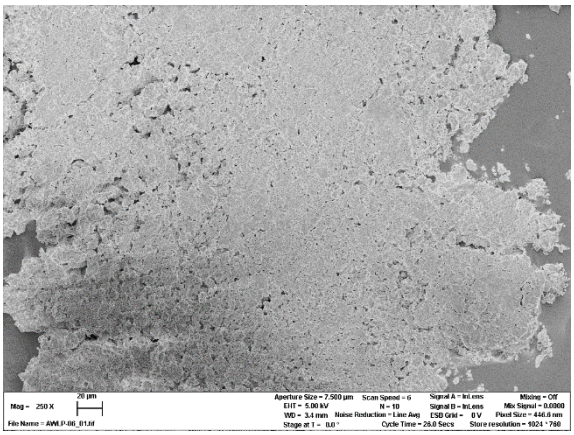

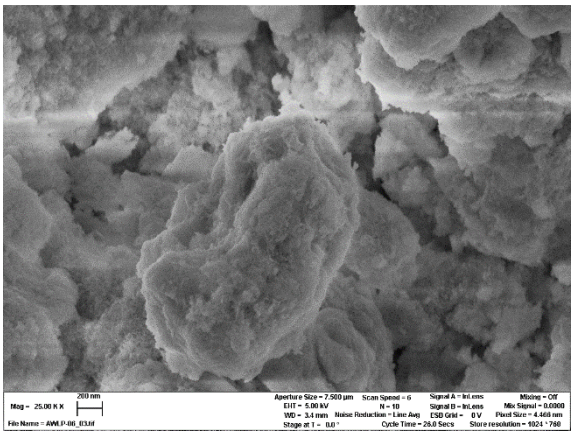

SEM images of HSiW/Al_2O_3 at magnifications of 250x and 25,000x.

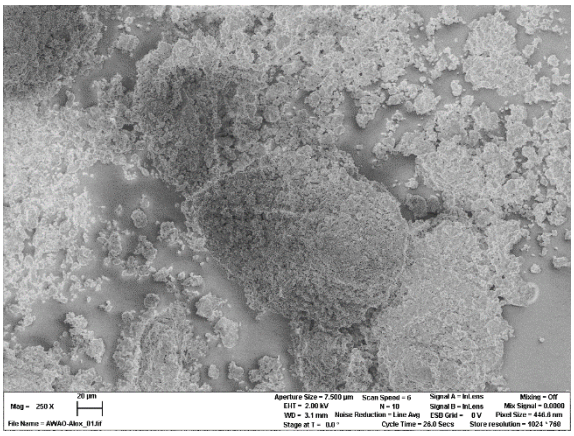

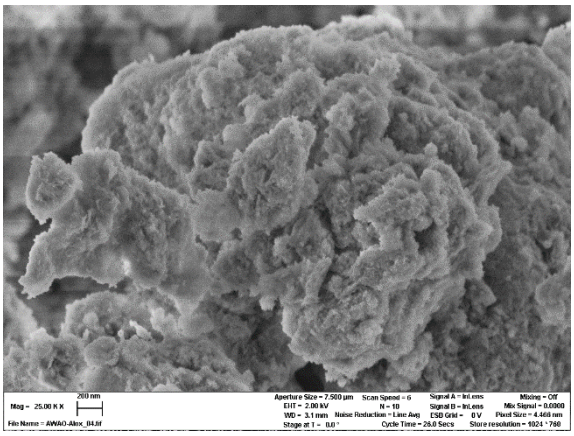

SEM images of Al_2O_3 at magnifications of 250x and 25,000x.

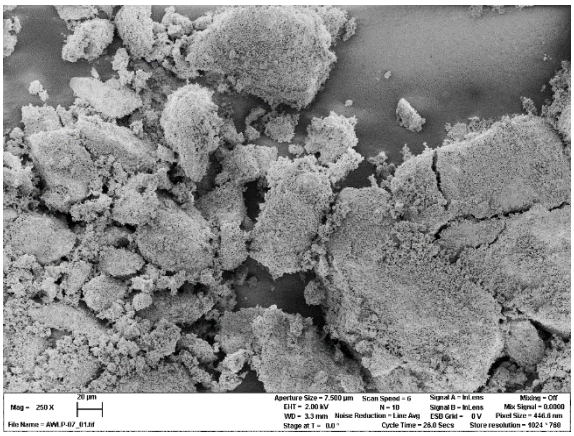

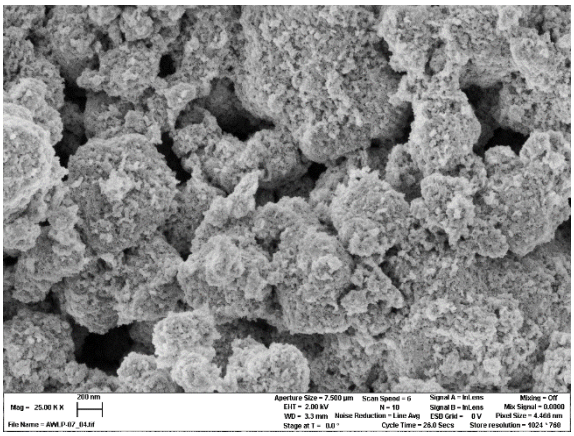

SEM images of $HSiW/TiO_2$ at magnifications of 250x and 25,000x.

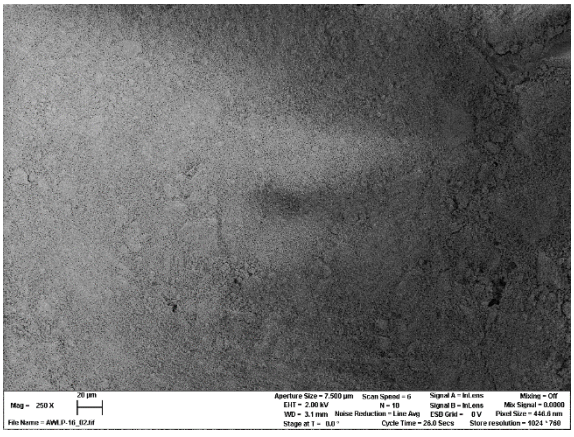

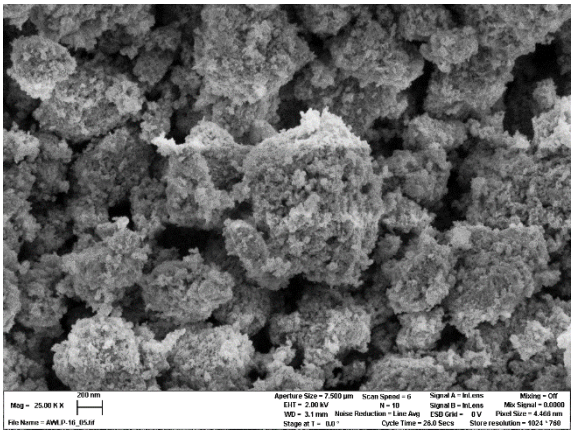

SEM images of TiO_2 at magnifications of 250x and 25,000x.

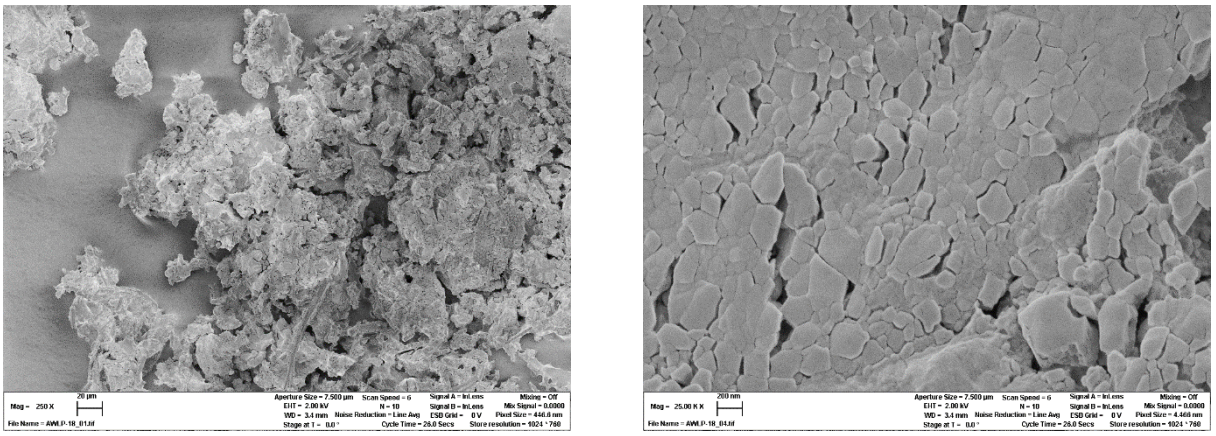

SEM images of HSiW/Celite at magnifications of 250x and 25,000x.

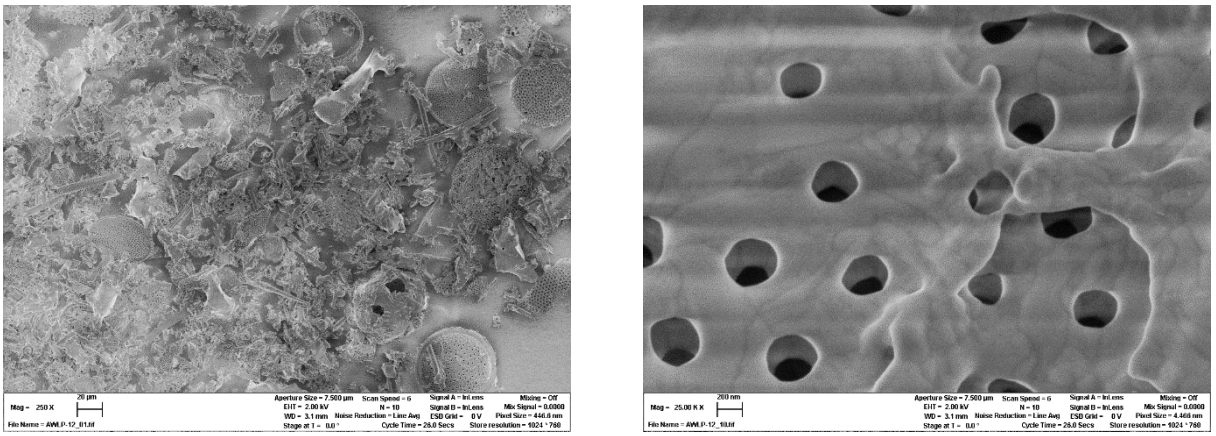

SEM images of Celite at magnifications of 250x and 25,000x.

Figure S 13: SEM Images of HSiW on different supports.

HSiW/ZrO_2

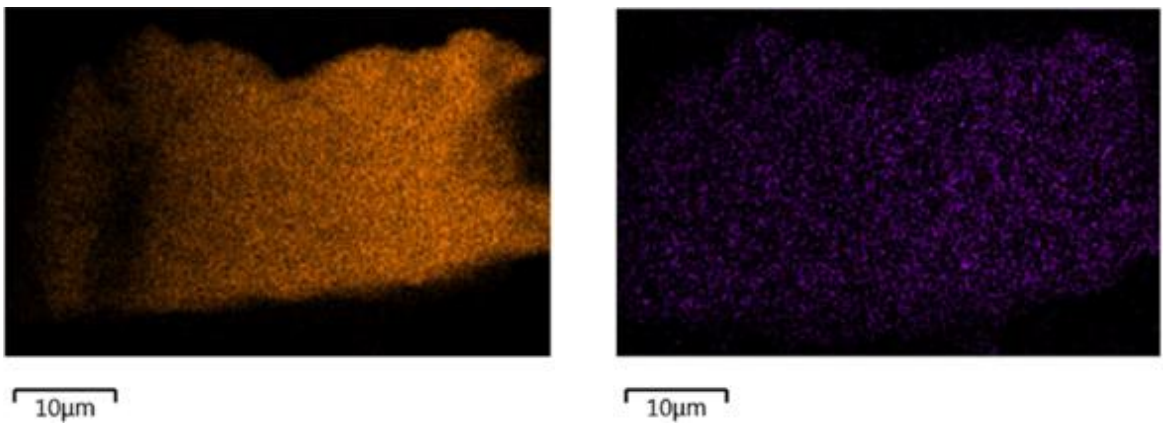

Zr W

HSiW/Al_2O_3

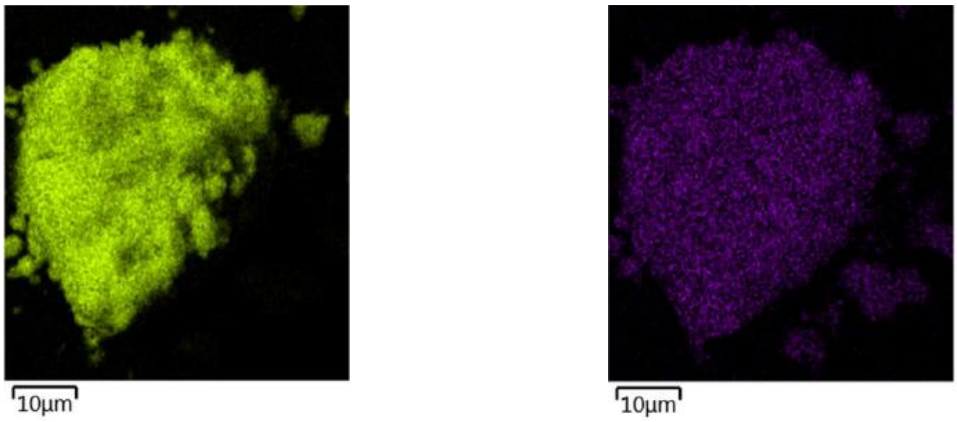

Al W

HSiW/TiO_2

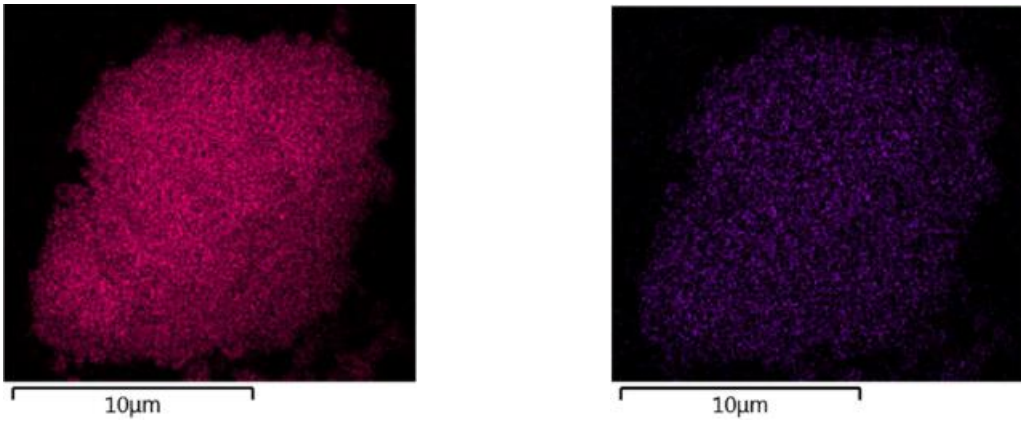

Ti W

HSiW/Celite

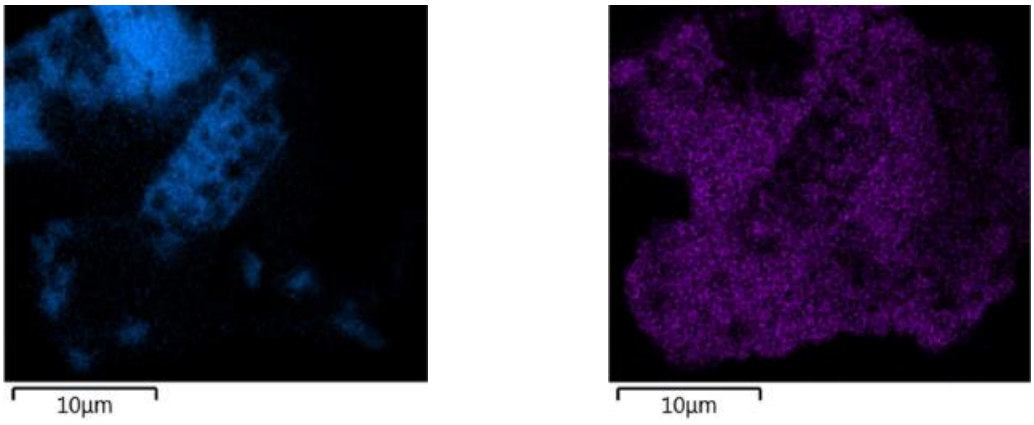

W

Figure S 14: SEM EDX-Mapping of HSiW on different supports.

Table S 4: Catalytic results of HSiW on different supports. Reaction conditions: T = 250 °C, p = 50 bar, H_2/CO_2 3/1, GHSV = 10000 h^{-1}.

catalyst	HSiW/ ZrO_2	ZrO_2	HSiW/ Al_2O_3	Al_2O_3	HSiW/ TiO_2	TiO_2	HSiW/ Celite	Celite
X_{CO_2} (%)	19.36	24.43	20.39	24.43	18.98	23.76	18.65	23.99
Y_{MeOH} (%)	3.32	12.75	4.23	12.34	3.35	12.41	3.51	13.18
Y_{DME} (%)	7.08	0.00	6.69	0.10	6.92	0.02	6.81	0.00
Y_{CO} (%)	12.50	11.68	12.82	12.03	12.17	11.35	11.74	10.81
S_{MeOH} (%)	14.50	52.19	17.80	50.42	14.95	52.18	15.93	54.95
S_{DME} (%)	30.91	0.00	28.17	0.42	30.84	0.10	30.86	0.00
S_{CO} (%)	54.59	47.81	54.02	49.17	54.21	47.72	53.21	45.05
P_{mass} ($g_{DME}\ g_{cat}^{-1}\ h^{-1}$)	0.48	0.00	0.45	0.01	0.47	0.00	0.46	0.00
P_{mol} ($mol_{DME}\ mol_{HPA}^{-1}\ h^{-1}$)	125.44	-	65.39	-	77.74	-	47.68	-

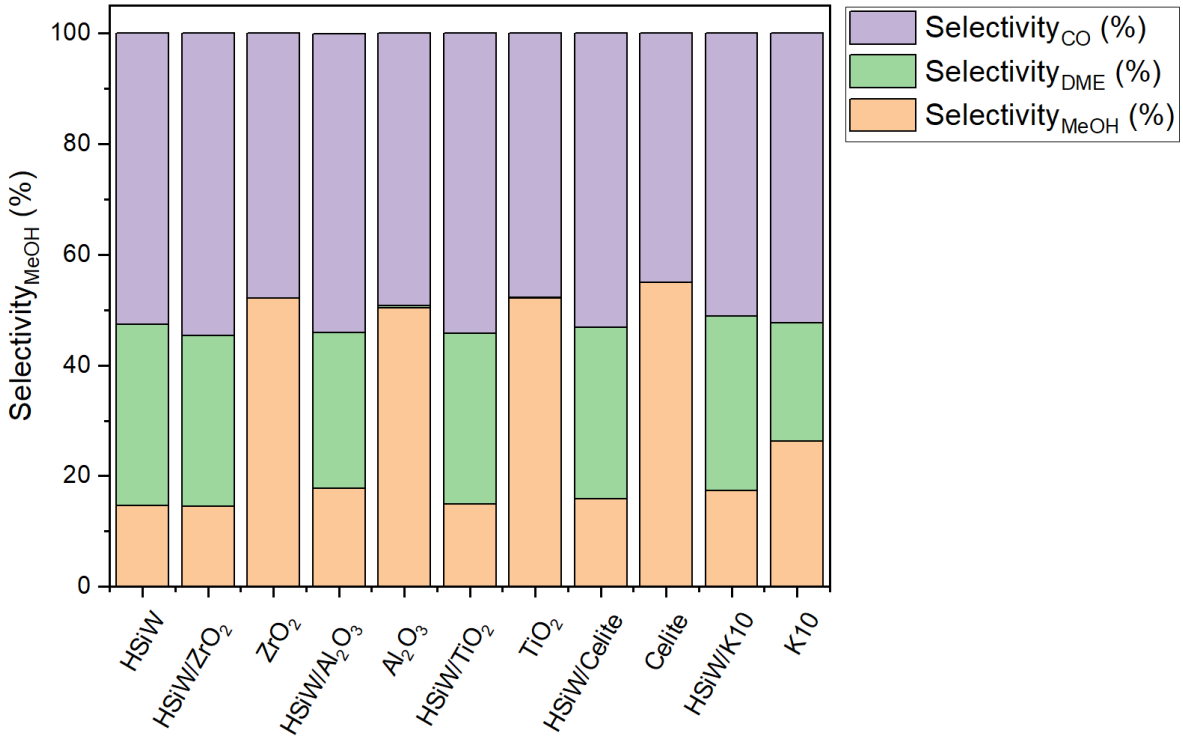

Figure S 15: Selectivities of HSiW on different supports. Reaction conditions: T = 250 °C, p = 50 bar, H_2/CO_2 3/1, GHSV = 10000 h^{-1}.

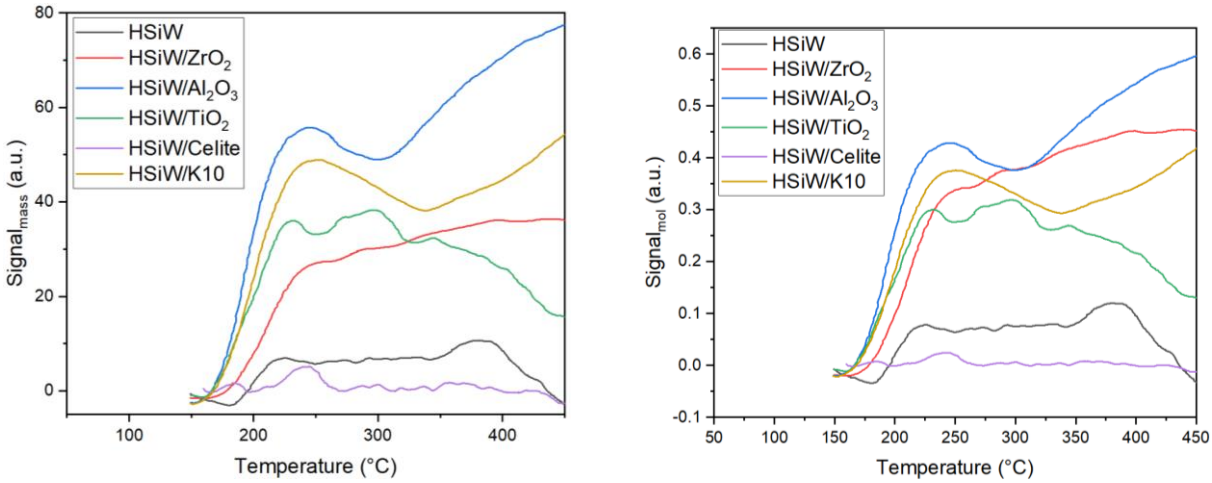

Figure S 16: NH_3-TPD analysis of HSiW on different supports, normalized to mass of catalyst (left) and normalized to molar mass of supported HPA (right).

Comparative Analysis with Previously-Reported Catalyst

The IR spectrum of HSiW/ZrO_2K exhibits characteristic Keggin vibration bands, confirming the preservation of the Keggin structure after impregnation (Figure S17). Elemental analysis confirms a slightly higher loading for HSiW/ZrO_2^K compared to HSiW/ZrO_2^W. N_2-physisorption further indicates similar surface areas, with marginally smaller pore diameters and pore volumes for HSiW/ZrO_2K (Table S5). Unlike the wet impregnation method used in this study, the modified synthesis procedure by Kubas utilized ethanol instead of water and reduced impregnation time, potentially leading to increased deposition and thus higher POM loading on the support material ZrO_2, as well as the slightly reduced pore volumes and diameters. However, these results should be interpreted cautiously, as the variations in elemental analysis and N_2 physisorption measurements are within the margin of error for both methods.

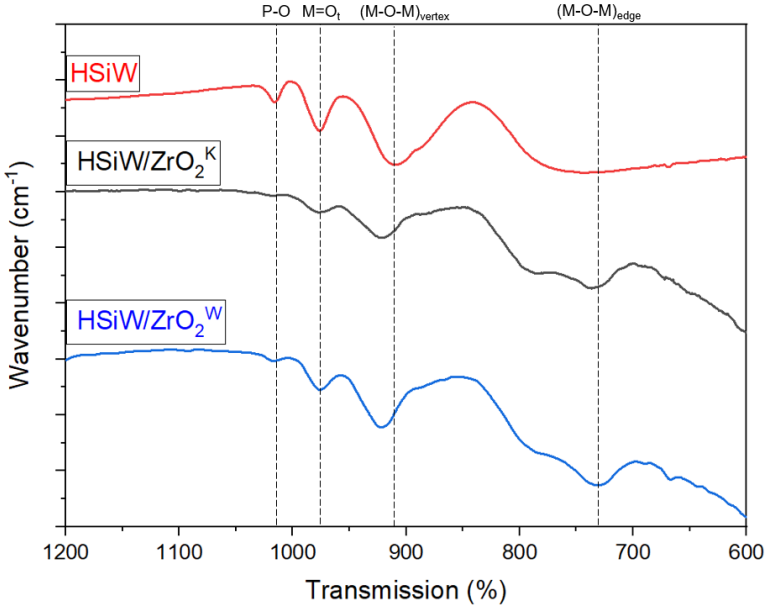

Figure S 17: IR spectra for HPA/ZrO_2 of current study (HPA/ZrO_2W) vs. catalyst from literature (HPA/ZrO_2K) and pure HiSW.

Table S 5: Textural properties and results of elemental analysis for HPA/ZrO_2 of current study (HPA/ZrO_2W) vs. catalyst from literature (HPA/ZrO_2K).

	$HSiW/ZrO_2^W$	$HSiW/ZrO_2^K$
Textural properties		
S_{BET} (m^2/g)	81	80
Ø pore diameter (nm)	3.40	3.38
Pore volume (mL/g)	0.18	0.11
Elemental analysis		
W (wt.%)	18.32	20.55
HPA (wt.%)	27.19	30.49
$Loading_{eff.}$ ($\mu mol_{HPA}\ g_{cat}^{-1}$)	80	90
$Loading_{theor.}$ ($\mu mol_{HPA}\ g_{cat}^{-1}$)	90	90

References

(1) Odyakov, V. F.; Zhizhina, E. G. A novel method of the synthesis of molybdovanadophosphoric heteropoly acid solutions, *React Kinet Catal Lett.* **2008**, *95,* pp. 21–28.

(2) Raabe, J.-C.; Poller, M. J.; Voß, D.; Albert, J. H8 PV5 Mo7 O40 - A Unique Polyoxometalate for Acid and RedOx Catalysis: Synthesis, Characterization, and Modern Applications in Green Chemical Processes, *ChemSusChem.* **2023**, *16,* e202300072.

(3) Raabe, J.-C.; Aceituno Cruz, J.; Albert, J.; Poller, M. J. Comparative Spectroscopic and Electrochemical Study of V(V)-Substituted Keggin-Type Phosphomolybdates and -Tungstates, *Inorganics.* **2023**, *11,* p. 138.

(4) Strickland, J. D. H. The Preparation and Properties of Silicomolybdic Acid. I. The Properties of Alpha Silicomolybdic Acid, *J. Am. Chem. Soc.* **1952**, *74,* pp. 862–867.

(5) Wesner, A.; Kampe, P.; Herrmann, N.; Eller, S.; Ruhmlieb, C.; Albert, J. Indium-based Catalysts for CO 2 Hydrogenation to Methanol: Key Aspects for Catalytic Performance, *ChemCatChem.* **2023**, *15*.

ChemCatChem

Supporting Information

Indium-based Catalysts for CO_2 Hydrogenation to Methanol: Key Aspects for Catalytic Performance

Anne Wesner, Philipp Kampe, Nick Herrmann, Sebastian Eller, Charlotte Ruhmlieb, and Jakob Albert*

Table of Contents

This document contains 8 Tables and 15 Figures on 20 pages.

Supplementary methods

Catalyst preparation

All chemicals were obtained commercially and used as received without further purification.

$CuO/ZnO/Al_2O_3$

Copper based methanol synthesis catalyst were obtained commercially via Alfa Aesar, product no. 45776.

In_2O_3/ZrO_2

In_2O_3/ZrO_2 catalysts have been prepared through impregnation by already published synthesis methods according Martin et al. (In_2O_3/ZrO_2 M-AA, M-SG)[12] or Schühle et al. (S-AA, S-SG)[13]. $In(NO_3)_3 \cdot x\ H_2O$ Puratronic® (≥99.999 %, Alfa Aesar, VWR 10708.22) was used as a precursor. ZrO_2 oxide by Alfa Aesar (VWR 43814.36, referred as ZrO_2 (AA)), or St. Gobain (SZ 31164 NORPRO, referred as ZrO_2 (SG)) were used as a support. Prior synthesis ZrO_2 pellets were granulated to a particle size of 80-250 µm.

Synthesis of In_2O_3/ZrO_2 according to Martin [12]. $In(NO_3)_3 \cdot x\ H_2O$ (6.84 g) was dissolved in 630 mL of ethanol and 216 mL of dist. water. ZrO_2 (18 g) was added to the solution and the suspension was stirred for 5 h in a rotatory evaporator (111 rpm, room temperature, 800 mbar). After the solvent was removed, the impregnated powder was dried (65 °C, 12 h), heated with 5 °C/min to 300 °C and calcined for 3 h.

Synthesis of In_2O_3/ZrO_2 according to Schühle [13]: The stock solution was prepared by dissolving $In(NO_3)_3 \cdot x\ H_2O$ (10 g) in 25 mL of dist. water. The suspension was prepared by adding ZrO_2 (17.1 g) to the $In(NO_3)_3 \cdot x\ H_2O$-stock solution (16.4 mL). An aqueous supernatant was removed in a rotary evaporator, followed by drying (65 °C, 12 h). Thereafter, the powder was heated with 5 °C /min to 300 °C and calcined for 3 h.

Promoted In_2O_3/ZrO_2 with different metals (Ce, Mg, Ni, Cu)

Bimetallic supported catalysts ($CuO/NOi/CeO_2/MgO\text{-}In_2O_3/ZrO_2$) have been prepared by co-precipitation. The used precursors were $In(NO_3)_3 \cdot x\ H_2O$ Puratronic® (≥ 99.999 %, Alfa Aesar, VWR 10708.22), $Ce(NO_3)_3 \cdot 6\ H_2O$ (99.5 %, Thermo Scientific, VWR ACRO218691000), $Mg(NO_3)_2 \cdot 6\ H_2O$ (≥ 98 %, Thermo Scientific,

VWR A10329.30), $Ni(NO_3)_2 \cdot 6\ H_2O$ (n.s., SuboLab GmbH) and $Cu(NO_3)_2 \cdot 3\ H_2O$ (99 %, Acros Organics). ZrO_2 (St. Gobain, SZ 31164 NORPRO, referred as ZrO_2 SG) and Na_2CO_3 (99,5 %, Grüssing) were used as a support material.

10 g Na_2CO_3 have been dissolved in 100 mL dist. H_2O. $In(NO_3)_3 \cdot x\ H_2O$ and the respective other metal-nitrate was dissolved in 250 mL dist. H_2O. The applied amounts of In_2O_3 and the metal-nitrates were calculated to be 10 wt.%. $NaHCO_3$-solution was added to the nitrate solution until a pH-value of 9.2 was reached and 20 g ZrO_2 were added. The suspension was stirred in a rotary evaporator (111 rpm, room temperature, 800 mbar) for 1 h and another 500 mL dist. H_2O were added afterwards. The mixture was filtered and washed until the washing solution reached a pH value of 7. The impregnated powder was dried (65 °C, 12 h), heated with 5 °C/min to 300 °C and calcined for 3 h.

NiO-In_2O_3/ZrO_2 catalysts have been prepared by different synthesis methods. The used precursors were $In(NO_3)_3 \cdot x\ H_2O$ Puratronic® (≥ 99.999 %, Alfa Aesar, VWR 10708.22), $Ni(NO_3)_2 \cdot 6\ H_2O$ (n.s. SuboLab GmbH) and Na_2CO_3 (99,5 %, Grüssing).

Wetness impregnation (WI)

$Ni(NO_3)_2 \cdot 6\ H_2O$ (0.747 g) was dissolved in 250 mL of dist. H_2O and In_2O_3/ZrO_2 (M-SG, 15 g) was added to the solution. The suspension was stirred for 1 h in a rotatory evaporator (111 rpm, room temperature, 850 mbar). After the solvent was removed, the impregnated powder was dried (65 °C, 12 h), heated with 5 °C/min to 300 °C and calcined for 3 h.

Co-precipitation (CP)

10 g Na_2CO_3 have been dissolved in 100 mL of dist. H_2O. $In(NO_3)_3 \cdot x\ H_2O$ (6.75 g) and $Ni(NO_3)_2 \cdot 6\ H_2O$ (1.24 g) were dissolved in 250 mL of dist. H_2O. $NaHCO_3$-solution was added to the nitrate solution until a pH-value of 9.2 was reached and 20 g ZrO_2 were added thereafter. The suspension was stirred in a rotary evaporator (111 rpm, room temperature, 800 mbar) for 1 h and treated with another 500 mL of dist. H_2O, followed by filtration and washing until the solution reached a pH value of 7. The impregnated powder was dried (65 °C, 12 h), heated with 5 °C/min to 300 °C and calcined for 3 h.

Chemical reduction (CR)

The synthesis method was derived from Zhang et al.[41] $Ni(NO_3)_2 \cdot 6\ H_2O$ (0.747 g) was dissolved in 250 mL of dist. H_2O and In_2O_3/ZrO_2 (M-SG) (15 g) was added to the solution. The suspension was stirred for 1 h in a rotary evaporator (111 rpm, room temperature, 800 mbar) and subsequently heated up to 80 °C. An aqueous solution of NaOH was prepared (n (Ni) : n (NaOH) = 1 : 3) and treated with $NaBH_4$ (n (Ni) : n ($NaBH_4$) = 1 : 4). The NaOH-solution was added dropwise to the suspension and the mixture was stirred for 2 h in a rotatory evaporator (111 rpm, 80 °C, 800 mbar). Afterwards, the mixture was washed with dist. H_2O until a pH value of 7 and the impregnated powder was dried (65 °C, 12 h) thereafter.

Catalyst characterization

ICP-OES

Inductively coupled plasma optical emission spectrometry (ICP-OES) was employed for elemental composition analysis of each catalyst. 100 mg of each sample were dissolved in a mixture of 5 mL conc. H_2SO_4 and 1 mL conc. HNO_3. Subsequently, the sample was atomized in an argon plasma and the resulting composition was quantified using optical emission spectrometry. The characterization was performed using an ASCOR-spectrometer (manufactured by Spectro) at the central element analysis service of the Department of Chemistry, University of Hamburg.

N_2-physisorption

Brunauer-Emmet-Teller (BET) surface area and Barrett-Joyner-Halenda (BJH) pore volume were determined by N_2-physisorption at -196 °C by an Autosorb iQ-MP/XR instrument from Anton Paar. Prior to analysis, the sample was degassed under vacuum at 200 °C for 10 h.

XRD

Powder X-ray diffraction (p-XRD), was used to determine the crystal structure and was carried out using a Panalytical MDP X'Pert Pro diffractometer operated in the Bragg-Brentano geometry with Cu Kα radiation (λ = 0.1541 nm). The measuring range of the diffraction angle was 10-80 ° and sampled using a rate of 0.013 ° every 0.3 s.

The average particle size of In_2O_3 on ZrO_2 size was determined using Scherrer-Debye equation[36]:

$$d = \frac{k\lambda}{\beta \cos\theta} \quad \text{(S1)}$$

where k represents the shape factor (0.89), λ the wavelength used in X-ray diffraction, β is the Full With at Half Maximum (FWHM) of the reflection and θ the Bragg angle. For the calculation the 2 2 2 reflection of In_2O_3 was used.

CO_2-TPD

CO_2-Temperature programmed desorption (CO_2-TPD) was used to determine CO_2 binding capacity and strength. Analysis have been carried out on a *ChemBET Pulsar* apparatus (Quantachrome Instruments). Prior to analysis, samples (0.3 g) were exposed to a He-gas flow (80 mL/min) and heated up to 200 °C (10 K/min) for 1 h to remove surface H_2O. The loading of the surface with CO_2 was also carried out at 200 °C, followed by cooling down to 50 °C. The sample was thereafter heated up under He gas flow (80 mL/min, 10 °C/min) to 700 °C and the desorbed CO_2 was measured via a *Thermal Conductivity Detector (TCD).*

H_2-TPR

H_2-Temperature programmed reduction (H_2-TPR) was used to determine the reducibility of the surface. Analysis have been carried out on a *ChemBET Pulsar* apparatus (Quantachrome Instruments). Prior to analysis, samples (0.3 g) were exposed to N_2-gas flow (80 mL/min) and heated up to 180 °C (10 °/min) for 1 h to remove surface H_2O, followed by cooling down to 100 °C. The sample was heated up again under H_2/N_2 (5/95 v/v) gas flow (80 mL/min, 10 °C/min) to 850 °C. The used H_2 was measured by via Thermal Conductivity Detector (TCD).

XPS

X-ray photoelectron spectroscopy (XPS) was used to determine the oxidation states of the surface elements. Analysis have been carried out using a Thermo Scientific system at room temperature with Al Kα-radiation (1484.6 eV) and a spot size of 400 µm. A flood gun was utilized to reduce charging effects of the samples. The resulting spectra were corrected by setting C1s binding energy at 284,8 eV. Data were processed by using Avantage 4.87 software.

Microscopy

High-resolution transmission electron microscopy (HRTEM) images were obtained using a double-corrected (CESCOR and CETCOR, CEOS) JEOL JEM 2200FS microscope with an in-column image filter (Ω-type), a high-angle annular dark-field (HAADF) detector, and a Gatan 4K UltraScan 1000 camera at an accelerating voltage of 200 kV. Energy-dispersive X-ray spectroscopy (EDX) elemental maps were obtained using a JEOL JED-2300 analysis station with a 100 mm2 silicon drift detector.

Catalytic evaluation

All experiments were performed in a continuous-flow high-pressure fixed-bed reactor setup (inner diameter 20 mm) made of stainless steel (1.4571), surrounded by a heating jacket (see Figure S1). The reactant gas mixture consisting of 25 % CO_2 (4.5 grade) and 75 % H_2 (5.0 grade) from Westfalen as well as N_2 (5.0 grade) from Air Liquide was conveyed into the reactor by mass-flow controllers (Bronkhorst Prestige FG-201CV). The reaction pressure was adjusted with a back-pressure regulator (Dutch Regulators). The catalyst bed temperature was controlled with an inside located thermocouple. Reactor inlet and outlet gas lines were heated to 180 °C with regard to preheat the reaction gas and to avoid condensation of methanol and water. Every 30 min, the outlet steam was sampled and analyzed by online gas chromatography (Bruker 450-GC). The GC has four columns (Restek U-Bond, Restek Q-Bond, Bruker Swax, Bruker Molsieve 5 Å), a methanizer (for CO_2 and CO quantification), two flame ionization detectors (FIDs) and one thermal conductivity detector (TCD).

5.0 or 4.0 g of catalyst with a particle size of 80-250 µm (mixed homogeneously with quartz beads) were filled into the reactor and held in place by a bed of quartz wool. Prior to reaction, the catalyst was pre-treated at 200 °C under flowing N_2 (300 Nml min^{-1}) for 1 hour. The Ni and Cu containing catalysts were pre-reduced using 10 % H_2/N_2 (500 Nml min^{-1}) at 200 °C for 1 h. Thereafter, the catalyst bed was heated to 300 °C and the reaction gas mixture with a CO_2/H_2 stoichiometric ratio of 1/3 was fed with a flow of 1200 Nml min^{-1} into the reactor, which was pressurized to 50 or 75 bar, respectively. Materials were tested 3 h under steady-state reaction conditions for performance comparison. Afterwards, the reactor was cooled to room temperature (3 K min^{-1}) under a continuous flow of nitrogen (1000 Nml min^{-1}) after reaction. The catalyst was removed and stored under Ar (4.6 grade. Heide Gas) for further analysis.

The yield Y_{MeOH}, selectivity S_{MeOH} and productivity P_{cat} were calculated according to the following equations.

$$Y_{\mathrm{MeOH}} = \frac{\dot{n}_{\mathrm{MeOH}}}{\dot{n}_{\mathrm{CO_2.in}}} \cdot 100\ \% \tag{S2}$$

$$S_{\mathrm{MeOH}} = \frac{\dot{n}_{\mathrm{MeOH.out}} - \dot{n}_{\mathrm{MeOH.in}}}{\dot{n}_{\mathrm{CO_2.in}} - \dot{n}_{\mathrm{CO_2.out}}} \cdot 100\ \% \tag{S3}$$

$$X_{CO_2} = \frac{Y_{\mathrm{MeOH}}}{S_{\mathrm{MeOH}}} \tag{S4}$$

$$P_{\mathrm{cat}} = \frac{\dot{m}_{\mathrm{MeOH.out}} \cdot M_{\mathrm{MeOH}}}{m_{\mathrm{cat}}} \tag{S5}$$

$$P_{\mathrm{surface}} = \frac{P_{cat} \cdot 1000\,\frac{mg}{g}}{S_{BET}} \tag{S6}$$

$$P_{\mathrm{metal}} = \frac{P_{cat}}{(\omega_{Indium} + \omega_{metal\ promoter})} \tag{S7}$$

The calculation of (2) to (4) was done as follows: the adjusted standard volume flow ($\dot{V}_{\mathrm{N}}$) and the known feed gas ($y_{i.\mathrm{in}}$) composition allowed the calculation of the molar flow of component *i* entering the reactor, under consideration of the ideal gas law.

$$\dot{n}_{i.\mathrm{in}} = \frac{p_{\mathrm{N}} \cdot y_{i.\mathrm{in}} \cdot V_{\mathrm{N}}}{R \cdot T_{\mathrm{N}}} \tag{S8}$$

In (8), p_N and T_N are standard pressure and temperature. As for the carbon balance of the reaction system, the total molar flow at the reactor outlet can be determined from the molar fractions of CO_2, CO and methanol known from online gas chromatograph analysis.

$$\dot{n}_{\mathrm{ges.out}} = \frac{\dot{n}_{\mathrm{CO_2.in}}}{y_{\mathrm{CO_2.out}} + y_{\mathrm{CO.out}} + y_{\mathrm{MeOH.out}}} \tag{S9}$$

The molar flow of the component *i*, at the reactor outlet was calculated as follows.

$$n_{i.out} = \dot{n}_{ges.out} \cdot y_{i.out} \tag{S10}$$

The gas hourly space velocity ($GHSV$) was used to relate the standard volume flow ($\dot{V}_{\mathrm{N}}$) to the catalyst volume (V_{cat}):

$$GHSV = \frac{\dot{V}_N}{V_{cat}} \tag{S11}$$

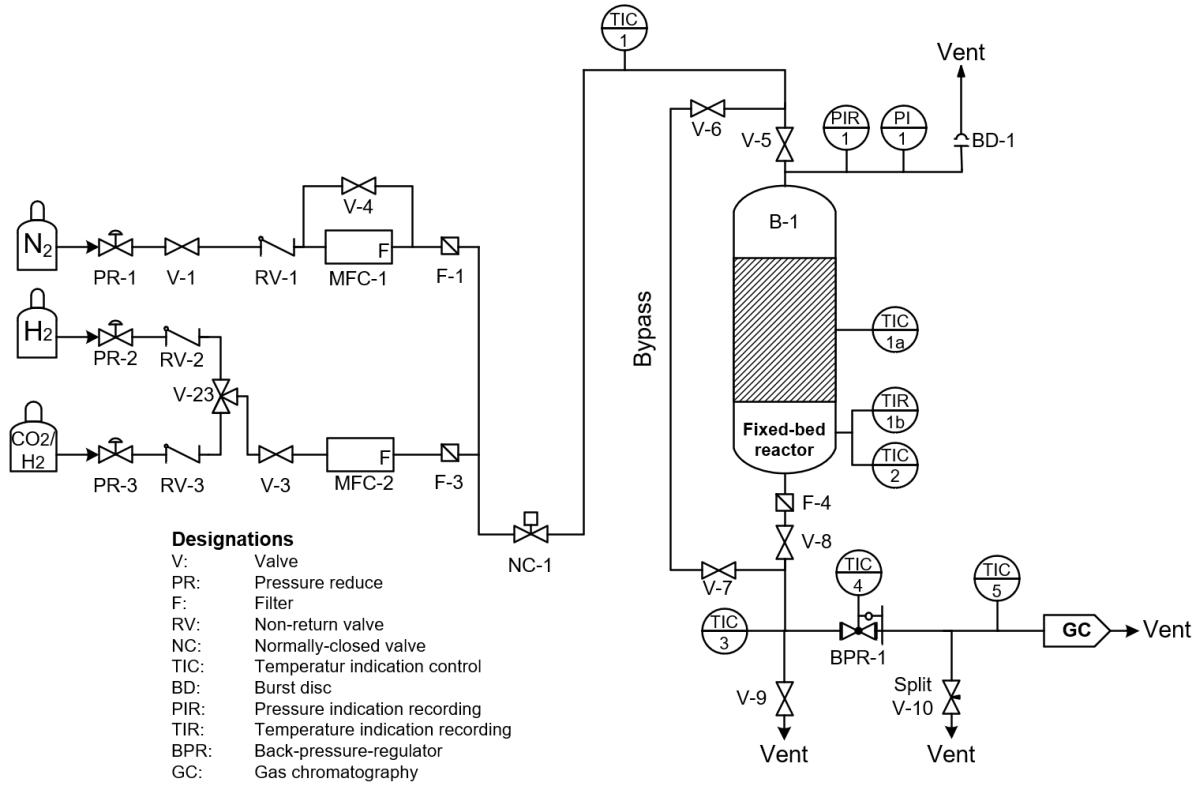

Figure S1. Instrumentation and piping diagram of the continuous-flow high-pressure fixed-bed reactor setup.

Supplementary catalytic results and characterization of In_2O_3/ZrO_2

Impact of different ZrO_2-supports and synthesis method on catalytic performance of In_2O_3/ ZrO_2-catalysts.

Table S1. Catalytic performance of In_2O_3/ZrO_2 (M-SG) and (S-AA) during a temperature ramp from 250 to 275 to 300 °C and back to 250 °C with 1200 NmL·min^{-1} at 50 and 75 bar.

		X / %					P_{cat} / $g_{MeOH}\ g_{cat}^{-1}\ h^{-1}$					$Y_{MeOH.CO2}$ / %					$S_{MeOH.CO2}$ / %				
In_2O_3/ZrO_2	T / °C	250	275	300	275	250	250	275	300	275	250	250	275	300	275	250	250	275	300	275	250
M-SG	75 bar	4.4	9.3	18.7	8.6	3.6	0.16	0.30	0.47	0.29	0.14	3.4	6.4	10.0	6.1	3.0	77.2	69.3	53.5	70.9	83.0
	50 bar	3.3	7.5	15.2	7.0	3.0	0.12	0.23	0.34	0.22	0.12	2.6	5.0	7.2	4.7	2.5	79.7	66.5	47.6	67.3	81.3
S-AA	75 bar	2.3	5.6	12.5	5.4	2.3	0.10	0.19	0.33	0.19	0.10	1.9	3.9	6.8	3.8	1.9	80.7	69.1	54.4	71.1	82.8
	50 bar	2.5	5.5	11.5	5.3	2.3	0.10	0.18	0.30	0.18	0.10	2.0	3.9	6.4	3.9	2.0	81.9	71.6	56.1	73.6	85

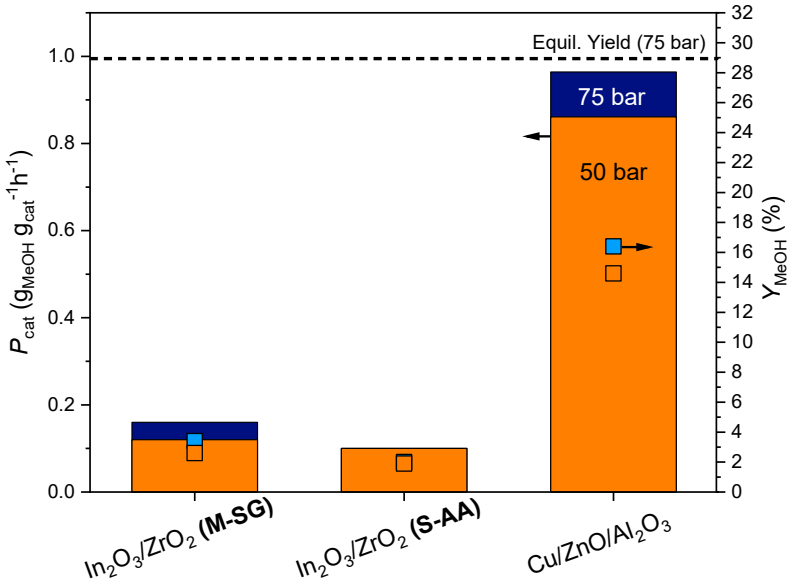

Figure S2. Methanol yield (squares) and productivity (bars) in dependency of total pressure p = 50 bar (orange) and p = 75 bar (blue) for different ZrO_2 supports (SG or AA) compared with the commercial Cu-based catalyst. Simulated equilibrium yield at T = 250 °C and p = 75 bar. Reaction conditions: CO_2/H_2 = 1/3; $GHSV$ = 8400 h^{-1}; TOS = 3 h; T = 250 °C; h_{bed} = 5.1 ± 0.1 cm.

Table S2. Evaluation of catalytic experiments using In_2O_3/ZrO_2 (M-AA), calculated arithmetic means and standard deviations at 75 bar and 300 °C.

	M-AA-1	M-AA-2	M-AA-2	M-AA-2	Arithmetic mean	Standard deviation
S_{CO2} (%)	66.1	65.5	58.8	57.3	61.9	4.52
Y_{CO2} (%)	8.47	8.54	8.47	8.62	8.53	0.071
P_{cat} ($g_{MeOH}\ g_{cat}^{-1}\ h^{-1}$)	0.399	0.403	0.399	0.406	0.402	0.003

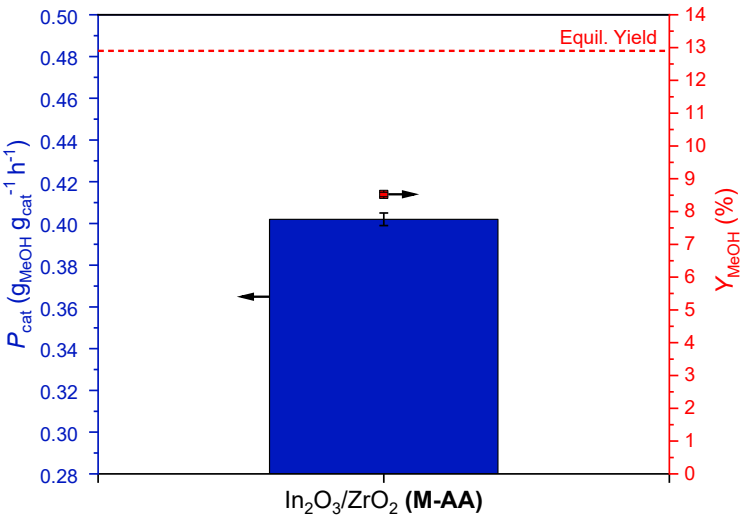

Figure S3. Methanol yield and active productivity of In_2O_3/ZrO_2 (M-AA) with calculated error bars out of two different batches and four experiments at 75 bar and 300 °C.

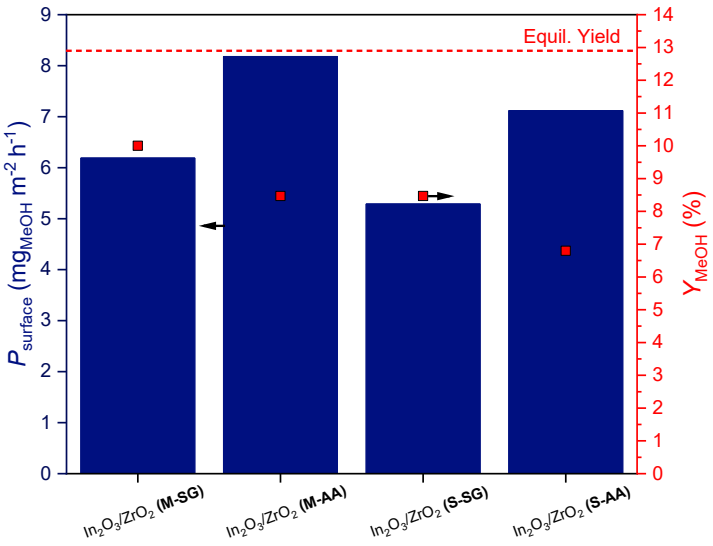

Figure S4. Influence of different ZrO_2 (SG or AA) supports and synthesis methods (M or S) on surface productivity $P_{surface}$, normalized to amount to the specific surfaces, and methanol yield in comparison to the calculated equilibrium yield. Reaction conditions: CO_2/H_2 = 1/3; GHSV = 8400 h^{-1}; *TOS* = 3 h; *T* = 300 °C; *p* = 75 bar; h_{bed} = 5.1 ± 0.1 cm.

a) ZrO_2 (AA)

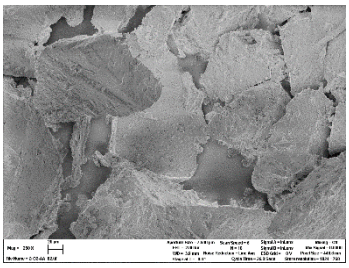

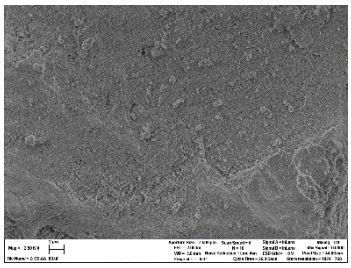

b) ZrO_2 (SG)

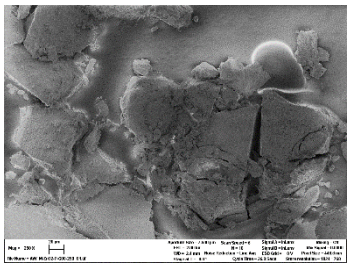

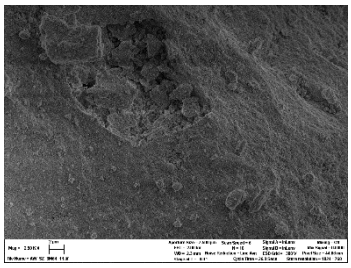

c) In_2O_3/ZrO_2 (S-AA)

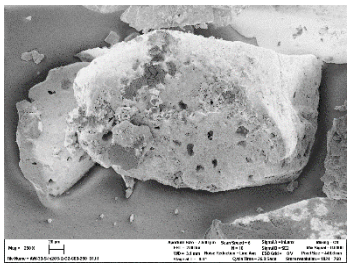

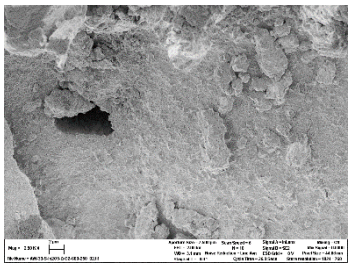

d) In_2O_3/ZrO_2 (M-SG)

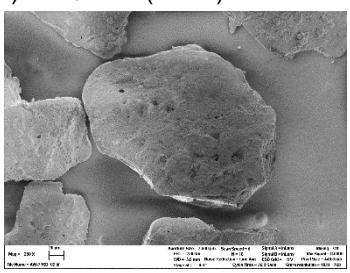

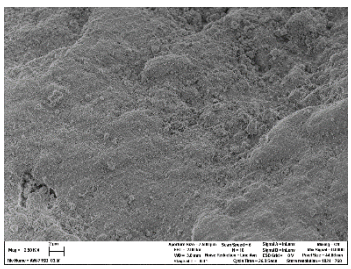

e) In_2O_3/ZrO_2 (S-SG)

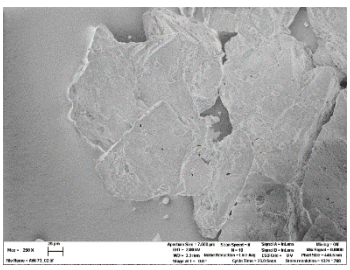

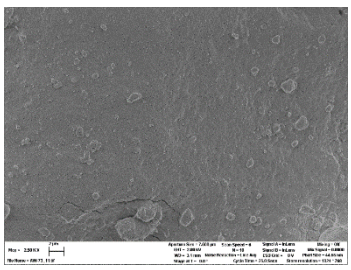

f) In_2O_3/ZrO_2 (M-AA)

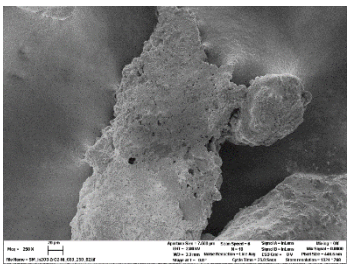

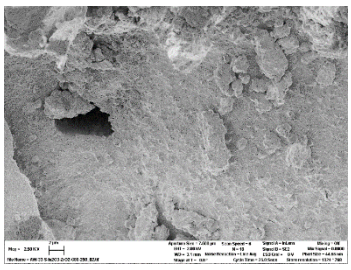

Figure S5. SEM images of a) ZrO_2 (AA) b) ZrO_2 (SG) c) In_2O_3/ZrO_2 (S-AA), d) In_2O_3/ZrO_2 (M-SG), e) In_2O_3/ZrO_2 (S-SG) and f) In_2O_3/ZrO_2 (M-AA).

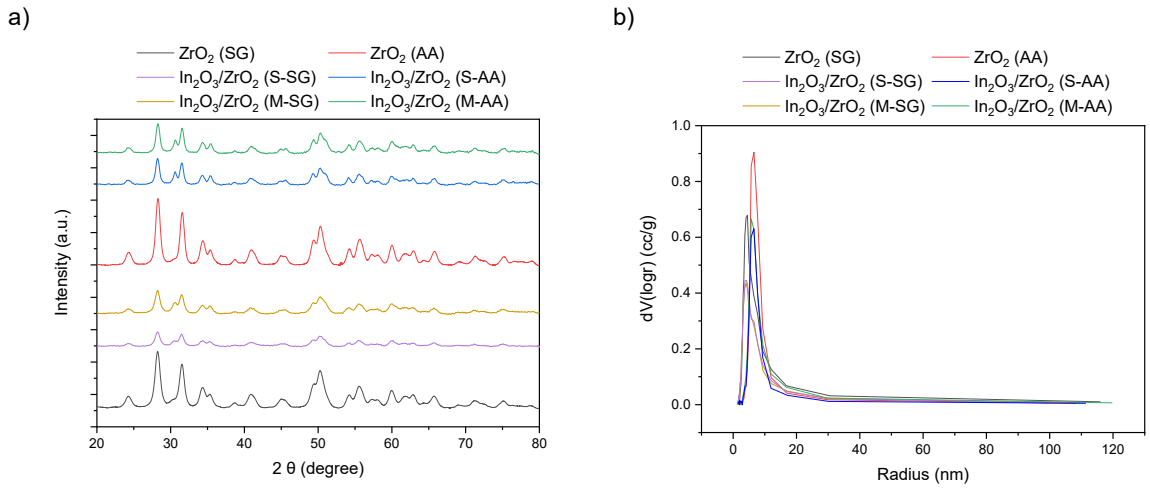

Figure S6. XRD patterns a) and pore size distribution determined by BJH method, b) for different ZrO_2 (AA and SG) and incorporated with In_2O_3 (S-AA, S-SG, M-AA and M-SG)

Table S3. Integral data of CO_2-TPD. Low (50 °C - 350 °C), high 350 °C - 650 °C and overall H_2 reduction capacity of ZrO_2 and In_2O_3/ZrO_2 material with In_2O_3/ZrO_2 (M-SG) as normed reference (1.00).

	nominal area of adsorption capacity		overall
	low	high	
ZrO_2 (SG)	1.67	0.17	0.66
ZrO_2 (AA)	1.21	0.19	0.52
In_2O_3/ZrO_2 (M-SG)	1.00	1.00	1.00
In_2O_3/ZrO_2 (S-SG)	0.59	1.12	0.95
In_2O_3/ZrO_2 (M-AA)	0.58	0.82	0.74
In_2O_3/ZrO_2 (S-AA)	0.50	0.75	0.67

Table S4 H_2-TPR integral data for low (110 °C - 420 °C), high 420 °C - 840 °C and overall area of ZrO_2 and In_2O_3/ZrO_2 material with In_2O_3/ZrO_2 (M-SG) as normed reference (1.00).

	nominal area of adsorption capacity		overall
	low	high	
ZrO_2 (SG)	0.02	0.00	0.01
ZrO_2 (AA)	0.03	0.00	0.01
In_2O_3/ZrO_2 (M-SG)	1.00	1.00	1.00
In_2O_3/ZrO_2 (S-SG)	1.08	1.05	1.06
In_2O_3/ZrO_2 (M-AA)	0.78	1.18	1.06
In_2O_3/ZrO_2 (S-AA)	0.74	0.82	0.80

Supplementary characterization of CuO-/NiO-/MgO-/CeO_2-In_2O_3/ZrO_2

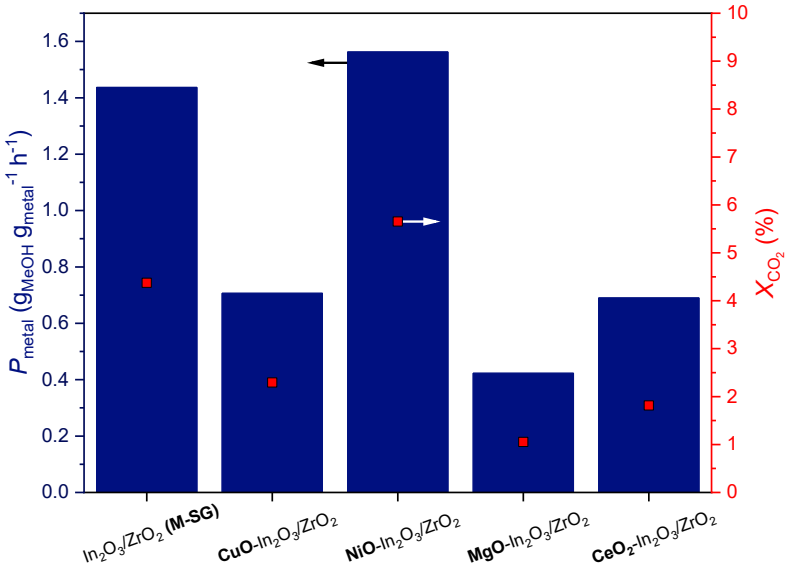

Figure S7. Catalytic performance of CuO-, NiO-, MgO- and CeO-promoted In_2O_3/ZrO_2 compared to In_2O_3/ZrO_2 (M-SG)**,** productivity P_{metal} normalized to amount of active metals, CO_2 conversion. Reaction conditions: CO_2/H_2 = 1/3; GHSV = 8300 h^{-1}; *TOS* = 3 h; *T* = 250 °C; *p* = 75 bar; h_{bed} = 5.1 ± 0.1 cm.

a) $CuO\text{-}In_2O_3/ZrO_2$

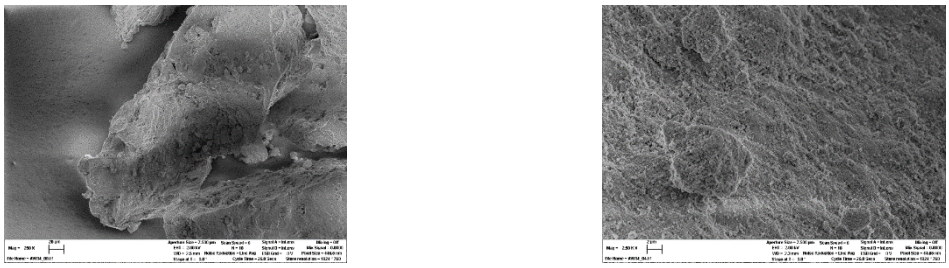

b) $NiO\text{-}In_2O_3/ZrO_2$

c) $MgO\text{-}In_2O_3/ZrO_2$

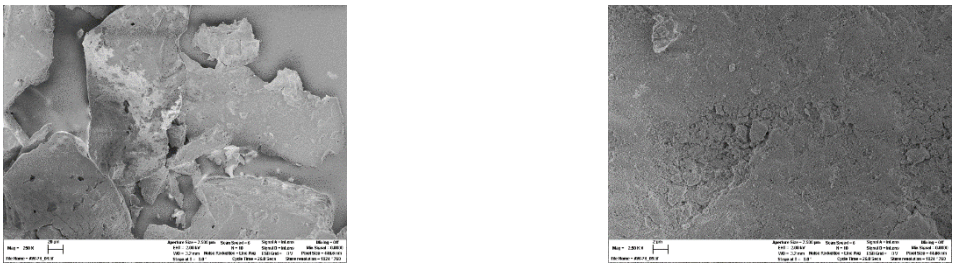

d) $CeO_2\text{-}\ In_2O_3/ZrO_2$

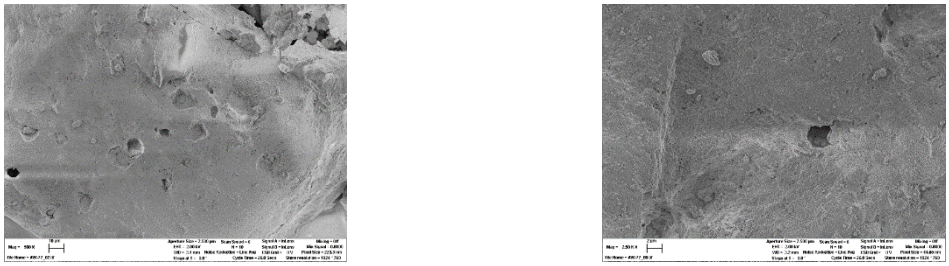

Figure S8. SEM images of a) $CuO\text{-}In_2O_3/ZrO_2$, b) $NiO\text{-}In_2O_3/ZrO_2$, c) $MgO\text{-}In_2O_3/ZrO_2$, d) $CeO_2\text{-}\ In_2O_3/ZrO_2$.

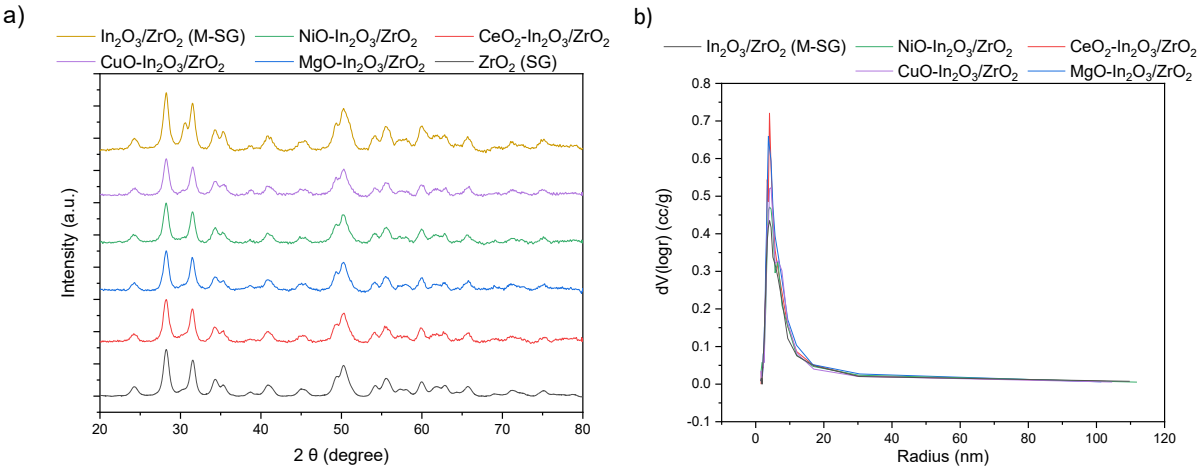

Figure S9. Analysis of CuO-, NiO-, MgO- and CeO_2-promoted In_2O_3/ZrO_2 compared to In_2O_3/ZrO_2 (M-SG): a) XRD pattern, b) pore size distribution (determined with BJH method).

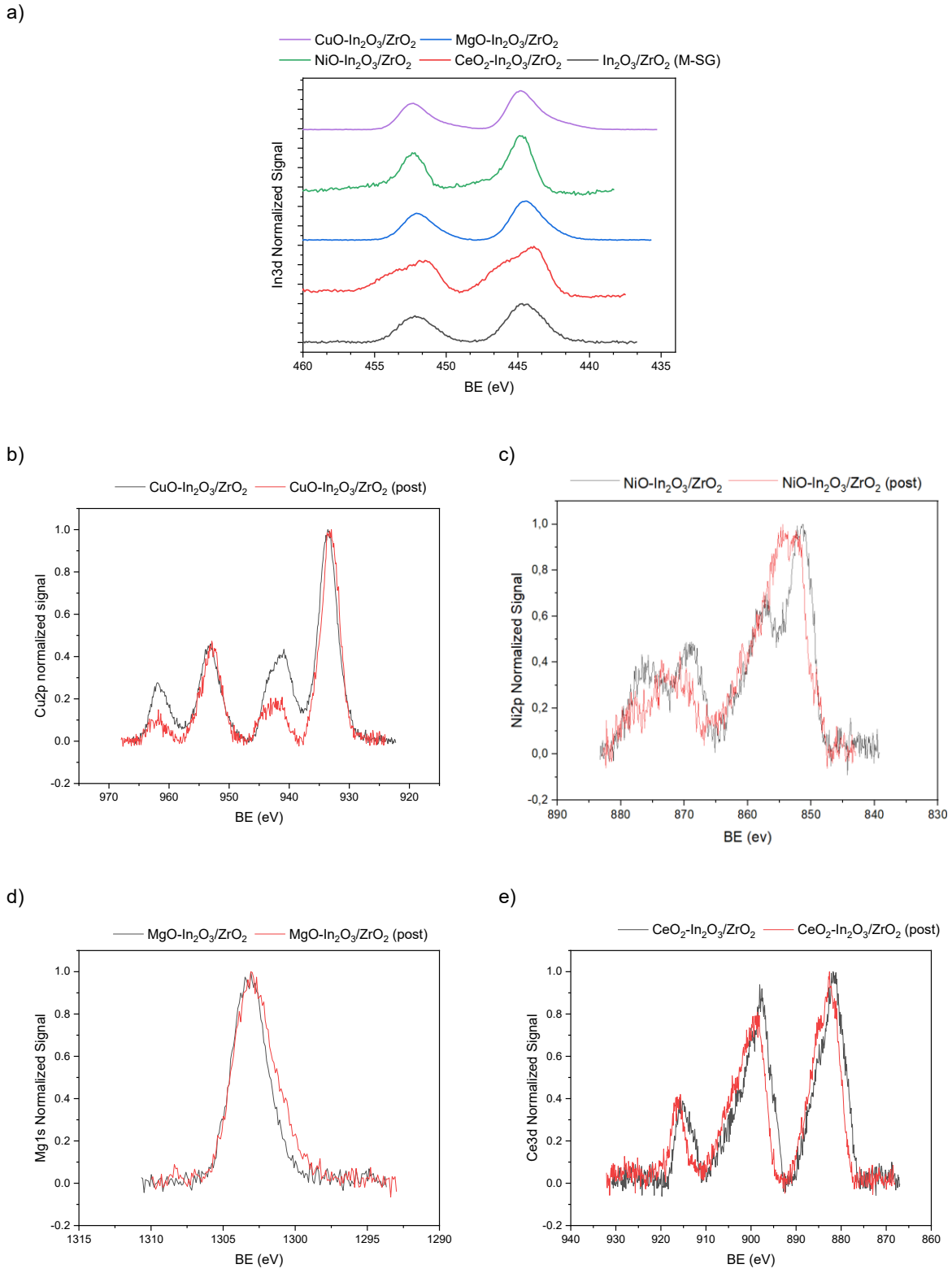

Figure S10. XPS spectra before (black) and after (red) reaction of a) In3d for CuO-, NiO-, MgO- and CeO_2-promoted In_2O_3/ZrO_2 compared to In_2O_3/ZrO_2 (M-SG), b) Cu2p for CuO-In_2O_3/ZrO_2, c) Ni2p for NOi-In_2O_3/ZrO_2, d) Mg1s for MgO-In_2O_3/ZrO_2 and e) Ce3d for CeO_2-In_2O_3/ZrO_2.

Table S5 Integral data of CO_2-TPD. Low (50 °C - 350 °C), high (350 °C - 650 °C) and overall area of CuO-/ NiO-/ MgO-/CeO_2-In_2O_3/ZrO_2 with In_2O_3/ZrO_2 (M-SG) as normed reference (1.00).

	nominal area of adsorption capacity		overall
	low	high	
CuO-In_2O_3/ZrO_2	2.30	1.15	1.53
NiO-In_2O_3/ZrO_2	1.73	1.48	1.56
MgO-In_2O_3/ZrO_2	2.89	0.85	1.52
CeO_2-In_2O_3/ZrO_2	1.26	0.63	0.83
In_2O_3/ZrO_2 (M-SG)	1.00	1.00	1.00

Table S6. H_2-TPR integral data for low (110 °C - 420 °C), high (420 °C - 840 °C) and overall area of CuO-/ NiO-/ MgO-/CeO_2-In_2O_3/ZrO_2 with In_2O_3/ZrO_2 (M-SG) as normed reference (1.00).

	nominal area of adsorption capacity		overall
	low	high	
CuO-In_2O_3/ZrO_2	1.78	0.69	1.01
NiO-In_2O_3/ZrO_2	1.31	0.90	1.02
MgO-In_2O_3/ZrO_2	0.53	0.75	0.68
CeO_2-In_2O_3/ZrO_2	0.81	0.79	0.80
In_2O_3/ZrO_2 (M-SG)	1.00	1.00	1.00

Supplementary characterization of NiO-In_2O_3/ZrO_2 (WI), (CR) and (CP)

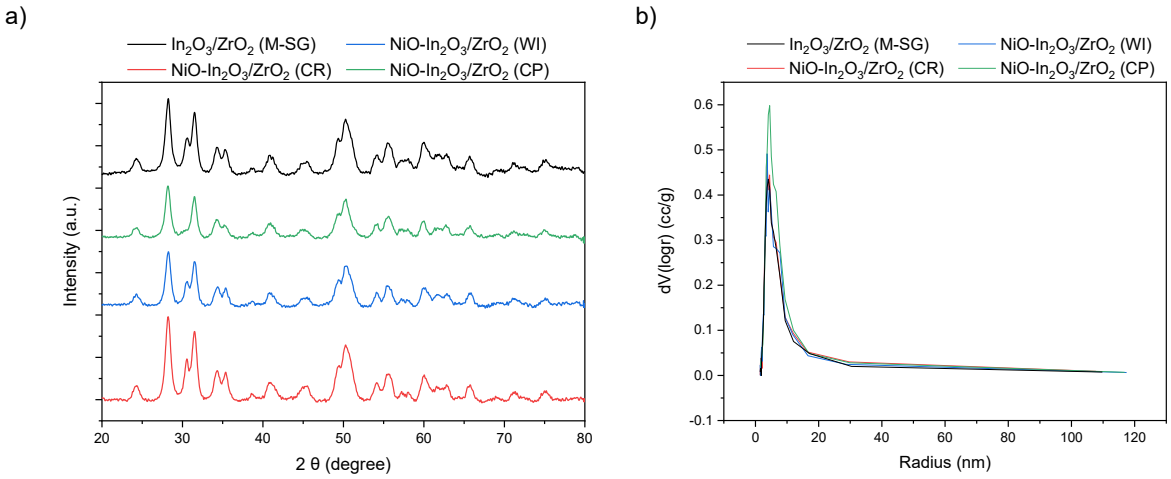

Figure S11. Analysis of NiO-In_2O_3/ZrO_2 prepared by WI, CR or CP compared with In_2O_3/ZrO_2 (M-SG): a) XRD pattern, b) pore size distribution (determined with BJH method).

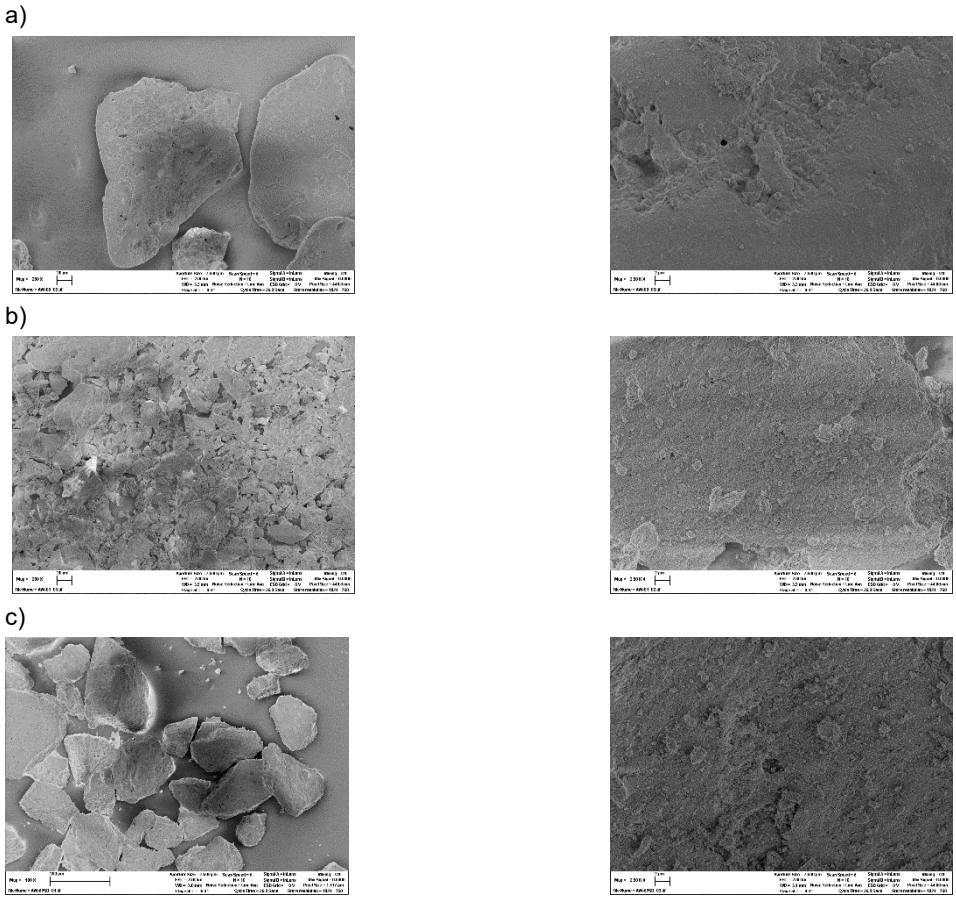

Figure S12. Backscattered electron analysis (left) and secondary electron analysis (right). SEM images of a) Ni-In_2O_3/ZrO_2 (WI), b) Ni-In_2O_3/ZrO_2 (CR) and c) Ni-In_2O_3/ZrO_2 (CP).

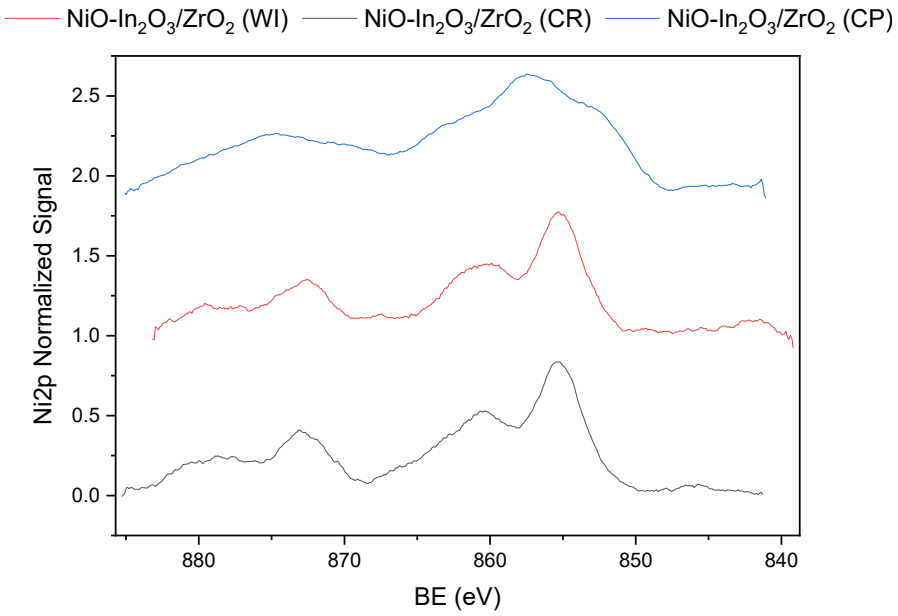

Figure S13. XPS spectra of Ni2p for Ni-In_2O_3/ZrO_2 prepared by WI, CP and CR.

Table S7. Integral data of CO_2-TPD. Low (50 °C - 350 °C), high (350 °C - 650 °C) and overall area of NiO-In_2O_3/ZrO_2 prepared by Wi, CR and CP with In_2O_3/ZrO_2 (M-SG) as normed reference (1.00).

	nominal area of adsorption capacity		overall
	low	high	
NiO-In_2O_3/ZrO_2 (WI)	1.64	1.71	1.69
NiO-In_2O_3/ZrO_2 (CR)	1.47	0.58	0.87
NiO-In_2O_3/ZrO_2 (CP)	1.70	0.53	0.91
In_2O_3/ZrO_2 (M-SG)	1.00	1.00	1.00

Table S8. H_2 TPR integral data for low (110 °C - 420 °C), high (420 °C - 840 °C) and overall area of NiO-In_2O_3/ZrO_2 prepared by Wi, CR and CP with In_2O_3/ZrO_2 (M-SG) as normed reference (1.00).

	nominal area of adsorption capacity		overall
	low	high	
NiO-In_2O_3/ZrO_2 (WI)	1.05	1.25	1.19
NiO-In_2O_3/ZrO_2 (CR)	0.75	0.70	0.72
NiO-In_2O_3/ZrO_2 (CP)	1.05	1.25	1.19
In_2O_3/ZrO_2 (M-SG)	1.00	1.00	1.00

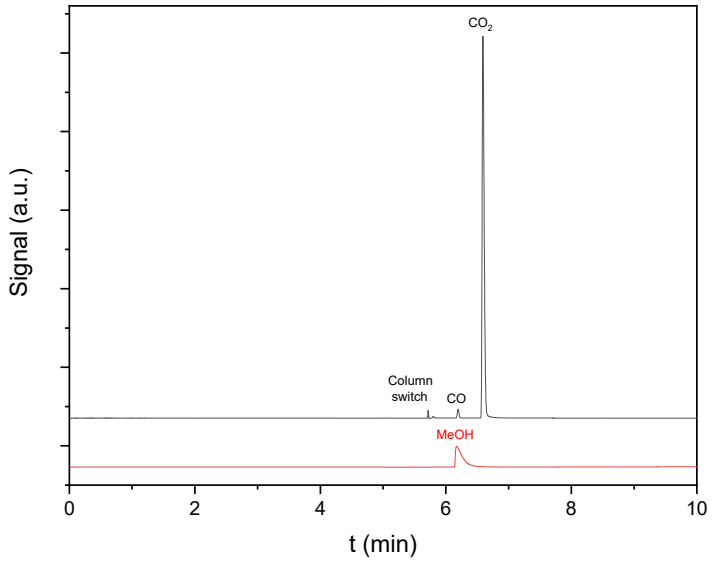

Figure S14. FID chromatogram for NiO-In_2O_3/ZrO_2 (WI): Valve switch-, CO-, CO_2- and MeOH peak. Reaction conditions: CO_2/H_2 = 1/3; GHSV = 4600 h^{-1}; T = 300 °C; p = 7.5 MPa; h_{bed} = 5.1 ± 0.1 cm.

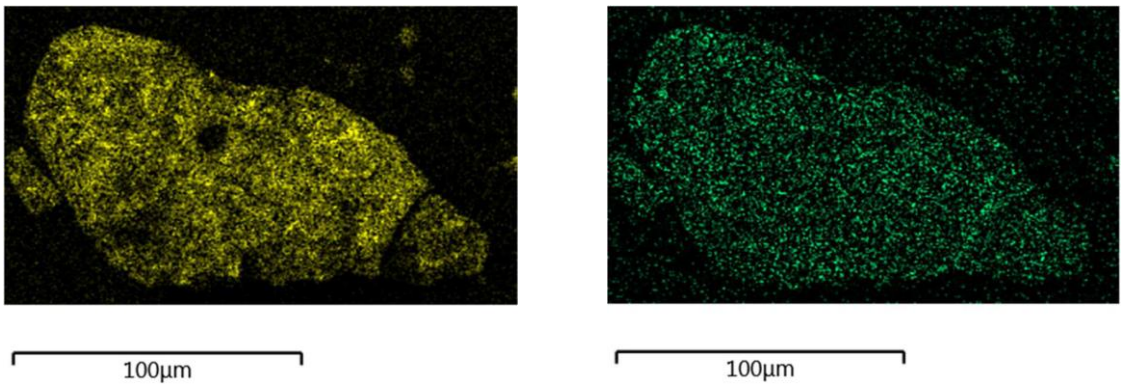

Figure S15. SEM-EDX elemental mapping images of Ni-In_2O_3/ZrO_2(WI) after 100 h TOS. In distribution left (yellow); Ni distribution right (green).

10. Acknowledgements

An dieser Stelle möchte ich all jenen danken, die zum Gelingen dieser Arbeit beigetragen haben.

Mein Dank gilt meinem ersten Gutachter Prof. Dr. Jakob Albert für die Aufnahme in seine Arbeitsgruppe, für die Bereitstellung des spannenden Forschungsthemas und die Betreuung während meiner praktischen Arbeiten.

En hjertelig tak til min vejleder ved DTU, Prof. Dr. Anders Riisager, for hans fremragende vejledning og for venligt at påtage sig rollen som andenbedømmer. Du har været en fremragende mentor.

Ich danke auch Prof. Dr. Lisa Vondung und Prof. Dr. Markus Fischer für die Übernahme der Prüfung meiner Disputation als Zweit- und DrittprüferIn.

Mein Dank gilt den wissenschaftlichen Serviceeinrichtungen der Universität Hamburg, insbesondere der Zentralen Elementanalytik, der Elektronenmikroskopie und der XRD-Abteilung. Ohne die Unterstützung bei den zahlreichen Messungen meiner Proben wäre diese Arbeit nicht möglich gewesen. Ein besonderer Dank geht dabei an Dr. Charlotte Ruhmlieb für die vielen fachlichen Diskussionen und dein stets offenes Ohr. Ebenso danke ich dem Stammpersonal am Institut der TMC, insbesondere Michael Gröger für deine jederzeit tatkräftige Unterstützung.

Ein Dank gilt auch dem Zentrallabor der Technischen Universität Hamburg – insbesondere Bo-Magnus Elfers – für die Durchführung zahlreicher Analysen, die wertvollen fachlichen Diskussionen und die vielfältige Unterstützung. Auch möchte ich Prof. Dr. Raimund Horn und seiner Arbeitsgruppe, einschließlich Dr. Oliver Korup, für den Zugang zu Labor für die Chemisorptionsmessungen sowie die stets verlässliche Hilfe danken.

Mein Dank gilt dem gesamten TMC-Arbeitskreis. Danke, Dr. Dorothea Voß, für deine unglaubliche Geduld und dafür, dass du immer für uns da warst – selbst in den stressigsten Zeiten. Mit all unseren Sorgen und Problemen konnten wir uns jederzeit an dich wenden, und du hast uns immer unterstützt. Ein riesiges Dankeschön geht an Dr. Maximilian J. Poller. Ohne dich hätte ich das hier nicht geschafft. Dein großes Fachwissen, deine Ruhe und dein Pragmatismus, wenn ich am Verzweifeln war, haben unendlich geholfen.

Besonders danken möchte ich meinen BürokollegInnen: Stefanie Wesinger - für die schöne Zeit im Büro und vor allem auch außerhalb, beim Klettern, Feiern, auf unseren Ausflügen und mit all unseren dummen Ideen. Jan Christian Raabe, dafür, dass du so ein außergewöhnlicher und einmaliger Mensch bist, der immer Sonne in unser Büro gebracht hat. Und Maximilian Papajewski – es war großartig, dich als Projektpartner an meiner Seite zu haben. Darüber hinaus danke ich: Michael Huber – besonders für deine Kreativität in Streiche spielen (aka Kressetastatur). André Wassenberg – du warst ein wunderbarer Vergnügungsbeauftragter und Laborkollege (danke auch fürs Ertragen meiner Musik !). Und Tobias Esser – danke für die schöne gemeinsame Zeit, auch wenn es bei uns ein wenig länger gedauert hat, bis wir warm geworden sind.

Einen herzlichen Dank auch an meine damaligen StudentInnen Simon Bisse, Leon Bacanli, Moritz Hilgers, Lasse Prawitt, Angela Ortmann und Nick Herrmann. Ihr habt unsere Projekte mit eurem Einsatz und eurer Motivation entscheidend vorangebracht, und es hat mir viel Freude gemacht, euch zu betreuen.

Mein Dank gilt außerdem meinen KooperationspartnerInnen Leonhard Schill, Sebastian Meier, Patrick Schühle, Franziska Hess, Valea Kim Wisniewski, Hristiana Velichkova und Bodo Fiedler. Danke für die tolle Zusammenarbeit, eure wichtigen Beiträge zu unseren Publikationen und die vielen hilfreichen Diskussionen.

Und dann die Menschen, wo Danke sagen eigentlich nicht mehr reicht, und die mir wahnsinnig viel bedeuten. Zuallererst Martin – du bist wirklich der beste große Bruder, den man sich wünschen kann. Marie, danke, dass du dich als Feel-good-Managerin so um uns alle kümmerst. Und Theo und Lea – ihr habt so viel mehr Liebe und Glück in mein Leben gebracht.

Charly und Kerstin - ihr seid zu meiner Familie geworden. Danke für die ganzen Jahre immer, immer und immer wieder auffangen, fürs mich aushalten, wenn es mir am schlechtesten ging (und auch am besten, wo ich auch nervig bin), fürs mit mir auf den Balkon gehen, wenn ich das gebraucht habe, für die Abende mit viel zu viel Wein und Skat… Ohne euch wäre ich nicht hier.

Danke an Lara, für die ganzen Dinge die ich so hier wirklich nicht hinschreiben kann, und für die du mir bis heute unverständlicherweise immer noch keine Rechnung gestellt hast. Sara, dafür dass du mich immer wieder dazu drängst, ein besserer Mensch zu sein. Philipp, für die ganzen Abende, wo ich so viel gelacht habe, dass mir mein Bauch weh getan hat, fürs mich-cheeren und für deine wunderbare Weltsicht. Und Paul, danke fürs zuhören, fürs Kopf immer wieder zurechtrücken. Und danke, dass du mir immer nachgezogen bist, und wir uns nie aus den Augen verloren haben.

Und danke Nils… fürs bemalen meiner Welt mit Schminke (und meiner Diss). IL

Eidesstaatliche Versicherung

Hiermit versichere ich an Eides statt, die vorliegende Dissertationsschrift selbst verfasst und keine anderen als die angegebenen Quellen und Hilfsmittel benutzt zu haben. Sofern im Zuge der Erstellung der vorliegenden Dissertationsschrift generative Künstliche Intelligenz (gKI) basierte elektronische Hilfsmittel verwendet wurden, versichere ich, dass meine eigene Leistung im Vordergrund stand und dass eine vollständige Dokumentation aller verwendeten Hilfsmittel gemäß der Guten wissenschaftlichen Praxis vorliegt. Ich trage die Verantwortung für eventuell durch gKI generierte fehlerhafte oder verzerrte Inhalte, fehlerhafte Referenzen, Verstöße gegen das Datenschutz- und Urheberrecht oder Plagiate.

Datum: 24.08.2025

Anne Wesner

Declaration on Oath

I hereby declare on oath that I have written this dissertation myself and have not used any sources or aids other than those specified. Insofar as electronic resources based on generative artificial intelligence (gKI) were used in the preparation of this thesis, I declare that my own work was in the foreground and that all resources used are fully documented in accordance with good scientific practice. I am responsible for any erroneous or distorted content, incorrect references, violations of data protection and copyright law or plagiarism that were generated by gKI.

Datum: 24.08.2025

Anne Wesner